Advanced histology methods for biodistribution and safety screening of next generation nanobiomaterials

A thesis submitted to The University of Dublin,

Trinity College for the degree of Doctor of Philosophy

August 2022

Submitted by:

Anna Elzbieta Bogdanska, BSc.

Under the supervision of:

Ussher Assistant Professor Dr. Adriele Prina-Mello, M.Sc., Ph.D.,

Dr. Oliviero Gobbo

Declaration

I declare that this thesis has not been submitted as an exercise for a degree at this or any other university and it is entirely my own work.

I agree to deposit this thesis in the University's open access institutional repository or allow the Library to do so on my behalf, subject to Irish Copyright Legislation and Trinity College Library conditions of use and acknowledgment.

I consent to the examiner retaining a copy of the thesis beyond the examining period, should they so wish (EU GDPR May 2018).

This thesis includes the unpublished and published work of others, duly acknowledged in the text wherever included.

Anna Bogdanska,
03/08/2022

“The gift of the great microscopist is the ability to think with the eyes and see with the brain”

Daniel Mazia

Summary

The overall aim of this PhD project was to improve histological methods used in the preclinical assessment of nanobiomaterials (NBMs) with particular focus on the semi-quantitative detection of a representative panel of NBMs in different tissue sections, improving their accumulation analysis in traditional 2D slides and 3D histology volumes. The structure of this thesis takes the form of seven chapters including an introduction, materials and methods, three results chapters, an overall discussion and conclusions with final chapter on future work.

Chapter 1, introductory opens with a definition of nanostructured materials and NBMs, discussing their classification and application in medical field. Following this, the preclinical assessment pathway for NBMs is briefly discussed including regulatory landscape and perspective. With *in vivo* studies being the final step in preclinical assessment of NBMs, particular focus was given to the different aspects of it, from biodistribution, toxicity and immune response. The research carried out in this PhD project was also centred around the area of histology and machine learning, both of which are expounded in separate sections. Finally, the chapter closes with stating the main hypothesis tested in this PhD project, and outlining the aims set out to prove the hypothesis.

Chapter 2, materials and methods comprises the techniques used throughout this PhD project. Subsequent three results chapters (chapter 3, 4, and 5) are presenting four case studies where toxicity and biodistribution of a representative panel of NBMs (two liposomes and three MNPs) were determined *in vivo* and *ex vivo*. Chapter 3 presents two *in vivo* studies, which were undertaken with the aim to develop a method which would detect liposomes in tissue sections. The general concept was to utilise a histological stain for lipid detection (Oil red O) in combination with other markers for fluorescent imaging. Experimental results presented in this chapter provided evidence that Oil red O stain can be used to trace liposomes in tissue section when combined with another marker to distinguish them from dietary fats. The following two results chapters (chapter 4 and 5) were focused on the magnetic iron oxide NBMs. The case study presented in chapter 4 utilises machine learning (ML) to provide objective and time efficient method for advanced quantitative histology studies. Furthermore, a series of consecutive sections from lung, liver, and kidney were used to generate 3D histology volumes which aimed to provide insights to biodistribution and aggregation of magnetic iron oxide NBMs in 3D. In chapter 5, the methodology developed in chapter 4 was progressed further by carrying out a quantitative histological analysis on traditional 2D tissue sections and 3D histology volumes, with particular focus on assessing the morphology of iron aggregates formed by two iron oxide NBMs in lungs. Additionally, specialised histology stains were used to determine the types of immune cells involved in the immune response to those NBMs

seen in lungs. Biodegradation of NBMs in lungs, liver, spleen, and kidney was also evaluated by means of immunofluorescent staining of dextran which was the main NBM coating investigated in the final case study.

Following the three results chapters is an overall discussion and conclusions chapter (chapter 6) which highlights the main findings from the in vivo case studies including a section on future work (chapter 7) outlining the experiments that will follow on from this research to further confirm the findings reported in this PhD project.

To complete this PhD project an extensive bibliography reporting the state of the art from the many research fields involved in this work. Finally, a comprehensive Appendix (chapter 8) is included where to expand in all technical, imaging and recorded processes which complete the data behind the main results presented.

Overall, the experimental research at the basis of this PhD provided qualitative and quantitative evidence supporting the identified aims thus proving the validity of the hypothesis set for this PhD project which was confirmed by the bulk of experimental results presented.

Acknowledgment

The work presented in this doctorate thesis was made possible with financial support from two European projects, the EUNCL (Grant ID: 654190) and the NoCanTher (Grant ID: 685795); both of which were funded by the European Commission under Horizon 2020. I am truly grateful for this funding which allowed me to achieve all of the results presented in this thesis and also present my research to a wider public in form of peer reviewed publications and conferences.

First and foremost, I would like to thank my supervisors who supported me on this journey and helped me become the scientist that I am today. A big thank you to Ussher Assistant Professor Adriele Prina-Mello for always encouraging me to aim higher and asking me the tough questions. I would also like to say a massive thank you to Dr. Oliviero Gobbo who was the first person to see a potential in me and encouraged me to persuade a doctorate degree. I would probably never have the courage to apply without his backing. I would also like to thank late Professor Yuri Volkov for infecting me with passion for microscopy and histopathology. Thank you for being my mentor and a fantastic example of the kind of researcher and teacher I hope to become one day.

I would also like to thank all the members of the Nanomedicine and Molecular imaging group, past and present. Thank you to Dr. Ciaran Maguire, Dr. Melissa Tutty and Dr. Gary Hannon for being great colleagues and friends. It was a privilege to work alongside of you all those years. I would also like to thank Dr. Dania Movia and Moreno Carrer for being an absolute joy to work with. I have been fortunate to meet a number of PhD students carrying out their research in TTMI, all of which have been there for me both professionally and personally. I will always be grateful that our paths have crossed.

There are many individuals from external institutions I would also like to thank for services and supplies for this project. I would like to thank Dr. Richard Flavin, Dr. Stephen Finn, and Dr. Anna Keogh from the Central Pathology Laboratory in St. James' Hospital for always being available to review my samples and provide your professional opinion. I would also like to thank all of the collaborators in SINTEF in Norway and CEA in France for supplying their material and sharing their characterisation data.

Finally, I would like to thank all of the strong women in my family and my chosen family. I would not be where I am today without my amazing mum and sister. Thank you both for believing in me and listening to me even when you did not understand what I was talking about. Also a big thank you to my best friend Ali for being my rock all those years.

Outputs

Peer reviewed publications

- Gary Hannon, **Anna Bogdanska**, Yuri Volkov, Adriele Prina-Mello "Comparing the Effects of Intracellular and Extracellular Magnetic Hyperthermia on the Viability of BxPC-3 Cells". *Nanomaterials*. 2020; 10(3):593. https://doi.org/10.3390/nano10030593

- Sharon A. O'Toole, Cathy Spillane, Yanmei Huang, Marie C. Fitzgerald, Brendan Ffrench, Bashir Mohamed, Mark Ward, Michael Gallagher, Tanya Kelly, Cathal O'Brien, Carmel Ruttle, **Anna Bogdanska**, Cara Martin, Dorinda Mullen, Elizabeth Connolly, Sarah A. McGarrigle, John Kennedy & John J. O'Leary "Circulating tumour cell enumeration does not correlate with Miller–Payne grade in a cohort of breast cancer patients undergoing neoadjuvant chemotherapy.", *Breast Cancer Res Treat*, **181,** 571–580 (2020). https://doi.org/10.1007/s10549-020-05658-7

- **Bogdanska. A.,** Gobbo. L., Volkov. Y., Prina-Mello. A., "3D volume segmentation and reconstruction. Supervised image classification and automated quantification of superparamagnetic iron oxide nanoparticles in histology slides for safety assessment ", *Nanotoxicology*. https://doi.org/10.1080/17435390.2021.1991502

- Fernández, Y., Movellan, J., Foradada, L., Giménez, V., García-Aranda, N., Mancilla, S., Armiñán, A., Borgos, S. E., Hyldbakk, A., **Bogdanska, A.,** Gobbo, O. L., Prina-Mello, A., Ponti, J., Calzolai, L., Zagorodko, O., Gallon, E., Niño-Pariente, A., Paul, A., Schwartz, S., Abasolo, I., Vicent, M. J., "In Vivo Antitumor and Antimetastatic Efficacy of a Polyacetal-Based Paclitaxel Conjugate for Prostate Cancer Therapy". *Adv. Healthcare Mater.* 2021, 2101544. https://doi.org/10.1002/adhm.202101544

Publication in preparation

- Hannon. G., **Bogdanska. A.,** Gobbo. O., Prina-Mello. A., "Biodistribution and Histological analysis of Iron-Dextran Nanoparticles in Wistar rats" (in submission)

Oral presentations

- **Anna Bogdanska,** Oliviero Gobbo, Adriele Prina-Mello "3D histology volumes; an innovative tool for assessment of biodistribution and aggregation of SPION *in vivo"*, 9th – 11th June 2021, NanoTech Poland 2021 - 11th International Conference, 9th-11th June 2021.

Poster Presentations

- Marco Alberti, **Anna Bogdanska**, Elvira Presti, Yuri Volkov, Adriele Prina-Mello "Multidisciplinary approach for the development of computational theranostics: translating ex vivo images into in silico models", 10th and 11th August 2017, Early Career Researchers Meeting, Queen's University Belfast.

- **Anna Bogdanska**, Oliviero Gobbo, Adriele Prina-Mello, Yuri Volkov "Semi-automated 3D segmentation of Superparamagnetic iron oxide nanoparticles (SPIONs) using histology images", 29th – 31st January 2020, NALS 2020, Madrid, Spain.

Credits

Base module (ST7007) taught as a part of the Postgraduate Diploma in Statistics (PCCS-STAT-1P) in Trinity College Dublin (15 ECTS).

Abstract

Over the past few decades nanobiomaterials (NBMs) have shown a promise in improving many areas of medicine such as diagnosis and treatment of diseases, with number of formulations currently approved for use by the regulators. However, there are still concerns regarding biodistribution, accumulation, and toxicity of NBMs in vivo as well as their impact on the immune system. To gain a better understanding on the complex interplay of NBMs with biological systems and structures, assays used in preclinical assessment of the next generation NBMs need to be expanded to address those specific concerns**.**

This PhD project aimed to contribute to the scientific knowledge on the biodistribution, accumulation, and toxicity of representative NBMs *in vivo* by improving their detection in tissue sections by means of accepted histological markers and methodologies. The second aim was to provide an efficient and objective method for semi-quantitative analysis of histological data by utilising machine learning. To achieve those goals, the research undertaken in this PhD project develops in four main case studies, where histological techniques were specifically tailored to the type of NBMs under investigation: namely liposome and iron oxide nanoparticles.

The first two case studies presented in chapter 3 were undertaken to address the lack for consistent microscopic detection of liposomes in histological tissue sections. For this purpose, two type of liposomes were selected as NBM models: a liposome containing fluorescent dye and a PEGylated liposome. By using histological stain for lipid detection (Oil red O), liposomes were successfully detected with fluorescent microscopy in different organs (liver, spleen, kidney, and small intestine). Moreover, by imaging fluorescent stain incorporated in the first liposome, or immunofluorescence labelled PEG of the second liposome, these NBMs were effectively discriminated from naturally occurring dietary lipids or fats.

The following two case studies presented in Chapter 4 and 5 addressed the need for a subjective and time efficient method for quantitative histology studies. This was achieved by utilising machine learning to assess biodistribution and morphology of aggregates formed by magnetic iron oxide nanoparticles, as NBMs in *in vivo* animal murine model. Perls' Prussian blue stained was used to stain iron in tissue sections, with quantitative analysis carried out in traditional 2D histology slides and 3D histology volumes reconstructed from a series of consecutive tissue sections. Data extrapolated from histology sides using this method provided information on patterns of accumulation of magnetic iron oxide NBMs in terms of number and size of aggregates formed in lungs, liver, kidney, and spleen following intravenous injection. Additionally, in the last case study, immune reaction in response to NBMs and their degradation *in vivo* was evaluated using

specialised histology stains. Results of this analysis suggested that dextran used to coat the magnetic iron oxide nanoparticles induced an acute immune response in lungs which was not seen in the NBM when this coating was degraded.

Overall, the work presented in this thesis highlights the extensive potential that tailored histology could have in evaluating the safety of NBMs *in vivo*. Various specialised stains allowed to detect NBMs in tissue sections on a microscopic level, to evaluate their degradation *in vivo* and type of immune reaction activated in response to the presence of these novel type of materials. Furthermore, traditional histological methods were brought into the twenty-first century by using ML to extrapolate quantitative data from representative images showing iron aggregates in 2D and 3D histology volumes. Future work in this area should evaluate if this type of analysis can be extended to assess the safety of other types of NBMs.

Table of Contents

1 Chapter 1: Introduction 1
1.1 Nanobiomaterials 1
1.1.1 Approved NBMs for medical applications 2
1.1.2 Types of NanoBioMaterials 3
1.1.3 Medical applications of NanoBioMaterials 6
1.2 Preclinical assessment 10
1.2.1 Regulatory landscape and perspective 10
1.3 Nanobiomaterials in vivo 11
1.3.1 Biodistribution 12
1.3.2 Toxicity and immune response 15
1.4 Role of histology in preclinical testing of NBMs 18
1.5 Machine Learning for bioimage processing 20
1.5.1 Trainable WEKA segmentation 21
1.5.2 Performance metrics 24
1.6 Hypothesis and aims 27
2 Chapter 2: Materials and methods 28
2.2 *In vivo* experiments 30
2.2.1 Animal housing 32
2.2.2 Monitoring animal wellbeing 32
2.2.3 Case study 1: In vivo toxicity and biodistribution of NIR-dye loaded liposome for imaging applications 32
2.2.4 Case study 2: In vivo toxicity and biodistribution of liposomal irinotecan 33
2.2.5 Case study 3: In vivo toxicity and biodistribution of MF66 MNPs 34
2.2.6 Case study 4: In vivo acute toxicity study of NOC0007 and RCL-01 MNPs 34
2.3 Histopathology 35
2.3.1 Cryopreserved tissue 35
2.3.2 Formalin fixed paraffin embedded tissue 37
2.4 Image acquisition 40
2.4.1 Brightfield microscopy 40
2.4.2 Automated microscope 40
2.4.3 Fluorescent imaging 41
2.5 Quantitative analysis 41
2.5.1 Sample preparation for Mass Spectroscopy 41
2.5.2 Sample preparation for iron quantification using inductively coupled plasma mass spectrometry 41
2.6 Machine learning for bioimage analysis 43
2.6.1 Model training 43
2.6.2 Model validation 43
2.6.3 Quantification of iron staining 44

2.6.4 Virtual 3D volume 45
2.7 Statistical analysis 45
3 Chapter 3: Histology assays for toxicity, accumulation and clearance of nanoliposomes . 47
3.1 Introduction 47
3.2 Experimental design 48
3.2.1 Case study 1: Safety study of dye-loaded lipid NBM 50
3.2.2 Case study 2: proof-of-concept SOP for liposome drug carrier biodistribution detection 51
3.3 Results 52
3.3.1 Case study 1: Safety study of a dye-loaded lipid NBM..... 52
3.3.2 Case study 2: proof-of-concept SOP for loaded liposome biodistribution detection 72
3.3.3 Quantitative analysis of biodistribution by MS 82
3.4 Discussion 83
3.5 Conclusion..... 87
4 Chapter 4: ML model for MNP quantification and 3D reconstruction from histology sections 88
4.1 Introduction 88
4.2 Experimental design 90
4.3 Results 92
4.3.1 Toxicity 92
4.3.2 Investigation of MNP accumulation..... 97
4.3.4 Iron quantification in histology sections 111
4.4 Discussion 115
4.5 Conclusion..... 118
5 Chapter 5: Histology study of toxicity and biodistribution of MNP *in vivo*..... 119
5.1 Introduction 119
5.3 Results 124
5.3.1 Clinical evaluation..... 124
5.3.2 Toxicity 127
5.3.3 Investigation of immune response and coating degradation..... 135
5.3.4 Investigation of MNPs accumulation in organs..... 154
5.3.5 Investigation of MNPs biodistribution in organs..... 161
5.3.6 Shape analysis of iron aggregates in lungs 176
5.4 Discussion 182
5.5 Conclusion..... 188
6 Overall discussion and conclusions 189
7 Future work..... 194
Bibliography..... 196
8 Appendix 207

8.1 Power calculation for *in vivo* studies 211
8.1.1 Power calculation for case study 1 211
8.1.2 Power calculation for case study 2 212
8.1.3 Power calculation for case study 4 213
8.2 In vitro experiments 214
8.2.1 Liposome uptake 214
8.2.2 MNPs uptake in vitro 216
8.3 *In vivo* experiments 219
8.3.1 Supplementary data for Case study 1: Novel dye-loaded lipid NBM 219
8.3.2 Supplementary data for Case study 2: proof of concept 237
8.3.3 Supplementary data for Case study 3: In vivo toxicity and biodistribution of MF66 MNPs 248
8.3.4 Supplementary data for case study 4: In vivo acute toxicity study of NOC0007 and RCL-01 256
8.3.5 Macro script for image pre-processing 290

List of Figures

Figure 1.1: Historical timeline of FDA approved NBMs and microparticles. 3
Figure 1.2: Schematic representation of NBM classification. 4
Figure 1.3: Considerations for *in vivo* testing of NBMs 12
Figure 1.4: Biodistribution of NBMs *in vivo* 14
Figure 1.5: Cells of the immune system 16
Figure 1.6: NBMs in H&E stained sections 19
Figure 1.7: Supervised machine learning for bioimage analysis 21
Figure 1.8: TWS software 22
Figure 1.9: Representative example of filters available in Fiji for image feature extraction 23
Figure 1.10: Graphical representation of pixel-based metrics 25
Figure 1.11: Visual representation of performance metrics 26
Figure 2.1: Schematic workflow for *in vivo* case studies 31
Figure 3.1: Experimental workflow for case study 1: dye-loaded lipid NBM 50
Figure 3.2: Experimental workflow for case study 2: liposomal irinotecan 51
Figure 3.3: Body weight variation over experiment duration 53
Figure 3.4: Liver pathology 7 days after intravenous injection of liposome 55
Figure 3.5: Spleen pathology 7 days after intravenous injection of liposomes 56
Figure 3.6: Kidney pathology 7 days after intravenous injection of liposomes 57
Figure 3.7: Lipid detection in liver tissue sections 59
Figure 3.8: Lipid detection in spleen tissue sections 60
Figure 3.9: Lipid detection in kidney tissue sections 61
Figure 3.10: Detection of lipids and NIR dye in female liver tissues sections 66
Figure 3.11: Detection of lipids and NIR dye in male liver 67
Figure 3.12: Detection of lipids and NIR dye in female spleen 68
Figure 3.13: Detection of lipids and NIR dye in male spleen 69
Figure 3.14: Detection of lipids and NIR dye in female kidney 70
Figure 3.15: Detection of lipids and NIR dye in male kidney 71
Figure 3.16: Pathological changes induced by irinotecan and liposomal irinotecan in liver, spleen and small intestines 74
Figure 3.17: Lipid detection with Oil Red O on different organ tissue sections 76
Figure 3.18: Immunofluorescent detection of lipids and PEG in liver 79
Figure 3.19: Immunofluorescent detection of lipids and PEG in small intestine 80
Figure 3.20: Immunofluorescent detection of lipid and PEG in spleen 81
Figure 3.21: Concentration of irinotecan (CPT-11), and its active metabolites SN-38 and SN-38 glucuronide in organs. 83
Figure 4.1: Experimental workflow for case study 3: *In vivo* toxicity and biodistribution of MF66 MNPs 91
Figure 4.2: Histological changes formed in lungs over time following injection of MNPs 93
Figure 4.3: Kidney pathology over time following injection of MNPs 94
Figure 4.4: Histological changes formed in liver over time following injection of MNPs 96
Figure 4.5: Local inflammation in liver induced by MNPs 97
Figure 4.6: Accumulation of MNPs in liver over time 98
Figure 4.7: Accumulation of MNPs in lungs over time 99
Figure 4.8: MNPs uptake by tissue specific macrophages 100
Figure 4.9: Accumulation of MNPs in kidney over time 101
Figure 4.10: Automated image analysis 104
Figure 4.11: Approaches for threshold selection 106
Figure 4.12: Performance evaluation of image segmentation algorithms 107
Figure 4.13: Performance evaluation of different segmentation methods 110
Figure 4.14: Quantification of Prussian blue staining 112
Figure 4.15: Representative images of 3D histology reconstruction and segmented 3D volume 114

Figure 5.1: Experimental workflow for case study 4: *In vivo* acute toxicity study of NOC0007 and RCL-01 123
Figure 5.2: Severity score 125
Figure 5.3: Body weight variation over experiment duration 126
Figure 5.4: Pathological changes in lung sections 128
Figure 5.5: Pathological changes in liver 130
Figure 5.6: Pathological changes in the spleen sections 132
Figure 5.7: Pathological changes in the kidney sections 133
Figure 5.8: Boxplot of pathological severity score 134
Figure 5.9: Mast cell activation in response to MNPs 136
Figure 5.10: Infiltration of mast cells in lung in response to NOC0007 MNPs 137
Figure 5.11: Infiltration of mast cells in the lung in response to RCL-01 MNPs 138
Figure 5.12: Detection of CD68+ cells and NOC 0007 dextran coating in lungs 140
Figure 5.13: Localisation of NOC 0007 in pulmonary macrophages 141
Figure 5.14: NOC 0007 accumulation in pulmonary vessel 141
Figure 5.15: Detection of CD68+ cells and RCL-01 dextran coating in lung 142
Figure 5.16: Localisation of RCL-01 in pulmonary macrophages 143
Figure 5.17: Detection of CD68+ cells and NOC 0007 dextran coating in liver 144
Figure 5.18: Detection of CD68+ cells and RCL-01 dextran coating in liver 145
Figure 5.19: Localisation of NOC 0007 in liver macrophages 146
Figure 5.20: Localisation of RCL-01 in liver macrophages 147
Figure 5.21: Detection of CD68+ cells and NOC0007 dextran coating in spleen 148
Figure 5.22: Detection of CD68+ cells and RCL-01 coating in spleen 149
Figure 5.23: Localisation of NOC 0007 in splenic macrophages 150
Figure 5.24: Localisation of RCL-01 in splenic macrophages 151
Figure 5.25: Detection of NOC 0007 dextran coating in kidney 152
Figure 5.26: Detection of RCL-01 dextran coating in kidney 153
Figure 5.27: MNPs distribution in lung 155
Figure 5.28: MNP distribution in liver 157
Figure 5.29: MNP distribution in spleen 159
Figure 5.30: MNP distribution in kidney 160
Figure 5.31: Performance evaluation of different segmentation methods 162
Figure 5.32: Segmentation of iron objects in lungs using different methods 163
Figure 5.33: Segmentation of iron objects in liver using different methods 164
Figure 5.34: Segmentation of iron objects in spleen using different methods 165
Figure 5.35: Segmentation of iron objects in kidney using different methods 166
Figure 5.36: Quantification of Prussian blue staining in NOC0007 treatment group 168
Figure 5.37: Quantification of Prussian blue staining in RCL-01 treatment group 169
Figure 5.38: Correlation between dose of NOC0007 MNPs and iron detected in histology sections 171
Figure 5.39: Correlation between dose of RCL-01 MNPs and iron detected in histology sections 172
Figure 5.40: Biodistribution of iron following injection with NOC0007 MNPs measured by quantitative, qualitative, and semi-quantitative techniques 174
Figure 5.41: Biodistribution of iron following injection with RCL-01 MNPs measured by quantitative, qualitative, and semi-quantitative techniques 175
Figure 5.42: Morphology of MNPs aggregates in histology slides 177
Figure 5.43: 3D reconstruction of lung sections from rats in NOC0007 experimental block 179
Figure 5.44: 3D reconstruction of lung sections from rats in RCL-01 experimental block 180
Figure 5.45: Morphology of MNPs aggregates in 3D histology volumes 181
Figure 5.46: Cascade of immune responses to intravenously administered MNPs 185

List of Tables

Table 2.1: Summary characterisation of nanobiomaterials as provided by the suppliers..... 29
Table 2.2: Scale conversion for images acquired with Nikon Eclipse E800 microscope 40
Table 2.3: Scale conversion for images acquired with LionHeartFX automated microscope 40
Table 2.4: Scale conversion for images acquired with Leica SP8 scanning confocal microscope41
Table 3.1: Summary characterisation of nanobiomaterials used in case study 1 and 2..... 49
Table 3.2: Full description of liposome accumulation and pathological changes in all organs from animals tested in case study 1..... 62
Table 3.3: Full description of liposome accumulation and pathological changes in all organs from animals tested in case study 2..... 77
Table 4.1: Full description of iron accumulation and pathological changes in all organs from animals tested in case study 3..... 102
Table 4.2: Initial model validation with 10-fold cross-validation. 109
Table 5.1: Physicochemical properties of NOC0007 and RCL-01 MNP..... 122

List of equations

Equation 1: Mathew's Correlation Coefficient (MCC) 44
Equation 2: F_1 score..... 44
Equation 3: Jaccard similarity coefficient (JSC) 44
Equation 4: Percent area of Perls' Prussian blue staining 45

List of supplementary figures

Supplementary figure 8.1: Sample size calculation for case study 1 212
Supplementary figure 8.2: Sample size calculation for case study 2 213
Supplementary figure 8.3: Cellular uptake of liposomes, PEG immunofluorescence labelling 215
Supplementary figure 8.4: Cellular uptake of SPION, Perls' Prussian blue 217
Supplementary figure 8.5: Cellular uptake of SPION, dextran immunostaining 218
Supplementary figure 8.6: H&E staining of female liver..... 219
Supplementary figure 8.7: H&E staining of male liver..... 220
Supplementary figure 8.8: H&E staining of female spleen..... 221
Supplementary figure 8.9: H&E staining ofmale spleen..... 222
Supplementary figure 8.10: H&E staining of female kidneys..... 223
Supplementary figure 8.11: H&E staining of male kidneys..... 224
Supplementary figure 8.12: Lipid content in female livers 225
Supplementary figure 8.13: Lipid content in male livers 226
Supplementary figure 8.14: Lipid accumulation in female spleen..... 227
Supplementary figure 8.15: Lipid accumulation in male spleen..... 228
Supplementary figure 8.16: Lipid accumulation in female kidneys..... 229
Supplementary figure 8.17: Lipid accumulation in male kidneys..... 230
Supplementary figure 8.18: Detection of lipids and IR-780 dye in female livers using fluorescent microscopy 231
Supplementary figure 8.19: Detection of lipids and IR-780 dye in male livers using fluorescent microscopy 232
Supplementary figure 8.20: Detection of lipids and IR-780 dye in female spleens using fluorescent microscopy 233
Supplementary figure 8.21: Detection of lipids and IR-780 dye in male spleens using fluorescent microscopy 234

Supplementary figure 8.22: Detection of lipids and IR-780 dye in female kidneys using fluorescent microscopy 235
Supplementary figure 8.23: Detection of lipids and IR-780 dye in male kidneys using fluorescent microscopy 236
Supplementary figure 8.24: Structural changes in liver following treatment with irinotecan or Onivyde® 237
Supplementary figure 8.25: Structural changes in spleen following treatment with irinotecan or Onivyde® 238
Supplementary figure 8.26: Structural changes in small intestines following treatment with irinotecan or Onivyde ® 239
Supplementary figure 8.27: Lipid accumulation in liver following treatment with irinotecan or liposomal irinotecan 240
Supplementary figure 8.28: Lipid accumulation in spleen following treatment with irinotecan or liposomal irinotecan 241
Supplementary figure 8.29: Lipid accumulation in small intestine following treatment with irinotecan or liposomal irinotecan 242
Supplementary figure 8.30: Immunofluorescent detection of lipids and PEG in liver 243
Supplementary figure 8.31: Immunofluorescent detection of lipids and PEG in small intestine 244
Supplementary figure 8.32: Immunofluorescent detection of lipids and PEG in spleen. 245
Supplementary figure 8.33: Pharmacokinetic profile of CPT-11, SN-38 and SN-38 glucuronide in plasma. 246
Supplementary figure 8.34: Faecal profile of CPT-11, SN-38 and SN-38G 247
Supplementary figure 8.35: Structural changes induced by MNPs in lungs 249
Supplementary figure 8.36: Structural changes induced by MNPs in kidneys 250
Supplementary figure 8.37: Structural changes induced by MNPs in liver 251
Supplementary figure 8.38: Accumulation of MNPs in lungs 252
Supplementary figure 8.39: Accumulation of MNPs in liver 253
Supplementary figure 8.40: Accumulation of MNPs in kidneys 254
Supplementary figure 8.41: Representative images selected for training WEKA classifier 255
Supplementary figure 8.42: Immune response in lungs following injection of NOC 0007 MNPs 266
Supplementary figure 8.43: Immune response in lungs following injection of RCL-01 MNPs 267
Supplementary figure 8.44: Pathological changes in liver following injection of NOC0007 .. 268
Supplementary figure 8.45: Pathological changes in liver following injection of RCL-01 269
Supplementary figure 8.46: Histological changes in spleen following NOC 0007 injection ... 270
Supplementary figure 8.47: Histological changes in spleen following RCL-01 injection 271
Supplementary figure 8.48: Histological changes in kidney following NOC 0007 injection ... 272
Supplementary figure 8.49: Histological changes in kidney following RCL-01 injection 273
Supplementary figure 8.50: Uptake of NOC0007 MNPs by lung macrophages 274
Supplementary figure 8.51: Uptake of RCL-01 MNPs by lung macrophages 275
Supplementary figure 8.52: Uptake of NOC0007 MNPs by Kupffer cells in liver 276
Supplementary figure 8.53: Uptake of RCL-01 MNPs by Kupffer cells in liver 277
Supplementary figure 8.54: Uptake of NOC0007 MNPs by splenic macrophages 278
Supplementary figure 8.55: Uptake of RCL-01 MNPs by splenic macrophages 279
Supplementary figure 8.56: Immunofluorescent detection of dextran in kidneys of animals injected with NOC0007 280
Supplementary figure 8.57: Immunofluorescent detection of dextran in kidneys of animals injected with RCL-01 281
Supplementary figure 8.58: Distribution and accumulation of NOC 0007 MNPs in lungs 282
Supplementary figure 8.59: Distribution and accumulation of RCL-01 MNPs in lungs 283
Supplementary figure 8.60: Distribution and accumulation of NOC 0007 MNPs in liver 284
Supplementary figure 8.61: Distribution and accumulation of RCL-01 MNPs in liver 285
Supplementary figure 8.62: Distribution and accumulation of NOC 0007 MNPs in spleen 286
Supplementary figure 8.63: Distribution and accumulation of RCL-01 MNPs in spleen 287
Supplementary figure 8.64: Distribution and accumulation of NOC 0007 MNPs in kidneys .. 288

Supplementary figure 8.65: Distribution and accumulation of RCL-01 MNPs in kidneys..... 289
Supplementary figure 8.66: Representative images selected for validating WEKA classifiers 291

List of supplementary tables

Supplementary table 8.1: List of reagents 207
Supplementary table 8.2: List of antibodies 208
Supplementary table 8.3: List of consumables 208
Supplementary table 8.4: Imaging equipment 208
Supplementary table 8.5: Software 208
Supplementary table 8.6: Severity score sheet for mice after drug administration 208
Supplementary table 8.7: Severity score sheet for rats after drug administration 210
Supplementary table 8.8: Full description of iron accumulation and pathological changes in all organs from animals tested inNOC0007 experimental block in case study 4 256
Supplementary table 8.9: Full description of iron accumulation and pathological changes in all organs from animals tested in RCL-01 experimental block in case study 4..... 261

List of Abbreviations

µM	micrometre
3D	Three-dimensional
ABC	Accelerated Blood Clearance
AFM	Atomic Force Microscopy
AI	Artificial Intelligence
CARPA	Complement Activation-Related Pseudoallergy
CEA-Leti	Commissariat à l'énergie atomique et aux énergies alternatives
COVID-19	coronavirus disease 2019
DNA	DeoxyriboNucleic Acid
DOX	doxorubicin
DSC	Dice Similarity Coefficient
EMA	European Medicines Agency
EU	Endotoxin Units
EUNCL	European Nanomedicine Characterisation Laboratory
FDA	Food and Drug Administration
FFPE	Formalin fixed paraffin embedded
FITC	Fluorescein IsoThioCyanate
FN	False Negative
FP	False Positive
FP7	7th Framework Programme for Research and Technological Development
FRF	Fast Random Forest
GUI	Graphical User Interface
H&E	Haematoxylin and Eosin
HPRA	Health Products Regulatory Authority
ICP-MS	Inductively coupled plasma mass spectrometry
IMS	Industrial Methylated Spirits
ip	intraperitoneal
ISO	International Organization for Standard
JSC	Jaccard Similarity Coefficient
LBCAM	Laboratory for Biological Characterisation of Advanced Materials
ML	Machine Learning
MMC	Matthews's correlation coefficient
MNP	Magnetic NanoParticle
MRI	Magnetic Resonance Imaging
MS	Mass Spectroscopy
MULTIFUN	Multifunctional Nanotechnology for selective detection and Treatment of cancer
NBM	NanoBioMaterial
NIR	Near-Infrared
NPs	NanoParticles
PBS	Phosphate Buffered Saline
PDAC	Pancreatic Ductal Adenocarcinoma
PEG	PolyEthylene Glycol

pEPR	particle Electron Paramagnetic Resonance
PET	Positron Emission Tomography
PVA	PolyVinyl Alcohol
RES	Reticulo Endothelial System
RGB	Red Green Blue
ROI	Region of Interest
ROS	Reactive Oxygen Species
RPMI	Gibco Roswell Park Memorial Institute Media
SCLC	Small Cell Lung Cancer
SEM	Scanning Electron Microscopy
SINTEF	Stiftelsen for industriell og teknisk forskning
siRNA	Small interfering RNA
SOP	Standard Operating Procedure
SPECT	Single Photon Emission Computed Tomography
SPION	Superparamagnetic Iron Oxide Nanoparticle
TGA	Therapeutic Goods and Administration, Australia
TN	True Negative
TP	True Positive
TTMI	Trinity Translational Medicine Institute
TWS	Trainable WEKA Segmentation
US-NCL	US Nanotechnology Characterization Laboratory
USPION	Ultrasmall Superparamagnetic Iron Oxide Particle
VADSs	Vaccine Adjuvant-Delivery Systems
VSPION	Very Small Superparamagnetic Iron Oxide Particle
WEKA	Waikato Environment for Knowledge Analysis

1 Chapter 1: Introduction

To begin, a foreword that defines and delimits the scope of this chapter; the chapter opens with an introduction to nanobiomaterials (NBMs) by providing general definition, brief history of NBMs approved for medical applications, and further description of different types of NBMs providing examples of their medical applications. The following section outlines preclinical assessment of NBMs with highlight on regulatory landscape and perspective. The third section of this chapter summarises current knowledge on interplay of NBMs with biological systems and structures *in vivo*, by discussing biodistribution, toxicity and immune response to those materials following intravenous administration. The following section presents how histology studies contribute to preclinical assessment of NBMs emphasising current limitations which were addressed in the aims of this thesis. Machine learning is then applied for bioimage processing in two of the results chapters in this thesis. Details on this technology are provided in the second last section of this chapter, where with the use of specific software applied to some examples, this will aim at providing sufficient information to understand how this technique can be applied to the results collected and analysed in chapter 4 and 5. In the final part of this introduction the outlining hypothesis and aims of research carried out in this doctorate project are presented.

1.1 Nanobiomaterials

General concept of nanotechnology was first introduced in 20th century. Since then, extensive research has been carried out in this area which is still growing exponentially. In general, nanostructured materials (also referred to in literature as nanomaterial) are defined by the European Commission as *'a natural, incidental or manufactured material containing particles, in an unbound state or as an aggregate or as an agglomerate where, for 50% or more of the particles in the number size distribution, one or more external dimensions is in the size range 1 nm – 100 nm.'* [1]. With regard to application of those materials for biomedical purposes, terms such as nanomedicine, nano-bio-interface, and more recently nanobiomaterials (NBMs) have been used interchangeably [2]. However, they can be further distinguished as follows: nanomedicine when referring to medicinal products; nano-bio-interfaces when referring to one specific component of any nano-object interacting with the environment; and NBMs when referring to a class of nanomaterials with biocompatibility or dedicated biological properties. For the past few decades there has been a rapid rise in the use of NBMs in a wide range of biological and biomedical applications such as tissue engineering [3], drug delivery [4], imaging, and combination of treatment and diagnostic known as theranostics [5, 6].

The use of NBMs in medical technologies has shown numerous advantages over currently available treatments such as longer retention time, improved solubility, higher carrier capability and fewer side effects [7, 8]. However, novel formulations fail to pass through regulatory approval due to complications in large-scale manufacturing and lack of quality control assays for characterisation [9-11]. Interaction of NBMs with biological systems is governed by a multitude of factors, including surface characteristics and size of material used [12]. Due to vast heterogeneity of formulations, there is no "one size fits all" in terms of assays used in early stages of NBM research. Nonetheless, number of NBMs have been approved for medical applications and are discussed in the next sub-section.

1.1.1 *Approved NBMs for medical applications*

Doxil®, was the first Food and Drug Administration (FDA) approved liposomal formulation, initially approved for the treatment of AIDS-related Kaposi's sarcoma in 1995 and later approved for treatment of recurrent ovarian cancer in 1998 for the treatment of certain cancers [13]. Since then, number of NBMs have been approved by FDA (Figure 1.1) and EMA for an array of applications. Most recently, during the coronavirus disease 2019 (COVID-19) situation, two vaccines employing liposomes as vaccine adjuvant-delivery systems (VADSs) for mRNA delivery we given an Emergency Use Authorization by the FDA, and conditional marketing authorisation by European medicines Agency (EMA) [14]. Spikevax® (previously COVID-19 Vaccine Moderna) and Comirnaty® (research name BNT162b2) from Pfizer/ BioNTech contain very similar lipid nanoparticles for mRNA delivery as well as PEGylated lipid to reduce opsonisation by serum proteins [15]. This approval has a potential to induce a paradigm shift in terms of the approval on the use of NBMs for clinical applications. However, novel formulations can still fail to pass through regulatory approval due to key issues such as large-scale manufacturing and lack of quality control assays for characterisation [16] which are further addressed in section 1.2.

The next sub-sections introduce two of the most researched types of NBMs for biomedical applications, presenting aspects critical for their translation into clinical products. Particular focus will be given to the biodistribution and the effects of those materials *in vivo*.

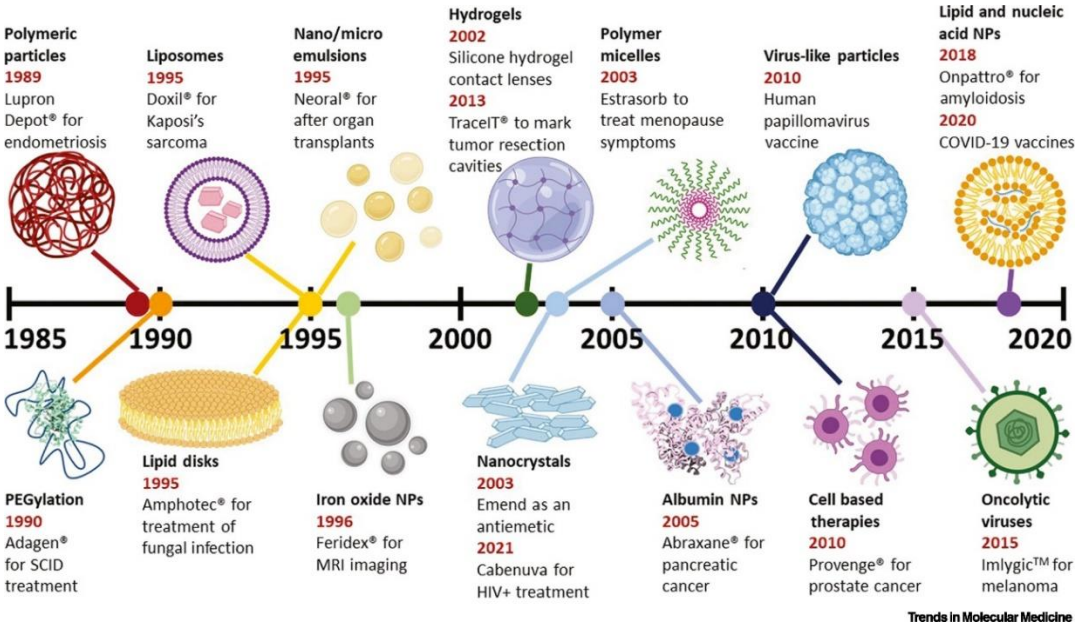

Figure 1.1: Historical timeline of FDA approved NBMs and microparticles.
Date indicates the year of first FDA approval with commercial name and indication. Figures are not to scale with each other. Abbreviation: COVID-19, coronavirus disease 2019; MRI, magnetic resonance imaging; SCID, severe combined immunodeficiency disease. Figure adapted from Batty *et al.* [17]

1.1.2 *Types of NanoBioMaterials*

NBMs can be broadly classified as organic (e.g.: liposomes, dendrimers, polymeric nanoparticles, micelles) or inorganic (Figure 1.2) from different families of materials such as ceramic and metallic (e.g.: gold and iron oxide), semiconductors (e.g.: quantum dots), and non-centrosymmetric materials (e.g.: second harmonic generation materials). Additionally, in the past decade increased research has focused on the combined use of organic-inorganic hybrid NBMs containing customised features of organic and inorganic nature and properties in the same system [18, 19]. For the purpose of this thesis, the following section will focus on one family of inorganic NBM material the metallic one, in particular the magnetic iron oxide nanoparticles, and one natural organic biodegradable NBM, in particular the liposome family. Highlights on their advantages and limitations in terms of their use for biomedical purposes will be presented.

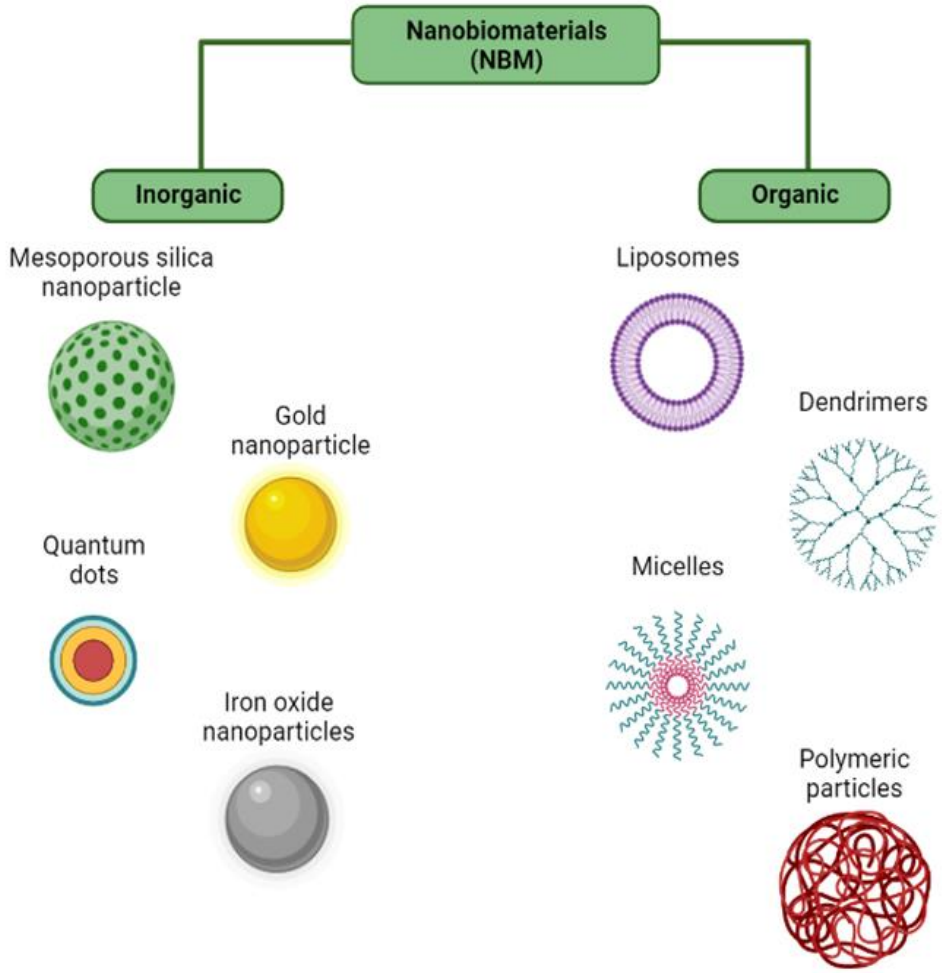

Figure 1.2: Schematic representation of NBM classification.
Examples of most widely used inorganic materials are presented on the left branch whereas organic materials are on the right branch. Figures are not to scale with each other. Created with BioRender.com.

1.1.2.1 Magnetic iron oxide nanoparticles

The most common forms of iron oxides in nature are magnetite (Fe_3O_4), maghemite (γ-Fe_2O_3), and hematite (α-Fe_2O_3) [20], with first two commonly used to formulate a metallic core of magnetic nanoparticles (MNPs). These types of particles are normally smaller than 100 nm and can be synthesized from any material characterized by some degree of magnetism [21]. Among this type of nanoparticles, superparamagnetic iron oxide nanoparticles (SPIONs) have gained interest due to their outstanding magnetic properties such as the superparamagnetic property. This means that they have a high, positive magnetic susceptibility, only in the presence of magnetic field exhibiting essentially no residual magnetism in the absence of magnetic field [22]. This means the SPIONS can be controlled in their energy and position via the application of a non-

invasive external magnetic field. This allows for the physical manipulation and localised heating of the particles and surrounding space. Within the SPIONS, these properties can be switched on and off by the application or not of the external magnetic field.

Based on their size, SPIONs can be categorised as very small superparamagnetic iron oxide particles (VSPIONs, <10 nm), ultrasmall superparamagnetic iron oxide particles (USPIONs, 10−50 nm), and superparamagnetic iron oxide particles (SPIONs, 50−180 nm) [23].

Apart from the safety aspects associated with dosing and exposure time, the toxicity of MNPs to be used for biomedical applications, depends on an array of factors which are part of the makeup of the NMBs. These are the coating/protective/biocompatibility material, the hydrodynamic diameter of the particle and its interaction with physiological fluid and tissue. The main factors contributing to the toxic effects associated with iron oxide MNPs are considered to be the release of iron ions from the MNP core. In a physiological environment, and when interaction with cells and tissue, these ions can diffuse intracellularly at lysosomal level, which react with hydrogen peroxide and leading to generation of Reactive Oxygen Species (ROS) [24]. For this reason, organic or polymeric coatings are commonly used to create a form of protective barrier for the metallic core of MNPs. Additionally, it is interesting to note that despite providing the protective function, some coating materials can induce an immune response. For example, activation of macrophages induced by polyethyleneimine-coated SPION [25] and activation of dendritic cells upon exposure to poly(vinylalcohol)-coated SPION [26]. Other significant toxic effects of iron oxide MNPs include inflammation, impaired mitochondrial function, membrane leakage of lactate dehydrogenase, increase in micronuclei, and chromosome condensation [27]. Interestingly, in several studies in patients reported no adverse events (or only minor) following the intravenous administration of MNPs [28, 29]. For this reason, MNPs with biocompatible coating such as dextran, are generally regarded safe. However, withdrawal from the market of two formulations containing dextran coated MNPs provides contradicting evidence on this matter. Feromoxtran 10 and Feridex were designed for imaging purposes, but due to the reports of toxic side effect such as hypersensitivity, hypotension and anaphylactic shock they were withdrawn from the market by the FDA in 2007 and 2008 respectively [30]. Those two examples highlight the need for more detailed safety assessment of novel MNPs prior to clinical application in order to prevent severe side effects in humans.

1.1.2.2 Liposome

Liposome can be described as a spherical vesicle composed of lipid bilayer enclosing an aqueous or lipid compartment. They can serve as carriers for numerous hydrophobic and hydrophilic molecules, transporting cargo of interest in the aqueous space or interpolated into the lipid bilayer. The properties of liposomes vary significantly depending on their lipid composition, size, surface charge, and method of preparation [31]. In fact, the lipid component determines fluidity, rigidity, and charge of the lipid bilayer, subsequently changing the properties of the liposome. Regarding their use for biomedical applications, liposomes are known to be non-toxic, biocompatible, and completely biodegradable. Furthermore, encapsulating chemotherapeutic agents in liposomes proved to improve their stability, efficacy, therapeutic index, and reduced toxicity of the encapsulated agent [32].

Despite many advantages of using liposomes for biomedical applications, there are also numerous limitations which must be considered as they present challenges for clinical translation. The most common disadvantages of liposomal technology arise partly from poor stability of those products in terms of their storage as well as in *in vivo* conditions. This is mostly due to potential lipids oxidation and hydrolysis, leakage, and loss of cargo molecules, as well as particle fission and fusion [33]. Liposome delivery systems are also known to be prone to a rapid clearance from the bloodstream due to their opsonisation of plasma components and uptake by macrophages of the reticuloendothelial system (RES), mainly in the liver and spleen. Sterically-stabilizing a liposomes with a hydrophobic polymer such as polyethylene glycol (PEG) had been shown to improve the efficacy of encapsulated agents by reducing *in vivo* opsonisation with serum components, and the rapid recognition and uptake by the RES [34]. However, PEGylated formulations that require multiple dosing regimens have been associated with loss of their long circulating properties in the so-called accelerated blood clearance (ABC) phenomenon. In this phenomenon, a second dose of PEGylated liposome is quickly cleared from the circulation when administered within a certain time interval from injection of the first dose due to an enhanced accumulation in liver [35]. Regardless of those limitations, sterically stabilised liposomal formulations currently dominate the FDA-approved NBM based products [36].

1.1.3 ***Medical applications of NanoBioMaterials***

Organic NBMs (liposomes specifically) are most commonly used for drug delivery systems [8], with inorganic NBMs taking the lead in imaging applications [37]. This section highlights

few of the applications of NBMs, with first two sub-sections discussing applications where both organic and inorganic NBMs have been utilised, followed by two sub-sections introducing applications where unique properties of iron oxide MNPs and liposomes respectively have been exploited for a specific treatment.

1.1.3.1 Drug delivery systems

Although NBMs have been designed to treat various diseases, their most important application has been in cancer, with many formulations already approved by the regulators. Using NBMs as drug delivery systems can improve several undesired properties of "free" drugs (i.e., not attached to or enclosed within NBM) , such as poor solubility, *in vivo* stability, pharmacokinetics, and biodistribution, enhancing their efficacy [38]. Due to their size, NBMs can be transported through capillaries, avoiding phagocytic clearance, resulting in extended circulation in blood. Another advantage of using NBMs for drug delivery is that they can be used for controlled drug release because the material properties are sensitive to temperature, pH, and biodegradability [39]. These systems are also promising because they can improve the stability of therapeutic agents against chemical/enzymatic degradation. The main requirement for using NBMs for drug delivery is that the drug should be loaded in such a manner that its functionality is not compromised.

MNPs can be used for drug delivery by either conjugating the therapeutic molecules on the surface or by co-encapsulating drug molecules along with magnetic particles within the coating material envelope [40]. Iron oxide MNPs exhibit high surface-to-volume ratio allowing for a higher loading capacity for the loaded molecule. By taking an advantage of both active and passive drug delivery approaches, MNPs are showing promising results in cancer chemotherapy [41, 42]. Additionally, recent studies have also focused on multimodal cancer therapies. For example, study reported by Hervault *et. al*. exploited properties on iron oxide MNPs for controlled drug delivery, by conjugating anticancer drug doxorubicin (DOX) to the pH- and thermo-responsive magnetic nanocarrier via acid-cleavable imine linker to provide advanced features for the targeted delivery of DOX molecules via the combination of magnetic targeting, and dual pH- and thermo-responsive behaviour which offers spatial and temporal control over the release of DOX [43].

Liposomes are the most clinically established NBMs for drug delivery. Modified liposomes have been shown to have excellent pharmacokinetic profiles for the delivery of number of

molecules such as Deoxyribonucleic acid (DNA), antisense oligonucleotide, Small interfering RNA (siRNA), proteins, and chemotherapeutic agents [44]. Numerous liposomal drugs with higher efficacy and lower toxicity than their non-nanoliposomal analogues have been approved for clinical use by FDA and EMA [45]. For example, PEGylated liposomal irinotecan (Onivyde®) was approved by the FDA for treatment of advanced pancreatic cancer in October 2015, followed by EMA designation as an 'orphan medicine' in October 2016. It was first developed for the treatment of metastatic adenocarcinoma of the pancreas, in combination with 5-fluorouracil (5-FU) and leucovorin, in patients who have been previously treated with gemcitabine. However, preliminary results from clinical trials indicate its potential to treat multiple solid tumours such as cervical cancer [46], oesophago-gastric cancer [47] and colorectal cancer [48], with main focus in treating pancreatic cancer.

1.1.3.2 Biomedical imaging

To date, different types of nanomaterials, such as dendrimers, liposomes, micelles, and inorganic nanoparticles, have been studied for molecular imaging [49, 50]. In comparison to NBMs for drug delivery, NBMs for imaging purposes should exhibit contrasting characteristics such as rapid biodegradation and/or elimination, with minimal incidence and intensity of side effects, as they are potentially also administered to healthy individuals [51].

A common medical application for MNPs is their use as contrast agents for magnetic resonance imaging (MRI). MRI is a non-invasive and high-resolution imaging technique used as the clinical standard for visualizing anatomical structures. SPIONs possess unique magnetic properties with strong shortening effects under longitudinal relaxation (T_1) and transverse relaxation (T_2) [52] [53]. In order to provide long shelf-life, SPIONs for MRI applications are generally coated with PEG, polyvinyl alcohol (PVA), or natural polysaccharides (dextran and modified chitosan) [54]. SPION contrast imaging has been used in research for multiple purposes such as cancer imaging, cardiovascular disease, inflammation disease, and macrophage imaging to name few [55, 56].

Researchers have been investigating use of liposomes for medical imaging since 1980 [57, 58]. Current research in this area focuses on improving target specificity of traditional imaging modalities such as MRI, positron emission tomography (PET), and single photon emission computed tomography (SPECT) by using functionalised liposomes containing an isotope [59] or a fluorophore [60, 61] Furthermore, liposomes have shown great promise in field of theranostics.

For example, recent study by Prasad *et al.* [62] capitalised on unique properties of multiple NBMs to synthetize targeted nanohybrids for in vivo bioimaging and near-infrared light mediated cancer therapy. Liposome was loaded with gold nanoparticles, graphene quantum dots and doxorubicin hydrochloride to exhibit photo-triggered chemotherapy. Furthermore, to achieve targeted delivery, surface of the liposome was functionalized with folic acid targeting ligands.

1.1.3.3 MNPs for Magnetic hyperthermia treatment

In recent years, research has focused on the use of SPIONs for magnetic hyperthermia which is a promising alternative to conventional cancer treatments as it could potentially reduce healthy tissue damage. Exceptional property of SPIONs is that they heat due to hysteresis loss, Neel relaxation, and eddy currents when exposed to an external alternating magnetic field [63]. In magnetic hyperthermia treatment, an external magnetic field is applied to SPIONs within the body to raise the temperature of surrounding cells above 42°C [64]. This form of therapy exhibits multitude of effects such as increase in blood flow and vessel permeability during heating, increase in the fluidity and permeability of membranes, and disruption to DNA-repair mechanisms resulting in apoptosis [65]. Moreover, hyperthermia can also be used to chemosensitise cancer cells [66]. Both *in vitro* [67] and *in vivo* [68] studies demonstrated benefits of this treatment in oncology. However, use of this technology is not limited to cancer. Recent study by Ding *et al*. [69] utilised MNPs to induce mild testicular hyperthermia as a mean of controllable male contraceptive, highlighting endless possibilities for applications of MNPs.

1.1.3.4 Vaccines

Concerns associated with conventional vaccines have prompted a development of novel subunit vaccines based on defined target antigens such as proteins, DNA, and RNA [70]. Liposomes are suitable vaccine adjuvant-delivery systems (VADSs), which protect antigens from the environmental damage, delivering them to specific lymphocytes, and also enhance the initiation of the immune response [71]. Outcome of the immune response depends on whether antigen is exposed on the surface of the liposome, encapsulated inside the lipid bilayer, or carried within the aqueous phase [72]. Additionally, formulation parameters (e.g., size, charge) can affect the retention of liposomes and associated antigens at the site of injection and subsequent trafficking to draining lymph nodes, which in turn influence magnitude of the immune response [73].

1.2 Preclinical assessment

The previous section highlighted benefits of using NBMs for biomedical applications. This section discusses why despite those advantages, the development and product translation of NBMs is still impacted by many issues at the preclinical level. These can be efficacy, safety, or quality related. To advance the progress of NBMs from research laboratory to clinical implementation, existing protocols for preclinical assessment need to be harmonised, and expanded with new analytical or experimental methods designed for the assessment of next generation nanomedicines. International efforts in this area are well recognised, and the Laboratory for Biological Characterisation of Advanced Materials (LBCAM) at Trinity Translational Medicine Institute (TTMI) is well positioned with the European and International landscape to contribute to addressing some of the aspects which are presented below, and some of which are objectives of the work presented in this thesis.

1.2.1 *Regulatory landscape and perspective*

NBMs for biomedical applications face several challenges in process of clinical translation such as lack of batch-to-batch reproducibility, complexity of the manufacturing processes, and wide gap between the scientific community and regulatory authorities [5]. At present, there is a lack of regulatory guidance regarding the specific requirements for advancing NBMs to clinical trials. Three main regulatory bodies, FDA, EMA, and Therapeutic Goods and Administration, Australia (TGA) do not follow common tests and procedures when evaluating safety and efficacy of NBMs [74]. In order to streamline approval process of NBMs for biomedical applications, the regulatory agencies need to be harmonised and provide clearly defined tests and procedures that need to be cleared by novel formulations prior to applying for approval [75]. Collaborative effort has been established between the EU and US in developing such standards and standardised approaches for the preclinical screening of NBMs. Several initiatives have been developed under the EU-US joint nano characterisation programmes.

Founded in 2015 by the European Union, the European Nanomedicine Characterisation (EUNCL) infrastructure was set to provide unbiased and transdisciplinary testing infrastructure to aid translation of next generation NBMs into clinical products. The EUNCL collaborated with the US Nanotechnology Characterization Laboratory (US-NCL) for the development of validated protocols to support the advance of NBMs in the biomedical industry.

The EUNCL developed and validated more than 30 Standard Operating Procedures (SOP) which have been shared with the Research and Development community [76]. This set of preclinical characterization assays for the NBMs formulations, include physical, chemical, *in vitro* and *in vivo* biological testing. This initiative contributed towards the harmonisation of preclinical requirements for NBMs. However, due to unique characteristics of any novel NBMs (or hybrids), the main methods for characterisation are widely established for the Physical Chemical Characterisation. This conceptualised into a "recommended assay cascade", which provided indication on the needs for tailoring any characterisation for each NBM depending on the material it is composed, of its physicochemical properties and established application. This is particularly applicable for the *in vitro* and *in vivo* testing where the specificities of the NBMS play a major role. Thus, grouping and similarities approach studies have been funded to support the characterisation of NBMs during scale up process.

The LBCAM was one of the partner members of EUNCL, providing expert advice, experimental design, and execution of *in vivo* safety testing on several NBMs. Research undertaken in this PhD project aimed to contribute to the assay cascade recommended by the EUNCL by expanding preclinical *in vivo* assessment with new analytical and experimental methods in the area of histology. Before further elaborating on the aims of this PhD project, the following section introduces the multifaceted interplay of NBMs with biological structures and systems.

1.3 Nanobiomaterials in vivo

The interaction of NBMs with biological systems and structures is a complex area of research. Biodistribution, toxicity, immune response, accumulation, metabolism and excretion of NBMs depends on route of administration as well as size, shape, and surface charge of the material itself, there are infinite possibilities as at to how they might behave in vivo. As a result, preclinical in vivo studies of NBMs have to be designed carefully to account for this multifactorial variability (Figure 1.3). This section will introduce general concepts in NBMs biodistribution, toxicity, immune response, and clearance following intravenous administration. This route of administration is the most common both in research and clinically approved NBMs. It is also the only route of administration used in the in vivo experiments throughout this thesis.

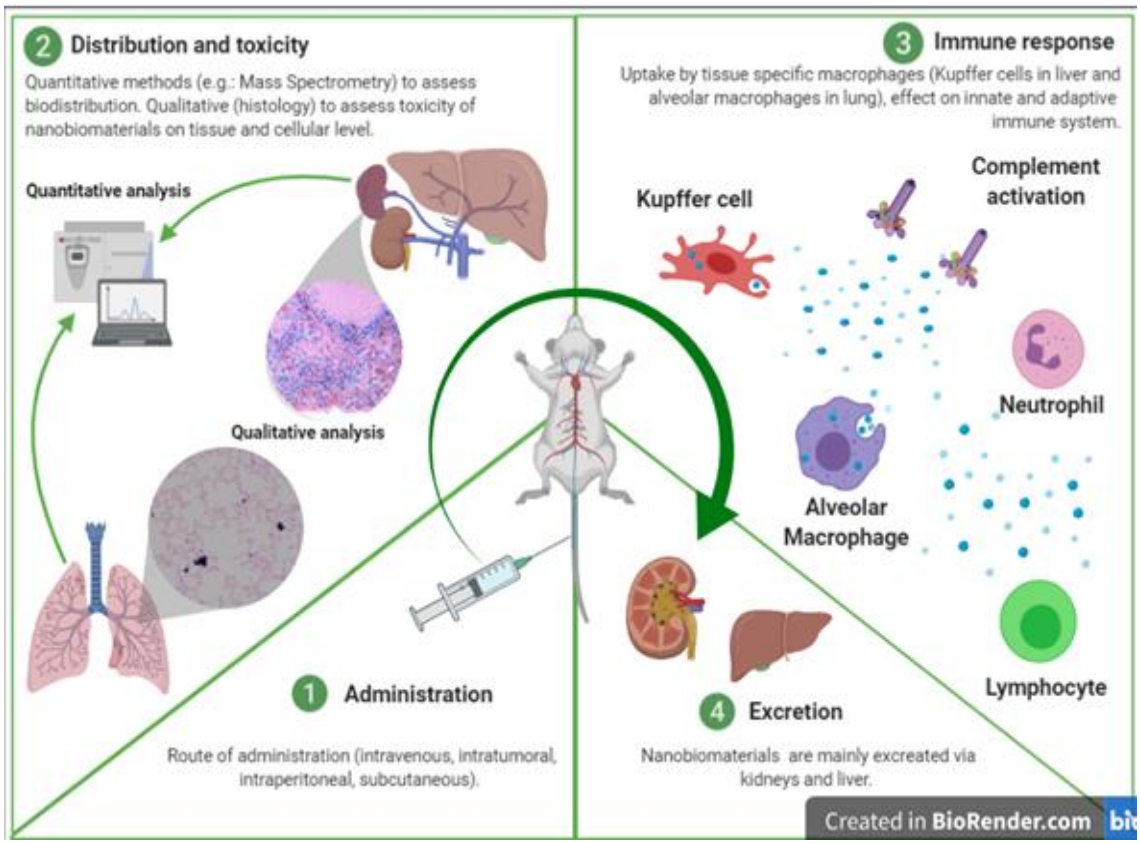

Figure 1.3: Considerations for *in vivo* testing of NBMs
Schematic representation of key aspects in *in vivo* testing of NBMs. Route of administration (number one, bottom left panel) strongly influences all features depicted in this diagram. Distribution and toxicity of NMBs (number two, top left panel) can be assessed using quantitative biochemical methods such as Mass Spectrometry or more qualitative methods such as histology staining. Top right panel (number three) highlights possible immune response to NBMs which are considered 'foreign' by the cells of immune system. Route of excretion (number four, bottom right panel) can also be examined with biochemical methods, by measuring contents of excretory products (urine and faeces).

1.3.1 *Biodistribution*

Biodistribution plays a significant role in the evaluation of NBM's diagnostic and therapeutic efficacy, biocompatibility, safety, and toxicity. Following an intravenous administration (as this is the most common route of parenteral administration), the vascular system controls the transport and residence of NBMs in each organ, and thus regulates NBMs flow, adhesion to the circulatory walls, binding, and distribution throughout the whole body (Figure 1.4). In addition, *in vivo* biodistribution of NBMs in healthy animal models is known to be composition-, size-, shape-, and surface charge-dependent.

Effect of size on biodistribution of NBMs have been extensively researched over the past

few decades. For example, study by Yang *et. al.* [77] evaluated biodistribution of carboxyl-coated iron oxide MNPs with a range of sizes (10, 20, 30, 40 nm) in mice. They reported on size dependent biodistribution with the smallest MNPs (10 nm) showing the highest uptake in the liver, whereas the largest MNPs (40 nm) showing the highest uptake in the spleen on day 1-post injection. Furthermore, the biodistribution of liposomes *in vivo* is also affected by size of the particle. For example, liposomes in blood vessels within the diameter range of 100-150 nm do not easily penetrate capillaries that perfuse tissues such as lung, kidney, and heart [78].

The shape of NBMs has also been shown to influence biodistribution and the phagocytic fate. For example, Champion and Mitragotri demonstrated that spherical NBMs undergo rapid phagocytosis by macrophages in comparison to NBMs with elliptical and elliptical disk shape [79]. Interestingly, NBM's shape also dictates the clearance pathway, where spherical and rod shaped NBMs tend to accumulate in liver and spleen, but disc like particles tend clear through kidneys [80].

Surface charge measured as zeta potential (ζ) is another factor strongly influencing biodistribution of NBMs *in vivo*. An extensive study on the effect of gold nanoparticle charge on their biodistribution was published by Elci *et al*. [81]. They found that surface charge has a notable effect on biodistribution of NBMs *in vivo*, specifically their sub-organ distribution as demonstrated by different pattern of accumulation in the glomeruli. Positively charged NBMs were found to accumulate in the glomeruli, whereas neutral and negatively charged materials were not.

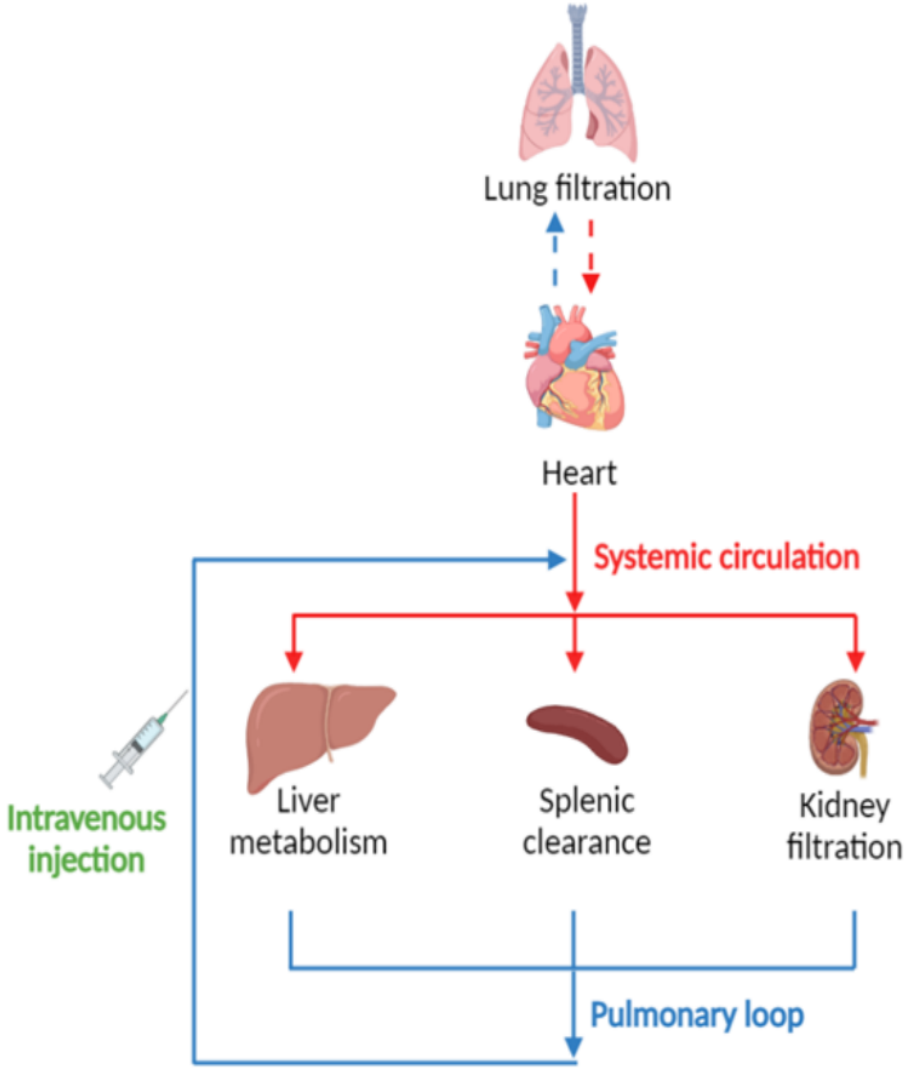

Figure 1.4: Biodistribution of NBMs *in vivo*
Graphical representation of biodistribution of NBMs to organs following an intravenous administration. Red lines represent oxygenated blood flow; blue lines represent deoxygenated blood flow. Figures are not to scale with each other. Created with BioRender.com.

Despite an extensive research on how different properties of NBMs influence their biodistribution following an intravenous injection, there is still a lack of knowledge on the dynamics of NBMs transport at the sub-organ level [82]. In order to understand this complex interaction, novel precise imaging techniques are required to simultaneously visualise NBMs and general structures of the organs in 3D down to cellular level.

1.3.2 *Toxicity and immune response*

Toxicity of NBMs to organs can present in a number of ways including pathological changes such as morphologic changes (gross, microscopic, and ultrastructural) and functional damage. The former is commonly assessed with histological techniques. Haematoxylin and Eosin (H&E) stain allows to visualise abnormal changes to structures and individual cells using brightfield microscopy. For example, in study by Wan *et al*., [83] lung injury and DNA damage in mice in response to intratracheally administered titanium and cobalt NBMs was demonstrated in H&E stained tissue sections. Immune response in form of inflammation infiltration can also be observed in H&E stained sections; however, this can be caused in response to damage caused by the material such as necrosis, or NBM itself. Research on the effect of NBMs on the immune system is currently expanding to address the knowledge gap on how different cells of the immune system respond to different materials.

The immune system is composed of organs/tissues, cells, and the products of cells such as cytokines and complement proteins. There are two branches of the immune system, innate and adaptive (Figure 1.5). Innate immune response is initiated within seconds, generating a non-specific inflammatory response when in contact with foreign bioactive agent such as pathogens and viruses. Cells of the innate immune system possess no immunological memory. In contrast, adaptive immune response is generated gradually over 3-4 days targeting specific antigens on pathogens and foreign materials by production of antibodies. Both branches of the immune system function cooperatively to provide a comprehensive response to a potential threat. NBMs can activate both innate and adaptive branches of immune system, initiating a response from different cells.

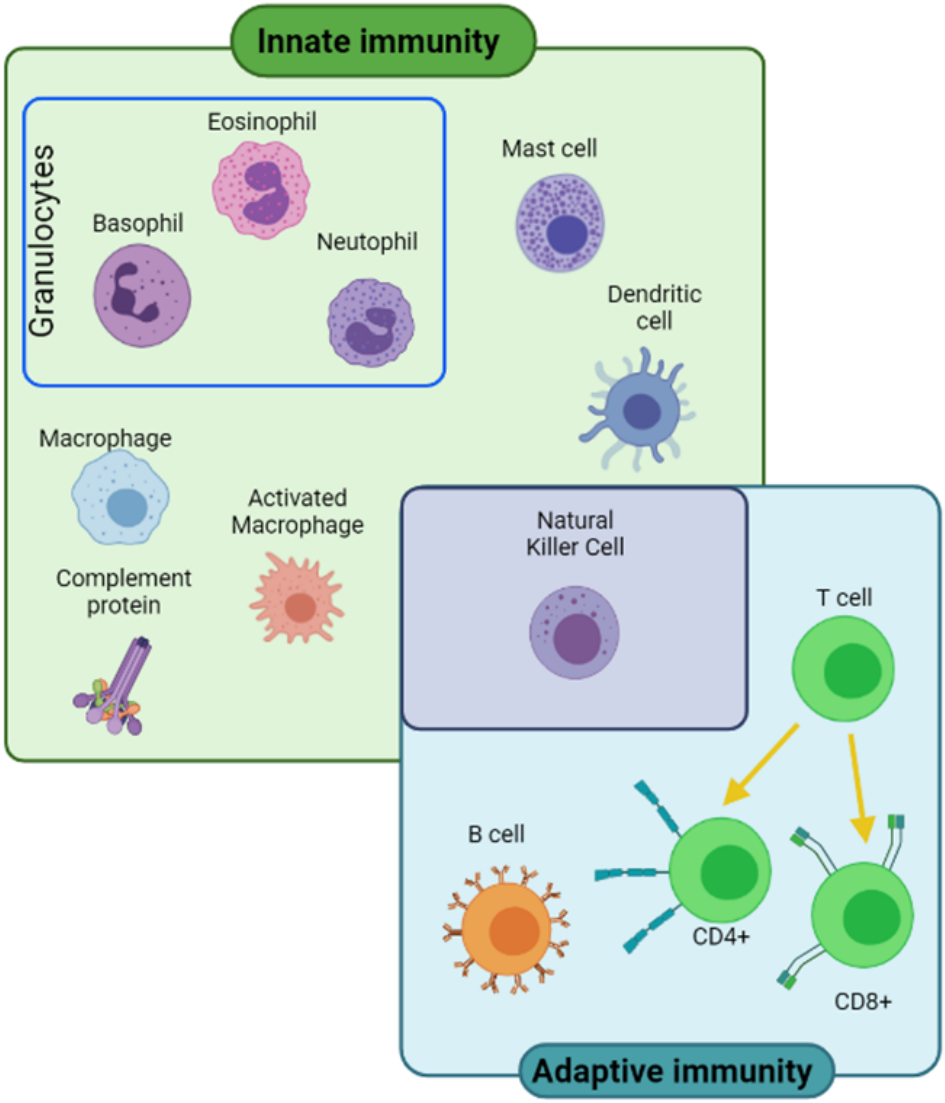

Figure 1.5: Cells of the immune system
Immune system is composed of two branches, innate (green background) and adaptive (blue background). Each of those branches contains cells and proteins with unique functions. Natural Killer cell is considered as a cell of both branches of the immune system which is depicted as a purple background. Figures are not to scale with each other. Created with BioRender.com.

Cells and proteins of the innate branch of the immune system act as a first line of defence against anything considered "foreign". NBMs often fall within this category, subsequently activating a response from the immune cells. Each cell of this branch has a unique mode of defence and interaction with NBMs. This area of research is still in early stages, however recent publications described few possible mechanisms:

i. **Eosinophils:** associated with allergic reactions, parasitic infections and chronic inflammation. They contain proteins which have a strong cytotoxic effect and a neurotoxin causing dysfunction in parasitic organisms. So far, it is unclear how NBMs could activate eosinophils and/or alter their structure. In the past few years,

several studies reported on potential mechanisms behind activation of human eosinophils with various NBMs [84, 85]. However, as this area of research is still relatively new, it will be years before we can fully comprehend interaction of NBMs with this type of immune cell.

ii. **Neutrophils:** the most common type of granulocytes. The cytoplasm of granulocytes contains three types of granules which contain various enzymes, complement activators, and antimicrobial peptides. Neutrophils are active phagocytes that use number of surface receptors to recognise infectious agents at the site of inflammation. Limited publications are available on the effect of NBMs on neutrophils, despite the fact that those cells are the first responders in an inflammatory reaction. Recent review article by Keshavan *et al*. [86] discussed what is known on this topic so far, and also highlighted the importance of understanding the interactions between nanomaterials and neutrophils for development of safe and effective NBMs for biomedical applications.

iii. **Mast cells:** contain secretory products such as histamine, heparin, eosinophil chemotactic factor, neutrophil chemotactic factor, cytokines and interleukins are stored in granules which are released when mast cell is activate recruiting other immune cells. Mast cells can be activated via binding of an antigen onto IgE antibodies present on their surface. Second activation mechanism is induced during complement protein activation.

iv. **Macrophages and dendritic cells:** antigen-presenting cells**.** Their function is to phagocytose foreign bioactive agent and process antigen material which they can present on their cell surface to the T cells.

v. **Complement activation (multiple cells involved):** the complement system is a biological cascade made up of multiple serum proteins. Upon intravenous injection, the NBMs, as any foreign body unrecognised by the immune system, can induce complement activation where complement proteins are cleaved into subunits. Some of those subunits can act as opsonin, inducing phagocytic cells to phagocytose foreign material to which this protein is bound. It is well documented that certain types of NBMs can activate complement system causing what is known as Complement activation-related pseudo-allergy (CARPA) [87]. Interestingly, PEG which is often used to coat NBMs to stabilize liposomes or improve biocompatibility has been shown to induce CARPA [88]. This highlights the need for detail safety studies of NBMs prior to clinical trials, as even materials believed to be safe can induce severe side effect *in vivo*.

Cells of the adaptive branch of the immune system include B and T lymphocytes, which are responsible for the production of antibodies. As previously mentioned, dextran and PEG are examples of materials used to improve biocompatibility and circulation of NBMs. Those materials are now known to influence the adaptive immune system which in turn produces acquired antibodies [89, 90]. These enhance the process of particle clearance by opsonization, activate the complement system, and induce the inflammatory response, occasionally accompanied by hypersensitivity reactions which can lead to anaphylactic shock and death. This type of the immune response could be tremendously problematic when NBMs are used for medical applications which require multiple doses such as chemotherapy or vaccines. On the other hand, since antibodies are widely used in an array of biological assays (e.g.: flow cytometry, enzyme-linked immunosorbent assay, immunohistochemistry), antibodies against specific coating material on NBMs could be utilised to detect those materials *in vitro* and *ex vivo*. Two case studies presented later on in this thesis work are benefitting from the use of anti-dextran and anti-PEG antibodies to detect NBMs in tissue sections by means of immunofluorescent staining. This technique is widely used in histology which is required by the regulators as part of the the preclinical dossier data preparation on the potential use of NBMs in medical technologies.

1.4 Role of histology in preclinical testing of NBMs

Histology is one of the gold standards in the field of toxicology, and in the emerging nanotoxicology field. In the latter, the toxicity of NBM and any immune response can be examined on tissue, cells and at subcellular level. As previously stated, it is also recommended during the *in vivo* safety evaluation at preclinical level as a part of any clinical investigation request to the regulatory agencies. Despite multiple advantages, for the NBM assessment, the current preclinical (also extended to clinical) histology is facing some shortcomings. For example, the detection of NBMs in histology sections highly depends on their chemical composition and detection level. Materials made from carbon and iron can be detected in commonly used Haematoxylin and Eosin (H&E) stain (Figure 1.6). However, organic particles such as liposomes cannot be always seen in H&E-stained sections due to their natural lipid composition. Moreover, imaging techniques that are currently used for microscopic detection of liposomes such as high-resolution transmission electron microscopy, can be expensive and time consuming. Conversely, techniques used in histology such as co-staining can provide cost and time effective solution for biodistribution and toxicity studies. For example, with suitable stains, specific type of immune response seen as influx of identified immune cells and specific location of liposomes could be evaluated in a single slide providing insight to accumulation and effect of those materials in

specific organs.

The second limitation of current histology applied in NBM research is that complex 3D biologic structures, such as organs or their constitutive organ units, are simplified to 2D biological assessment or during histological sample preparation. With novel NBMs being designed to target specific sites, such a, for instance, hepatic stellate cells in liver or mesangial cells of glomeruli in the kidney, it is necessary to observe those sub-organs in 3D to achieve accurate evaluation [91]. In the past few years, number of researchers have extended the use of digital microscopy to three dimensions by stacking digital images of serial sections [92]. This technique could be consequently used in safety assessment of NBMs provided that those materials can be visualised using a brightfield or fluorescent microscope.

Further into the limitations of current histology, is that even with specialised stains used for the detection of NBMs, these studies are considered only as qualitative investigation. Scoring (or grading) methods have been introduced to provide semi-quantitative tools for extracting data from histology samples for analysis and group comparisons [93]. However, those methods are highly subjective, with person-to-person variability in results. To obtain more quantitative results, representative photomicrographs need to be manually segmented for further analysis. As this process is extremely time consuming, computerised segmentation of photomicrographs is highly needed to obtain repeatable and accurate results with minimal user input.

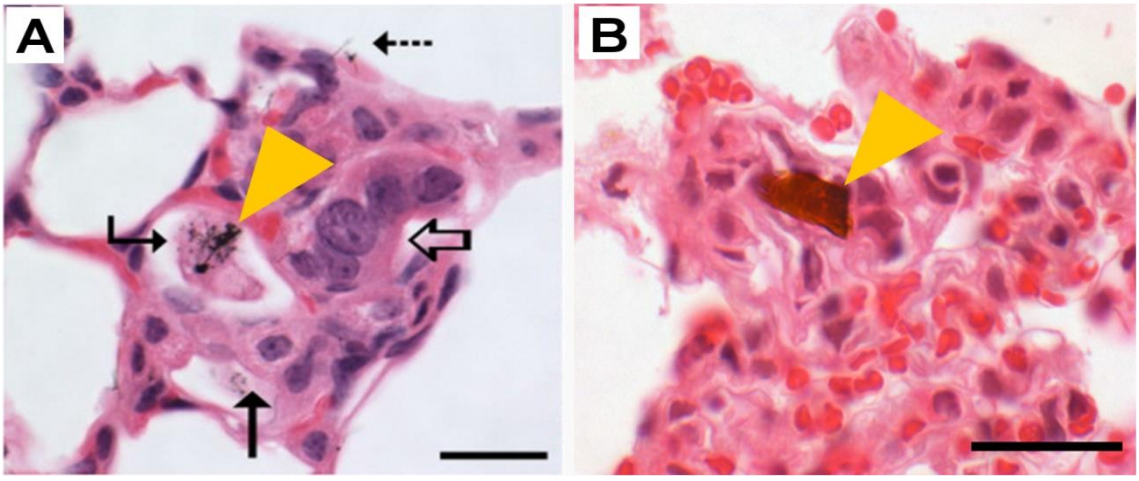

Figure 1.6: NBMs in H&E stained sections
(A) Photomicrograph from the lung of a mouse 28 days after aspirating 20µg multi-walled carbon nanotubes; Scale bar 20 µm. Adapted from Porter *et al.*[94]; (B) Photomicrograph of H&E stained rat lung section 7 days after intravenous injection of 30 mg/kg of SPION; scale bar 25 µm. Orange arrowhead indicates NBMs.

In order to address some of the above reported limitations and to address the shortfalls in semi- to quantitative assessment for NBM toxicity, the next section introduces the use of machine learning (ML) for quantitative analysis of bioimages; examples are also presented for clarity. Then, Chapters 4 and 5 exploits using this technique for semi- to quantitative histology studies of iron oxide MNPs by comparing traditional 2D tissue sections and then expanding to 3D histology volumes. To provide clear and widely applicable use of the ML, the general concepts of machine learning will be introduced based on the dedicated software adopted in this PhD research project. Machine Learning terminology and methods will be detailed in their technical aspects applied to bioimage analysis.

1.5 Machine Learning for bioimage processing

Microscopy is an indispensable part of modern biological research (both *in vitro* and *in vivo*), with new state-of-the-art equipment allowing for more efficient and detailed imaging. However, immense amount of complex data created using these systems has led to an increased demand for automated or semi-automated processing and analysis [95].

Image segmentation is one of the key techniques used in the processing of biological images for multiple purposes, such as counting objects (e.g.: specific cells, micro metastasis, sub organs), measuring object distribution, and measuring shape and appearance of individual objects [96]. Manual segmentation is a laborious process prone to bias. Computerized segmentation provides a solution to achieve consistent and accurate results from a number of images with minimal user input and associated operator-dependent error [97]

In recent decades, artificial intelligence (AI) [98] has been widely used in many areas, ranging from proteomics and drug discovery [99] to its application in FDA approved diagnostic tools [100]. Machine learning (ML) is considered a branch of AI, where a set of representative data is used to develop algorithms based on patterns which can be used to make predictions; simply put, it is learning through experience. Generally, machine learning algorithms can be categorised as:

a) Unsupervised: independent ability to find patterns

b) Supervised: classification and prediction algorithms are based on provided examples.

Classification is a common machine learning discipline where a training data is generated by manually labelling representative examples according to predefined classes (Figure 1.7). In terms of image analysis, a series of features are extracted to discriminate the classes. As a result,

a segmented image is generated with each pixel assigned to a predefined class. Numerous software platforms are available for bioimage analysis using ML. Fiji (also referred to as Fiji/ImageJ) is an open source software commonly used by researchers for image processing and analysis [101]. For purpose of this thesis, a Trainable WEKA (Waikato Environment for Knowledge Analysis) Segmentation [102] plugin from Fiji was used as its user-friendly graphical user interface (GUI) was designed for users with limited knowledge of machine learning. The following sections will therefore use this software as an example to introduce some of the concepts of ML in bioimage analysis.

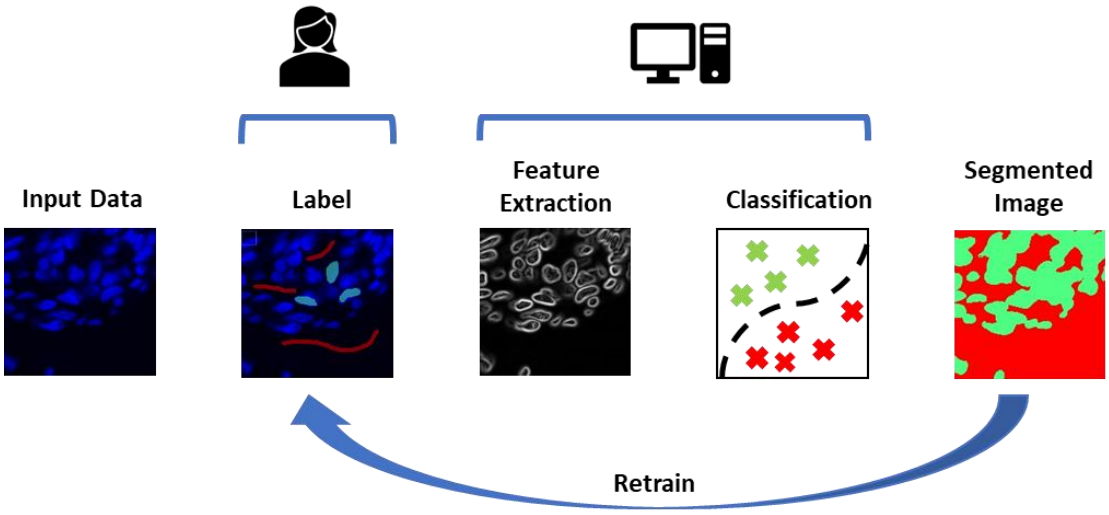

Figure 1.7: Supervised machine learning for bioimage analysis
Graphical representation of the workflow applied in the supervised machine learning for bioimage analysis. Input data should include representative images of the entire dataset, as for variability in staining intensity, example of control (positive and negative), and example of test samples. Images are manually annotated by a specialist to "train" the software with data for determining parameters for each predefined class. In the example shown, two classes were selected as nuclei seen in blue in original image (left hand side), annotated with green label (right hand side), and black background annotated in red. The software adopts pattern and features recognition, and builds a classifier based on the extracted parameters. These are used to assign pixels to each predefined class. In the final step, images are segmented to discriminate between different classes. The entire process can be repeated to retrain the classifier if needed to provide for better accuracy.

1.5.1 *Trainable WEKA segmentation*

Trainable WEKA Segmentation (TWS) plugin for Fiji is an open source machine learning tool for pixel classification and segmentation using supervised image classification approach, extensively used to develop methods for high-throughput image analysis [98, 103] and 3D segmentation [104]. GUI makes TWS easy to use (Figure 1.8A) for researchers with limited experience in programming who need to perform advanced bioimage analysis.

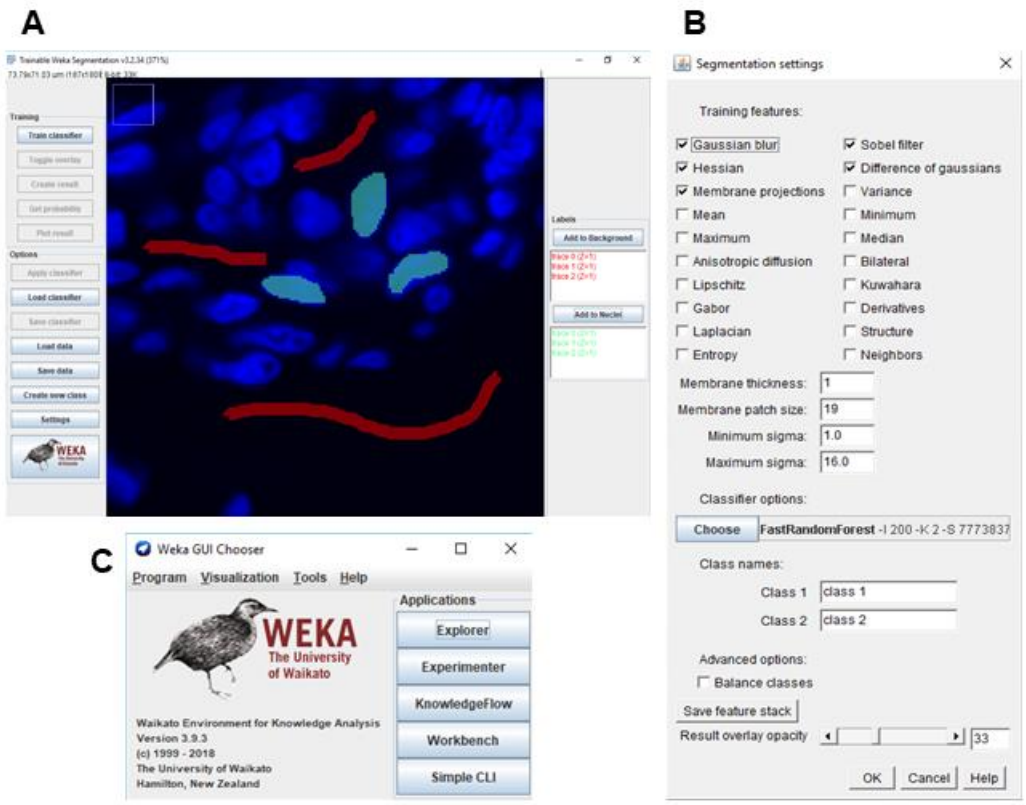

Figure 1.8: TWS software
User friendly GUI in WEKA (A) allows to manually draw regions of interest which can be added to predefined classes seen on the right had side of the menu. By default, there are two classes which can be renamed using the settings menu (B) and where more classes can be added. Additionally, the settings menu allows to select training features for the classifier. Data extracted from the training images can be further assessed using one of the options in WEKA GUI chooser (C). For example, the performance of the classifier can be assessed using WEKA explorer.

Settings menu in TWS (Figure 1.8B) allows to select classifier and suitable parameters to train classification model. Image features are extracted using filters included as a part of Fiji. The features available in TWS can be categorised as:

a) Edge detectors: Laplacian, Sobel, difference of Gaussians, Hessian matrix, Gabor

b) Texture filters: minimum, maximum, median, variance, entropy, structure tensor etc

c) Noise reduction filters: Gaussian blur, bilateral filter, Anisotropic diffusion, Kuwahara and Lipschitz

d) Membrane detectors: localise membrane like structures

An effect of different filters on a binary image is shown in Figure 1.9.

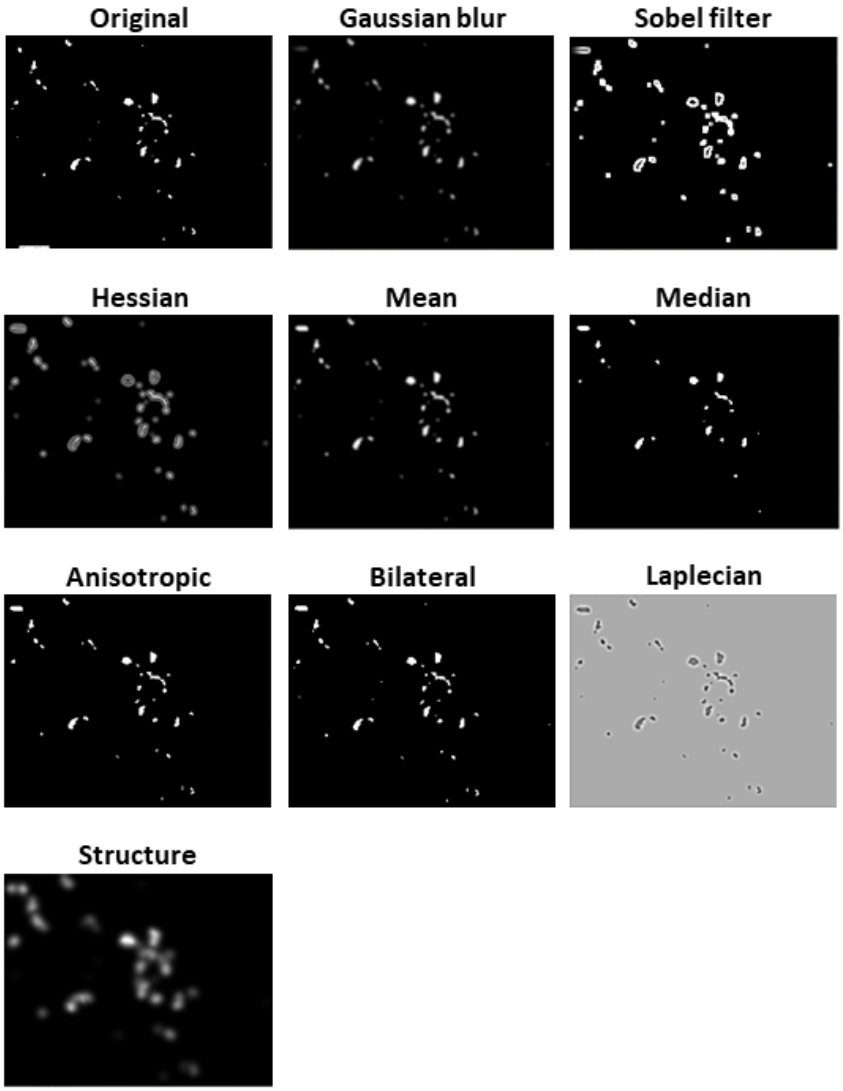

Figure 1.9: Representative example of filters available in Fiji for image feature extraction
Fiji provides a number of filters for feature extraction . As shown in this example these filters can improve an image to detect objects of interest (white objects in original image). However, not every filter will be suitable for every image as shown here with Hessian filter which diminished quality of the original image.

Fast Random Forest (FRF) is selected as a default classifier in TWS; this algorithm is a multithreaded implementation of the Random Forest classifier. This supervised learning algorithm builds 'forest' containing multiple decision trees such that each tree depends on the values of random vector [105]. Default settings in TWS build a model with 200 trees and 2 random features, those settings can be changed to improve performance and reduce processing time. Number of classes can also be changed and renamed as needed. Example image in Figure 1.8 had two classes, nuclei seen in blue and black background. Classes are colour coded as seen in example image where class 1 (background) is in red, and class 2 (nuclei) is in green. Regions of interest (ROI) representative of objects to be classified are manually drawn and added to each class. Train classifier button initiates the training process. Once completed, segmented image is

overlaid on original image used for training. More labels can be added to retrain the classification model to improve performance. Data generated during training process can be saved and examined in WEKA's Explorer environment (Figure 1.8C). In the explorer, performance can be analysed using training data by calculating performance statistics such as percent of correctly classified instances, precision, recall and F-measure for each class. This type of analysis can be indicative of how model will perform, however as data is obtained from ROI's used for training, performance metrics can be overestimated. It is therefore advised to add an additional method to validate the model which will be discussed in next section.

The TWS gives two options for generating results. 'Create results' option generates segmented red, green, blue (RGB) images with each object colour coded in a class colour. 'Get probability' option generates probability maps which are binary images where the pixel intensity value represents computer's certainty that a specific pixel belongs to a specific class. Probability maps give more flexibility in terms of post-processing and further analysis where additional steps such as thresholding can be introduced to improve accuracy.

1.5.2 *Performance metrics*

The performance of segmentation method can be evaluated using multiple metrics. Those methods not only assess the final result, but also provide a figure which has to be optimised by tuning the classifier parameters [106]. Classified images are evaluated by comparing them to manually segmented images referred to as 'ground truth'. Figure 1.10A shows an example of histology image. Tissue seen in pink was manually segmented (orange segment in Figure 1.10B) to create a ground truth image which was overlaid onto binary image generated by TWS (orange contour in Figure 1.10 C). Number of true positive (TP), true negative (TN), false positive (FP) and false negative (FN) pixels is determined (Figure 1.10C) to calculate overlap-based metrics. This process is repeated for each class to measure performance of the model.

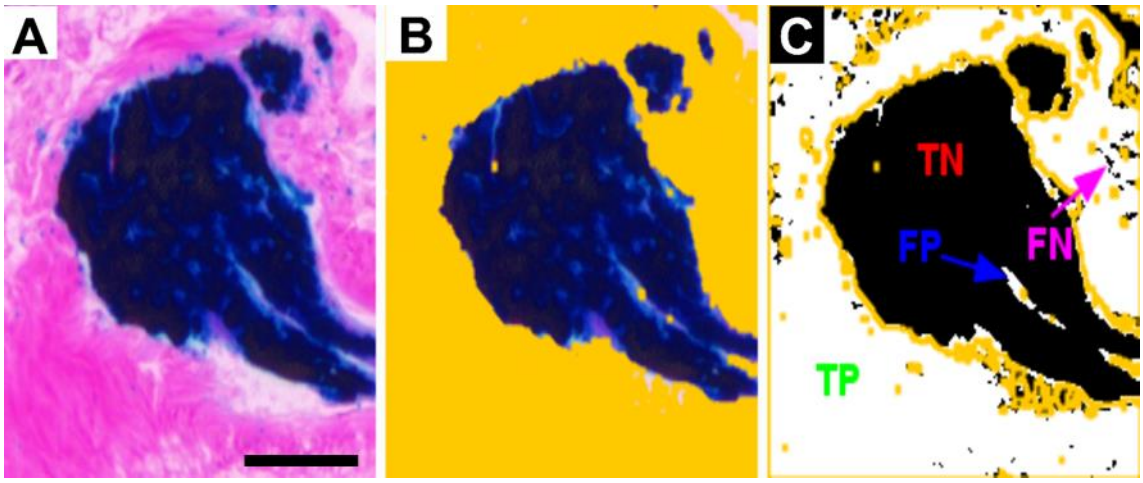

Figure 1.10: Graphical representation of pixel-based metrics
(A) Original photomicrograph of lung tissue (pink) with iron aggregate (blue), (B) area manually segmented (orange) as ground truth for tissue; (C) overlay of ground truth outline (orange line) onto binary image generated using TWS; Pixels are categorized as True Positive (TP), True Negative (TN), False Positive (FP) or False Negative (FN).Scale bar in the original image represents 25 µm.

Multiple statistical metrics can be used to measure the performance of the classifier. Dice coefficient [107] and Jaccard index [108] (Figure 1.11) are commonly used metrics in segmentation. Dice Coefficient (also known as F1 measure) is two times the area of overlap divided by the total number of pixels in both images. Jaccard index (also known as Intersection - Over - Union) is the area of overlap between the predicted segmentation and the ground truth image divided by the area of union between the predicted segmentation and the ground truth. Both of those metrics range from 0 to 1 (0 to 100%) with 0 signifying no overlap and 1 signifying perfectly overlapping segmentation.

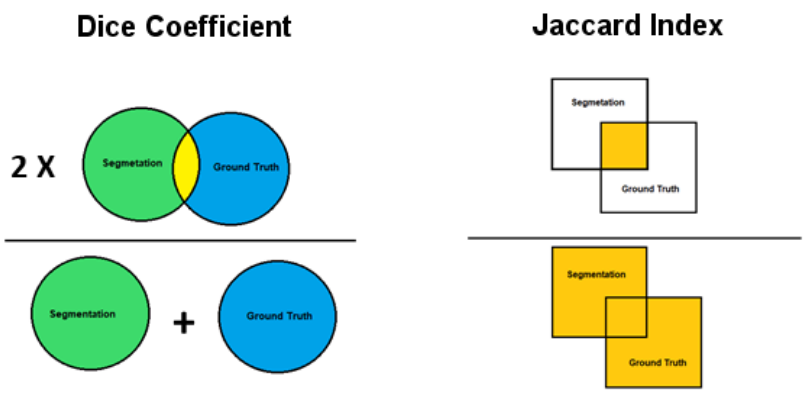

Figure 1.11: Visual representation of performance metrics
Dice coefficient and Jaccard index are two most commonly used statistics to measure performance of a classifier. Dice coefficient is calculated as twice the area of overlap (seen in yellow) between two images divided by a sum of areas of two images. Jaccard index is calculated by dividing an area of overlap of two images (orange square in the nominator) divided by the area of union of two images.

Accuracy is another example of commonly used metrics. It is defined as a ratio between the correctly classified samples to the total number of samples [109]. However, accuracy and Jaccard index are biased with respect to data imbalance where one class dominates the image, while other class(es) make up small portion of the image [110, 111]. Alternative measures are unaffected by this data imbalance calculating more reliable measure of classifier model performance. For example, Matthews's correlation coefficient (MCC) accounts for all four pixel-based metrics (TP, TN, FP and FN) overcoming data imbalance. MCC ranges in the interval -1 to 1, indicating perfect misclassification and perfect classification respectively [112]. Selecting the right evaluation metric is crucial in achieving the optimal classifier during the training process [113]. As all metrics have their own intrinsic advantages and disadvantages, and it is advised to use the most suitable ones simultaneously when assessing performance of the classifier. In terms of NBMs research, recent article by Winkler [114] emphasised the role of AI and ML in nano safety. Focus of this publication was on the use of ML to model nanomaterials datasets relevant to their possible adverse biological or ecological impacts, the use of these data to progress the "safe-by-design" paradigm, and their use by regulators of nanomaterials. Furthermore, the author discussed the list of ambitious milestones set by the participants of the exploratory workshop on Quantitative Nanostructure Toxicity Relationships held in 2011 in the Netherlands [115]. One of the two-year milestones included developing better methods for tracking nanoparticles in the body. Those two areas of research (ML in nano safety and methods for detection of NBMs) were a foundation for experimental work undertaken in this PhD project as outlined in the next section

1.6 Hypothesis and aims

As presented in section 1.2.1, the lack of regulatory guidelines in terms of standardised assessment criteria for advancing NBMs for biomedical applications into clinic, it is particularly true when it comes to the evaluation of the in vivo safety data for NBMs. While histology studies are recommended by the regulators in preclinical safety studies, there is an untapped potential in terms of how those techniques are used in NBMs research. More information regarding interaction of those materials with biological structures can be extrapolated from histology slides by adding specialised stains for the detection of NBMs in tissue sections. This also enable the quantitative analysis on histology images. Therefore, to contribute to the expansion of the scientific knowledge in this area, this PhD experimental research-based project is conceptually designed to address the following hypothesis:

"Can an extensive histological analysis add highly valuable details on biodistribution, toxicity and immune response to NBMs for the *in vivo* preclinical assessment?"

To validate this hypothesis, this thesis follows case-studies design, with in-depth histological analysis carried out on two types of NBMs commonly used for biomedical applications and medical technology: liposomes and Iron Oxide Magnetic Nanoparticles (referred to from this point as MNPs).

The following aims are set for assessing the liposomes:

i. To identify, test and verify a suitable histology stain for liposome detection.

ii. To differentiate between liposomes and naturally occurring lipids.

Whereas the following aims are set for assessing the iron oxide MNPs:

i. To perform qualitative and semi-quantitative analysis on iron deposits detected in various tissue sections with the use of ML.

ii. To reconstruct organ samples in 3D volumes for elucidating the complex distribution of particle accumulation in *in vivo* studies.

The next four chapters present the methodological procedures and results highlighting the key findings obtained during this PhD project. Corroborating and supporting technical data, imaging, and results are included in the appendix (chapter 8) where to provide depth of the work carried out.

2 Chapter 2: Materials and methods

This chapter will present an introduction to the nanobiomaterials (NBMs) fingerprinting as technical properties characterised within the methods developed within the extensive involvement of the LBCAM with EU FP7 and Horizon2020 projects (e.g., MULTIFUN, EUNCL, NoCanTher). The in vivo experimental design and rationale for the investigation of selected nanobiomaterials is here presented concerning the details of the methodologies, protocols and step by step investigation approach taken across the 4 case studies which are at the make of the results for this thesis. From animal license, welfare and handling to organs and tissue harvesting, preparation, imaging and recording, and statistical analysis are here presented. The key findings and results are presented in the next chapters. The extended list of materials and equipment used throughout this project are reported in the appendix (Supplementary table 8.1 to 8.5) for convenience and reproducibility.

2.1 Nanobiomaterials

As described, several NBMs were chosen as representative materials for this study. The summary of the physico chemical characterisation properties of each NBM used in this PhD project are reported in Table 2.1. This information was provided by the suppliers of the material, with characterisation carried out in line with the most relevant techniques available. As stated, the materials are all supplied within the framework of large collaborative European projects where the LBCAM was one of the partners involved in the pre-clinical testing for these.

Table 2.1: Summary characterisation of nanobiomaterials as provided by the suppliers

Listed materials were used in *in vivo* studies. These were divided in relevant case studies as presented and results reported in chapters 3, 4, and 5 as outlined in the top row.

Case study	Case study 1 (chapter 3) *In vivo* toxicity and biodistribution of NIR-dye loaded liposome for imaging applications	Case study 1 (chapter 3) *In vivo* toxicity and biodistribution of NIR-dye loaded liposome for imaging applications	Case study 2 (chapter 3) *In vivo* toxicity and biodistribution of liposomal irinotecan	Case study 3 (chapter 4) *In vivo* toxicity and biodistribution of MF66 MNPs	Case study 4 (chapter 5) *In vivo* acute toxicity study of NOC0007 and RCL-01 MNPs	Case study 4 (chapter 5) *In vivo* acute toxicity study of NOC0007 and RCL-01 MNPs
Name	LipImage™815 (referred to in thesis as dye-loaded liposome)	Lipidots (referred to in this thesis as carrier control)	Onivyde™	MF66 MNPs	NOC0007 MNPs	RCL-01 MNPs
Type of material	Lipid nanoparticles with IR780-Oleyl dye	Lipid nanoparticles, filled with soybean oil	Liposomal irinotecan	Magnetite (Fe_3O_4)	Maghemite (γ-Fe_2O_3)	Iron Oxide
Primary size (nm)	N/A	N/A	N/A	12 ± 3	14	50 ± 25
Coating	Myrj™S40	Myrj™S40	Polyethylene glycol (PEG)	DMSA	Dextran 40kD	Dextran
Hydrodynamic diameter (nm)	46 ± 1	46 ± 1	~ 110	89 ± 0.5	122.6	149
Zeta Potential (mV)	- 2.5 ± 0.5	- 2.5 ± 0.5	~ -16	- 46 ± 0.7	-6.5	-20.5
Polydispersity index (PDI)	0.093	0.094	<0.1	0.36		0.26
Endotoxin (EU/ml)	<1 In solution with lipid concentration of 94 mg/ml; Measured with chromogenic LAL assay	<1 In solution with lipid concentration of 92 mg/ml; Measured with chromogenic LAL assay	<1 In a solution containing 4.3 mg/mL irinotecan free base; Measured with chromogenic LAL assay	N/A	<1.6 In a solution with iron concentration of 130 mg/ml; Measured with turbidimetric-kinetic method	0.4 In a solution with iron concentration of 72 mg/ml; Measured with turbidimetric-kinetic method
Supplier	Supplied by collaborator at CEA Letti, Grenoble, France.	Supplied by collaborator at CEA Letti, Grenoble, France.	Purchased from Pfizer	Supplied by collaborator from IMDEA, Madrid, Spain	Supplied by collaborator from IMDEA, Madrid, Spain	Purchased from Resonant Circuits Limited

2.2 *In vivo* experiments

This section is focused at providing the general information and details for the *in vivo* study at the basis of this PhD work. The section will present the key aspect relevant to *in vivo* animal study from welfare and wellbeing to housing and clinical evaluation. For convenience, the graphical representation of the experimental design for each case study is reported in the specific chapters: chapter 3 liposomes; chapter 4 iron oxide MNPs and chapter 5 novel iron oxide MNPs. However, in order to provide the basic experimental workflow the key aspects are here presented in Figure 2.1.

In vivo studies presented in this thesis were a part of collaborative European projects funded by the European Commission (EUNCL, MultiFun, and NoCanTher) aiming to bring novel nanobiomaterials to clinical trials. To satisfy requirements of the regulators (EMA and FDA), studies in small rodents presented in this thesis were carried out as a part of the pre-clinical assessment essential to apply for marketing authorisation.

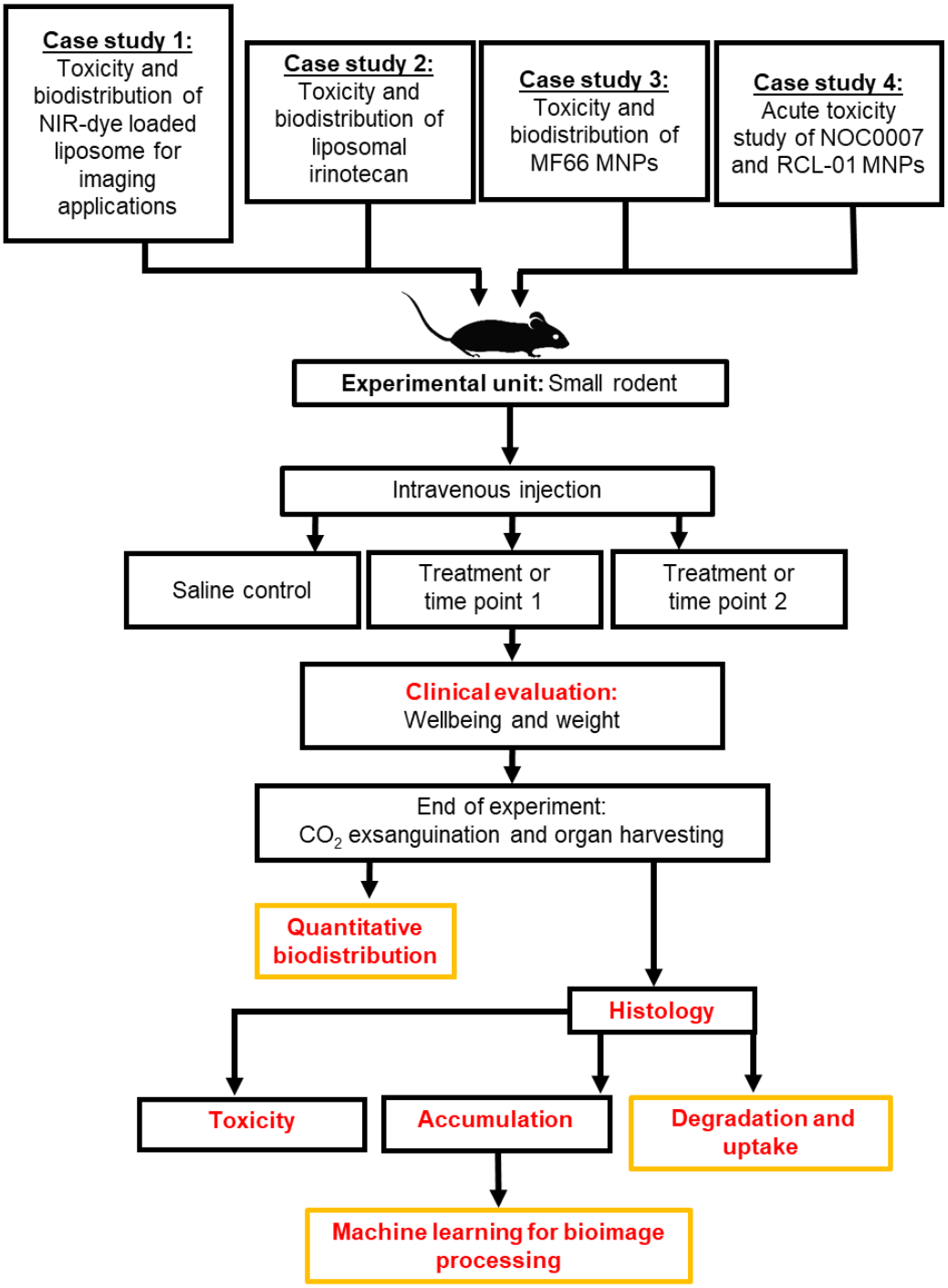

Figure 2.1: Schematic workflow for *in vivo* case studies
From top to bottom, first row of the diagram introduces four case studies which will be discussed in this thesis. Small rodents (rat or mice) were used as experimental unit in all studies, with intravenous injection selected as a route of administration of the material tested. Animals' wellbeing was monitored by measuring weight and assessing wellbeing on a daily basis. At the end of the experiment animals were humanely euthanized, and organs of interest were harvested for the analysis outlined in boxes shown in the bottom four rows. Red text indicates points at which data was collected and will be presented in the results chapters 3 to 5. Orange boxes indicate analysis, which was not adequate for every case study used, details listed in black boxes remained constant in all four case studies.

2.2.1 *Animal housing*

The experimental protocols employed in this thesis were approved by the Animal Research Ethics Committee of the Trinity College Dublin and complied with Health Products Regulatory Authority (HPRA) Ireland, in accordance with the Directive 2010/63/EU; Project license number AE19136/P073 and AE19136/P089 Animals were supplied by Trinity College Dublin BioResources Unit (unless otherwise stated) and housed in a thermo-regulated environment with a 12 h light/dark cycle for at least 1 week before the experiments. Food and water were available at libitum. Animal procedures cwerearried out by fully trained and licensed personnel (HPRA individual authorisation number AE19136/I104 and AE19136/I450) whom at all stages assessed and recorded the well-being of the animals according to the severity score sheet (Supplementary table 8.6 and Supplementary table 8.7). At the end of experiment, animals were humanely euthanized in accordance with HPRA Ireland. Details on species, strain, sex, number of animals and procedures carried out are detailed in relevant chapters in the results sections.

2.2.2 *Monitoring animal wellbeing*

Clinical signs such as body weight, activity, appearance, and behaviour can be an early indicator of severe adverse effects and toxicity. For this reason, animals were monitored daily for the duration of the study. Wellbeing of the animals was assessed and recorded according to severity score sheet (Supplementary table 8.6 and Supplementary table 8.7 in the appendix). Change in animal body weight over experiment duration was recorded daily as a percent of initial weight before administration, and was calculated for each animal individually to account for natural variation in initial weight prior to experiment.

2.2.3 *Case study 1: In vivo toxicity and biodistribution of NIR-dye loaded liposome for imaging applications*

The aim of this *in vivo* study was to assess toxicity, biodistribution, organ accumulation, and degradation of NIR dye-loaded liposome (here called LipImage^{TM}815) in comparison to its liposome carrier control (here called Lipidots). This study was approved by the Animal Research Ethics Committee at Trinity College Dublin and the Health Products Regulatory Authority (Project license number: AE19136/P073). The number of mice per group was based on a power calculation for weight carried out in G*Power; details of the calculations are provided in the appendix section 8.1.1.

Preliminary *in vivo* studies of LipiImage^{TM}815 were carried out by the collaborator on this project where imaging properties were assessed in 6 week old healthy FVB female mice [116]. To investigate biodistribution, degradation and toxicity of this nanobiomaterials, *in vivo* study carried out as a part of this PhD project used pathogen-free, healthy male and female C57BL/6 mice (body weight 23 ± 2 g) supplied by Harlan Laboratories, UK. Animalswere randomly assigned to three experimental groups: saline control, LipImage^{TM}815 (lipid concentration 100 mg/kg) and carrier control Lipidots (soybean oil loaded lipid; lipid concentration 100 mg/kg), each containing three males and four females. Weight and wellbeing of the animals were recorded daily following the injection. Animals were humanely euthanized seven days post injection via CO_2 exsanguination in accordance with HPRA Ireland. Organs of interest were harvested, washed thrice in saline and cryopreserved in OCT (Thermo Scientific) as detailed under section 2.3.1 cryopreserved tissue.

2.2.4 *Case study 2: In vivo toxicity and biodistribution of liposomal irinotecan*

The *in vivo* study was carried out as a proof-of-concept standard operating procedure (SOP) study where a liposome anti-cancer drug recently approved by the regulators was used as a model NBM to optimise a protocol for detecting PEGylated liposomes in tissue sections. For this purpose, liposomal formulation of irinotecan sold under commercial name Onivyde® was selected as a model nanobiomaterial. Study design was based on the information obtained from the assessment report of this formulation published by EMA [117] where a single dose toxicity was assessed in male Sprague Dawley rats with three animals per treatment group. *In vivo* study undertaken as a part of this PhD thesis was carried out in nine pathogen-free, healthy male Wistar rats (body weight 245 g ± 23 g) were randomly assigned to three experimental blocks: saline control, irinotecan, and Onivyde®. Rats were anesthetised by an intraperitoneal (i.p.) injection of a mixture of ketamine (60 mg/kg; Vetalar; Pfizer; Ireland) and medetomidine hydrochloride (0.5 mg/kg; Domitor; Pfizer; Ireland). The left femoral vein was cannulated with heparinized permanent polyurethane intravascular tubing for blood sampling. Rats in the control group (n = 3) were injected with saline through the tail vein; Rats in two experimental groups (n = 3 per group) were injected with irinotecan (20 mg/kg; Sigma-Aldrich; lot number WXBC1849V), or liposomal irinotecan at a dose of 20 mg/kg of irinotecan equivalent through the tail vein. The anaesthetic reversal agent, atipamezole hydrochloride solution (Antisedan, Pfizer, Ireland), was injected ip. at 5 mg/kg. Blood samples (approximately 400µl) were collected in heparinized tubes at the following times: 15 min; 30 min; 1 h; 2 h; 4 h; 6 h; 24 h and 48 h after drug injection. In each case, blood was replaced by an equal volume of isotonic solution. Faecal samples were collected if available at 6 h, 24 h and 48 h post injection. Animals were humanely euthanized 48 h post injection via CO_2 exsanguination in accordance with HPRA Ireland. Organs of interest

were harvested, washed thrice in saline, and cryopreserved in OCT as detailed under section 2.3.1 cryopreserved tissue. The study was approved by the internal Animal Research Ethics Committee at Trinity College Dublin and the Health Products Regulatory Authority (Project license number: AE19136/P073). Details of the power calculation used to determine number of animals per group are included in the appendix, section 8.1.2.

2.2.5 *Case study 3: In vivo toxicity and biodistribution of MF66 MNPs*

To investigate toxicity and biodistribution of MF66 MNPs with MRI and particle electron paramagnetic resonance (pEPR), pathogen-free male and female BALB/c mice (body weight 23 g ± 2 g) purchased from Harlan Laboratories, were injected with 100 µl of MNP solution at 10 mg Fe/ml or saline (control) through the tail vein, and randomly assigned to experimental groups at the post-injection time points (3 h, 24 h, 48 h, 72 h and 5 weeks). Animals were humanely euthanized at selected time points by injection of a high dose of pentobarbital in accordance with HPRA Ireland. Organs of interest were washed twice in saline and processed for paraffin embedding as detailed in section 2.3.1 formalin fixed paraffin embedded tissue.

2.2.6 *Case study 4: In vivo acute toxicity study of NOC0007 and RCL-01 MNPs*

Two formulations used in this study were designed for intratumoral injection for cancer hyperthermia treatment. As a part of the safety evaluation prior to clinical trial, study presented here was designed to mimic a 'failed' intratumoral injection and a worst-case scenario where all injected material reached the bloodstream. This study was approved by the Animal Research Ethics Committee at Trinity College Dublin and the Health Products Regulatory Authority (Project license number: AE19136/P089). Details of sample size for calculation ca be found in the appendix section 8.1.3. Forty-eight pathogen-free, healthy female Wistar rats (body weight 245 g ± 23 g) were randomly assigned to two experimental blocks (NOC0007 and RCL-01). Within each block, animals were further divided into four treatment groups: Saline injection, 30 mg/kg MNPs, 45 mg/kg MNPs, 60 mg/kg MNPs. Single dose intravenous injection (1 mL total volume) was given via tail vein. Weight and wellbeing of the animals was recorded according to the severity score sheet (Supplementary table 8.7) at 0.5, 1, and 2 hours post injection and then daily until study completion on day 7, at which point animals were humanely euthanized via CO_2 exsanguination in accordance with HPRA Ireland. Organs of interest (lungs, liver, spleen and kidneys) were washed trice in saline and processed for paraffin embedding as detailed in section 2.3.1 formalin fixed paraffin embedded tissue.

2.3 Histopathology

This section provides protocols for preparation of tissue samples for histological staining. The section is divided into two main sub-sections detailing protocols for cryopreserved tissue samples used for the liposome *in vivo* studies (two case studies presented in chapter 3), and formalin fixed paraffin embedded tissue samples used for the *in vivo* studies of MNPs (presented in chapter 4 and 5). Different methods for tissue preservation were selected based on the composition of NBMs examined. All histological findings reported in the results chapters 3, 4, and 5 were verified by a certified pathologist from Central Pathology Laboratory in St. James's hospital in Dublin.

2.3.1 *Cryopreserved tissue*

2.3.1.1 Sample preparation

Harvested organs were sampled according to "Revised guides for organ sampling and trimming in rats and mice" published by Registry of Industrial Toxicology Animal-data and North American Control Animal Database [118], To ensure coherence between studies, tissue samples were collected from the same location within an organ in every case study. Samples were immediately embedded in OCT (Thermo Scientific) using disposable plastic moulds and frozen by floating the mould in Isopentane (ACROS Organics) bath cooled to -20˚C. Frozen tissue blocks were stored at approximately -80˚C prior to sectioning. 10 µm thick serial sections were cut on multiple levels of the block using cryostat (Leica, CM1850 UV), with at least 50µm between every level.Sections were retrieved onto positively charged microscope glass slides, air dried and stored at approximately -80˚C prior to staining.

2.3.1.2 H&E staining for frozen sections

Slides were immersed in cold formalin for 10 minutes to fix the tissue and washed in few changes of distilled water prior to staining. Slides were immersed in Harris haematoxylin (RAL Diagnostics, France) for 5 minutes, rinsed in running tap water for 5 minutes, differentiated in 1% acid alcohol and counterstained with Eosin (Sigma-Aldrich) for 3 minutes. Slides were then dehydrated by passing them through a series of alcohol baths at incrementing concentrations and two baths with xylene (Honeywell, Germany). Slides were then mounted using DPX mounting media (Thermo Scientific) and examined under light microscopy (Nikon Eclipse E800) equipped with 0.5x, 10x, 20x, 40x, and 100x lenses. Representative images were acquired using a QCapture Pro software V 6.0.0.605 (MediaCybernetics).

2.3.1.3 Oil red O (ORO) for lipid detection

Staining was carried out according to previously published protocol [119] with slight modifications. Oil red O (Sigma-Aldrich) stock was prepared from powder to a 0.5% w/v solution in isopropyl alcohol (Fisher Scientific) by mixing on magnetic stirrer at room temperature overnight. Stock solution was stored at room temperature up to 6 months. Cryosections were warmed to -20°C for 1 hour, followed by 1 hour fixation in ice cold 10% formalin. Excess formalin was removed by three rinses in deionised water for 30 seconds. ORO working solution was prepared fresh by mixing stock solution with distilled water in 1.5:1 ratio respectively (e.g., 30 ml of ORO stock solution in 20 ml of water). Working solution was incubated for 10 minutes at room temperature and filtered using vacuum filtration system (VWR) with 0.45 µm pore size. This solution was stable for up to 3 hours. Slides were rinsed in 60% isopropyl alcohol for 30 seconds, immersed in ORO working solution for 10 minutes, followed by another 30 second rinse in 60% isopropyl alcohol. Sections were counterstained with haematoxylin solution according to Gill II (Merk) and rinsed in running tap water for 3 minutes. Slides were stained in batches, with each batch containing section from omentum for a positive lipid control. Slides were then mounted using Aquatex® aqueous mounting media (Merk) and examined under light microscope (Nikon Eclipse E800) equipped with 0.5x, 10x, 20x, 40x, and 100x lenses. Representative images were acquired using a QCapture Pro software V 6.0.0.605 (MediaCybernetics).

2.3.1.4 Oil red O staining for fluorescence

To examine lipids stained by Oil red O together with IR780-Oleyl dye loaded in the liposome a previously published protocol [120] was used with modifications. Cryosections were warmed to -20°C for 1 hour, followed by fixation in 4% formaldehyde at room temperature for 1 hour. Sections were rinsed three times in deionised water, permeabilised with 0.5% Triton X-100 in PBS for 5 minutes and washed for 5 minutes in three changes of PBS. Slides were then immersed in Oil red O working solution for 20 minutes. Slides were rinsed three times in deionised water followed by 10 minutes in running tap water. Sections were mounted with ProLong diamond antifade mountant (Invitrogen) and covered with coverslip. Images were acquired with 20x lens on a Lionheart™ FX automated microscope (BioTek) using Gen5 software V 3.04.17. Objects of interest were detected using the following filters: nuclei with DAPI filter (excitation 377nm, emission 447nm), lipids with CY5 filter (excitation 628nm, emission 685nm), IR780-Oley dye with CY7 filter (excitation 716 nm, emission 809nm). Organs of animals injected with saline or carrier control were used to account for any autofluorescence in two channels of

interest.

2.3.1.5 PEG immunostaining combined with Oil Red O for fluorescence

To examine lipids stained by oil red O together with immunolabelled polyethylene glycol (PEG) a previously published protocol [120] was used with modifications. Cryosections were warmed to -20°C for 1 hour, followed by fixation in 4% formaldehyde at room temperature for 1 hour. Sections were rinsed three times in deionised water, permeabilised with 0.5% Triton X-100 in PBS for 5 minutes and washed for 5 minutes in three changes of PBS. Sections were incubated overnight at 4°C with anti-polyethylene glycol primary antibody (RevMAb) diluted 1:250 in 5% BSA; for staining control cells were incubated in the same conditions in 5% BSA without the antibodies. Sections were then washed three times with PBS prior to detection with ReadyProbes™ Alexa Fluor® 488 Donkey anti-rabbit IgG Antibody (Invitrogen, Bio-Sciences Ltd) as per manufacturer's guidelines. Nuclei were stained with Hoechst 33342 (Invitrogen, Bio-Sciences Ltd) at 1:1000 dilution. After washing in three changes of PBS, 5 minutes each, slides were immersed in oil red O for 20 minutes. Slides were rinsed three times in deionised water followed by 10 minutes in running tap water. Sections were mounted with ProLong diamond antifade mountant (Invitrogen) and covered with coverslip. Images were acquired with 40x lens on a Leica SP8 confocal microscope (Leica) using Leica Application Suite X (LAS X). Objects of interest were detected using the following settings on the software: nuclei excitation 405nm, emission 410 - 495nm; lipids excitation 552nm, emission 592 - 750nm; PEG excitation 488 nm, emission 495 – 592 nm. Initial optimisation of the protocol was carried out *in vitro* in HepG2 cells as detailed in the appendix chapter 8 under section 8.1.1.

2.3.2 ***Formalin fixed paraffin embedded tissue***

2.3.2.1 Sample preparation

Organs were sampled for histology according to "Revised guides for organ sampling and trimming in rats and mice" published by Registry of Industrial Toxicology Animal-data and North American Control Animal Database [118]. Tissue samples were collected from the same location in every case study to ensure coherence between different studies. Specimens were formalin fixed for 24 hours and processed for paraffin embedding in tissue processor (Leica, TP1020) by passing through series of ascending ethanol baths followed by three changes of xylene and infiltration with wax. Tissue was embedded into paraffin block on tissue embedder (Leica, EG1150H). 5 µm thick serial sections were cut on multiple levels of the block using rotary microtome (Leica, RM2235), with at least 50µm between every level. Sections were retrieved onto positively charged microscope glass slides (Thermo Scientific) and dried in the oven at 37˚C

overnight.

2.3.2.2 Haematoxylin and Eosin (H&E) staining

Sections were stained according to haematoxylin & eosin staining method (IHC world protocol [121]), with minor changes. Briefly, sections were de-paraffinized in two changes of xylene (Honeywell) and hydrated with decreasing concentrations of IMS to distilled water; sections were immersed in Harris haematoxylin (RAL Diagnostics), rinsed in running tap water, differentiated in 1% acid alcohol and counterstained with Eosin (Sigma-Aldrich). Slides were then dehydrated by passing them through a series of alcohol baths at incrementing concentrations and two baths with xylene (Honeywell). Slides were then mounted using DPX mounting medium (Thermo Scientific) and examined under light microscopy (Nikon Eclipse E800) equipped with 0.5x, 10x, 20x, 40x, and 100x lenses. Representative images were acquired using a QCapture Pro software V 6.0.0.605 (MediaCybernetics).

2.3.2.3 Perls' Prussian blue for ferric iron detection

Staining was performed as detailed in a previous publication [122] on particles examined in this study. Minor changes were introduced. Briefly, rehydrated sections were covered with equal parts of hydrochloric acid (HCl) (Honeywell) and potassium ferrocyanide (Honeywell) for 20 min. Slides were washed in distilled water and counterstained with Eosin (Sigma-Aldrich) for 5 min. Following incubation periods, slides were rinsed with distilled water before being dehydrated in a graded series of industrial methylated spirit (IMS) (Lennox) rinses. Slides were then cleared in two baths of xylene (Honeywell) and cover-slipped with DPX mounting medium (Thermo Scientific) and examined under light microscope (Nikon Eclipse E800) equipped with 0.5x, 10x, 20x, 40x, and 100x lenses. Representative images were acquired using a QCapture Pro software V 6.0.0.605 (MediaCybernetics). Slides were stained manually, with each batch containing spleen section for positive iron control, and skin section for negative control. Prior to staining tissue sections, a protocol was optimized *in vitro* using BxPC-3 cells which were treated with a series of concentrations of two MNPs. Details of this experiment can be found in the appendix, with detailed protocol in section 8.1.2.1.

2.3.2.4 Toluidine blue staining

Sections were de-paraffinized in two changes of xylene (Honeywell) and hydrated with decreasing concentrations of IMS (Lennox, Ireland) to distilled water. Toluidine stock solution was prepared from powder to a 1% w/v solution in 70% ethanol. Staining solution was prepared fresh, by mixing stock solution with 1% w/v sodium chloride (Fisher Scientific) solution (pH 2.5) in 1:10 ratio respectively. Sections were stained in the working solution for 2 minutes, followed with wash in three changes of distilled water. Sections were counterstained in eosins solution

diluted to 0.5% v/v in 70% alcohol. Slides were then dehydrated by passing them through a series of alcohol baths at incrementing concentrations and two baths with xylene (Honeywell). Slides were then mounted using DPX mounting medium (Thermo Scientific) and examined under light microscopy (Nikon Eclipse E800) equipped with 0.5x, 10x, 20x, 40x, and 100x lenses. Representative images were acquired using a QCapture Pro software V 6.0.0.605 (MediaCybernetics).

2.3.2.5 Immunofluorescence

Sections were de-paraffinized in two changes of xylene (Honeywell) and hydrated with decreasing concentrations of IMS (Lennox) to distilled water. Heat antigen retrieval was carried out by submerging slides in citrate buffer (DiaPath) and bringing them to boil in a microwave for 30 minutes. Slides were cooled to room temperature and washed twice in PBS for 5 minutes, followed by Permeabilisation step in 0.4% triton-X in PBS for 10 minutes. Tissue autofluorescence was blocked with TrueBlack® Lipofuscin Autofluorescence Quencher (Biotium) according to manufacturer's pre-treatment protocol. Sections were secured with Liquid blocker pen (Ted Pella) and subjected to blocking with 5% normal goat serum (Invitrogen) for 1 hour at room temperature in humid chamber. Primary antibody solution was prepared in 1% normal goat serum (Invitrogen) by combining mouse anti-dextran primary antibody (STEMCELL Technologies) at 1:100 dilution with rabbit anti-rat CD68 primary antibody (Invitrogen) at 1:500 dilution. Incubation with primary antibodies was carried out in dark humid chamber for 2 hours at room temperature. Slides were subjected to three 5-minute washes in PBS (Fisher Scientific) prior to detection with secondary antibodies. Mouse anti-dextran antibody was detected with goat anti-mouse secondary antibody conjugated with AlexaFluor488 (Invitrogen); rabbit anti-rat primary antibodies were detected with goat anti-rabbit secondary antibody conjugated with Alexa Fluor 594 (Invitrogen) diluted according to manufacturer's guidelines. Sections were incubated with secondary antibodies for 1 hour at room temperature in dark humid chamber, followed by three 5-minute washes in PBS, and 15-minute incubation with Hoechst (Invitrogen) for nuclei staining diluted at 1:1000 in PBS. Sections were washed trice in PBS and mounted with ProLong diamond antifade mountant (Invitrogen). Images were acquired with 40x lens on a Leica SP8 confocal microscope (Leica) using Leica Application Suite X (LAS X). Prior to staining tissue sections, a protocol was optimized *in vitro* using BxPC-3 cells which were treated with a series of concentrations of two MNPs. Details of this experiment can be found in the appendix, with detailed protocol in section 8.1.2.2.

2.4 Image acquisition

Throughout this project different imaging equipment were used to acquire a high quality images to present observed histological changes and to allow semi-quantitative analysis where applicable. The following section outlines specifications of the equipment used.

2.4.1 *Brightfield microscopy*

Slides stained with traditional histological stains (H&E, Oil red O, Perls' Prussian blue, and Toluidine blue) were examined under light microscope (Nikon Eclipse E800) equipped with 10x, 20x, 40x, and 100x lenses. Slides were initially observed using a 10x lens, moving up in magnification if required. Representative images were acquired using a QCapture Pro software V 6.0.0.605 (MediaCybernetics), using lens specified under each figure legend. Images were calibrated according to the scale conversion (Table 2.2) calculated using reference images of graticule.

Table 2.2: Scale conversion for images acquired with Nikon Eclipse E800 microscope

Lens used	Scale conversion
10 x	1.13 pixels/µm
20x	2.22 pixels/µm
40x	4.46 pixels/µm
100x	11.02 pixels/µm

2.4.2 *Automated microscope*

Images acquired using an automated microscope LionHeartFX (BioTek) equipped with 4x, 10x, and 20x lens. Microscope was operated using Gen5 software (V 3.04.17). Images were calibrated according to the scale conversion (Table 2.3) calculated using reference images of graticule.

Table 2.3: Scale conversion for images acquired with LionHeartFX automated microscope

Lens used	Scale conversion
10x	1.27 pixels/µm
20x	2.54 pixels/µm

2.4.3 *Fluorescent imaging*

Leica SP8 scanning confocal microscope (Leica) equipped with 10x, 20x, 40x, and 63x was used to obtain high quality fluorescent images. Leica Application Suite X (LAS X) was used to operate the microscope and acquire images using 40x and 63x. Images were calibrated according to the scale conversion (Table 2.4) calculated using reference images of graticule.

Table 2.4: Scale conversion for images acquired with Leica SP8 scanning confocal microscope

Lens used	Scale conversion
40x	7.04 pixels/µm
63x	8.32 pixels/µm

2.5 Quantitative analysis

2.5.1 *Sample preparation for Mass Spectroscopy*

Organ samples in case study 2: proof-of-concept SOP for liposome drug carrier biodistribution detection were prepared according to a peer-reviewed protocol [123]. Briefly, organs were excised from the sacrificed rats and stored frozen at - 80˚C until homogenization. Frozen tissues were thawed, chopped and weighed at 4˚C. 50 ± 20 mg of chopped tissue was homogenized in 2 mL of ice-cold homogenizing solution (pH 7.4) containing 250 mM sucrose (Fluka Analytical), 1 mM EDTA dehydrate (Avantor performance material) and 10 mM potassium phosphate (Fisher Scientific Ltd.) with TissueLyser LT (QUIAGEN) using 3mm Tungsten Carbide Bead (QUIAGEN). Homogenization was paused for 30 s after every 60 s of homogenization at 30 Hz. The homogenization was repeated 3-4 times until a uniform homogenate was obtained. Tissue extract was stored at approximately -80˚C prior to analysis. Prepared samples where then shipped under dry ice to Stiftelsen for industriell og teknisk forskning (SINTEF) partner in Norway for Liquid Chromatography / Mass Spectrometry (MS) analysis. SINTEF was the chosen partner for LC/MS since the group develop specific assays for NBM quantification under the EUNCL H2020 project.

2.5.2 *Sample preparation for iron quantification using inductively coupled plasma mass spectrometry*

The following protocol was kindly provided by Dr. Gary Hannon as he carried out the analysis during his post-doctorate project in the Nanomedicine and Molecular Imaging group in

Trinity College.

Tissue samples was dissolved in 67-69 % trace-element nitric acid (Fischer Scientific) at a concentration that is ten times the weight of the sample (i.e. 1 g of tissue would be dissolved in 10 ml nitric acid) in 15 ml tubes (Eppendorf). For lung, kidney and spleen, an entire organ (left side) is dissolved in acid; for liver, a vertical slice is made along the major lobe with the aim of approximately 1 g of this tissue being used for iron quantification. The tubes are then heated to 60 °C and left overnight. The dissolved samples are then diluted into trace-element water (Fischer Scientific) for subsequent Inductively coupled plasma mass spectrometry (ICP-MS) analysis. Prepared samples were sent to the London Metallomics Facility at Kings College London for ICP-MS analysis using the NexION 350D. The procedure involved a seven standard calibration curve between 1 µg/L and 10,000 µg/L and standard controls every twenty samples as an internal quality control. Additionally, a calibration control yttrium-89 was utilised as an internal standard.

2.6 Machine learning for bioimage analysis

Chapter 1 introduced the ML for bioimage analysis, detailing terminology and software used in this thesis. The following sections provide in depth protocols, which were implemented to semi-quantitatively and qualitatively assess iron aggregates in tissue sections obtained from animals injected with MNPs. Results of those analysis are presented further on in the thesis in results chapter 4 and 5.

2.6.1 *Model training*

Trainable WEKA segmentation (TWS) plugin in Fiji (v3.2.34) [102] was used for pixel classification and segmentation. Four segmentation classes were created: background, tissue, nanoparticles and artefacts. In total, three classifiers were trained to overcome variability in corresponding features of different tissue samples. The following features were selected: Gaussian blur, Anisotropic diffusion, and bilateral filter for noise reduction; difference of Gaussian for edge detector; mean and median for texture filters. Default settings were kept for membrane thickness and membrane patch size (1 and 19 respectively) with maximum sigma changed to 2. The default Fast Random Forest (FRF) classifier was selected with following options: maxDepth = 0; numFeatures = 2; numTrees = 100.

From images acquired for iron quantification (2D images), five images per organ were randomly assigned to train the classifier using a standard desktop set up (Intel® Core™ i5-3570 CPU @ 3.40GHz, 8.00 GB RAM, x64-based processor). The time taken to generate the data from nine images was roughly five minutes and reflects the expected resource time needed for a mid-range student or analysts' PC. Classified images were evaluated by comparing resulting probability maps to the visual evaluation of a trained pathologist and the automated detection system was retrained if needed. Step-by-step screencast on method described here to train and validate the classifier was recorded and made available for download from the open repository https://gitlab.com/abogdans/weka_4_iron_quantification .

2.6.2 *Model validation*

During training, classifiers' performance was evaluated within the WEKA's Explorer Environment via 10-fold cross-validation. Data was split into ten folds with each fold data further split into training set (90% of data) with remainder used for testing. Once trained and validated, classifiers were saved and applied to the remaining data.

Test images were duplicated and manually segmented for tissue and nanoparticles creating

ground truth images used to calculate number of True Positive (TP), True Negative [124], False Positive (FP) and False Negative (FN) pixels in images obtained from different threshold methods (Figure 1). Probability map images generated by WEKA were subjected to a threshold step with value set between 191 to 255, representative of pixel belonging to a class with certainty higher than 75%, and threshold value between 127 to 255, representative of pixel belonging to a class with certainty higher that 50%. Additionally, original histology images used for training the classifier were converted to 8-bit format and subjected to a manual threshold to highlight area of iron positive staining or tissue. This method is referred to as default since it represents traditional approach to image segmentation and quantification. Resulting binary images were used to evaluate performance of each method in comparison to ground truth image.

Following overlap-based metrics were used:

Mathews' Correlation Coefficient was calculated using equation 1 [112]:

Equation 1: Mathew's Correlation Coefficient (MCC)

$$\mathrm{MCC} = \frac{\mathrm{TP} * \mathrm{TN} - \mathrm{FP} * \mathrm{FN}}{\sqrt{(\mathrm{TP} + \mathrm{FN}) * (\mathrm{TP} + \mathrm{FP}) * (\mathrm{TN} + \mathrm{FN}) * (\mathrm{TN} + \mathrm{FP})}}$$

F_1 score was calculated using equation 2 [112]:

Equation 2: F_1 score

$$\mathrm{F_1score} = \frac{2 * \mathrm{TP}}{2 * (\mathrm{TP} + \mathrm{FP} + \mathrm{FN})}$$

Jaccard similarity coefficient (JSC) [108] was calculated using equation 3:

Equation 3: Jaccard similarity coefficient (JSC)

$$\mathrm{JSC} = \frac{\mathrm{TP}}{\mathrm{TP} + \mathrm{FP} + \mathrm{FN}}$$

The value of F_1 score, DSC and JSC ranges from 0 to 1, indicating no spatial overlap between two sets of binary segmentation to complete overlap, respectively. The value for MCC ranges from -1 to 1, indicating perfect misclassification and perfect classification respectively.

2.6.3 *Quantification of iron staining*

Quantification of iron staining was performed using an open source software ImageJ/FIJI (NIH) [101]. Probability map images obtained from TWS were converted to 8-bit format and subjected to a threshold with set value between 191 to 255 incorporating pixels which were

assigned to a class with 75% certainty or higher. Image analysis was coded in macro-language (appendix) and performed on probability map images obtained from TWS classification. The percentage of iron was calculated using equation 4:

Equation 4: Percent area of Perls' Prussian blue staining

$$\%\ \text{area of PPB staining} = \frac{\text{area of PPB positive staining } (\mu m^2)}{\text{area of tissue staining } (\mu m^2)} \times 100$$

2.6.3.1 Shape analysis of iron aggregates from 2D histology sections

Circularity and roundness of the objects segmented as iron aggregates was measured using the particle analysis plugin in Fiji software [125].

2.6.4 *Virtual 3D volume*

Consecutive sections (5 μm thick) were stained with PPB to expose iron aggregates. Slides were imaged with an automated microscope (LionheartFX, BioTek) using 10x lens. Images were acquired with Gen5 software (V 3.04.17) using montage option, resulting in a number of tiles, which were stitched together with linear blend. Full images were manually aligned into virtual stack using TrakEM2 plugin [126] in Fiji and loaded onto TWS. Trained classifier was used to segment four classes of interest, resulting probability map stack was subjected to post processing step where each class stack was converted to an 8-bit format, threshold was applied with lower-level set to 191 and upper level of 255, assigned a pseudo colour (corresponding to that used by TWS), and merged into one stack. Icy v2.0.3.0 (open community platform for bioimage informatics, http://icy.bioimageanalysis.org/) software with built in Visualization Toolkit (3DVTK) for 3D computer graphics [127] was used to generate 3D volumes.

2.6.4.1 Shape analysis of iron aggregates in 3D histology volumes

Elongation and flatness of objects segmented as iron aggregates in 3D histology volumes was measured using 3D Geometrical measure available as a part of the BioVoxxel Toolbox in Fiji [128].

2.7 Statistical analysis

Initial data exploration was carried out using the statistical computer package Minitab V19

(Minitab Statistical Software, United Kingdom) licenced by Trinity College Dublin. Statistical calculations and graphing of data were carried out using the statistical computer package GraphPad Prism V.9.0.0 (121) for Windows (GraphPad Software, San Diego, USA), licenced by Trinity College Dublin. Both parametric and non-parametric tests were used. Specifications on how results are expressed, and statistical test used can be found in table and figure legends. In each case, a p value < 0.05 was considered statistically significant.

3 Chapter 3: Histology assays for toxicity, accumulation and clearance of nanoliposomes

3.1 Introduction

The advantages and limitations of histology studies in preclinical assessment of NBMs were discussed in Chapter 1. One of the shortcomings of histological techniques in this area of research is their inability to detect certain types of NBMs. Liposomes fall into this category, greatly limiting the techniques which can be used to examine biodistribution of those materials *in vivo*. The biochemical methods used to determine biodistribution of those materials measure concentration of cargo carried by the liposome such as drug or a dye. However, due to destructive nature of those methods it cannot be determined whether this cargo is still within the liposome and whether it was sequestered by specific cells. To complement qualitative biochemical analysis used to assess biodistribution, research undertaken as part of this study aimed to develop a method which would detect liposomes in histology sections.

The results presented in this chapter were obtained from two *in vivo* case studies undertaken by the LBCAM in Trinity College Dublin as one of the partner members of EUNCL, the recently completed EU H2020 infrastructure project. Due to vast heterogeneity of NBMs, there is no "one size fits all" in terms of assays used in early stages of NBMs research, therefore experimental design for these studies were tailored specifically to the NBM used. The general concept was to utilize a histological stain for lipid detection (Oil red O) to visualise liposomes in tissue sections. In order to discriminate between natural lipids and NBMs, the fluorescent properties of Oil red O (ORO) were used to examine co-localisation with cargo of liposome used in first case study, or coating material on liposome used in the second case. This type of analysis has two-fold advantage; firstly, evaluation of biodistribution and localisation of liposomes down to cellular level, secondly, evaluation of degradation by assessing co-localisation between different components of the NBM under observation.

The first case study assessed the safety of an innovative dye-loaded lipid NBM synthesized by one of the EU H2020 projects' collaborator. The encapsulated-dye liposome was designed as a contrast agent for near-infrared fluorescence *in vivo* diagnostic imaging agent. This NBM is composed of lecithin phospholipids with a lipid core (soybean oil and wax) containing IR780-Oleyl dye for fluorescent imaging. The study presented here took an advantage of this fluorescent dye, to confirm whether staining tissue sections with ORO is a suitable method for detection of liposomes.

The second case study presented in this chapter was a proof-of-concept standard operating procedure (SOP) study where a liposome drug carrier NBM was used to optimise a protocol for detecting PEGylated liposomes in tissue sections. To this purpose, a recently approved anti-cancer drug, liposomal irinotecan (Onivyde®; nal-IRI; also known as PEGylated liposomal irinotecan) was used. In this case, since the majority of liposomes approved for biomedical applications are used as delivery systems, the NMB carrier did not contain a tracer such as fluorophore for their detection. The latter limitation was addressed by "thinking outside of liposome" and visually detecting this type of NBMs by combining lipid stain with immunofluorescent detection of material used for coating.

The overall hypothesis for the experiments undertaken in this chapter was: "liposomes can be detected in *ex vivo* tissue sections with histology stain used for lipid staining". The main objective to support this hypothesis was to discriminate between the engineered liposomes and the naturally present lipids in organs (dietary lipids and lipid storage) by visual detection of lipids and its cargo or coating material.

3.2 Experimental design

Two case studies presented in this chapter were a part of a large multidisciplinary analytical cascade developed and implemented within the framework of the EUNCL. They were designed, organized and operated according to the highest EU regulatory and quality standards in order to provide a full analysis of chosen NBMs for medical applications, from characterisation to pre-clinical *in vivo* studies. The latter was carried out within this PhD work with the processing of the organs, histology sectioning, staining, observation and recording of events all reported in this chapter. While the experimental *in vivo* design, implementation and organs collection was carried out under the supervision of Dr Oliviero Gobbo, processing of the organs, histology sectioning, staining, observation and recording of events was carried out within this PhD work.

In case study 1, Near-infrared (NIR)-dye loaded liposome designed for imaging purposes was assessed for toxicity and adaptive immune response. Case study 2 on the other hand focused on assessing initial accumulation and side effects occurring up to 48 hours post injection of an irinotecan loaded liposome (clinical product under the commercial name: Onivyde®) commercialised by Ipsen. Table 3.1 outlines physicochemical properties of the nanobiomaterials used in the two case studies presented in this chapter and doses used. Additionally, graphical representation of the experimental workflow for case study 1 and 2 are shown in Figures 3.1 and

3.2 respectively.

Table 3.1: Summary characterisation of nanobiomaterials used in case study 1 and 2
Summary of the physicochemical properties of the materials used in case study 1 and 2.

Case study	**Case study 1** ***In vivo* toxicity and biodistribution of NIR-dye loaded liposome for imaging applications**	**Case study 1** ***In vivo* toxicity and biodistribution of NIR-dye loaded liposome for imaging applications**	**Case study 2** ***In vivo* toxicity and biodistribution of liposomal irinotecan**
Name	LipImage™815 (referred to in thesis as dye-loaded liposome)	Lipidots (referred to in this thesis as carrier control)	Onivyde™
Type of material	Lipid nanoparticles with IR780-Oleyl dye	Lipid nanoparticles, filled with soybean oil	Liposomal irinotecan
Primary size (nm)	N/A	N/A	N/A
Coating	Myrj™S40	Myrj™S40	Polyethylene glycol (PEG)
Hydrodynamic diameter (nm)	46 ± 1	46 ± 1	~ 110
Zeta Potential (mV)	- 2.5 ± 0.5	- 2.5 ± 0.5	~ -16
Polydispersity index (PDI)	0.093	0.094	<0.1
Endotoxin (EU/ml)	<1 In solution with lipid concentration of 94 mg/ml; Measured with chromogenic LAL assay	<1 In solution with lipid concentration of 92 mg/ml; Measured with chromogenic LAL assay	<1 In a solution containing 4.3 mg/mL irinotecan free base; Measured with chromogenic LAL assay
Supplier	Supplied by collaborator at CEA Letti, Grenoble, France.	Supplied by collaborator at CEA Letti, Grenoble, France.	Purchased from Pfizer

3.2.1 *Case study 1: Safety study of dye-loaded lipid NBM*

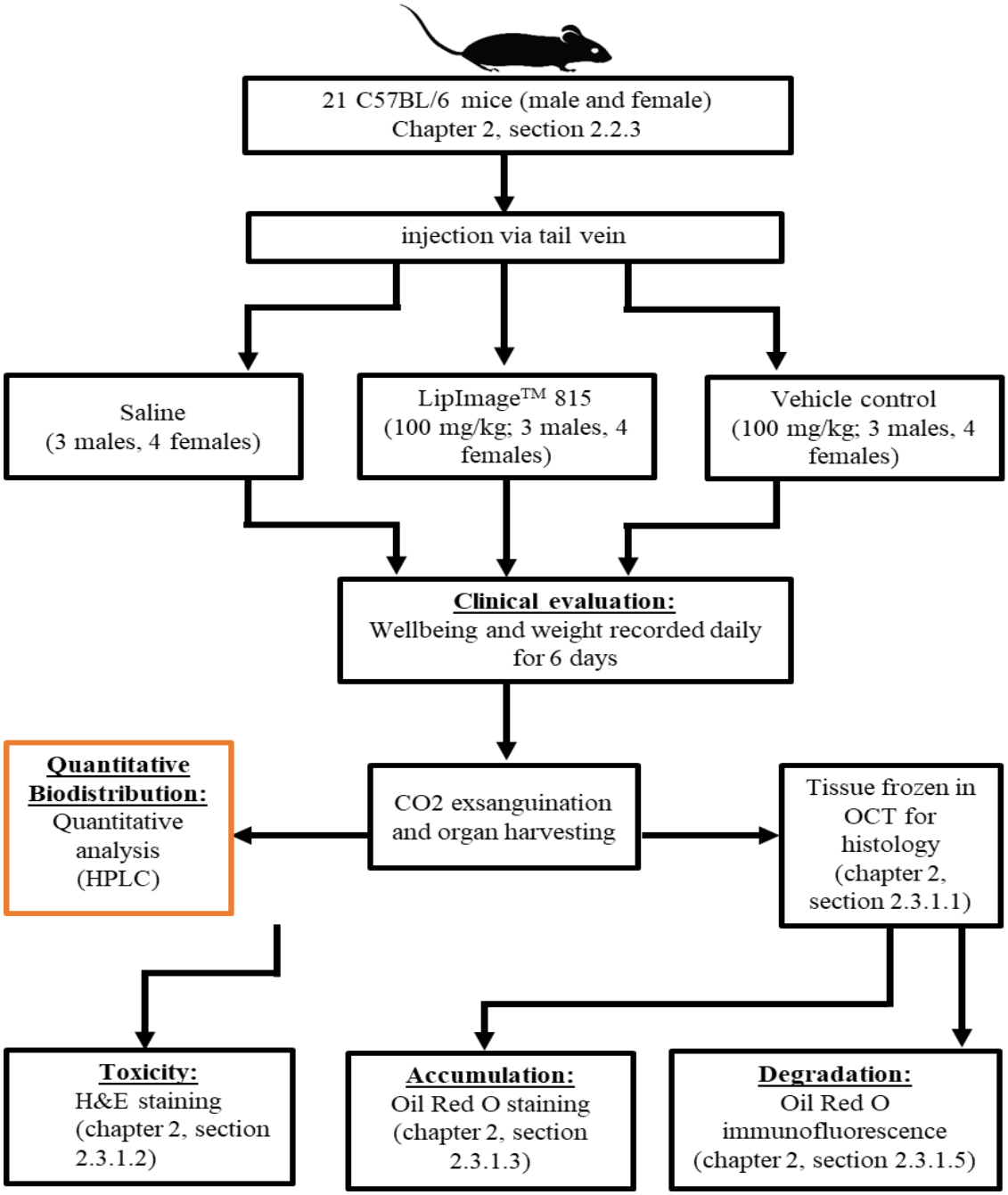

Figure 3.1: Experimental workflow for case study 1: dye-loaded lipid NBM
In vivo experimental workflow for the safety study of dye-loaded lipid NBM. From top to bottom, the first three rows of the diagram present details on the animals used, route of administration, and type and dose of material administered. Clinical evaluation of the animals was recorded daily for 6 days following the injection. On day 6, animals were euthanized with CO_2, and organs of interest were harvested, and cryopreserved for further analysis. Note: quantitative biodistribution (orange box) was not part of this thesis but planned in the overall scale of the European project. Boxes in the bottom row highlight histological methods utilized in this thesis to determine tissue toxicity, accumulation, and degradation of the NBMs used. Specific protocols related to case study are reported in chapter 2 under the specific technique utilized. The study was approved by the internal Animal Research Ethics Committee at Trinity College Dublin and the Health Products Regulatory Authority, project license number: AE19136/P073.

3.2.2 *Case study 2: proof-of-concept SOP for liposome drug carrier biodistribution detection*

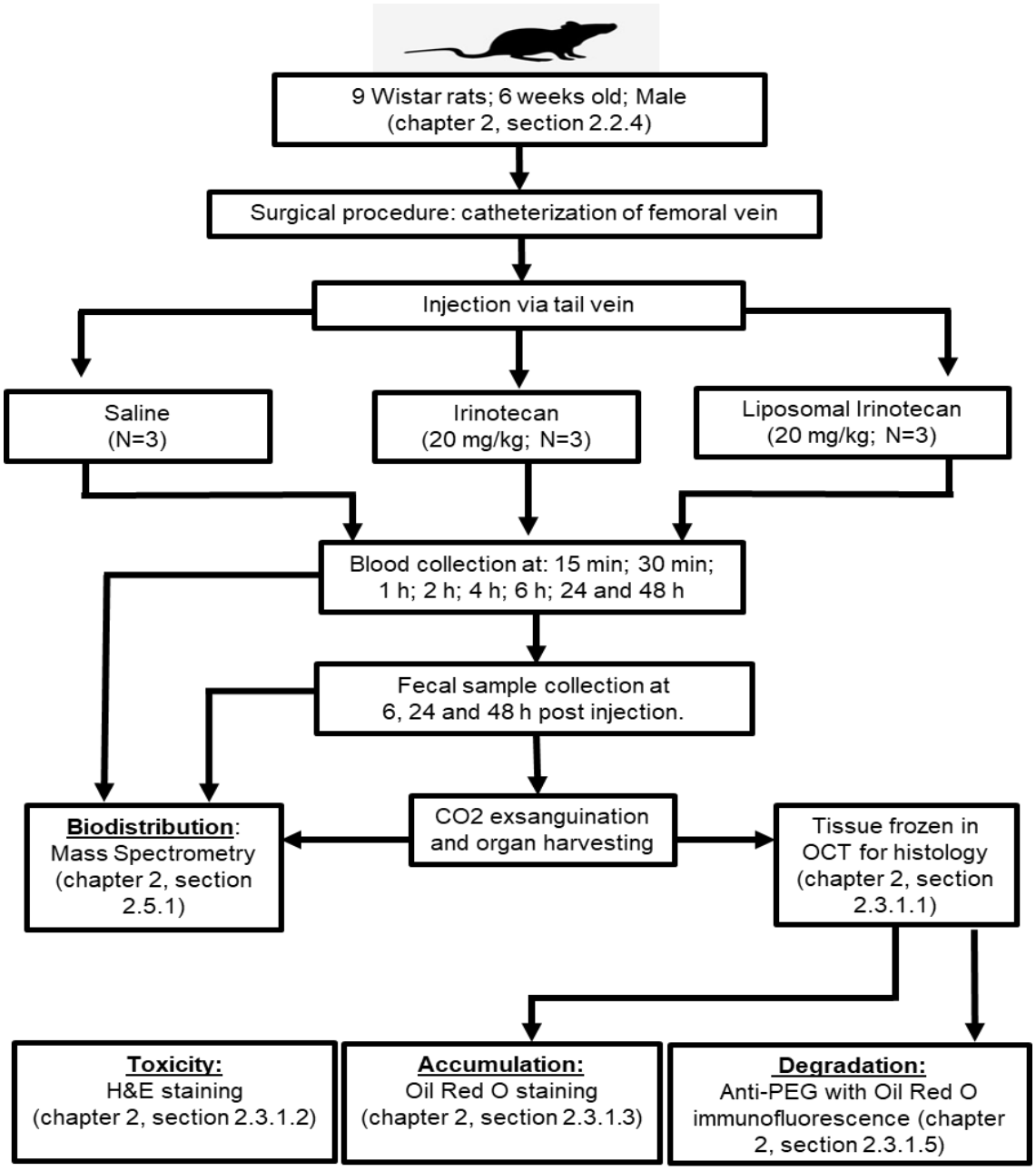

Figure 3.2: Experimental workflow for case study 2: liposomal irinotecan
In vivo experimental workflow for the safety study of safety study of Onivyde®. From top to bottom, the first four rows of the diagram present details on the animals used, surgical procedure, route of administration, and type and dose of material administered. When available, blood and faecal samples were collected at time post injection indicated in the diagram to evaluate pharmacokinetic profile and excretion of the injected drug. Forty-eight hours post injection animals were euthanized with CO_2, and organs of interest were harvested, and cryopreserved for further analysis. Boxes in the bottom row highlight histological methods utilized in this thesis to determine tissue toxicity, accumulation, and degradation of the NBMs used. Dose is given as irinotecan equivalent. Full protocols can be found in indicated sections in Chapter 2. The study was approved by the internal Animal Research Ethics Committee at Trinity College Dublin and the Health Products Regulatory Authority, project license number: AE19136/P073.

3.3 Results

Results presented in this section were observed and recorded during two safety studies of NIR-dye loaded liposome and liposomal irinotecan. The results presented in this chapter focus on the assessment of toxicity and accumulation of those lipid based NBMs in organs, which was evaluated using a number of histological techniques.

3.3.1 *Case study 1: Safety study of a dye-loaded lipid NBM*

Fluorophores, approved for near-infrared (NIR) fluorescence imaging in humans, face a number of limitations such as poor optical properties [129], aggregation, and strong adsorption on plasma proteins [130] which in turn regulate their biodistribution [131]. To overcome those limitations, collaborators at the Commissariat à l'énergie atomique et aux énergies alternatives (CEA-Leti) in France designed and manufactured novel NIR dye called IR780-Oley dye encapsulated within the liposome, industrial commercial name Lipimage™ 815. The selected lipid carrier was produced with ingredients already approved for human use with high biocompatibility and fabrication process free of toxic solvents. Results of the safety study of this novel nanoimaging contrast agent are presented in this section. *In vivo* study in mice was conducted as part of a SOP development at preclinical level at Trinity College as a part of the EUNCL consortium.

3.3.1.1 Animal wellbeing

Initial *in vivo* animal assessment was carried out as part of the body weigh variation in mice over experiment duration, see Figure 3.3. In females (Figure 3.3 A) no significant changes in weight were seen in animals treated with NIR dye-loaded liposome or soybean oil-filled carrier control when compared to males injected with saline. The same was seen in males (Figure 3.3 B). There was also no sign of pain or distress seen in the animals until the endpoint of this study.

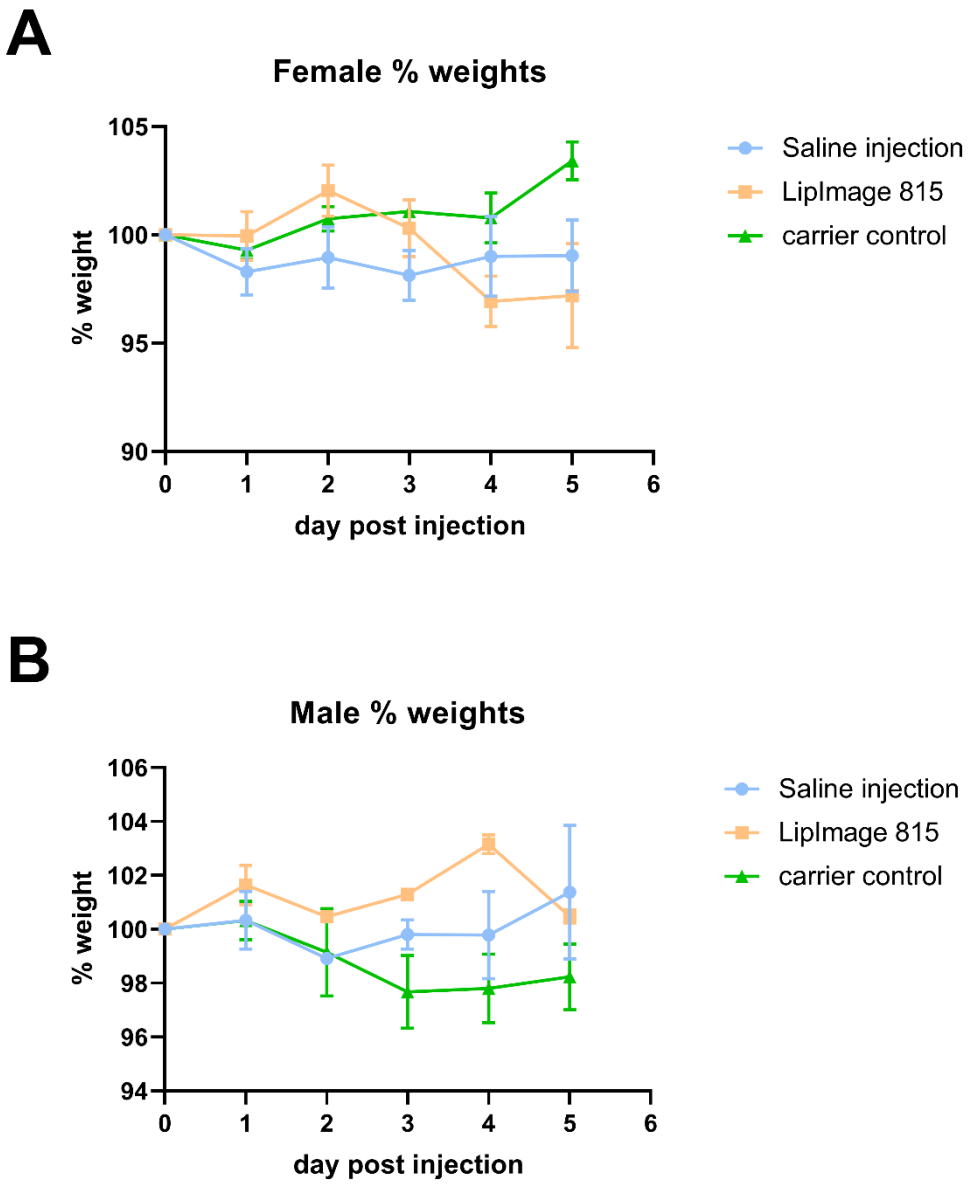

Figure 3.3: Body weight variation over experiment duration
Percent change in body weight (y-axis) over experiment duration (x-axis) in female (A) and male (B) mice following intravenous injection of saline (light blue ●), LipImage™ 815 (orange ■) or carrier control (green ▲) at 100 mg/kg lipid concentration. Data expressed as mean ± SEM (n = 3 for males and n = 4 for females).

3.3.1.2 Toxicity

Gross examination of the explanted organs did not reveal any abnormal macroscopic changes indicative of toxicity. H&E stained sections were examined under the light microscope to assess tissue morphology and cellular changes indicative of toxicity. Due to differences or rates of change in the physiology, anatomy, hormonal, behaviour, biochemistry and genetics between females and males, histopathological changes were also evaluated separately. For both genders,

no abnormal changes suggestive of toxicity or immune response were seen in liver (Figure 3.4), spleen (Figure 3.5) or kidney (Figure 3.6) in response to NIR dye-loaded liposome or soybean oil-filled liposome used as carrier control. This was seen across all animals used in this study regardless of gender and treatment as shown in the representative images in the appendix (Supplementary figures Supplementary figure 8.6Supplementary figure 8.11).

Confirmation of the results presented in this section was sought by an independent certified pathologist from the St. James' Central Pathology Laboratory, St. James's Hospital, Dublin Ireland. These findings were confirmed, as summarised in Table 3.2.

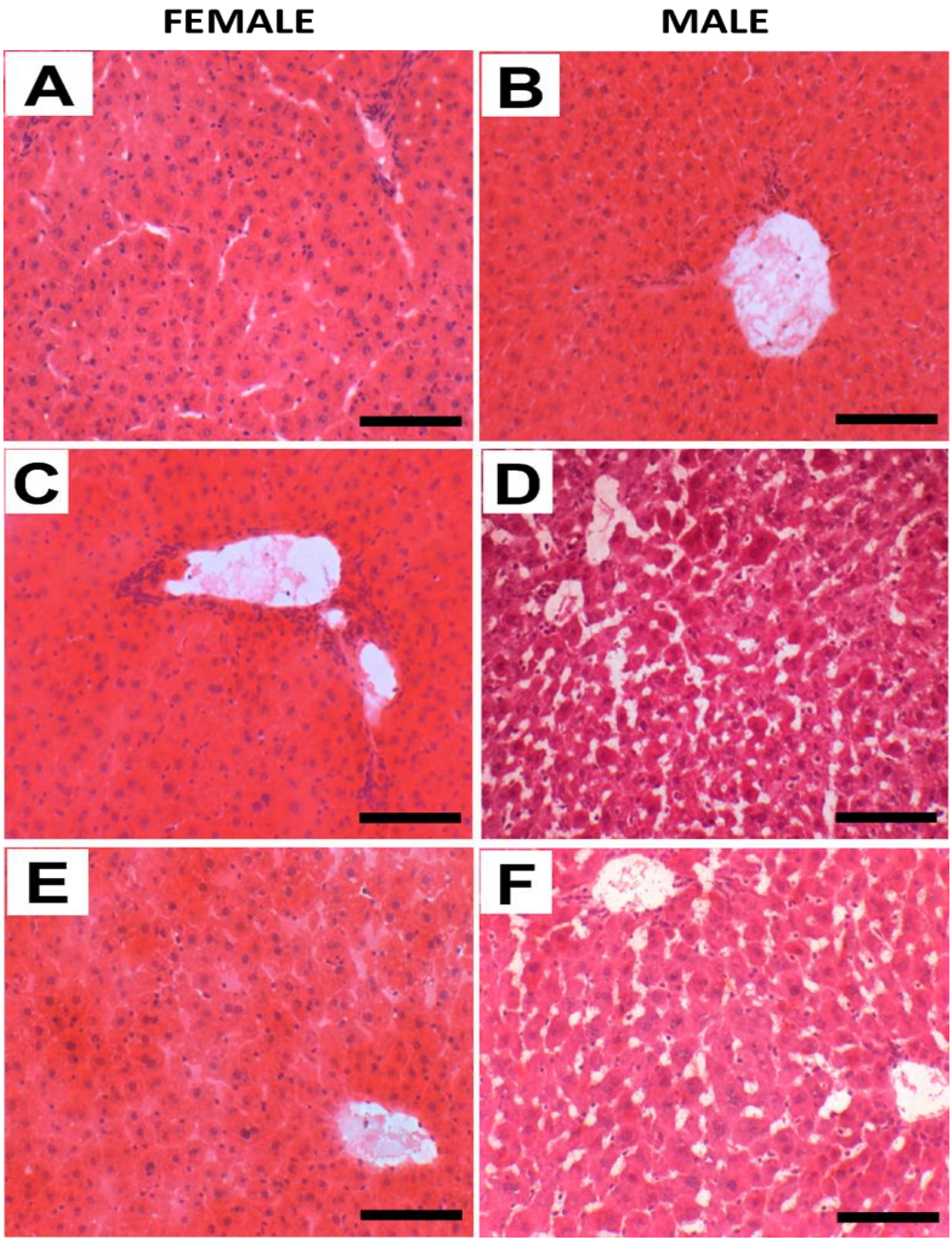

Figure 3.4: Liver pathology 7 days after intravenous injection of liposome
Representative photomicrographs of H&E stained liver tissue sections of C57BL/6 mice following intravenous injection of liposome (females n=4, males n=3). 10µm thick sections were collected at four levels across the block, with at least 50 µm distance between levels. No abnormal changes suggestive of toxicity or immune response were seen in females (left column) or males (right column) injected with NIR dye-loaded liposome at 100 mg/kg concentration (C and D), or soybean-oil loaded liposome as carrier control at 100 mg/kg concentration (E and F) when compared to livers of animals injected with saline (A and B). Representative images were acquired with 20x lens; Scale bar represents 100 µm.

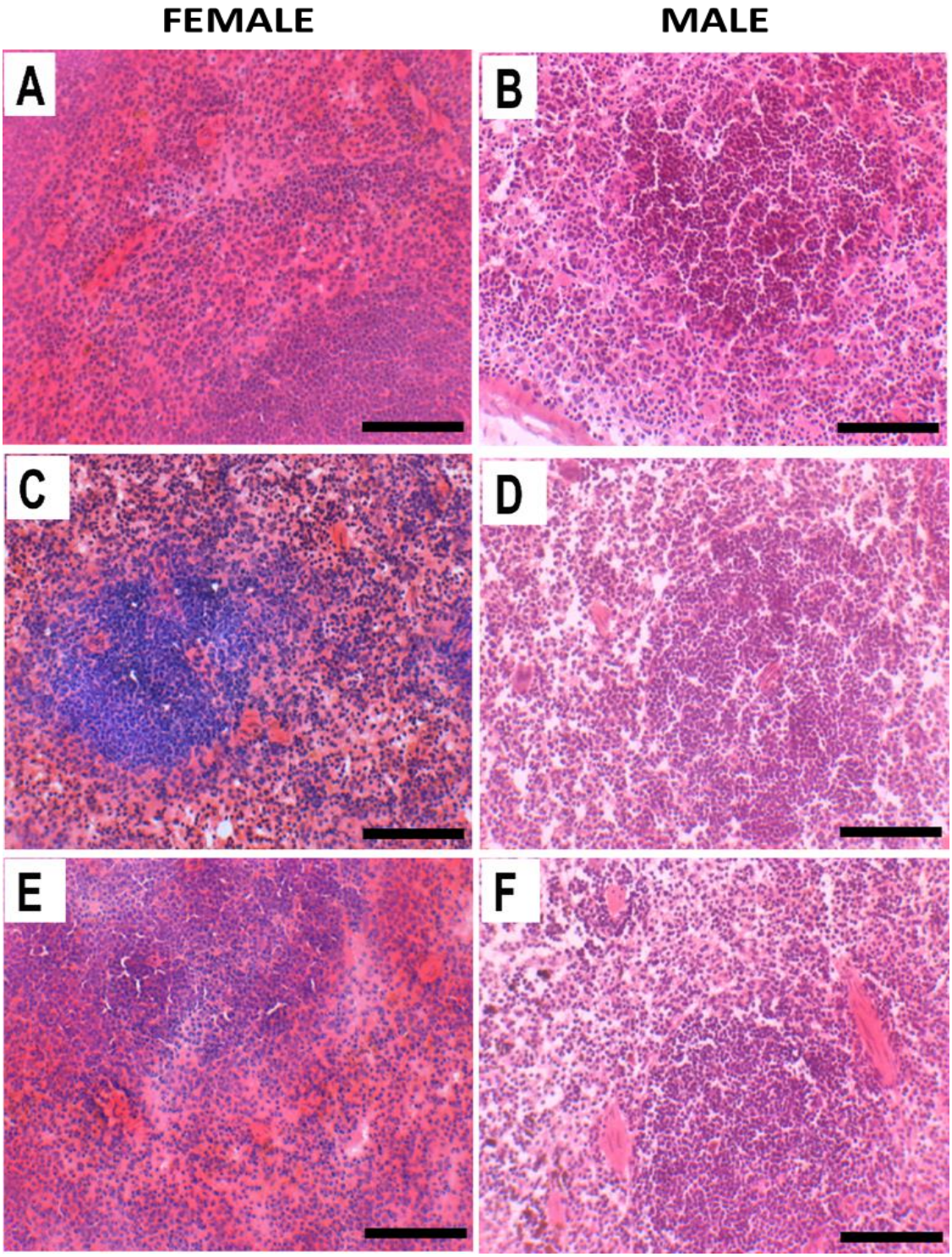

Figure 3.5: Spleen pathology 7 days after intravenous injection of liposomes
Representative photomicrographs of H&E stained spleen tissue sections of C57BL/6 mice following intravenous injection of liposome (females n=4, males n=3). 10µm thick sections were collected at four levels across the block, with at least 50 µm distance between levels. No abnormal changes suggestive of toxicity or immune response were seen in females (left column) or males (right column) injected with NIR dye-loaded liposome at 100 mg/kg concentration (C and D), or soybean oil-loaded liposome as carrier control at 100 mg/kg concentration (E and F) when compared to spleens of animals injected with saline (A and B). Representative images were acquired with 20x lens; Scale bar represents 100 µm.

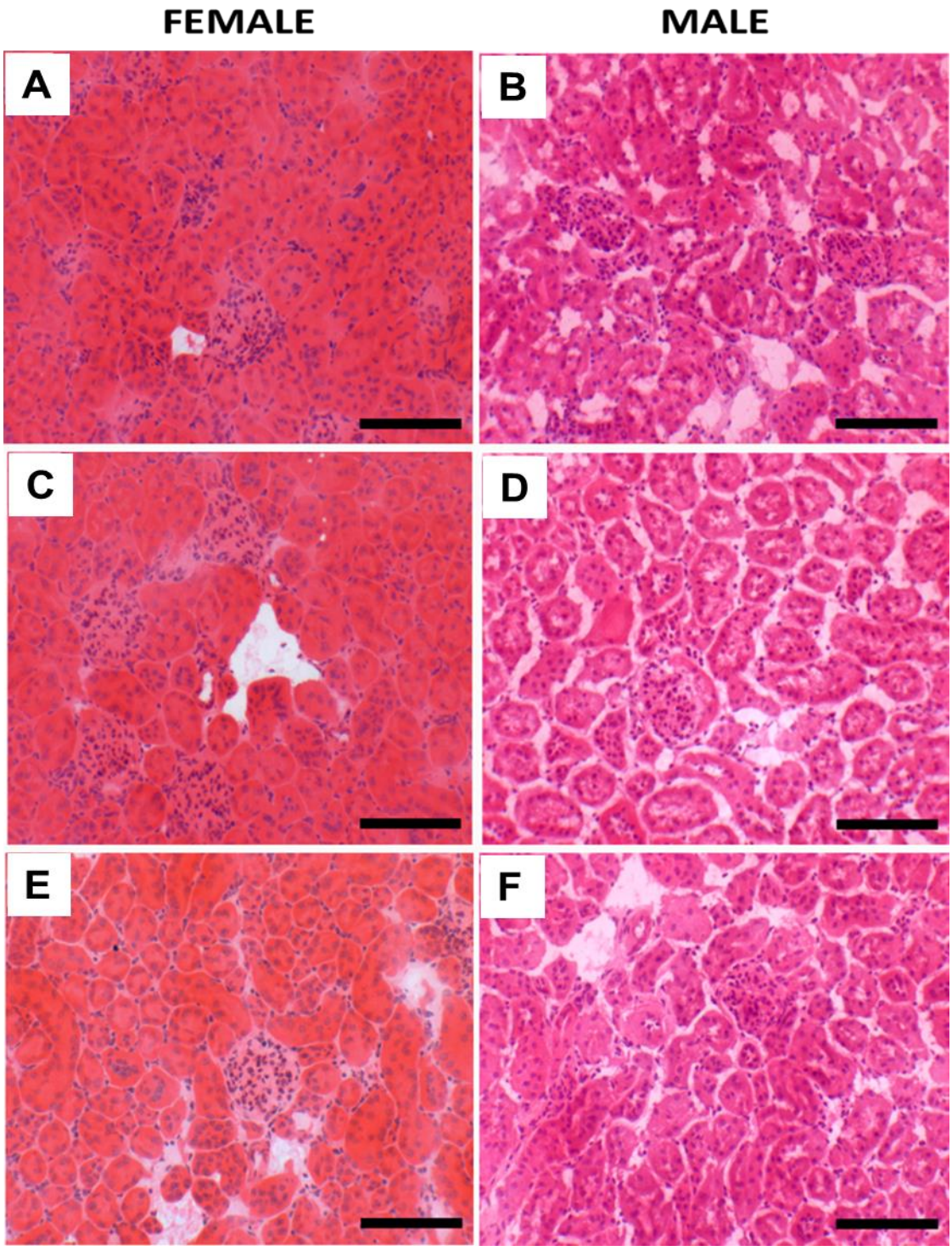

Figure 3.6: Kidney pathology 7 days after intravenous injection of liposomes
Representative photomicrographs of H&E stained kidney tissue sections of C57BL/6 mice following intravenous injection of liposome (females n=4, males n=3). 10µm thick sections were collected at four levels across the block, with at least 50 µm distance between levels. No abnormal changes suggestive of toxicity or immune response were seen in females (left column) or males (right column) injected with NIR dye-loaded liposome at 100 mg/kg concentration (C and D), or soybean-oil filled liposome as carrier control at 100 mg/kg concentration (E and F) when compared to livers of animals injected with saline (A and B). Representative images were acquired with 20x lens; Scale bar represents 100 µm.

3.3.1.3 Determination of NBM accumulation in tissue by selective histological staining

Qualitatively, visual assessment of lipid accumulation in all tissue organs investigated was carried out by using a fat-soluble stain ORO. This stain is used in histopathology for staining neutral triglycerides and lipids.

Interestingly, among all organs analysed in mice, the livers of female mice injected with NIR dye-loaded liposome had the most abundant lipid staining (Figure 3.7). Similar results were observed in kidney (Figure 3.9), where the number of lipid vacuoles was seen in renal tubules of female mice injected with NIR dye-loaded liposome or soybean oil-filled liposome as carrier control. This was seen across all females used in this study (Supplementary figure 8.12). A small number of lipid vacuoles was also seen in renal tubules of males injected with NIR dye-loaded liposome, however in comparison to vehicle control (soybean oil-filled liposome) or aqueous saline those changes were deemed not significant for all males used in this study (supplementary figure 8.14). Additionally, no significant accumulation of lipids was seen in the livers of males injected with NIR-dye loaded liposomes, or the soybean oil-loaded carrier control (Supplementary figure 8.13). For both genders, no lipids were detected in the spleen tissues (Figure 3.8), across all animals (Supplementary figure 8.14 and Supplementary figure 8.15).

Confirmation of the results presented in this section was sought by an independent certified pathologist from the St. James' Central Pathology Laboratory, St. James's Hospital, Dublin Ireland. These findings were confirmed, as summarised in table Table 3.2: Full description of liposome accumulation and pathological changes in all organs from animals tested in case study 1.

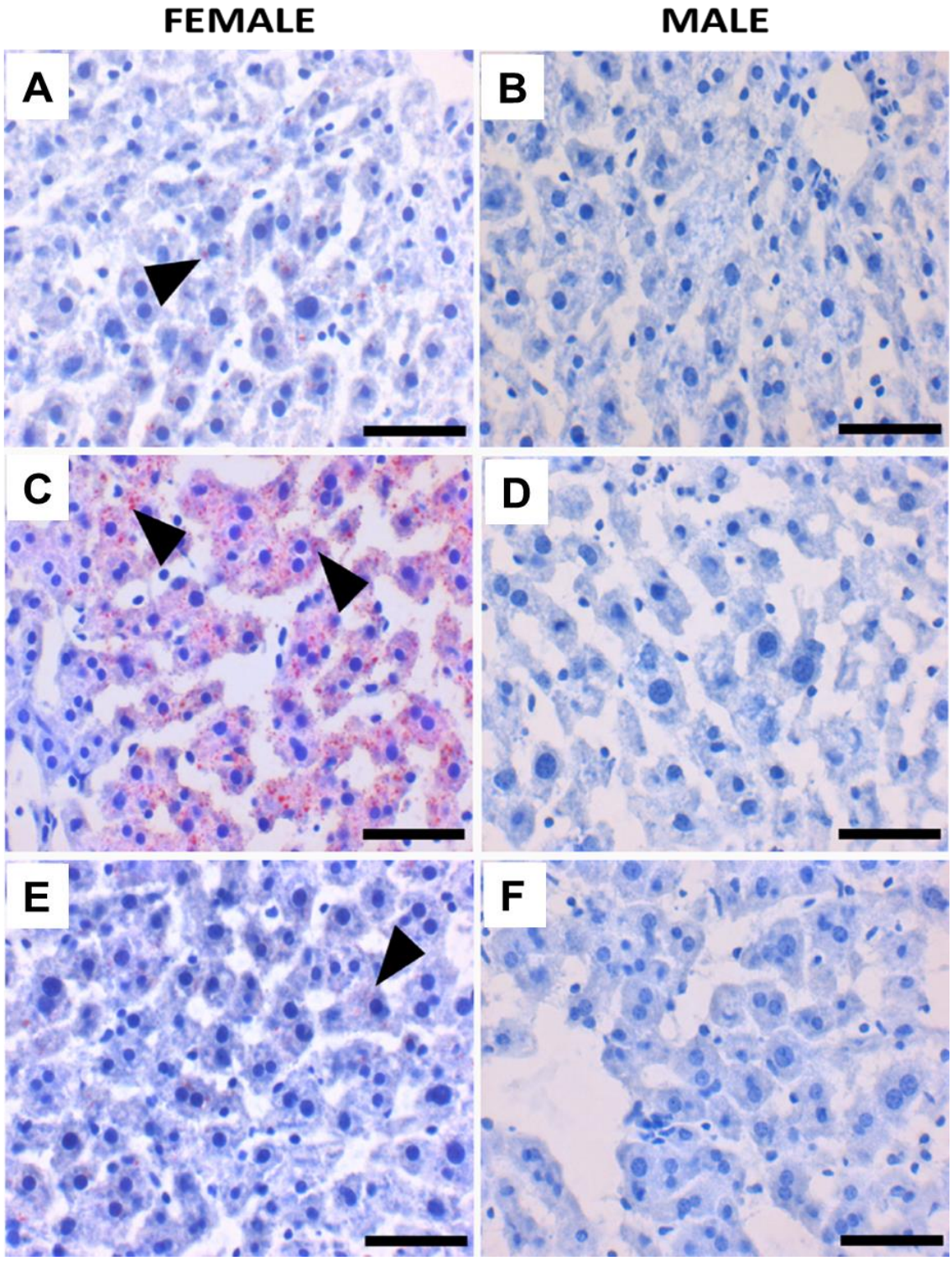

Figure 3.7: Lipid detection in liver tissue sections
Representative photomicrographs of Oil Red O stained liver sections highlighting difference in lipid content (seen as bright red vacuoles indicated by black arrowheads) between females (left column, n=4) and males (right column, n=4). C57BL/6 mice were injected with either saline (A and B), NIR dye-loaded liposome at 100 mg/kg concentration (C and D), or soybean-oil filled liposome (vehicle control) at 100 mg/kg concentration (E and F). 10µm thick sections were collected at four levels across the block with at least 50 µm distance between levels. Representative images were acquired with 40x lens. Scale bar represents 50 µm.

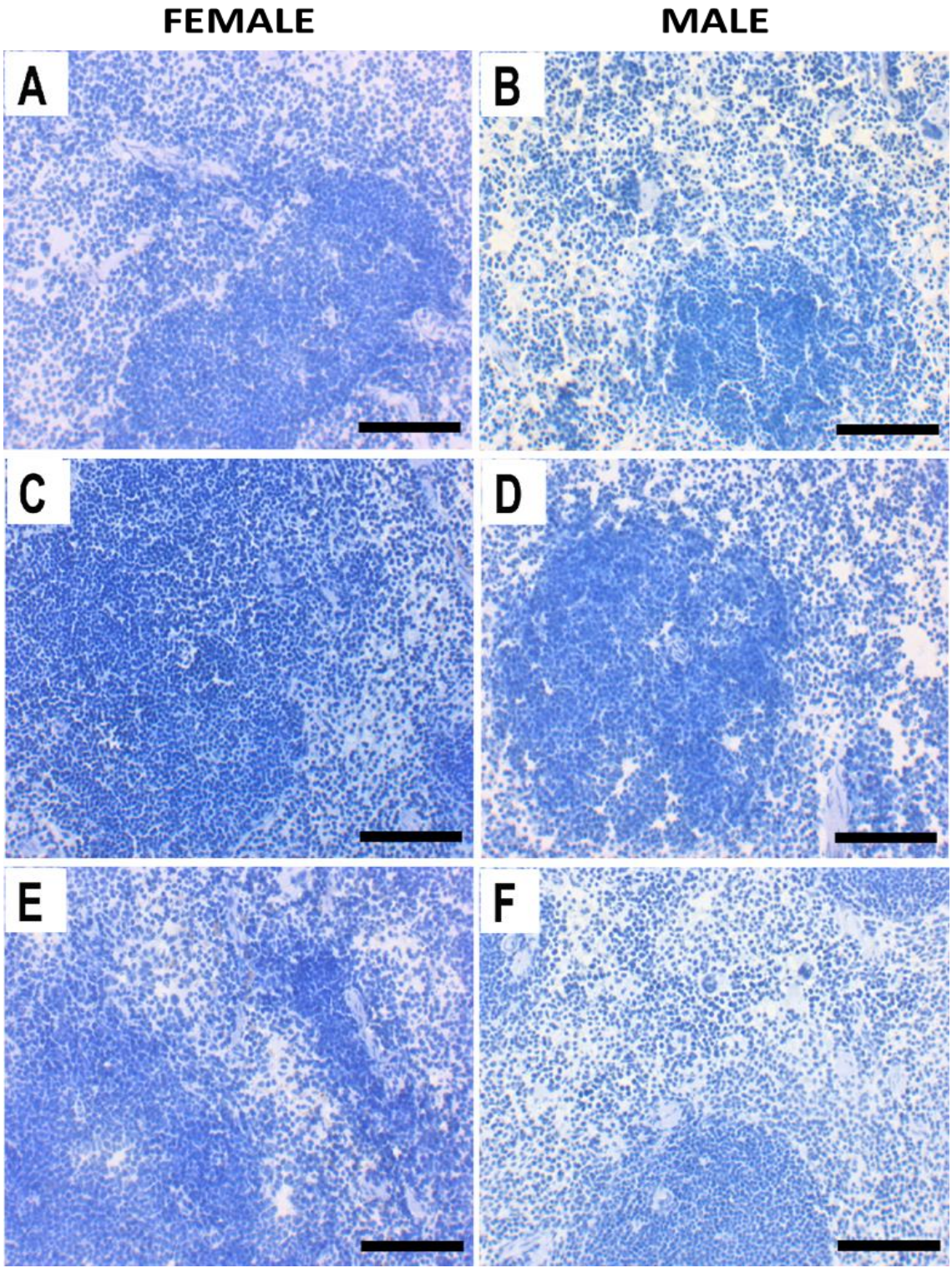

Figure 3.8: Lipid detection in spleen tissue sections
Representative photomicrographs of Oil Red O stained spleen sections. Lipid accumulation was not seen in C57BL/6 mice injected with either saline (A and B), NIR dye-loaded liposome at 100 mg/kg concentration (C and D), or soybean oil-filled liposome (vehicle control) at 100 mg/kg concentration (E and F) in both females (left column, n=4) and males (right column, n=3). 10µm thick sections were collected at four levels across the block with at least 50 µm distance between levels. Representative images were acquired with 40x lens. Scale bar represents 50 µm.

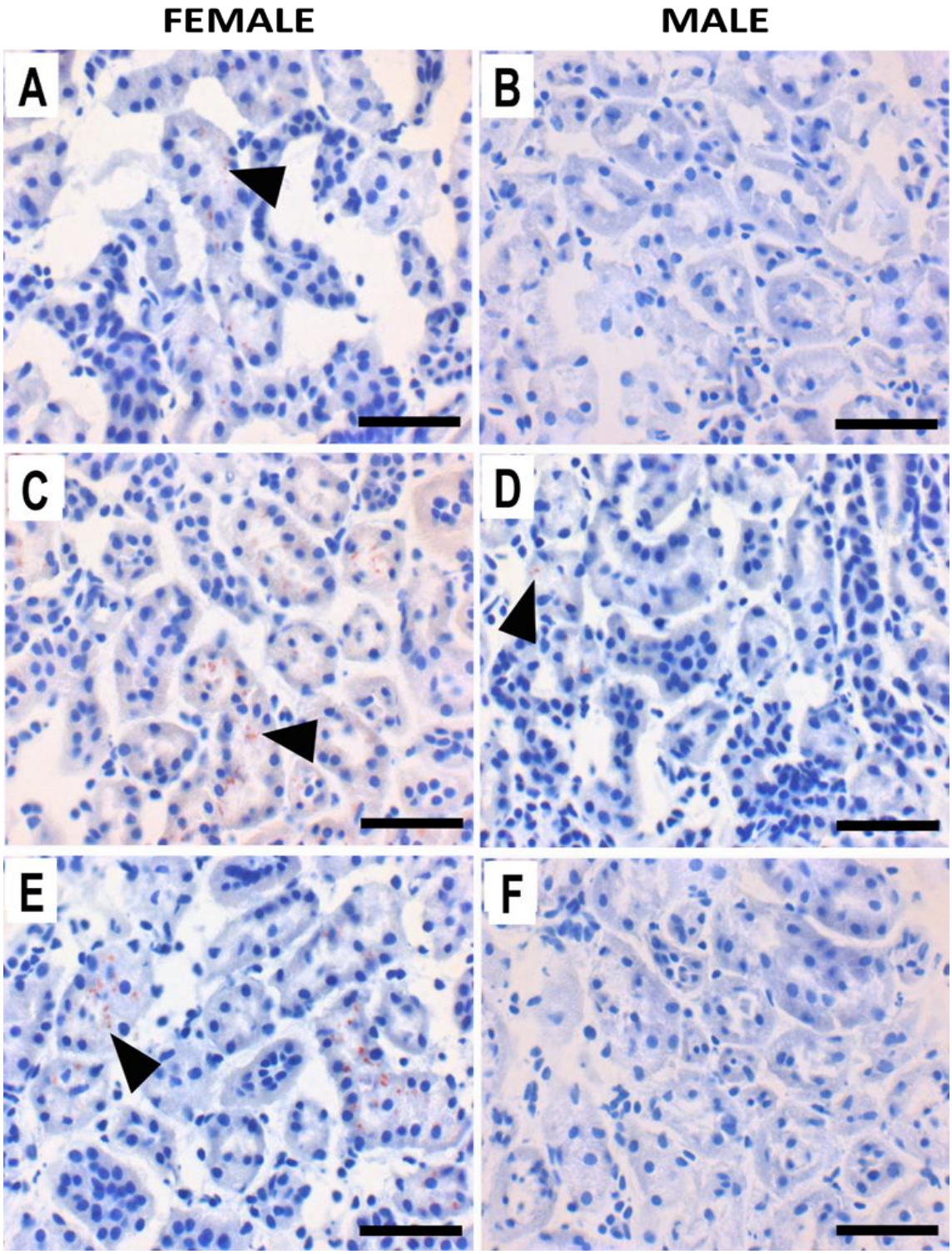

Figure 3.9: Lipid detection in kidney tissue sections
Representative photomicrographs of Oil Red O stained kidney sections from C57BL/6 mice. Lipids can be seen as bright red vacuoles indicated by the black arrowheads. Animals were injected with either saline (A and B), or NIR dye-loaded liposome at 100 mg/kg concentration (C and D), or soybean-oil filled liposome (vehicle control) at 100 mg/kg concentration (E and F). Females (left column, n=4) showed higher accumulation of lipids in the tubules in comparison to males (right column, n=3). 10µm thick sections were collected at four levels across the block with at least 50 µm distance between levels. Representative images were acquired with 40x lens. Scale bar represents 50 µm.

Table 3.2: Full description of liposome accumulation and pathological changes in all organs from animals tested in case study 1

Summary of findings reported by the certified pathologist from St. James' Central Pathology Laboratory on histological changes and accumulation of lipids for slices obtained from the organs of experimental animal used in case study 1. NAD: nothing abnormal detected

Animal ID	Sex	Treatment	Organ	Diagnosis	Lipid accumulation
1	Female	LipImage 815	Liver	NAD	Number of lipid vacuoles present in the hepatocytes
			Spleen	NAD	No lipids detected
			Kidney	NAD	Number of lipid vacuoles present in the renal tubules
2	Female	LipImage 815	Liver	NAD	Number of lipid vacuoles present in the hepatocytes
			Spleen	NAD	No lipids detected
			Kidney	NAD	Number of lipid vacuoles present in the renal tubules
3	Female	LipImage 815	Liver	NAD	Number of lipid vacuoles present in the hepatocytes
			Spleen	NAD	No lipids detected
			Kidney	NAD	Number of lipid vacuoles present in the renal tubules
4	Female	LipImage 815	Liver	NAD	Number of lipid vacuoles present in the hepatocytes
			Spleen	NAD	No lipids detected
			Kidney	NAD	Number of lipid vacuoles present in the renal tubules
5	Male	LipImage 815	Liver	NAD	No lipids detected
			Spleen	NAD	No lipids detected
			Kidney	NAD	No lipids detected
6	Male	LipImage 815	Liver	NAD	No lipids detected
			Spleen	NAD	No lipids detected
			Kidney	NAD	No lipids detected
7	Male	LipImage 815	Liver	NAD	No lipids detected
			Spleen	NAD	No lipids detected
			Kidney	NAD	No lipids detected
8	Female	Lipid control	Liver	NAD	Evidence of lipid vacuoles in the hepatocytes
			Spleen	NAD	No lipids detected

			Kidney	NAD	Small number of lipid vacuoles in renal tubules
9	Female	Lipid control	Liver	NAD	Evidence of lipid vacuoles in the hepatocytes
			Spleen	NAD	No lipids detected
			Kidney	NAD	No lipids detected
10	Female	Lipid control	Liver	NAD	Evidence of lipid vacuoles in the hepatocytes
			Spleen	NAD	No lipids detected
			Kidney	NAD	No lipids detected
11	Female	Lipid control	Liver	NAD	Evidence of lipid vacuoles in the hepatocytes
			Spleen	NAD	No lipids detected
			Kidney	NAD	No lipids detected
12	Male	Lipid control	Liver	NAD	No lipids detected
			Spleen	NAD	No lipids detected
			Kidney	NAD	No lipids detected
13	Male	Lipid control	Liver	NAD	No lipids detected
			Spleen	NAD	No lipids detected
			Kidney	NAD	No lipids detected
14	Male	Lipid control	Liver	NAD	No lipids detected
			Spleen	NAD	No lipids detected
			Kidney	NAD	No lipids detected
15	Female	saline	Liver	NAD	No lipids detected
			Spleen	NAD	No lipids detected
			Kidney	NAD	Evidence of lipid vacuoles in the renal tubule
16	Female	saline	Liver	NAD	No lipids detected
			Spleen	NAD	No lipids detected
			Kidney	NAD	Evidence of lipid vacuoles in the renal tubule
17	Female	saline	Liver	NAD	No lipids detected
			Spleen	NAD	No lipids detected
			Kidney	NAD	Evidence of lipid vacuoles in the renal tubule
18	Female	saline	Liver	NAD	Evidence of lipid vacuoles in the hepatocytes

			Spleen	NAD	No lipids detected
			Kidney	NAD	No lipids detected
19	Male	saline	Liver	NAD	No lipids detected
			Spleen	NAD	No lipids detected
			Kidney	NAD	No lipids detected
20	Male	saline	Liver	NAD	No lipids detected
			Spleen	NAD	No lipids detected
			Kidney	NAD	No lipids detected
21	Male	saline	Liver	NAD	No lipids detected
			Spleen	NAD	No lipids detected
			Kidney	NAD	No lipids detected

To discriminate between naturally occurring lipids and the liposomes, further investigation was carried out using fluorescent imaging.

Fluorescent imaging of female liver tissue section confirmed that females injected with NIR dye loaded liposome have a higher number of lipid vacuoles present in the hepatocytes in comparison to animals injected with saline or control (filled with soybean oil) (Figure 3.10 and Supplementary figure 8.18). No florescence was detected in far red channel (excitation 716 nm, emission 809 nm) indicating that by the time of the analysis NIR dye was either completely metabolised or excreted. The opposite was seen in male liver tissue sections (Figure 3.11 and Supplementary figure 8.19), where lipids and dye were found in the same location within individual hepatocytes as indicated by the orange arrowhead in Figure 3.11. No fluorescence was seen in males injected with saline or soybean oil filled carrier control, confirming that faint fluorescent signal seen in animals injected with NIR dye loaded liposome is the IR780-Oley dye encapsulated in the liposome.

The fluorescent imaging of spleen tissue sections showed similar pattern in both genders. Fluorescent dye was detected in both female (Figure 3.12 and Supplementary figure 8.20) and male (Figure 3.13 and Supplementary figure 8.21) mice injected with NIR dye-loaded liposome. Signal detected in females was weaker in comparison to that seen in males suggesting direct effect of sex on the metabolism and excretion of this NBM. Interestingly, a number of lipid vesicles was seen in spleens of females (Figure 3.12) and males (Figure 3.13) which was undetected with

brightfield microscopy (Figure 3.8). Additionally, there was a distinct overlap between lipid positive staining and signal from IR780-Oley dye suggesting successful detection of liposomes still containing their cargo material six days post injection. Those hypothetical liposomes were located in the marginal zone and white pulp suggesting potential immune response from cells of adaptive branch of immune system.

Lipids were also detected in renal tubules of both female (Figure 3.14 and Supplementary figure 8.22) and male (Figure 3.15 and Supplementary figure 8.23) mice. A faint signal from IR780-Oley dye was also detected in renal tubules of males injected with NIR dye loaded liposome, which was co-localised with lipid vesicles as indicated by the orange arrowhead in the representative Figure 3.15.

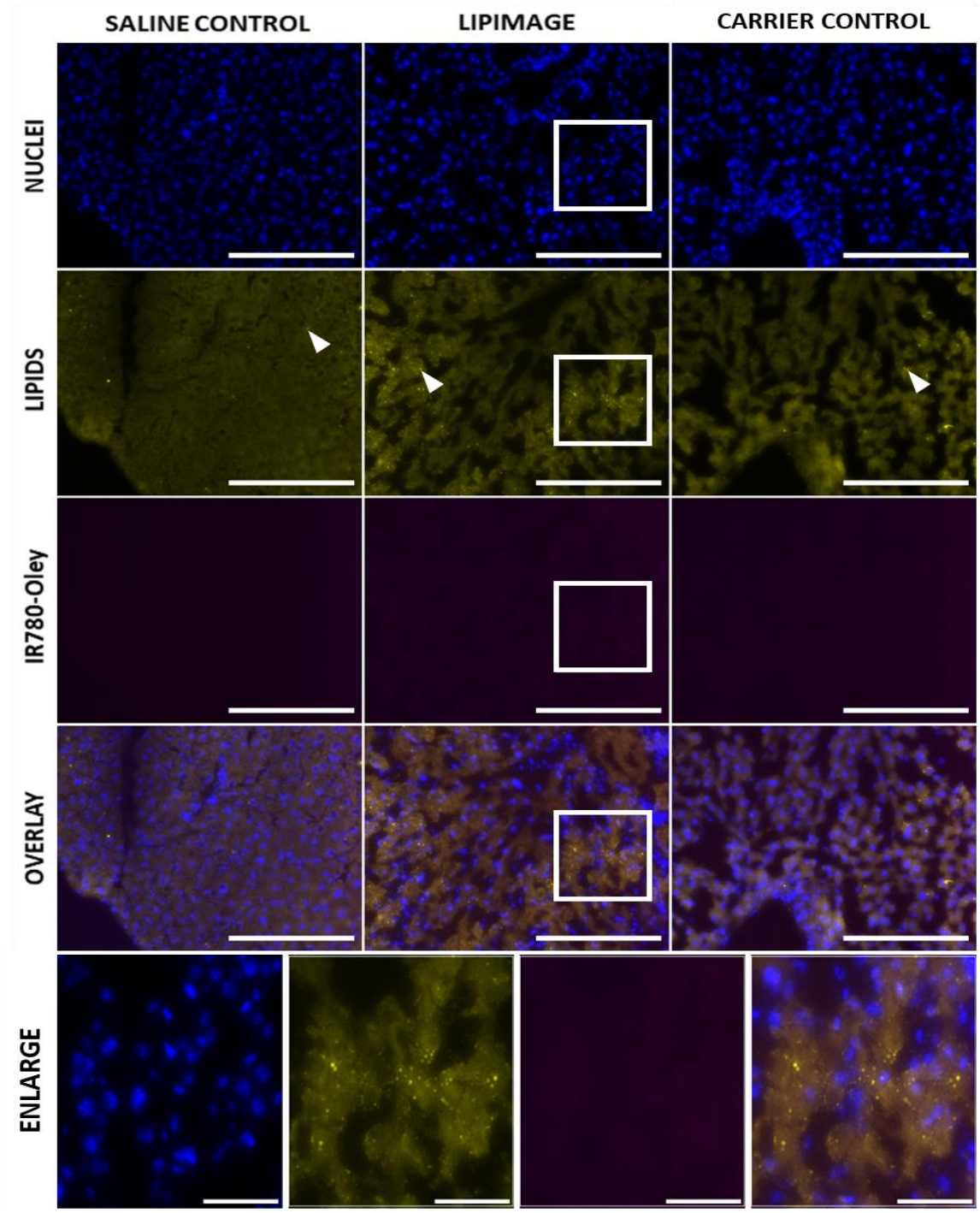

Figure 3.10: Detection of lipids and NIR dye in female liver tissues sections

Representative photomicrographs of liver sections from C57BL/6 female mice (n=4) injected with saline (left column), NIR dye-loaded liposome at 100 mg/kg concentration (middle column), or vehicle control liposome filled with soybean-oil (right column). . 10µm thick sections were collected at four levels across the block with at least 50 µm distance between levels. For better visualisation, objects of interest were assigned pseudo colour in the images as follows: nuclei are seen in blue, lipids in yellow, IR-780 dye in magenta. Lipids were detected in all animals regardless of treatment. Enlarged images of the areas highlighted with white boxes are shown in the bottom panel. Representative images were acquired with 20x lens. Scale bar represents 200µm in the original images, and 50µm in the enlarged images

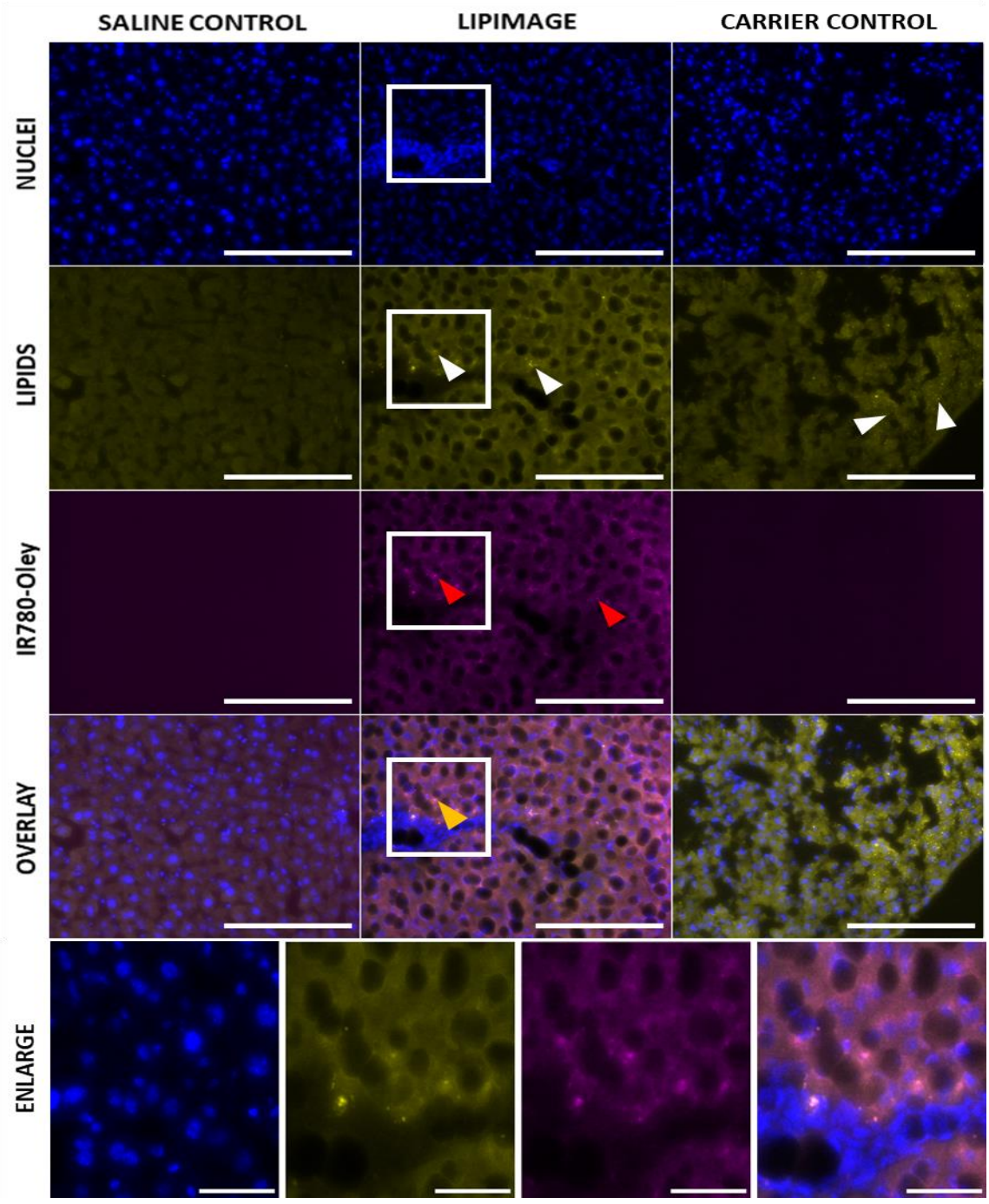

Figure 3.11: Detection of lipids and NIR dye in male liver
Representative photomicrographs of liver sections from C57BL/6 male mice (n=3) injected with saline (left column), NIR dye-loaded liposome at 100 mg/kg concentration (middle column), or vehicle control liposome filled with soybean-oil (right column). 10µm thick sections were collected at four levels across the block with at least 50 µm distance between levels. For better visualisation, objects of interest were assigned pseudo colour in the images as follows: nuclei are seen in blue, lipids in yellow, IR-780 dye in magenta. Lipids were detected in animals injected with two liposomal formulations as indicated by the white arrowheads in second row. Co-localisation (orange arrowheads in fourth row) of lipid and IR780-Oley dye (red arrowheads in third row) was seen in animals injected with NIR dye-loaded liposome. Enlarged images of the areas highlighted with white boxes are shown in the bottom panel. Representative images were acquired with 20x lens. Scale bar represents 200µm in the original images, and 50µm in the Enlarged images.

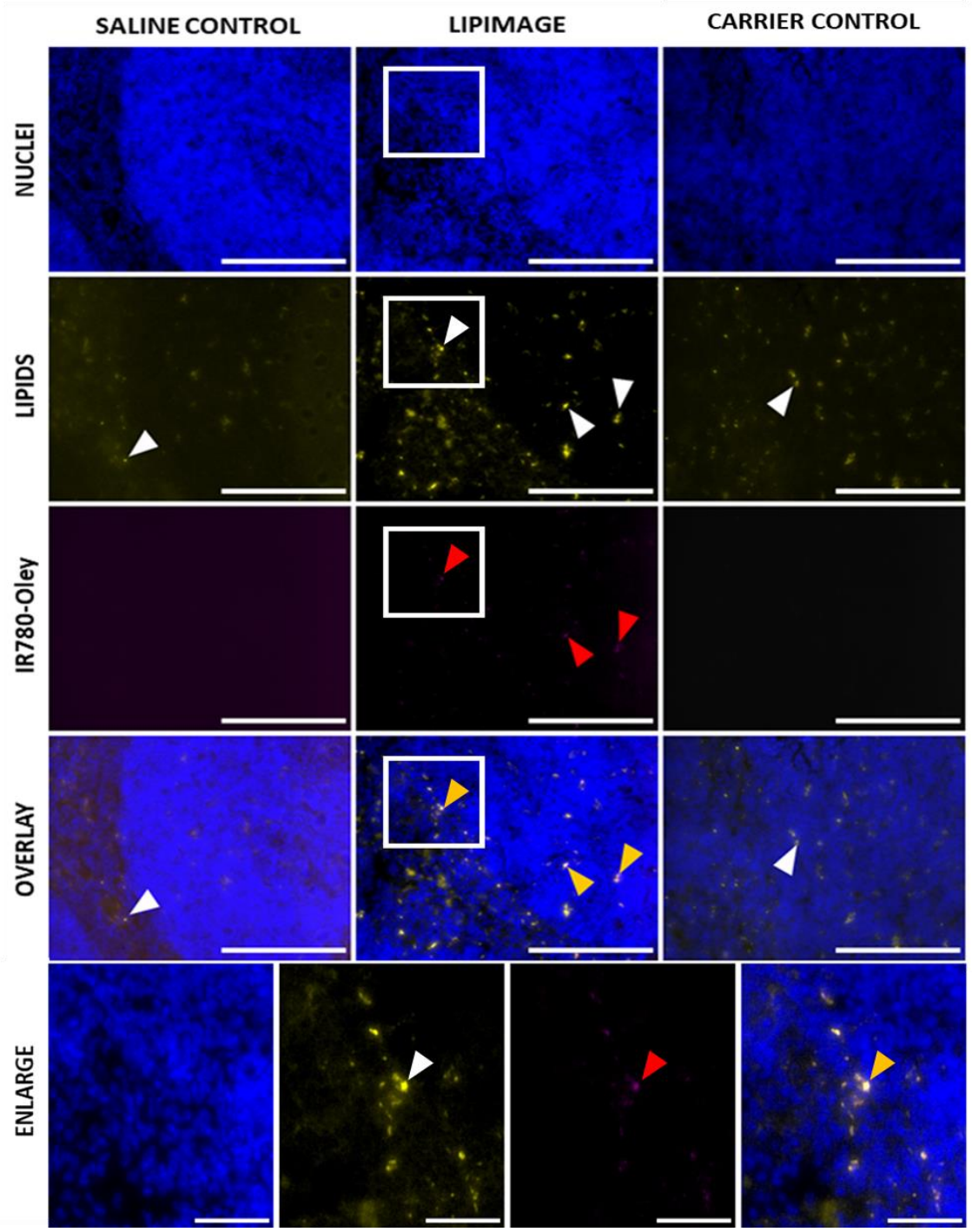

Figure 3.12: Detection of lipids and NIR dye in female spleen
Representative photomicrographs of spleen sections from C57BL/6 female mice (n=4) injected with saline (left column), NIR dye-loaded liposome at 100 mg/kg concentration (middle column), or vehicle control liposome filled with soybean-oil (right column). 10µm thick sections were collected at four levels across the block with at least 50 µm distance between levels. For better visualisation, objects of interest were assigned pseudo colour in the images as follows: nuclei are seen in blue, lipids in yellow, IR-780 dye in magenta. Lipids were detected in all animals regardless of the treatment as indicated by the white arrowheads in second and fourth rows. Co-localisation (orange arrowheads in fourth row) of lipid and IR780-Oley dye (red arrowheads in third row) was seen in animals injected with NIR dye-loaded liposome. Enlarged images of the areas highlighted with white boxes are shown in the bottom panel. Representative images were acquired with 20x lens. Scale bar represents 200µm in the original images, and 50µm in the enlarged images

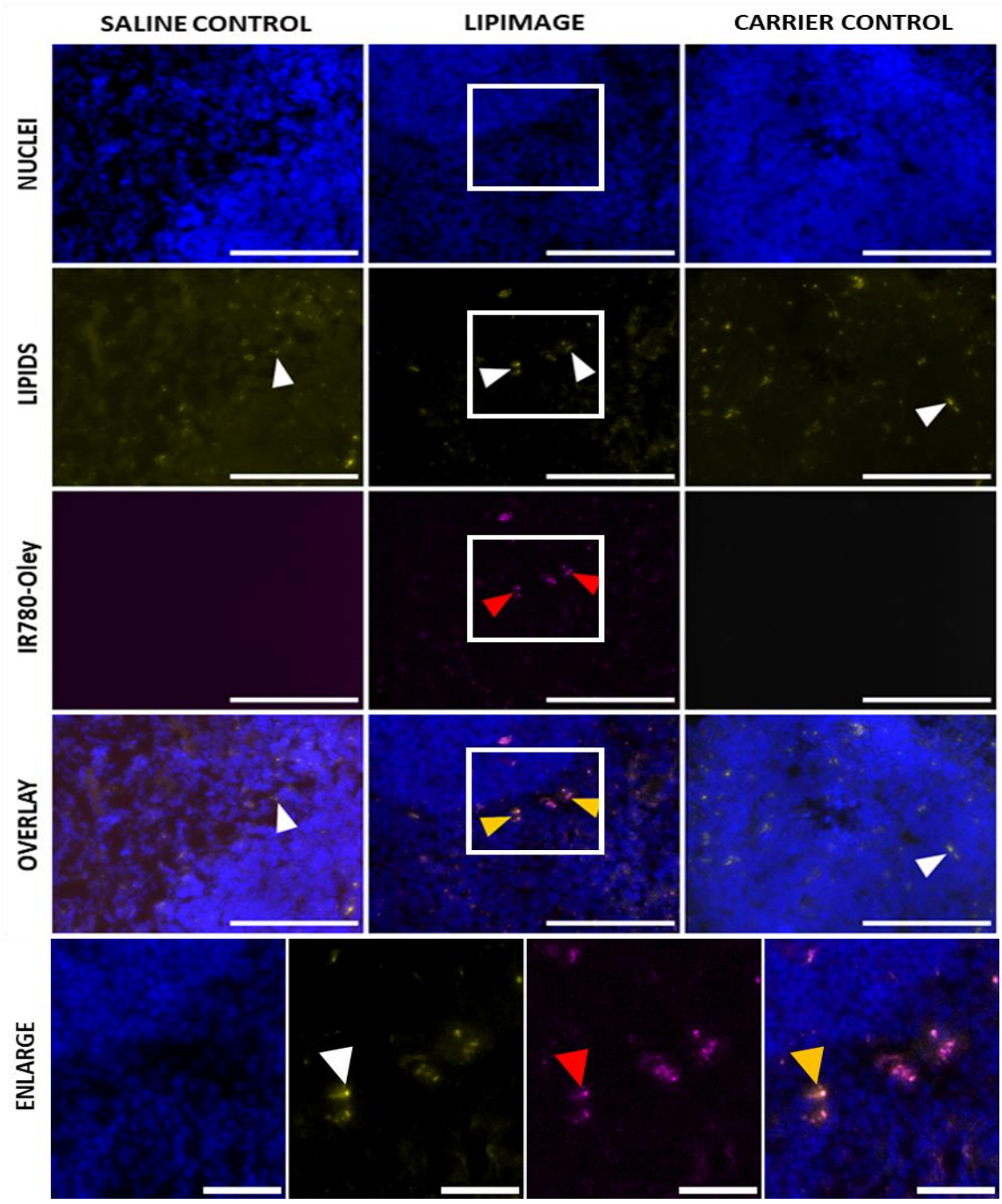

Figure 3.13: Detection of lipids and NIR dye in male spleen
Representative photomicrographs of spleen sections from C57BL/6 male mice (n=3) injected with saline (left column), NIR dye-loaded liposome at 100 mg/kg concentration (middle column), or vehicle control liposome filled with soybean-oil (right column). 10µm thick sections were collected at four levels across the block with at least 50 µm distance between levels. For better visualisation, objects of interest were assigned pseudo colour in the images as follows: nuclei are seen in blue, lipids in yellow, IR-780 dye in magenta. Lipids were detected in all animals regardless of the treatment as indicated by the white arrowheads in second and fourth rows. Co-localisation (orange arrowheads in fourth row) of lipid and IR780-Oley dye (red arrowheads in third row) was seen in animals injected with NIR dye-loaded liposome. Enlarged images of the areas highlighted with white boxes are shown in the bottom panel. Representative images were acquired with 20x lens. Scale bar represents 200µm in the original images, and 50µm in the enlarged images

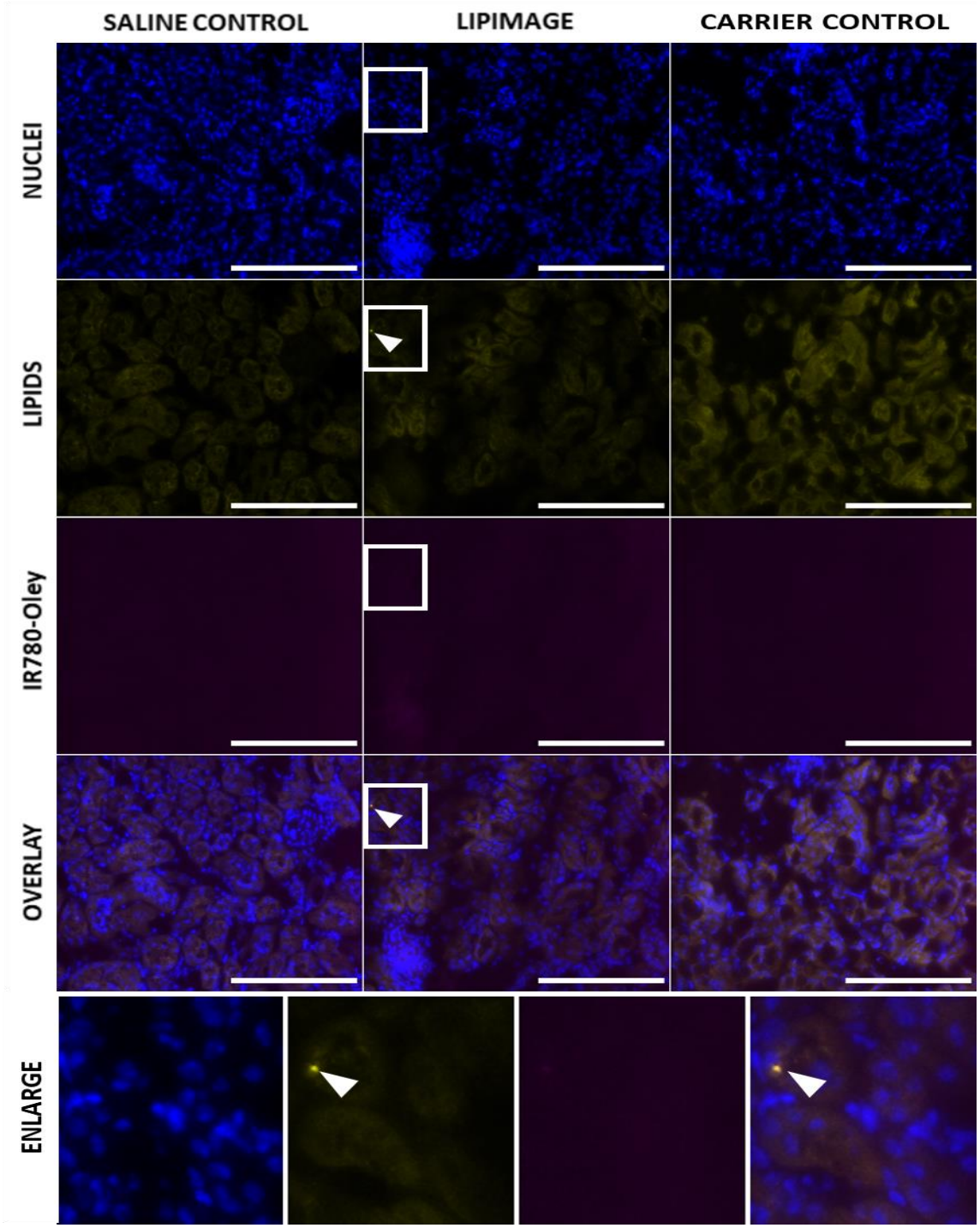

Figure 3.14: Detection of lipids and NIR dye in female kidney
Representative photomicrographs of kidney sections from C57BL/6 female mice (n=4) injected with saline (left column), NIR dye-loaded liposome at 100 mg/kg concentration (middle column), or vehicle control liposome filled with soybean-oil (right column). 10µm thick sections were collected at four levels across the block with at least 50 µm distance between levels. For better visualisation, objects of interest were assigned pseudo colour in the images as follows: nuclei are seen in blue, lipids in yellow, IR-780 dye in magenta. Lipids were only detected in females injected with NIR dye-loaded liposome as indicated by the white arrowheads in second and fourth rows. Enlarged images of the areas highlighted with white boxes are shown in the bottom panel. Representative images were acquired with 20x lens. Scale bar represents 200µm in the original images, and 50µm in the enlarged images

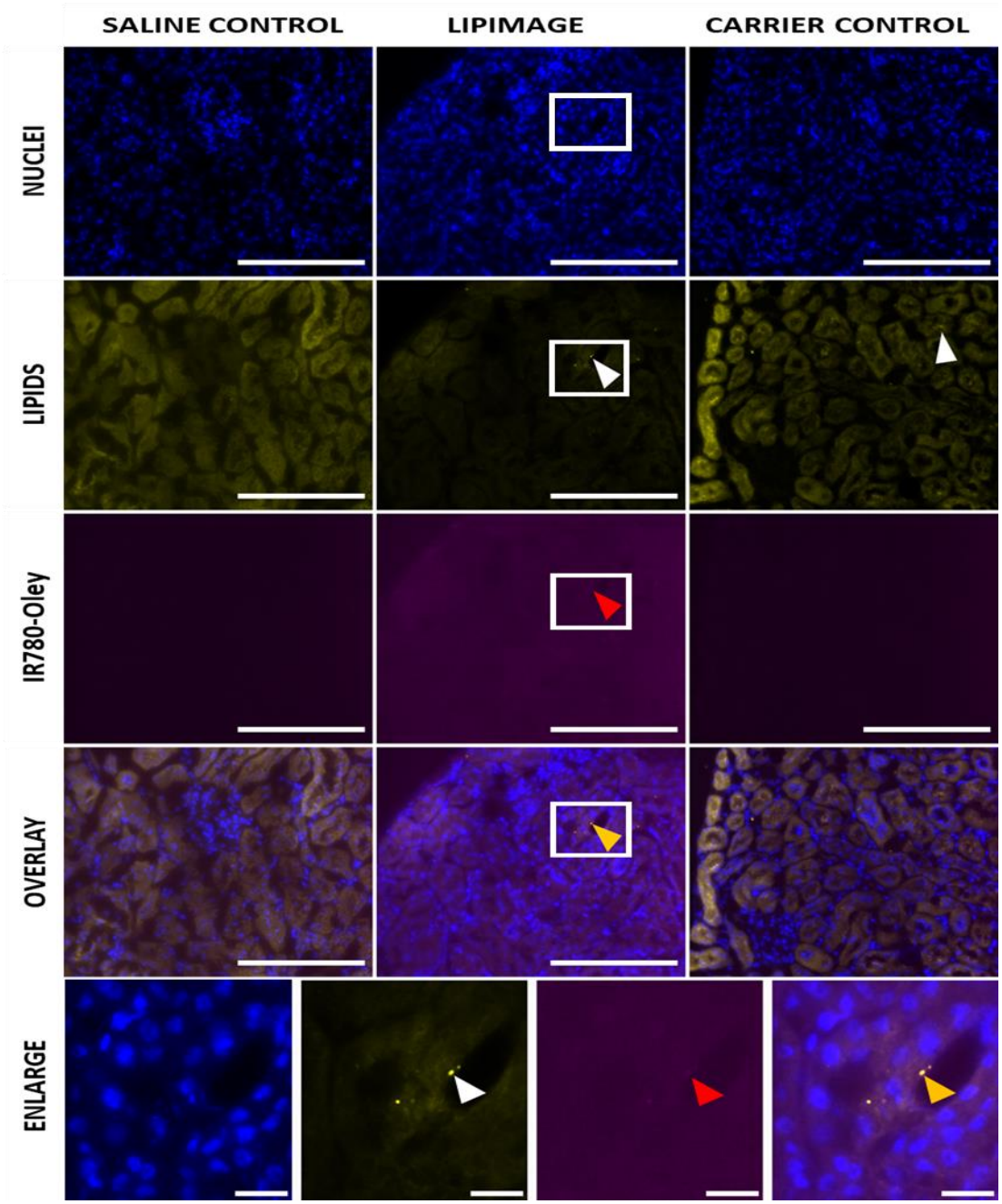

Figure 3.15: Detection of lipids and NIR dye in male kidney

Representative photomicrographs of kidney sections from male C57BL/6 m9ice (n=3) injected with saline (left column), NIR dye-loaded liposome at 100 mg/kg concentration (middle column), or vehicle control liposome filled with soybean-oil (right column). 10µm thick sections were collected at four levels across the block with at least 50 µm distance between levels. For better visualisation, objects of interest were assigned pseudo colour in the images as follows: nuclei are seen in blue, lipids in yellow, IR-780 dye in magenta. Lipids were detected in animals injected with two liposomal formulations as indicated by the white arrowheads in second and fourth rows. Co-localisation (orange arrowheads in fourth row) of lipid and IR780-Oley dye (red arrowheads in third row) was seen in males injected with NIR dye-loaded liposome. Enlarged images of the areas highlighted with white boxes are shown in the bottom panel. Representative images were acquired with 20x lens. Scale bar represents 200µm in the original images, and 50µm in the enlarged images

In summary, liposomes containing IR780-Oley were successfully detected ex vivo in tissue sections using fluorescent imaging. This novel approach to liposome detection in tissue sections lead to an unexpected finding showing the effect of animal's sex on the stability of NIR dye. Lipids stained with ORO overlapped with fluorescent signal from NIR dye allowing for discrimination between NBMs and naturally occurring lipids in males. This was not possible for the carrier control containing soybean oil, emphasising the need for a suitable marker for detection of liposomes not containing a dye or a fluorophore. This limitation was addressed in the second in vivo case study presented in the next sub-section.

3.3.2 *Case study 2: proof-of-concept SOP for loaded liposome biodistribution detection*

Irinotecan (CPT-11) is a camptothecin derivative with a broad spectrum of antitumor activity in clinical models with responses observed in colorectal [132], lung [133, 134], cervical [135, 136] and ovarian cancers. Due to numerous limitations of irinotecan, such as poor water solubility, quick inactivation at physiological pH and low conversion to active metabolite [137]. To this objective extensive research at preclinical level has been carried out to develop new delivery methods [138]. Onivyde®, as CPT-11 encapsulated PEGylated liposome, was first developed for the treatment of metastatic adenocarcinoma of the pancreas, in combination with 5-fluorouracil (5-FU) and leucovorin, in patients who have been previously treated with gemcitabine. However, preliminary results from clinical trials indicate its potential to treat multiple solid tumours [46-48]. This formulation was approved by the FDA for treatment of advanced pancreatic cancer in October 2015, followed by EMA designation as an 'orphan medicine' in October 2016.

Since its first approval, FDA has granted Fast Track designation for Onivyde® in two more applications. Currently ongoing Phase 3 randomised study (NAPOLI-3; NCT04083235) [139-141] is conducted to assess safety and efficacy of Onivyde® in combination with 5-fluorouracil/leucovorin (5-FU/LV) and oxaliplatin together, known as NALIRIFOX as first-line treatment in patients with previously untreated, unresectable, locally advanced and metastatic pancreatic ductal adenocarcinoma (PDAC). Second Phase 3 randomised study (RESILIENT; NCT03088813) is conducted to assess safety and efficacy of Onivyde® as a monotherapy for small cell lung cancer (SCLC) in patients who have progressed on or after a first-line platinum-based regiment [142-144].

All the clinical evidence presented, highlights the continuous growing interest in the use of Onivyde® to treat multiple cancers as monotherapy and in combination with other treatments emphasize the need for consistent and appropriate preclinical testing models to fully understand interaction of nanomedicines with biological systems for successful translation into clinic. For this reason, Onivyde® was adopted as a model NBM to develop and optimise a SOP for detecting PEGylated liposomes in tissue section. The results presented in this section concentrate on toxicity and biodistribution of this NBM in comparison to its free drug counterpart. Supplementary data on pharmacokinetics and clearance is provided in the appendix, supplementary figure 8.32 and 8.33 respectively.

3.3.2.1 Toxicity

It is well documented that Irinotecan is known to cause chemotherapy-associated steatohepatitis, therefore in the SOP work the search for steatosis in the liver was expected. To evaluate drug induced tissue toxicity, three main organs of interest were processed for histopathological examination. In this study, there were no major changes suggesting toxicity observed in spleen and small intestine in both treatment groups. This was seen across all animals used in this study (Supplementary figure 8.24). In liver, however (Figure 3.16), a lipid type bodies were seen in the hepatocytes in both groups. This change was seen in 2 out of 3 animals in each treatment group (Supplementary figure 8.24)

Confirmation of the results presented in this section was sought by an independent certified pathologist from the St. James' Central Pathology Laboratory, St. James's Hospital, Dublin Ireland. The pathologist was blinded to experimental conditions. Findings reported in this case study were confirmed, as summarised in Table 3.3: Full description of liposome accumulation and pathological changes in all organs from animals tested in case study 2.

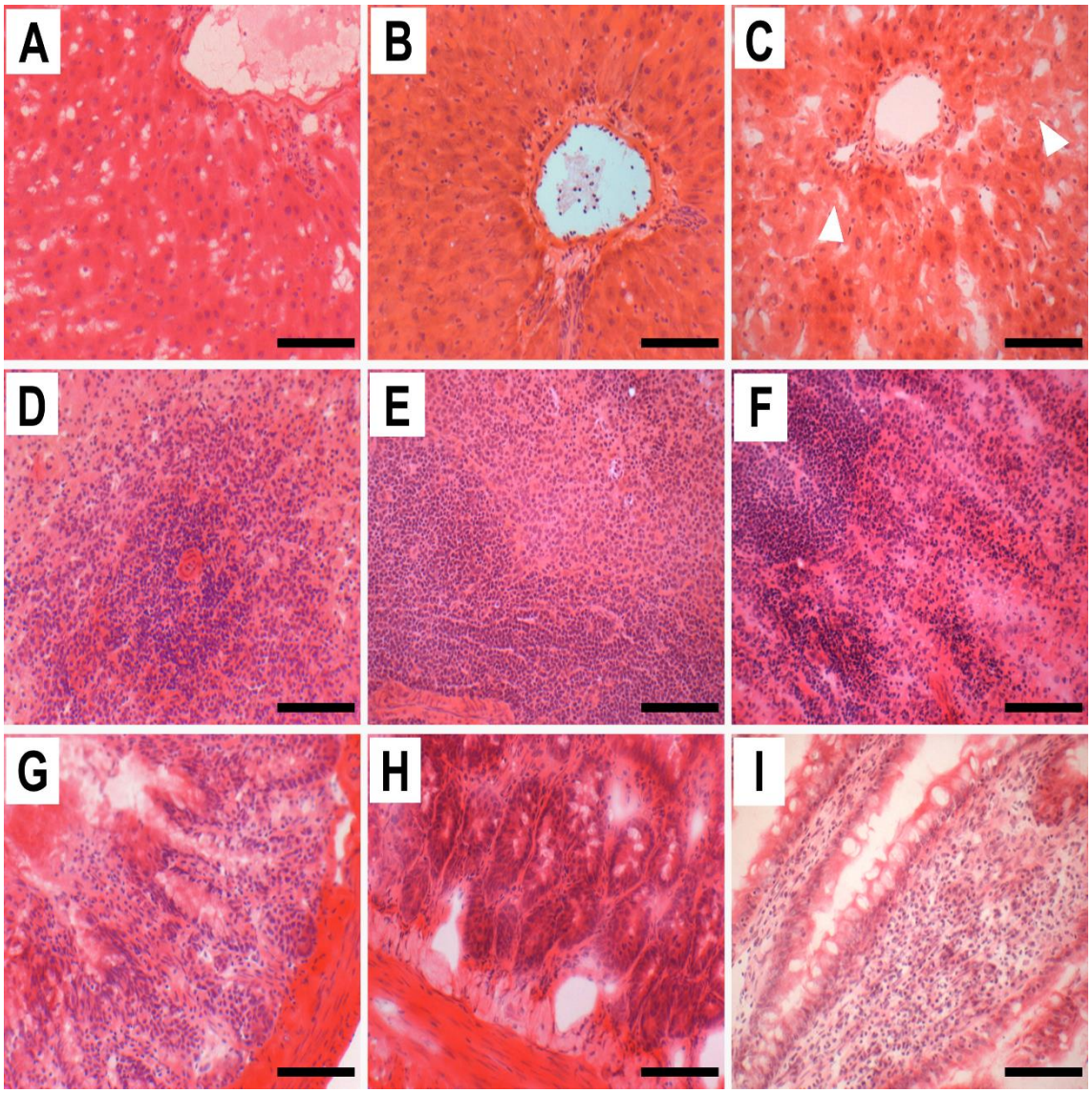

Figure 3.16: Pathological changes induced by irinotecan and liposomal irinotecan in liver, spleen and small intestines

Representative photomicrographs of H&E stained liver (A-C), spleen (D-F), and small intestine (G-I) of male Wistar rats (n=3). Animals were injected with either saline (left column), Irinotecan at 20 mg/kg (middle column), or liposomal Irinotecan at 20 mg/kg (right column). Animals were culled 48h post injection and harvested organs were cryopreserved by freezing in OCT media. 10µm sections were cut with a cryostat, and collected at four levels through the block spaced at least 50 µm apart. Sections were stained with H&E stain, and examined using a brightfield microscope. Representative images were acquired with 20x lens. Scale bar represents 100 µm.

3.3.2.2 Determination of Liposome accumulation in organs by selective histological staining

In both treatment groups, several animals showed positive staining in the liver hepatocytes (Figure 3.17 B and C) and in the lacteal in small intestines (Figure 3.17 H and I). However, accumulation of lipids was higher in animals injected with liposomal irinotecan (Supplementary figure 8.27 and Supplementary figure 8.29). Furthermore, multiple macrophages with lipid vacuoles were seen in the white pulp of spleen (Figure 3.17 F). This was seen in 3 out of 3 animals treated with liposomal irinotecan, and only 1 out of 3 animals treated with Irinotecan (Supplementary figure 8.28).

Confirmation of the results presented in this section was sought by an independent certified pathologist from the St. James' Central Pathology Laboratory, St. James's Hospital, Dublin Ireland. These findings were confirmed, as summarised in Table 3.3: Full description of liposome accumulation and pathological changes in all organs from animals tested in case study 2..

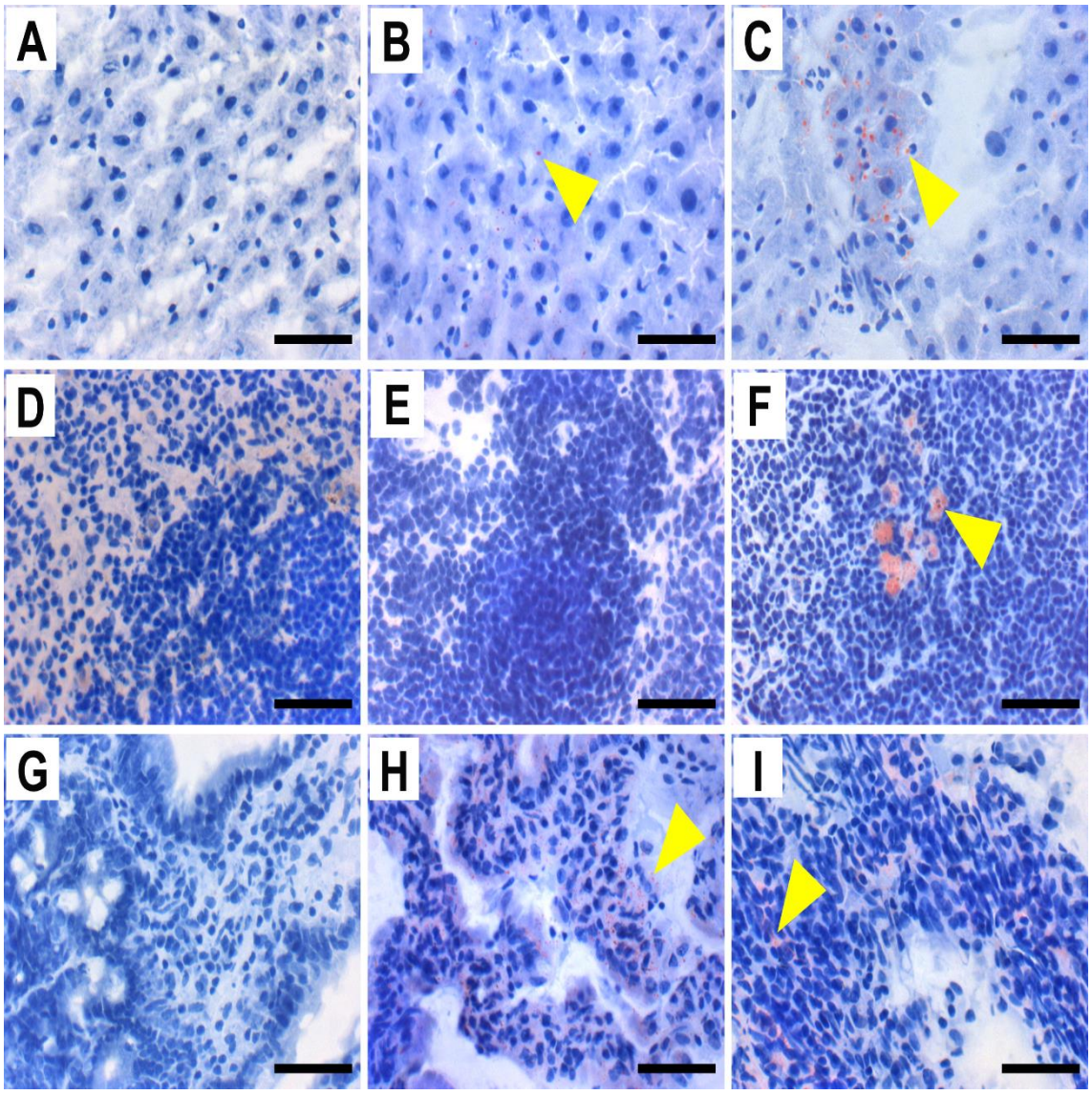

Figure 3.17: Lipid detection with Oil Red O on different organ tissue sections
Representative photomicrographs of liver (A-C), spleen (D-E) and small intestine (G-I) from male Wistar rats (n=3) injected with saline (left column) irinotecan at 20 mg/kg (middle column), or Onivyde® at 20 mg/kg of Irinotecan equivalent (right column). Animals were culled 48h post injection and harvested organs were cryopreserved by freezing in OCT media. 10µm sections were cut with a cryostat, and collected at four levels through the block spaced at least 50 µm apart. Collected sections were stained with ORO stain, and examined using a brightfield microscope. Lipid droplets are visible as bright red deposits (yellow arrowhead). Representative images were acquired with 40x lens. Scale bar represents 50 µm.

Table 3.3: Full description of liposome accumulation and pathological changes in all organs from animals tested in case study 2.

Summary of findings reported by the certified pathologist from St. James' Central Pathology Laboratory on histological changes and accumulation of lipids for slices obtained from the organs of experimental animal used in case study 2. NAD: nothing abnormal detected

Animal ID	Treatment	Organ	Diagnosis	Lipid accumulation
1	Onivyde®	Liver	NAD	Small number of lipid vacuoles in the hepatocytes
		Spleen	NAD	Lipid loaded macrophages in the white pulp
		Small intestine	NAD	Positive lipid staining in the lacteal
2	Saline	Liver	NAD	No lipids detected
		Spleen	NAD	NAD
		Small intestine	NAD	NAD
3	Irinotecan	Liver	NAD	No lipids detected
		Spleen	NAD	NAD
		Small intestine	NAD	NAD
4	Irinotecan	Liver	Vacuoles in the hepatocytes	No lipids detected
		Spleen	NAD	Lipid loaded macrophages in the white pulp
		Small intestine	NAD	NAD
5	Onivyde®	Liver	Vacuoles in the hepatocytes	Small number of lipid vacuoles in the hepatocytes
		Spleen	NAD	Lipid loaded macrophages in the white pulp
		Small intestine	NAD	Positive lipid staining in the lacteal
6	Saline	Liver	NAD	No lipids detected
		Spleen	NAD	NAD
		Small intestine	NAD	NAD
7	Saline	Liver	NAD	No lipids detected
		Spleen	NAD	NAD
		Small intestine	NAD	NAD
8	Irinotecan	Liver	Vacuoles in the hepatocytes	No lipids detected
		Spleen	NAD	NAD
		Small intestine	NAD	NAD
9	Onivyde®	Liver	Vacuoles in the hepatocytes	Small number of lipid vacuoles in the hepatocytes
		Spleen	NAD	Lipid loaded macrophages in the white pulp
		Small intestine	NAD	Positive lipid staining in the lacteal

In order to discriminate between naturally occurring lipids and the liposome, tissue sections were stained with ORO together with immunolabelling of PEG. Sections were examined under laser scanning confocal microscope to visually assess co-localisation of the liposome and PEG coating.

PEG was detected in liver (Figure 3.18), small intestine (Figure 3.19), and spleen (Figure 3.20) of the animals injected with Onivyde®. Furthermore, in all three organs, PEG co-localised with lipid positive areas (as indicated by white arrowheads in representative figures), suggesting that number of liposomes was not degraded in any of those organs at 48 hours post intravenous injection. Additionally, free PEG (not co-localised with lipids) was seen in the splenic white pulp (Figure 3.20). These finding were consistent between the animals within each treatment group (Supplementary figure 8.30, Supplementary figure 8.31, and Supplementary figure 8.32 in chapter 8).

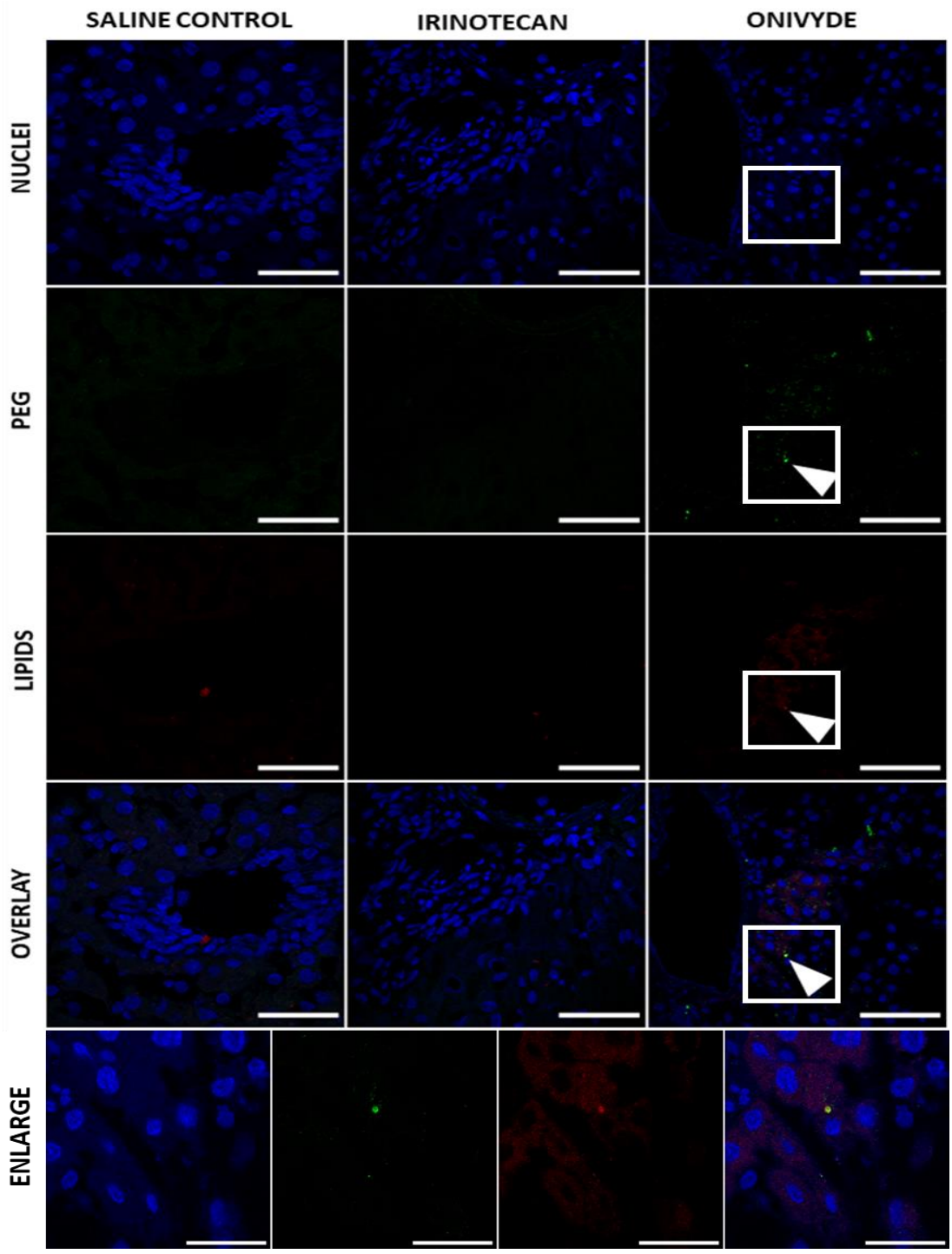

Figure 3.18: Immunofluorescent detection of lipids and PEG in liver
Representative photomicrographs of liver from male Wistar rats (n=3) injected with saline (left column), free irinotecan at 20 mg/kg concentration (middle column), or Onivyde® at 20 mg/kg of irinotecan equivalent (right column). Animals were culled 48h post injection and harvested organs were cryopreserved by freezing in OCT media. 10µm sections were cut with a cryostat, and collected at four levels through the block spaced at least 50 µm apart. Objects of interest were assigned pseudo colour as follows: nuclei in blue, PEG in green, lipids in red. Co-localisation of lipid and PEG (white arrowheads) was seen in the animals injected with Onivyde®. Enlarged images of the areas highlighted with white boxes are shown in the bottom panel. Representative images were acquired with 63x lens. Scale bar represents 50µm in the original images, and 25µm in the enlarged images.

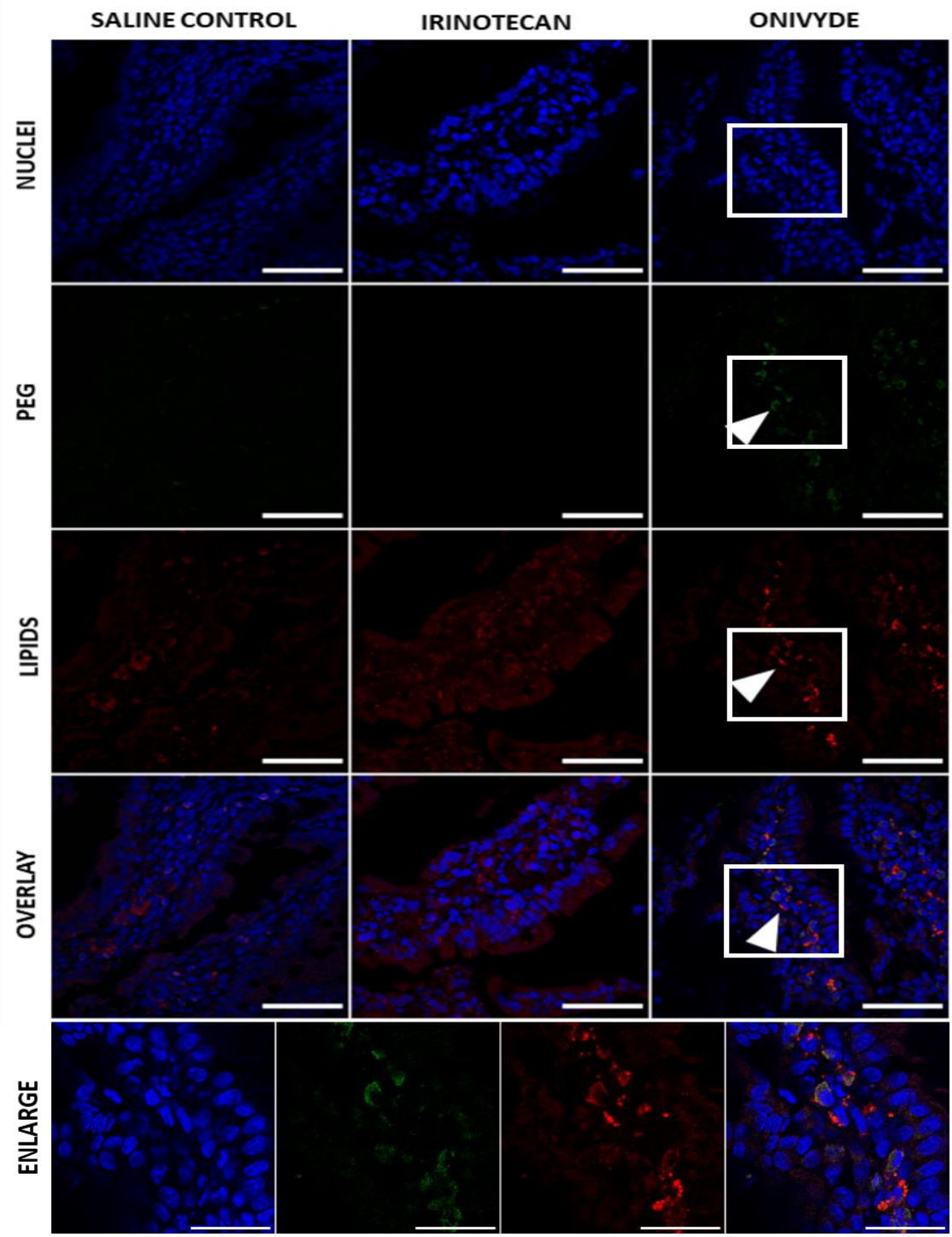

Figure 3.19: Immunofluorescent detection of lipids and PEG in small intestine
Representative photomicrographs of small intestines from male Wistar rats (n=3) injected with saline (left column), free irinotecan at 20 mg/kg concentration (middle column), or Onivyde® at 20 mg/kg of irinotecan equivalent (right column). Animals were culled 48h post injection and harvested organs were cryopreserved by freezing in OCT media. 10µm sections were cut with a cryostat, and collected at four levels through the block spaced at least 50 µm apart. Objects of interest were assigned pseudo colour as follows: nuclei in blue, PEG in green, lipids in red. Co-localisation of lipid and PEG (white arrowheads) was seen in the lacteal of the animals injected with Onivyde®. Enlarged images of the areas highlighted with white boxes are shown in the bottom panel. Representative images were acquired with 63x lens. Scale bar represents 50µm in the original images, and 25µm in the enlarged images.

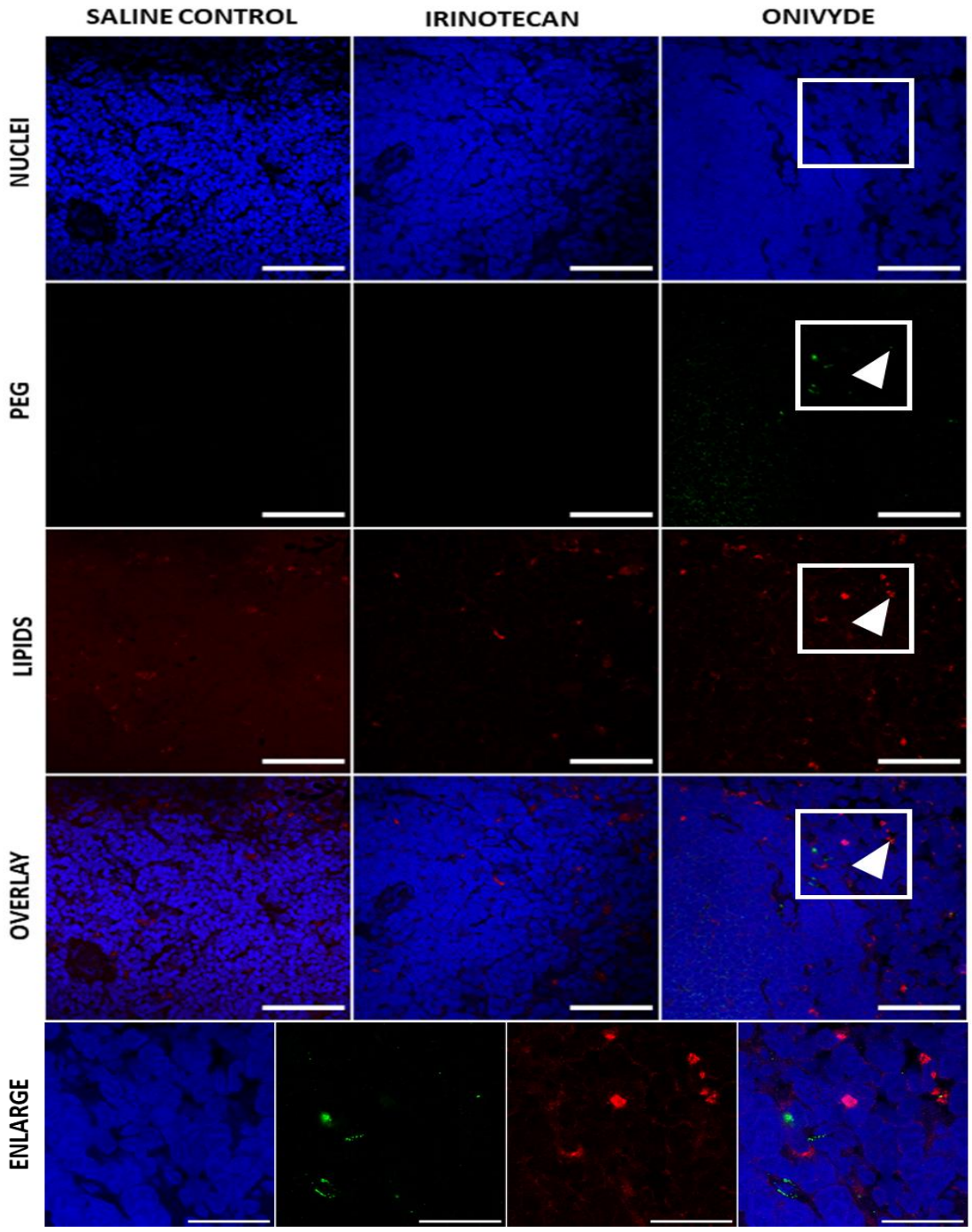

Figure 3.20: Immunofluorescent detection of lipid and PEG in spleen
Representative photomicrographs of spleen from male Wistar rats (n=3) injected with saline (left column), free irinotecan at 20 mg/kg concentration (middle column), or Onivyde® at 20 mg/kg of irinotecan equivalent (right column). Animals were culled 48h post injection and harvested organs were cryopreserved by freezing in OCT media. 10µm sections were cut with a cryostat, and collected at four levels through the block spaced at least 50 µm apart. Objects of interest were assigned pseudo colour as follows: nuclei in blue, PEG in green, lipids in red. Co-localisation of lipid and PEG (white arrowheads) was seen in the animals injected with Onivyde®. Enlarged images of the areas highlighted with white boxes are shown in the bottom panel. Representative images were acquired with 63x lens. Scale bar represents 50µm in the original images, and 25µm in the enlarged images.

3.3.3 *Quantitative analysis of biodistribution by MS*

The results of immunofluorescent staining indicated presence of the liposomes in liver, small intestine and spleen. The co-localisation of PEG coating with lipid suggested that the liposomes were not metabolised at 48 h post injection. This was in line with the results from the mass spectrometry carried out by SINTEF, EUNCL H2020 project partner.

The quantitative analysis showed that the concentration of CPT-11 in the Onivyde®-treated group was much higher than in the free-chemical diffusive irinotecan-treated group; as it was measured in the majority of the organs assessed (Figure 3.21). The highest concentration of CPT-11 was detected in the spleen of the Onivyde®-treated animals, with concentration 10-fold higher than the one detected in liver and small intestine. This proves that the free formulation is being metabolised faster compared to its liposomal form, supporting results of the fluorescent microscopy which showed intact liposomes within those organs

Different trend was observed for the concentration of an active metabolite of irinotecan, SN-38 (Figure 3.21B). Spleen had a higher SN-38 concentration in irinotecan-treated animals compared to animals treated with Onivyde®. Liver and small intestine are involved in the metabolism of CPT-11. In those organs, concentration of SN-38 in irinotecan treated animals was almost half the SN-38 concentration in the Onivyde®-treated animals. The opposite was seen in spleen, where concentration of SN-38 was about two-fold higher than that detected in the spleen of Onivyde®-treated animals. In both groups, the highest concentration of SN-38G (Figure 3.21C) was found in the small intestines.

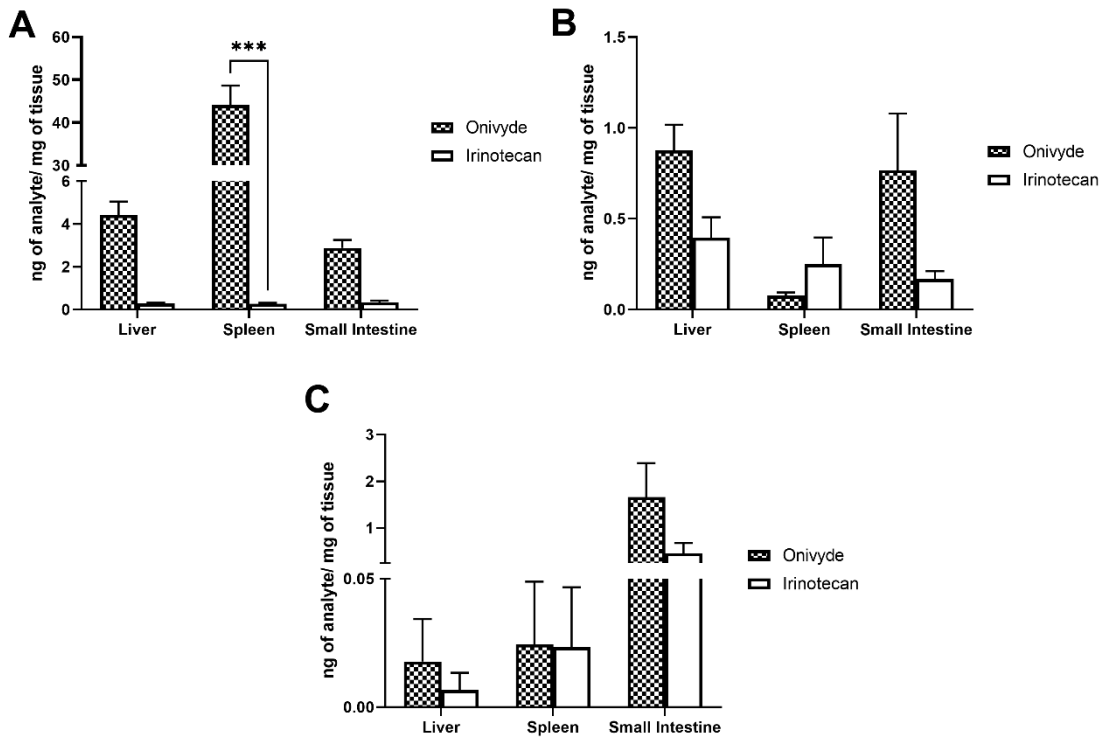

Figure 3.21: Concentration of irinotecan (CPT-11), and its active metabolites SN-38 and SN-38 glucuronide in organs.
Tissue profile of CPT-11 (A), SN-38 (B) and SN-38G (C) 48h after single dose intravenous injection of Onivyde® (checker pattern) or irinotecan (white fill) at 20 mg/kg irinotecan equivalent. Statistical significance was determined using Two-way ANOVA with Tukey's multiple comparison test; ** $p \leq 0.01$, *** $p \leq 0.001$. Data points represent mean ± SEM, n= 3. MS analysis was carried out by Dr. Sven Even Borgos and Dr. Astrid Hyldbakk at SINTEF, Norway.

In summary, liposomes were successfully detected *ex vivo* in tissue sections using combination of traditional histological stain for lipids ORO and immunofluorescent labelling of the coating material PEG. This was further confirmed with a quantitative analysis, where levels of CPT-11 were much higher in animals treated with Onivyde® in comparison to animals treated with irinotecan, suggesting a protective function of the liposome slowing down the metabolism of the drug.

3.4 Discussion

The characterisation of liposome shape and presence in tissue can be done by a few imaging techniques such as Scanning Electron Microscopy (SEM) or Atomic force microscopy (AFM) [145]. However, those techniques are time consuming and relatively expensive. Histological method proposed in this chapter provides a cost-effective solution where tissue sections can be stained simultaneously and imaged in a fraction of time required by more advanced microscopy,

examining a larger area of the sample. Up to date very few studies attempted to detect liposomes in histology sections. For example, recent publication by Fonseca-Gomes *et al.* [146] examined biodistribution of organic NBMs (liposomes, solid lipid nanoparticles and poly(lactic-co-glycolic acid) nanoparticles) in histology sections by using polarized light. The optical birefringence of those nanoparticles allowed for scoring tissue distribution and density. Two case studies presented in this chapter, provided strong evidence that ORO stain could also be used for this type of analysis.

Studies presented in this chapter are not the first attempt to detect lipid based NBMs in tissue using ORO. Rizk *et al.* failed to detect lipid particles with ORO stain in neural cell culture and brain tissue [147]. It was concluded that ORO staining is a nonspecific method that should be avoided for determining the intracellular distribution of lipid carriers. From the results presented in this chapter, the two cases are contradicting the previous statement made by Rizik *et al*. To address the reported lack of specificity, co-localisation of lipids with either cargo dye or coating material was assessed to distinguish between naturally occurring lipids and the liposome.

As stated, the first case study presented in this chapter assessed safety of a dye-loaded lipid NBM for NIR fluorescent imaging. No indication of toxicity was reported from the initial preclinical evaluation or histopathology. The biodistribution was visually assessed with ORO stain. Livers of female mice injected with NIR dye-loaded liposomes had the most abundant lipid staining (Figure 3.7). Similarly, this was observed in kidney (Figure 3.9), where number of lipid vacuoles were seen in the renal tubules of female mice injected with NIR dye-loaded liposomes or soybean oil-filled carrier control. Differences, or rates of change in the physiology, anatomy, hormones, behaviour, biochemistry and genetics between male and female can all influence toxicokinetics [148]. Results from brightfield and fluorescent microscopy presented in this chapter indicated differences between male and female mice in terms of the rate of metabolising the liposomes seen by different patterns of lipid accumulation. Furthermore, IR780-Oley dye was detected in males at 6 days post injection of the liposome, which was not seen in females. Previous studies on this NBM carried out in female BALB/cJ RJ mice [116] measured fluorescence macroscopically with a NIR imaging system in various organs at 30 minutes, 4 hours, and 24 hours post injection. A decrease in fluorescence signal was found in kidney and spleen between 4 hours and 24 hours which is in line with the results reported here were no fluorescence was detected in those organs 6 days post injection.

Further investigation into this material was carried out in a phase-0/phase I study in beagle dogs [149], where biodistribution was also assessed by measuring fluorescence macroscopically

with a NIR imaging system. Method presented here for microscopic detection of those liposomes in tissue sections provided valuable information regarding specific location within tissues which is important when assessing safety of NBMs. Lipid NBMs containing IR780-Oley dye were found in the marginal zone of the spleen (Figure 3.12 and Figure 3.13) which is rich in B lymphocytes. As previously discussed in the introductory chapter (chapter 1), B lymphocytes can produce antibodies against PEG, which was used as a coating material for LipImage™815. Therefore, presence of this NBM in the marginal zone suggests an immune response to second injection of this material is possible and should be examined in multiple dose *in vivo* study.

In the second case study presented, a nanoliposomal formulation of chemotherapeutic drug irinotecan was chosen as a model PEGylated liposome. PEG is widely used as coating material to stabilise the liposome and prevent clearance by the innate immune system, which is a prerequisite for biomedical applications. Therefore, in terms of detecting this type of NBMs in tissue sections on a microscopic level, PEG was chosen as a target for immunofluorescent staining combined with ORO.

First, toxicity of irinotecan and Onivyde® was assessed with histological methods. Sections were stained with H&E and evaluated for signs of tissue or cellular damage. Changes in liver in form of lipid type bodies were observed in both treatment groups. This was expected as irinotecan is known to cause steatosis. In the report published by EMA [117], gastrointestinal tract and hematologic system are listed as target organs of toxicity in single and repeated dose toxicity studies in mice, rats and dogs. At the doses used in this study, no significant changes suggestive of toxicity were seen in spleen or small intestine.

To detect lipid accumulation, sections consecutive to H&E were stained with lipid specific stain, Oil red O. Several animals in both treatment groups showed positive staining in liver and small intestine (Figure 3.17, Supplementary figure 8.27, and Supplementary figure 8.29) with a visually observed variation in the amount of lipids present. Interestingly, a number of lipid-laden cells were detected in the splenic white pulp of all animals injected with Onivyde® (Supplementary figure 8.28). Combination of immunofluorescent staining against PEG and ORO stain was used to confirm location of liposomes in tissue section. This method was specifically beneficial when assessing small intestine. Initial examination of ORO stained sections of small intestine revealed accumulation of lipids in the lacteal which is a lymphatic capillary that absorbs dietary fat. Immunofluorescent staining against PEG combined with ORO stain allowed to discriminate between dietary fats and liposomes (Figure 3.19 and Supplementary figure 8.31) highlighting the benefit of combining two stains. PEG and ORO stain were also co-localised in

liver (Supplementary figure 8.30) and spleen (Supplementary figure 8.32) indicating that liposomes were still intact at 48 hours post injection.

Quantitative assessment was carried out by high sensitivity LC/MS within a large experimental design as part of the EUNCL H2020 project to measure levels of CPT-11 and its two metabolites SN-38 and SN-38G in tissue samples in order to confirm histology findings. Levels of metabolites detected in the organs confirmed that by encapsulating the drug in the liposome, a prolonged circulation was achieved. Similar results to the ones presented here were previously reported by EMA in the assessment report of Onivyde® [117]. After a single 90 min IV infusion of Onivyde® or irinotecan at 10 mg/kg of irinotecan equivalent, an increased level of CPT-11 and SN-38 were found in plasma, bile, and spleen of Long Evans rats treated with liposomal formulation.

It is interesting to point out that one of the limitations of MS analysis is that, to be quantitative, it involves a chemical or mechanical homogenization of tissue sample, which also destroys the liposomes. Therefore, this technique raise some level of uncertainty when investigated in the context of the NBM accumulation in the organ; whether high concentration of CPT-11 seen in different organs of animals injected with Onivyde® (Figure 3.21A) was still encapsulated within the liposome at 48h post injection or if it was released. By developing a suitable method for relatively simple, time and cost-effective detection of liposomes in tissue section, additional information can be extrapolated to complement such quantitative analysis. In the proof-of-concept study presented here, the spleen from animals injected with Onivyde® had the highest concentration of CPT-11 indicating that potentially liposomes were still intact, or in large fragments. This was confirmed by fluorescent imaging where PEG was found to co-localise with lipids (Figure 3.20 and Supplementary figure 8.32).

No toxicity was reported from the histological assessment of the two case studies presented in this chapter, nonetheless future studies on those NBMs should be undertaken to investigate a potential immunogenic response to PEG, which was used as a coating material for all the NBMs tested here. Previous studies undertaken in a pig model by Kozma *et al* showed that anti-PEG IgM concentration in blood peaks at 7-9 days after IV injection of pegylated liposomes at the dose 0.1 mg/kg) [88]. Since two case studies presented here lasted shorter than 7 days (6 days post injection for case study 1, and 48 hours for case study 2), it would be important to investigate the long-term effects of those NBMs.

3.5 Conclusion

In conclusion, the limitations of using ORO as a suitable stain for liposome, previously described in literature, were overcame by assessing the slides under the fluorescent microscope after the initial observation under brightfield microscopy. This allowed to achieve more precise determination of cellular location of the liposomes. Furthermore, assessing the co-localisation of either cargo material or coating material provided a better understanding on the degradation of this material *in vivo*, and furthermore distinguishing with the naturally occurring lipids. Overall, the liposomal formulations tested in the two case studies discussed in this chapter were found to be safe to be further pre-clinically investigated *in vivo*, as no significant signs of toxicity were reported from the histological analysis.

4 Chapter 4: ML model for MNP quantification and 3D reconstruction from histology sections

4.1 Introduction

As discussed in Chapter 1, magnetic hyperthermia treatment is one of the applications of MNPs, which is a promising alternative to conventional cancer treatments as it could potentially reduce healthy tissue damage [150]. Particles with approximately 10 nm diameter show optimal superparamagnetic properties [151], however aggregation can significantly reduce their heating potential by the decreased surface area [152], increasing their toxicity, and immune implications *in vivo* [153]. Furthermore, excessive accumulation of MNPs can result in toxic implications such as DNA damage, oxidative stress, epigenetic events and inflammatory processes [154]. Therefore, a thorough evaluation of MNPs biodistribution following *in vivo* administration and any induced toxicity such as local inflammation, tissue damage or necrosis is a key step in advancing them into clinic [155].

Toxicologic histopathology is an important component of preclinical *in vivo* studies of nanoparticles as it allows for assessment of their interaction with the cellular microenvironment [156]. Microscopic visualization in tissue sections is still one of the most common techniques used to evaluate biodistribution of nanoparticles following *in vivo* administration [157, 158]. Certain types of nanoparticles can be visualized by light microscopy in tissue sections stained with conventional histopathology stain. For example, Prussian blue staining is frequently used in MNPs biodistribution studies, as this technique is relatively inexpensive and enables to study accumulation of nanoparticles at cellular and tissue level [159, 160]. Despite numerous advantages, histology is facing shortcomings in studies of nanoparticles for biomedical applications.

Histology is considered a qualitative method when assessing nanoparticle biodistribution [161]. Despite Prussian blue stain being one of the gold standards in biodistribution studies of iron oxide nanoparticles, limited studies are available on quantitative analysis of iron content in tissues after staining [162-164]. Furthermore, representative two-dimensional (2D) histological sections do not provide details on three-dimensional (3D) distribution with respect to biological structures such as blood vessels and lymphatics, which play an important role in nanoparticle transport and clearance. 2D sections also provide limited information on size and shape of MNPs aggregates. The lack of more quantitative histological studies is mainly due to time consuming

process of image acquisition and segmentation of sufficient number of images required to avoid statistical bias.

Recent advances in digital pathology and machine learning show a promise in significantly reducing processing time [165, 166]. Additionally, computerized segmentation provides a solution to achieve consistent and accurate results on a number of images with minimal user input, reducing associated operator-dependent error [97]. This new branch of pathology called computational pathology (CAPTH), has already been used for quantification of pathological changes [167, 168], which were previously manually counted or visually assessed by pathologist. It would be therefore beneficial if similar methodology could be applied to preclinical assessment of nanoparticles to provide reliable representation of nanoparticle biodistribution in the whole organ.

The overall aim of this chapter was to establish methods for evaluation of MNP distribution and accumulation *in vivo* using histology tissue sections. Adding this methodology to the current pre-clinical assay cascade used for the safety assessment of new generation medical technologies would enhance the process of translation into the clinic. The overall aim can be broken down into the following objectives:

1. To train and validate a machine learning model for semi-quantitative analysis of histological stain for MNP accumulation in tissue.
2. To reconstruct selected organ tissue slice samples in 3D volumetric images to understand the complexity of particle distribution into tissues *in vivo.*

The background that brought to these aims is based on the questions raised by the MultiFun consortium (Multifunctional Nanotechnology for selective detection and Treatment of Cancer), which was funded under EU 7th Framework Programme for Research and Technological Development (FP7) between 2011 and 2015. The MultiFun consortium has successfully developed and validated a novel and minimally invasive nanotechnology system to improve cancer diagnosis and treatment [169-171]. The latter includes a synergistic effect between the therapeutic effect produced by magnetic hyperthermia and that due to selective drug delivery to tumour cells. One of the requirements for advancing these formulations into the clinic is determining conditions that control the MNP magnetic heat release, and how to control the heat exposure. Number of studies used computational modelling for this purpose, examining the effect of size, shape and assembly of individual MNPs [172], as well as the effects of interaction between those particles [173] on heating profile. In order to provide such *in silico* studies with more biologically relevant information on shape and size of the aggregates formed by MNP in

various tissues, this chapter focuses on developing a semi-automated method for extrapolating such data from histological sections using machine learning.

The experimental work described in this chapter was carried out as a continuation of work undertaken under the MultiFun EC FP7 project, in the context of providing advanced *in vivo* quantitative histological models to be then adopted and applied under the follow up EU H2020 project called NoCanTher (NoCanTher project) [174] which is presented in the next chapter. Results presented in this chapter were published in scientific peer-review journal and disseminated in form of an original research manuscript entitled: "3D volume segmentation and reconstruction. Supervised image classification and automated quantification of superparamagnetic iron oxide nanoparticles in histology slides for safety assessment" [175].

4.2 Experimental design

The case study presented in this chapter is part of a larger multidisciplinary work developed and implemented within the framework of MULTIFUN FP7 project. While the experimental *in vivo* design, implementation and organs collection was carried out under the supervision of Dr Oliviero Gobbo (individual authorisation number AE19136/I104) while training Dr Kieran Crosbie Staunton as a part of his doctorate research [176], the processing of the organs, histology sectioning, staining, observation and recording of events was carried out within this PhD work. This provided a set of good quality tissue sections from different organs to be used for the development of the Machine Learning (ML) models for semi quantitative analysis of the section. Furthermore, the image processing also enable the 3D rendering and volume reconstructions as shown in the results section

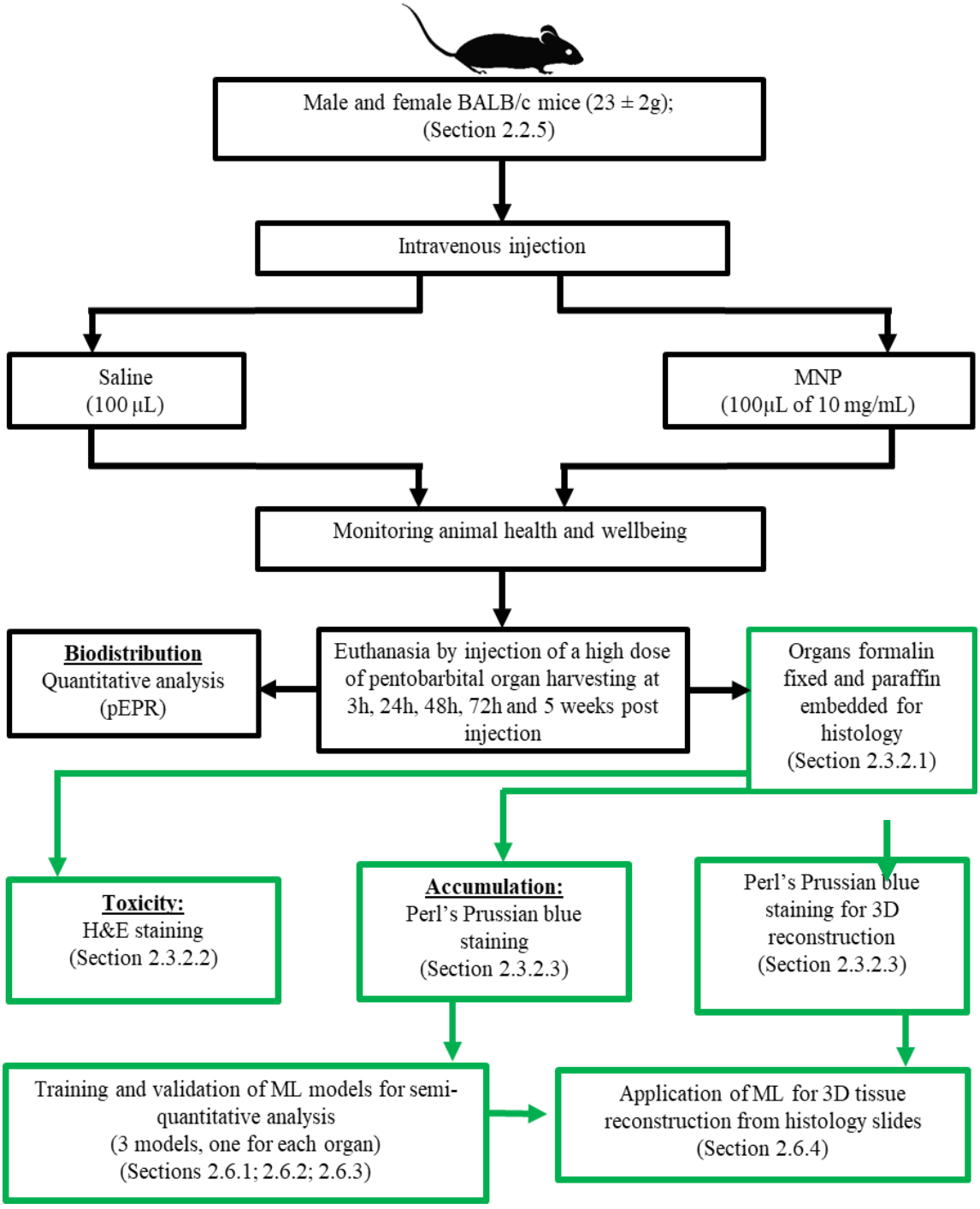

Figure 4.1: Experimental workflow for case study 3: *In vivo* toxicity and biodistribution of MF66 MNPs

In vivo study design to assess pharmacokinetics and biodistribution of MNP. From top to bottom, first five rows (black boxes) provide details on animals used in this study, route and dose of the solution injected, and method used for quantitative biodistribution. This part of the *in vivo* study was conducted as a part of Dr. Kieran Crosbie-Staunton's PhD thesis, who presented the results in his doctorate thesis [176]. The bottom two rows (green boxes) outline histological methods used to evaluate toxicity and accumulation of MNPs in organs, results of which are presented in this chapter. Full protocols can be found in chapter 2, under specified sections.

4.3 Results

Following the experimental flow presented, tissue samples were processed into wax blocks and used for the preclinical assessment by means of histological analysis as part of this research work. Tissue slides where observed and recorded and the results here presented are part of the toxicity and accumulation response of the MNPs. Semi-quantitative histology with use of ML was then carried out. Finally, consecutive selected tissue samples were used to generate 3D segmented volumes based on 3D histology volumes, where the accumulation of MNPs is shown in 3D.

4.3.1 *Toxicity*

H&E stained sections of lung, liver and kidney were examined to assess tissue morphology and cellular changes indicative of MNPs induced toxicity. No significant abnormal changes were noted in lungs (Figure 4.2) and kidneys (Figure 4.3) when compared to sections from control animals. This was a case for all animals used in this study as also presented in an extensive tissue sections observation reported, in the Supplementary figure 8.38, Supplementary figure 8.39, and Supplementary figure 8.40, which are provided for completeness. In lungs, MNP aggregates were seen as a granular brown material predominantly in the pulmonary vessels such as the one seen in Figure 4.2D in the branch of pulmonary artery.

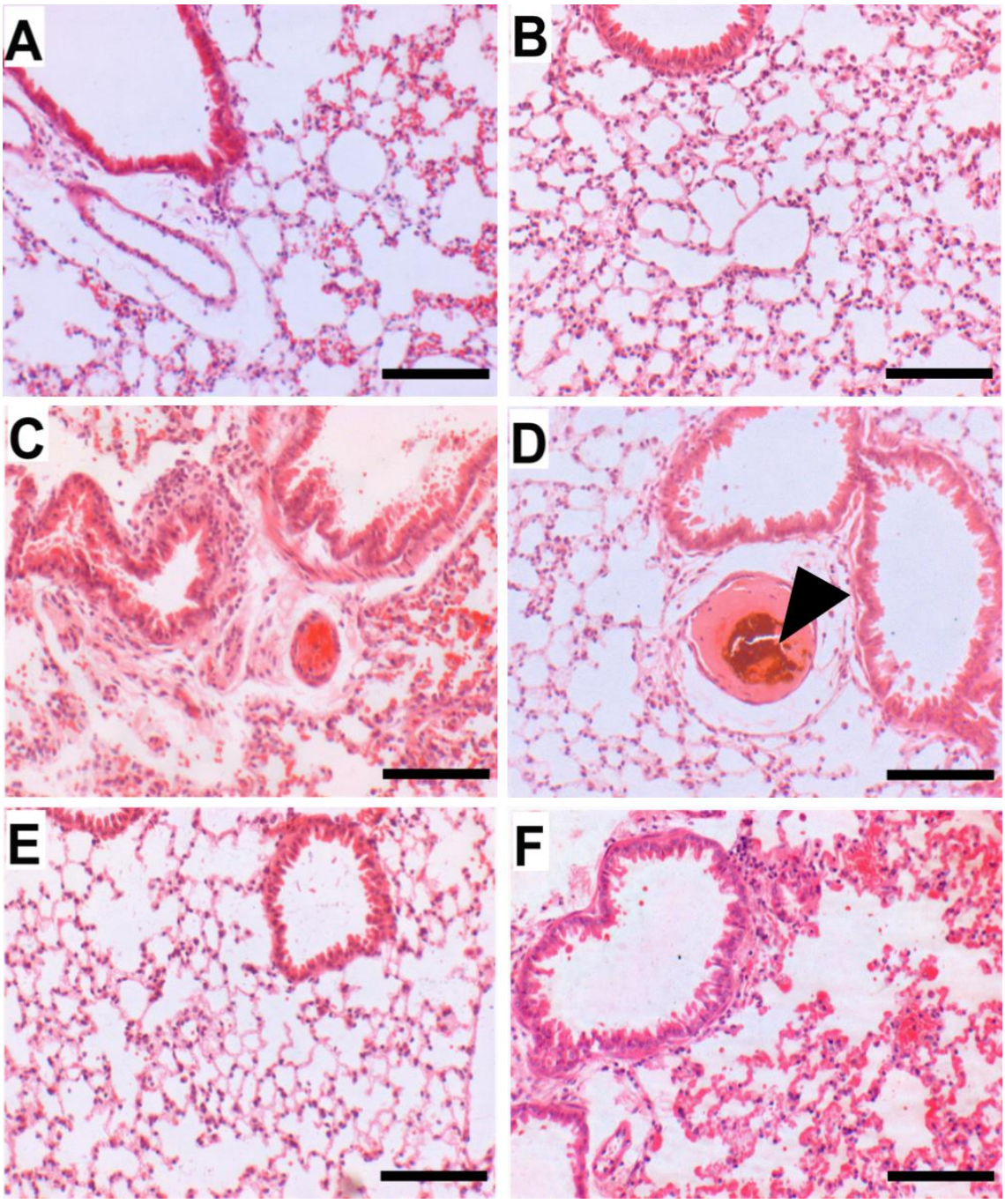

Figure 4.2: Histological changes formed in lungs over time following injection of MNPs
Representative photomicrographs of H&E stained lung tissue sections of BALB/c mice injected with 100µl of saline (A) or 100µl of 100 mg/ml MNP solution MNP solution (B-F) sacrificed post injection at 3h (B), 24h (C), 48h (A and D), 72h (E) and 5 weeks (F). Tissue was formalin fixed and paraffin embedded. 5µm thick sections were cut with rotary microtome and collected at three levels through the block spaced at least 50 µm apart. MNPs aggregates were seen as granular brown deposits (arrowhead in figure D). No other changes indicative of toxicity or inflammation were seen. Scale bar represents 100 µm.

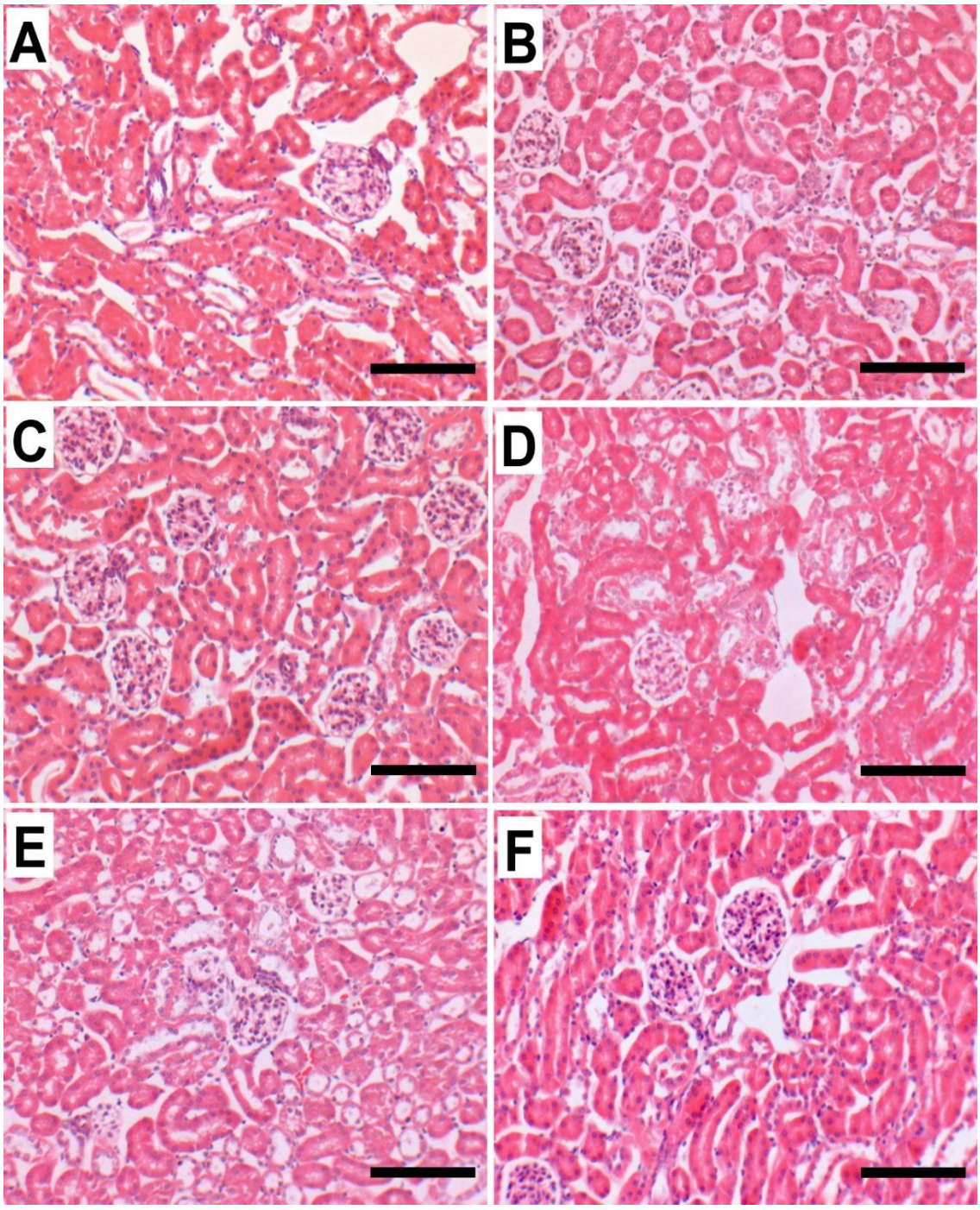

Figure 4.3: Kidney pathology over time following injection of MNPs
Representative photomicrographs of H&E stained kidney sections of BALB/c mice injected with 100µl of saline (A)) or 100µl of 10 mg/ml MNP solution (B-F) and sacrificed post injection at 3h (B), 24h (C), 48h (A and D), 72h (E) and 5 weeks (F). Tissue was formalin fixed and paraffin embedded. 5µm thick sections were cut with rotary microtome and collected at three levels through the block spaced at least 50 µm apart. There were no changes indicative of toxicity or inflammation. Scale bar represents 100 µm.

In liver, numerous foci of inflammation (Figure 4.4 F) were seen from 24 hours post injection up to 5 weeks. As these foci of inflammation can occur spontaneously in rodent liver, a consecutive slide stained with Perls' Prussian blue was used to determine whether this infiltration of immune cells formed in response to iron (Figure 4.5). Iron was seen as blue deposit in Perls' Prussian blue stained slides (Figure 4.5 B), indicating that foci of inflammation formed in response to iron accumulation. Additionally, cytoplasmic vacuolation (white spaces in the hepatocytes in Figure 4.4 C) was seen from 24 hours to 72 hours post injection with MNPs. This was not seen in any of the animals sacrificed at 5 weeks post injection suggesting regeneration of the hepatocytes. No other changes were seen at any time post injection in any of the animals examined (Supplementary figure 8.39).

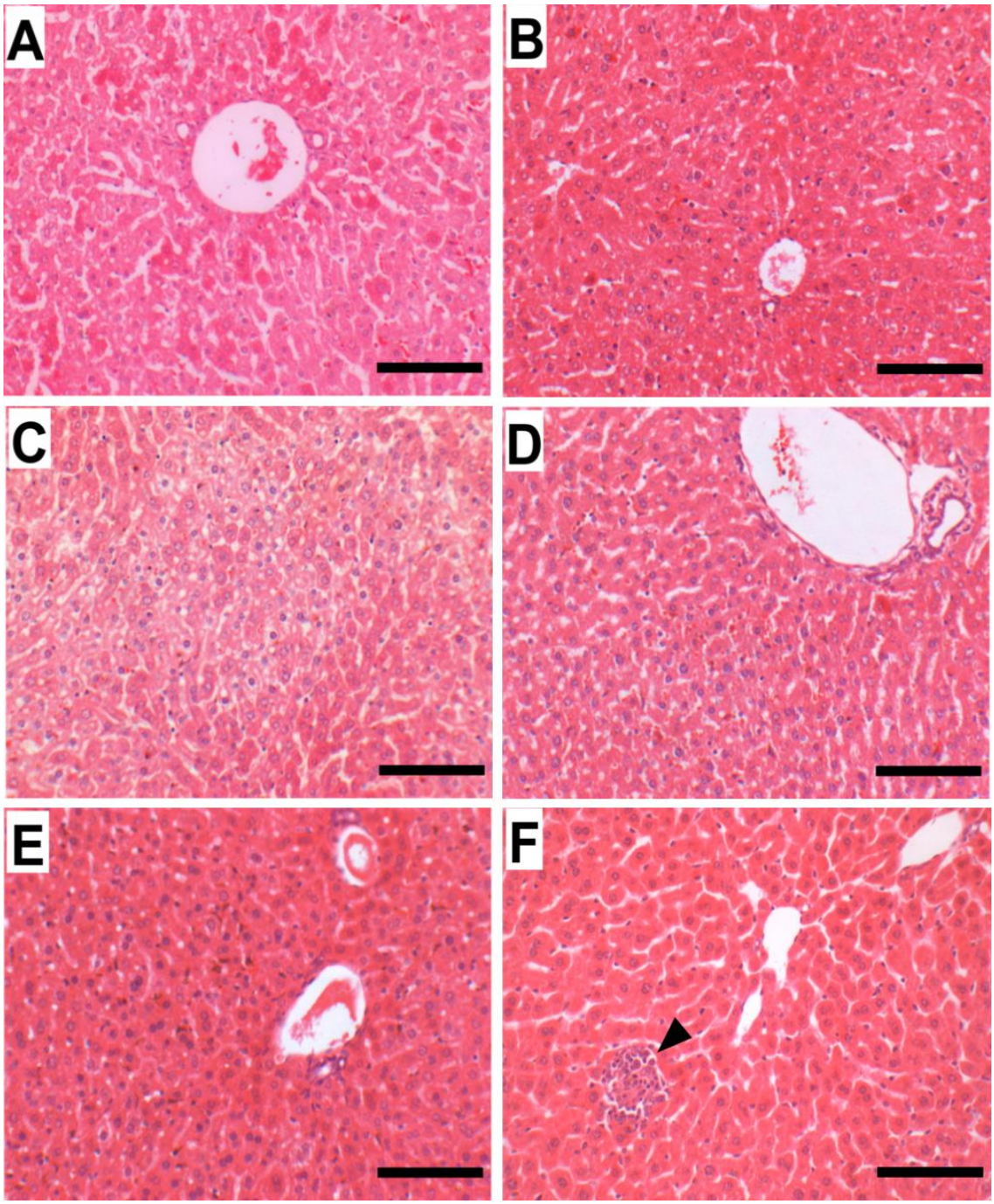

Figure 4.4: Histological changes formed in liver over time following injection of MNPs
Representative photomicrographs of H&E stained liver sections of BALB/c mice injected with 100µl of saline (A) or) or 100µl of 10 mg/ml MNP solution (B-F) and sacrificed post injection at 3h (B), 24h (C), 48h (A and D), 72h (E) and 5 weeks (F). Tissue was formalin fixed and paraffin embedded. 5µm thick sections were cut with rotary microtome and collected at three levels through the block spaced at least 50 µm apart. Focus of mild inflammation (black arrowhead in figure F). No other changes suggestive of toxicity or inflammation were seen in the tissue sections. Scale bar represents 100 µm

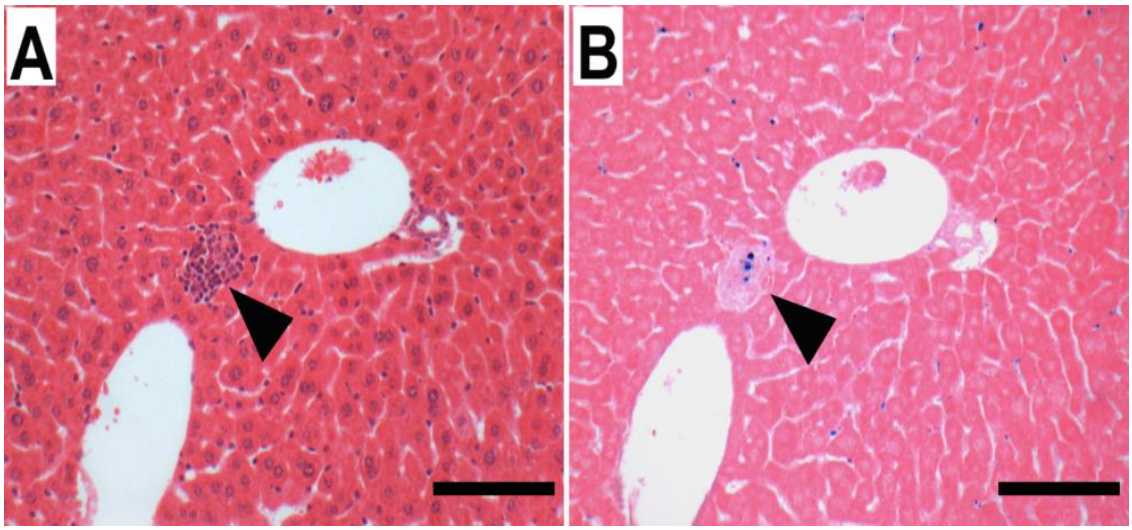

Figure 4.5: Local inflammation in liver induced by MNPs
Representative photomicrographs of H&E (A) and Perls' Prussian blue (B) stained consecutive sections of BALB/c mouse liver showing formation of mild focal inflammation (granuloma) in response to presence of MNPs (black arrowhead). Tissue was formalin fixed and paraffin embedded. 5µm thick consecutive sections were cut with rotary microtome and collected at three levels through the block spaced at least 50 µm apart. Iron aggregates are visible as blue deposits in figure B. Scale bar represents 50 µm.

4.3.2 *Investigation of MNP accumulation*

An increase in iron content over time was observed in liver (Figure 4.6) and lung (Figure 4.7) compared to control tissue. In liver, iron aggregates were mainly visible in the hepatic sinusoids and in the cytoplasm of Kupffer cells at every time point used in this study. In lungs, iron was observed as early as 3 hours post injection of MNPs (Figure 4.7 B). Large aggregates (with area greater than 1000 μm^2) were observed in branches of pulmonary arteries at 24 and 48 hours post injection of MNPs (Figure 4.7 C and D). By 72 hours post injection, iron staining within the cytoplasm of pulmonary macrophages was identified (Figure 4.7 E and F), suggesting phagocytic clearance. However, iron aggregates in pulmonary vessels were found up until 5 weeks post injection.

Accumulation of iron tissue specific macrophages in liver and lung was confirmed with consecutive sections stained with H&E as shown in figure 1.8. Iron be seen as granular brown material in the cytoplasm of Kupffer cells in the liver stained with H&E (Figure 4.8 A) and as a granular blue material in cytoplasm of pulmonary macrophages in lung (Figure 4.8 D) and Kupffer cells in liver (Figure 4.6B) in Perls' Prussian blue stained slides.

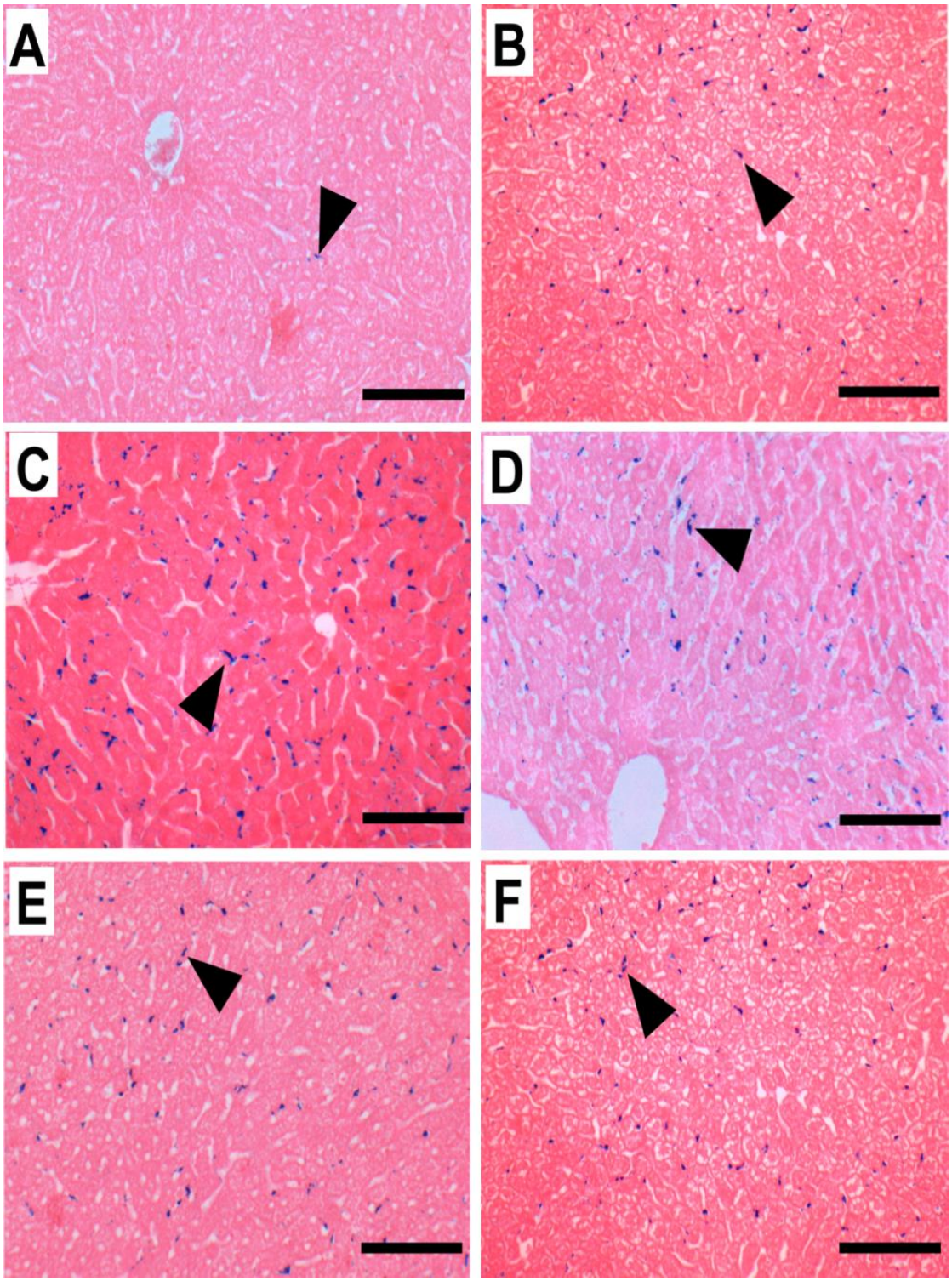

Figure 4.6: Accumulation of MNPs in liver over time
Representative photomicrographs of Perls' Prussian blue (PPB) stained BALB/c mouse liver sections showing accumulation and distribution of MNPs (black arrows). Animals were injected with 100µl of saline (A)) or 100µl of 10 mg/ml MNP solution (B-F) and sacrificed post injection at 3h (B), 24h (C), 48h (A and D), 72h (E) and 5 weeks (F). Tissue was formalin fixed and paraffin embedded. 5µm thick sections were cut with rotary microtome and collected at three levels through the block spaced at least 50 µm apart. Scale bar represents 100 µm

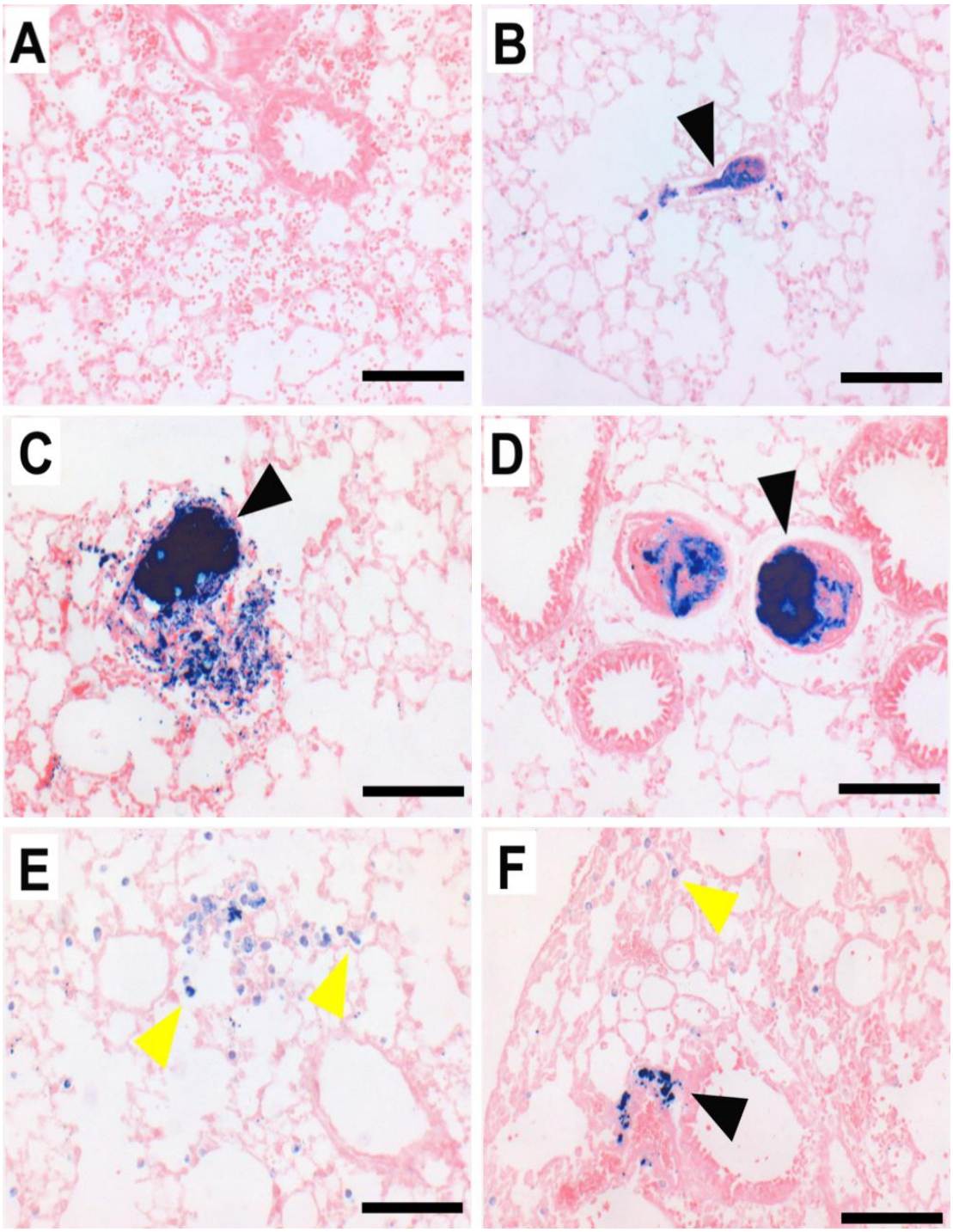

Figure 4.7: Accumulation of MNPs in lungs over time
Representative photomicrographs of PPB stained BALB/c mouse lung sections showing accumulation and distribution of MNPs (black arrowhead). Yellow arrowheads highlight uptake by pulmonary macrophages. Animals were injected with 100µl of saline (A), or 100µl of 10 mg/ml MNP solution (B-F) and sacrificed post injection at 3h (B), 24h (C), 48h (D), 72h (A and E) and 5 weeks (F). Tissue was formalin fixed and paraffin embedded. 5µm thick sections were cut with rotary microtome and collected at three levels through the block spaced at least 50 µm apart. Scale bar represents 200 µm.

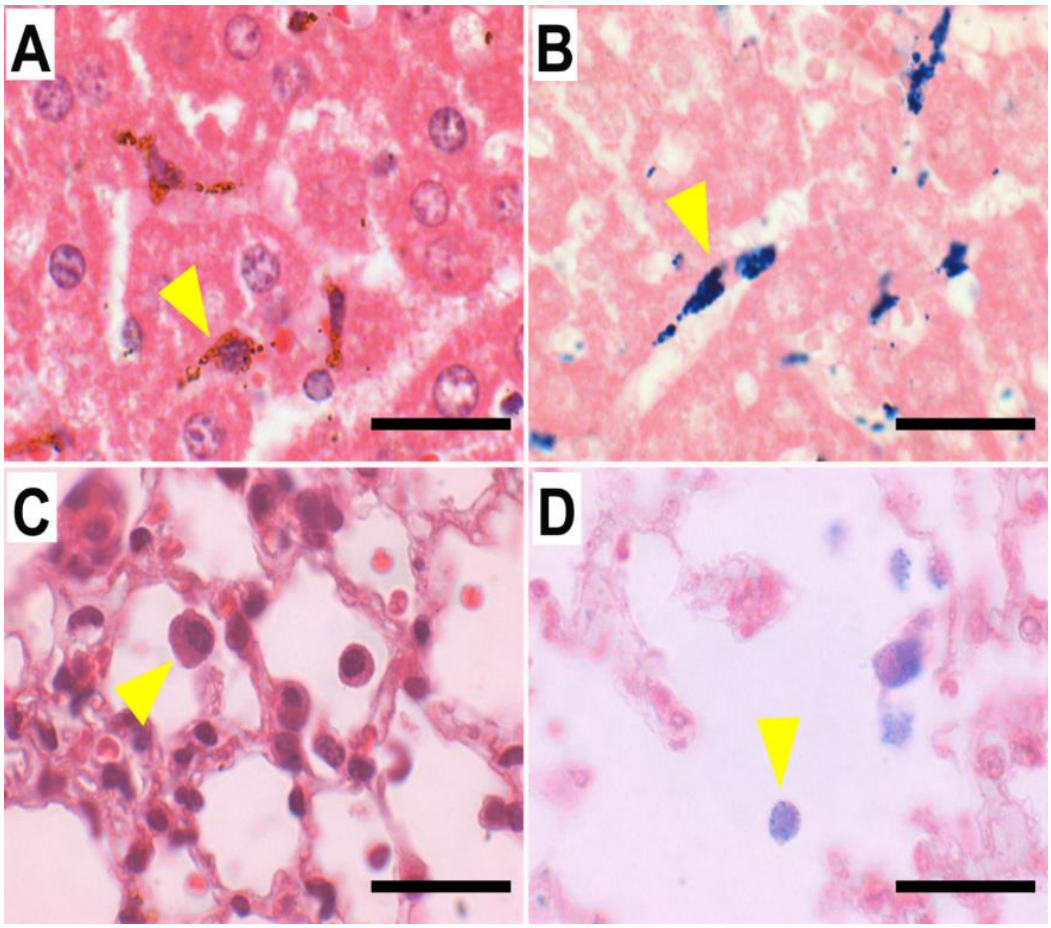

Figure 4.8: MNPs uptake by tissue specific macrophages
Representative photomicrographs of BALB/c mouse liver and lung sections stained with H&E (A and C respectively) or PPB (B and D respectively). Tissue was formalin fixed and paraffin embedded. 5µm thick sections were cut with rotary microtome and collected at three levels through the block spaced at least 50 µm apart. Yellow arrowheads indicate tissue specific macrophages with iron contained within the cytoplasm; scale bar represents 25 µm.

In kidneys (Figure 4.9), iron was mainly observed in proximal tubules at 24 hours and 48 hours post injection. Evidence of iron accumulation was also seen in Bowman's capsule at 48 hours post injection (Figure 4.9 D). Staining intensity diminished by 72 hours post injection and was not observed at 5 weeks post injection suggesting complete clearance of MNPs. Differences in staining intensity and number of stained objects between control and treated animals were too subtle to conclude whether it is significantly different. Semi-quantitative analysis of Perls' Prussian blue stained slides was carried out with use of the machine learning to calculate percent area of iron in tissue, as well as number and size of stained objects.

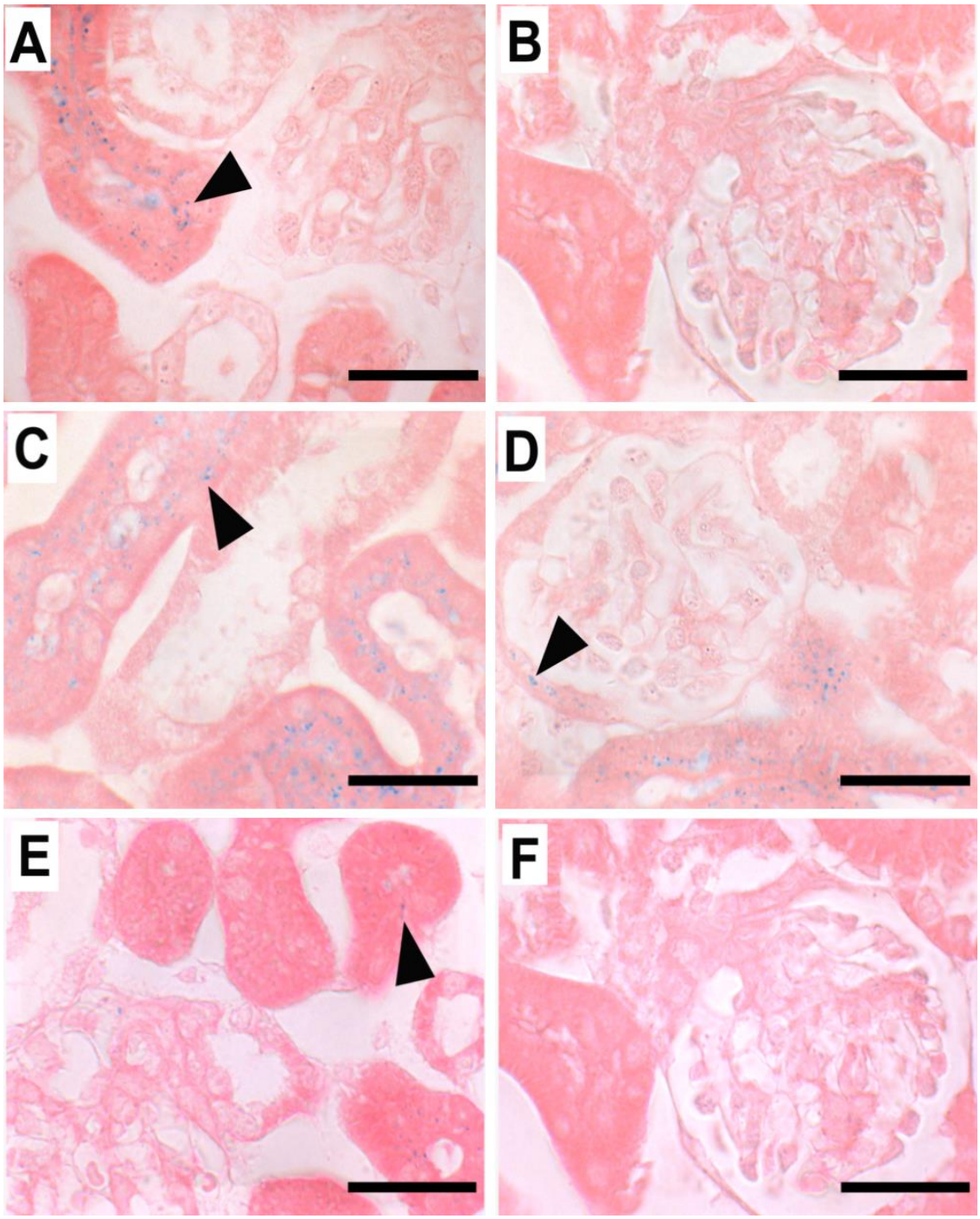

Figure 4.9: Accumulation of MNPs in kidney over time
Representative photomicrographs of PPB stained BALB/c mouse kidneys sections showing accumulation and distribution of MNPs (black arrows). Animals were injected with either saline (A) or 100µl of 10 mg/ml MNP solution (B-F) and sacrificed post injection at 3h (B), 24h (C), 48h (D), 72h (A and E) and 5 weeks (F). Tissue was formalin fixed and paraffin embedded. 5µm thick sections were cut with rotary microtome and collected at three levels through the block spaced at least 50 µm apart. Iron was detected mainly in the renal tubules (A, C, and E), with minimal accumulation in the Bowman's capsule (D). Scale bar represents 50 µm

Confirmation of the results presented on toxicity and iron accumulation was sought by an independent certified pathologist from the St. James' Central Pathology Laboratory, St. James's Hospital, Dublin Ireland. These findings were confirmed, as summarised in Table 4.1.

Table 4.1: Full description of iron accumulation and pathological changes in all organs from animals tested in case study 3

Summary of findings reported by the certified pathologist from St. James' Central Pathology Laboratory on histological changes and accumulation of iron for slices obtained from the organs of experimental animal used in case study 3. Pathologist was blinded to experimental conditions. NAD: nothing abnormal detected

Animal ID	Treatment	Time post injection	Organ	Diagnosis	Iron accumulation
1	MNPs (100µl @3mg/ml)	3 h	Liver	NAD	No iron detected
			Lung	NAD	Number of small iron aggregates seen in the vasculature
			Kidney	NAD	No iron detected
2	MNPs (100µl @3mg/ml)	3 h	Liver	NAD	Iron in the cytoplasm of Kupffer cells
			Lung	NAD	No iron detected
			Kidney	NAD	No iron detected
3	MNPs (100µl @3mg/ml)	24 h	Liver	NAD	Iron in the cytoplasm of Kupffer cells
			Lung	NAD	No iron detected
			Kidney	NAD	Iron in the proximal tubules
4	MNPs (100µl @3mg/ml)	24 h	Liver	Small foci of inflammation	Iron in the cytoplasm of Kupffer cells
			Lung	NAD	Iron aggregates seen in the vasculature
			Kidney	NAD	Iron in the proximal tubules
5	MNPs (100µl @3mg/ml)	48 h	Liver	NAD	Iron in the cytoplasm of Kupffer cells
			Lung	NAD	No iron detected
			Kidney	NAD	Iron in the proximal tubules
6	MNPs (100µl @3mg/ml)	48 h	Liver	Small foci of inflammation	Iron in the cytoplasm of Kupffer cells
			Lung	NAD	Large iron aggregates seen in the vasculature; iron in the cytoplasm of pulmonary macrophages
			Kidney	NAD	Iron in the proximal tubules
7	MNPs (100µl @3mg/ml)	72 h	Liver	Small foci of inflammation	Iron in the cytoplasm of Kupffer cells
			Lung	NAD	Iron in the cytoplasm of pulmonary macrophages
			Kidney	NAD	Iron in the proximal tubules
8	MNPs (100µl @3mg/ml)	72 h	Liver	NAD	Iron in the cytoplasm of Kupffer cells
			Lung	NAD	Large iron aggregates seen in the vasculature; iron in the

					cytoplasm of pulmonary macrophages
			Kidney	NAD	Iron in the proximal tubules
9	MNPs (100µl @3mg/ml)	5 weeks	Liver	Small foci of inflammation	No iron detected
			Lung	NAD	No iron detected
			Kidney	NAD	No iron detected
10	MNPs (100µl @3mg/ml)	5 weeks	Liver	Small foci of inflammation	Iron in the cytoplasm of Kupffer cells
			Lung	NAD	Iron aggregates seen in the vasculature; iron in the cytoplasm of pulmonary macrophages
			Kidney	NAD	No iron detected
11	Saline	24 h	Liver	NAD	No iron detected
			Lung	NAD	No iron detected
			Kidney	NAD	No iron detected
12	Saline	48 h	Liver	NAD	No iron detected
			Lung	NAD	No iron detected
			Kidney	NAD	Iron in the proximal tubules

4.3.3 *Training and validation of machine learning model for iron quantification in histology slides.*

Trainable WEKA segmentation plugin in Fiji was used for image classification of Prussian blue stained images. Three models were trained, one for each tissue type. As performance of the classifier is dependent on quality of the training data and feature selection, images included in the training set represented diversity in obtained data in terms of size of iron deposits, intensity of blue staining and variation in tissue structure (Supplementary figure 8.41). Resulting probability maps (Figure 4.10 C) are binary images where the pixel intensity value represents the computer's certainty that a specific pixel belongs to a specific class. To achieve an accurate result, a threshold step was introduced with a value cut-off set between 191 and 255. This range was representative of pixels assigned to a class by WEKA with certainty or above 75% (Figure 4.10 D). Other methods for thresholding such as value cut-off representative of certainty above 50% (Figure 4.10 E) and default automatic threshold in Fiji (Figure 4.10 F) resulted in much higher number of pixels selected as nanoparticles, which in turn would result in overestimation of particles present in tissue.

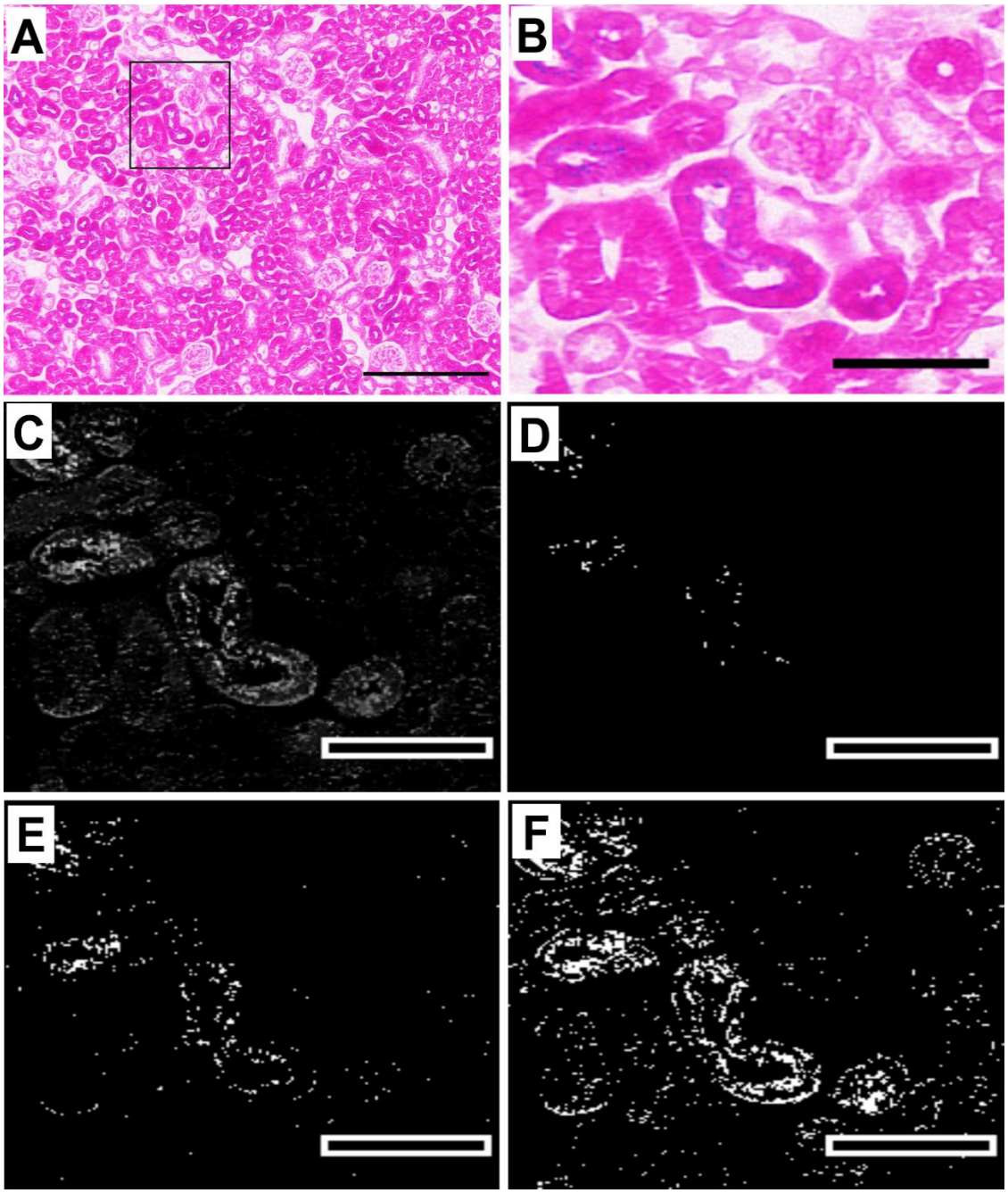

Figure 4.10: Automated image analysis
Representative image of a kidney section of BALB/c mouse injected with 100µl of 10 mg/ml of MNP solution 24 hours post injection. (A) Digitized PPB-stained section showing iron accumulation, (B) enlargement of boxed area in figure A, (C) probability map of pixels assigned as nanoparticles, (D) binary image of pixels assigned to a class with over 75% certainty, (E) binary image of pixels segmented as iron with over 50% certainty, (F) result of automatic default threshold preformed on probability map. Scale bar represents 200 µm in figure A and 50 µm in figures B to F.

In order to apply a threshold to RGB colour image, first it needs to be converted to a grayscale. While this approach is adequate for images with intensely stained iron aggregates, it can affect quantification of much smaller and fainter aggregates such as the ones observed in this study in kidneys. Figure 4.11 shows effect of converting an original RGB image (Figure 4.11 A and B) to an 8-bit image (Figure 4.11 C) or splitting it to red, green and blue channel (Figure 4.11 D, E and F respectively) on visibility of faintly stained iron aggregates. Both of those conversions reduced visibility of MNPs potentially producing a false negative result in terms of iron quantification. This was confirmed by subjecting image seen in Figure 4.11 D to a number of thresholds available to transform into binary images in Fiji. Out of 16 global thresholds, 5 produced reasonable binary representations. However, those algorithms cannot distinguish between a nanoparticle and a staining artefact (black object in Figure 4.11 B) due to greyscale conversion required in image pre-processing (Figure 4.12).

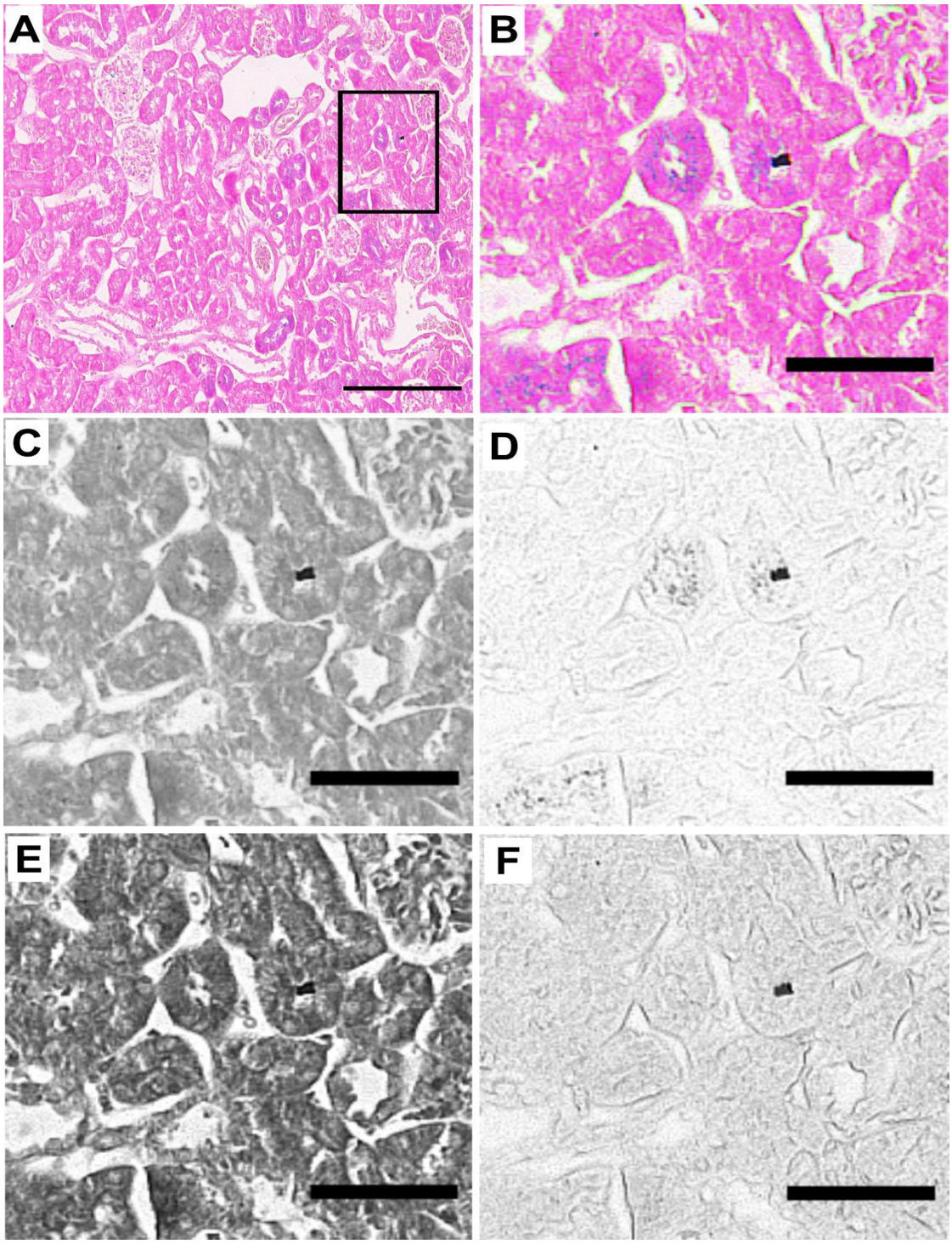

Figure 4.11: Approaches for threshold selection
Representative image of a kidney section from a BALB/c mouse injected with 100µl of 10 mg/ml MNP solution. Animal was sacrificed 24 hours post injection. (A) Digitized PPB-stained section showing iron accumulation, (B) enlargement of boxed area in figure A, (C) image conversion to 8-bit greyscale, (D) red channel extraction, (E) green channel extraction, (F) blue channel extraction. Scale bar represents 200 µm in figure A and 50 µm in figures B to F.

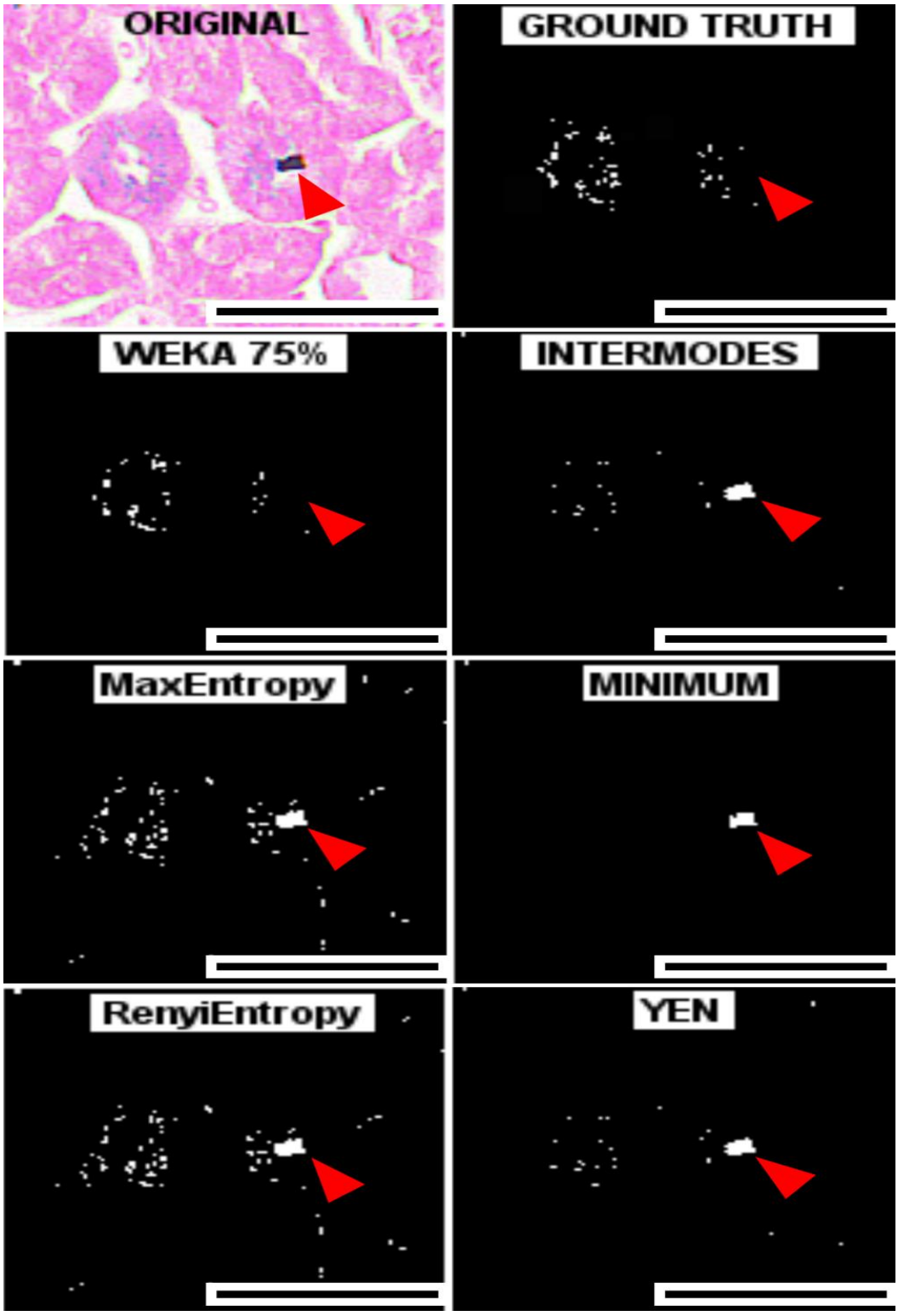

Figure 4.12: Performance evaluation of image segmentation algorithms
Output binarization images generated by manual segmentation (ground truth), WEKA with 75% certainty thresholding, or five of the threshold algorithms available in FIJI. Red arrowhead highlights an area where staining artefact was observed in original image. Scale bar represents 50µm.

During classifier training, model's performance was evaluated in WEKA's Explorer Environment, where data extrapolated from representative images used for training was used to run 10-fold cross-validation. Final performance statistics for each model are shown in Table 4.2. Overall, the classification models used in this study performed well with high precision value (>0.90). However, as the data obtained during training is acquired from regions of interest (ROIs) manually drawn by the user and not from an entire image, the calculated performance metrics might not be truly representative of classifier's performance. To overcome this limitation, a second validation step was introduced.

Images obtained from the classifier were compared to manually segmented ground truth images of tissue and nanoparticles using overlap-based metrics (Figure 4.13). For the tissue counterstained with eosin in PPB slides (Figure 4.13 A, C, and E), 75% and 50% certainty threshold on probability maps from WEKA performed similarly to long-stablished method of manually selecting threshold value in 8-bit image (referred to as default) in images from lung and kidney. For liver samples, MCC for 75% threshold is lower compared to a default method. As WEKA classifier is a pixel-based classification, this lower performance in comparison to a ground truth image results from small vacuoles naturally occurring in the hepatocytes (especially in older mice) being classified as a background. As being assigned to a different class, overlap metrics count those pixels as false negative when compared to ground truth image. For nanoparticle class, 75% threshold method performed better in comparison to default threshold on 8-bit image across all three types of tissue. This difference is especially prominent in kidney (Figure 4.14F). By converting an original RGB photomicrograph to grayscale, some objects stained with Perls' Prussian blue are lost as it can be seen in example in Figure 4.11. Furthermore, F_1 score and MCC values calculated from a full image (Figure 4.12) were lower to those reported from 10-fold cross validation in WEKA's Explorer Environment (Table 4.2), emphasizing that this method of validating classifiers' performance may not be sufficient in image segmentation problems.

Table 4.2: Initial model validation with 10-fold cross-validation.
Performance of different classifiers (top row) in segmenting tissue and iron in representative images calculated with WEKA explorer menu. Number of statistics (left column) were used, each ranging from 0-1, where 1 indicates a perfect classifier.

	Classifier	**Liver**	**Lung**	**Kidney**
Precision	Tissue	0.986	0.988	0.991
	Nanoparticles	1.000	0.974	0.939
Recall	Tissue	0.996	0.994	0.994
	Nanoparticles	0.959	0.973	0.841
F_1 score	Tissue	0.991	0.991	0.993
	Nanoparticles	0.979	0.973	0.888
MCC	Tissue	0.988	0.990	0.991
	Nanoparticles	0.979	0.972	0.889

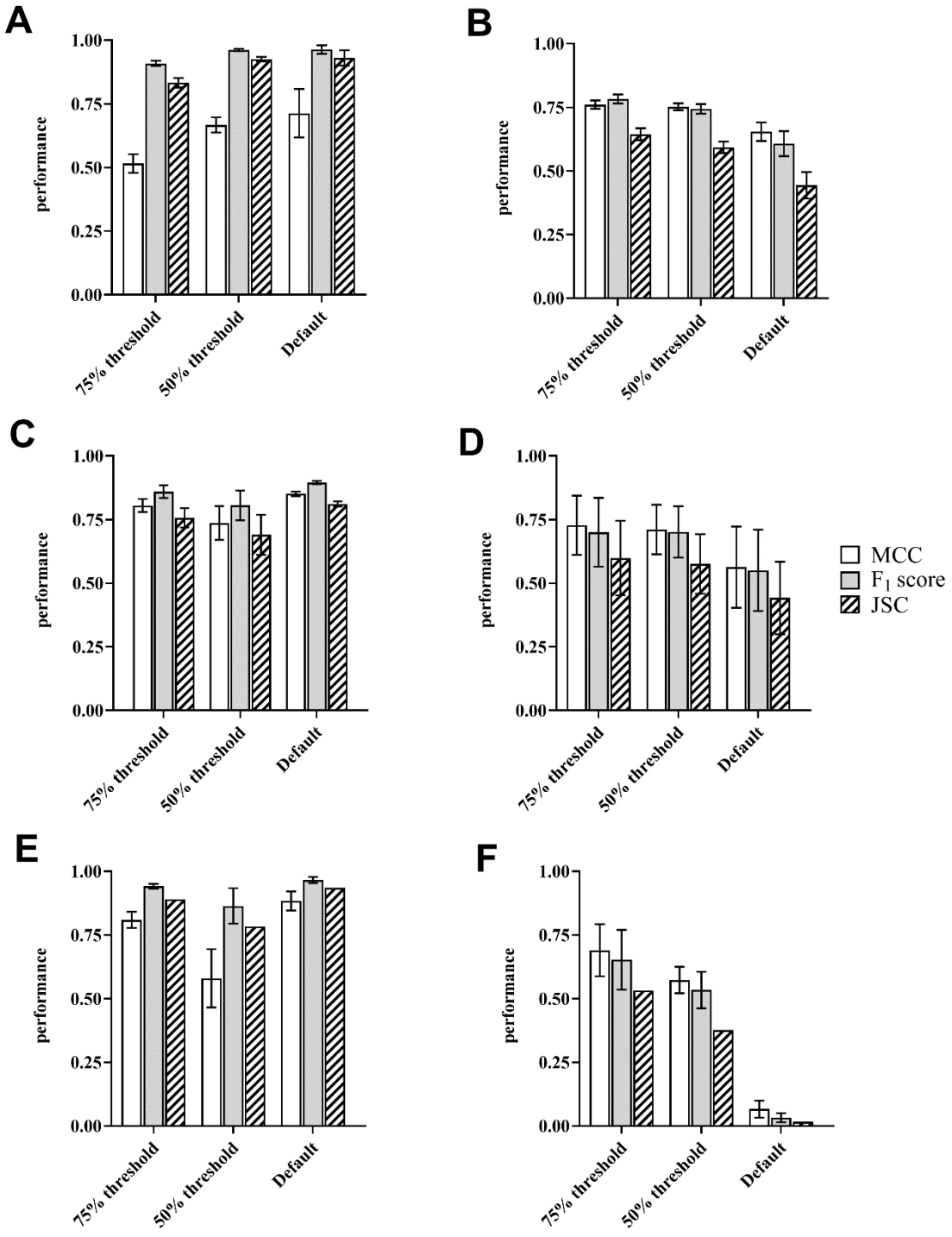

Figure 4.13: Performance evaluation of different segmentation methods

Performance of the different methods to iron and tissue segmentation in organs. Representative images were segmented using WEKA, with resulting probability maps' thresholds to represent pixels assigned to a class with certainty above 75% (75% threshold) or 50% (50% threshold). Default segmentation algorithm from FIJI was used for comparison as one of the traditionally used methods for semi-quantification of histological stains. Overlap metrics between manually segmented ground truth images and three segmentation methods were calculated for pixels classified as tissue in liver, lung, and kidney (A, C and E respectively) and for pixels classified as nanoparticles in liver, lung and kidney (B, D and F respectively). Data shown as mean ± SEM. MCC: Matthew's Correlation Coefficient; JSC: Jaccard Similarity Coefficient

4.3.4 *Iron quantification in histology sections*

To estimate visually observed increase of iron in liver, lungs and kidneys following MNP injection, quantification of Prussian blue staining was performed using trained classifier. In liver, statistical analysis suggested a significant increase in iron concentration from 3 hours up to 72 hours post injection compared to control sections (Figure 4.14 A). MNPs were almost completely cleared from the liver by 5 weeks post injection as indicated by a non-significant difference in concentration in comparison to control animals. Concentration of iron in lungs and kidneys was elevated following MNP injection, however this was found not to be statistically significant in comparison to organs from control animals.

In order to determine factor contributing to observed increase in the percent area, size (figure 4.14 B) and number of Prussian blue stained objects (figure 4.14 C) was calculated. In liver, aggregates did not increase significantly in size over time; there was an increase in number of aggregates up to 24 hours post injection of MNP, which began to decline subsequently. An opposite trend was observed in lungs, where size of the aggregates increased over time, with largest MNP aggregates detected at 48 hours post injection; number of objects also increased up to 48 hours post injection, however not with the same magnitude. In kidney, MNP aggregates did not increase in size over time, suggesting that observed increase in percent area of PPB stain was due to higher number of detected objects. Statistical analysis revealed a significantly lower iron content at 3 hours, 48, 72 hours and 5 weeks post injection of MNP in comparison to animals injected with saline (Figure 4.14 C).

.

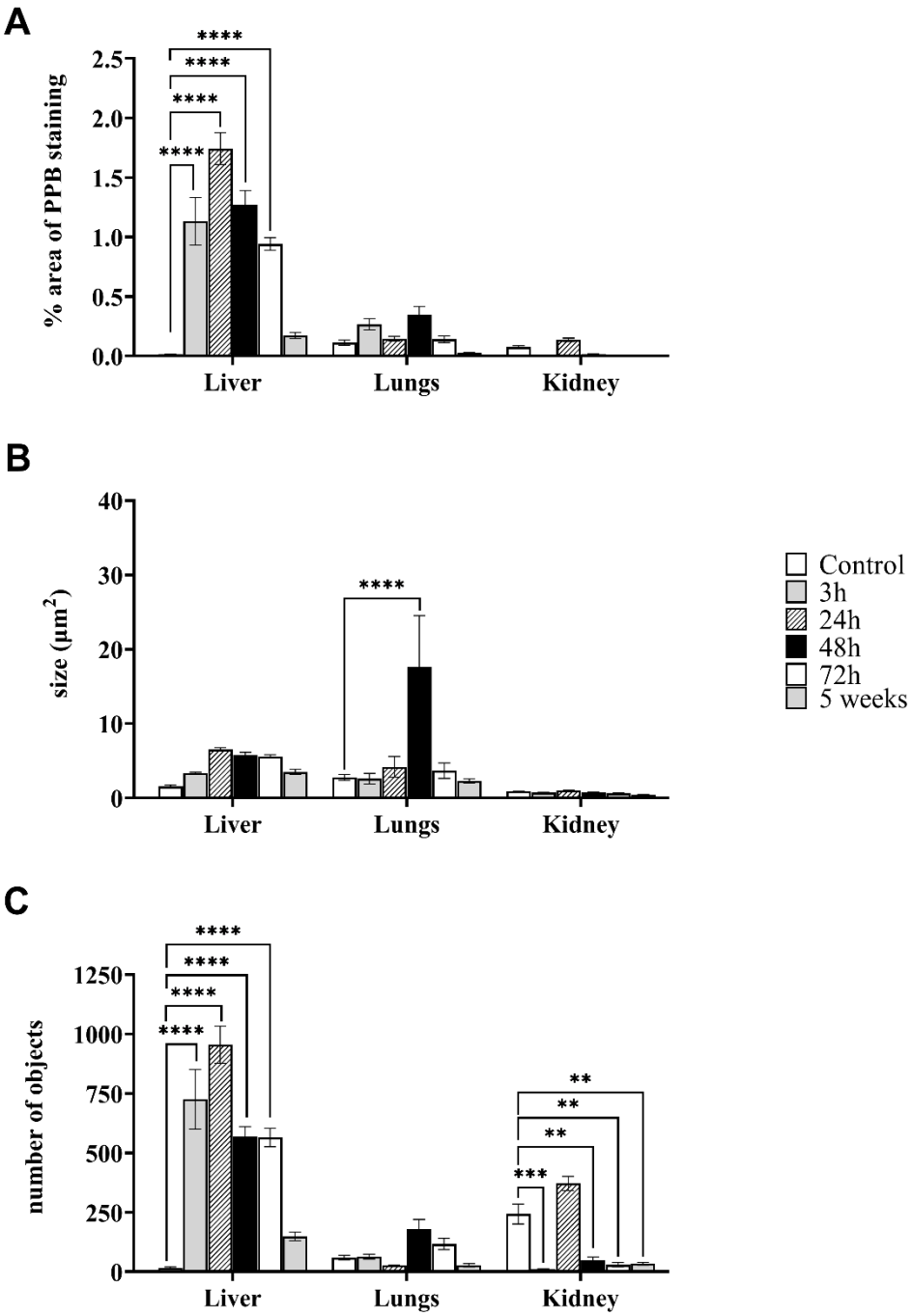

Figure 4.14: Quantification of Prussian blue staining
Quantification of the Prussian blue stained objects in liver, lung, and kidney tissue. (A) Percent area of PPB staining in tissue, (B) average size of detected aggregates, (C) number of detected objects. Statistical significance was determined using Two-way ANOVA with Bonferroni's multiple comparison test. ** $p \leq 0.01$, *** $p \leq 0.001$. Data points represent mean ± 95% Confidence Intervals of the mean; n=54 (two animals per time point, three slides per tissue, nine images per slide).

4.3.5 *3D virtual model*

Based on the quantification results, three samples (one for each organ) were selected for 3D reconstruction as they showed a clear increase in iron concentration in comparison to control samples. Nineteen consecutive 5μm sections from each tissue sample were stained with Perl's Prussian blue, imaged using automated microscope, manually aligned into a virtual stack and segmented using trained classifiers. Resulting stack of probability maps was post-processed by applying threshold representative of certainty above 75% that given pixel belongs to a particular class. Icy software with build in 3DVTK enabled the visualization of the stacks in 3D (Figure 4.15).

One of the limitations of traditional histology stacks imaging is the inability to remove certain components such as background for a better visualization and further analysis. Probability maps obtained by TWS are seen by imaging software as channels and can be easily switched on and off or be extracted separately for further analysis such as assessing the geometrical shape of the aggregates. This allowed for a clearer visualization of MNPs present in tissue samples, which are obscured in original histology stacks, such as the ones seen in the kidney sample in Figure 4.15. Although iron aggregate formed in the pulmonary vessel was clearly visible in the histology stack (middle figure in top row of Figure 4.15), its full geometry was unknown before examining a segmented 3D volume.

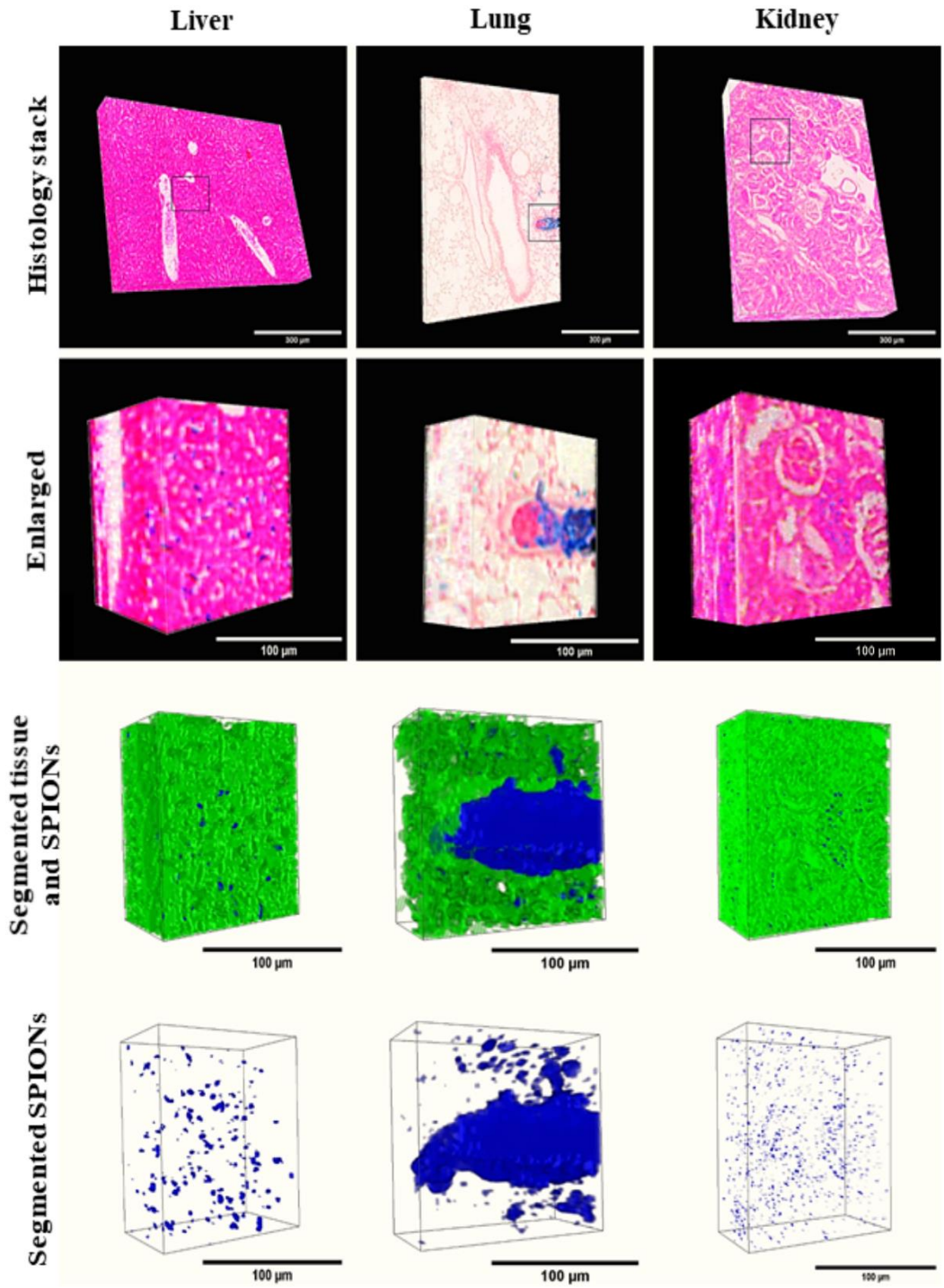

Figure 4.15: Representative images of 3D histology reconstruction and segmented 3D volume
Initial images acquired in brightfield were reconstructed into virtual stack; each of the segmented classes was then assigned a pseudo-colour (tissue in green; nanoparticles in blue; not shown here background in red and artefacts in yellow) for representative 3D volume; channel representing nanoparticles. Volume dimensions in top row images: x = 800 µm, y = 600 µm, z = 95 µm, scale bar represents 300 µm. Volume dimensions in enlarged images: x = 150 µm, y = 150 µm, z = 95 µm, scale bar represents 100 µm.

4.4 Discussion

In this chapter, an extensive histological analysis was carried out to assess toxicity and accumulation of MNP *in vivo*. As physical and chemical characteristics of magnetic nanoparticles and route of administration will impact their pharmacokinetics, toxicity and biodistribution [177], novel formulations have to be carefully examined prior to clinical trials [178].

The MNPs used in this study with a 12 ± 3 nm core diameter were coated in dimercaptosuccinic acid (DMSA). No indications of toxicity were observed in lung and kidney. Similar findings were reported in study by Yang *et al,* [77] where effect of size on biodistribution and toxicokinetics of iron oxide nanoparticles was investigated. In liver, small foci of inflammation were observed in response to MNP from 24 hour to 5 weeks post injection. In study by Feng *et al*. [179] slight mononuclear cell infiltration in the portal area of liver was also noted in BALB/c mice 2 weeks post injection of polyethylene glycol (PEG) coated iron oxide nanoparticles with 10 nm and 30 nm core Long-term *in vivo* toxicity studies (60 to 90 days post injection) would be required to determine whether those changes would resolve without complications once MNPs are completely cleared from the liver. In terms of DMSA coated iron oxide nanoparticles, *in vivo* studies of 12 nm core and 8.5 nm core were carried out in Wistar rats [180] and nonhuman primates (*Cebus* spp.) [181] respectively. In both species, no alterations were observed in the organs, at any time point up to 60 days after nanoparticle treatment. Overall, the lack of pathological changes in lung and kidneys as well as mild changes in the liver suggest that MF66 MNPs, assessed in this study, do not cause toxicity in those organs at the doses used.

For the accumulation results, positive iron staining was detected in lung and liver as early as 3 hours post injection (Figure 4.7). Relatively large MNP aggregates were detected in pulmonary vessels from 3 hours post injection up to 5 weeks, despite evidence of phagocytic clearance at 72 hours post injection. Although no changes suggestive of toxicity were reported in lungs, presence of those aggregates can result in severe consequence. In study by Chaves *et al.* [182], mice injected with DMSA coated magnetite nanoparticles with an average diameter of 9.4 ± 0.01 nm presented with breathing difficulties and died immediately after injection containing 100µL of 2.0×10^{16} particle/cm^3. Post-mortem examination revealed vast amount of magnetic nanoparticles clustered inside capillaries.

Liver is well known site of accumulation of iron oxide nanoparticles [183, 184]. In this study, iron was detected mainly in the hepatic sinusoids and in the cytoplasm of Kupffer cells. Both coating and iron core can be degraded within lysosomes of the Kupffer cells, and core can

be metabolised into other forms of iron [185]. For example, Lunov *et. al*. [186] demonstrated degradation of the carboxydextran shell of ferucarbotran (also known as Resovist) iron oxide nanoparticles by macrophages using fluorescent imaging and Dynamic Light Scattering Therefore, the presence of MF66 MNPs in Kupffer cells suggests their clearance, which is desired, as iron overload in liver can also lead to significant toxicity.

In kidney, iron was mainly observed in proximal tubules at 24 hours and 48 hours post injection. Proximal tubules have been shown to express several iron transporter proteins [187, 188], involved in iron reabsorption from tubular fluid. Iron is either stored in ferritin and utilized by the cells of the renal tubular epithelium, or exported via the basolateral membrane of tubular epithelial cells into the interstitium or circulation [189]. Positive iron staining was also seen in Bowman's capsule at 48 hours post injection. Staining intensity diminished by 72 hours post injection and was not observed at 5 weeks post injection suggesting complete clearance of MNPs. Similar findings were reported by Bellusci *et. al.* [190] who demonstrated accumulation of iron in the renal tubules at multiple time points over 21 days post injection of manganese ferrite nanoparticles with a mean core diameter of about 8 nm functionalized with citric acid In the study presented here, surprisingly no iron positive staining was seen after 3 hours post injection. Processes behind renal iron homeostasis in response to MNP are not yet fully understood. However, as previous work showed the effect of MNP particles on renal function as an increase in urine flow rate and decrease in tubular fluid reabsorption 20 – 60 minutes following MNPs administration [191],this was also seen in this study. Therefore it can be hypothesized that low iron concentration in proximal tubules at 3 hours post injection of MNPs in comparison to control could potentially be due to the same processes.

Semi-qualitative histological analysis (Figure 4.14) revealed that increase of iron in liver and kidney up to 48 h post injection of MNPs reported by pEPR [192] was due to increase in number of aggregates. Conversely when it was observed and quantified in lung, the increase in iron concentration is caused by an increase in the size of the aggregates. Aggregation of MNP in pulmonary vasculature can cause a life-threatening obstruction, however as size of the aggregates started to diminish from 72 hours post injection onwards, it can be concluded that aggregation of the material is slowly cleared out of the lung. Traditionally, results of histological analysis were reported as presence or absence of iron staining [180], or using histological score where for example "0" indicated "no staining", and "4" indicated "severe staining" [193]. In recent publications, the Prussian blue stained areas (μm^2) were measured to estimate the amount of nanoparticles accumulated in tissue [97, 163, 194]. In the study presented here, the use of ML was exploited for semi-qualitative and quantitative analysis of iron in tissue sections. In total,

three classification models were trained to overcome the variability in corresponding features of different tissue samples. Performance metrics indicated, that each model accurately classified tissue and iron in histological photomicrographs. For semi-quantitative analysis, percent area of Prussian blue staining was measured. Previous work undertaken during MultiFun project examined biodistribution and pharmacokinetic properties of similar particle using particle electron paramagnetic resonance (pEPR) and Magnetic Resonance Imaging (MRI) [192]. The results presented here show similar trend in biodistribution of MNP, with majority of iron detected in liver.

In order to maximize information obtained from histology samples, 2D digital images obtained from consecutive sections were reconstructed into 3D virtual volumes. Nanoparticle transport and clearance depend on their interaction with blood vessels, lymphatics and other biological structures. This interaction cannot be fully apprehended from traditional 2D histological slides which provide a snapshot of complex 3D structures. With the aid of ML, 3D volumes representing distribution of MNPs in liver, lung and kidney were generated in this study using standard desktop setup within 50 work hours, which is only a fraction of what was previously required using manual segmentation [104, 195]. As paraffin embedded tissue was used, complementary immunohistological analysis can be carried out in future studies to detect any biological markers of interest. Furthermore, with the ability to separate MNPs from other structures, the 3D volumes can provide details on aggregation via measurement of various shape descriptors. Up to date, approaches to visualize nanoparticles in intact tissues, involves making samples optically transparent using chemical and physical methods [196-199] or combining multiple imaging methods such as in vivo X-ray and ex vivo fluorescence imaging [200]. Despite numerous advantages of those approaches, they require specialized imaging equipment and algorithms or the use of fluorescent probes, which may limit their application in research. The methods used in this study allowed for a relatively simple and quick reconstruction of 2D histological images to 3D volumes without specialized equipment or powerful computer.

The method also presented for semi-quantitative distribution and mapping analysis which could be more informative, and less time and labor-intensive techniques such as ICP-MS or pEPR. The information acquired and processed from the semi-quantitative histology studies can provide comprehensive dataset on MNP size and number of aggregates, as well as their location within tissue which can have direct implication in the clearance rate of particles from the organs. Undoubtedly, this can contribute to pre-clinical safety profile of MNPs, as indicated in the objective of this study.

4.5 Conclusion

Histological analysis confirmed DMSA-coated MNPs used in this study were biocompatible as no obvious signs of toxicity were observed in liver, lung or kidney. Uptake of the material by tissue specific phagocytic cells and the decrease in iron staining over time, suggested the clearance of MNPs from those organs.

Furthermore, semi-quantitative histological analysis carried out with use of ML, extrapolated additional information on size and number of MNPs aggregates in tissue, providing complementary information to the quantitative measurements carried out such as pEPR or inductively coupled plasma mass spectrometry (ICP-MS).

5 Chapter 5: Histology study of toxicity and biodistribution of MNP *in vivo*

5.1 Introduction

In chapter 4, toxicity and biodistribution of one of the magnetic iron oxide nanoparticles (MNPs) developed under MultiFun consortium was assessed. In the course of four years, the MultiFun consortium developed formulations based on multifunctional MNP with an anticancer drug and a target peptide to capitalize on synergistic therapeutic effect produced by the combination of magnetic hyperthermia and intracellular drug delivery. *In vitro* and *in vivo* studies on those nanoformulations showed efficacy and safety against breast and pancreatic cancer [169, 171, 201]. Those initial results have led to further funding by the European Commission under Horizon 2020 framework. The Nanomedicine upscaling for early clinical phases of multimodal cancer therapy (NoCanTher) EU funded project aims to scale-up production of the patented MNP design from the MultiFun (patent filed PCT/EP2015/056631) and translate the most promising nanoscale formulation to early clinical development for pancreatic cancer.

The NoCanTher consortium[1] kicked off in 2016 and involves eleven institutions from five different countries (Ireland, France, Germany, Spain, and the UK) and three different sectors (academia, industry and clinical). The main objective of this international collaboration is to assess bare nanoparticles (i.e., not containing chemotherapeutic drug or ligand for active targeting) and multifunctional nanoparticles in advanced preclinical models, with former being used in a clinical study. As one of the collaborators on this project, the Nanomedicine and Molecular Imaging group in Trinity College Dublin carried out an *in vivo* toxicity study in Wistar rats on two bare nanoparticles synthesized by the collaborators to determine acute toxicity and biodistribution seven days post single, high dose intravenous injection. The results from the histology part of this study are detailed in this chapter.

The methodological approach undertaken in this chapter was based on that developed in chapter 4. As two MNPs used in this study shared similar physicochemical properties (core size < 50nm, dextran coating, negative charge, hydrodynamic diameter < 150nm), the main aims of the *in vivo* studies presented in this chapter were to:

1. Assess histological changes induced in organs in response to intravenous administration of MNPs.

[1] NoCanTher website - https://cordis.europa.eu/project/id/685795

2. Investigate MNP’ interactions with immune cells by means of specialized staining.
3. Obtain quantitative data from histological sections stained for iron detection.
4. Carry out quantitative morphological analysis of iron aggregates in traditional 2D histology slides and 3D histology volumes.

5.2 Experimental objectives and design

Two lead MNPs for hyperthermia treatment were used in the *in vivo* study for the evaluation of acute toxicity and organ damage in response to a single, high dose injection. The overall aim of this study was to mimic a 'failed' intratumoral injection and a worst-case scenario where all injected material reached the bloodstream. The main objective was to determine the concentration at which acute effects occur, their manifestation and their level of severity. Physicochemical properties of MNPs used in this study are summarised in Table 5.1. The study design, which was carried out in two experimental blocks is reported in the graphical representation in Figure 5.1. Experimental work presented in this chapter is complementary to the work of Dr. Gary Hannon at the LBCAM (TTMI, TCD) [202].

While the experimental *in vivo* design and implementation was carried out under the supervision of Dr Oliviero Gobbo, organ harvesting and processing, histology sectioning, staining, observation and recording of events was carried out within this PhD work.

Table 5.1: Physicochemical properties of NOC0007 and RCL-01 MNP
Summary of the physicochemical properties of the materials used in case study 4.

Name	NOC0007 MNPs	RCL-01 MNPs
Type of material	Maghemite (γ-Fe2O3)	Iron Oxide
Primary size (nm)	14	50 ± 25
Coating	Dextran 40kD	Dextran
Hydrodynamic diameter (nm)	122.6	149
Zeta Potential (mV)	-6.5	-20.5
Polydispersity index (PDI)		0.26
Endotoxin (EU/ml)	<1.6 In a solution with iron concentration of 130 mg/ml, measured with turbidimetric-kinetic method	0.4 In a solution with iron concentration of 72 mg/ml, Measured with turbidimetric-kinetic method
Supplier	Supplied by collaborator from IMDEA, Madrid, Spain	Purchased from Resonant Circuits Limited
Animal model used	Wistar rats (body weight 245 g ± 23 g) female	Wistar rats (body weight 245 g ± 23 g) female
Volume injected (ml)	1	1

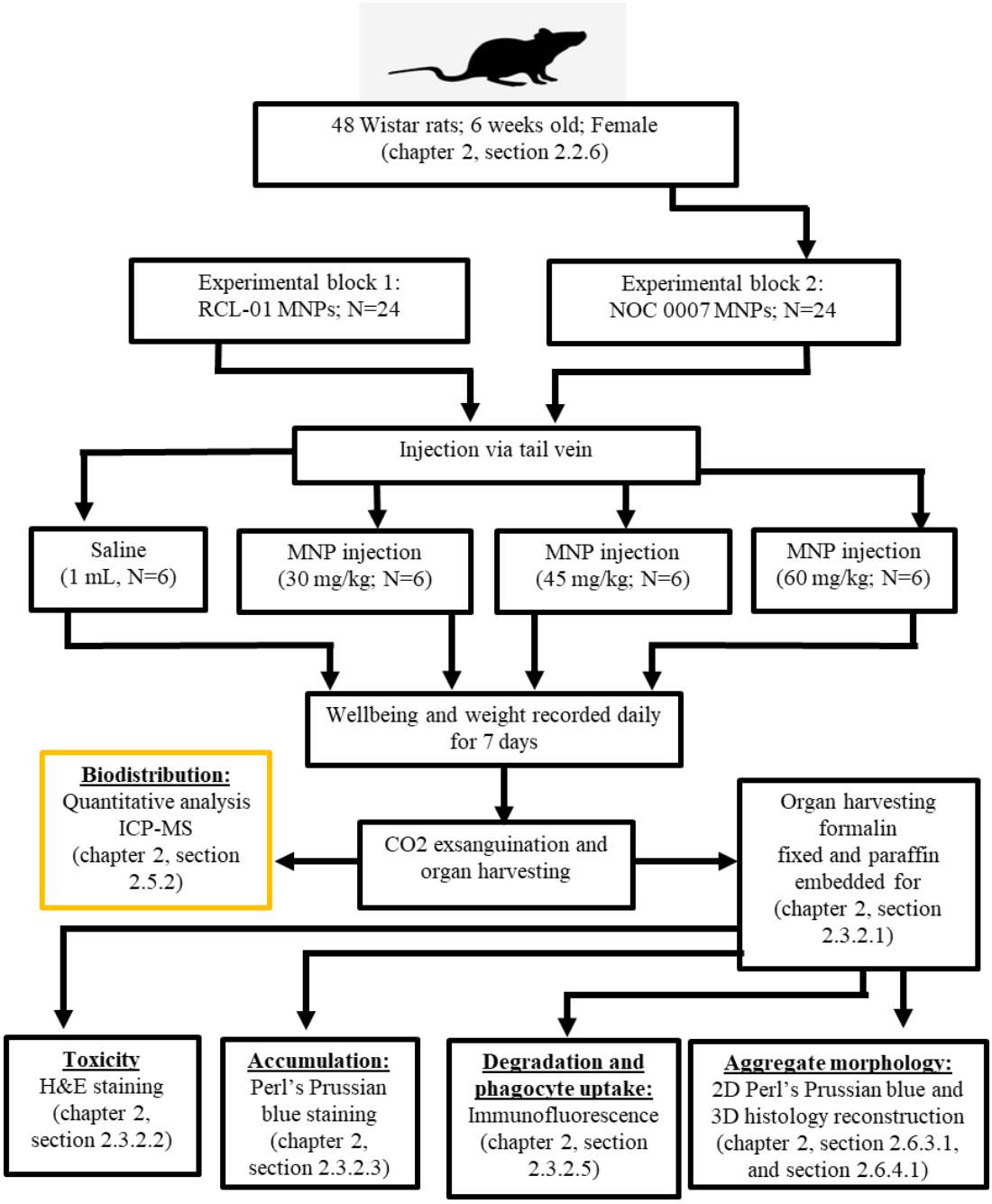

Figure 5.1: Experimental workflow for case study 4: *In vivo* acute toxicity study of NOC0007 and RCL-01

In vivo study was designed in accordance with ISO 10993-11:2018 (biological evaluation of medical devices) to mimic a 'failed' intratumoural injection and a worst-case scenario where all injected material reached the bloodstream. From top to bottom, first four rows of the diagram present details on the animals used, route of administration, and type and dose of material administered. Clinical evaluation of the animals was recorded daily for 7 days following the injection. On day 7, animals were euthanized with CO_2, and the organs of interest were harvested, formalin fixed, and paraffin embedded for further analysis. Note: quantitative biodistribution (orange box) was carried out by Dr Gary Hannon as a part of his work for the doctorate thesis [202]. Boxes in the bottom row, highlight histological methods utilized in this thesis to determine tissue toxicity, accumulation, and degradation of the MNPs used. Specific protocols related to case study are reported in chapter 2 under the specific technique utilized. Project license number: AE19136/P089

5.3 Results

Results presented in this section were observed and recorded during the seven-day acute exposure *in vivo* toxicity study of NOC0007 and RCL-01 MNPs. This was followed by a histology study where pathological changes, immune response, degradation, and accumulation of MNPs was assessed. Finally, ML for bioimage analysis was used to measure levels of iron in organs, number, size and shape of the aggregates formed. The latter was also evaluated in the 3D segmented volumes based on 3D histology volume of lungs.

5.3.1 *Clinical evaluation*

For both MNPs, there were significant differences in severity scores between control animals and treatment groups at 30-minute time point post injection (Figure 5.2) for both MNP examined. For RCL-01, statistically significant difference in scores was also observed over time in animals injected at 60 mg/kg (Figure 5.2 B). Other clinical signs suggestive of toxicity of MNP were reported in animals injected with NOC0007, which presented with scaring at the site of injection resulting in necrotic tail and tail loss in several animals (3/6 rats at 30 mg/kg; 4/6 rats at 45 mg/kg; 6/6 rats at 60 mg/kg). Diarrhoea was also reported soon after injection in four animals treated with higher doses (1/6 rats at 45 mg/kg; 3/6 rats at 60 mg/kg). As those animals did not show signs of pain according to Rat Grimace Scale used to monitor animal's pain by the National Centre for the Replacement Refinement and Reduction of Animals in Research (NC3Rs) [203], their score was reported as 0 after one hour post injection.

Change in animal body weight over experiment duration was recorded as a percent of initial weight before administration. This was calculated for each animal individually to account for natural variation in initial weight prior to experiment. Any change in weight above 10% of the initial weight is considered significant. No significant changes in weigh were seen over experiment duration in both treatment groups (Figure 5.3).

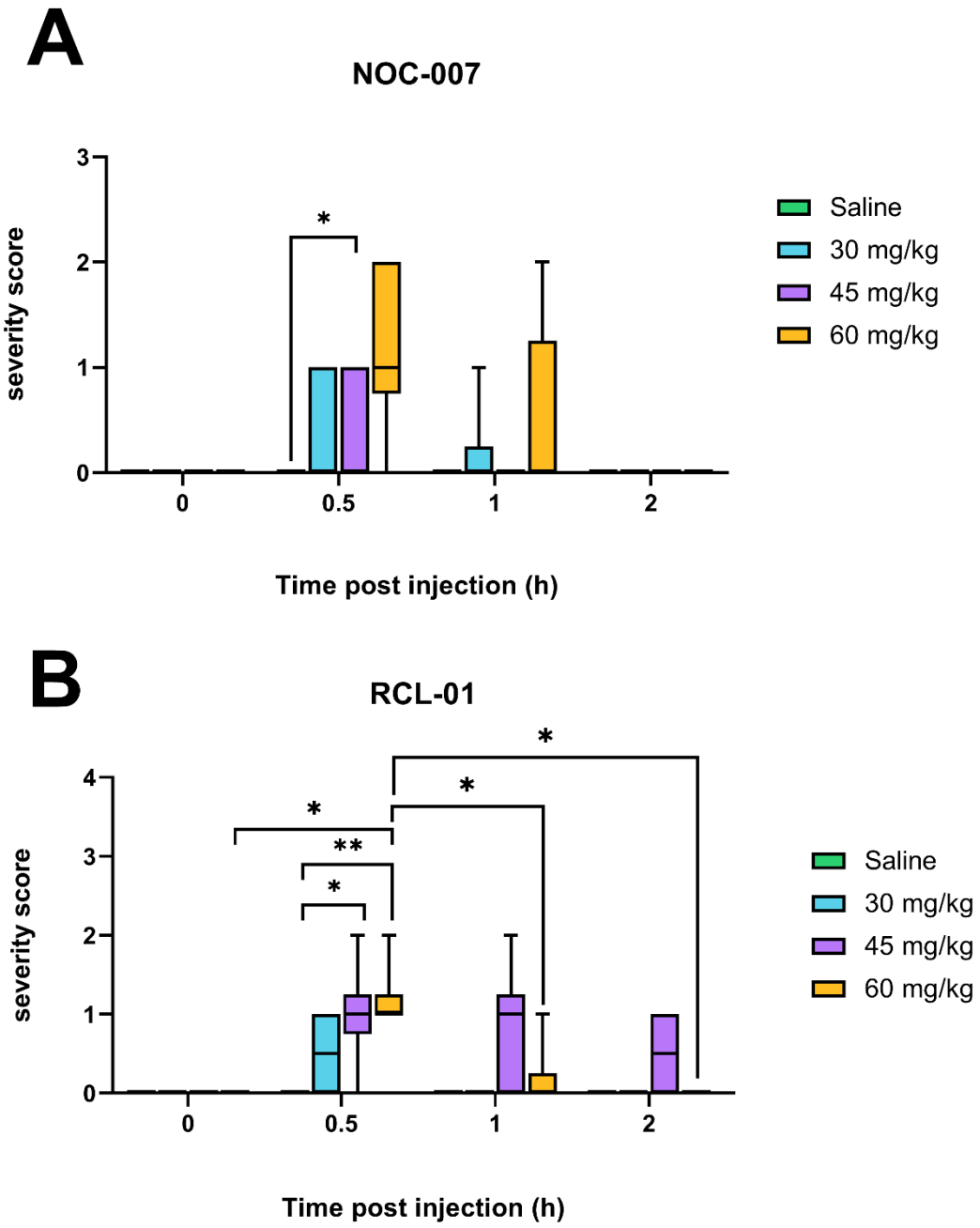

Figure 5.2: Severity score

Boxplot of severity score for animals treated with NOC0007 (A) or RCL-01 (B). Maximum obtainable score was 4. Within each box, horizontal lines denote median values; boxes extend from the 5th to the 95th percentile of each group's distribution of values. Statistical significance between treatments at individual time points was calculated using Kruskal-Wallis test with post-hoc Mann-Whitney U test.

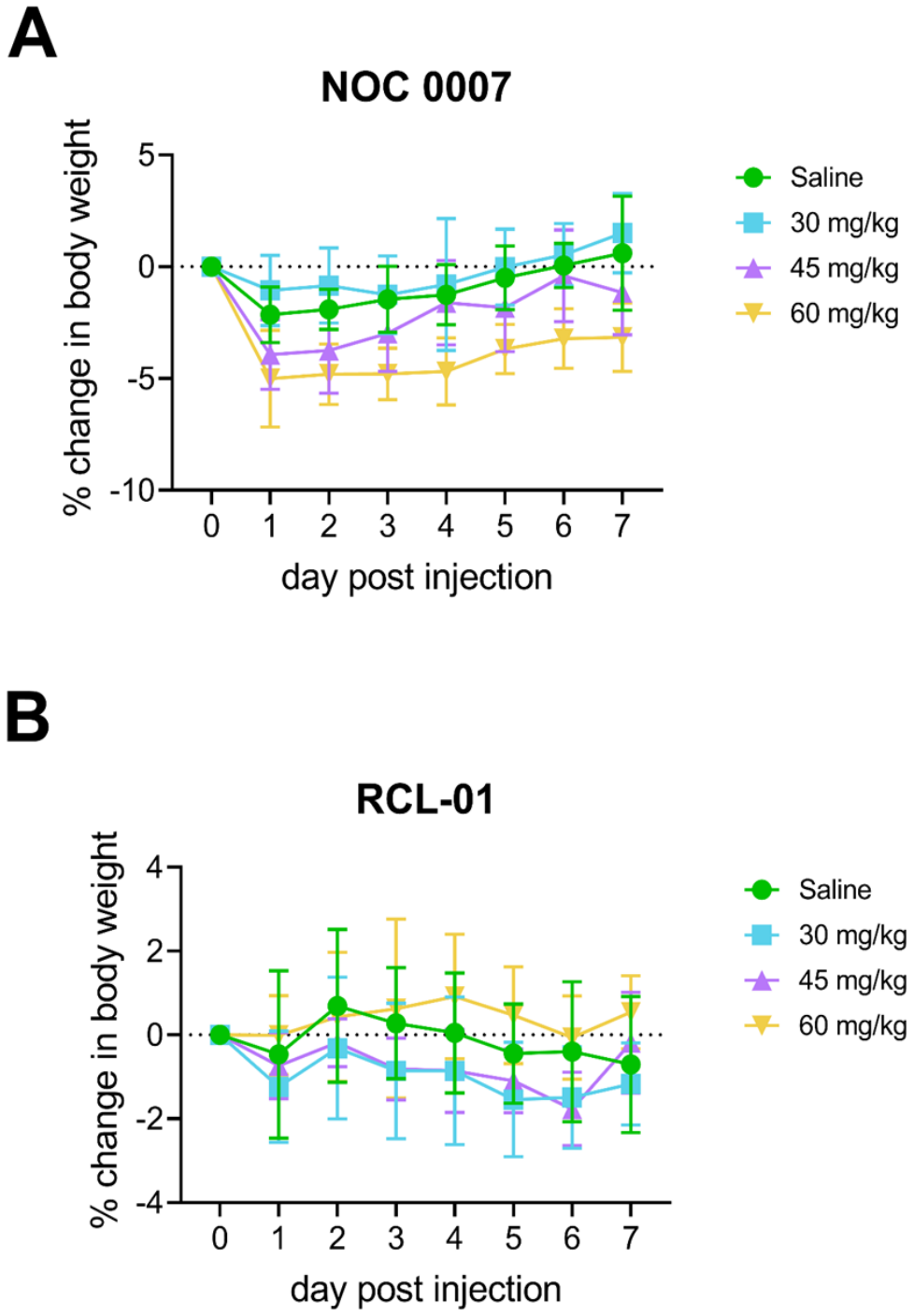

Figure 5.3: Body weight variation over experiment duration
Percent change in body weight (y-axis) in Wistar rats over experiment duration (x-axis) in animals in NOC 0007 experimental block (A) and RCL-01 experimental block (B). Control animals were injected with saline (green ●); MNP were administered at 30 mg/kg (blue ■), 45 mg/kg (purple ▲) or 60 mg/kg (yellow ▼) on day 0 of the experiment. Data expressed as mean ± SD (n = 6).

5.3.2 *Toxicity*

In both treatment groups influx of immune cells into perivascular and peribronchial space was observed on H&E stained lung sections (Figure 5.4) regardless of dose of MNPs used. Types of immune cells observed varied between two particles, with NOC 0007 treated animals showing increase of eosinophils and mast cells in the area, regardless of dose used. RCL-01 treated animals also shown an influx of immune cells, with majority of eosinophils. No histological changes were reported in other structures of the lungs. Interestingly, in animals treated with NOC 0007 MNPs, number of iron aggregates seen a granular brown deposits formed shapes resembling a rectangular (Figure 5.4 B). This was not observed in RCL-01 treated animals, where iron deposits were mainly seen in the macrophages (Figure 5.4 F).

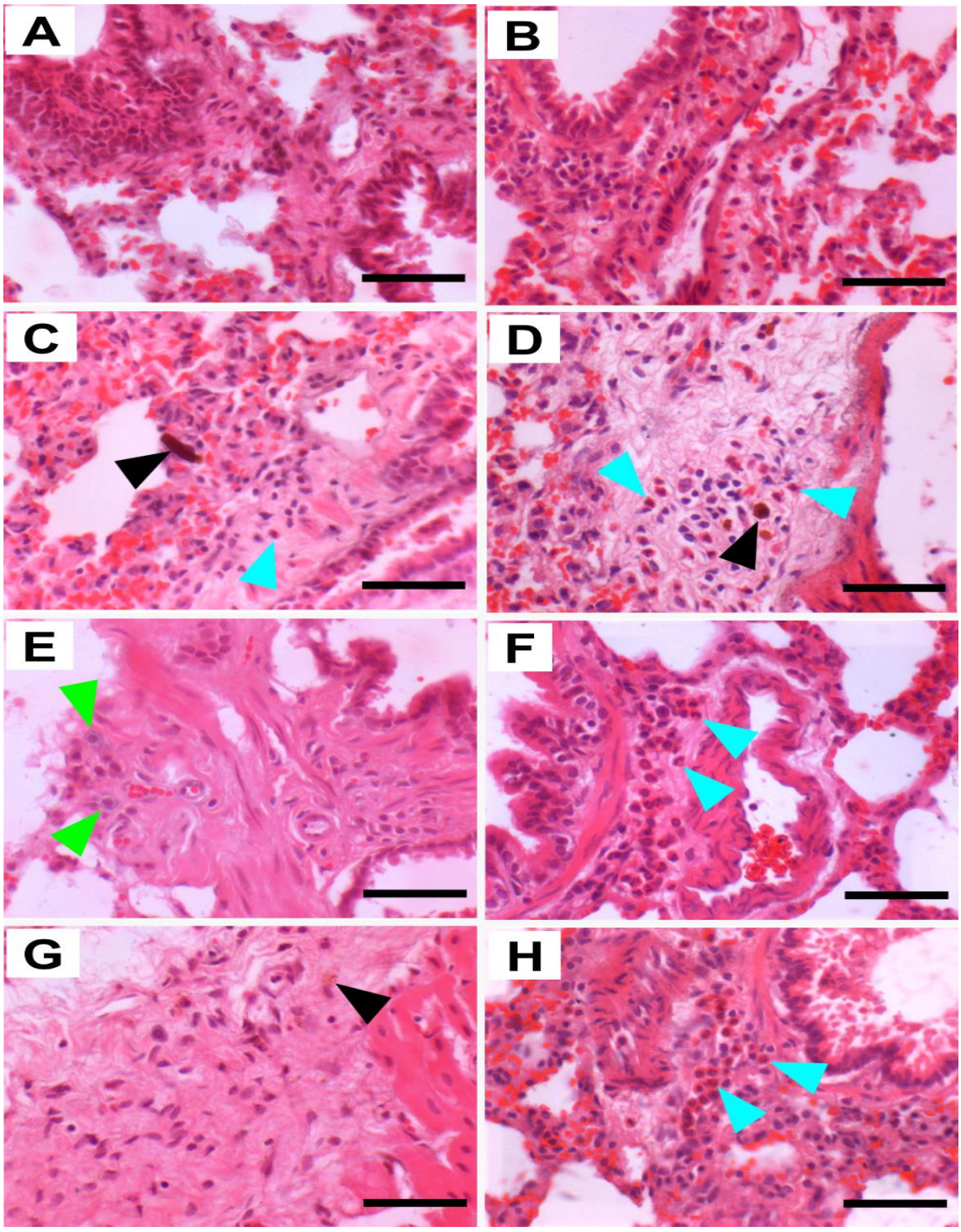

Figure 5.4: Pathological changes in lung sections

Representative photomicrographs of H&E stained lung sections of Wistar rats (n=6) showing an immune infiltrate in perivascular and peribronchial space formed in response to MNPs. Animals were injected with either saline (A and B), or MNP at 30 mg/kg (C and D), 45 mg/kg (E and F) and 60 mg/kg (G and H). Animals were sacrificed 7 days post injection. Tissue was formalin fixed and paraffin embedded. 5µm thick sections were cut with rotary microtome and collected at four levels through the block spaced at least 50 µm apart. Left column shows photomicrographs of sections from animals in NOC 0007 treatment group, right column from RCL-01 treatment group. Black arrowheads: iron; Light blue arrowheads: eosinophils; Green arrowheads: mast cells. Scale bar represents 100 µm.

In liver, mild hepatic congestion was seen in the majority of animals in NOC0007 and RCL-01 treatment groups (Figure 5.5), in animals injected with the MNPs as well as the control animals injected with saline (Supplementary figure 8.44 and Supplementary figure 8.45).

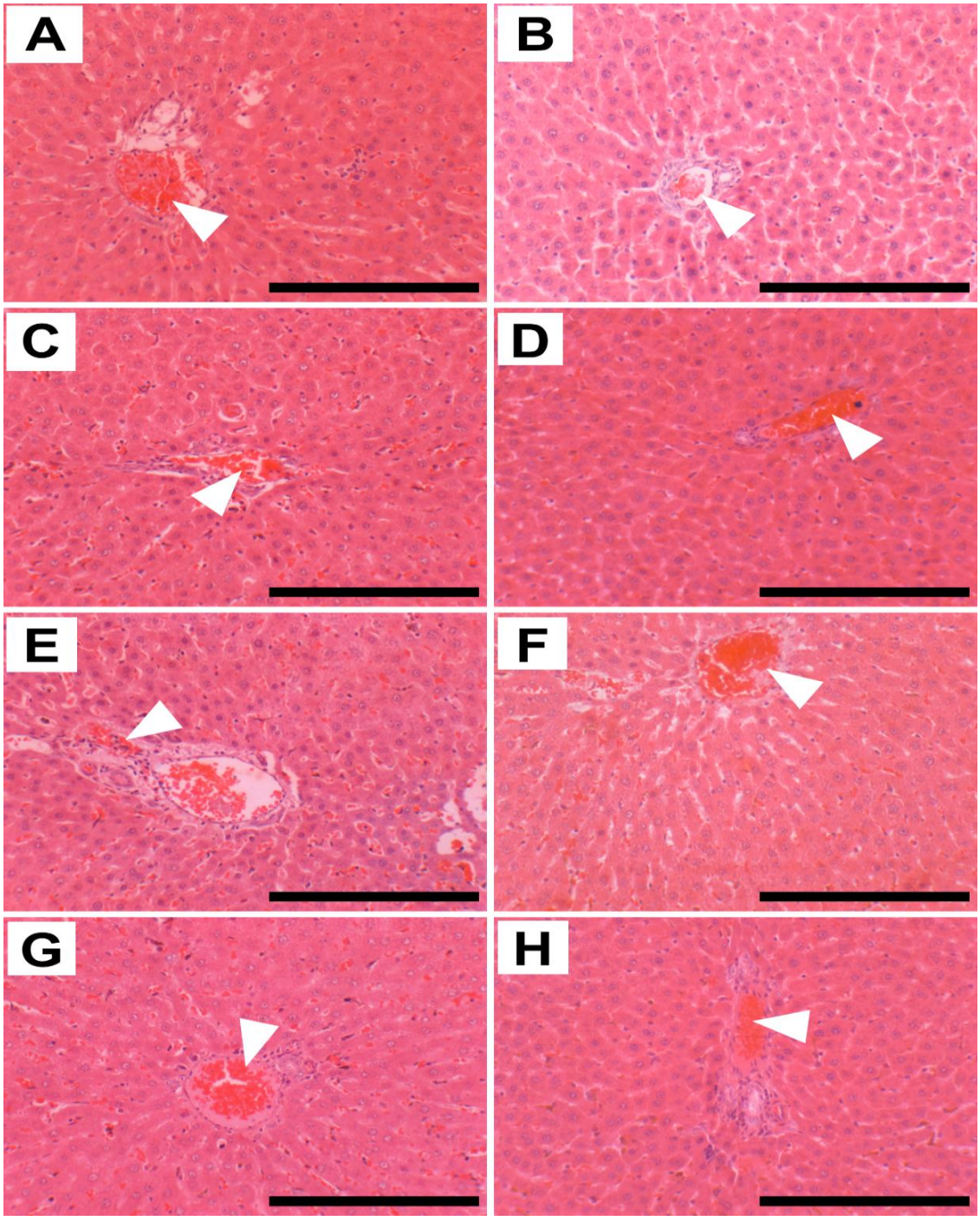

Figure 5.5: Pathological changes in liver

Representative photomicrographs of H&E stained liver sections of Wistar rats (n=6) showing congestion in the vasculature (white arrowheads). This was seen in control animals injected with saline (A and B), or MNPs at 30 mg/kg (C and D), 45 mg/kg (E and F) and 60 mg/kg (G and H). Animals were sacrificed 7 days post injection. Tissue was formalin fixed and paraffin embedded. 5µm thick sections were cut with rotary microtome and collected at four levels through the block spaced at least 50 µm apart. Right hand side column shows photomicrographs of sections from animals in NOC 0007 treatment group, left hand side column from RCL-01 treatment group. Scale bar represents 100 µm.

Extramedullary haematopoiesis was seen in the splenic red pulp (Figure 5.6). This change was characterised by increased number of erythroid precursor cells as well as megakaryocytes (yellow arrowhead in Figure 5.6 B, C and D). This change was noted in the control animals as well as the ones injected with the MNPs. No significant changes were seen in the white pulp in any of the animals in both treatment groups (Supplementary figure 8.46 and Supplementary figure 8.47).

Number of histological changes suggestive of toxicity were seen in kidneys (Figure 5.7). These changes included: calcification, tubule dilation, cytoplasmic vacuolation in tubule, cytoplasmic alterations in renal tubule, tubule degeneration, tubule regeneration, cellular infiltration in the interstitium, and glomerular atrophy with widening of the glomeruli space. Similarly, to pathological changes reported in the liver and spleen, no significant difference in the degree of changes was seen between the control animals and those injected with the increasing dose of MNPs.

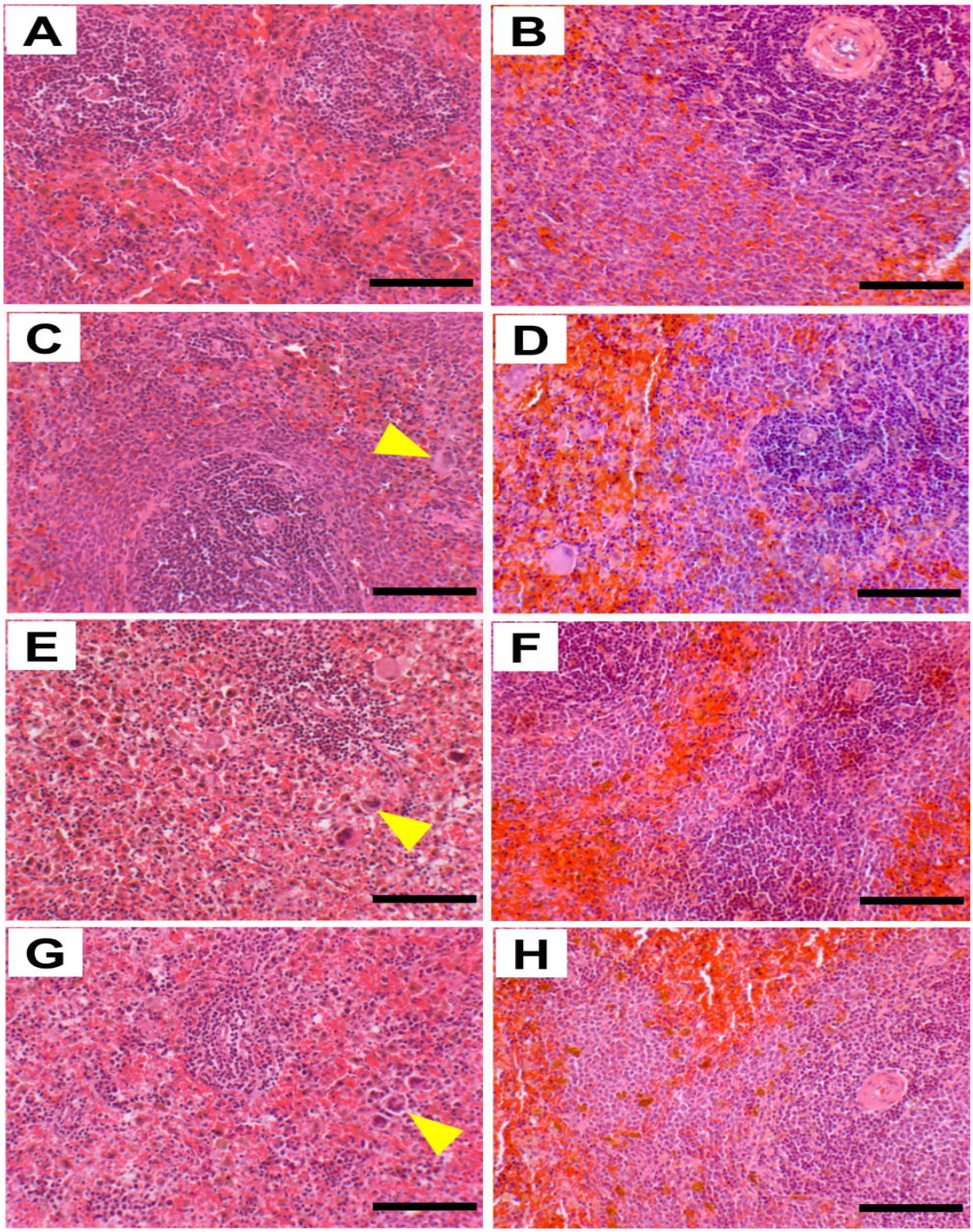

Figure 5.6: Pathological changes in the spleen sections

Representative photomicrographs of H&E stained spleen sections from Wistar rats (n=6) showing an increased number of megakaryocytes in the red pulp of animals injected with MNPs. Photomicrographs from control animals injected with saline are shown in the top row (A and B). Animals were injected with the MNP at 30 mg/kg (C and D), 45 mg/kg (E and F) and 60 mg/kg (G and H). Animals were sacrificed 7 days post injection. Tissue was formalin fixed and paraffin embedded. 5µm thick sections were cut with rotary microtome and collected at four levels through the block spaced at least 50 µm apart. Left column shows photomicrographs of sections from animals in NOC 0007 treatment group, right column from RCL-01 treatment group. Yellow arrowheads indicate megakaryocytes. Scale bar represents 100 µm.

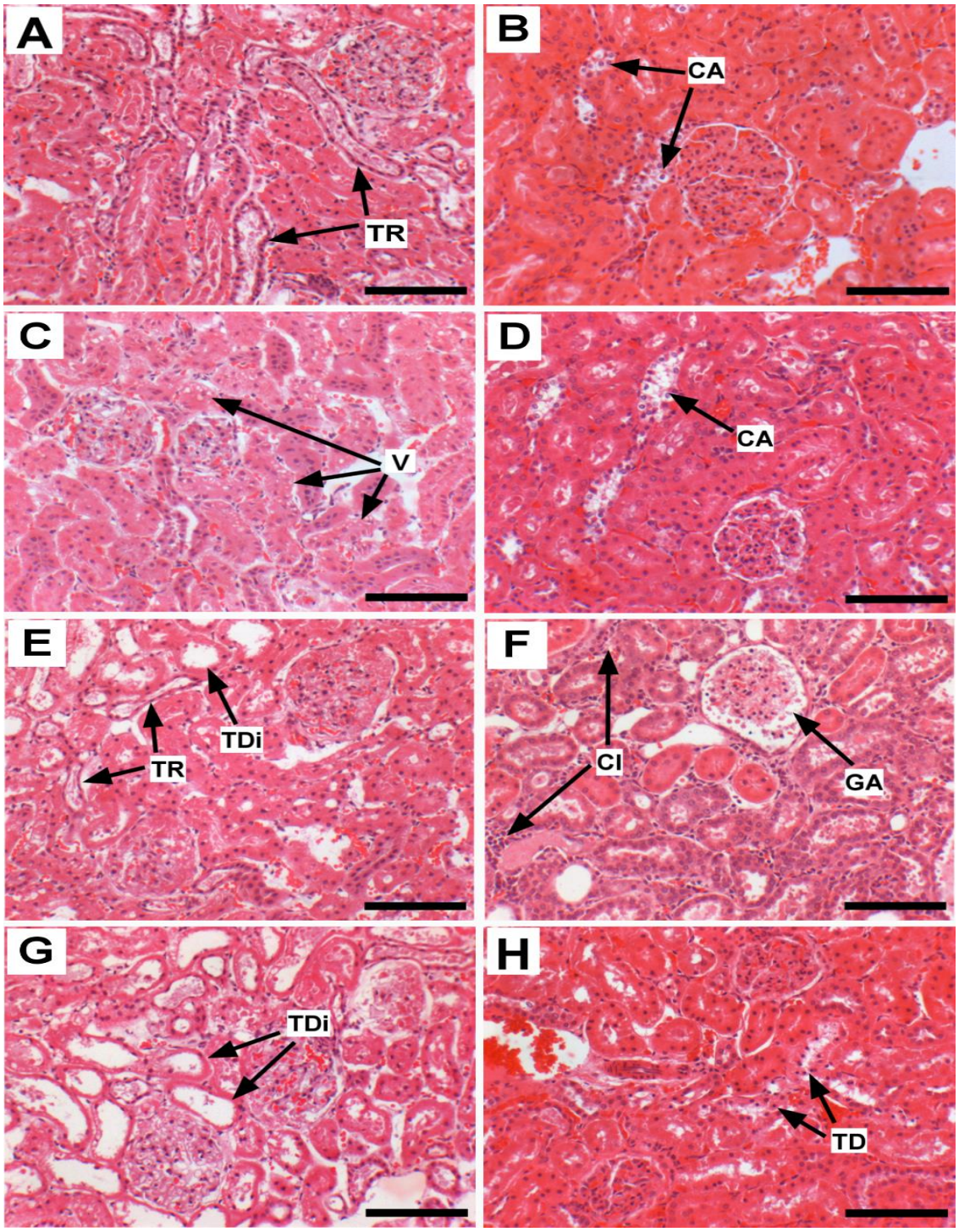

Figure 5.7: Pathological changes in the kidney sections

Representative photomicrographs of H&E stained kidney sections from Wistar rats (n=6) showing abnormal histological changes. Animals were injected with either saline (A and B), or MNP at 30 mg/kg (C and D), 45 mg/kg (E and F) and 60 mg/kg (G and H). Animals were sacrificed 7 days post injection. Tissue was formalin fixed and paraffin embedded. 5µm thick sections were cut with rotary microtome and collected at four levels through the block spaced at least 50 µm apart. Left column shows photomicrographs of sections from animals in NOC 0007 treatment group, right column from RCL-01 treatment group. TR: tubule regeneration, V: vacuolation, TDi: tubule dilation, CA: cytoplasmic alterations, CI: cell infiltrate, GA: glomerular atrophy, TD: tubule degeneration. Scale bar represents 100 µm.

All of the findings reported from the assessment of H&E stained slides were in line with the ones reported by the two registrar pathologists from the Central Pathology Laboratory in St. James's Hospital Dublin, as detailed in Supplementary table 8.8 and Supplementary table 8.9. The pathologists made their assessment blinded to the treatments given to the animals. Furthermore, pathological changes were rated using a 4-tier severity scale as shown in Figure 5.8. Although number of changes were identified in animals from across different treatment groups, severity score showed no significant differences between the control animals and those injected with MNPs.

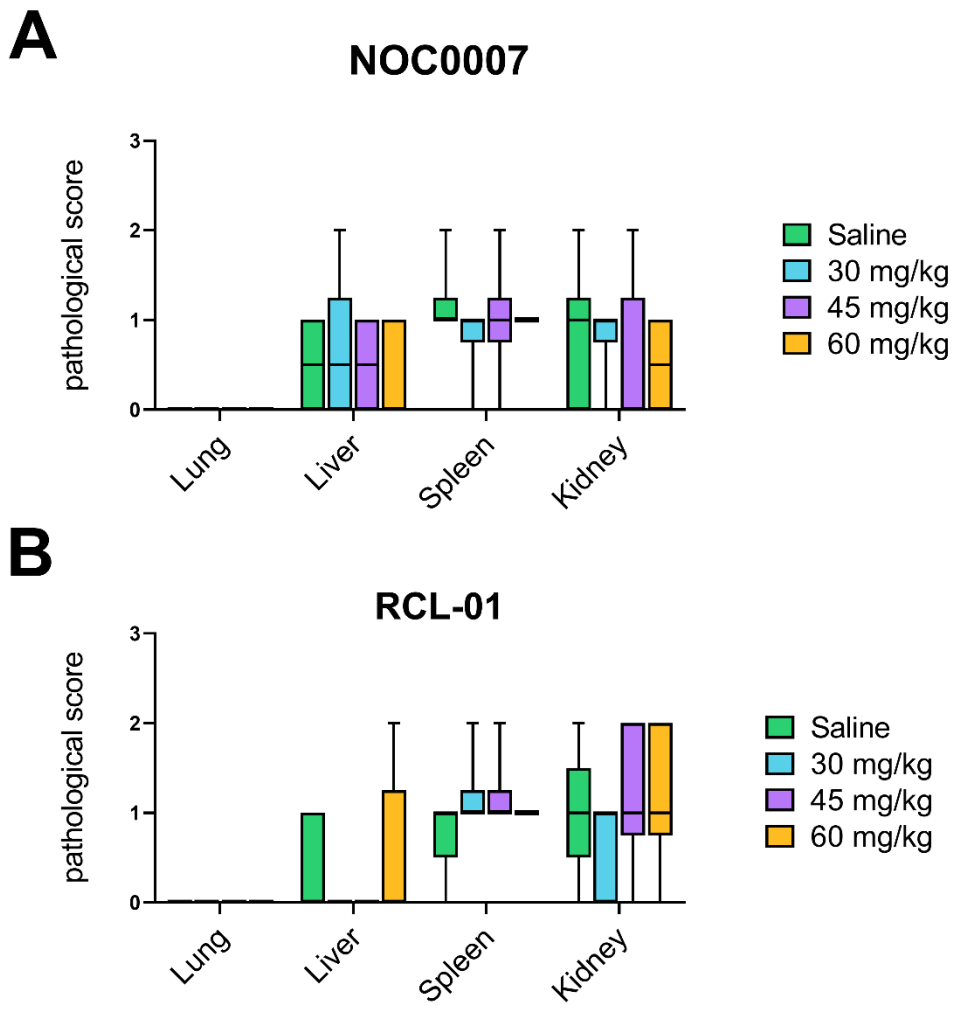

Figure 5.8: Boxplot of pathological severity score
Identification of histological changes severity in organs of animals from NOC0007 experimental block (A) and RCL-01 experimental block (B) rated blindly by a pathologist. Histology score followed a 4-tier severity scale: 0, normal structures; 1, minor changes; 2, mild changes; 3, severe pathological changes. Within each box, horizontal lines denote median values; boxes extend from the 5th to the 95th percentile of each group's distribution of values (n=5-6). Statistical significance was calculated using Mann-Whitney U test.

The next section discusses results obtained from two specialised stains which were used to further investigate the interaction of the MNPs with the cells of the innate immune system. First staining, modified toluidine blue staining was used to further investigate response of mast cells and eosinophils to iron accumulated in the perivascular and peribronchial space in the lungs. Second staining, immunofluorescent staining was used to determine uptake of MNPs by tissue specific macrophages and degradation of the dextran coating.

5.3.3 *Investigation of immune response and coating degradation*

Initial results from H&E stained sections provided preliminary indication of different immune response and accumulation of NOC0007 and RCL-01 in organs. In order to gain insights into mechanisms behind those findings, two specialised stains were optimised to further investigate response of the cells of innate immune system and the degradation of dextran coating.

5.3.3.1 Mast cell response

Toluidine blue staining is an established method for the identification and quantification of mast cells. Due to co-localization of mast cells and eosinophils observed in perivascular and peribronchial space on H&E stained slides, a modified toluidine blue stain incorporating eosin was used for better visualisation of those cells. Figure 5.9 shows accumulation of immune cells in peribronchial connective tissue. As mast cells are distributed mainly in the connective tissue throughout the body, their presence in peribronchial space was expected. Resting mast cells were predominant in control animals (Figure 5.9 A and B).

In animals treated with NOC 0007 several mast cells appeared to be activated as characterised by release of granules from the cytoplasm. However, visual assessment of the slides did not indicate a significant increase in number of mast cells as shown in the low magnification images in Figure 5.10. In RCL-01 treated animals, number of degranulating mast cells was visually increased in comparison to control animals, as shown in low magnification images in Figure 5.11. Moreover, degranulating mast cells were surrounded with eosinophils.

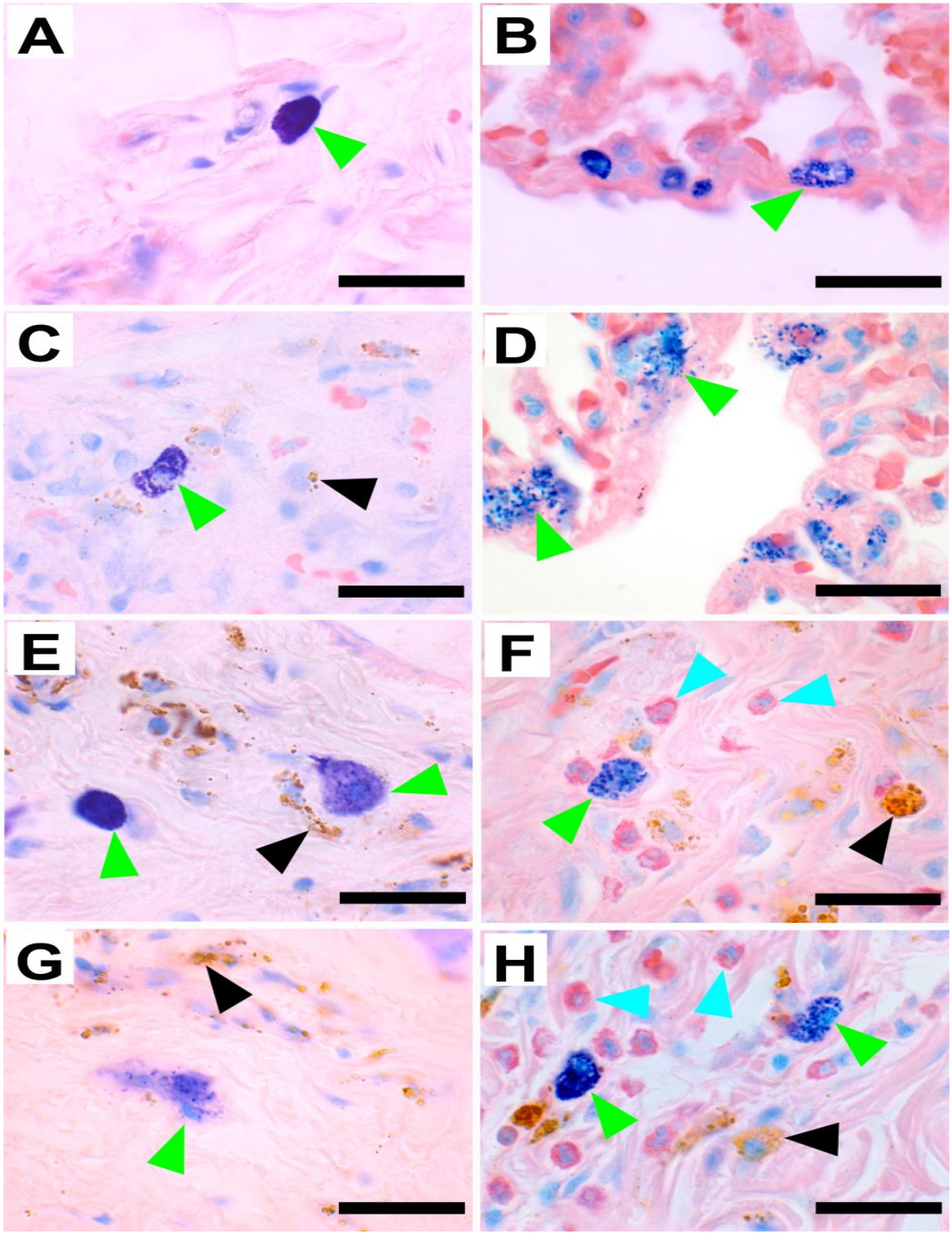

Figure 5.9: Mast cell activation in response to MNPs

High magnification photomicrographs of Toluidine blue stained lung sections of Wistar t
Rats (n=6) showing degranulation of mast cells stained in dark blue/purple. Animals were injected with either saline (A and B), or MNP at 30 mg/kg (C and D), 45 mg/kg (E and F) and 60 mg/kg (G and H). Animals were sacrificed 7 days post injection. Tissue was formalin fixed and paraffin embedded. 5µm thick sections were cut with rotary microtome and collected at four levels through the block spaced at least 50 µm apart. Left column shows photomicrographs of sections from animals in NOC 0007 treatment group, right column from RCL-01 treatment group. Black arrowhead: iron aggregates; Green arrowhead: mast cells; Light blue arrowhead: eosinophils. Scale bar represents 25 µm.

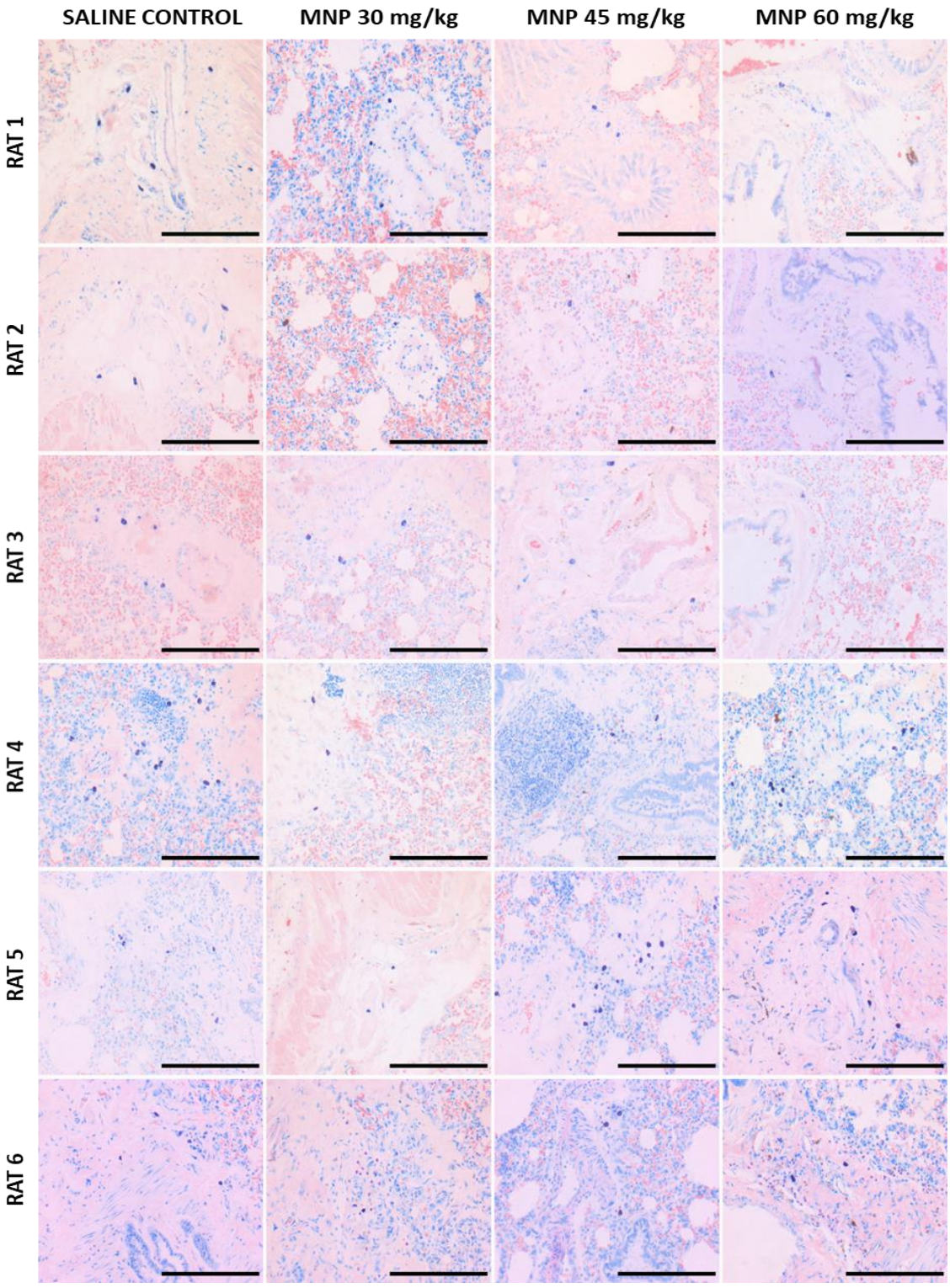

Figure 5.10: Infiltration of mast cells in lung in response to NOC0007 MNPs
Toluidine blue attaining showing the presence of mast cells (dark blue/purple cells) in the perivascular and peribronchial region in lungs of Wistar rats (n=6) injected with saline (left hand side column), or NOC0007 MNPs at 30mg/kg, 45 mg/kg, or 60 mg/kg. Animals were sacrificed 7 days post injection. Tissue was formalin fixed and paraffin embedded. 5µm thick sections were cut with rotary microtome and collected at four levels through the block spaced at least 50 µm apart. Images were acquired with Nikon Eclipse E800 brightfield microscope using 20x lens; scale bar represents 100 µm.

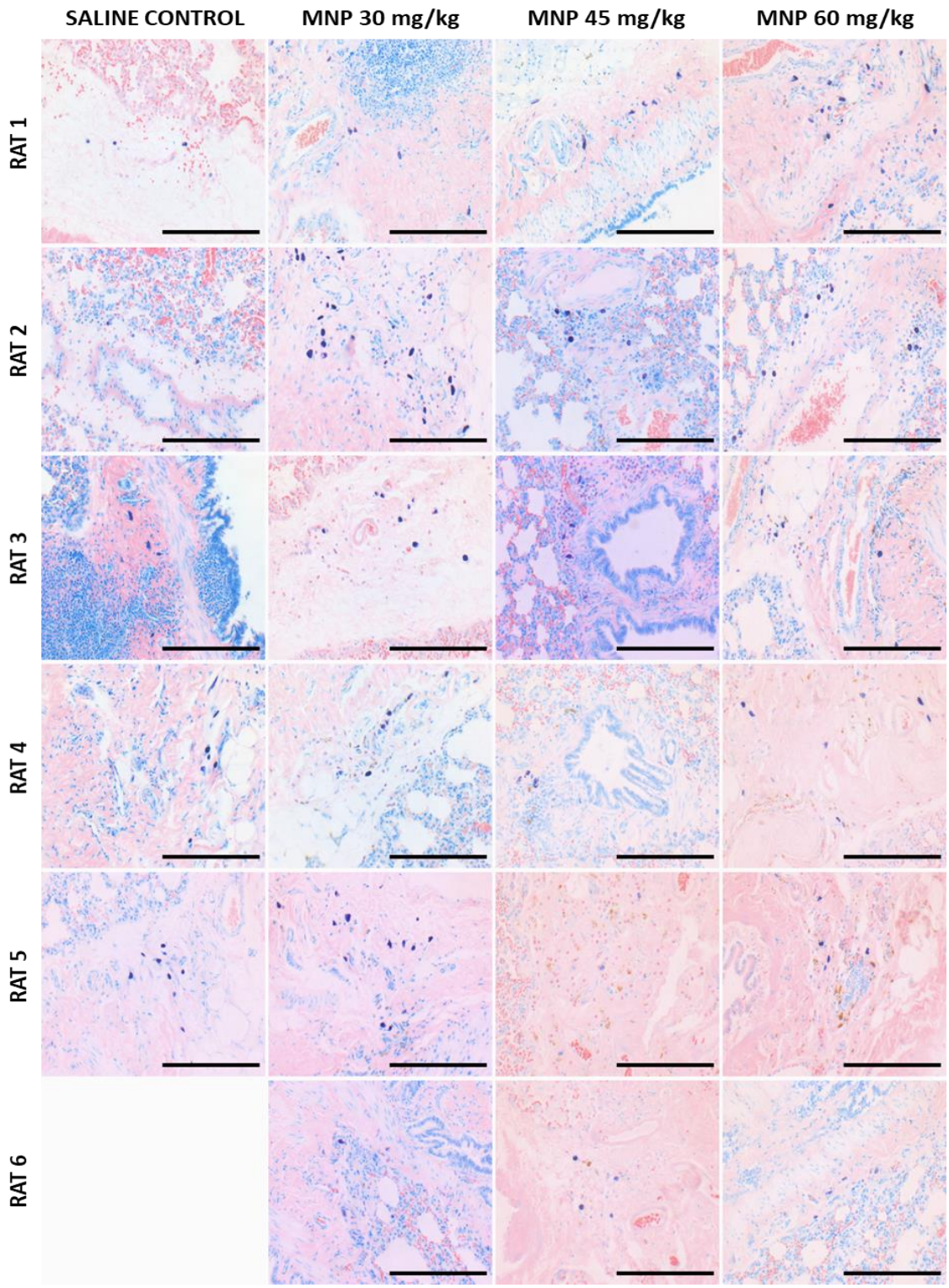

Figure 5.11: Infiltration of mast cells in the lung in response to RCL-01 MNPs
Toluidine blue attaining showing the presence of mast cells (dark blue/purple cells) in the perivascular and peribronchial region in lungs of Wistar rats (n=6) injected with saline (left hand side column), or RCL-01 MNPs at 30mg/kg, 45 mg/kg, or 60 mg/kg. Animals were sacrificed 7 days post injection. Tissue was formalin fixed and paraffin embedded. 5µm thick sections were cut with rotary microtome and collected at four levels through the block spaced at least 50 µm apart. Images were acquired with Nikon Eclipse E800 brightfield microscope using 20x lens; scale bar represents 100 µm.

5.3.3.2 MNPs uptake and degradation by phagocytes

Both NOC0007 and RCL-01 were coated with dextran, which is commonly used to prevent the agglomeration and toxicity of MNPs. However, signs indicative of toxicity were seen in H&E stained tissue sections across different organs and relatively large aggregates were present in pulmonary vasculature of animals injected with NOC 0007. In this section, immunofluorescent staining was used to verify if the dextran coating was degraded at the time of the analysis.

Regardless of MNP dose used, dextran was not detected in lungs of animals injected with NOC 0007 MNPs (Figure 5.12 and Supplementary figure 8.50). Brightfield images showed that those particles formed relatively large aggregates in the vasculature. Interestingly, immunofluorescent staining revealed that those aggregates are in fact clusters of macrophages loaded with iron as demonstrated in Figure 5.13 and supplementary figure 8.60. This was not evident in neither H&E nor PPB stained sections (Figure 5.14), as iron completely obscured the visibility of cell nuclei.

In lungs of RCL-01 treated animals, dextran was only detected in animals treated with 60 mg/kg of MNPs (Figure 5.15 and Supplementary figure 8.51). It was predominantly found in the cytoplasm of CD68+ cells within perivascular and peribronchial connective tissue and in the pulmonary macrophages (Figure 5.16).

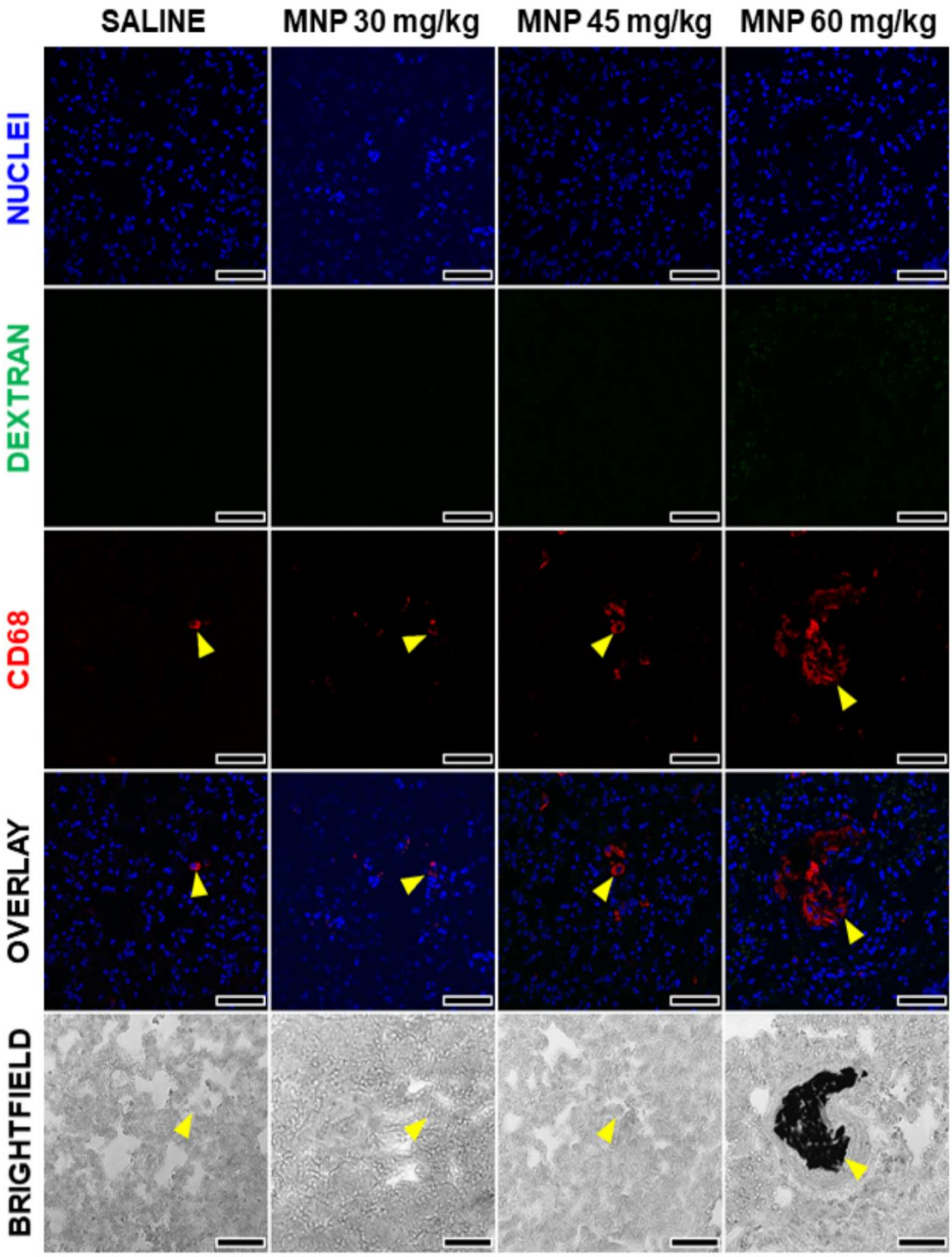

Figure 5.12: Detection of CD68+ cells and NOC 0007 dextran coating in lungs
Representative immunofluorescent images showing uptake of NOC 0007 MNPs by the CD68+ macrophages in the lungs (yellow arrowheads) of Wistar rats (n=3). Animals were sacrificed 7 days post injection. Tissue was formalin fixed and paraffin embedded. 5µm thick sections were cut with rotary microtome and collected at four levels through the block spaced at least 50 µm apart. Dextran was not detected in the lungs of animals injected with the MNPs, regardless of dose used. Nuclei were counterstained with Hoechst. Scale bar represents 50µm.

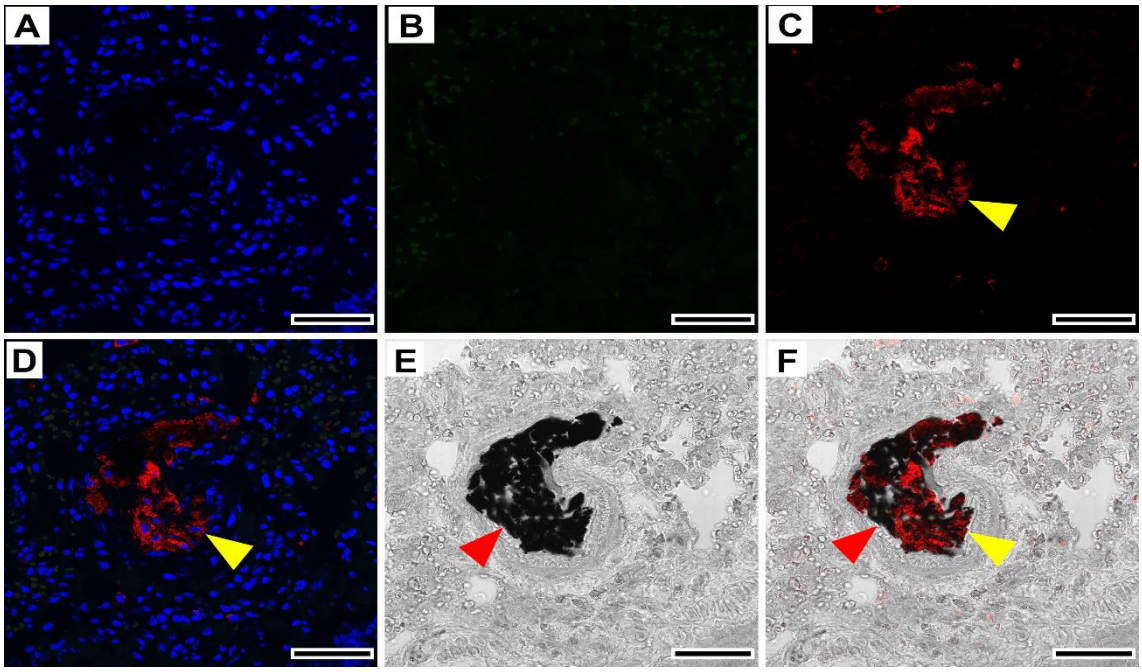

Figure 5.13: Localisation of NOC 0007 in pulmonary macrophages
High magnification photomicrographs of lung sections from Wistar rats (n=3) treated with NOC 0007 MNPs at 60 mg/kg. A: Nuclei; B: Dextran; C: CD68; D: overlay of A, B and C; E: brightfield image; F: overlay of all channels. Yellow arrowhead indicates macrophages stained with anti-CD68 antibody; Red arrowhead indicates iron. Scale bar represents 50µm.

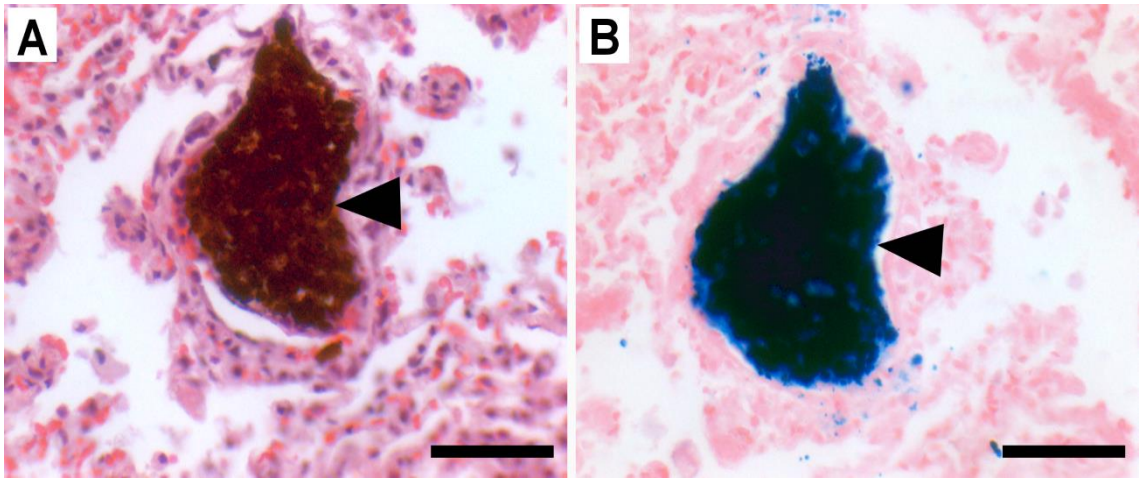

Figure 5.14: NOC 0007 accumulation in pulmonary vessel
High magnification photomicrographs of consecutive lung sections from Wistar rat treated with NOC 0007 MNPs at 60 mg/kg stained with H&E (A) or PPB (B) showing an iron aggregate formed in the blood vessel (black arrowhead). Scale bar represents 50 µm.

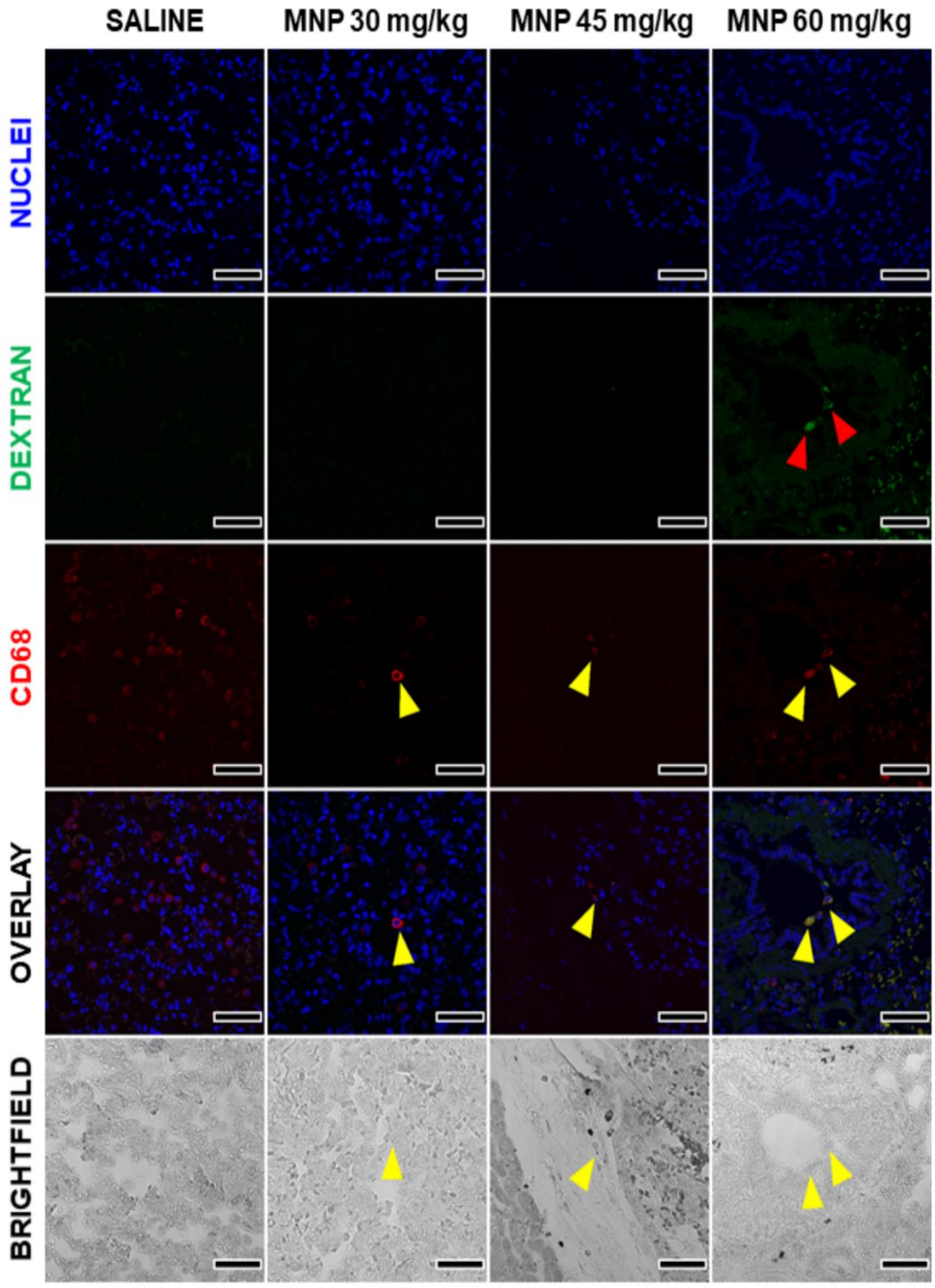

Figure 5.15: Detection of CD68+ cells and RCL-01 dextran coating in lung
Representative photomicrographs showing uptake of RCL-01 MNPs by CD68+ pulmonary macrophages (yellow arrowheads) in Wistrar rats (n=3). Animals were sacrificed 7 days post injection. Tissue was formalin fixed and paraffin embedded. 5µm thick sections were cut with rotary microtome and collected at four levels through the block spaced at least 50 µm apart. Red arrowheads indicate dextran which co-localised with the CD68+ cells. Scale bar represents 50µm.

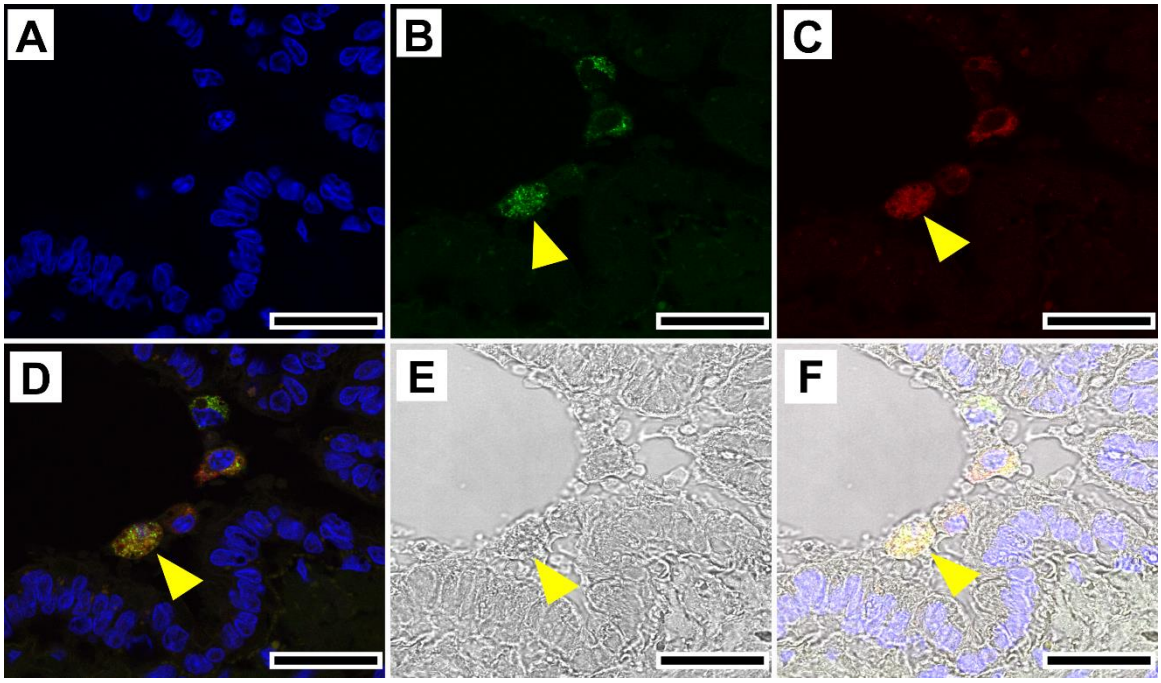

Figure 5.16: Localisation of RCL-01 in pulmonary macrophages
High magnification photomicrographs showing uptake of RCL-01 MNPs by pulmonary macrophages In Wistar rats (yellow arrowhead). Animal was injected with the MNPs at 60 mg/kg. Animals were sacrificed 7 days post injection. Tissue was formalin fixed and paraffin embedded. 5µm thick sections were cut with rotary microtome and collected at four levels through the block spaced at least 50 µm apart. A: Nuclei; B: Dextran; C: CD68; D: overlay of A, B and C; E: brightfield image; F: overlay of all channels. Scale bar represents 25µm.

Similar trend was seen in liver. Dextran was not detected in the examined animals injected with NOC 0007 MNPs at any of the doses used (Figure 5.17 and Supplementary figure 8.52). However, brightfield images confirmed presence of iron in the cytoplasm of Kupffer cells (Figure 5.19). In contrast, dextran was detected in animals injected with RCL-01 MNPs at all investigated doses (Figure 5.18 and Supplementary figure 8.53). Magnified images confirmed co-localization of dextran and iron within the cytoplasm of Kupffer cells which were identified by CD68 positive staining as shown in representative Figure 5.20.

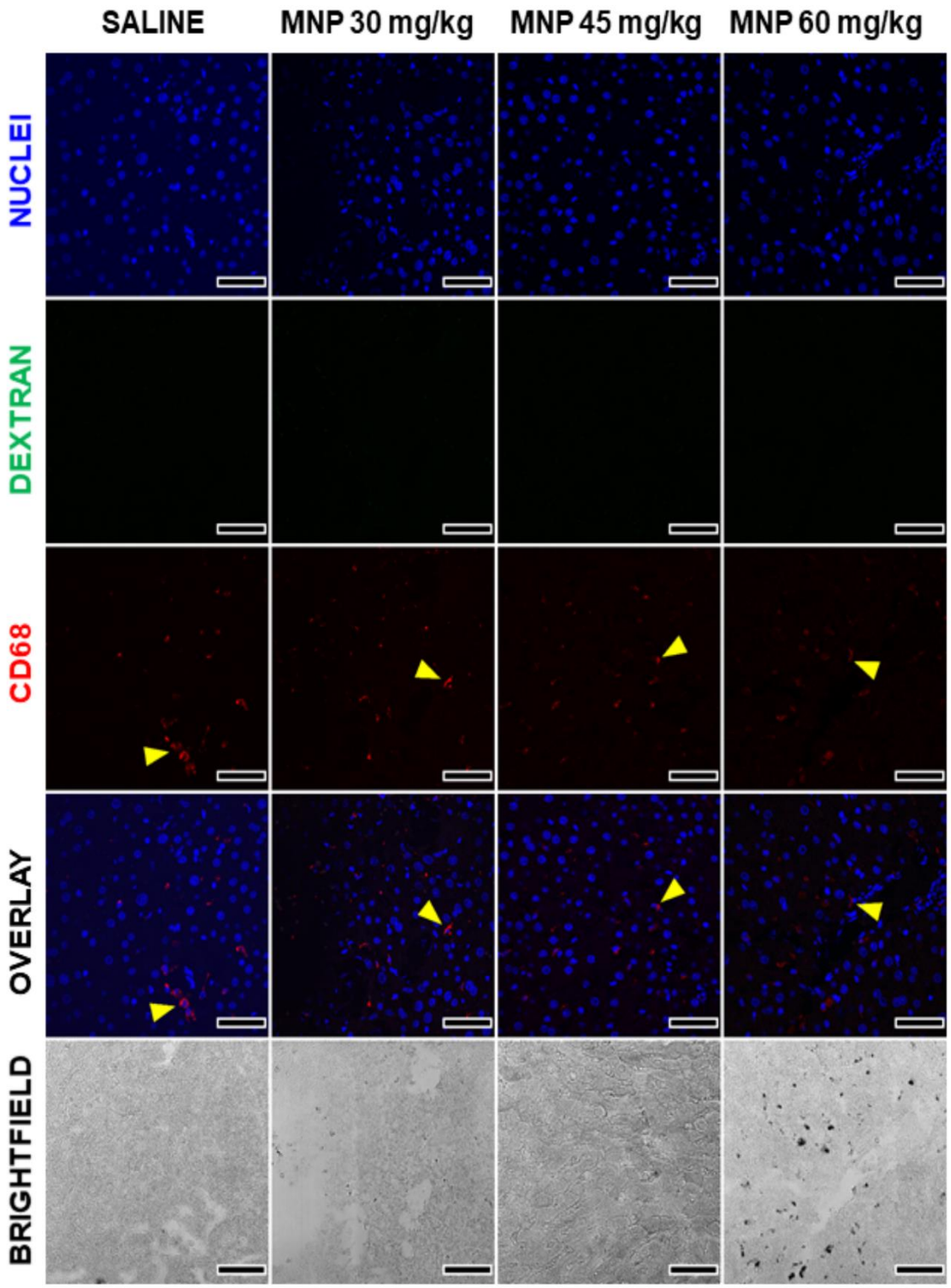

Figure 5.17: Detection of CD68+ cells and NOC 0007 dextran coating in liver
Representative photomicrographs showing uptake of NOC 0007 MNPs by CD68+ Kupffer cells in the liver of Wistar rats (n=3) (yellow arrowhead). Animals were sacrificed 7 days post injection. Tissue was formalin fixed and paraffin embedded. 5µm thick sections were cut with rotary microtome and collected at four levels through the block spaced at least 50 µm apart. Dextran was not detected in the control animals, or ones injected with the MNPs, regardless of dose used. Scale bar represents 50µm.

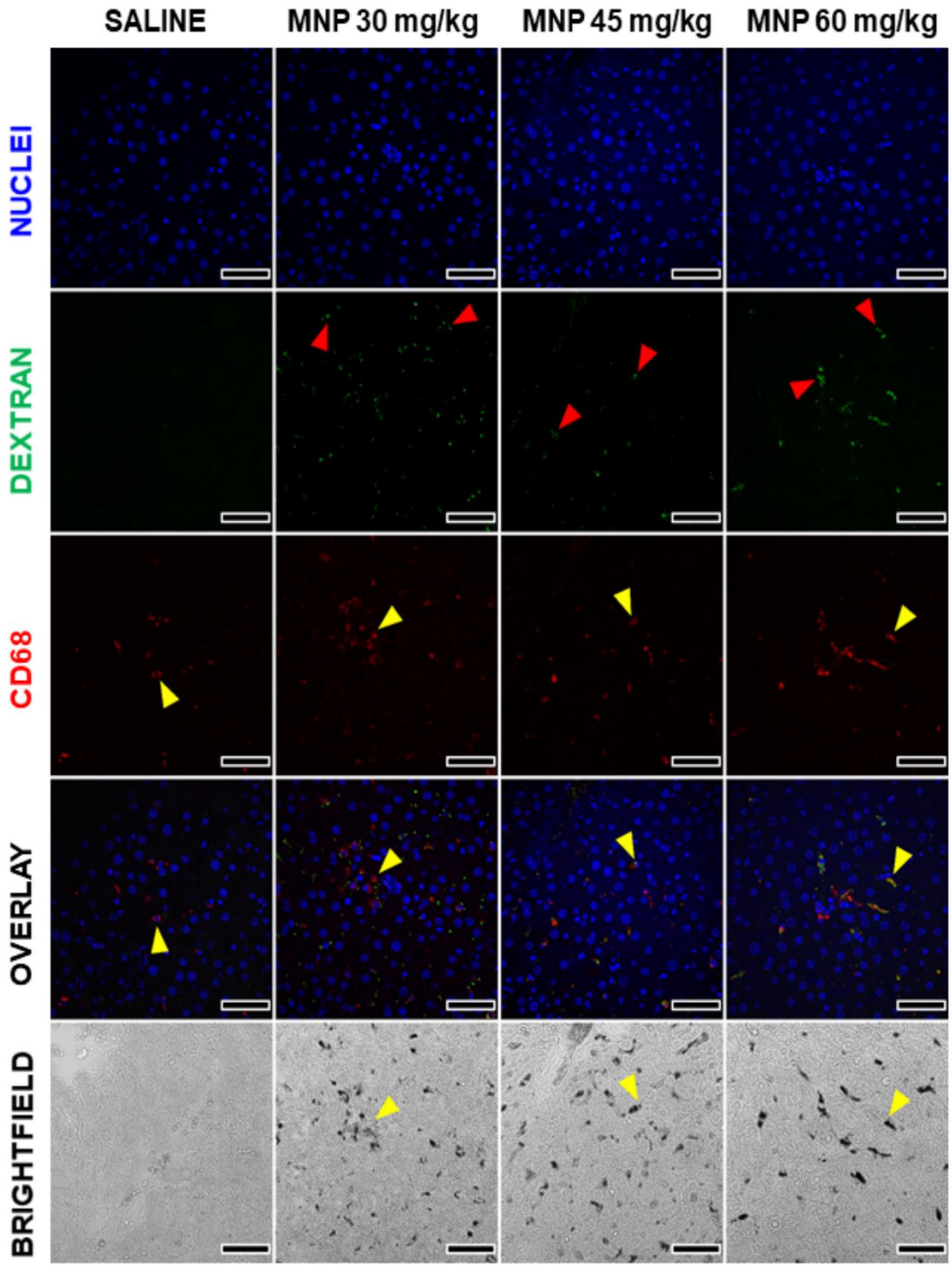

Figure 5.18: Detection of CD68+ cells and RCL-01 dextran coating in liver
Representative photomicrographs showing uptake of RCL-01 MNPs by CD68+ Kupffer cells in the liver (yellow arrowhead) Wistar rats (n=3). Animals were sacrificed 7 days post injection. Tissue was formalin fixed and paraffin embedded. 5µm thick sections were cut with rotary microtome and collected at four levels through the block spaced at least 50 µm apart. Red arrowhead indicates dextran, which was detected in the animals injected with MNPs, at all doses used. Scale bar represents 50µm.

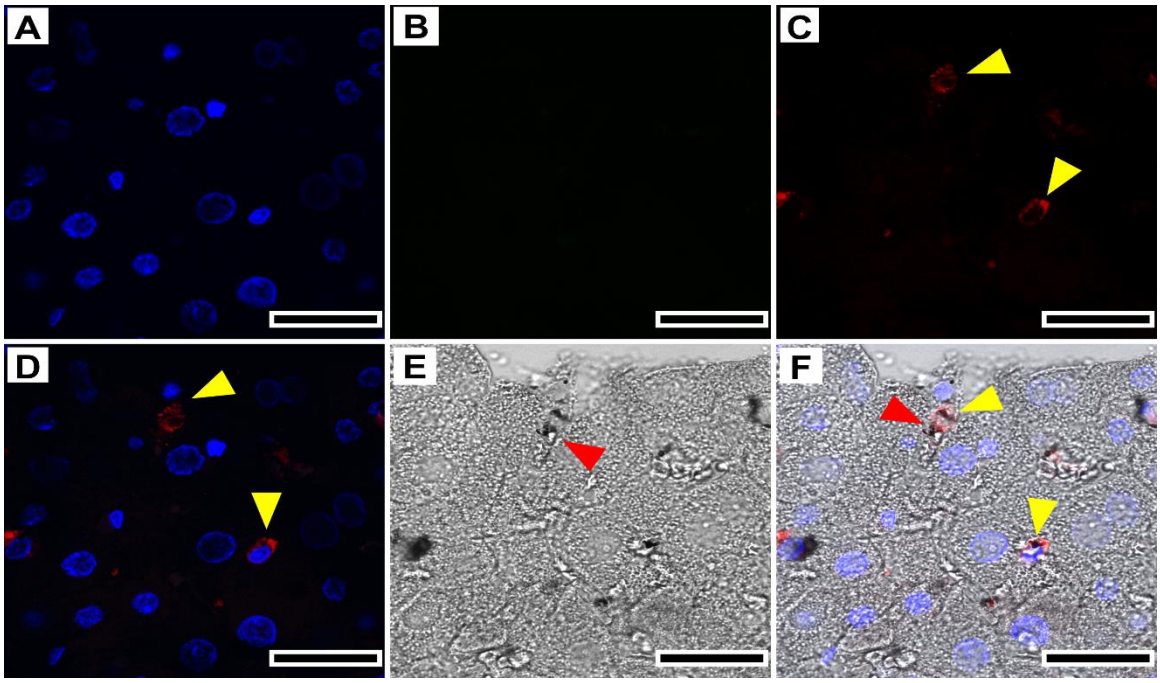

Figure 5.19: Localisation of NOC 0007 in liver macrophages

High magnification photomicrographs showing uptake of NOC0007 by CD68+ Kupffer cells (yellow arrowheads) in the liver of Wistar rats (n=3) injected with NOC0007 at 60 mg/kg. Animals were sacrificed 7 days post injection. Tissue was formalin fixed and paraffin embedded. 5µm thick sections were cut with rotary microtome and collected at four levels through the block spaced at least 50 µm apart. Red arrowhead indicates iron. A: Nuclei; B: Dextran; C: CD68; D: overlay of A, B and C; E: brightfield image; F: overlay of all channels. Scale bar represents 25µm.

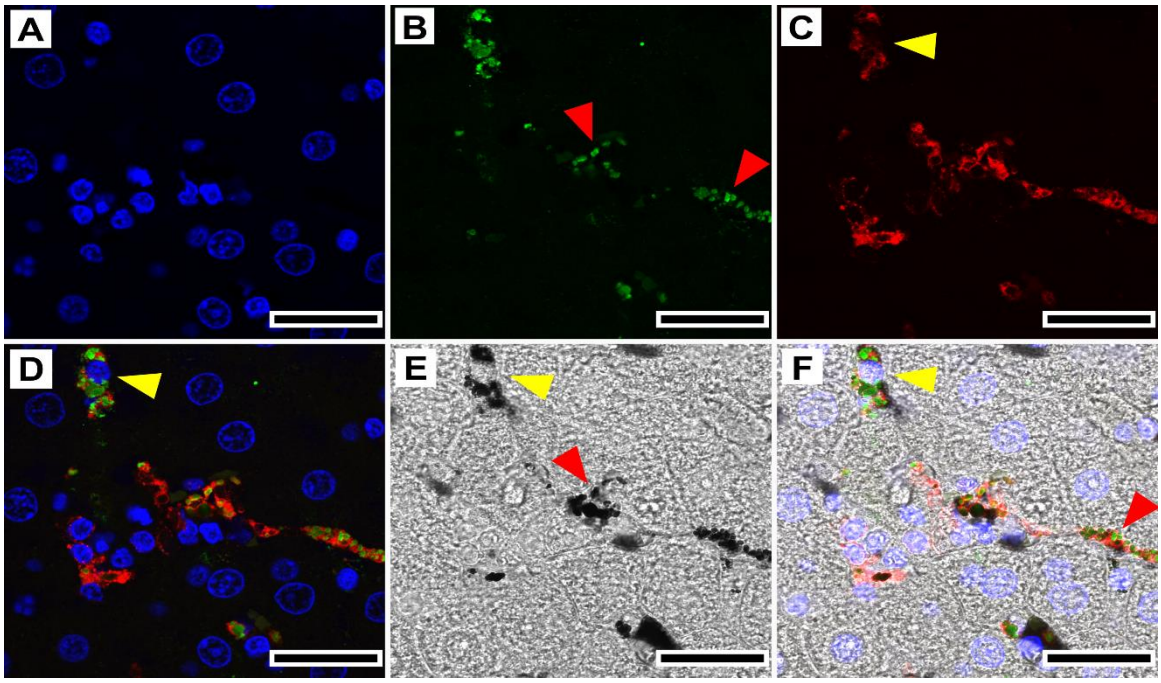

Figure 5.20: Localisation of RCL-01 in liver macrophages
High magnification photomicrographs showing uptake of dextran coated RCL-01 (red arrowhead) by CD68+ Kupffer cells (yellow arrowhead) in the liver of Wistar rats (n=3) injected with RCL-01 at 60 mg/kg. Animals were sacrificed 7 days post injection. Tissue was formalin fixed and paraffin embedded. 5µm thick sections were cut with rotary microtome and collected at four levels through the block spaced at least 50 µm apart. A: Nuclei; B: Dextran; C: CD68+ cells; D: overlay of A, B and C; E: brightfield image; F: overlay of all channels. Scale bar represents 25µm.

Dextran was not detected in the spleens of the NOC 0007 injected animals (Figure 5.21 and Supplementary figure 8.54). Similarly, to findings reported in liver, iron seen in brightfield images was confirmed to be located within splenic macrophages (Figure 5.23) on a border of red pulp and marginal zone and within the marginal zone.

RCL-01 treated animals also followed the trend observed for this MNP, with dextran consistently detected at all three doses used (Figure 5.22 and Supplementary figure 8.55). Magnified images confirmed co-localization of dextran and iron within the cytoplasm of splenic macrophages which were identified by CD68 positive staining as shown in representative, Figure 5.24. Cells containing iron and dextran were located in the marginal zone of white pulp and in the red pulp.

Dextran was not detected in kidneys of the animals injected with NOC0007 (Figure 5.25), or RCL-01 (Figure 5.26) at any of the injected doses. This was consistent in samples from three animals per dose which were used for this staining (Supplementary figure 8.56 and Supplementary figure 8.57).

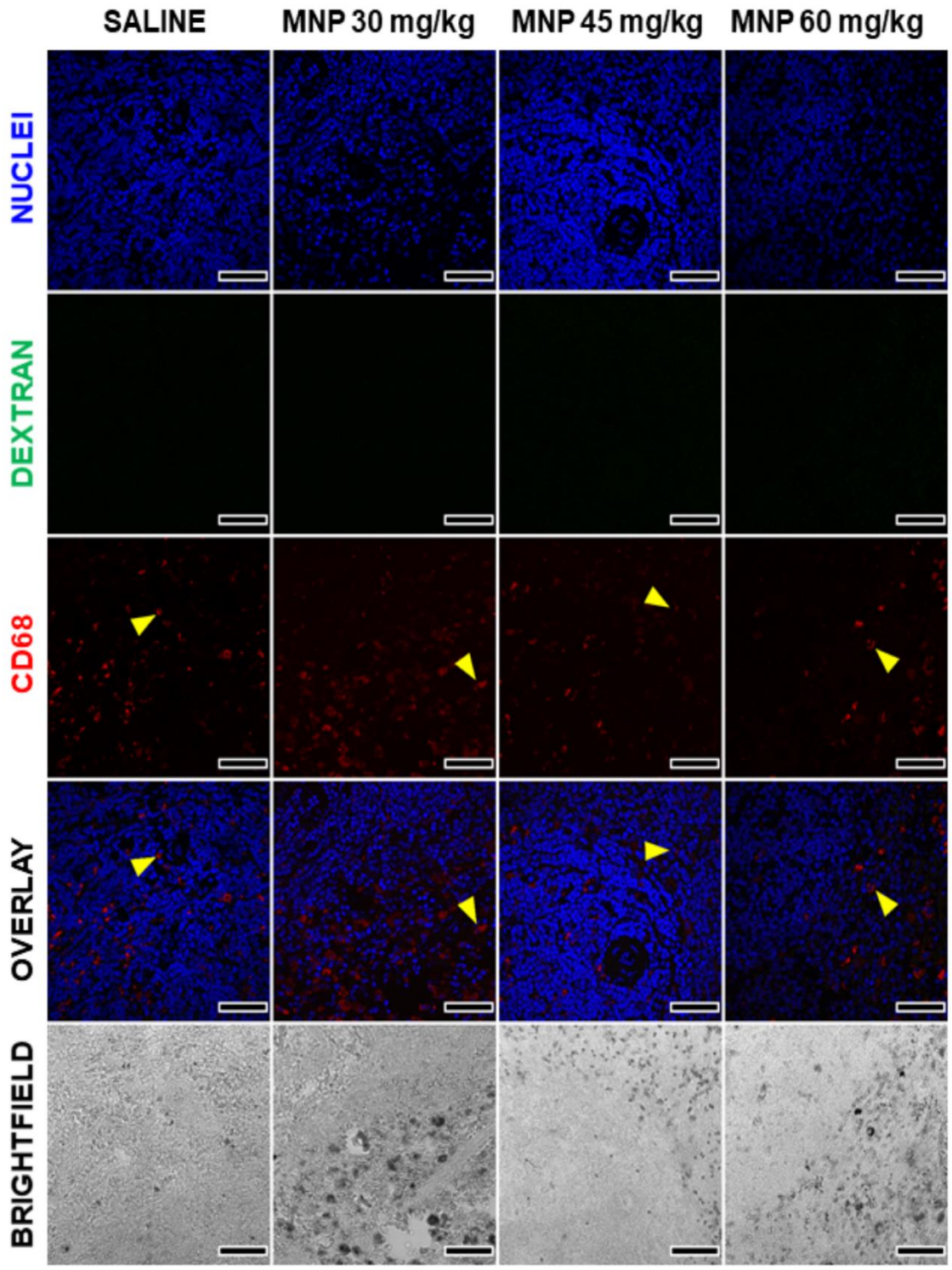

Figure 5.21: Detection of CD68+ cells and NOC0007 dextran coating in spleen

Representative photomicrographs showing uptake of NOC0007 MNPs by the splenic macrophages (yellow arrowhead) in Wistar rats (n=3) located in the marginal zone. Animals were sacrificed 7 days post injection. Tissue was formalin fixed and paraffin embedded. 5µm thick sections were cut with rotary microtome and collected at four levels through the block spaced at least 50 µm apart. Dextran was not detected in the control animals, or the ones injected with the MNPs, regardless of the dose used. Scale bar represents 50µm.

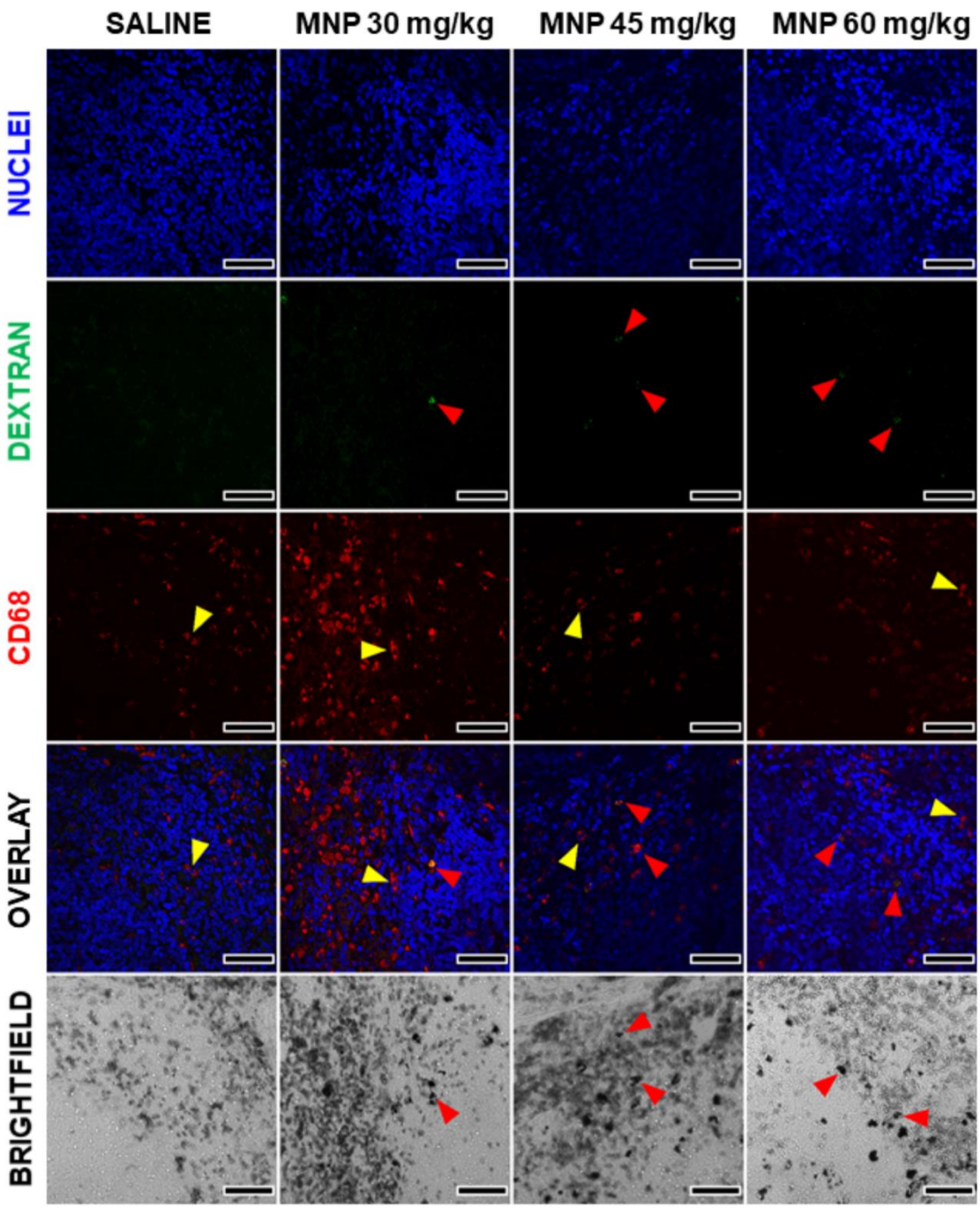

Figure 5.22: Detection of CD68+ cells and RCL-01 coating in spleen

Representative photomicrographs showing uptake of RCL-01 MNPs by the splenic macrophages (yellow arrowhead) of Wistar rats (n=3) in the marginal zone and on the border of red pulp and marginal zone. Animals were sacrificed 7 days post injection. Tissue was formalin fixed and paraffin embedded. 5µm thick sections were cut with rotary microtome and collected at four levels through the block spaced at least 50 µm apart. Dextran (red arrowheads) was seen in the animals injected with the MNPs at all three doses tested. Scale bar represents 50µm.

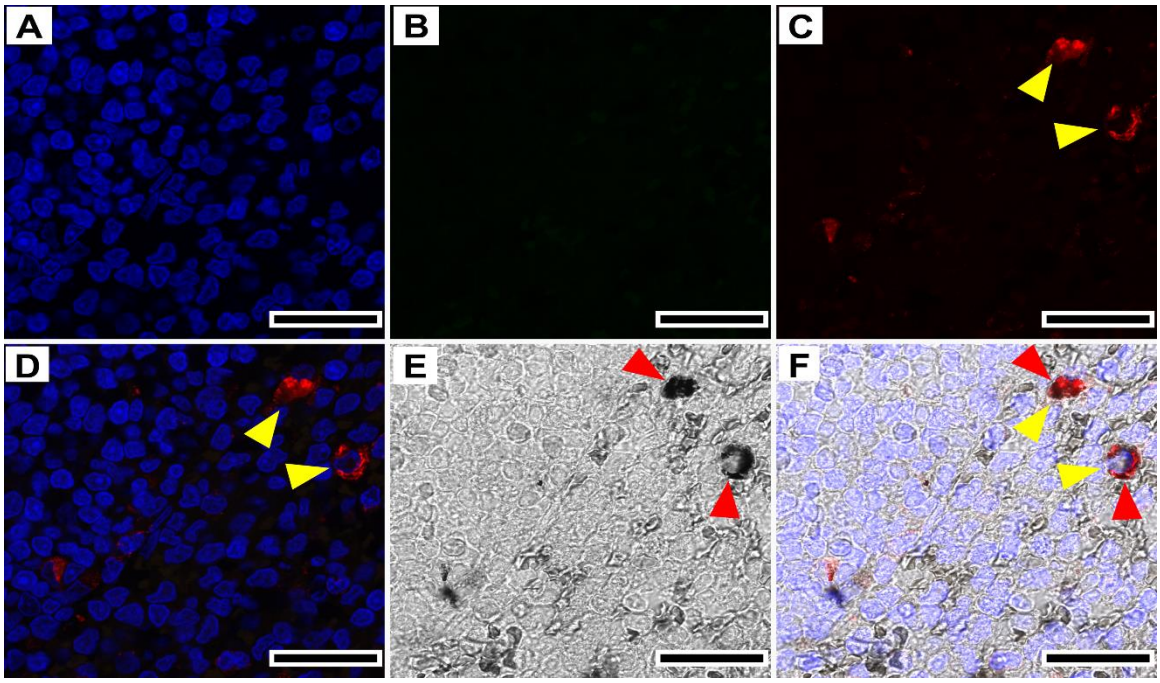

Figure 5.23: Localisation of NOC 0007 in splenic macrophages
High magnification photomicrographs showing uptake of NOC 0007 MNPs (red arrowhead) by the CD68+ splenic macrophages (yellow arrowhead) in WIstar rats (n=3). Animal was injected with RCL-01 at 60 mg/kg. Animals were sacrificed 7 days post injection. Tissue was formalin fixed and paraffin embedded. 5µm thick sections were cut with rotary microtome and collected at four levels through the block spaced at least 50 µm apart. A: Nuclei; B: Dextran; C: CD68+ cells; D: overlay of A, B and C; E: brightfield image; F: overlay of all channels. Scale bar represents 25µm.

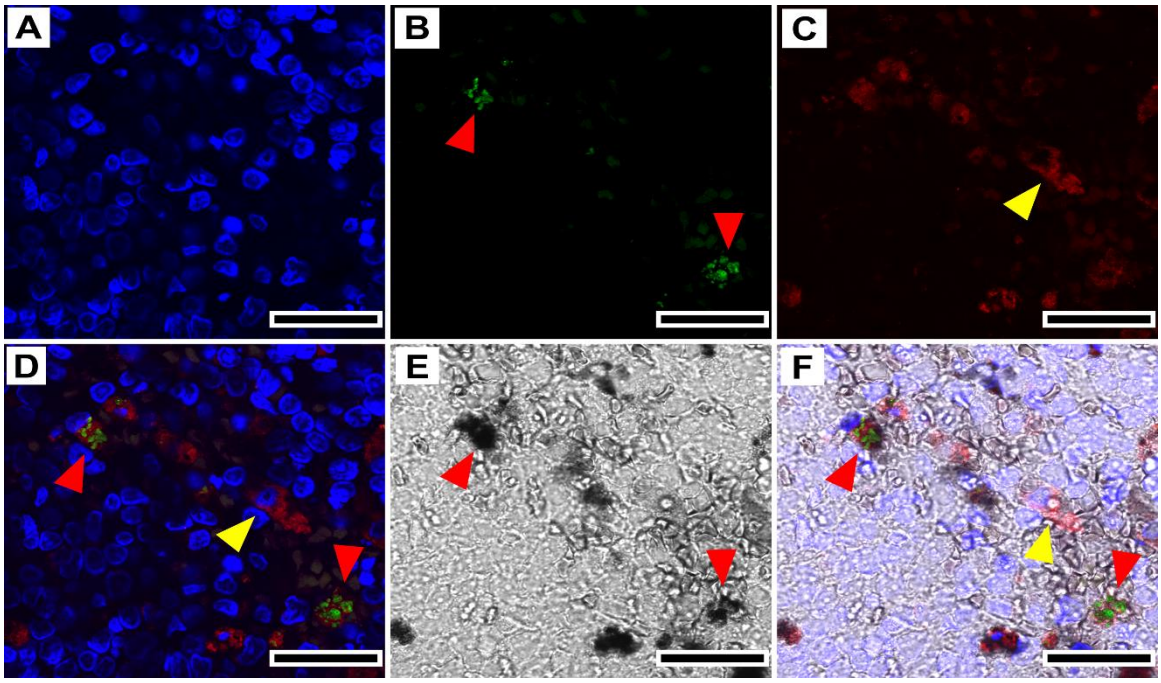

Figure 5.24: Localisation of RCL-01 in splenic macrophages
High magnification photomicrographs showing uptake of RCL-01 MNPs (red arrowhead) by the splenic macrophages (yellow arrowhead) in the marginal zone in Wistar rats (n=3). Animal was injected with RCL-01 at 60 mg/kg dose, and sacrificed 7 days post injection. Tissue was formalin fixed and paraffin embedded. 5µm thick sections were cut with rotary microtome and collected at four levels through the block spaced at least 50 µm apart. A: Nuclei; B: Dextran; C: CD68; D: overlay of A, B and C; E: brightfield image; F: overlay of all channels. Scale bar represents 25µm.

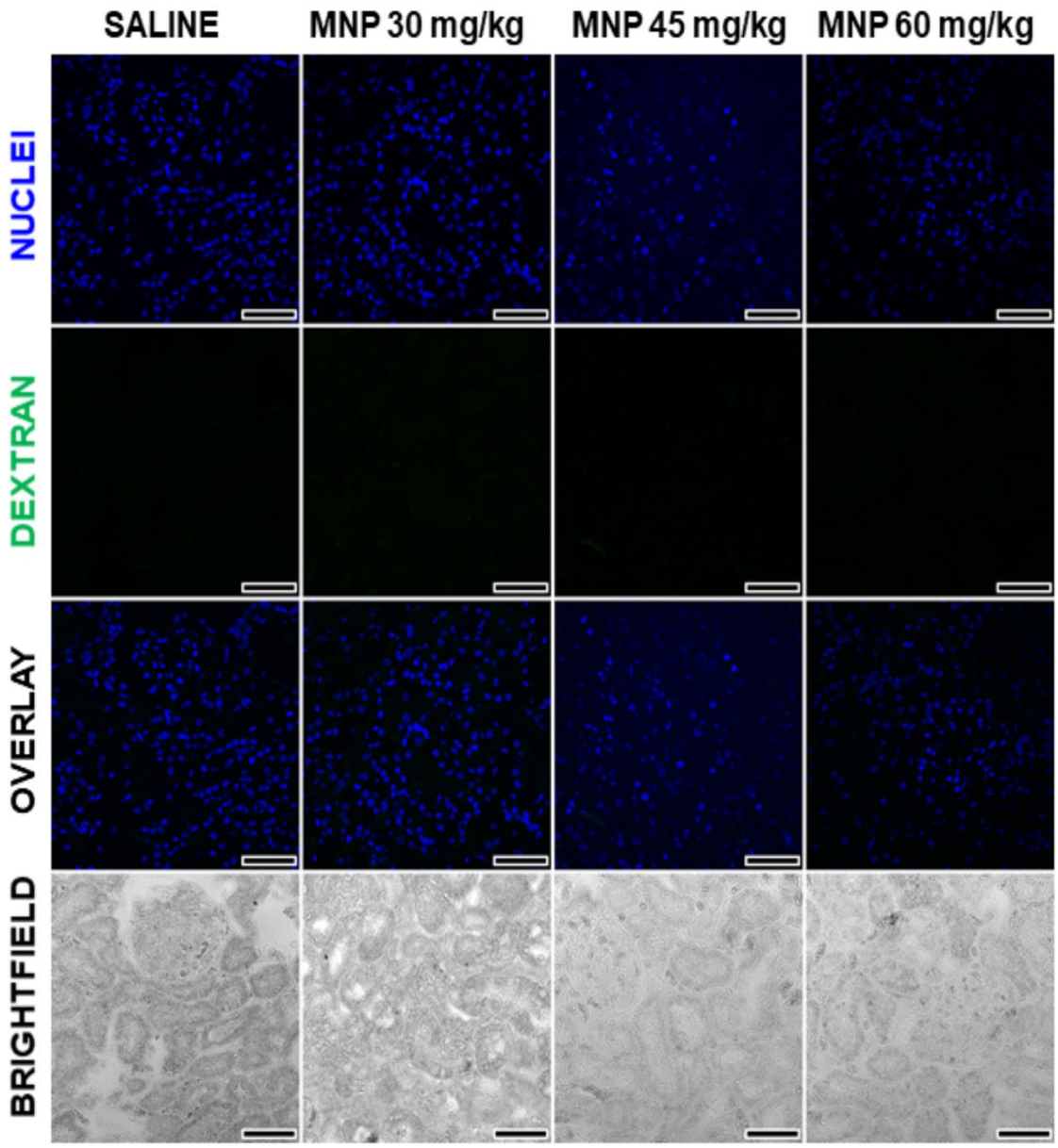

Figure 5.25: Detection of NOC 0007 dextran coating in kidney

Representative photomicrographs of kidney sections from Wistar rats (n=3) injected with NOC 0007 MNPs. Animals were sacrificed 7 days post injection. Tissue was formalin fixed and paraffin embedded. 5µm thick sections were cut with rotary microtome and collected at four levels through the block spaced at least 50 µm apart. Dextran was not detected in any of the animals examined. Scale bar represents 50µm.

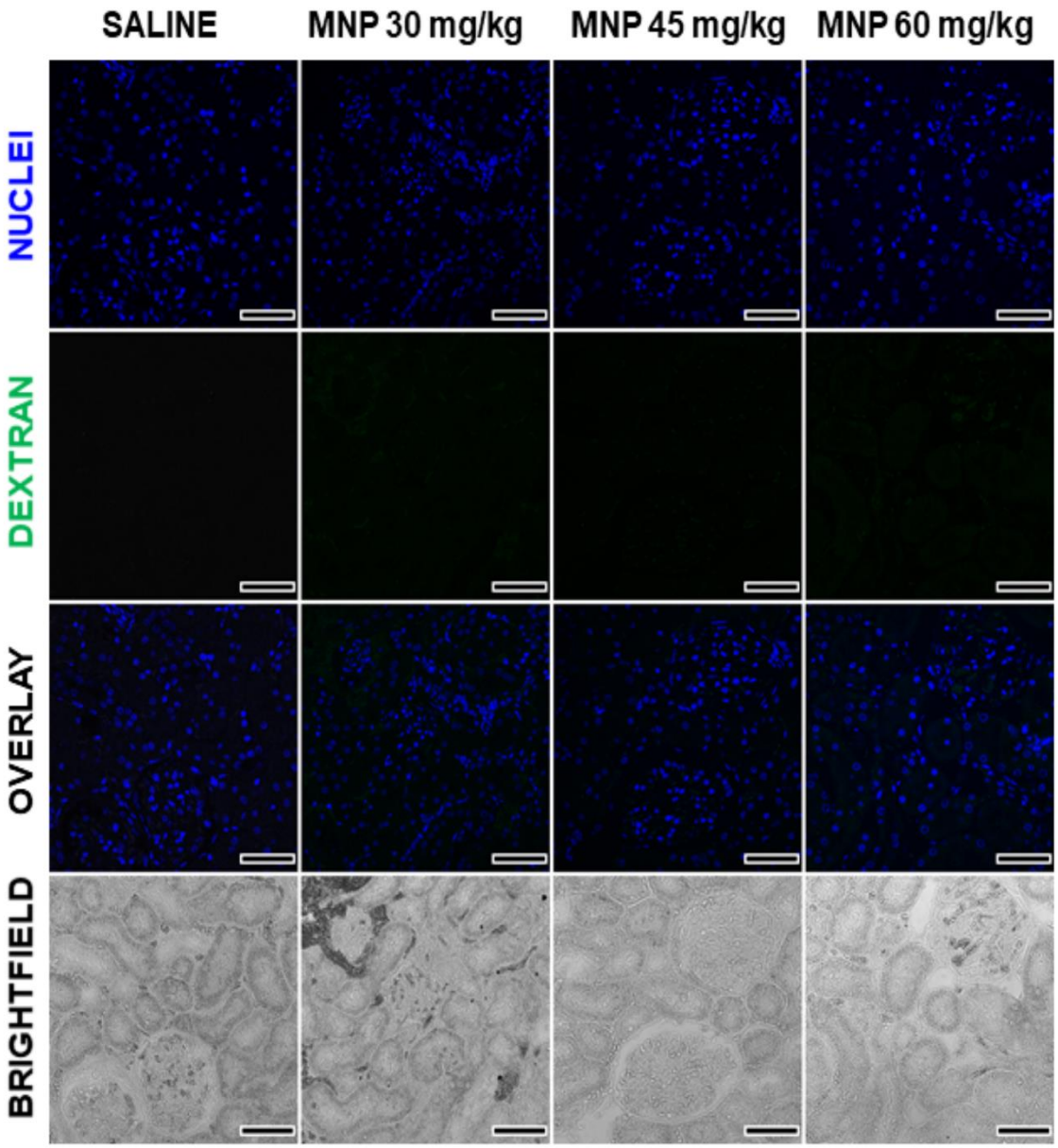

Figure 5.26: Detection of RCL-01 dextran coating in kidney
Representative photomicrographs of kidney sections from Wistar rats (n=3) injected with RCL-01 MNPs. Animals were sacrificed 7 days post injection. Tissue was formalin fixed and paraffin embedded. 5µm thick sections were cut with rotary microtome and collected at four levels through the block spaced at least 50 µm apart. Dextran was not detected in any of the animals examined. Scale bar represents 50µm.

Spleen and kidney are both naturally rich in iron, making it challenging to discriminate between endogenous iron, and exogenous iron from MNPs. The detection of dextran coating with means of immunofluorescent staining was hypothesized to solve this issue. Dextran coating of MNPs would be the first component subjected to degradation *in vivo* and therefore may not be detectable at the time of analysis as seen here in the tissue samples harvested seven days post injection with NOC 0007. Overall, these results support the advantages of carrying out quantitative studies on tissue sections stained with PPB as presented in the following section.

5.3.4 *Investigation of MNPs accumulation in organs*

The first section of results briefly discussed differences in shape of aggregates observed between two MNPs in H&E-stained sections. This was confirmed in PPB-stained sections (Figure 5.27), where an array of shapes was observed in lungs of animals treated with NOC 0007 (Figure 5.27B and C). This phenomenon was seen across all treatments doses as shown in Supplementary figure 8.58. In contrast, the aggregates observed in RCL-01 treated animals had a uniform shape close to a circle. In terms of localization of those aggregates, NOC 0007 MNPs accumulated preferentially in the vasculature (pulmonary veins and smaller capillaries), with minimal accumulation in perivascular and peribronchial space. This was seen in 3 out of 6 animals injected at 30 mg/kg, 4 out of 6 animals injected at 45 mg/kg, and 3 out of 6 animals injected at 60 mg/kg. In animals treated with 60 mg/kg of MNPs, aggregates in the vasculature were relatively large, causing almost complete obstruction (Figure 5.27G). Different pattern of accumulation was observed for RCL-01 treated animals, where the majority of iron was present in the macrophages in perivascular and peribronchial spaces (Supplementary figure 8.59).

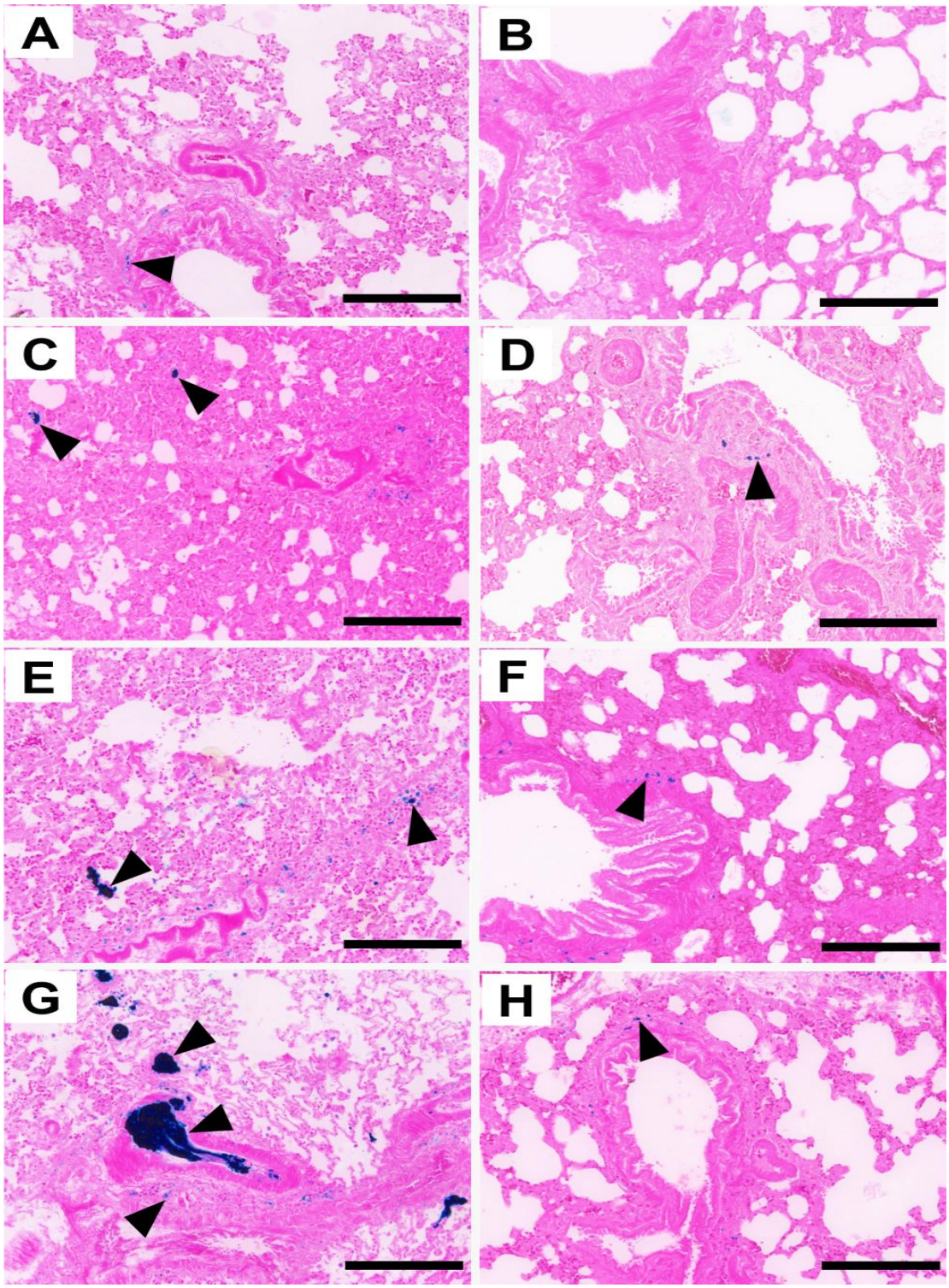

Figure 5.27: MNPs distribution in lung

Representative photomicrographs of PPB stained lung sections from Wistar rats showing different patterns of accumulation and distribution of iron (black arrows). Animals were injected with either saline (A and B), or MNP at 30 mg/kg (C and D), 45 mg/kg (E and F) and 60 mg/kg (G and H); n=6. Animals were sacrificed 7 days post injection. Tissue was formalin fixed and paraffin embedded. 5µm thick sections were cut with rotary microtome and collected at four levels through the block spaced at least 50 µm apart. Left column shows photomicrographs of sections from animals in NOC 0007 treatment group, right column from RCL-01 treatment group. Scale bar represents 200 µm.

In contrast, biodistribution and accumulation of iron was more uniform for NOC 0007 and RCL-01 in liver (Figure 5.28). Both particles were found in sinusoids, phagocytosed by the resident macrophages also known as Kupffer cells. These findings were consistent across the animals as shown in Supplementary figure 8.60 and Supplementary figure 8.61. Additionally, presence of faint iron staining in the hepatocytes of the animals from RCL-01 experimental block was reported by the pathologist. This was seen in 2 out of 6 control animals injected with saline, 1 out of 6 animals injected with the RCL-01 at 45 mg/kg, and 3 out of 6 animals injected with the RCL-01 at 60 mg/kg.

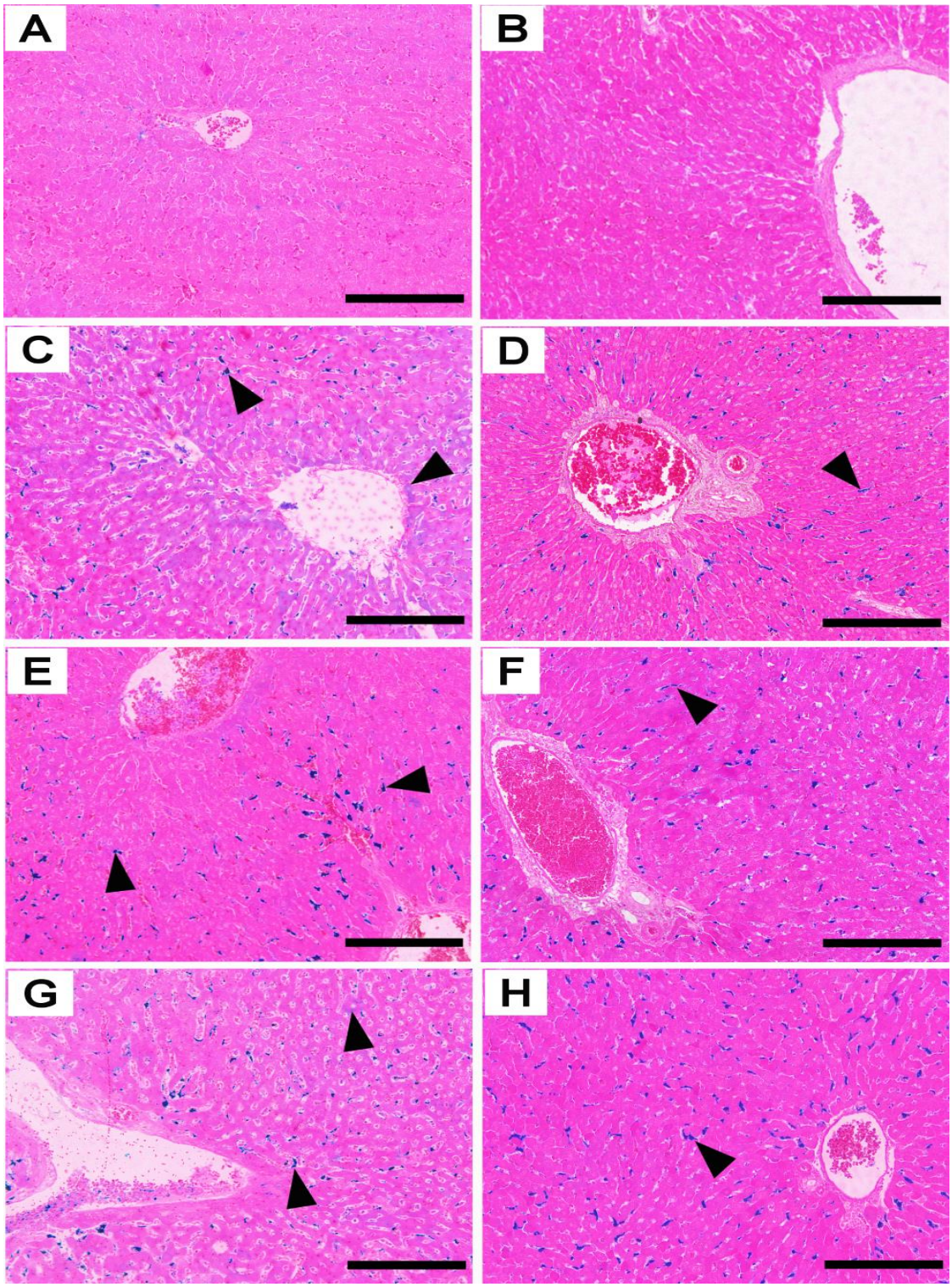

Figure 5.28: MNP distribution in liver

Representative photomicrographs of PPB stained liver sections from Wistar rats showing accumulation and distribution of iron (black arrows). Animals were injected with either saline (A and B), or MNP at 30 mg/kg (C and D), 45 mg/kg (E and F) and 60 mg/kg (G and H); n=6. Animals were sacrificed 7 days post injection. Tissue was formalin fixed and paraffin embedded. 5µm thick sections were cut with rotary microtome and collected at four levels through the block spaced at least 50 µm apart. Left column shows photomicrographs of sections from animals in NOC 0007 treatment group, right column from RCL-01 treatment group. Scale bar represents 200 µm

Spleen is naturally rich in iron due to splenic red pulp macrophages which are specialized in iron recycling. Therefore, it is challenging to visually determine whether iron accumulation is spleen was increased due to presence of MNPs (Figure 5.29). The only noticeable difference between control animals and those injected with MNPs was presence of iron loaded macrophages in the marginal zone of white pulp. This was seen in both NOC 0007 (Supplementary figure 8.62) and RCL-01 (Supplementary figure 8.63) treated animals.

Similar can be said about kidney, where no obvious visual differences were seen between control animals and those treated with MNPs due to kidneys function in iron homeostasis as previously discussed in Chapter 4. Iron was detected in the cortex area located mainly within cytoplasm of renal tubule cells (Figure 5.30), and also in the glomeruli (Figure 5.30B) within glomerular capillaries and in the cytoplasm of podocytes. This was seen in NOC0007 injected animals (Supplementary figure 8.64) and RCL-01 injected animals (Supplementary figure 8.65) regardless of the dose used.

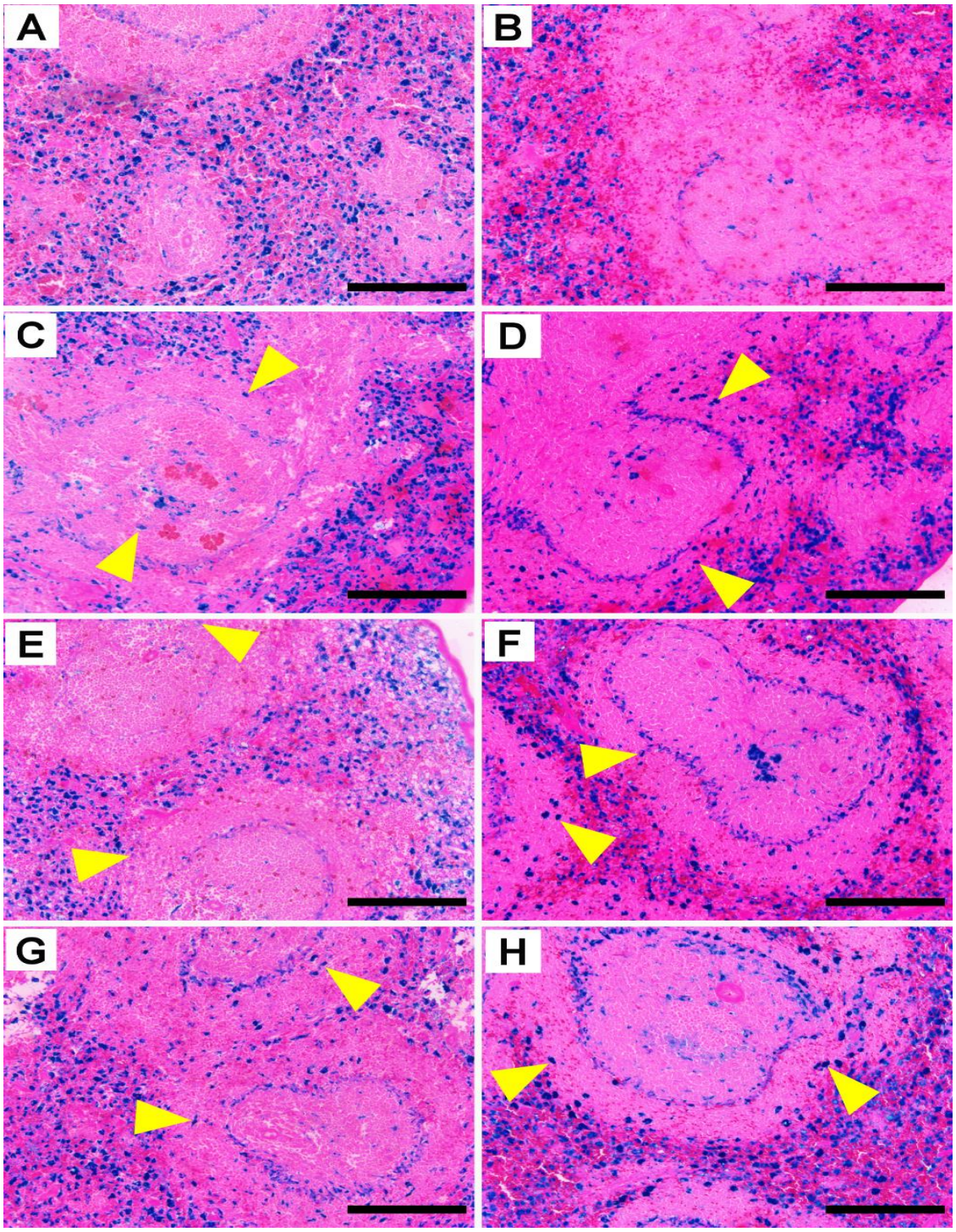

Figure 5.29: MNP distribution in spleen

Representative photomicrographs of PPB stained spleen sections from Wistar rats showing accumulation and distribution of iron (blue deposits). Animals were injected with either saline (A and B), or MNP at 30 mg/kg (C and D), 45 mg/kg (E and F) and 60 mg/kg (G and H); n=6. Animals were sacrificed 7 days post injection. Tissue was formalin fixed and paraffin embedded. 5µm thick sections were cut with rotary microtome and collected at four levels through the block spaced at least 50 µm apart. Left column shows photomicrographs of sections from animals in NOC 0007 treatment groupright column from RCL-01 treatment group. Yellow arrowheads indicate iron loaded macrophages in marginal zone of white pulp. Scale bar represents 200 µm.

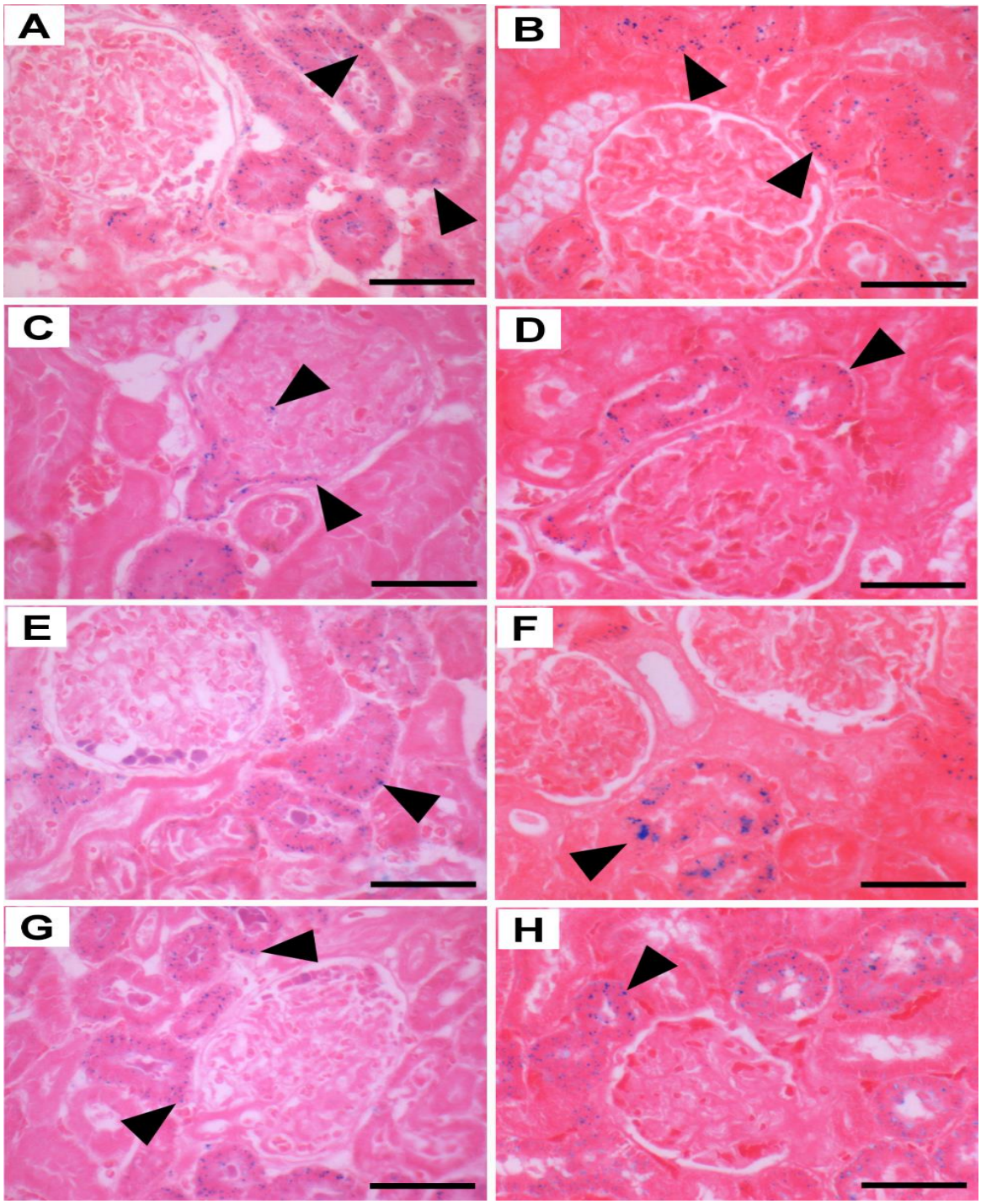

Figure 5.30: MNP distribution in kidney

Representative photomicrographs of PPB stained kidney sections of Wistar rats showing accumulation and distribution of iron (black arrowhead). Animals were injected with either saline (A and B), or MNP at 30 mg/kg (C and D), 45 mg/kg (E and F) and 60 mg/kg (G and H); n=6. Animals were sacrificed 7 days post injection. Tissue was formalin fixed and paraffin embedded. 5µm thick sections were cut with rotary microtome and collected at four levels through the block spaced at least 50 µm apart. Left column shows photomicrographs of sections from animals in NOC 0007 treatment group, right column from RCL-01 treatment group. Scale bar represents 50 µm.

In summary, iron accumulation was seen in all of the organs analysed in this study. From the visual assessment, differences between the control animals and those injected with the MNPs were clear in the lungs and liver sections. As spleen and kidneys are both naturally rich in iron, it was challenging to determine whether there was an increase in iron contents due to the injection with the MNPs.

5.3.5 *Investigation of MNPs biodistribution in organs*

To overcome the limitations of visual assessment, semi-quantitative assessment measuring iron content in tissue sections was performed using ML. Obtained results were compared against the two gold standards used to evaluate iron content in organs, a quantitative measurement using ICP-MS, and qualitative pathological scoring.

5.3.5.1 Training and validation of ML model for semi-quantitative and qualitative assessment of iron in histological tissue sections

This section focuses on utilising ML for advanced bioimage analysis in line with method developed in Chapter 4 of this thesis. In total, four classifiers were trained, one for each organ, using five representative images from each organ (Supplementary figure 8.66).

To validate the classifiers, images used for training the classifiers were manually segmented for tissue and iron to create ground truth images, which were used to measure the overlap with images obtained from other segmentation methods. Three different statistics, MCC, F_1score, and JSC were used to measure the performance. Additionally, the performance of long-established method of manually selecting threshold value in 8-bit image (referred to as set threshold) and one of the thresholding algorithms (Intermodes) available in Fiji software were also compared against ground truth images. Calculated performance metrics shown in figure 5.29 highlight that images segmented by WEKA classifier which were subjected to a threshold step representative of a certainty above 75% that a pixels belonging to each class produced more accurate results in comparison to 50% certainty threshold and two traditionally used methods. This is especially evident in case of iron deposits detected in kidney (Figure 5.29 F) and pixels segmented as tissue in liver, spleen, and kidney (Figure 5.29 D, F and H respectively). Visual representation of how those methods performed to segment iron in different tissues are provided in figures 5.30 to 5.33. Representative photomicrograph of kidney (Figure 5.35) contained a graphene shaving from a pencil used to label the slides. It is important to note that only image segmented by WEKA classifier thresholded for pixels assigned to iron class with more than 75% certainty correctly omitted this type of a staining artefact.

Validated classifiers were then used for quantitative and qualitative analysis of visually observed iron deposits to determine whether there was a statistically significant difference between control and test animals.

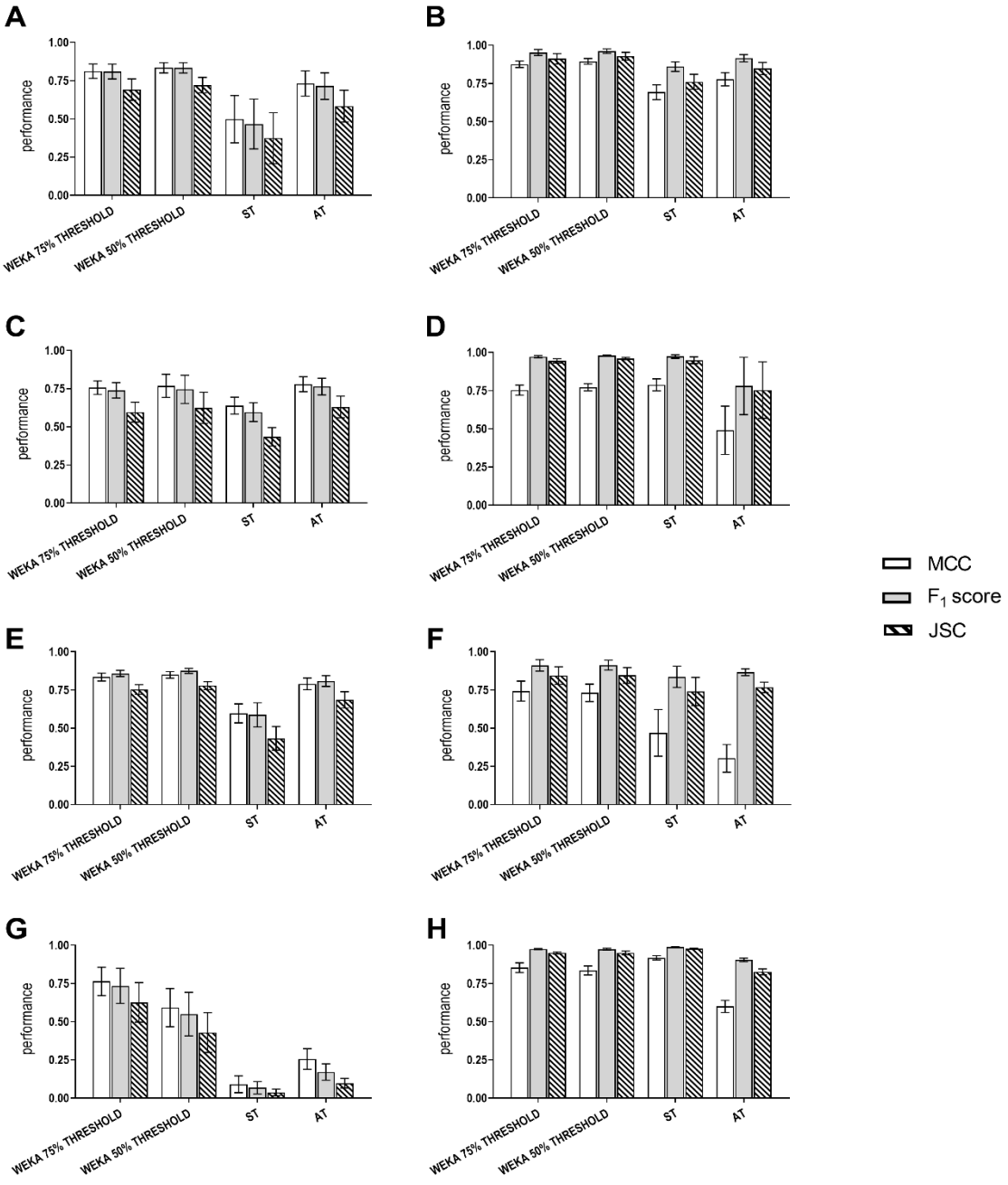

Figure 5.31: Performance evaluation of different segmentation methods
Performance of the different methods to iron and tissue segmentation in photomicrographs of histology sections. Overlap metrics were calculated for pixels classified as iron in lung, liver, spleen, and kidney (A, C, E and G respectively) and for pixels classified as tissue in lung, liver, spleen, and kidney (B, D, F and H respectively). Metrics range from 0 to 1, with 1 indicating a perfect overlap with manually ground truth image. Data shown as mean ± SEM. ST: set threshold; AT: automatic threshold (Intermodes); MCC: Mathew's Correlation Coefficient; JSC: Jaccard Similarity Coefficient.

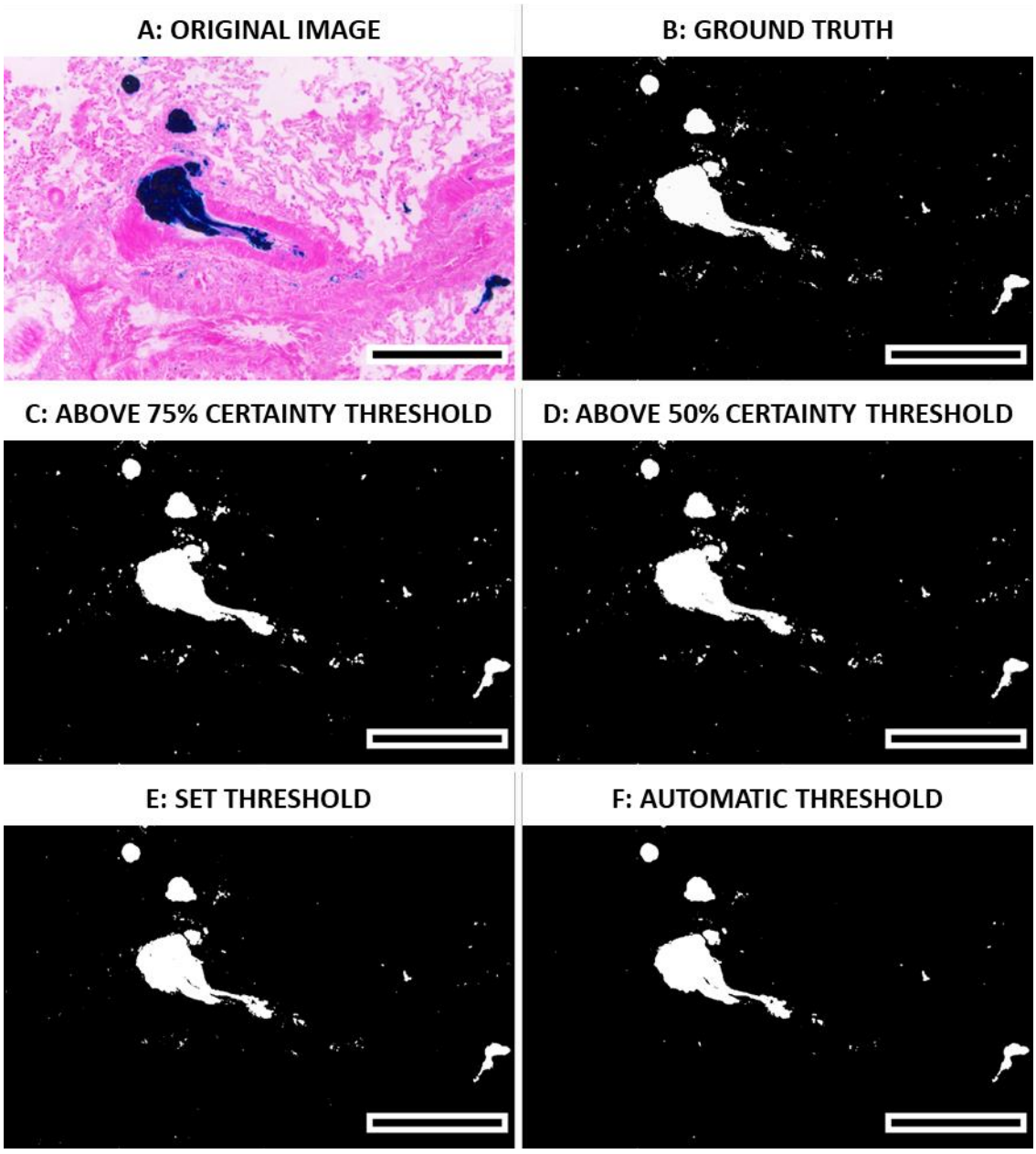

Figure 5.32: Segmentation of iron objects in lungs using different methods
Representative image of a lung section of Wistar rat injected with NOC0007 MNPs at 60 mg/kg of MNP. (A) Digitized PPB-stained section showing iron accumulation in blue, (B) manually segmented ground truth image, (C) binary image of pixels assigned to a class with over 75% certainty, (D) binary image of pixels assigned to a class with over 50% certainty, (E) result of a set threshold, (F) automatic default threshold in Fiji preformed on probability map. Scale bar represents 250 µm.

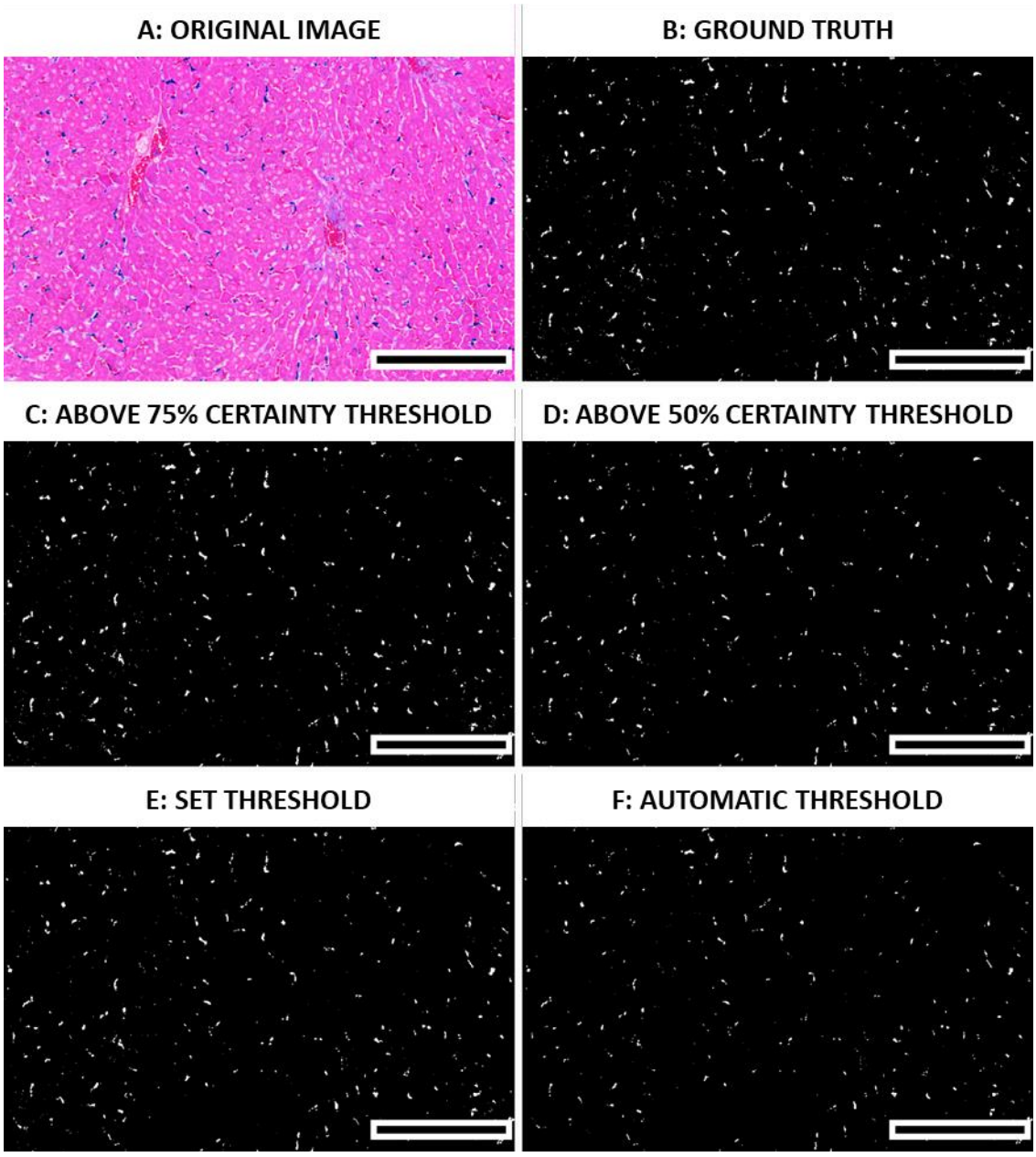

Figure 5.33: Segmentation of iron objects in liver using different methods
Representative image of a liver section of Wistar rat injected with RCL-01 MNPs at 60 mg/kg of MNP. (A) Digitized PPB-stained section showing iron accumulation in blue, (B) manually segmented ground truth image, (C) binary image of pixels assigned to a class with over 75% certainty, (D) binary image of pixels assigned to a class with over 50% certainty, (E) result of a set threshold, (F) automatic default threshold in Fiji preformed on probability map. Scale bar represents 250 µm.

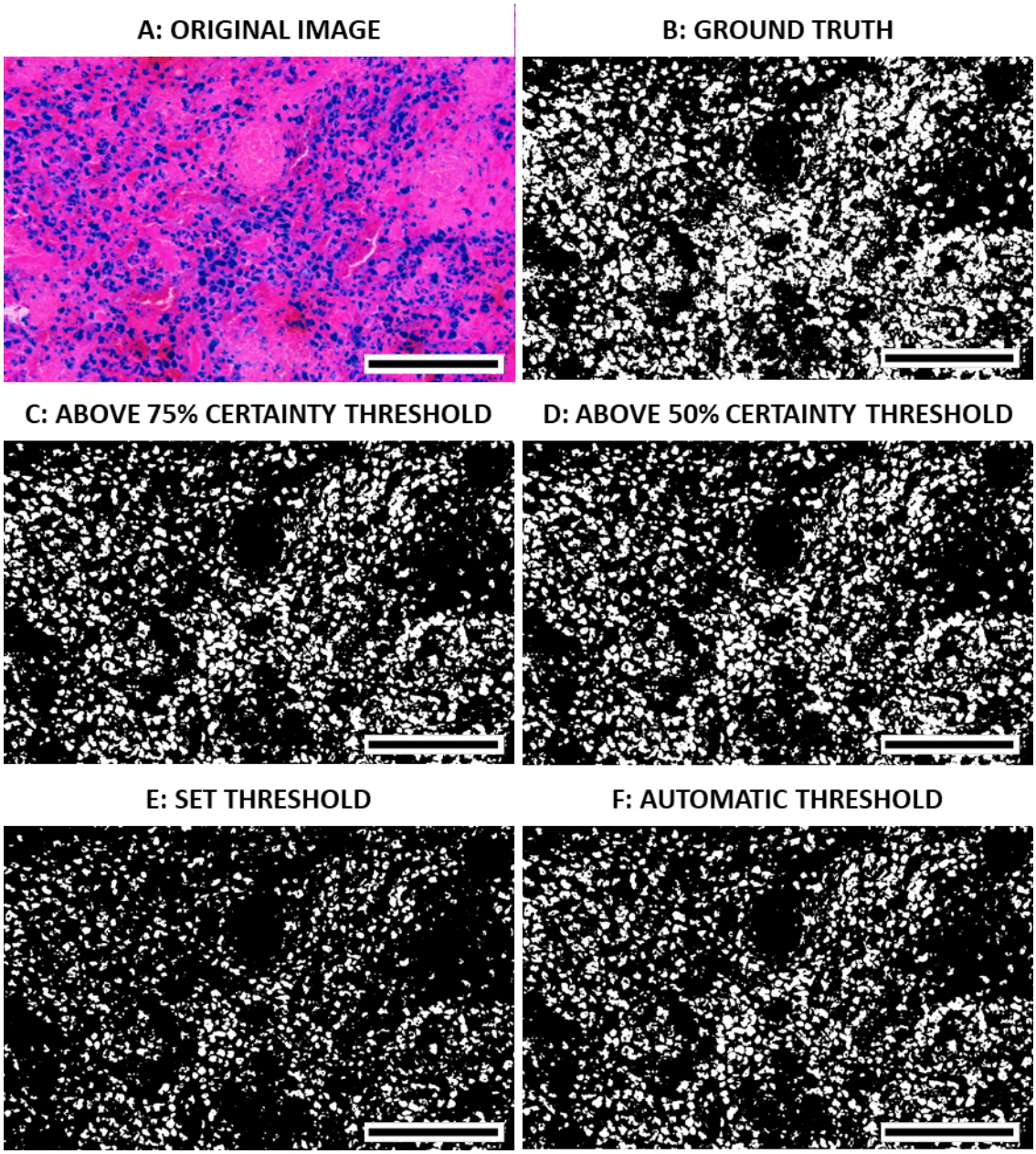

Figure 5.34: Segmentation of iron objects in spleen using different methods
Representative image of a spleen section of Wistar rat injected with saline. (A) Digitized PPB-stained section showing iron accumulation in blue, (B) manually segmented ground truth image, (C) binary image of pixels assigned to a class with over 75% certainty, (D) binary image of pixels assigned to a class with over 50% certainty, (E) result of a set threshold, (F) automatic default threshold in Fiji preformed on probability map. Scale bar represents 250 µm.

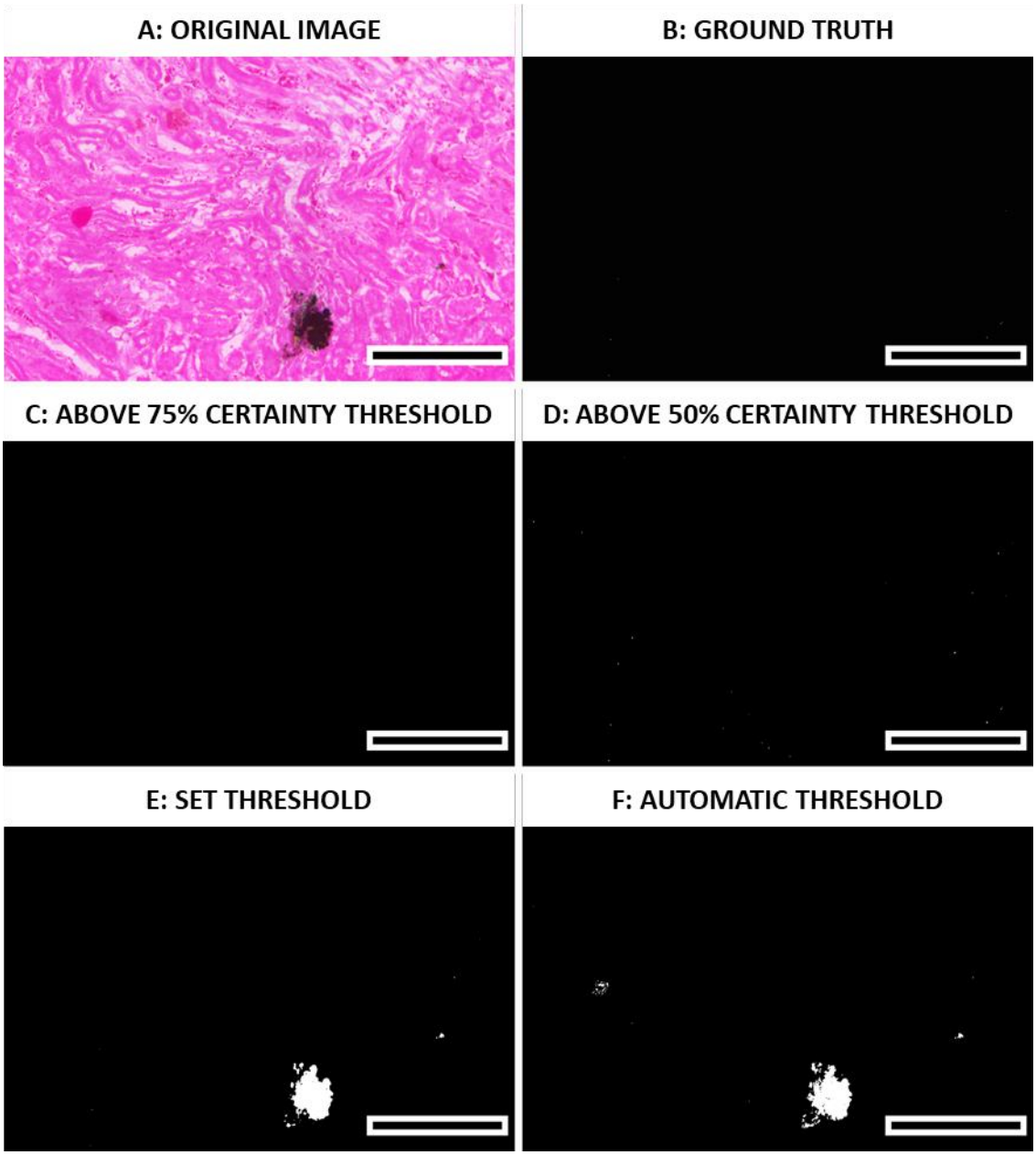

Figure 5.35: Segmentation of iron objects in kidney using different methods
Representative image of a kidney section of Wistar rat injected with RCL-01 at 30 mg/kg. (A) Digitized PPB-stained section showing a staining artefact seen in black, (B) manually segmented ground truth image, (C) binary image of pixels assigned to a class with over 75% certainty, (D) binary image of pixels assigned to a class with over 50% certainty, (E) result of a set threshold, (F) automatic default threshold in Fiji preformed on probability map. Scale bar represents 250 µm.

In chapter 4, the quantification of iron in histology slides was carried out on nine representative images acquired from three slides collected across tissue sample at three levels spaced at least 50 µm apart. Similarly, the quantification of iron in this *in vivo* study was carried out in rats rather than mice, the number of representative images was increased to ten images acquired from four sections collected at different levels across tissue sample to account for larger

size of each organ.

The results of the semi-quantitative analysis of PPB-stained slides in NOC0007 and RCL-01 treatment group respectively are shown in Figure 5.36 and Figure 5.37. As expected, liver and spleen showed the highest iron content in both treatment groups due to their role in iron homeostasis. The statistical analysis showed significant difference between liver of control animals and those injected with MNPs at three different doses for both NOC0007 and RCL-01. This significance was seen for all three parameters measured, with both number and size of detected iron deposits increasing with increasing dose of MNPs injected.

In contrast, no significant difference was found for % area of PPB staining in spleen. For both MNPs used in this study, the number of detected objects was directly proportional to the increasing doses, with strong statistical significance observed between control animals and those injected with NOC0007 at 30 mg/kg and 60 mg/kg (Figure 5.36 B). This was not the case for size of iron aggregates, which was found to be inversely proportional to the injected dose. This difference showed strong statistical significance between control and RCL-01 treated animals regardless of dose used, and also between different doses (Figure 5.37 C).

In lungs, all three parameters used for quantitative analysis increased with increasing dose of MNPs injected in both treatment groups. For NOC0007, animals injected with a dose of 60 mg/kg showed strong statistical significance across all the parameters when compared with the control animals. Additionally, a strong statistical difference was reported for number of detected objects between control animals and animals injected with NOC0007 at 30 mg/kg or 45 mg/kg (Figure 5.36 B). For RCL-01, treatment at 45 mg/kg and 60 mg/kg showed significant increase in the % area of PPB staining (Figure 5.37 A), with latter also showing statistically significant increase in number of detected objects (Figure 5.37 B) and size of the aggregates. Increase in size of iron aggregates was directly proportional to dose (Figure 5.37 C), with strong statistical difference between control animals and the ones injected with MNPs at 45 mg/kg and 60 mg/kg, with additional significant difference found between those two doses.

No significant differences in the iron levels in kidneys were found between the control animals and those injected with the MNPs, regardless of type of the material and dose. There were also no significant differences between the doses used in both NOC0007 and RCL-01 treatment groups.

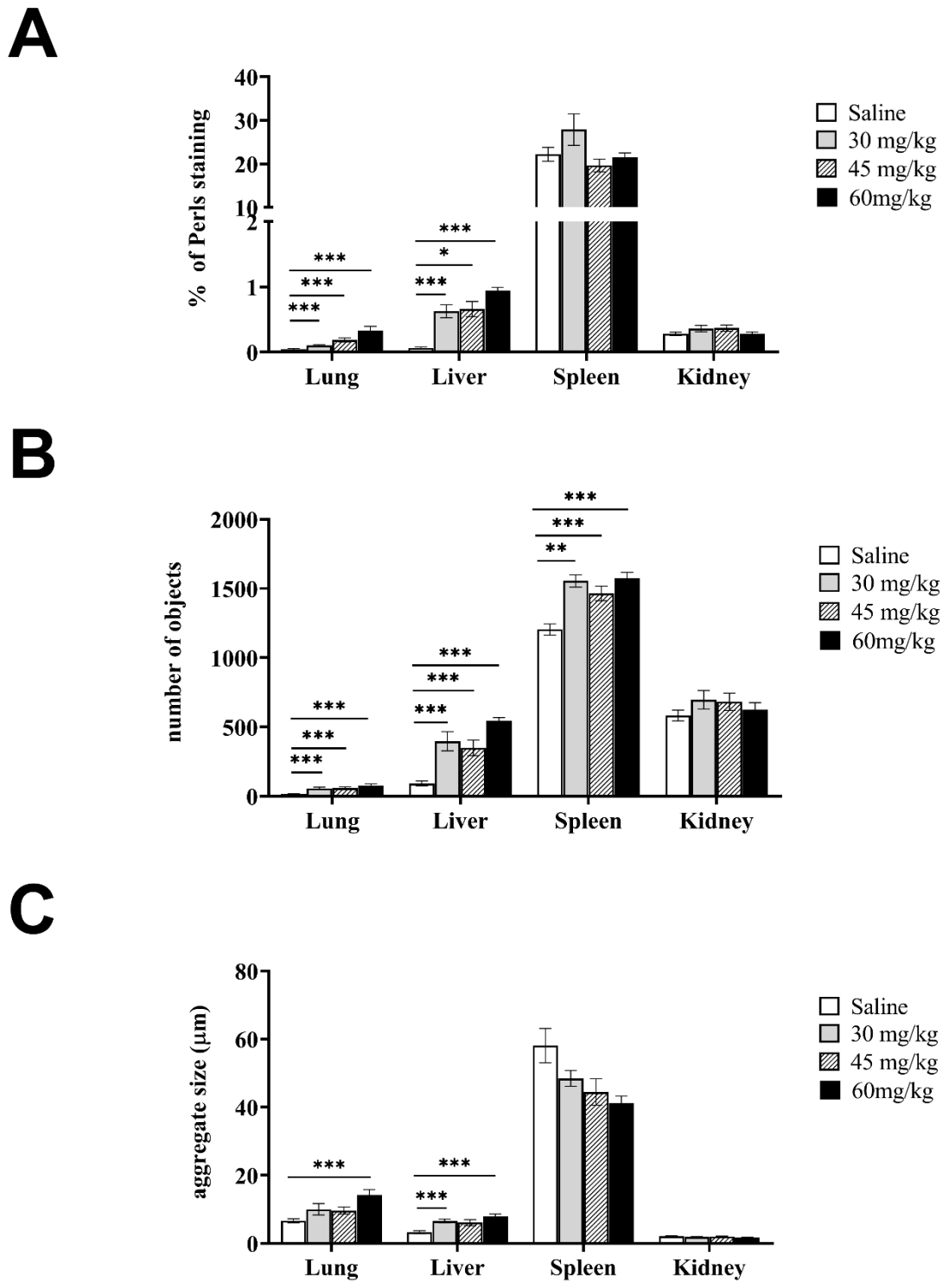

Figure 5.36: Quantification of Prussian blue staining in NOC0007 treatment group
Semi-quantification of the Prussian blue stained objects in lung, liver, spleen, and kidney using ML image segmentation. (A) Percent area of PPB staining in tissue, (B) average number of detected aggregates, (C) average size of detected objects. Statistical significance was determined using Mann-Whitney U test; * $p \leq 0.05$, ** $p \leq 0.01$, *** $p \leq 0.001$. Data points represent mean ± standard error of mean; n=240 in terms of images analysed; n=6 in terms of animal per treatment.

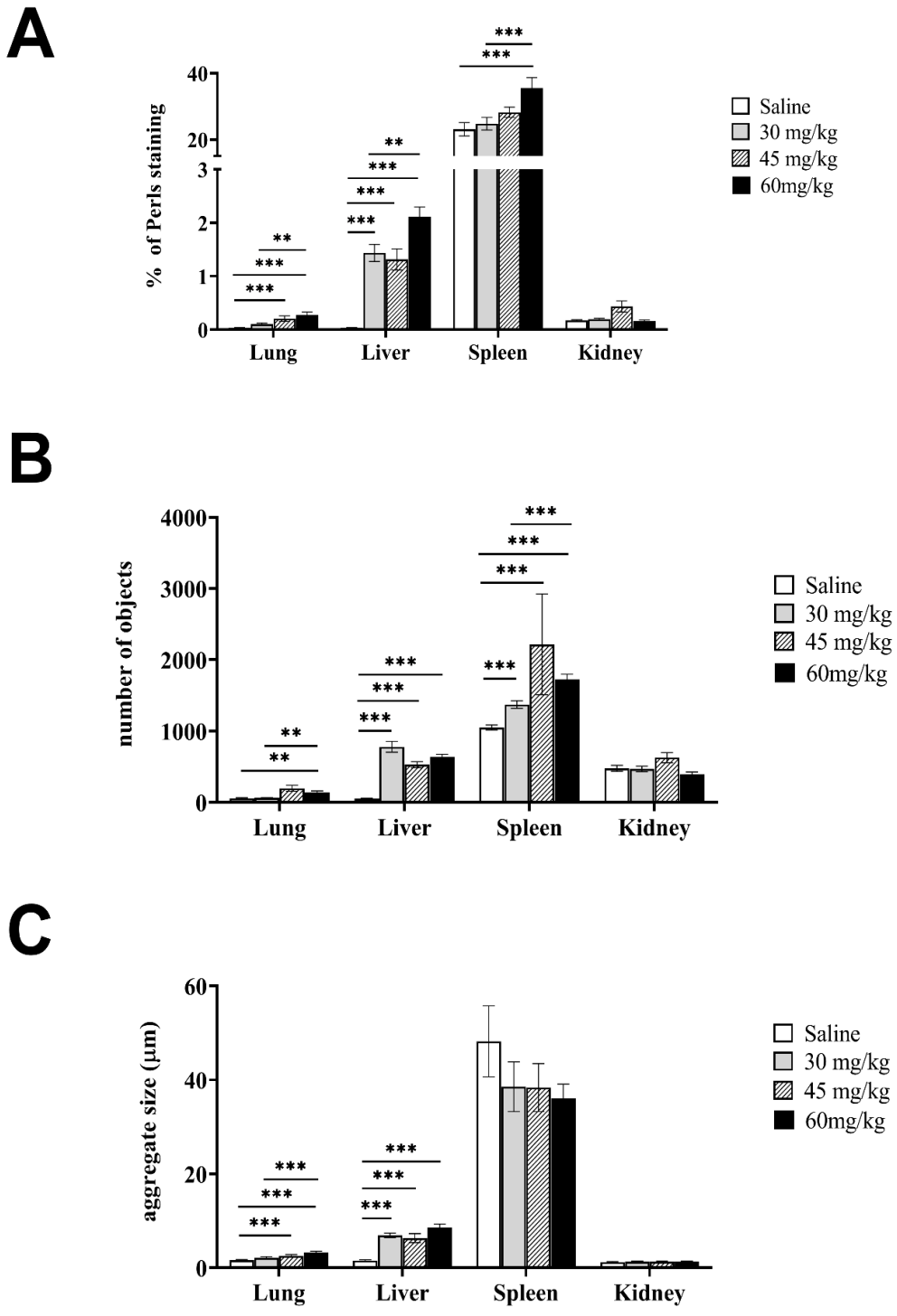

Figure 5.37: Quantification of Prussian blue staining in RCL-01 treatment group
Semi-quantification of the Prussian blue stained objects in lung, liver, spleen, and kidney using ML image segmentation. (A) Percent area of PPB staining in tissue, (B) average number of detected aggregates, (C) average size of detected objects. Statistical significance was determined using Mann-Whitney U test; * $p \leq 0.05$, ** $p \leq 0.01$, *** $p \leq 0.001$. Data points represent mean ± standard error of mean; n=240 in terms of images analysed; n=6 in terms of animal per treatment.

Data extrapolated from PPB stained slides was also used for additional analysis on correlation between dose of MNPs and three parameters used for quantitative analysis of iron content in tissue.

In NOC0007 treatment group, significant positive correlation between dose and % area of Perls' staining (Figure 5.38 A), number of detected objects (Figure 5.38 B), and size of objects (Figure 5.38 C) was found for lung and liver with calculated p-value ≤ 0.05. Significant positive correlation was also found between dose and size of objects detected in spleen, with calculated p-value ≤ 0.01.

In RCL-01 treatment group, a linear dose response between the injected dose and the % area of Perls' staining was seen in liver and spleen, with calculated p-value ≤ 0.05 (Figure 5.39 A). Size of detected objects in lung and liver also showed a linear dose response with calculated p-value ≤ 0.05 and p-value ≤ 0.001 respectively (Figure 5.39 C). No significant correlation was found between dose of MNPs and number of detected objects (Figure 5.39 B).

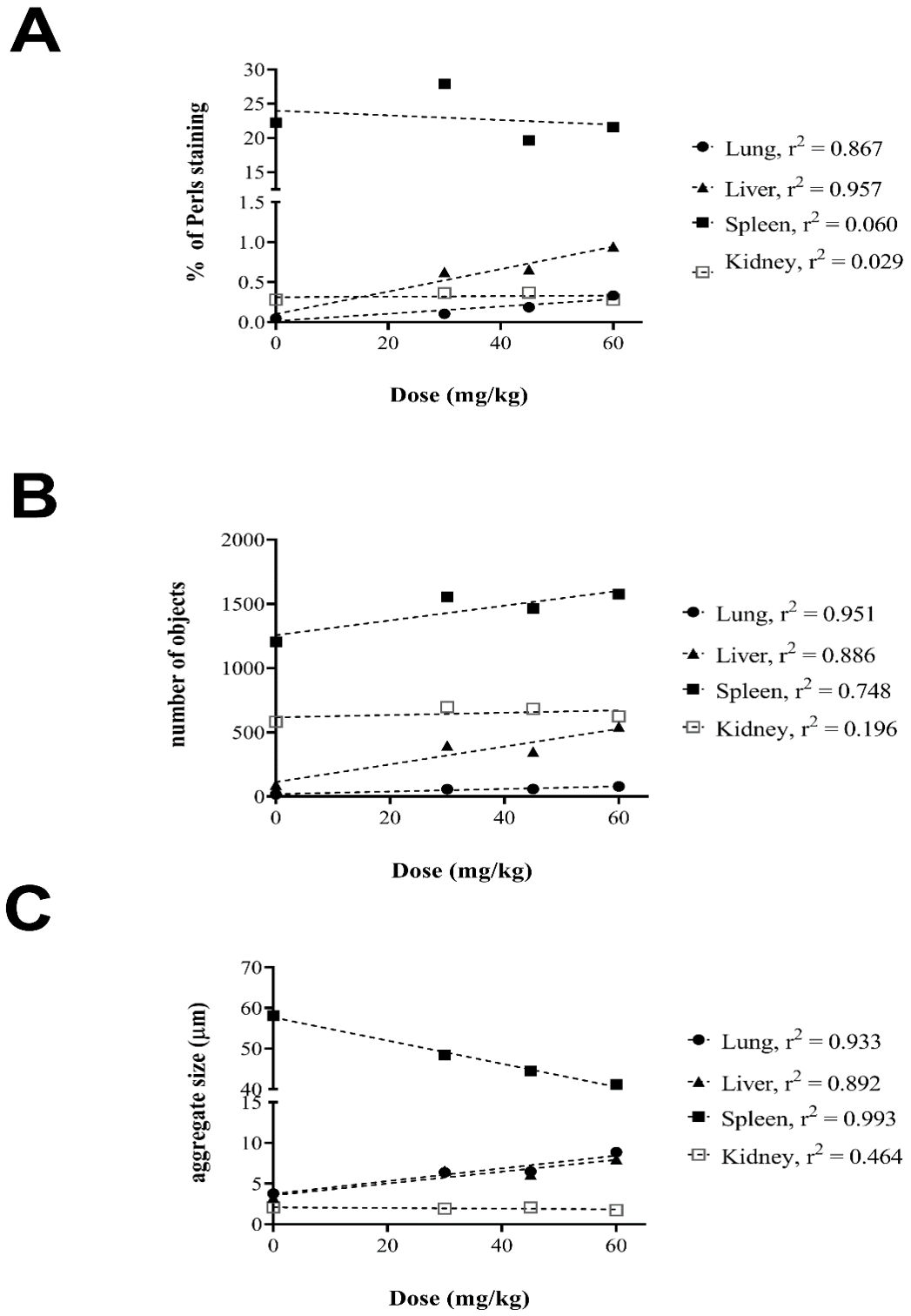

Figure 5.38: Correlation between dose of NOC0007 MNPs and iron detected in histology sections
Graphical representation of the relationship between the expression of the area occupied by iron in the total area of tissues and the dose of the NOC 0007 MNPs administered to rats. Data shown as mean, n=6 animals. Reported r^2 value was calculated using Pearson correlation coefficient with one-tailed p-value and 95% confidence interval.

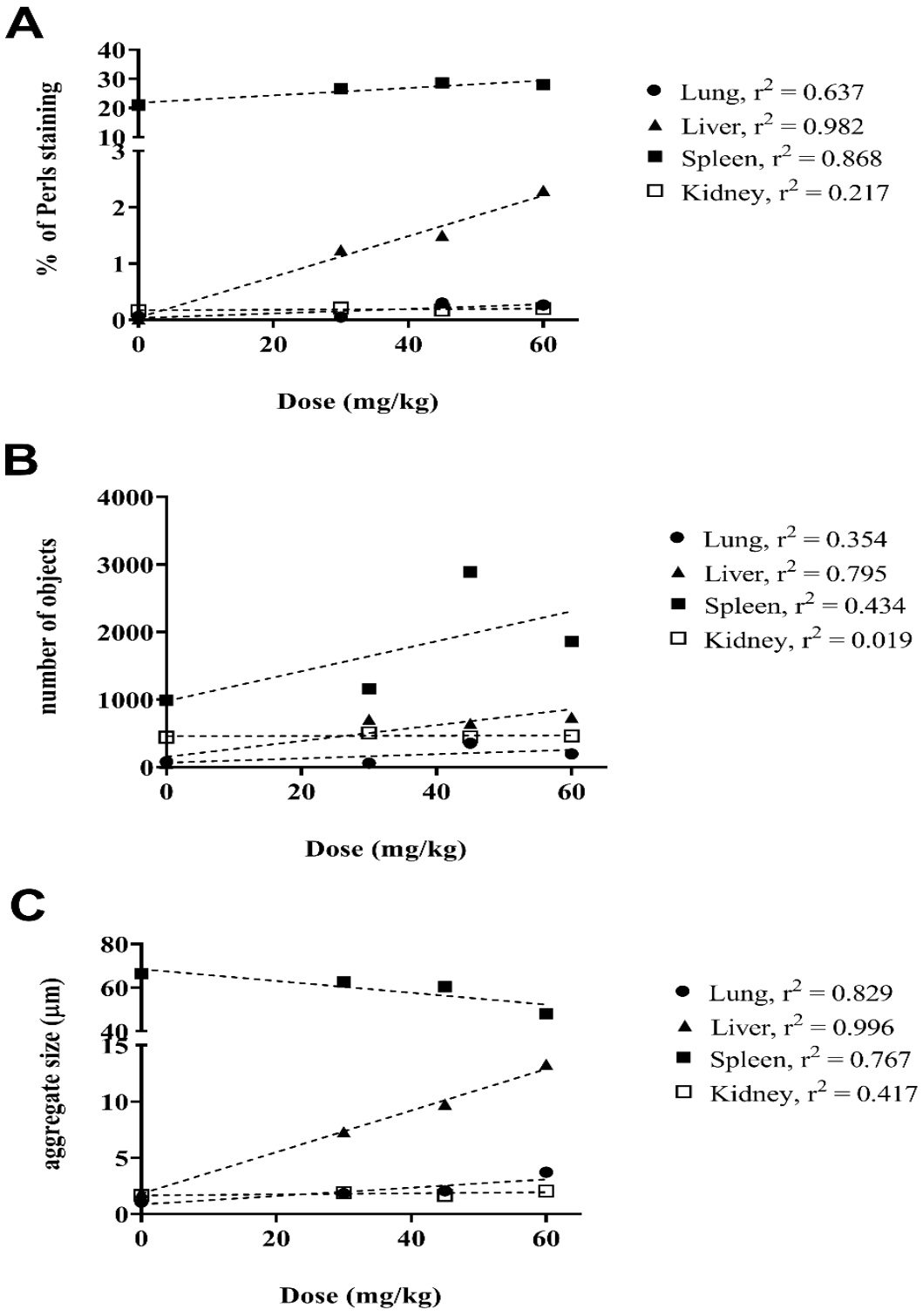

Figure 5.39: Correlation between dose of RCL-01 MNPs and iron detected in histology sections
Graphical representation of the relationship between the expression of the area occupied by iron in the total area of tissues and the dose of the RCL-01 MNPs administered to rats. Data shown as mean, n=6 for MNPs and n=5 for saline control. Reported r^2 value was calculated using Pearson correlation coefficient with one-tailed p-value and 95% confidence interval.

Three techniques were used to evaluate levels of iron in organs, semi-quantitative % area of Prussian blue staining calculated using ML, quantitative measurement using ICP-MS, and qualitative pathological score. Results of the ICP-MS analysis were kindly provided by Dr. Gary Hannon from the LBCAM group, whereas pathological scoring was performed by the histopathology registrar from Central Pathology Laboratory in St. James's hospital, Dr. Anna Keogh. Pathological score followed 5-tier scale from 0 (absent/background staining) to 4 (severe staining easily visible using a 2.5x objective).

For NOC007 (Figure 5.40), results obtained from histology images using ML (Figure 5.40 C) were found to mirror those reported from quantitative analysis (Figure 5.40 C), with highest levels of iron reported in the spleen. Pathology scoring also indicated that spleen had the highest content of iron (Figure 5.40 B), however pathologist have not reported any differences between treatment groups highlighting limitations of the human eye. The same was seen for RCL-01 (Figure 5.41), where both ICP-MS and ML showed a dose-depended increase in iron content in spleen, which was not reported by the pathologist.

The pathology score and ML technique both showed a dose-depended increase in iron content within lungs of NOC0007 injected animals, which was not seen in the results of ICP-MS. However, all three techniques showed a dose dependent increase of iron in lungs of animals injected with RCL-01. This was not the case for liver and kidney samples, where all three techniques showed divergence for both NOC0007 and RCL-01.

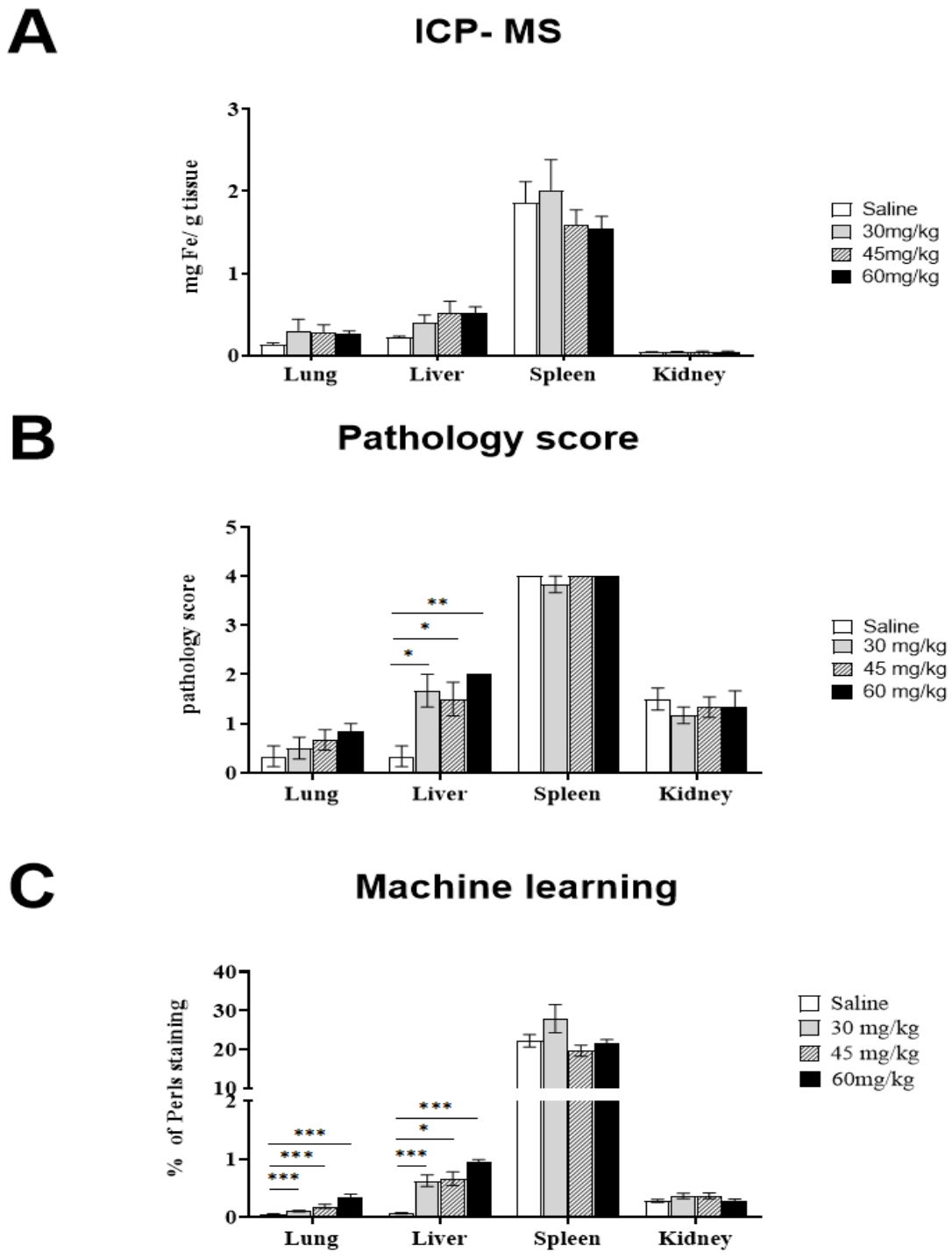

Figure 5.40: Biodistribution of iron following injection with NOC0007 MNPs measured by quantitative, qualitative, and semi-quantitative techniques

Iron levels in organs 7 days post injection with NOC0007 measured quantitatively with A: ICP-MS; B: qualitatively with pathological score following 5-tier scale from 0 (absent/background staining) to 4 (severe staining easily visible using a 2.5x objective); C: semi-quantitatively with ML for bioimage analysis. Statistical significance was determined using 2-way Anova with post-hoc Tukey's multiple comparisons test in A, and Mann-Whitney U test in B and C. * $p \leq 0.05$, ** $p \leq 0.01$, *** $p \leq 0.001$. Data points represent mean ± standard error of mean; n=6 animal per treatment.

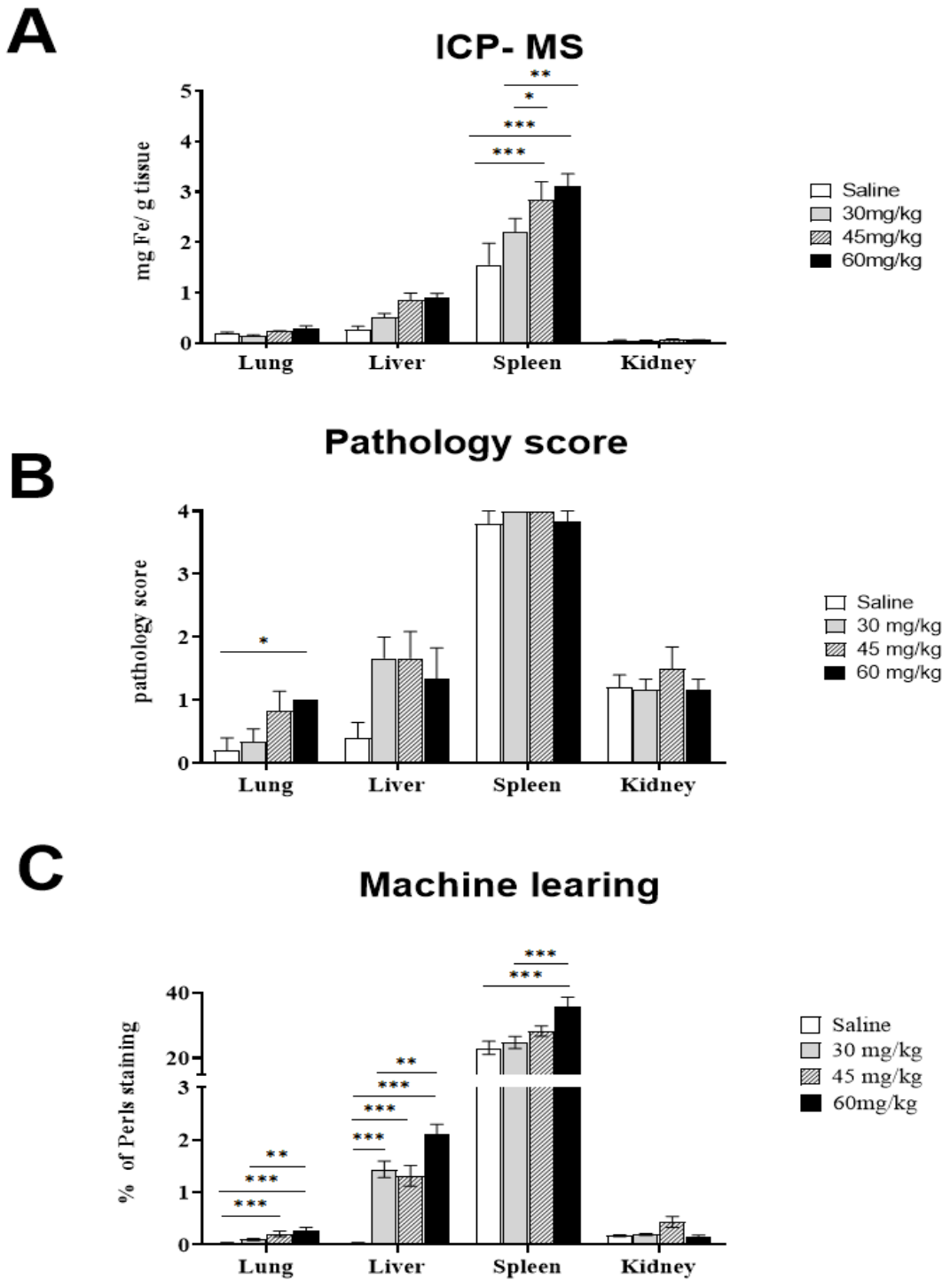

Figure 5.41: Biodistribution of iron following injection with RCL-01 MNPs measured by quantitative, qualitative, and semi-quantitative techniques

Iron levels in organs 7 days post injection with RCL-01 measured quantitatively with A: ICP-MS; B: qualitatively with pathological score following 5-tier scale from 0 (absent/background staining) to 4 (severe staining easily visible using a 2.5x objective); C: semi-quantitatively with ML for bioimage analysis. Statistical significance was determined using 2-way Anova with post-hoc Tukey's multiple comparisons test in A, and Mann-Whitney U test in B and C. * $p \leq 0.05$, ** $p \leq 0.01$, *** $p \leq 0.001$. Data points represent mean ± standard error of mean; n=5-6 animal per treatment.

While the results of ICP-MS, pathological scoring, and ML were in agreement in terms of levels of iron seen in the lungs, differences in the shape of the aggregated were clearly visible, for instance, in sections stained with H&E (Figure 5.4) and PPB (Figure 5.27). In the following section, shape descriptors were used to provide a quantitative assessment for morphology of those aggregates in both traditional 2D histology sections and in reconstructed 3D histology volumes.

5.3.6 *Shape analysis of iron aggregates in lungs*

As previously reported in chapter 4, the aggregation of MNPs can significantly reduce their heating potential, as well as affect the immune reaction and possible toxicity *in vivo*. With visible differences between shapes of the aggregates formed in lungs for two MNPs tested in this case study (figure 5.4 and figure 5.24), the aim of this section was to quantitatively assess morphology of those aggregates in traditional 2D histology sections and in 3D histology volumes generated from a series of consecutive sections. The methodological approach implemented in this section to generate 3D histology volumes will follow the same methodology and process as described in detail in chapter 4.

5.3.6.1 2D histology slides

For RCL-01, over 50% or iron aggregates in the control animals was found to resemble a perfect circle with roundness and circularity close to 1 (top right-hand corner in Figure 5.42). The increasing dose of RCL-01 MNPs resulted in a change of aggregate morphology as indicated by the dose dependent decrease in the percentage of circular objects.

Morphology of iron aggregates found in the lungs of NOC0007 injected animals did not correlate with the dose of MNPs. Moreover, no significant differences were found between the saline control (top left-hand corner in Figure 5.42) and MNPs injected animals.

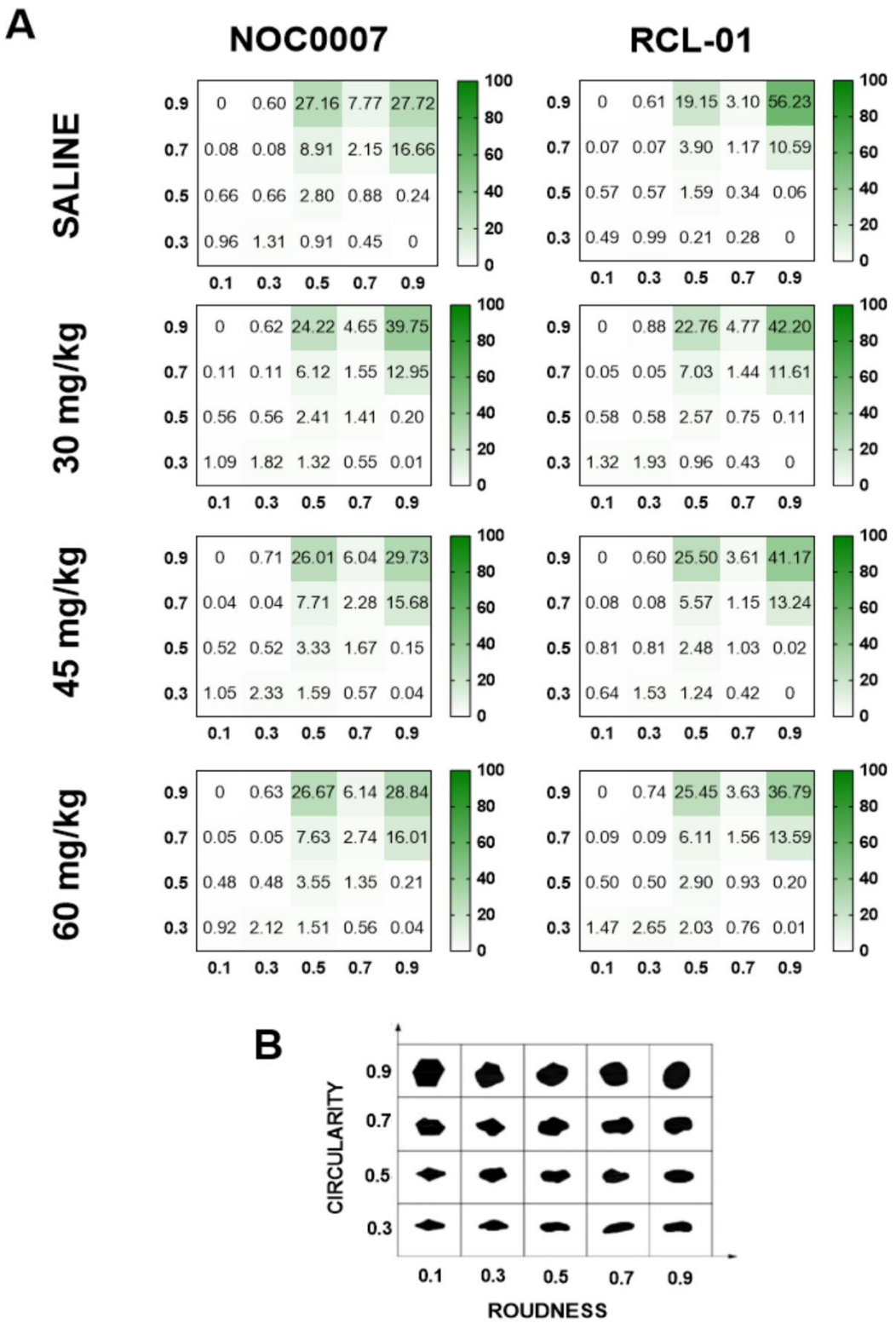

Figure 5.42: Morphology of MNPs aggregates in histology slides

Morphology of iron aggregates was measured using two shape descriptors, roundness (x-axis) and circularity (y-axis). (A) Heat maps colour-coded for percent of aggregates falling within predefined ratios for shape description. (B) graphical representation of aggregate shapes, adapted Krumbein and Sloss [204]. Results shown as mean; n=240 in terms of images analysed; n=6 in terms of animal per treatment.

Morphology of an iron deposit observed in traditional 2D histology slides depends on the orientation of cut made. Although international guidelines on the orientation of the cut with respect to an entire organ were followed, it is impossible to determine orientation of the iron aggregate within the organ. For this reason, shape analysis was also carried out on 3D histology volumes, results of which are discussed in the next section.

5.3.6.2 3D histology volumes

In Chapter 4, 3D histology volumes were generated from nineteen 5µm thick consecutive sections stained with PPB. Images acquired for reconstruction had dimensions of 800 µm x 600 µm, resulting in final reconstruction with volume equivalent to 0.046 mm^3. In this Chapter, larger 3D histology volumes were generated to account for a larger tissue area of organs extracted from rats in comparison to mice used in the previous chapter. Here, twenty 5µm thick consecutive sections stained with PPB were used for this reconstruction. Acquired images had dimension of 2000 µm x 1300 µm, resulting in final reconstruction with volume equivalent to 0.260 mm^3. Representative 3D volumes highlighting accumulation of iron in lungs of the animals injected with NOC 0007 or RCL-01 respectively are shown in Figure 5.43 and Figure 5.44.

Contrasting to the previous section, there were no significant differences between NOC 0007 and RCL-01 with regard to morphology of iron aggregates (Figure 5.45). In both cases, the majority of aggregates (> 45%) across all treatments had a flat elongated morphology. With the second most frequent shape (> 30%) resembling a disk with a circular but flat morphology. The remainder of the detected objects were reported as perfect sphere with elongation and flatness ratio close to 1. Increase in spherical objects appears to be dose-dependent for both NOC0007 and RCL-01. Additional analysis evaluating size distribution of objects categorized as different shapes could potentially indicate whether those shapes are formed due to cellular uptake such as the one shown with immunofluorescent staining in the previous section.

With reconstructed 3D histology volume, variability and uncertainty in the reported shape morphology of the iron aggregates formed in lungs was reduced as the orientation of the cut made when preparing tissue sections become irrelevant.

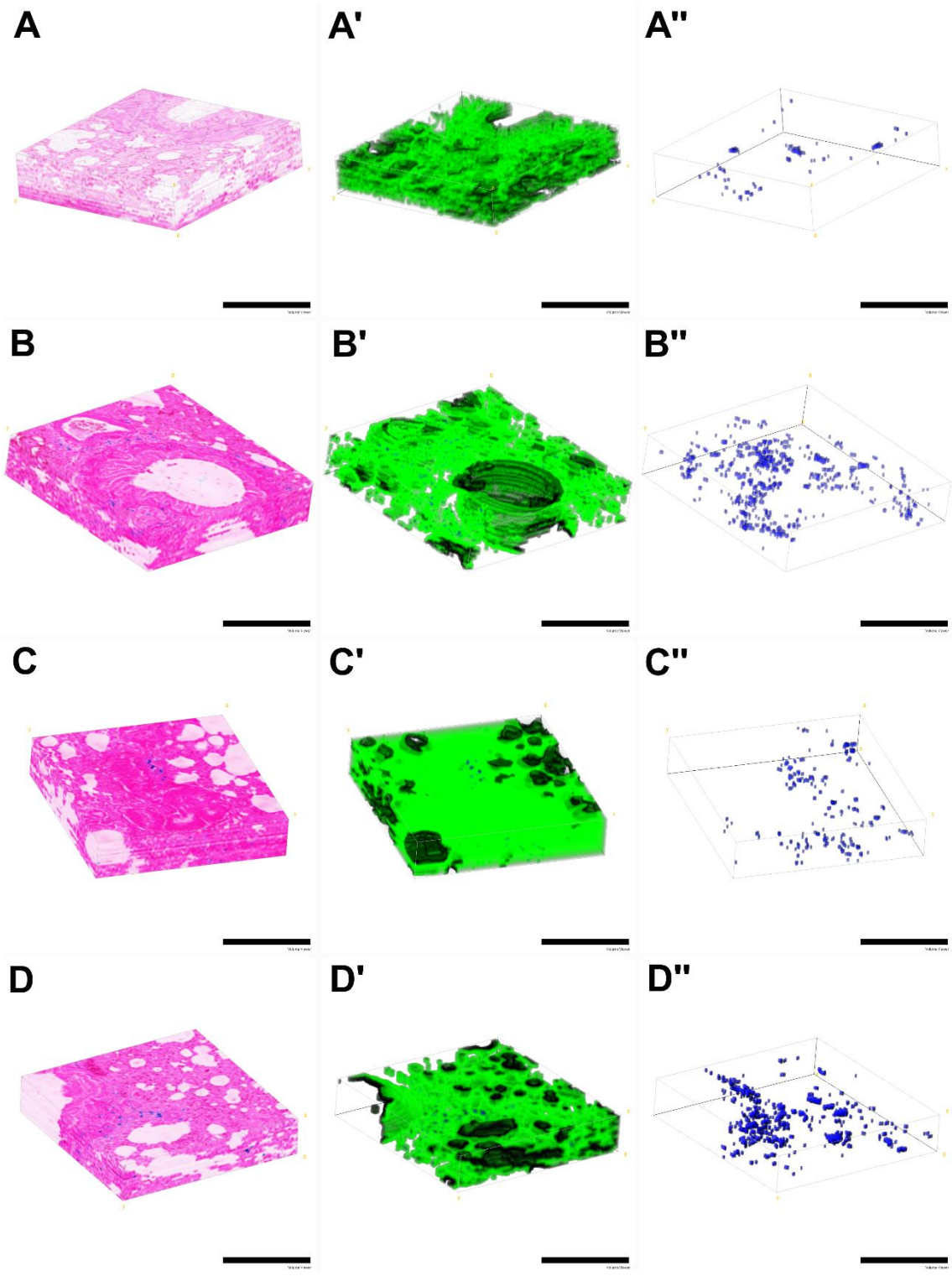

Figure 5.43: 3D reconstruction of lung sections from rats in NOC0007 experimental block
Brightfield images of Perls' Prussian blue stained lung sections reconstructed into virtual stack (A, B, C and D); 3D volume reconstruction of tissue (green) and iron deposits (blue) segmented with WEKA (A', B', C' and D'); 3D volume reconstruction of iron deposits segmented by WEKA (A'', B'', C'' and D''); Animals were injected with: saline (A, A' and A''); 30 mg/kg MNPs (B, B' and B''); 45 mg/kg MNPs (C, C' and C''), and 60 mg/kg MNPs (D, D' and D''). Volume dimensions: x = 500 µm, y = 500 µm, z = 100 µm, scale bar represents 250 µm.

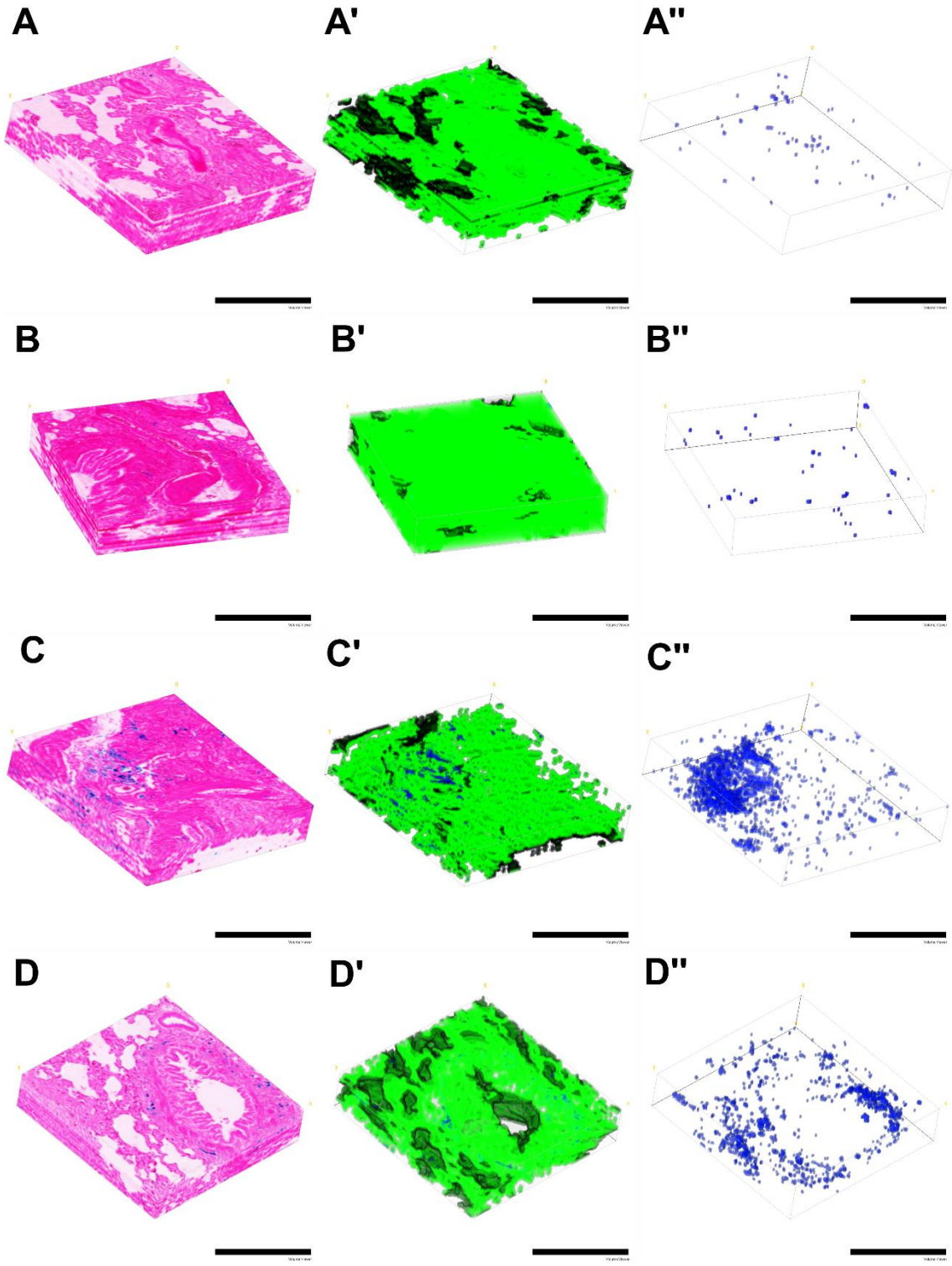

Figure 5.44: 3D reconstruction of lung sections from rats in RCL-01 experimental block
Brightfield images of Perls' Prussian blue stained lung sections reconstructed into virtual stack (A, B, C and D); 3D volume reconstruction of tissue (green) and MNPs (blue) segmented with WEKA (A', B', C' and D'); 3D volume reconstruction of MNPs segmented by WEKA (A'', B'', C'' and D''); Animals were injected with: saline (A, A' and A''); 30 mg/kg MNPs (B, B' and B''); 45 mg/kg MNPs (C, C' and C''), and 60 mg/kg MNPs (D, D' and D''). Volume dimensions: x = 500 µm, y = 500 µm, z = 100 µm, scale bar represents 250 µm.

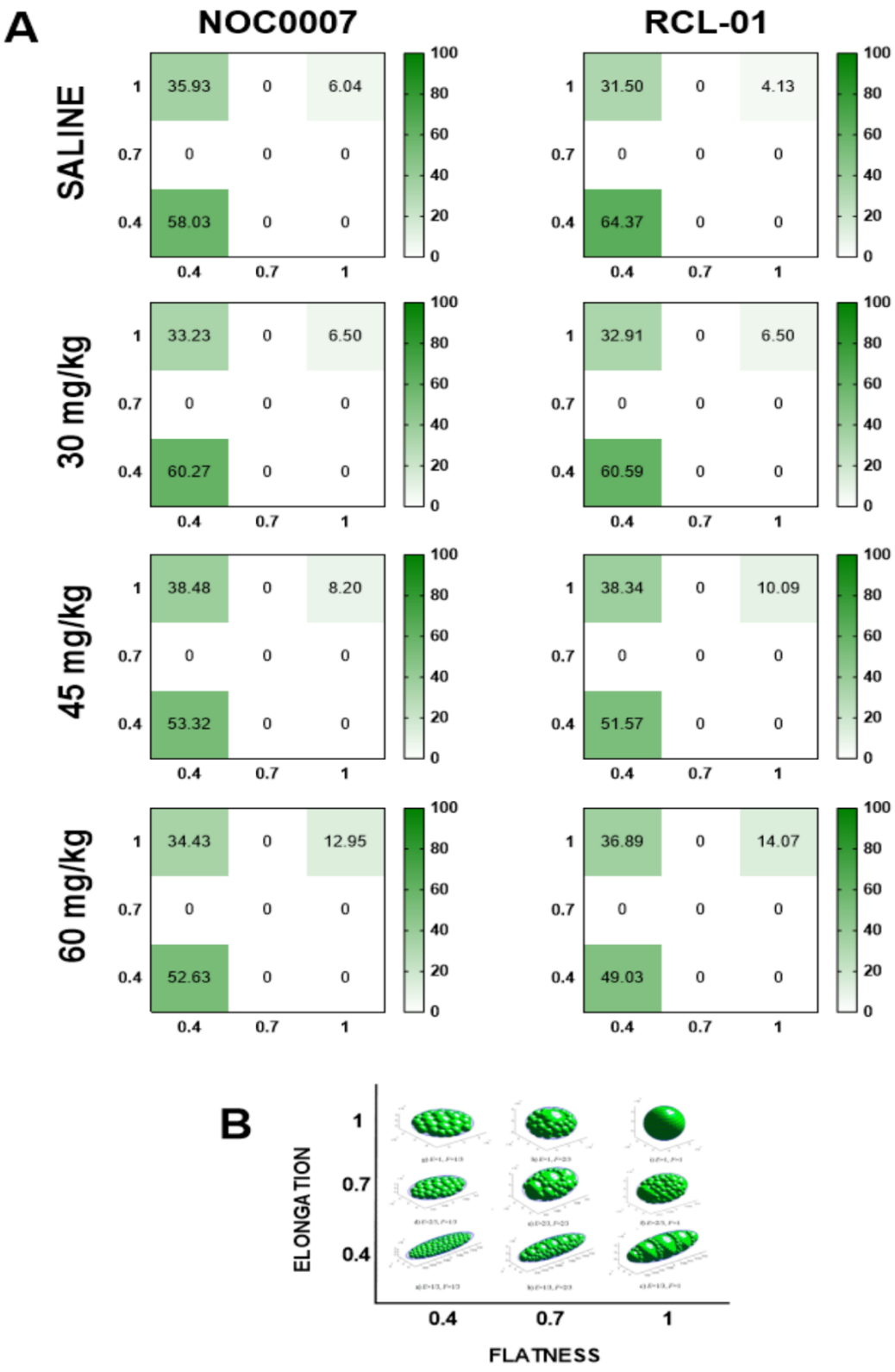

Figure 5.45: Morphology of MNPs aggregates in 3D histology volumes
Morphology of iron aggregates in 3D was measured using flatness (x-axis) and elongation (y-axis). (A) Heat maps colour-coded for percent of aggregates falling within predefined ratios for shape description. (B) graphical representation of aggregate shapes, modified from Zhou *et al.* [205]. n=6.

5.4 Discussion

The results presented in this chapter were obtained as a part of a multinational collaboration aiming to scale-up production of the patented MNP design and translate one of these nanoformulations to early clinical development to treat pancreatic ductal adenocarcinoma with magnetic hyperthermia. As a part of this consortium, the Nanomedicine and Molecular Imaging group in Trinity College Dublin carried out an *in vivo* study in Wistar rats to mimic a 'failed' intratumoral injection where all material reaches the bloodstream. Results from the extensive histological analysis carried out on samples obtained during this *in vivo* study were presented in this chapter.

Two bare MNPs as solid core inorganic nanoparticle coated with dextran and no drug or ligand loads or coated, referred to throughout this thesis as NOC 0007 and RCL-01 were used to test main hypothesis of this chapter, whether MNPs with similar physicochemical properties exhibit comparable biodistribution and toxicity *in vivo*.

NOC 0007 is composed of maghemite (γ-Fe_2O_3) core measuring 14 nm. The MNPs were coated with 40kD dextran with hydrodynamic diameter of 122.6 nm and with -6.5 mV zeta potential. RCL-01 on the other hand, is composed of iron core measuring 50 ± 25 nm. Similarly, to NOC0007, particles were coated with dextran with hydrodynamic diameter of 149 nm and with -20.5 mV zeta potential.

Initial clinical evaluation of the animals' wellbeing provided early indication of severe adverse effects and toxicity induced by MNPs. In both experimental groups, significant difference in the severity score was observed 30 minutes post injection between control animals and those injected with MNPs. However, all animals fully recovered by 2-hour post injection. Similar findings were previously reported by Bourrinet *et al.* [206]. In their preclinical assessment of ferumoxtran-10 (USPION contrast agent for lymph node detection), rats that received 126 mg Fe/kg in a single dose intravenous injection showed clinical signs of toxicity in form of swollen snout and/or paws, dark body areas, laboured respiration, and red crust around the nose within 10 minutes after dosing. In the same *in vivo* study, animals receiving 400 mg Fe/kg presented with clinical signs of toxicity during dosing which included hypoactivity, ataxia, and darkening of the entire body and/or tail. In both cases, the reported clinical signs lasted up to 24 hours, apart from body darkened areas in the animals injected with higher dose, which progressively disappeared within nine days post injection. In the study reported here, animals presented with diarrhoea and scaring at the site of injection resulting in necrotic tail and tail loss reported in number of animals

injected with NOC 0007. Those observations could be indicative of hypersensitivity, which is known to occur in response to iron infusion [207]. No significant changes were seen in body weight of any the animals up to the end of experiment.

Toxicity and immune response in lungs, liver, spleen, and kidneys was assessed with means of histopathology. Signs of toxicity and immune response were noted in all organs, regardless of type and dose of MNPs. Influx of inflammatory cells was seen in the perivascular and peribronchial space in the lungs of animals injected with MNPs (Figure 5.4). Types of the immune cells varied between two MNPs, with NOC 0007 inducing an influx of mast cells and eosinophils, and RCL-01 prompting a strong response from eosinophils.

NOC 0007 and RCL-01 MNPs also induced changes in spleen in the form of extramedullary haematopoiesis at all doses examined. Similar effect was observed in a study conducted by Awaad [208] at 2 weeks post intravaginal installation of 13.4 ± 3.2 nm core MNPs in mice at dose equivalent to 45 mg Fe/mouse . Kidneys of animals used in study presented here also had a number of histological changes (Figure 5.7). With a number of those changes occurring naturally in rats (as seen with control animals) [209], it was challenging to determine which, if any, of those changes formed in response to toxicity of MNPs. Vacuoles were observed in renal tubules of rats injected with NOC 0007 and RCL-01 (Figure 5.7 B). Interestingly, similar changes were observed in early research on the effect of dextran on lysosomal ultrastructure and protein digestion in renal proximal tubule [210]. Wistar rats injected with a solution containing dextran T-40 at a dose of 5 g/kg of body weight showed prominent vacuoles in proximal tubules 1 hour post injection. As both NOC0007 and RCL-01 stabilized with dextran, this finding instigates a question regarding what part of MNPs contributes to toxicity *in vivo*. This aspect should be investigated in the future studies where dextran used for coating MNPs is injected into the animal for comparison.

Despite number of changes suggestive of toxicity were seen in all of the organs examined, pathological severity score provided by the registrar pathologist showed no significant differences between the control animals and those injected with the MNPs (Figure 5.8).

Modified Toluidine blue stain was used to further examine mast cells and eosinophils seen in H&E stained lung sections. In NOC 0007 injected animals, mast cells were identified around areas where iron was accumulated, with number of those cells appearing to be activated as characterised by release of granules from the cytoplasm (Figure 5.9B, C, and D). Number of degranulating mast cells was visually increased in RCL-01 injected animals in comparison to

control animals and those injected with NOC 0007. Moreover, degranulating mast cells were surrounded with eosinophils (Figure 5.9 F, G, and H). Histamine is one of the secretory products of mast cells. It is a ubiquitous mediator whose effects are mediated by number of receptors present on the surface of eosinophils [211]. One of those receptors, H1, is known to increase expression of C3b receptors on eosinophils [212]. Analysis on complement activation by MNPs carried out by Dr. Gary Hannon as a part of his doctorate thesis revealed an increase of C3b in response to RCL-01 [213]. Conjointly, results obtained from Toluidine blue staining and complement activation assay imply the following response to intravenous injection with RCL-01 (Figure 5.46). Upon injection, C3b opsonin binds to the surface of MNPs priming them for engulfment by phagocytic cells. Complement protein activation leads to activation of mast cells and release of histamine which is a chemoattractant for eosinophils also increasing C3b receptors on their surface. Hypothetically, RCL-01 coated with C3b could be phagocytosed for degradation by eosinophils with increased number of C3b receptor. However, uptake of MNPs by eosinophils was beyond the scope of this projects and would need to be further investigated in the future to confirm this theory. Additionally, levels of histamine over time could also be measured in future in vivo to fully evaluate the response of mast cells to MNPs.

Proposed cascade for immune response to RCL-01 relies on complement activation. Research in this area demonstrated that dextran can activate or inhibit complement system activation both in free and in MNP-bound form [214]. Furthermore, literature on the exact pathway of complement activation by dextran coated MNPs is limited. A study in mice carried out by Banda *et. al.* [215] showed that complement was activated via the lectin (sugar recognition) pathway in response to 20 kDa dextran coated SPIO nanoworms. However, it is unknown if the same pathway would be activated by MNPs with other sugar coating.

PPB staining of lung sections from animals injected with NOC 0007 revealed large aggregates formed in the vasculature, suggesting potential degradation of dextran coating. This was confirmed by immunofluorescent staining for dextran, which was not detected in any of the organs of the animals injected with NOC 0007, regardless of dose used (Figure 5.12 and supplementary figure 8.60). Interestingly, immunofluorescent staining for CD68 used in combination with anti-dextran antibody revealed that large aggregates formed in vasculature of animals injected with the highest dose of NOC 0007 were in fact a cluster of macrophages rather than an iron aggregate (Figure 5.13 and Figure 5.14). This was not detected in neither H&E, nor PPB staining (Figure 5.4 and Figure 5.27 respectively). Heavy iron overload seen in those macrophages completely obscured any features used to characterise cells in traditional histology sections. In contrast to NOC 0007, dextran was still detected bound to RCL-01 MNPs in lung,

liver and spleen at 7 days post injection. This finding further confirms that cascade of immune events observed in this study was most likely activated in response to dextran coating rather than particle core composed of iron.

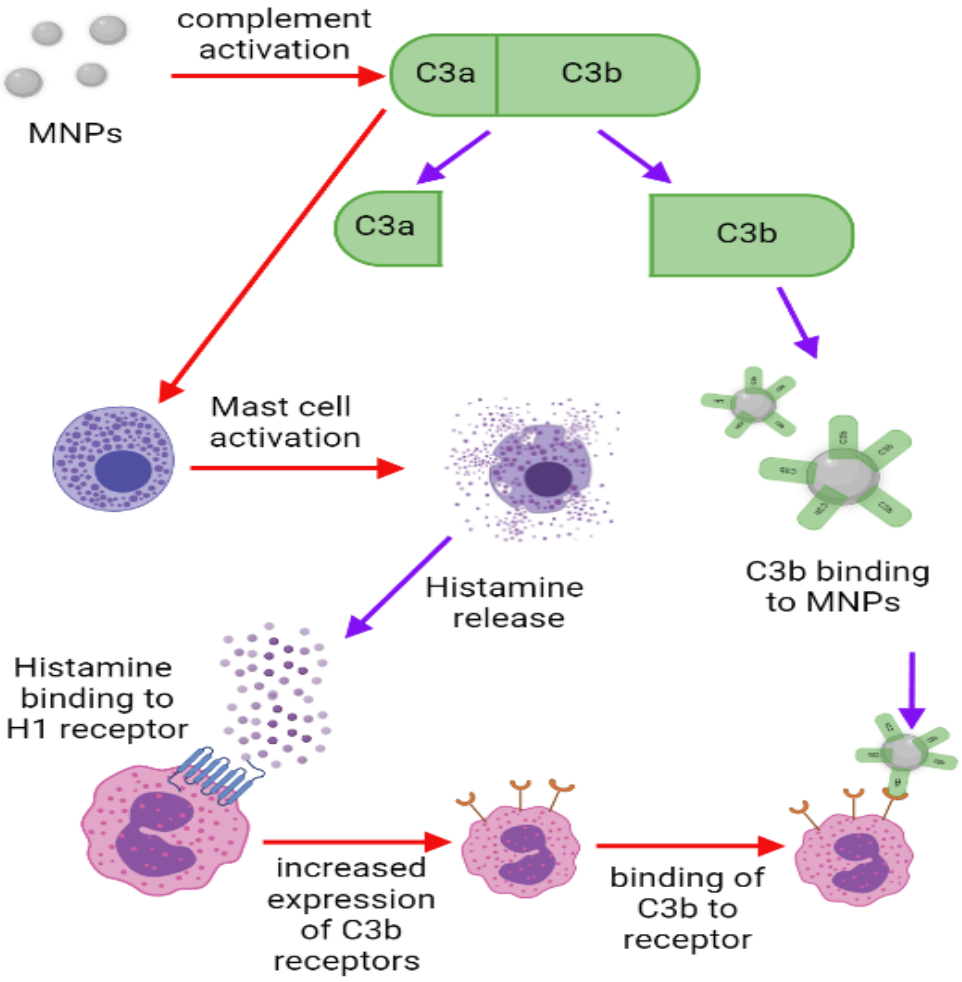

Figure 5.46: Cascade of immune responses to intravenously administered MNPs
Graphical representation of cascade of immune responses activated by RCL-01 MNPs. Red arrows represent activation of different components of immune system; purple arrows represent other events occurring simultaneously. Figures are not to scale with each other. Created with BioRender.com.

In the past few years, researchers have applied immunofluorescent staining of dextran coating on MNPs for quantitative analysis *in vitro* [216]. However, as dextran coating would be the first component subjected to degradation *in vivo*, it may not be detectable at the time of analysis as seen in this study with NOC 0007 MNPs. Therefore, for the purpose of detection and quantitative analysis of iron in tissue sections PPB stain is the most reliable even though it cannot discriminate between endogenous and exogenous iron.

To correlate the histological and immunological impacts observed in various organs with accumulation of MNPs, tissue sections stained with PPB stain for iron detection were first examined visually. Differences in the accumulation of two MNPs were observed in both liver and lungs. In liver, iron was detected within the cytoplasm of resident macrophages (Kupffer cells) in MNPs injected animals in both experimental blocks (Figure 5.28). However, in livers of RCL-01 injected animals, faint iron staining was also noted in the cytoplasm of hepatocytes, regardless of dose used. Dissimilar accumulation pattern was also distinct in the lungs, where not only location of iron aggregates, but also their size and shape differed for two MNPs (Figure 5.27). Injection of NOC 0007 resulted in a formation of relatively large aggregates within the vasculature, which as described in previous chapter of this thesis can be life threatening. NOC 0007 and RCL-01 showed similar biodistribution in kidney, with iron staining present predominantly in renal tubules (Figure 5.30). Control animals also had noticeable iron staining in the same location, which is in line with results presented in a previous chapter. Similar iron content was also found in the spleens of control animals injected with saline and those injected with the MNPs. High numbers of iron laden cells were seen in the marginal zone of white pulp and in the red pulp (Figure 5.29). In order to determine whether iron accumulation was significantly higher in the organs of animals injected with the MNPs in comparison to control animals, semi-quantitative analysis of PPS in tissue sections was carried out with the use of ML.

Performance metrics measuring overlap of the images segmented by the ML with the manually segmented ground truth images confirmed that WEKA classifiers trained for segmenting tissue and iron in histology images were as effective as the other two methods (set and automatic threshold) used the past (Figure 5.31). Furthermore, similarly to results presented in chapter 4, WEKA classifier outperformed all other methods in detecting iron in kidney sections. Validated classifiers were used for a semi-quantitative analysis where percent area of iron was calculated from representative images, with additional qualitative analysis of number and size of objects detected with PPB stain (Figure 5.36 and Figure 5.37). For both MNPs, spleen had the highest accumulation of iron as indicated by percent area of PPB stain, number, and size of detected iron aggregates, with liver coming second. The increase in percent area and size of iron objects in the liver was directly proportional to increasing dose of both NOC0007 and RCL-01 as confirmed by statistically significant correlation (Figure 5.38 and Figure 5.39). This was also seen in the lungs of NOC0007 injected animals. Furthermore, size of the iron aggregates in the spleen of NOC0007 was also found to correlate with dose used. Percent area of PPB stain detected in the lungs and liver of RCL-01 injected animals was also found to correlate with the dose used.

Results on the iron levels in tissues obtained with the semi-quantitative analysis of PPB

were compared against two gold standards used for this purpose. ICP-MS is one of the quantitative techniques used in the area of MNPs research to determine biodistribution of this material. On the other hand, traditional histological scoring or grading is regarded as qualitative technique. As shown in Figure 5.40 and Figure 5.41, data on the iron levels in tissues obtained for the histology section with means of ML mirrored quantitative results from ICP-MS analysis. Pathological grading provided by the registrar pathologist failed to differentiate iron levels observed in the livers and spleens of the control animals and those injected with the MNPs. This was mainly due to high levels of endogenous iron found naturally in those organs in rats, highlighting shortcomings of this technique in evaluating biodistribution of the MNPs. Based on the similarities between the results of ICP-MS and semi-qualitative image analysis using ML it can be concluded that the latter can be used to estimate levels of iron in tissue, as well as number and size of the aggregates formed.

To maximise information obtained from images segmented with ML, shape descriptors were used to quantitatively assess morphology of the iron aggregates in lungs using traditional 2D histology sections and reconstructed 3D histology volumes. There is a lack of literature where similar analysis was carried out to measure morphology of the aggregates in organs, making this study a first of its kind. Shape descriptors calculated from 2D histology slides confirmed that morphology of iron deposits varied between two experimental blocks (Figure 5.42). For NOC0007, no difference was seen in the morphology of iron objects found in the control animals and those injected with increasing dose of MNPS. In contrast, increasing doses of RCL-01 seemed to affect the morphology of iron aggregates, with decrease in the number of objects resembling a circle. Looking at graphical representation of morphological shapes demonstrated in Figure 5.42 B together with photomicrograph of histological sections, it can be hypothesized that detected objects are primarily iron-laden resident macrophages. Pulmonary macrophages would have a circularity and roundness close to 1, and macrophages seen in perivascular and peribronchial space having an ellipse shape.

Contrasting to shape analysis in 2D histology slides, investigation on 3D histology volumes showed no significant differences between NOC 0007 and RCL-01 with regard to morphology of iron aggregates. In both cases, majority of aggregates (> 49 %) across all treatments had a flat elongated morphology, with the second most frequent shape (> 30%) resembling a disk with a circular but flat morphology. Additional analysis evaluating size distribution of objects categorized as different shapes could potentially indicate whether those shapes are formed due to cellular uptake such as the one hypothesised based on analysis in 2D. Orientation of cut made to a sample when preparing histology slide can influence appearance of different shapes. Analysis

on 3D volumes rather than traditional 2D histology sections reduces variability and uncertainty in reported shape morphology as the orientation of cut made when preparing tissue sections becomes irrelevant. In recent years number of studies employed computer simulations to predict the magnetic properties depending on the shape of the MNPs in a specific volume [217, 218]. Furthermore, computer simulations can be used to predict temperature distribution, the mass concentration, and the heat transfer in tumours such as the one recently detailed by Suleman and Riaz [219], who carried out 3D *in silico* study of breast cancer hyperthermia using MNPs. Their study was carried out on a theoretical model of a breast tumour of 10 mm radius surrounded by a normal tissue of 30 mm radius constructed on a COMSOL Multiphysics software. The 3D volumes obtained from histology slides such as the ones presented in this chapter could provide a more biologically relevant model for those types of *in silico* simulations, where the accumulation of MNPs within a complex structure of an organ or tumour can be defined on a microscopic level.

5.5 Conclusion

The *in vivo* toxicity study presented in this chapter, as an advanced case study, was designed to mimic a 'failed' intratumoral injection and a worst-case scenario where all injected material reached the bloodstream during intratumoral injection. From the histology assessment the results showed minimal toxicity and immune response in organs at seven days post injection with increasing doses of NOC0007 and RCL-01 MNPs. Furthermore, uptake of the MNPs by the phagocytic cells in lungs, liver, and spleen was confirmed with the immunofluorescent staining. Co-labelling with the anti-dextran antibody determined that the two materials tested show a different rate of degradation within those cells.

Moreover, iron levels in organs were measured using three different techniques: quantitative measurement via ICP-MS; qualitative histological scoring carried out by registrar pathologist; and semi-quantitative evaluation using ML segmentation of histological images. The latter was found to mirror the results of ICP-MS (gold standard in this area of research), confirming that the here proposed method provides relatively accurate evaluation of the iron content in tissue. In addition, this semi-quantitative method can be used to gain further data on additional parameters such as the number, size, and morphology of the aggregates formed in organs by MNPs, all of which are not provided by the other two methods.

Overall, it can be concluded that the three methods adopted independently provided the same outcome, both materials examined can be regarded as safe for further pre-clinical investigation.

6 Overall discussion and conclusions

As highlighted in the literature presented in chapter 1, despite of the immense advancement over the past few decades of nanotechnology applied to biomaterials, there are still several unanswered questions regarding the way NBMs get assessed for safety. Furthermore, the lack of regulatory guidance regarding the specific characterization and screening requirements for advancing promising NBMs to clinical trials, is particularly impacting the toxicity and safety evaluation *in vivo*. Although histology studies are recommended by the regulators, they are not used at their full potential, with the majority of published studies reporting only on the H&E stained tissue sections used to examine pathological changes. Having identified this gap at preclinical level, the overall goal of this PhD project was to develop advanced histological methodologies to be used for the preclinical safety studies of NBMs. The experimental-based research was driven by the need to investigate the biodistribution, accumulation and toxicity profile of representative NBMs: liposomes and iron oxide magnetic nanoparticles.

Lipid based NBMs are one of the materials which prove challenging in terms of tracing their biodistribution *in vivo*. From the safety perspective, it is important to determine in what cells and structures within the organ NBMs accumulate in, as it can provide details on the route of their excretion and potential immune implications. Current methods of detection include labelling liposomes with an appropriate marker for visualisation (e.g., fluorescent dye or a radionucleotide) prior to administration. The disadvantage of this method is that the addition of probes and dyes to a membrane system can potentially interfere with the properties of the liposomal delivery system [220]. To overcome this limitation, research undertaken as a part of two *in vivo* case studies presented in chapter 3 aimed to develop a method utilising histological techniques to detect liposomes *ex vivo* in tissue sections. This was achieved by using a histological stain for lipid detection (Oil red O) to visualise liposomes which were differentiated from natural lipids by examining co-localisation with a dye encapsulated inside the liposome used in first case study (safety study of dye-loaded lipid NBM), or coating material on liposome used in the second case study (proof-of-concept SOP for liposome drug carrier biodistribution detection). Overall, strong evidence was provided to demonstrate that Oil red O staining is a good method for detecting liposomes in tissue sections using fluorescent microscopy provided that a second fluorescent marker is used to differentiate them from naturally occurring lipids. One of the limitations to this method is the rate of degradation of the NBM *in vivo.* Without the marker for co-labelling, it would be impossible to discriminate between the liposome and naturally occurring lipids. For example, since coating material is the first part of the NMB to be exposed to different components *in vivo*, it is also the first part to be degraded. For this reason, studies with a coating material used

as a second marker are limited to short term studies (few hours to few days post injection) only. With that said, the detection of lipid NBMs with fluorescent imaging dyes is still more advantageous than some of the other techniques such as SEM or AFM which can be expensive, time consuming, and only examine a small area of provided tissue sample. Using Oil red O for fluorescent microscopy allows to prepare multiple sections simultaneously, at a relatively low cost. In past published literature, Oil red O was used for characterisation of Collagen-Liposome-Chondroitin Sulfate Matrix [221] and for detection of lipid vectors in neural cell culture and in brain tissue [147]. In this PhD project, the use of this staining, combined with other standard histopathology staining (H&E) provided in depth understanding on the accumulation of the liposomes in number of organs and impact on the surrounding tissue. To the best of my knowledge, this is the first time Oil red O was used in combination with another marker for fluorescent detection of liposomes *in vitro* or *ex vivo*, making the research presented in this thesis first of its kind. Therefore the results presented in chapter 3, combined with the optimised methodologies of chapter 2, contribute to the understanding of the liposome accumulation in various organs, tissues and associated potential immune response.

Iron oxide magnetic nanoparticles (MNPs) was the second representative material of choice for this PhD project, as presented in chapter 4 and 5. The two case studies were designed to assess MNPs toxicity and immune response when used as medical technology in magnetic hyperthermia applications. From the safety perspective, it is important to determine the levels of iron accumulated in organs, as its overload can lead to toxicity. Furthermore, the data on biodistribution and organ accumulation of MNPs is required by the regulators as part of the clinical dossier for parenteral applications. Unlike liposomes, iron can be detected in tissue sections using Perls' Prussian blue stain. However, limited studies are available on semi-quantitative analysis of iron content in tissues after staining due to time consuming image processing required for the analysis. To overcome this hurdle, a methodology for computerized segmentation using Machine Learning (ML) was developed during this PhD thesis, as presented in chapter 4, achieving consistent and accurate results as proven by the calculated statistics used to validate the ML model. Furthermore, the accuracy of this method in estimating the levels of iron accumulation in tissues was confirmed in chapter 5, by means of gold standards for biodistribution through quantitative measurement via ICP-MS, and also evaluated via histopathology standard practice via large tissue slides scoring. Interestingly, the results obtained via the tissue image processing and ML segmentation mirrored the conclusions reported from the ICP-MS quantitative technique, were a dose-dependent increase in iron concentration was seen in several organs. The findings from the histological tissues scoring captured the general aspects associated with the MNP accumulation and biodistribution across all organs and animals exposed.

Nonetheless, it did not provide sufficient evidence to clearly report on the differences in the iron levels between the control and MNP exposed animals. This was particularly evident, for instance, in the spleen of control animals and those injected with the MNPs. However, the iron MNP case study provided the ground for consideration on the use of parallel, or complementary, techniques to adopt when observing, recording and assessing the accumulation of iron in tissues.

The application of the semi-quantitative method using ML was initially used on representative images from traditional 2D histology sections and was then advanced to 3D histology volumes, as presented in chapter 5 where shape of different iron aggregates in lung tissue was measured using shape descriptors. Interestingly, one of the formulations (RCL-01) showed to be more spherical in the type of aggregates observed in the animals injected with increasing doses of this MNP. To the best of my knowledge, this is the first study where the morphology of the aggregates formed by MNPs in tissue was assessed semi-quantitatively by ML using shape descriptors. As shape and size of the aggregates can influence the rate of clearance, this type of analysis can significantly contribute to the safety studies of MNPs.

To maximize the information obtained from the histology sections, two specialised stains were adopted in chapter 5 to evaluate the effect of MNPs on the cells of innate branch of the immune system. Modified toluidine blue stain was used to investigate the response of mast cells to MNPs accumulated in the lung. Mast cells were found to be activated by RCL-01 as indicated by their degranulation. Furthermore, number of eosinophils were also found in the same area, indicating a release of chemoattractant histamine by the mast cells, suggesting a response similar to an allergic reaction. Immunofluorescent staining was used to confirm the uptake of the MNPs by phagocytic cells and assess the degradation of the MNP dextran coating. This was achieved using immunofluorescent co-staining for dextran and phagocytic cell marker CD68. Interestingly, by using this technique, it was determined that iron aggregates, present in pulmonary vasculature of animals injected with NOC0007, were in fact contained within the phagocytic cells. Such in depth analysis was not observed and consistently recorded with the H&E or Perls' Prussian blue stained sections due to the partial or complete masking of the cellular features such as nuclei by the solid dark iron nanoparticle or aggregates. Furthermore, the results obtained from immunofluorescent staining indicated that dextran coating was still present on RCL-01 MNPs but was degraded in NOC0007 MNPs. Moreover, combined results of these stains and the results from the complement activation assay provided by the collaborator on the project confirmed an onset of an immune response cascade associated to the intravenously administered dextran coated RCL-01 MNPs. In brief, upon the MNP injection, C3b opsonin in the blood bound to the surface of MNPs priming it for engulfment by phagocytic cells. Simultaneously, complement protein

activation lead to activation of mast cells and release of histamine which acted as a chemoattractant for eosinophils also increasing C3b receptors on their surface. Despite the indication of an immune response to RCL-01, only mild pathological changes suggestive of toxicity were reported in all of the organs examined. This leads to the conclusion that both NOC0007 and RCL-01 can be regarded as safe for further preclinical assessment, as even at the relatively high doses, minimal pathological changes and immune response was seen.

Case studies presented in this thesis were undertaken as a part of pre-clinical investigation of novel nanobiomaterials where biodistribution and toxicity was investigated in histology sections. Although results presented here answered scientific questions set out at the beginning of the project, there are numerous aspects which need to be addressed in future studies. To account for sex differences at various physiological levels which could impact accumulation and degradation of NBMs such as the ones reported in case study 1, both male and female animals should be included in further investigations unless formulation is designed for gender specific disease (e.g.: ovarian cancer, prostate cancer). Furthermore, histological analysis should be standardised in terms of number of sections and investigating specific location or cell types within the organ. Recent advances in automation of histology studies such as development of automated stainers, whole slide scanners and use of artificial intelligence to extrapolate numerical data from images will improve reproducibility and comparability between studies.

Overall, the amount of evidence and experimental results presented in this thesis demonstrated how advanced tissue preparation and staining methodologies in histology can improve the safety profile analysis and assessment of NBMs at preclinical level. Similarly, to other assays used for preclinical investigations of NBMs, the methods used in this work were specifically tailored at investigating the physicochemical properties of the material under study, thus allowing the detection in organs *ex vivo* and improving the semi-quantitative analysis presented by the ML.

Overall looking at the specific aims set at the beginning of this thesis, for liposomes, (chapter 1 section 1.6):

i. To identify, test and verify a suitable histology stain for liposome detection.
ii. To differentiate between liposomes and naturally occurring lipids.

In the two case studies presented in chapter 3, liposomes were detected in a number of organs using Oil red O. Differentiation between naturally occurring lipids and liposomes was achieved by using a secondary marker in fluorescent imaging.

Whereas when looking at the specific aims set for assessing the iron oxide MNPs:

i. To perform qualitative and semi-quantitative analysis on iron deposits detected in various tissue sections with the use of ML.
ii. To reconstruct organ samples in 3D volumes for elucidating the complex distribution of particle accumulation in in vivo studies.

In chapter 4, semi-quantitative and qualitative assessment of iron levels in organs was achieved with use of ML for image segmentation. This method was further validated in chapter 5, where the obtained results were compared against the two gold standard techniques (ICP-MS and histology scoring) used to measure iron levels in tissue.

It can be therefore concluded that all the aims set out at the beginning of this PhD project were fully achieved providing strong evidence in support of the validity and positive response to the main hypothesis at the basis of the experimental-based research developed in this thesis.

Furthermore, from the bulk of evidence and data acquired, analysed and processed over the four case studies relevant to two NBM categories it can be concluded that these materials resulted to have a low toxicity profile and therefore can be considered to be safe for further clinical investigation.

7 Future work

As this PhD project had several objectives aimed at overcoming or resolving some of the limitations of current histopathology when applied to NBM, there are many more challenges to overcome in the future.

Number of chemicals (e.g. CPT-11) and lipids (e.g. soybean oil) possess autofluorescent properties which could potentially be examined to serve as a secondary marker for detection of liposomes in tissue sections. Therefore, future studies on this particle could use those properties for detection of liposomes simultaneously evaluating the metabolic state of cargo drug. Additionally, as discussed in previous section, method presented here for detection of liposomes is limited to rate of degradation. In both *in vivo* studies undertaken in this PhD project a single endpoint was used to evaluate biodistribution and accumulation of intravenously administered NBM. To fully examine accuracy of immunofluorescent co-staining for liposome detection *ex vivo*, a time course study should be carried out ranging from few hours post injection to several days.

Recently, research on MNPs for hyperthermia treatment shifted towards *in silico* studies where computational simulations are used to predict optimal conditions to achieve maximum therapeutic effect with minimal side effects [222, 223]. Up to date, studies in this area are based on the theoretical tumour models created in a specialised software such as COMSOL Multiphysics software. In this PhD project 3D histology volumes were segmented with use of ML to generate 3D volumes showing accumulation and aggregation of MNPs in different organs. Those segmented volumes can potentially be used in the future *in silico* experiments to predict optimal settings for a hyperthermia treatment in biologically relevant environments on a microscopic scale. Preliminary research in this area was carried out by the Nanomedicine and Molecular Imaging group in Trinity College Dublin using representative photomicrograph of a Perls' Prussian blue stained lung section to build a model for predicting thermal ablation [224]. It is anticipated that similar model will be developed in the future using segmented 3D volumes presented in this thesis. Furthermore, future work should focus on generating 3D volumes from co-labelled slides to visualize other aspects of the tissues such as blood vessels or localise specific cells. Such models would allow appropriate orientation and evaluation of the cellular biodistribution of NBMs. Further collaborative work with clinical histopathologists could create the ground for setting up the basis for ML adoption under the preclinical *in vivo* investigation with a view to maximise the outcome from ever animal study, reduce the number of animals used and also provide a predictive tool for *in silico* modelling.

Furthermore, *in vivo* studies presented in this thesis were limited to assessing organ specific toxicity of nanobiomaterials using histology. Future studies should include additional biochemical tests of plasma biomarkers associated with organ damage, as this type of assessment would be more adequate for clinical trials. Based on the findings presented in this thesis, these should include markers of liver damage such as alkaline phosphatase, aspartate transaminase, and alanine transaminase, as well as markers used to assess renal function including creatinine and kidney injury molecule-1.

Bibliography

1. Rauscher, H., et al., *Towards a review of the EC Recommendation for a definition of the term "nanomaterial" Part 1: Compilation of information concerning the experience with the definition*, J.R.C.I.f.H.a.C. Protection, Editor. 2014, Publications Office of the European Union: Online.
2. Pandit, A. and D.I. Zeugolis, *Twenty-five years of nano-bio-materials: have we revolutionized healthcare?* Nanomedicine, 2016. **11**(9): p. 985-987. https://doi.org/10.2217/nnm.16.42
3. Kumar, P., et al., *Comprehensive Survey on Nanobiomaterials for Bone Tissue Engineering Applications.* Nanomaterials, 2020. **10**(10). https://doi.org/10.3390/nano10102019
4. De Jong, W.H. and P.J.A. Borm, *Drug delivery and nanoparticles:applications and hazards.* International journal of nanomedicine, 2008. **3**(2): p. 133-149. https://doi.org/10.2147/IJN.S596
5. Singh, D., F. Dilnawaz, and S.K. Sahoo, *Challenges of moving theranostic nanomedicine into the clinic.* Nanomedicine, 2020. **15**(2): p. 111-114. https://doi.org/10.2217/nnm-2019-0401
6. Chen, F., E.B. Ehlerding, and W. Cai, *Theranostic nanoparticles.* Journal of nuclear medicine : official publication, Society of Nuclear Medicine, 2014. **55**(12): p. 1919-1922. https://doi.org/10.2967/jnumed.114.146019
7. Salama, L., et al., *Emerging Nanopharmaceuticals and Nanonutraceuticals in Cancer Management.* Biomedicines, 2020. **8**(9): p. 347. https://doi.org/10.3390/biomedicines8090347
8. Ventola, C.L., *Progress in Nanomedicine: Approved and Investigational Nanodrugs.* P & T : a peer-reviewed journal for formulary management, 2017. **42**(12): p. 742-755.
9. Hua, S., et al., *Current Trends and Challenges in the Clinical Translation of Nanoparticulate Nanomedicines: Pathways for Translational Development and Commercialization.* (1663-9812 (Print)).
10. Gioria, S., et al., *Are existing standard methods suitable for the evaluation of nanomedicines: some case studies.* Nanomedicine, 2018. **13**(5): p. 539-554. https://doi.org/10.2217/nnm-2017-0338
11. Halamoda-Kenzaoui, B., et al., *Mapping of the available standards against the regulatory needs for nanomedicines.* Wiley interdisciplinary reviews. Nanomedicine and nanobiotechnology, 2019. **11**(1): p. e1531-e1531. https://doi.org/10.1002/wnan.1531
12. Almeida, J.P.M., et al., *In vivo biodistribution of nanoparticles.* Nanomedicine, 2011. **6**(5): p. 815-835. https://doi.org/10.2217/nnm.11.79
13. Anselmo, A.C. and S. Mitragotri, *An overview of clinical and commercial impact of drug delivery systems.* Journal of controlled release : official journal of the Controlled Release Society, 2014. **190**: p. 15-28. https://doi.org/10.1016/j.jconrel.2014.03.053
14. Agency, E.M. *Conditional marketing authorisation*. 2021 [cited 2021; Available from: https://www.ema.europa.eu/en/human-regulatory/marketing-authorisation/conditional-marketing-authorisation.
15. Tenchov, R., et al., *Lipid Nanoparticles—From Liposomes to mRNA Vaccine Delivery, a Landscape of Research Diversity and Advancement.* ACS Nano, 2021. https://doi.org/10.1021/acsnano.1c04996
16. Hua, S., et al., *Current Trends and Challenges in the Clinical Translation of Nanoparticulate Nanomedicines: Pathways for Translational Development and Commercialization.* Frontiers in Pharmacology, 2018. **9**(790). https://doi.org/10.3389/fphar.2018.00790
17. Batty, C.J., E.M. Bachelder, and K.M. Ainslie, *Historical Perspective of Clinical Nano and Microparticle Formulations for Delivery of Therapeutics.* Trends in Molecular Medicine, 2021. **27**(6): p. 516-519. https://doi.org/10.1016/j.molmed.2021.04.002
18. Ananikov, V.P., *Organic-Inorganic Hybrid Nanomaterials.* Nanomaterials (Basel, Switzerland), 2019. **9**(9): p. 1197. https://doi.org/10.3390/nano9091197
19. Di Martino, A., et al., *Organic-inorganic hybrid nanoparticles controlled delivery system for anticancer drugs.* International Journal of Pharmaceutics, 2017. **526**(1): p. 380-390. https://doi.org/10.1016/j.ijpharm.2017.04.061
20. Ali, A., et al., *Synthesis, characterization, applications, and challenges of iron oxide nanoparticles.* Nanotechnology, science and applications, 2016. **9**: p. 49-67. https://doi.org/10.2147/NSA.S99986
21. Williams, H.M., *The application of magnetic nanoparticles in the treatment and monitoring of cancer and infectious diseases.* Bioscience Horizons: The International Journal of Student Research, 2017. **10**. https://doi.org/10.1093/biohorizons/hzx009
22. Elias, A. and A. Tsourkas, *Imaging circulating cells and lymphoid tissues with iron oxide nanoparticles.* Hematology, 2009. **2009**(1): p. 720-726. https://doi.org/10.1182/asheducation-2009.1.720

23. Corot, C., et al., *Recent advances in iron oxide nanocrystal technology for medical imaging.* Advanced Drug Delivery Reviews, 2006. **58**(14): p. 1471-1504. https://doi.org/10.1016/j.addr.2006.09.013
24. Tăculescu, E., et al., *Preclinical Aspects on Magnetic Iron Oxide Nanoparticles and Their Interventions as Anticancer Agents: Enucleation, Apoptosis and Other Mechanism*. 2018.
25. Mulens-Arias, V., et al., *Polyethylenimine-coated SPIONs trigger macrophage activation through TLR-4 signaling and ROS production and modulate podosome dynamics.* Biomaterials, 2015. **52**: p. 494-506. https://doi.org/10.1016/j.biomaterials.2015.02.068
26. Blank, F., et al., *Biomedical nanoparticles modulate specific CD4+ T cell stimulation by inhibition of antigen processing in dendritic cells.* Nanotoxicology, 2011. **5**(4): p. 606-621. https://doi.org/10.3109/17435390.2010.541293
27. Singh, N., et al., *Potential toxicity of superparamagnetic iron oxide nanoparticles (SPION).* Nano Reviews, 2010. **1**(1): p. 5358. https://doi.org/10.3402/nano.v1i0.5358
28. Hamm, B., et al., *Contrast-enhanced MR imaging of liver and spleen: First experience in humans with a new superparamagnetic iron oxide.* Journal of Magnetic Resonance Imaging, 1994. **4**(5): p. 659-668. https://doi.org/10.1002/jmri.1880040508
29. Toth, G.B., et al., *Current and potential imaging applications of ferumoxytol for magnetic resonance imaging.* Kidney international, 2017. **92**(1): p. 47-66. https://doi.org/10.1016/j.kint.2016.12.037
30. Shah, A. and M.A. Dobrovolskaia, *Immunological effects of iron oxide nanoparticles and iron-based complex drug formulations: Therapeutic benefits, toxicity, mechanistic insights, and translational considerations.* Nanomedicine : nanotechnology, biology, and medicine, 2018. **14**(3): p. 977-990. https://doi.org/10.1016/j.nano.2018.01.014
31. Simão, A.M.S., et al., *Liposomal systems as carriers for bioactive compounds.* Biophysical reviews, 2015. **7**(4): p. 391-397. https://doi.org/10.1007/s12551-015-0180-8
32. Zamboni, W.C., *Concept and Clinical Evaluation of Carrier-Mediated Anticancer Agents.* The Oncologist, 2008. **13**(3): p. 248-260. https://doi.org/10.1634/theoncologist.2007-0180
33. Nkanga, C., et al., *General Perception of Liposomes: Formation, Manufacturing and Applications*. 2019.
34. Sercombe, L., et al., *Advances and Challenges of Liposome Assisted Drug Delivery.* Frontiers in pharmacology, 2015. **6**: p. 286-286. https://doi.org/10.3389/fphar.2015.00286
35. Abu Lila, A.S., H. Kiwada, and T. Ishida, *The accelerated blood clearance (ABC) phenomenon: Clinical challenge and approaches to manage.* Journal of Controlled Release, 2013. **172**(1): p. 38-47. https://doi.org/10.1016/j.jconrel.2013.07.026
36. Beltrán-Gracia, E., et al., *Nanomedicine review: clinical developments in liposomal applications.* Cancer Nanotechnology, 2019. **10**(1): p. 11. https://doi.org/10.1186/s12645-019-0055-y
37. Anselmo, A.C. and S. Mitragotri, *Nanoparticles in the clinic.* Bioengineering & translational medicine, 2016. **1**(1): p. 10-29. https://doi.org/10.1002/btm2.10003
38. Nasimi, P. and M. Haidari, *Medical Use of Nanoparticles: Drug Delivery and Diagnosis Diseases.* International Journal of Green Nanotechnology, 2013. **1**: p. 1943089213506978. https://doi.org/10.1177/1943089213506978
39. Rizvi, S.A.A. and A.M. Saleh, *Applications of nanoparticle systems in drug delivery technology.* Saudi pharmaceutical journal : SPJ : the official publication of the Saudi Pharmaceutical Society, 2018. **26**(1): p. 64-70. https://doi.org/10.1016/j.jsps.2017.10.012
40. Wahajuddin and S. Arora, *Superparamagnetic iron oxide nanoparticles: magnetic nanoplatforms as drug carriers.* International journal of nanomedicine, 2012. **7**: p. 3445-3471. https://doi.org/10.2147/IJN.S30320
41. A. Abdelaziz, O., et al., *Superparamagnetic Iron Oxide Nanoparticles (SPIONs): Preparation and Recent Applications.* 2020. https://doi.org/10.3390/ma12040617
42. Janko, C., et al., *Functionalized Superparamagnetic Iron Oxide Nanoparticles (SPIONs) as Platform for the Targeted Multimodal Tumor Therapy.* Frontiers in oncology, 2019. **9**: p. 59-59. https://doi.org/10.3389/fonc.2019.00059
43. Hervault, A., et al., *Doxorubicin loaded dual pH- and thermo-responsive magnetic nanocarrier for combined magnetic hyperthermia and targeted controlled drug delivery applications.* Nanoscale, 2016. **8**(24): p. 12152-12161. https://doi.org/10.1039/C5NR07773G
44. Bamrungsap, S., et al., *Nanotechnology in therapeutics: a focus on nanoparticles as a drug delivery system.* Nanomedicine, 2012. **7**(8): p. 1253-1271. https://doi.org/10.2217/nnm.12.87
45. Simonazzi, A., et al., *Nanotechnology applications in drug controlled release*. 2018. p. 81-116.

46. Chang, T.C., et al., *Phase I study of nanoliposomal irinotecan (PEP02) in advanced solid tumor patients.* Cancer Chemotherapy and Pharmacology, 2015. **75**(3): p. 579-586. https://doi.org/10.1007/s00280-014-2671-x
47. Roy, A.C., et al., *A randomized phase II study of PEP02 (MM-398), irinotecan or docetaxel as a second-line therapy in patients with locally advanced or metastatic gastric or gastro-oesophageal junction adenocarcinoma†.* Annals of Oncology, 2013. **24**(6): p. 1567-1573. https://doi.org/10.1093/annonc/mdt002
48. Benoist, C., et al., *PEPCOL: a GERCOR randomized phase II study of nanoliposomal irinotecan PEP02 (MM-398) or irinotecan with leucovorin/5-fluorouracil as second-line therapy in metastatic colorectal cancer.* Cancer Medicine, 2016. **5**(4): p. 676-683. https://doi.org/10.1002/cam4.635
49. Kim, J., N. Lee, and T. Hyeon, *Recent development of nanoparticles for molecular imaging.* Philosophical Transactions of the Royal Society A: Mathematical, Physical and Engineering Sciences, 2017. **375**(2107): p. 20170022. https://doi.org/10.1098/rsta.2017.0022
50. Nune, S.K., et al., *Nanoparticles for biomedical imaging.* Expert opinion on drug delivery, 2009. **6**(11): p. 1175-1194. https://doi.org/10.1517/17425240903229031
51. Kiessling, F., et al., *Nanoparticles for Imaging: Top or Flop?* Radiology, 2014. **273**(1): p. 10-28. https://doi.org/10.1148/radiol.14131520
52. Thomas, R., I.-K. Park, and Y.Y. Jeong, *Magnetic Iron Oxide Nanoparticles for Multimodal Imaging and Therapy of Cancer.* International Journal of Molecular Sciences, 2013. **14**(8). https://doi.org/10.3390/ijms140815910
53. Jeon, M., et al., *Iron Oxide Nanoparticles as T1 Contrast Agents for Magnetic Resonance Imaging: Fundamentals, Challenges, Applications, and Prospectives.* Advanced Materials, 2021. **33**(23): p. 1906539. https://doi.org/10.1002/adma.201906539
54. Dulińska-Litewka, J., et al., *Superparamagnetic Iron Oxide Nanoparticles-Current and Prospective Medical Applications.* Materials (Basel, Switzerland), 2019. **12**(4): p. 617. https://doi.org/10.3390/ma12040617
55. Jin, R., et al., *Superparamagnetic iron oxide nanoparticles for MR imaging and therapy: design considerations and clinical applications.* Current Opinion in Pharmacology, 2014. **18**: p. 18-27. https://doi.org/10.1016/j.coph.2014.08.002
56. Mahmoudi, M., et al., *Superparamagnetic iron oxide nanoparticles: promises for diagnosis and treatment of multiple sclerosis.* ACS chemical neuroscience, 2011. **2**(3): p. 118-140. https://doi.org/10.1021/cn100100e
57. Williams, B.D., et al., *Imaging in rheumatoid arthritis using liposomes labelled with technetium.* British medical journal (Clinical research ed.), 1986. **293**(6555): p. 1143-1144. 10.1136/bmj.293.6555.1143-a
58. Henze, A., et al., *Radio-opaque liposomes for the improved visualisation of focal liver disease by computerized tomography.* Computerized Medical Imaging and Graphics, 1989. **13**(6): p. 455-462. https://doi.org/10.1016/0895-6111(89)90286-3
59. Lamichhane, N., et al., *Liposomes: Clinical Applications and Potential for Image-Guided Drug Delivery.* Molecules, 2018. **23**(2). https://doi.org/10.3390/molecules23020288
60. Cheng, M.H.Y., et al., *Stable J-aggregation of an aza-BODIPY-lipid in a liposome for optical cancer imaging.* Angewandte Chemie, 2019. https://doi.org/10.1002/anie.201907754
61. Li, S., et al., *Novel Multifunctional Theranostic Liposome Drug Delivery System: Construction, Characterization, and Multimodality MR, Near-Infrared Fluorescent, and Nuclear Imaging.* Bioconjugate Chemistry, 2012. **23**(6): p. 1322-1332. https://doi.org/10.1021/bc300175d
62. Prasad, R., et al., *Liposomal nanotheranostics for multimode targeted in vivo bioimaging and near-infrared light mediated cancer therapy.* Communications Biology, 2020. **3**(1): p. 284. https://doi.org/10.1038/s42003-020-1016-z
63. Moroz, P., S.K. Jones, and B.N. Gray, *Magnetically mediated hyperthermia: current status and future directions.* International Journal of Hyperthermia, 2002. **18**(4): p. 267-284. https://doi.org/10.1080/02656730110108785
64. Nelson, N.R., J.D. Port, and M.K. Pandey, *Use of Superparamagnetic Iron Oxide Nanoparticles (SPIONs) via Multiple Imaging Modalities and Modifications to Reduce Cytotoxicity: An Educational Review.* Journal of Nanotheranostics, 2020. **1**(1). https://doi.org/10.3390/jnt1010008
65. Rodrigues, H.F., G. Capistrano, and A.F. Bakuzis, *In vivo magnetic nanoparticle hyperthermia: a review on preclinical studies, low-field nano-heaters, noninvasive thermometry and computer simulations for treatment planning.* International Journal of Hyperthermia, 2020. **37**(3): p. 76-99. https://doi.org/10.1080/02656736.2020.1800831

66. Chatterjee, D.K., P. Diagaradjane, and S. Krishnan, *Nanoparticle-mediated hyperthermia in cancer therapy.* Therapeutic delivery, 2011. **2**(8): p. 1001-1014. https://doi.org/10.4155/tde.11.72
67. Hannon, G., et al., *Comparing the Effects of Intracellular and Extracellular Magnetic Hyperthermia on the Viability of BxPC-3 Cells.* Nanomaterials, 2020. **10**(3). https://doi.org/10.3390/nano10030593
68. Shetake, N.G., et al., *Magnetic nanoparticle-mediated hyperthermia therapy induces tumour growth inhibition by apoptosis and Hsp90/AKT modulation.* International Journal of Hyperthermia, 2015. **31**(8): p. 909-919. https://doi.org/10.3109/02656736.2015.1075072
69. Ding, W., et al., *Magnetic Testis Targeting and Magnetic Hyperthermia for Noninvasive, Controllable Male Contraception via Intravenous Administration.* Nano Letters, 2021. **21**(14): p. 6289-6297. https://doi.org/10.1021/acs.nanolett.1c02181
70. Moyer, T.J., A.C. Zmolek, and D.J. Irvine, *Beyond antigens and adjuvants: formulating future vaccines.* The Journal of clinical investigation, 2016. **126**(3): p. 799-808. https://doi.org/10.1172/JCI81083
71. Wang, N., M. Chen, and T. Wang, *Liposomes used as a vaccine adjuvant-delivery system: From basics to clinical immunization.* Journal of controlled release : official journal of the Controlled Release Society, 2019. **303**: p. 130-150. https://doi.org/10.1016/j.jconrel.2019.04.025
72. Nisini, R., et al., *The Multirole of Liposomes in Therapy and Prevention of Infectious Diseases.* Frontiers in Immunology, 2018. **9**(155). https://doi.org/10.3389/fimmu.2018.00155
73. Watson, D.S., A.N. Endsley, and L. Huang, *Design considerations for liposomal vaccines: influence of formulation parameters on antibody and cell-mediated immune responses to liposome associated antigens.* Vaccine, 2012. **30**(13): p. 2256-2272. https://doi.org/10.1016/j.vaccine.2012.01.070
74. Kad, A., et al., *An Elucidative Review to Analytically Sieve the Viability of Nanomedicine Market.* Journal of Pharmaceutical Innovation, 2020. https://doi.org/10.1007/s12247-020-09495-5
75. Halamoda Kenzaoui, B., Box, H., Van Elk, M., Gaitan, S., Geertsma, R., Gainza Lafuente, E., Owen, A., Del Pozo, A., Roesslein, M. and Bremer, S, *Anticipation of regulatory needs for nanotechnology-enabled health products.* 2019. https://data.europa.eu/doi/10.2760/599552
76. Germain, M., et al., *Delivering the power of nanomedicine to patients today.* Journal of Controlled Release, 2020. **326**: p. 164-171. https://doi.org/10.1016/j.jconrel.2020.07.007
77. Yang, L., et al., *Size dependent biodistribution and toxicokinetics of iron oxide magnetic nanoparticles in mice.* Nanoscale, 2015. **7**(2): p. 625-636. https://doi.org/10.1039/C4NR05061D
78. Kraft, J.C., et al., *Emerging research and clinical development trends of liposome and lipid nanoparticle drug delivery systems.* Journal of pharmaceutical sciences, 2014. **103**(1): p. 29-52. https://doi.org/10.1002/jps.23773
79. Champion, J.A. and S. Mitragotri, *Role of target geometry in phagocytosis.* Proceedings of the National Academy of Sciences of the United States of America, 2006. **103**(13): p. 4930-4934. https://doi.org/10.1073/pnas.0600997103
80. Rawal, M., A. Singh, and M.M. Amiji, *Quality-by-Design Concepts to Improve Nanotechnology-Based Drug Development.* Pharmaceutical Research, 2019. **36**(11): p. 153. https://doi.org/10.1007/s11095-019-2692-6
81. Elci, S.G., et al., *Surface Charge Controls the Suborgan Biodistributions of Gold Nanoparticles.* ACS Nano, 2016. **10**(5): p. 5536-5542. https://doi.org/10.1021/acsnano.6b02086
82. Baboci, L., et al., *The Dual Role of the Liver in Nanomedicine as an Actor in the Elimination of Nanostructures or a Therapeutic Target.* Journal of oncology, 2020. **2020**: p. 4638192-4638192. https://doi.org/10.1155/2020/4638192
83. Wan, R., et al., *Cobalt nanoparticles induce lung injury, DNA damage and mutations in mice.* Particle and Fibre Toxicology, 2017. **14**(1): p. 38. https://doi.org/10.1186/s12989-017-0219-z
84. Vallières, F., et al., *Activation of human AML14.3D10 eosinophils by nanoparticles: Modulatory activity on apoptosis and cytokine production.* Journal of Immunotoxicology, 2016. **13**(6): p. 817-826. https://doi.org/10.1080/1547691X.2016.1203379
85. Vanharen, M. and D. Girard, *Activation of Human Eosinophils with Nanoparticles: a New Area of Research.* Inflammation, 2020. **43**(1): p. 8-16. https://doi.org/10.1007/s10753-019-01064-4
86. Keshavan, S., et al., *Nano-bio interactions: a neutrophil-centric view.* Cell Death & Disease, 2019. **10**(8): p. 569. https://doi.org/10.1038/s41419-019-1806-8
87. Hannon, G., et al., *Immunotoxicity Considerations for Next Generation Cancer Nanomedicines.* Advanced Science, 2019. **6**(19): p. 1900133. https://doi.org/10.1002/advs.201900133

88. Kozma, G.T., et al., *Pseudo-anaphylaxis to Polyethylene Glycol (PEG)-Coated Liposomes: Roles of Anti-PEG IgM and Complement Activation in a Porcine Model of Human Infusion Reactions.* ACS Nano, 2019. **13**(8): p. 9315-9324. https://doi.org/10.1021/acsnano.9b03942
89. Ziv, O., R.R. Avtalion, and S. Margel, *Immunogenicity of bioactive magnetic nanoparticles: Natural and acquired antibodies.* Journal of Biomedical Materials Research Part A, 2008. **85A**(4): p. 1011-1021. https://doi.org/10.1002/jbm.a.31518
90. Kozma, G.T., et al., *Anti-PEG antibodies: Properties, formation, testing and role in adverse immune reactions to PEGylated nano-biopharmaceuticals.* Advanced Drug Delivery Reviews, 2020. **154-155**: p. 163-175. https://doi.org/10.1016/j.addr.2020.07.024
91. Ishizawa, K., et al., *Evaluation of tissue-clearing techniques for intraorgan imaging of distribution of polymeric nanoparticles as drug carriers.* Drug Development and Industrial Pharmacy, 2020. **46**(12): p. 2061-2069. https://doi.org/10.1080/03639045.2020.1843476
92. Magee, D., et al., *Histopathology in 3D: From three-dimensional reconstruction to multi-stain and multi-modal analysis.* Journal of Pathology Informatics, 2015. **6**(1): p. 6-6. 10.4103/2153-3539.151890
93. Gibson-Corley, K.N., A.K. Olivier, and D.K. Meyerholz, *Principles for valid histopathologic scoring in research.* Veterinary pathology, 2013. **50**(6): p. 1007-1015. https://doi.org/10.1177/0300985813485099
94. Porter, D.W., et al., *Mouse pulmonary dose- and time course-responses induced by exposure to multi-walled carbon nanotubes.* Toxicology, 2010. **269**(2): p. 136-147. https://doi.org/10.1016/j.tox.2009.10.017
95. Meijering, E., et al., *Imagining the future of bioimage analysis.* Nature Biotechnology, 2016. **34**(12): p. 1250-1255. https://doi.org/10.1038/nbt.3722
96. Uchida, S., *Image processing and recognition for biological images.* Development, growth & differentiation, 2013. **55**(4): p. 523-549. https://doi.org/10.1111/dgd.12054
97. Rodrigues, D., et al., *Quantitative histochemistry for macrophage biodistribution on mice liver and spleen after the administration of a pharmacological-relevant dose of polyacrylic acid-coated iron oxide nanoparticles.* Nanotoxicology, 2017. **11**(2): p. 256-266. https://doi.org/10.1080/17435390.2017.1291865
98. Miller, N., et al., *High-Throughput Image Analysis of Lipid-Droplet-Bound Mitochondria.* bioRxiv, 2020: p. 2020.03.10.985929. https://doi.org/10.1101/2020.03.10.985929
99. Gupta, R., et al., *Artificial intelligence to deep learning: machine intelligence approach for drug discovery.* Molecular diversity, 2021: p. 1-46. https://doi.org/10.1007/s11030-021-10217-3
100. Benjamens, S., P. Dhunnoo, and B. Meskó, *The state of artificial intelligence-based FDA-approved medical devices and algorithms: an online database.* npj Digital Medicine, 2020. **3**(1): p. 118. https://doi.org/10.1038/s41746-020-00324-0
101. *Fiji/ImageJ*. [cited 2021; Available from: https://imagej.net/software/fiji/.
102. Arganda-Carreras, I., et al., *Trainable Weka Segmentation: a machine learning tool for microscopy pixel classification.* Bioinformatics, 2017. **33**(15): p. 2424-2426. https://doi.org/10.1093/bioinformatics/btx180
103. Sikpa, D., et al., *Automated detection and quantification of breast cancer brain metastases in an animal model using democratized machine learning tools.* Scientific Reports, 2019. **9**(1): p. 17333. https://doi.org/10.1038/s41598-019-53911-x
104. Caffrey, B.J., et al., *Semi-automated 3D segmentation of human skeletal muscle using Focused Ion Beam-Scanning Electron Microscopic images.* Journal of Structural Biology, 2019. **207**(1): p. 1-11. https://doi.org/10.1016/j.jsb.2019.03.008
105. Breiman, L., *Random Forests.* Machine Learning, 2001. **45**(1): p. 5-32. https://doi.org/10.1023/A:1010933404324
106. Luque, A., et al., *The impact of class imbalance in classification performance metrics based on the binary confusion matrix.* Pattern Recognition, 2019. **91**: p. 216-231. https://doi.org/10.1016/j.patcog.2019.02.023
107. Dice, L.R., *Measures of the Amount of Ecologic Association Between Species.* Ecology, 1945. **26**(3): p. 297-302. https://doi.org/10.2307/1932409
108. Jaccard, P., *Nouvelles recherches sur la distribution florale*. 1908, Lausanne: Rouge.
109. Sokolova, M., N. Japkowicz, and S. Szpakowicz. *Beyond Accuracy, F-Score and ROC: A Family of Discriminant Measures for Performance Evaluation*. in *AI 2006: Advances in Artificial Intelligence*. 2006. Berlin, Heidelberg: Springer Berlin Heidelberg.

110. Daskalaki, S., I. Kopanas, and N. Avouris, *Evaluation of classifiers with uneven class distribution problem.* Applied Artificial Intelligence, 2006. **20**(5): p. 381-417. https://doi.org/10.1080/08839510500313653
111. Tharwat, A., *Classification assessment methods.* Applied Computing and Informatics, 2021. **17**(1): p. 168-192. https://doi.org/10.1016/j.aci.2018.08.003
112. Chicco, D. and G. Jurman, *The advantages of the Matthews correlation coefficient (MCC) over F1 score and accuracy in binary classification evaluation.* BMC Genomics, 2020. **21**(1): p. 6. https://doi.org/10.1186/s12864-019-6413-7
113. Valuations, E. *A review on evaluation metrics for data classification evaluations*. 2015.
114. Winkler, D.A., *Role of Artificial Intelligence and Machine Learning in Nanosafety.* Small, 2020. **16**(36): p. 2001883. https://doi.org/10.1002/smll.202001883
115. *Quantitative nanostructure-toxicity relationships workshop*. [cited 2021; Available from: https://www.nanowerk.com/news/newsid=19941.php.
116. Jacquart, A., et al., *LipImage™ 815: novel dye-loaded lipid nanoparticles for long-term and sensitive in vivo near-infrared fluorescence imaging.* Journal of Biomedical Optics, 2013. **18**(10): p. 1-9. https://doi.org/10.1117/1.JBO.18.10.101311
117. Agency, E.M., *Assessment report*. 2016.
118. Ruehl-Fehlert, C., et al., *Revised guides for organ sampling and trimming in rats and mice – Part 1: A joint publication of the RITA1 1RITA: Registry of Industrial Toxicology Animal-data.* . Experimental and Toxicologic Pathology, 2003. **55**(2): p. 91-106. https://doi.org/10.1078/0940-2993-00311
119. Mehlem, A., et al., *Imaging of neutral lipids by oil red O for analyzing the metabolic status in health and disease.* Nature Protocols, 2013. **8**(6): p. 1149-1154. https://doi.org/10.1038/nprot.2013.055
120. Koopman, R., G. Schaart, and M.K. Hesselink, *Optimisation of oil red O staining permits combination with immunofluorescence and automated quantification of lipids.* Histochemistry and Cell Biology, 2001. **116**(1): p. 63-68. https://doi.org/10.1007/s004180100297
121. IHC WORLD, L. *H&E staining method and protocol*. 2003 [cited 2017 September]; Available from: http://www.ihcworld.com/_protocols/special_stains/HE_Harris.htm.
122. Edge, D., et al., *Pharmacokinetics and bio-distribution of novel super paramagnetic iron oxide nanoparticles (SPIONs) in the anaesthetized pig.* Clinical and Experimental Pharmacology and Physiology, 2016. **43**(3): p. 319-326. https://doi.org/10.1111/1440-1681.12533
123. Graham, J., *Homogenization of Mammalian Tissues.* TheScientificWorldJOURNAL, 2002. **2**. https://doi.org/10.1100/tsw.2002.849
124. Martinkova, P., et al., *Iron Oxide Nanoparticles: Innovative Tool in Cancer Diagnosis and Therapy.* Advanced Healthcare Materials, 2018. **7**(5): p. 1700932. https://doi.org/10.1002/adhm.201700932
125. *Particle Analysis* [cited 2021; Available from: https://imagej.net/imaging/particle-analysis.
126. *TrakEM2*. [cited 2021; Available from: https://imagej.net/plugins/trakem2/.
127. de Chaumont, F., et al., *Icy: an open bioimage informatics platform for extended reproducible research.* Nature Methods, 2012. **9**(7): p. 690-696. https://doi.org/10.1038/nmeth.2075
128. *BioVoxxel Toolbox*. [cited 2021; Available from: https://imagej.net/plugins/biovoxxel-toolbox.
129. Landsman, M.L., et al., *Light-absorbing properties, stability, and spectral stabilization of indocyanine green.* Journal of Applied Physiology, 1976. **40**(4): p. 575-583. https://doi.org/10.1152/jappl.1976.40.4.575
130. Benson, R.C. and H.A. Kues, *Fluorescence properties of indocyanine green as related to angiography.* Physics in Medicine and Biology, 1978. **23**(1): p. 159-163. https://doi.org/10.1088/0031-9155/23/1/017
131. Desmettre, T., J.M. Devoisselle, and S. Mordon, *Fluorescence Properties and Metabolic Features of Indocyanine Green (ICG) as Related to Angiography.* Survey of Ophthalmology, 2000. **45**(1): p. 15-27. https://doi.org/10.1016/S0039-6257(00)00123-5
132. Fuchs, C., E.P. Mitchell, and P.M. Hoff, *Irinotecan in the treatment of colorectal cancer.* Cancer Treatment Reviews, 2006. **32**(7): p. 491-503. https://doi.org/10.1016/j.ctrv.2006.07.001
133. Kondo, R., et al., *A Phase II Study of Irinotecan for Patients with Previously Treated Small-Cell Lung Cancer.* Oncology, 2018. **94**(4): p. 223-232. https://doi.org/10.1159/000486622
134. Rothenberg, M.L., *Irinotecan (CPT-11): Recent Developments and Future Directions–Colorectal Cancer and Beyond.* The Oncologist, 2001. **6**(1): p. 66-80. https://doi.org/10.1634/theoncologist.6-1-66

135. Look, K.Y., et al., *A Phase II Trial of CPT-11 in Recurrent Squamous Carcinoma of the Cervix: A Gynecologic Oncology Group Study.* Gynecologic Oncology, 1998. **70**(3): p. 334-338. https://doi.org/10.1006/gyno.1998.5129
136. Verschraegen, C.F., et al., *Phase II study of irinotecan in prior chemotherapy-treated squamous cell carcinoma of the cervix.* Journal of Clinical Oncology, 1997. **15**(2): p. 625-631. 10.1200/jco.1997.15.2.625
137. Kurzrock, R., et al., *Safety, pharmacokinetics, and activity of EZN-2208, a novel conjugate of polyethylene glycol and SN38, in patients with advanced malignancies.* Cancer, 2012. **118**(24): p. 6144-6151. https://doi.org/10.1002/cncr.27647
138. Messerer, C.L., et al., *Liposomal Irinotecan.* Formulation Development and Therapeutic Assessment in Murine Xenograft Models of Colorectal Cancer, 2004. **10**(19): p. 6638-6649. https://doi.org/10.1158/1078-0432.CCR-04-0221
139. Wainberg, Z.A., et al., *NAPOLI-3: An open-label, randomized, phase III study of first-line liposomal irinotecan + 5-fluorouracil/leucovorin + oxaliplatin versus nab-paclitaxel + gemcitabine in patients with metastatic pancreatic ductal adenocarcinoma.* Journal of Clinical Oncology, 2020. **38**(15_suppl): p. TPS4661-TPS4661. 10.1200/JCO.2020.38.15_suppl.TPS4661
140. Wainberg, Z.A., et al., *First-line liposomal irinotecan with oxaliplatin, 5-fluorouracil and leucovorin (NALIRIFOX) in pancreatic ductal adenocarcinoma: A phase I/II study.* European Journal of Cancer, 2021. **151**: p. 14-24. https://doi.org/10.1016/j.ejca.2021.03.028
141. Ramnaraign, B.H., et al., *A phase II, open-label pilot study evaluating the safety and activity of liposomal irinotecan (Nal-IRI) in combination with 5-FU and oxaliplatin (NALIRIFOX) in preoperative treatment of pancreatic adenocarcinoma (NEO-Nal-IRI Study).* Journal of Clinical Oncology, 2021. **39**(3_suppl): p. TPS446-TPS446. 10.1200/JCO.2021.39.3_suppl.TPS446
142. Paz-Ares, L.G., et al., *RESILIENT part II: an open-label, randomized, phase III study of liposomal irinotecan injection in patients with small-cell lung cancer who have progressed with platinum-based first-line therapy.* Journal of Clinical Oncology, 2020. **38**(15_suppl): p. TPS9081-TPS9081. 10.1200/JCO.2020.38.15_suppl.TPS9081
143. Ponce, S., et al., *1793P RESILIENT part 1: Pharmacokinetics of second-line (2L) liposomal irinotecan in patients with small cell lung cancer (SCLC).* Annals of Oncology, 2020. **31**: p. S1038-S1039. 10.1016/j.annonc.2020.08.1554
144. Paz-Ares, L., et al., *P48.14 RESILIENT Part 2: A phase 3 Study of Liposomal Irinotecan in Patients with Small-Cell Lung Cancer in the Second-Line Setting.* Journal of Thoracic Oncology, 2021. **16**(3): p. S505. 10.1016/j.jtho.2021.01.884
145. Robson, A.-L., et al., *Advantages and Limitations of Current Imaging Techniques for Characterizing Liposome Morphology.* Frontiers in Pharmacology, 2018. **9**(80). https://doi.org/10.3389/fphar.2018.00080
146. Fonseca-Gomes, J., et al., *In vivo Bio-Distribution and Toxicity Evaluation of Polymeric and Lipid-Based Nanoparticles: A Potential Approach for Chronic Diseases Treatment.* International journal of nanomedicine, 2020. **15**: p. 8609-8621. https://doi.org/10.2147/IJN.S267007
147. Rizk, T., et al., *Pitfalls in the detection of lipid vectors in neural cell culture and in brain tissue.* Journal of Biomedical Materials Research Part A, 2004. **68A**(2): p. 360-364. https://doi.org/10.1002/jbm.a.20060
148. Mohammadpour, R., et al., *Subchronic and chronic toxicity evaluation of inorganic nanoparticles for delivery applications.* Advanced Drug Delivery Reviews, 2019. **144**: p. 112-132. https://doi.org/10.1016/j.addr.2019.07.006
149. Sayag, D., et al., *Phase-0/phase-I study of dye-loaded lipid nanoparticles for near-infrared fluorescence imaging in healthy dogs.* European Journal of Pharmaceutics and Biopharmaceutics, 2016. **100**: p. 85-93. https://doi.org/10.1016/j.ejpb.2016.01.001
150. Kandasamy, G. and D. Maity, *Recent advances in superparamagnetic iron oxide nanoparticles (SPIONs) for in vitro and in vivo cancer nanotheranostics.* International Journal of Pharmaceutics, 2015. **496**(2): p. 191-218. https://doi.org/10.1016/j.ijpharm.2015.10.058
151. Ferrero, R., et al., *Influence of shape, size and magnetostatic interactions on the hyperthermia properties of permalloy nanostructures.* Scientific Reports, 2019. **9**(1): p. 6591. https://doi.org/10.1038/s41598-019-43197-4
152. Mejías, R., et al., *Cell-Promoted Nanoparticle Aggregation Decreases Nanoparticle-Induced Hyperthermia under an Alternating Magnetic Field Independently of Nanoparticle Coating, Core Size, and Subcellular Localization.* ACS Applied Materials & Interfaces, 2019. **11**(1): p. 340-355. https://doi.org/10.1021/acsami.8b18451

153. Patil, R.M., et al., *Comprehensive cytotoxicity studies of superparamagnetic iron oxide nanoparticles.* Biochemistry and Biophysics Reports, 2018. **13**: p. 63-72. https://doi.org/10.1016/j.bbrep.2017.12.002
154. Singh, N., et al., *Potential toxicity of superparamagnetic iron oxide nanoparticles (SPION).* Nano reviews, 2010. **1**: p. 10.3402/nano.v1i0.5358. 10.3402/nano.v1i0.5358
155. Shreffler, J.W., et al., *Overcoming Hurdles in Nanoparticle Clinical Translation: The Influence of Experimental Design and Surface Modification.* International journal of molecular sciences, 2019. **20**(23): p. 6056. https://doi.org/10.3390/ijms20236056
156. Metselaar, J.M. and T. Lammers, *Challenges in nanomedicine clinical translation.* Drug Delivery and Translational Research, 2020. **10**(3): p. 721-725. https://doi.org/10.1007/s13346-020-00740-5
157. Hubbs, A.F., et al., *Nanotechnology: toxicologic pathology.* Toxicologic pathology, 2013. **41**(2): p. 395-409. https://doi.org/10.1177/0192623312467403
158. Ostrowski, A., et al., *Overview about the localization of nanoparticles in tissue and cellular context by different imaging techniques.* Beilstein Journal of Nanotechnology, 2015. **6**: p. 263-280. 10.3762/bjnano.6.25
159. Pham, B.T.T., et al., *Biodistribution and Clearance of Stable Superparamagnetic Maghemite Iron Oxide Nanoparticles in Mice Following Intraperitoneal Administration.* International journal of molecular sciences, 2018. **19**(1): p. 205. https://doi.org/10.3390/ijms19010205
160. Zhu, X.-M., et al., *Enhanced cellular uptake of aminosilane-coated superparamagnetic iron oxide nanoparticles in mammalian cell lines.* International journal of nanomedicine, 2012. **7**: p. 953-64. https://doi.org/10.2147/IJN.S28316
161. Arms, L., et al., *Advantages and Limitations of Current Techniques for Analyzing the Biodistribution of Nanoparticles.* Frontiers in Pharmacology, 2018. **9**: p. 802. https://doi.org/10.3389/fphar.2018.00802
162. Gramoun, A., et al., *Monitoring the effects of dexamethasone treatment by MRI using in vivo iron oxide nanoparticle-labeled macrophages.* Arthritis research & therapy, 2014. **16**: p. R131. https://doi.org/10.1186/ar4588
163. Yu, Q., et al., *Biodistribution and Toxicity Assessment of Superparamagnetic Iron Oxide Nanoparticles In Vitro and In Vivo.* Current Medical Science, 2018. **38**(6): p. 1096-1102. https://doi.org/10.1007/s11596-018-1989-8
164. Beckmann, N., et al., *Macrophage labeling by SPIO as an early marker of allograft chronic rejection in a rat model of kidney transplantation.* Magnetic Resonance in Medicine, 2003. **49**(3): p. 459-467. https://doi.org/10.1002/mrm.10387
165. Meijs, M., et al., *Robust Segmentation of the Full Cerebral Vasculature in 4D CT of Suspected Stroke Patients.* Scientific Reports, 2017. **7**(1): p. 15622. https://doi.org/10.1038/s41598-017-15617-w
166. Januszewski, M., et al., *High-precision automated reconstruction of neurons with flood-filling networks.* Nature Methods, 2018. **15**(8): p. 605-610. https://doi.org/10.1038/s41592-018-0049-4
167. Al-Janabi, S., et al., *Evaluation of Mitotic Activity Index in Breast Cancer Using Whole Slide Digital Images.* PLOS ONE, 2014. **8**(12): p. e82576. https://doi.org/10.1371/journal.pone.0082576
168. Saha, M., et al., *An Advanced Deep Learning Approach for Ki-67 Stained Hotspot Detection and Proliferation Rate Scoring for Prognostic Evaluation of Breast Cancer.* Scientific Reports, 2017. **7**(1): p. 3213. https://doi.org/10.1038/s41598-017-03405-5
169. Kossatz, S., et al., *High Therapeutic Efficiency of Magnetic Hyperthermia in Xenograft Models Achieved with Moderate Temperature Dosages in the Tumor Area.* Pharmaceutical Research, 2014. **31**(12): p. 3274-3288. https://doi.org/10.1007/s11095-014-1417-0
170. Ludwig, R., et al., *Nanoparticle-based hyperthermia distinctly impacts production of ROS, expression of Ki-67, TOP2A, and TPX2, and induction of apoptosis in pancreatic cancer.* International journal of nanomedicine, 2017. **12**: p. 1009-1018. https://doi.org/10.2147/IJN.S108577
171. Kossatz, S., et al., *Efficient treatment of breast cancer xenografts with multifunctionalized iron oxide nanoparticles combining magnetic hyperthermia and anti-cancer drug delivery.* Breast cancer research : BCR, 2015. **17**(1): p. 66-66. https://doi.org/10.1186/s13058-015-0576-1
172. Gavilán, H., et al., *How size, shape and assembly of magnetic nanoparticles give rise to different hyperthermia scenarios.* Nanoscale, 2021. **13**(37): p. 15631-15646. 10.1039/D1NR03484G
173. Torche, P., et al., *Thermodynamics of interacting magnetic nanoparticles.* Physical Review B, 2020. **101**(22): p. 224429. https://doi.org/10.1103/PhysRevB.101.224429

174. European Commission CORDIS. *Nanomedicine upscaling for early clinical phases of multimodal cancer therapy*. 2016 [cited 2019 18 January]; Available from: https://cordis.europa.eu/project/rcn/200812/factsheet/en.
175. Bogdanska, A., et al., *3D volume segmentation and reconstruction. Supervised image classification and automated quantification of superparamagnetic iron oxide nanoparticles in histology slides for safety assessment.* Nanotoxicology, 2021: p. 1-17. https://doi.org/10.1080/17435390.2021.1991502
176. Crosbie-Staunton, K., *Multiparametric evaluation of magnetic nanoparticles for theranostic applications in breast and pancreatic cancer*, in *Department of Clinical Medicine*. 2016, Trinity College, the University Dublin.
177. Mahmoudi, M., et al., *Assessing the In Vitro and In Vivo Toxicity of Superparamagnetic Iron Oxide Nanoparticles.* Chemical Reviews, 2012. **112**(4): p. 2323-2338. https://doi.org/10.1021/cr2002596
178. Gobbo, O.L., et al., *Magnetic Nanoparticles in Cancer Theranostics.* Theranostics, 2015. **5**(11): p. 1249-1263. 10.7150/thno.11544
179. Feng, Q., et al., *Uptake, distribution, clearance, and toxicity of iron oxide nanoparticles with different sizes and coatings.* Scientific Reports, 2018. **8**(1): p. 2082. https://doi.org/10.1038/s41598-018-19628-z
180. Ruiz, A., et al., *Biodistribution and pharmacokinetics of uniform magnetite nanoparticles chemically modified with polyethylene glycol.* Nanoscale, 2013. **5**(23): p. 11400-11408. https://doi.org/10.1039/C3NR01412F
181. Monge-Fuentes, V., et al., *Biodistribution and biocompatibility of DMSA-stabilized maghemite magnetic nanoparticles in nonhuman primates (Cebus spp.).* Nanomedicine, 2011. **6**(9): p. 1529-1544. https://doi.org/10.2217/nnm.11.47
182. Chaves, S.B., et al., *Light microscopy and magnetic resonance characterization of a DMSA-coated magnetic fluid in mice.* IEEE Transactions on Magnetics, 2002. **38**(5): p. 3231-3233. 10.1109/TMAG.2002.802495
183. Jain, T.K., et al., *Biodistribution, Clearance, and Biocompatibility of Iron Oxide Magnetic Nanoparticles in Rats.* Molecular Pharmaceutics, 2008. **5**(2): p. 316-327. https://doi.org/10.1021/mp7001285
184. Huang, J., et al., *Effects of Nanoparticle Size on Cellular Uptake and Liver MRI with Polyvinylpyrrolidone-Coated Iron Oxide Nanoparticles.* ACS Nano, 2010. **4**(12): p. 7151-7160. https://doi.org/10.1021/nn101643u
185. Nairz, M., et al., *"Pumping iron"-how macrophages handle iron at the systemic, microenvironmental, and cellular levels.* Pflugers Archiv : European journal of physiology, 2017. **469**(3-4): p. 397-418. https://doi.org/10.1007/s00424-017-1944-8
186. Lunov, O., et al., *Lysosomal degradation of the carboxydextran shell of coated superparamagnetic iron oxide nanoparticles and the fate of professional phagocytes.* Biomaterials, 2010. **31 34**: p. 9015-22. https://doi.org/10.1016/j.biomaterials.2010.08.003
187. Scindia, P.Y., M.D.J. Leeds, and M.D.S. Swaminathan, *Iron Homeostasis in Healthy Kidney and its Role in Acute Kidney Injury.* Seminars in Nephrology, 2019. **39**(1): p. 76-84. https://doi.org/10.1016/j.semnephrol.2018.10.006
188. Smith, C.P. and F. Thévenod, *Iron transport and the kidney*. Biochimica et Biophysica Acta (BBA) - General Subjects, 2009. **1790**(7): p. 724-730. https://doi.org/10.1016/j.bbagen.2008.10.010
189. Martines, A.M.F., et al., *Iron metabolism in the pathogenesis of iron-induced kidney injury*. Nature Reviews Nephrology, 2013. **9**(7): p. 385-398. https://doi.org/10.1038/nrneph.2013.98
190. Bellusci, M., et al., *Biodistribution and acute toxicity of a nanofluid containing manganese iron oxide nanoparticles produced by a mechanochemical process.* International journal of nanomedicine, 2014. **9**: p. 1919-1929. https://doi.org/10.2147/IJN.S56394
191. Edge, D., et al., *Assessment of renal function in the anaesthetised rat following injection of superparamagnetic iron oxide nanoparticles.* Canadian Journal of Physiology and Pharmacology, 2016. **95**(4): p. 443-446. https://doi.org/10.1139/cjpp-2016-0405
192. Gobbo, O.L., et al., *Biodistribution and pharmacokinetic studies of SPION using particle electron paramagnetic resonance, MRI and ICP-MS.* Nanomedicine, 2015. **10**(11): p. 1751-1760. https://doi.org/10.2217/nnm.15.22
193. Hall, A.P., et al., *Comparison of Computerized Image Analysis with Traditional Semiquantitative Scoring of Perls' Prussian Blue Stained Hepatic Iron Deposition.* Toxicologic Pathology, 2013. **41**(7): p. 992-1000. https://doi.org/10.1177/0192623313476576

194. Tsuchiya, K., et al., *Histological study of the biodynamics of iron oxide nanoparticles with different diameters.* International journal of nanomedicine, 2011. **6**: p. 1587-1594. https://doi.org/10.2147/IJN.S22189
195. Berning, M., Kevin M. Boergens, and M. Helmstaedter, *SegEM: Efficient Image Analysis for High-Resolution Connectomics.* Neuron, 2015. **87**(6): p. 1193-1206. https://doi.org/10.1016/j.neuron.2015.09.003
196. Sindhwani, S., et al., *Exploring Passive Clearing for 3D Optical Imaging of Nanoparticles in Intact Tissues.* Bioconjugate Chemistry, 2017. **28**(1): p. 253-259. https://doi.org/10.1021/acs.bioconjchem.6b00500
197. Sindhwani, S., et al., *Three-Dimensional Optical Mapping of Nanoparticle Distribution in Intact Tissues.* ACS Nano, 2016. **10**(5): p. 5468-5478. https://doi.org/10.1021/acsnano.6b01879
198. Kingston, B.R., et al., *Assessing micrometastases as a target for nanoparticles using 3D microscopy and machine learning.* Proceedings of the National Academy of Sciences, 2019. **116**(30): p. 14937. https://doi.org/10.1073/pnas.1907646116
199. Yang, L., et al., *Three-Dimensional Quantitative Co-Mapping of Pulmonary Morphology and Nanoparticle Distribution with Cellular Resolution in Nondissected Murine Lungs.* ACS Nano, 2019. **13**(2): p. 1029-1041. https://doi.org/10.1021/acsnano.8b07524
200. Yang, L., et al., *Multimodal Precision Imaging of Pulmonary Nanoparticle Delivery in Mice: Dynamics of Application, Spatial Distribution, and Dosimetry.* Small, 2019. **15**(49): p. 1904112. https://doi.org/10.1002/smll.201904112
201. Sanhaji, M., et al., *The phenotype of target pancreatic cancer cells influences cell death by magnetic hyperthermia with nanoparticles carrying gemicitabine and the pseudo-peptide NucAnt.* Nanomedicine: Nanotechnology, Biology and Medicine, 2019. **20**: p. 101983. https://doi.org/10.1016/j.nano.2018.12.019
202. Hannon, G., *Assessing the potential of iron oxide nanoparticles to treat cancer through magnetic hyperthermia*, in *Clinical Medicine*. 2020, Trinity College Dublin.
203. Sotocina, S.G., et al., *The Rat Grimace Scale: A Partially Automated Method for Quantifying Pain in the Laboratory Rat via Facial Expressions.* Molecular Pain, 2011. **7**: p. 1744-8069-7-55. https://doi.org/10.1186/1744-8069-7-55
204. *Stratigraphy and Sedimentation By W. C. Krumbein and L. L. Sloss. viii + 497 pp., 123 figs., W. H. Freeman & Co., San Francisco, 1951. Price $5.00.* Geological Journal, 1951. **1**(1): p. i-i. https://doi.org/10.1002/gj.3350010110
205. Zhou, C., et al., *Influence of particle shape on aggregate mixture's performance: DEM results.* Road Materials and Pavement Design, 2019. **20**(2): p. 399-413. https://doi.org/10.1080/14680629.2017.1396236
206. Bourrinet, P., et al., *Preclinical Safety and Pharmacokinetic Profile of Ferumoxtran-10, an Ultrasmall Superparamagnetic Iron Oxide Magnetic Resonance Contrast Agent.* Investigative Radiology, 2006. **41**(3). 10.1097/01.rli.0000197669.80475.dd
207. Rampton, D., et al., *Hypersensitivity reactions to intravenous iron: guidance for risk minimization and management.* Haematologica, 2014. **99**(11): p. 1671-1676. https://doi.org/10.3324/haematol.2014.111492
208. Awaad, A., *Histopathological and immunological changes induced by magnetite nanoparticles in the spleen, liver and genital tract of mice following intravaginal instillation.* The Journal of Basic & Applied Zoology, 2015. **71**: p. 32-47. https://doi.org/10.1016/j.jobaz.2015.03.003
209. Seely, J.C., G.C. Hard, and B. Blankenship, *Chapter 11 - Kidney*, in *Boorman's Pathology of the Rat (Second Edition)*, A.W. Suttie, Editor. 2018, Academic Press: Boston. p. 125-166.
210. Christensen, E.I. and A.B. Maunsbach, *Effects of dextran on lysosomal ultrastructure and protein digestion in renal proximal tubule.* Kidney International, 1979. **16**(3): p. 301-311. https://doi.org/10.1038/ki.1979.132
211. Ezeamuzie, C.I. and E. Philips, *Histamine H(2) receptors mediate the inhibitory effect of histamine on human eosinophil degranulation.* British journal of pharmacology, 2000. **131**(3): p. 482-488. https://doi.org/10.1038/sj.bjp.0703556
212. Anwar, A.R. and A.B. Kay, *H1-receptor dependence of histamine-induced enhancement of human eosinophil C3b rosettes.* Clinical and experimental immunology, 1980. **42**(1): p. 196-199.
213. Hannon, G., *Assessing the potential of iron oxide nanoparticles to treat cancer through magnetic hyperthermia*, in *School of medicine*. 2020, Trinity College Dublin.
214. Fülöp, T., et al., *Complement activation in vitro and reactogenicity of low-molecular weight dextran-coated SPIONs in the pig CARPA model: Correlation with physicochemical features and*

clinical information. Journal of Controlled Release, 2018. **270**: p. 268-274. https://doi.org/10.1016/j.jconrel.2017.11.043
215. Banda, N.K., et al., *Mechanisms of complement activation by dextran-coated superparamagnetic iron oxide (SPIO) nanoworms in mouse versus human serum.* Particle and Fibre Toxicology, 2014. **11**(1): p. 64. https://doi.org/10.1186/s12989-014-0064-2
216. Jasmin, et al., *Tracking stem cells with superparamagnetic iron oxide nanoparticles: perspectives and considerations.* International journal of nanomedicine, 2017. **12**: p. 779-793. https://doi.org/10.2147/IJN.S126530
217. Essajai, R., et al., *Shape-dependent structural and magnetic properties of Fe nanoparticles studied through simulation methods.* RSC Advances, 2019. **9**(38): p. 22057-22063. https://doi.org/10.1039/C9RA03047F
218. Manzin, A., R. Ferrero, and M. Vicentini, *From Micromagnetic to In Silico Modeling of Magnetic Nanodisks for Hyperthermia Applications.* 2021. **4**: p. 2100013. https://doi.org/10.1002/adts.202100013
219. Suleman, M. and S. Riaz, *3D in silico study of magnetic fluid hyperthermia of breast tumor using Fe3O4 magnetic nanoparticles.* Journal of Thermal Biology, 2020. **91**: p. 102635. https://doi.org/10.1016/j.jtherbio.2020.102635
220. Robson, A.-L., et al., *Advantages and Limitations of Current Imaging Techniques for Characterizing Liposome Morphology.* Frontiers in pharmacology, 2018. **9**: p. 80-80. 10.3389/fphar.2018.00080
221. Craciunescu, O., et al., *Preparation and Characterization of a Collagen-Liposome-Chondroitin Sulfate Matrix with Potential Application for Inflammatory Disorders Treatment.* Journal of Nanomaterials, 2014. **2014**: p. 903691. https://doi.org/10.1155/2014/903691
222. Sanz, B., et al., *In Silico before In Vivo: how to Predict the Heating Efficiency of Magnetic Nanoparticles within the Intracellular Space.* Scientific Reports, 2016. **6**(1): p. 38733. https://doi.org/10.1038/srep38733
223. Suleman, M. and S. Riaz, *In silico study of hyperthermia treatment of liver cancer using core-shell CoFe2O4@MnFe2O4 magnetic nanoparticles.* Journal of Magnetism and Magnetic Materials, 2020. **498**: p. 166143. https://doi.org/10.1016/j.jmmm.2019.166143
224. Alberti, M. and A. Prina-Mello, *Smart model of intrinsic loss power of SPIONs in hyperthermia treatment.* Journal of Magnetism and Magnetic Materials, 2020. **502**: p. 166493. https://doi.org/10.1016/j.jmmm.2020.166493
225. Vejjasilpa, K., et al., *Antitumor efficacy and intratumoral distribution of SN-38 from polymeric depots in brain tumor model.* Experimental Biology and Medicine, 2015. **240**(12): p. 1640-1647. https://doi.org/10.1177/1535370215590819
226. Slatter, J.G., et al., *Pharmacokinetics, Metabolism, and Excretion of Irinotecan (CPT-11) Following I.V. Infusion of CPT-11 in Cancer Patients.* Drug Metabolism and Disposition, 2000. **28**(4): p. 423-433.

8 Appendix

Supplementary table 8.1: List of reagents

Name	Manufacturer	Product code
10% Neutral Buffered Formalin	DiaPath	F0043
2-propanol	Fisher Scientific Ltd.	P/7507/7
Aquatex® aqueous mounting media	Merk	HC860590
Atipamezole hydrochloride	Pfizer	N/A
Citrate Buffer	DiaPath	T0050
DPX mountant	Thermo Scientific	LAMB/DPX
EDTA dehydrate	Avantor performance material	4040-00
Eosin Y	Sigma-Aldrich	HT110280-2.5L
FBS	Sigma-Aldrich	F7524
Gill II Haematoxylin	Merk	HX99311375
Harris Haematoxylin	RAL DIAGNOSTICS	361075-1000
Histo-Clear II	National Diagnostics	HS-202
Hoechst 33342	Invitrogen	H3570
Hydrochloric acid	Honeywell	30721-2.5L
Industrial Methylated Spirits (IMS)	Lennox	CRTSI0330716
Irinotecan hydrochloride	Sigma-Aldrich	101710411
Isopentane	ACROS Organics	126470010
Ketamine	Pfizer	N/A
Medetomidine hydrochloride	Pfizer	N/A
Nanoliposomal irinotecan (Onivyde®)	Merrimack	N/A
Normal Goat Serum	Invitrogen	10000C
Nuclear Fast Red	Sigma-Aldrich	60700-5G
Oil red O	Sigma-Aldrich	1002367522
Optimal Cutting Temperature (OCT) compound	Thermo Scientific	361603E
Penicillin-Streptomycin	Sigma-Aldrich	P4333-100ML
Phosphate Buffered Saline (PBS) Tablets	Fisher Scientific Ltd.	1282-1680
Potassium ferrocyanide	Honeywell	P3289-100G
Potassium phosphate	Fisher Scientific Ltd.	P285-500
ProLong diamond antifade mountant	Invitrogen	P36961
Rhodamine Phalloidin	Invitrogen	R415
RPMI	ThermoFisher Scientific	21875091
Sucrose	Fluka Analytical	60-090-557
Triton X-100	Sigma-Aldrich	93443
TrueBlack® Lipofuscin Autofluorescence Quencher	Biotium	23007
Xylenes	Honeywell	16446

Supplementary table 8.2: List of antibodies

Target	Species produced	Manufacturer	Conjugated	Reference	Country
Dextran	Mouse	STEMCELL Technologies	No	60026	Canada
CD68	Rabbit	Invitrogen	No	PA5-81594	China
rabbit IgG	Goat	Invitrogen	Alexa Fluor 594	R37117	USA
rabbit IgG	Goat	Invitrogen	Alexa Fluor 488	R37118	USA
Polyethylene Glycol	Rabbit	RevMAb Biosciences	No	31-1008-00	USA

Supplementary table 8.3: List of consumables

Product	Manufacturer	Product code
Catheter	Linton instruments	C10PU-RFA1310
Coverslip 0.13-0.17 mm thick	Fisher scientific	1237-3128
Microtome blades	Thermo Scientific	12191830
Needles	VWR International	613-2012
Plastic moulds	Ted Pella	27147-2
Superfrost microscopic slides	VWR International	631-0108
Syringe	ThermoFisher Scientific	S7510-1
Tungsten beads	QUIAGEN	69997
8-well chamber slides	Corning Incorporated	354118

Supplementary table 8.4: Imaging equipment

Name	Manufacturer	Model
Automated microscope	BioTek	LionheartTMFX
Light Microscope	Nikon	Eclipse E800
Confocal Microscope	Leica	SP8

Supplementary table 8.5: Software

Name	Publisher	Version
Gen5	BioTek	3
GraphPad Prism	GraphPad Software, San Diego, USA	V.5.01
Icy	BioImage Analysis unit, Institut Pasteur	1.9.10.0
Fiji	Wayne Rasband National Institutes of Health	1.51s

Supplementary table 8.6: Severity score sheet for mice after drug administration

Each day, the animals received a score based on body weight, activity, appearance and behaviour. Each score is associated with a specific action. The scoring system was approved by the HPRA; project license number AE19136/P073.

Score	Variables measured	Clinical signs of sickness	Care to be provided
0	Body weight Activity Appearance	Clinically normal	Baseline weight prior injection.
1	Body weight Activity Appearance/behaviour	Weight loss <10% Decreased Normal	Keep record in the monitoring log. Weight animal daily
2	Body weight Activity Appearance	Weight loss >10% Reduced Normal + dehydration[1]	Provide moistened food pellets on floor of the cage. Check temperature. At this stage, we will rehydrate the animal with daily subcutaneous injections of saline.
3	Body weight Activity Temperature Appearance	Weight loss >15% Animal is not moving willingly + a hunched posture cold when handled Dirty (decrease in grooming behaviour)	Separate weak mouse from stronger mice. Monitor and weight, animal 2 times per day. At this stage, the animal will receive water and food to compensate the dehydration and weight loss by oral gavage. A hypothermic animal will placed in an individual cage under an infrared lamp or a heating pad will be placed under the cage.
4	Body weight Activity Temperature Appetite	-Weight loss >20% -Animal is not moving + a hunched posture[2] -Inability to obtain food & water -Hind-limb paralysis or weakness -Persistent hypothermia -Anaemia as indicated by symptoms such as pale feet, or haematological measures	This animal must be euthanized immediately. It will be humanely sacrificed with CO_2 followed by post mortem analysis.

[1]When dehydrated the skin on the back of the neck stays tented up if pulled gently and released.

[2]head down, feet close together.

Supplementary table 8.7: Severity score sheet for rats after drug administration

Each day, the animals received a score based on body weight, activity, appearance and behaviour. Each score is associated with a specific action. The scoring system was approved by the HPRA; project license number AE19136/P089.

Score	Variables measured	Clinical signs of sickness	Care to be provided
0	Body weight Activity Appearance	Clinically normal	Baseline weight prior to injection.
1	Body weight Activity Appearance/behaviour	Weight loss <10% Decreased Normal Oculo-nasal discharge	Keep record in the monitoring log. Weight animal daily.
2	Body weight Activity Appearance/behaviour	Weight loss >10% Reduced Normal + dehydration piloerection Peer interaction and transient vocalisation subdued behaviour	Provide moistened food pellets on floor of the cage. Check temperature. Rehydrate with daily subcutaneous injections of saline. If pain suspected, administrate 0.05-0.1 mg/kg of buprenorphine subcutaneously.
3	Body weight Activity Appearance/behaviour	Weight loss >15% Animal is not moving willingly + a hunched posture, cold when handled. Dirty (decrease in grooming	Separate weak animal. Monitor and weight twice a day. Animal should receive water and food by oral gavage to compensate for dehydration and weight loss. A hypothermic animal should be placed in an individual cage under an infrared lamp or heating pad should be placed under the cage. If pain suspected, administrate 0.05-0.1 mg/kg of buprenorphine subcutaneously.
4	Body weight Activity Appearance/behaviour	Weight loss >20% Animal is not moving + a hunched posture. Inability to obtain food and water. Hind-limb paralysis or weakness Persistent hypothermia Anaemia as indicated by symptoms such as pale feet, or haematological measures	Animal must be euthanized immediately. Humane euthanasia with CO_2 followed by post mortem analysis.

8.1 Power calculation for *in vivo* studies

Proper consideration was afforded to experimental design throughout this project to ensure the minimum number of animals will be used. The experiments were based on well-established protocols and sample size calculations contained in previous projects undertaken by the group as well as data from the existing research literature. The numbers were also based on the power calculation in regards to previous results, with experimental design consulted with experienced biostatistician. The following subsections contain verbatim justification on the number of animals used submitted to the HPRA as a part of the application for project authorisation.

8.1.1 *Power calculation for case study 1*

The number of mice per group is based on a power calculation for weight carried out in G*Power. We have set the power to 0.9 and we have applied a Bonferroni correction to the significance level since you are interested in 3 concentrations of nanoparticle being compared to nanoparticle alone. A Bonferroni correction was applied to the significance levels for the power calculations to compensate for the number of statistical tests carried out. We have added an extra mouse per group due to difficulties which may occur during repeated injections through the tail vein. Indeed, it may be impossible to inject a mouse after a few injection and in this case we will not be able to include it in our statistical analysis.

Group	Treatment	No. of animals
1	Nanoparticle alone	7
2	Highest dose NP-Drug	7
3	Lower dose NP-Drug	7
4	Intermediate dose NP-Drug	7

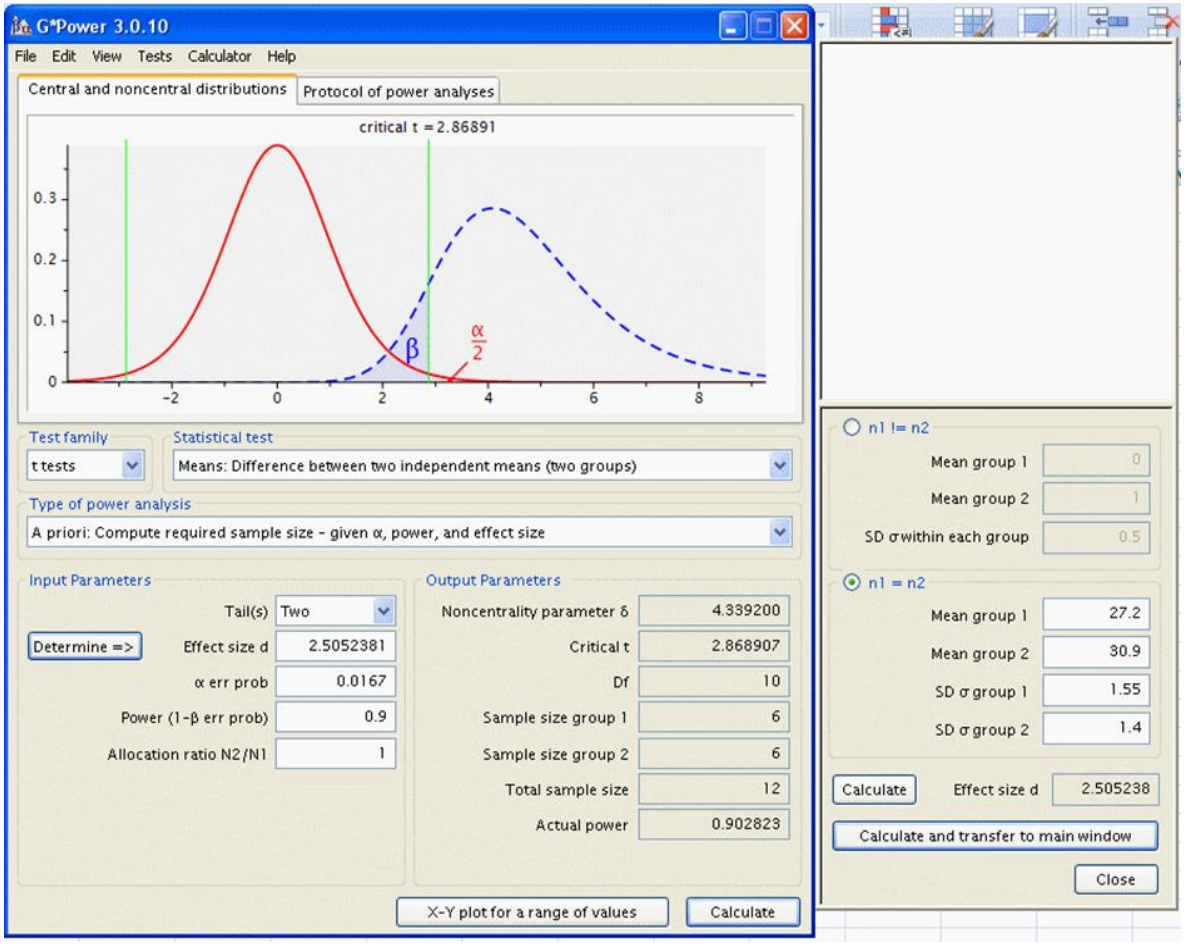

Supplementary figure 8.1: Sample size calculation for case study 1
Main window of G*Power software after a priori sample size calculation with the effect size calculator window shown to the right.

8.1.2 *Power calculation for case study 2*

The number of rats per group is based on a power calculation for AUC carried out in G*Power. We have set the power to 0.9 and we have applied a Bonferroni correction to the significance level since we are interested in 2 concentrations of nanoparticle being compared to free drug. A Bonferroni correction was applied to the significance levels for the power calculations to compensate for the number of statistical tests carried out.

Group	Treatment	No. of animals
1	Free drug	5
2	Highest dose NP-Drug	5

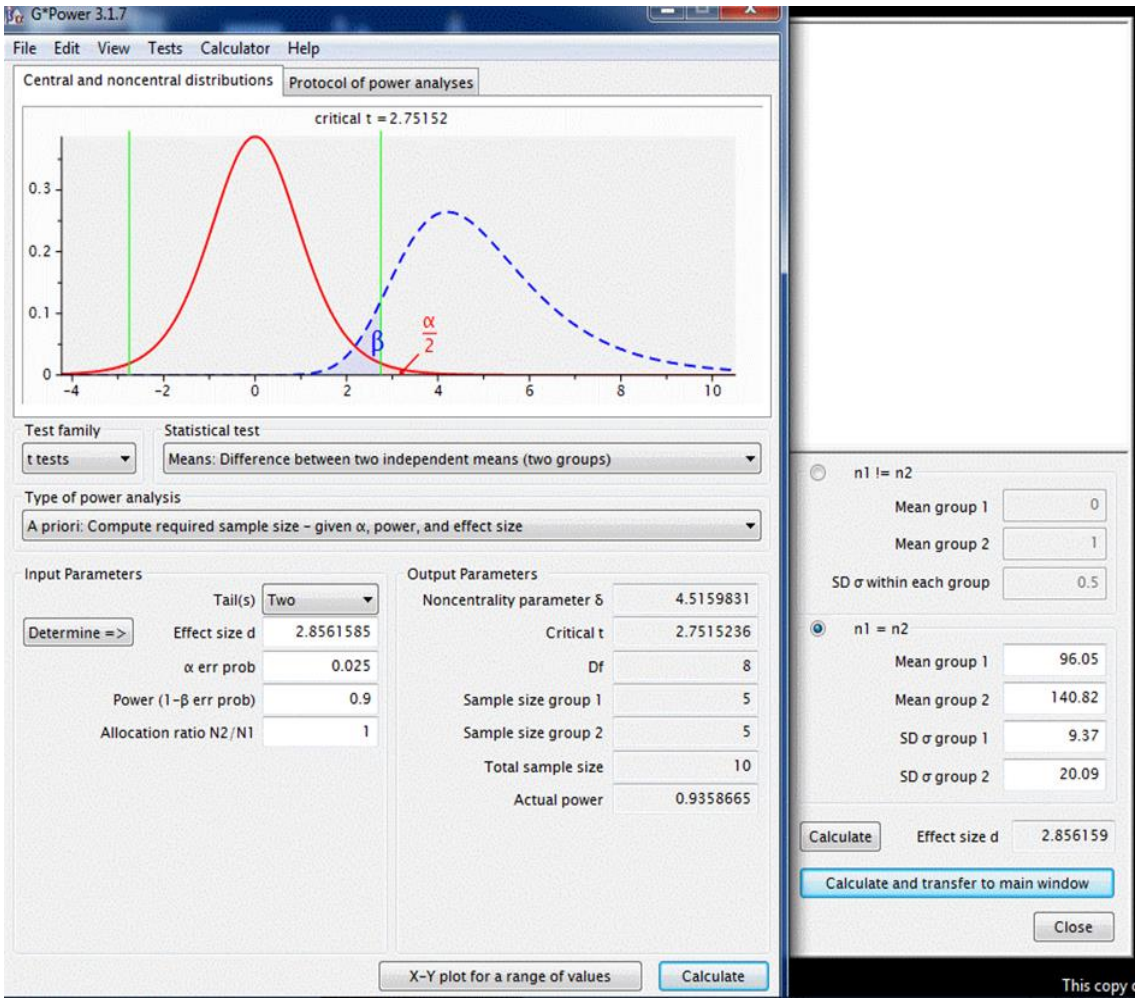

Supplementary figure 8.2: Sample size calculation for case study 2
Main window of G*Power software after a priori sample size calculation with the effect size calculator window shown to the right.

8.1.3 *Power calculation for case study 4*

Proper consideration has been afforded to experimental design to ensure the minimum number of animals will been used. We will use a randomised block design with 2 blocks of 3 reps per treatment. Including the vehicle controls this will give 20 error degrees of freedom. The two blocks will also give an indication on the repeatability of the two blocks. 6 rats will then be used for training PhD students and revising the catheter procedure. We will then use randomised block ANOVA followed by post hoc testing with Tukey's test to analyse results. This will also enable us to change the drug dose after the first block experiment if no side effects are observed.

8.2 In vitro experiments

8.2.1 *Liposome uptake*

Human liver hepatocellular carcinoma (HepG2) cells (supplied by SINTEF, Norway) were cultured in RPMI 1640 culture media (Life Technologies, UK) supplemented with 10% FBS and 1% penicillin-streptomycin (Invitrogen, Ireland) at 10,000 U/ml and 10,000 µg/ml respectively. Cells were maintained under a humidified atmosphere of 95% air/5% CO_2 at 37°C. Cells were seeded in 8-well chamber slides (Corning Incorporated, USA) at 20,000 cells per well. After 24 hours incubation at 37°C, different concentrations of liposome nanoparticles, from 50 to 1500 µg⁄mL were added for 24 hours to the culture medium.

8.2.1.1 Polyethylene Glycol (PEG) immunostaining

Following exposure to NPs, cells were washed three times with PBS (Fisher Scientific, Ireland), fixed for 30 minutes with 3.7% paraformaldehyde (Sigma-Aldrich, Ireland) at room temperature and permeabilised with 0.1% Triton-X (Sigma-Aldrich, Ireland) in PBS for 5 min. Unspecific staining was blocked with 30 minutes incubation in 5% Bovine serum albumin (BSA) in PBS at room temperature. Cells were incubated overnight at 4°C with anti-polyethylene glycol primary antibody (RevMAb, San Francisco, USA) diluted 1:500 in 5% BSA; for staining control cells were incubated in the same conditions in 5% BSA without the antibodies. Cells were then washed three times with PBS prior to detection with ReadyProbes™ Alexa Fluor® 488 Donkey anti-Rabbit IgG Antibody (Invitrogen, Bio-Sciences Ltd) as per manufacturers guidelines. Nuclei were stained with Hoechst 33342 (Invitrogen, Bio-Sciences Ltd). F-actin was stained with rhodamine phalloidin (Invitrogen, Bio-Sciences Ltd). Following three washes with PBS, slides were dried, mounted with ProLong diamond antifade mountant and imaged on Nikon TE300 fluorescent microscope.

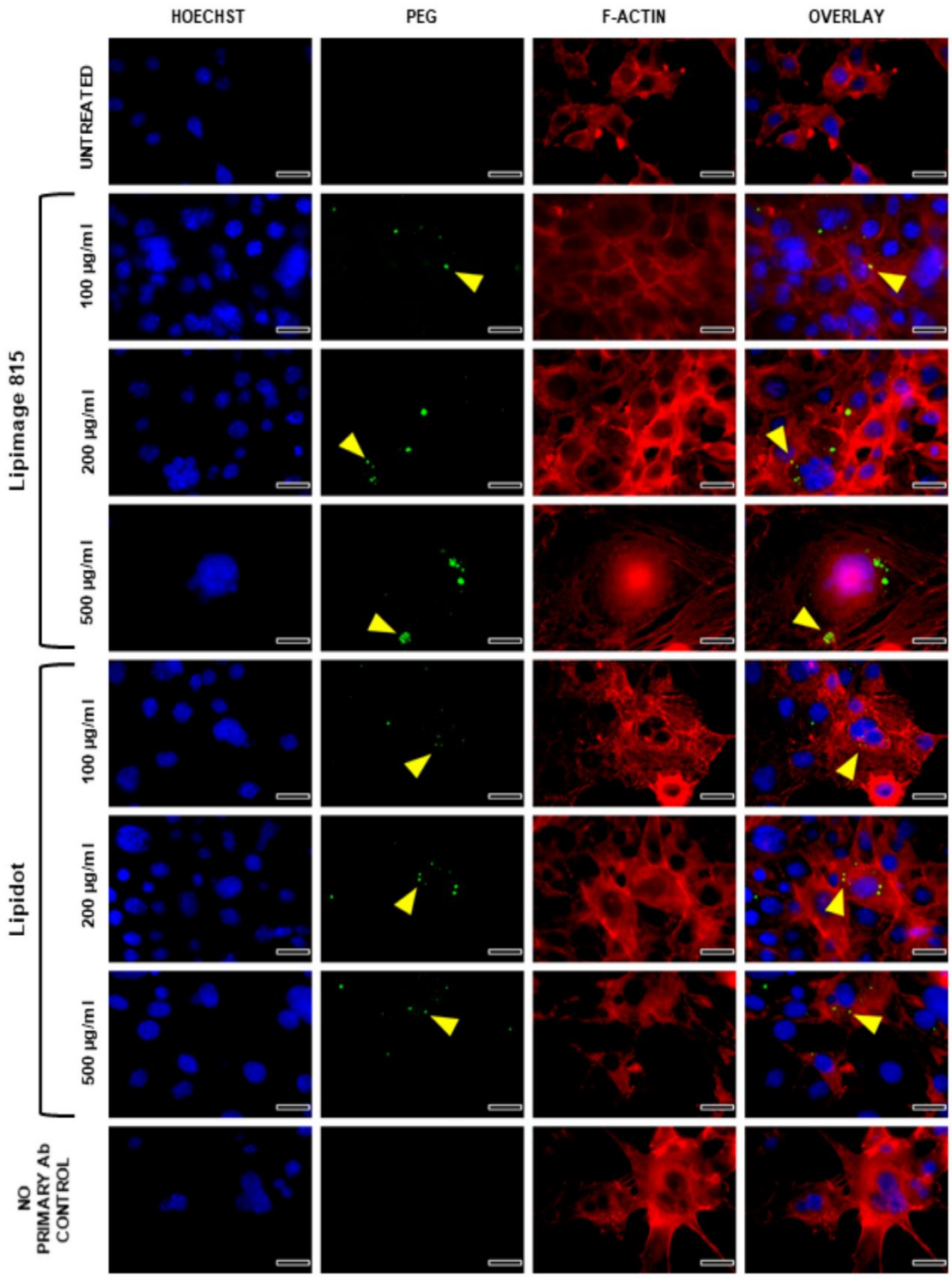

Supplementary figure 8.3: Cellular uptake of liposomes, PEG immunofluorescence labelling
Representative photomicrographs of HepG2 cells following 24 hour incubation with culture media (untreated) or 100 µg/mL, 200 µg/mL and 500 µg/mL of liposome. Cells were seeded in 8-well chamber slides at 10,000 cells/well and incubated at standard culturing conditions for 24 hours prior to treatment with nanobiomaterials. Yellow arrowheads highlight areas of positive PEG staining (green). Scale bar represents 25 µm.

8.2.2 *MNPs uptake in vitro*

BxPC-3 cells (ATCC, CRL-1687; pancreatic adenocarcinoma of a female human aged 61) were cultured in RPMI 1640 culture media (Life Technologies, UK) supplemented with 10% Fetal Bovine Serum (FBS) (Sigma, USA) and 1% penicillin-streptomycin (Invitrogen, Dublin, Ireland) at 10,000 U/ml and 10,000 µg/ml respectively. Cells were maintained under a humidified atmosphere of 95% air/5% CO2 at 37°C. Cells were seeded in 8-well chamber slides (Corning incorporated, USA) at 20,000 cells per well. After 24 hours incubation at 37°C, different concentrations of iron oxide nanoparticles, from 0 to 3000 µg⁄ml were added for 24 hours to the culture medium.

8.2.2.1 Perls' Prussian blue staining of cells

Following exposure to NPs, cells were washed three times with Phosphate-Buffered Saline (PBS) (Fisher Scientific, Dublin, Ireland), fixed for 30 minutes with 3.7% paraformaldehyde (Sigma-Aldrich, Dublin, Ireland) at room temperature, washed three times with PBS and incubated with iron staining solution made up of equal part of 4% HCl and 4% potassium ferrocyanide for 20 minutes. Cells were washed three times in PBS and counterstained with Eosin for 5 minutes. Slides were rinsed with distilled water before being dehydrated in a graded series of IMS rinses. Slides were then cleared in two baths of Xylene and cover-slipped with DPX mounting medium. Brightfield images were acquired with Nikon Eclipse E800M equipped with coloured camera.

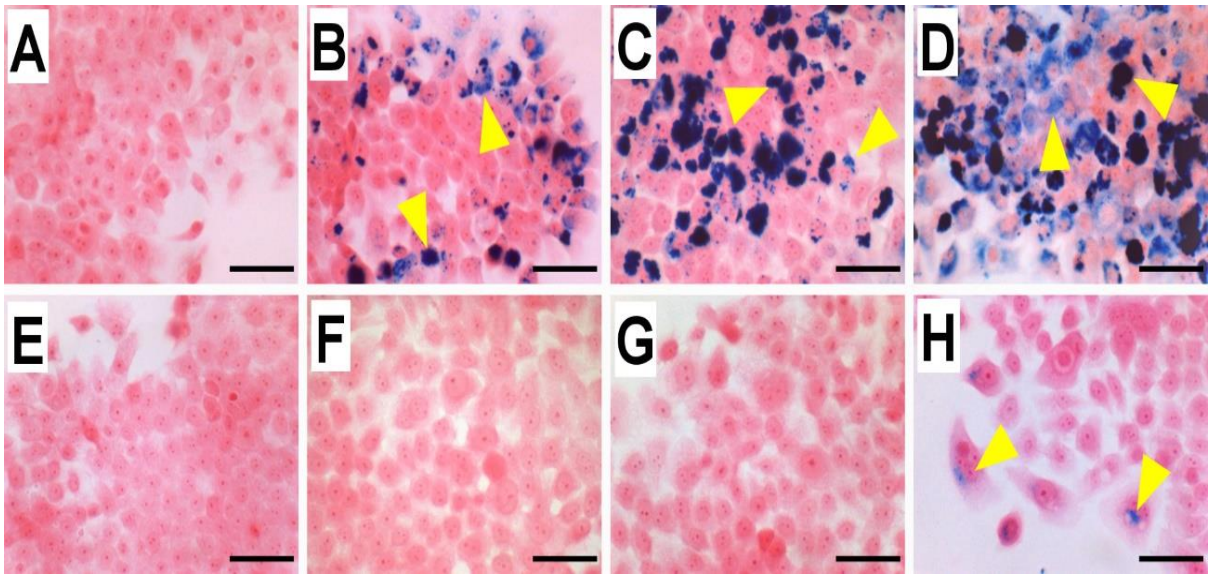

Supplementary figure 8.4: Cellular uptake of SPION, Perls' Prussian blue
Representative photomicrographs of BxPC-3 cells stained with Perls' Prussian blue following 24 hour incubation with saline (A and E), 47 µg/mL of MNPs (B and F), 750 µg/mL of SPION (C and G) or 3000 µg/mL of MNPs. Cells were seeded in 8-well chamber slide at 10,000 cells/well, and incubated at standard culturing conditions for 24 hours prior to treatment with MNPs. Cells in top row were treated with NOC0007 formulation; cells in bottom row were treated with RCL-01 formulation. Iron aggregates are visible as blue deposits (yellow arrowhead). Scale bar represents 50 µm.

8.2.2.2 Dextran immunostaining of cells

Following exposure to NPs, cells were washed three times with Phosphate-Buffered Saline (PBS) (Fisher Scientific, Dublin, Ireland), fixed for 30 minutes with 3.7% paraformaldehyde (Sigma-Aldrich, Dublin, Ireland) at room temperature and permeabilised with 0.1% Triton-X (Sigma-Aldrich, Ireland) in PBS for 5 min. Unspecific staining was blocked with 30 minutes incubation in 5% Normal Goat Serum (Invitrogen, Ireland) in PBS at room temperature. Cells were incubated overnight at 4°C with anti-dextran antibody (STEMCELL Technologies, USA) diluted 1:100 in 5% BSA; for staining control cells were incubated in the same conditions in 5% BSA without the antibodies. Cells were then washed three times with PBS prior to detection of primary antibody with ReadyProbes™ Alexa Fluor® 488 Donkey anti-Rabbit IgG Antibody (Invitrogen, Bio-Sciences Ltd) as per manufacturers guidelines. Nuclei were stained with Hoechst 33342 (Invitrogen, Bio-Sciences Ltd). F-actin was stained with rhodamine phalloidin (Invitrogen, Bio-Sciences Ltd). Following three washes with PBS, slides were dried, mounted with ProLong

diamond antifade mountant and imaged on Nikon TE300 fluorescent microscope.

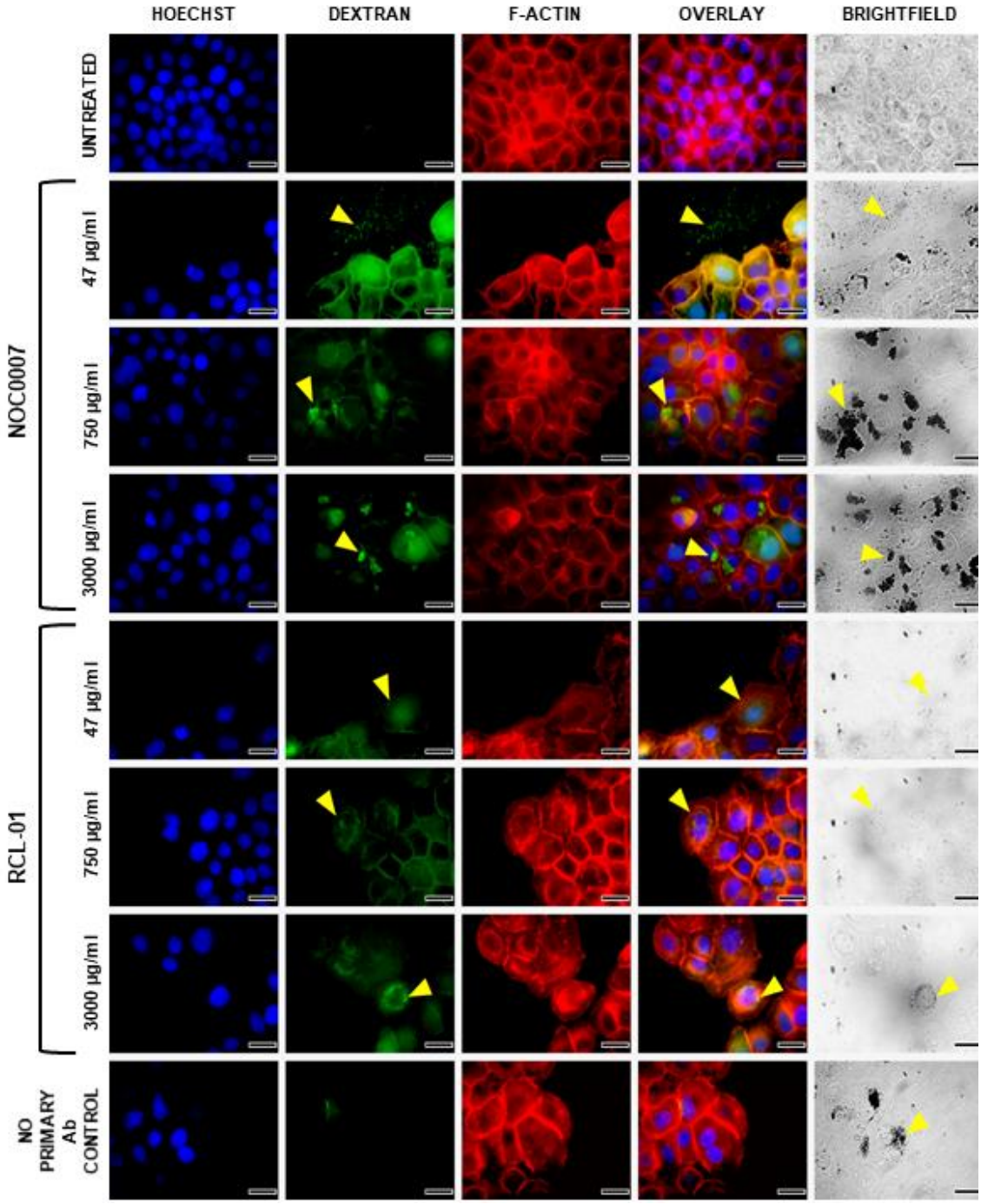

Supplementary figure 8.5: Cellular uptake of SPION, dextran immunostaining
Representative photomicrographs of BxPC-3 cells following 24 hour incubation with culture media (untreated), 47 µg/mL of SPION, 750 µg/mL of SPION or 3000 µg/mL of SPION. Cells were seeded in 8-well chamber slide at 10,000 cells/well, and incubated at standard culturing conditions for 24 hours prior to treatment with MNPs. Yellow arrowheads highlight areas of overlap of dextran (green) and iron deposits (black granular material in brighfield images). Scale bar represents 25 µm.

8.3 *In vivo* experiments

8.3.1 *Supplementary data for Case study 1: Novel dye-loaded lipid NBM*

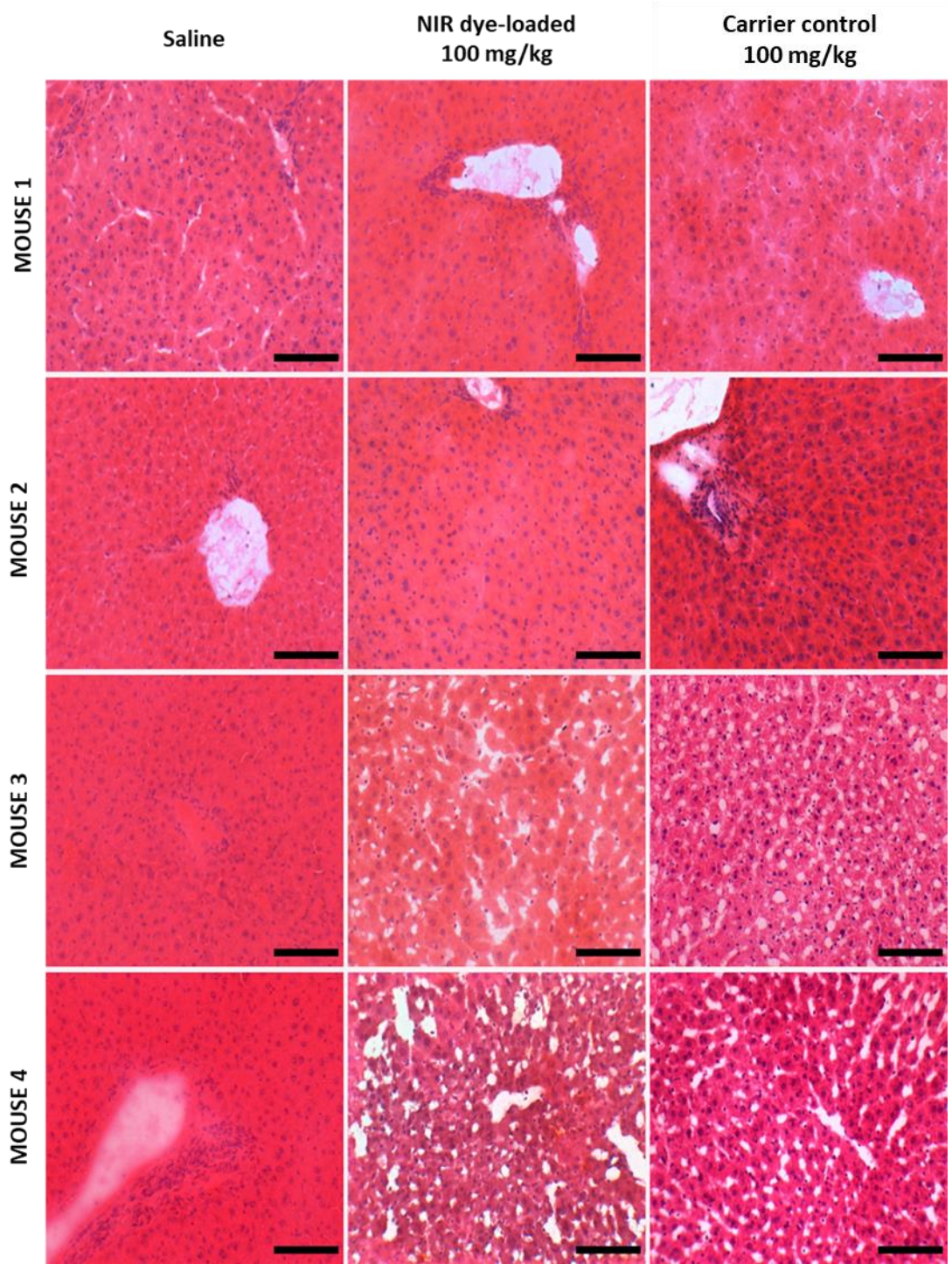

Supplementary figure 8.6: H&E staining of female liver
Representative photomicrographs of H&E stained liver tissue collected from female C57BL/6 mice used in this study. No abnormal changes suggestive of toxicity or immune response in response to injection with NIR dye-loaded liposome at 100 mg/kg concentration (middle column) or soybean-oil filled liposome as vehicle control at 100 mg/kg concentration (right column) when compared to livers of animals injected with saline (left column). Representative images were acquired with 20x lens; Scale bar represents 100 µm.

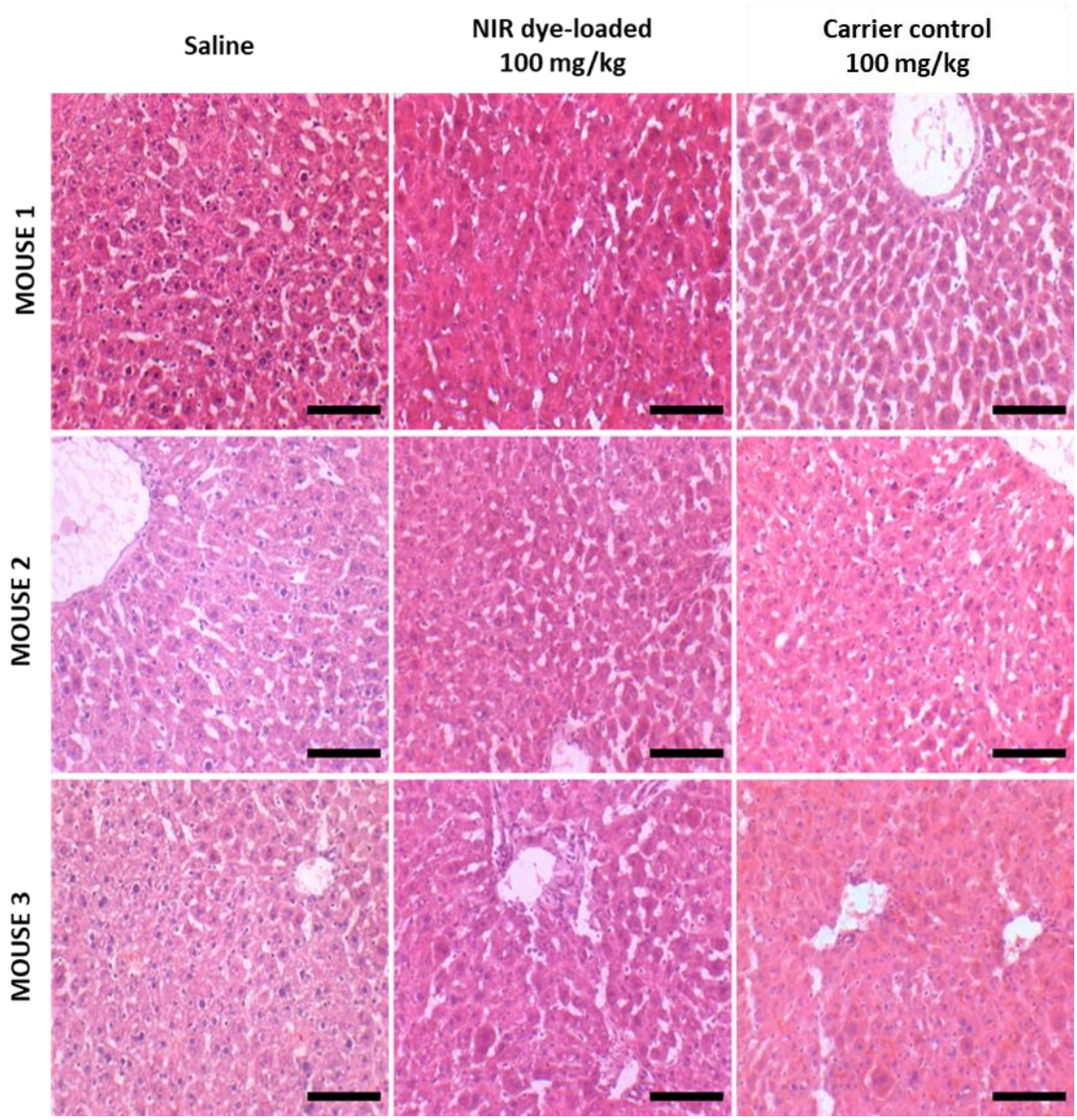

Supplementary figure 8.7: H&E staining of male liver

Representative photomicrographs of H&E stained liver tissue collected from male C57BL/6 mice used in this study. No abnormal changes suggestive of toxicity or immune response in response to injection with NIR dye-loaded liposome at 100 mg/kg concentration (middle column) or soybean-oil filled liposome as vehicle control at 100 mg/kg concentration (right column) when compared to livers of animals injected with saline (left column). Representative images were acquired with 20x lens; Scale bar represents 100 µm.

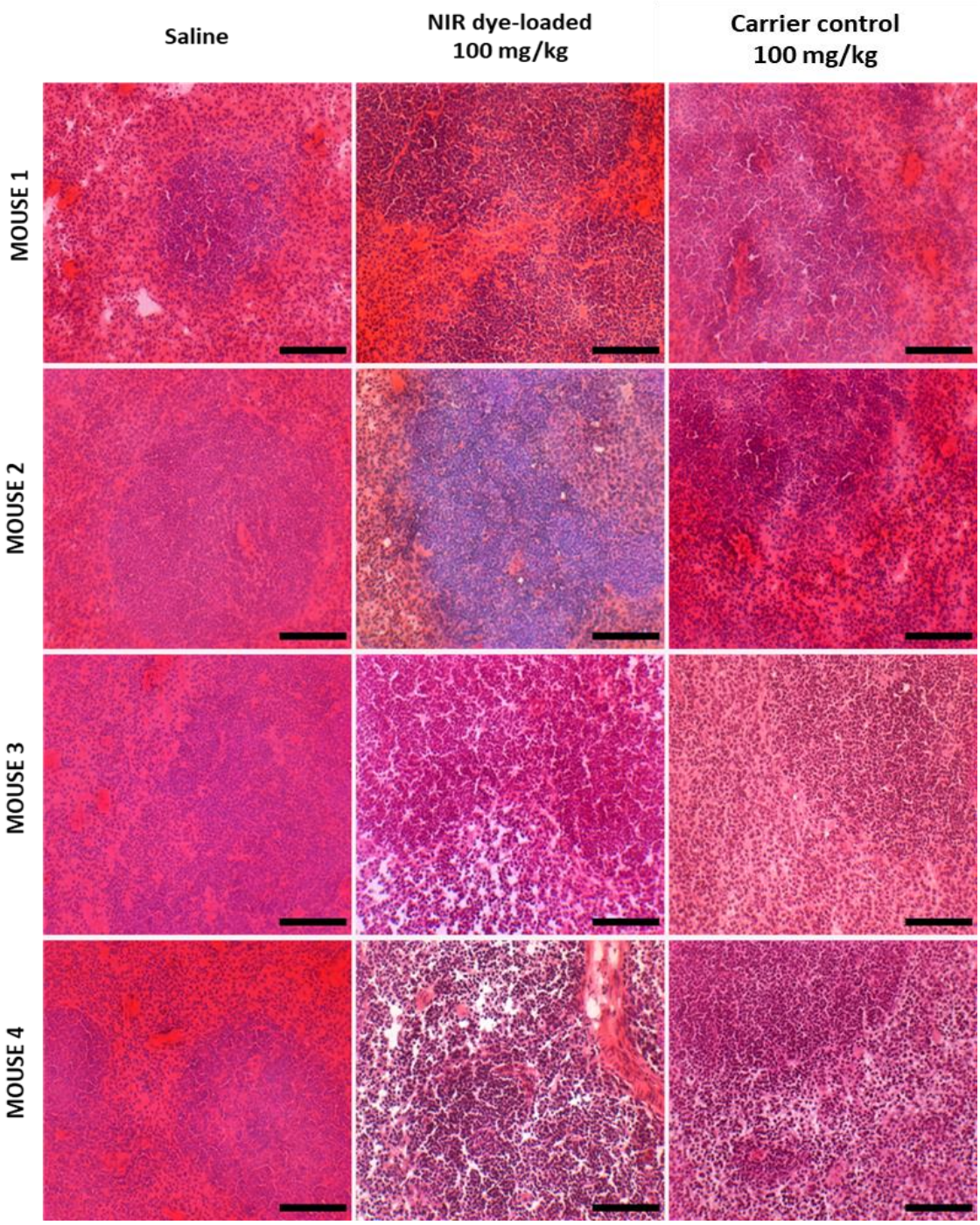

Supplementary figure 8.8: H&E staining of female spleen
Representative photomicrographs of H&E stained spleen tissue collected from female C57BL/6 mice used in this study. No abnormal changes suggestive of toxicity or immune response in response to injection with NIR dye-loaded liposome at 100 mg/kg concentration (middle column) or soybean-oil filled liposome as vehicle control at 100 mg/kg concentration (right column) when compared to livers of animals injected with saline (left column). Representative images were acquired with 20x lens; Scale bar represents 100 µm.

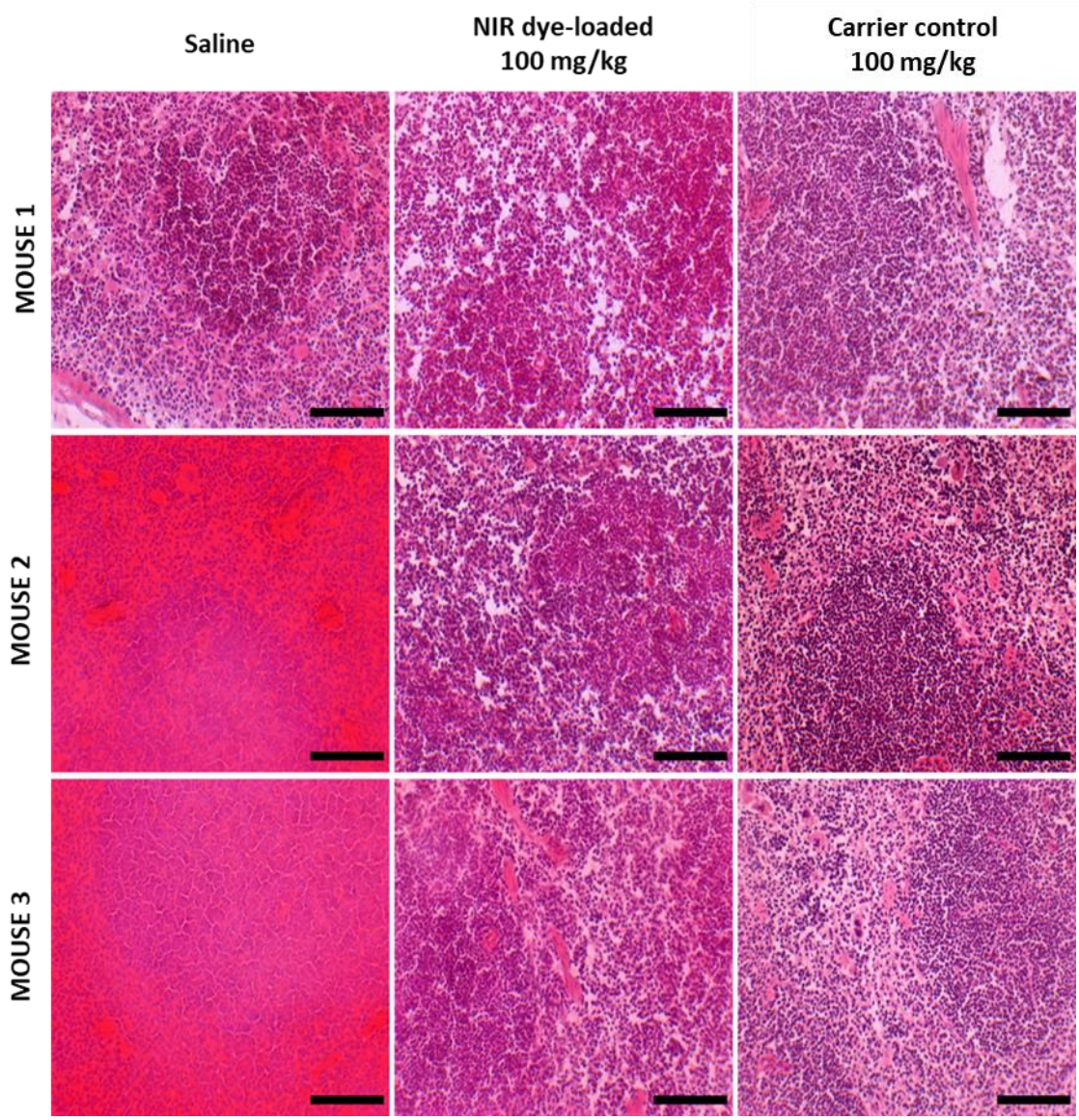

Supplementary figure 8.9: H&E staining ofmale spleen
Representative photomicrographs of H&E stained spleen tissue collected from male C57BL/6 mice used in this study. No abnormal changes suggestive of toxicity or immune response in response to injection with NIR dye-loaded liposome at 100 mg/kg concentration (middle column) or soybean-oil filled liposome as vehicle control at 100 mg/kg concentration (right column) when compared to livers of animals injected with saline (left column). Representative images were acquired with 20x lens; Scale bar represents 100 µm.

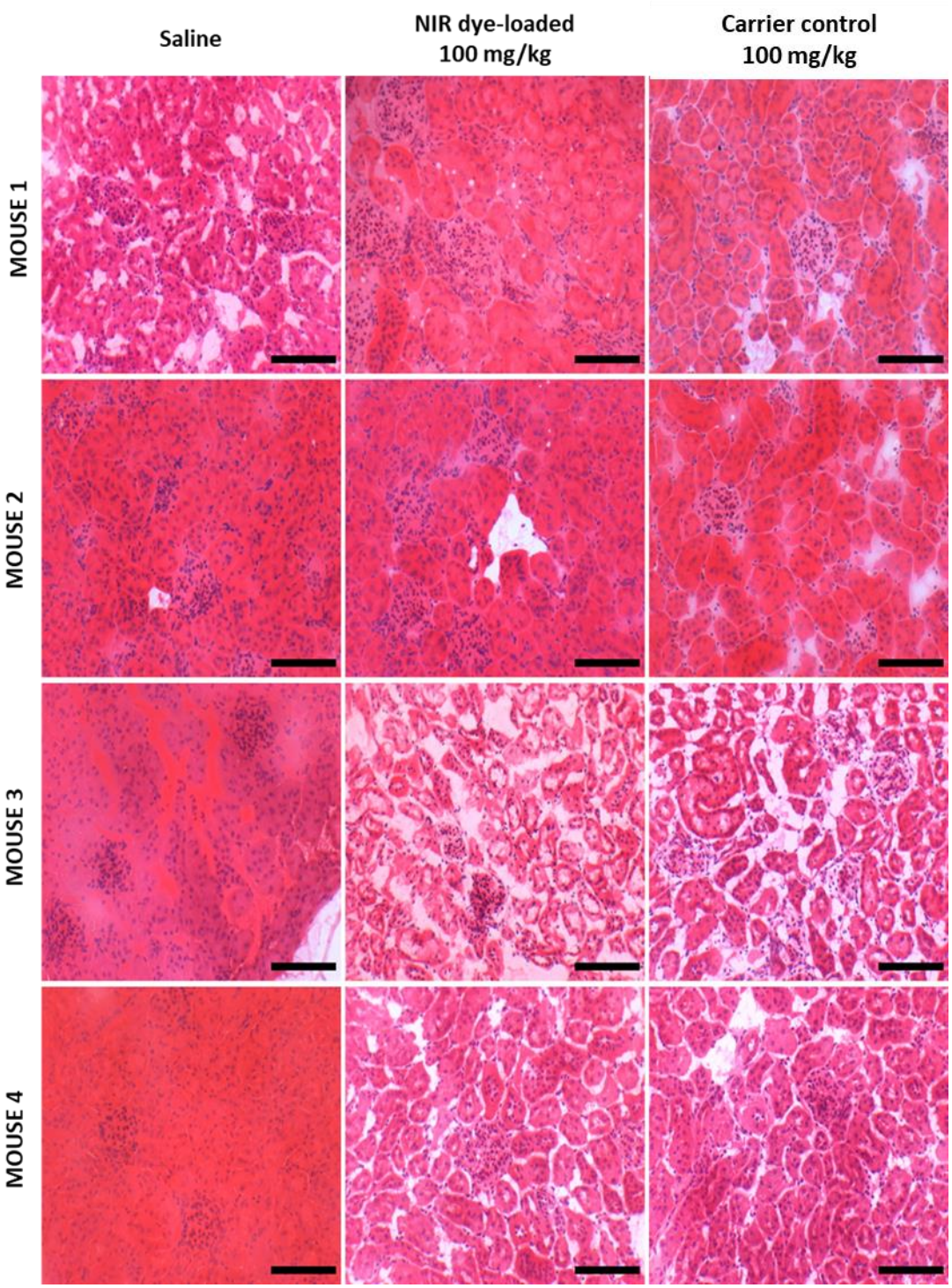

Supplementary figure 8.10: H&E staining of female kidneys

Representative photomicrographs of H&E stained kidney tissue collected from female C57BL/6 mice used in this study. No abnormal changes suggestive of toxicity or immune response in response to injection with NIR dye-loaded liposome at 100 mg/kg concentration (middle column) or soybean-oil filled liposome as vehicle control at 100 mg/kg concentration (right column) when compared to livers of animals injected with saline (left column). Representative images were acquired with 20x lens; Scale bar represents 100 µm.

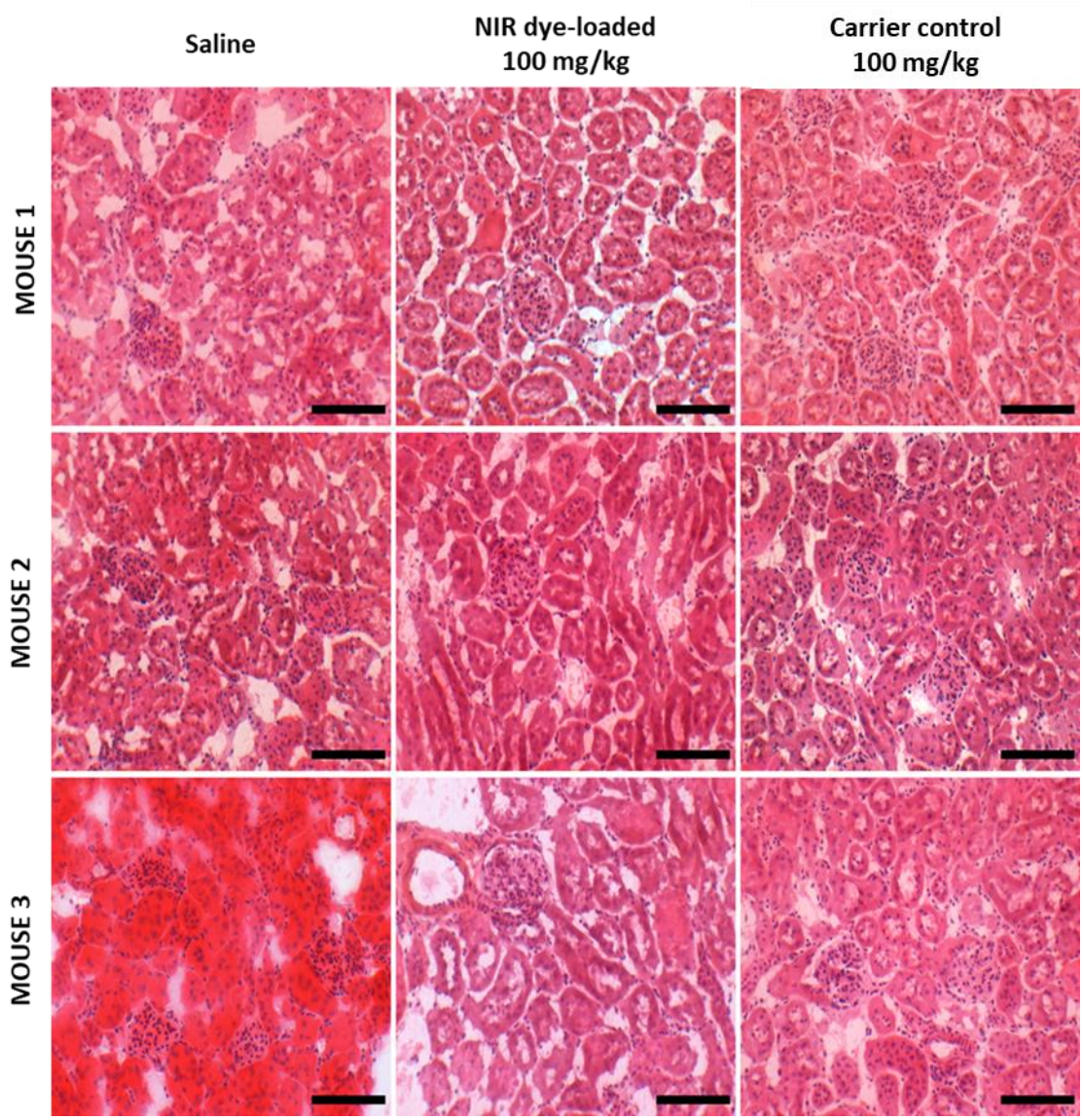

Supplementary figure 8.11: H&E staining of male kidneys
Representative photomicrographs of H&E stained kidney tissue collected from male C57BL/6 mice used in this study. No abnormal changes suggestive of toxicity or immune response in response to injection with NIR dye-loaded liposome at 100 mg/kg concentration (middle column) or soybean-oil filled liposome as vehicle control at 100 mg/kg concentration (right column) when compared to livers of animals injected with saline (left column). Representative images were acquired with 20x lens; Scale bar represents 100 µm.

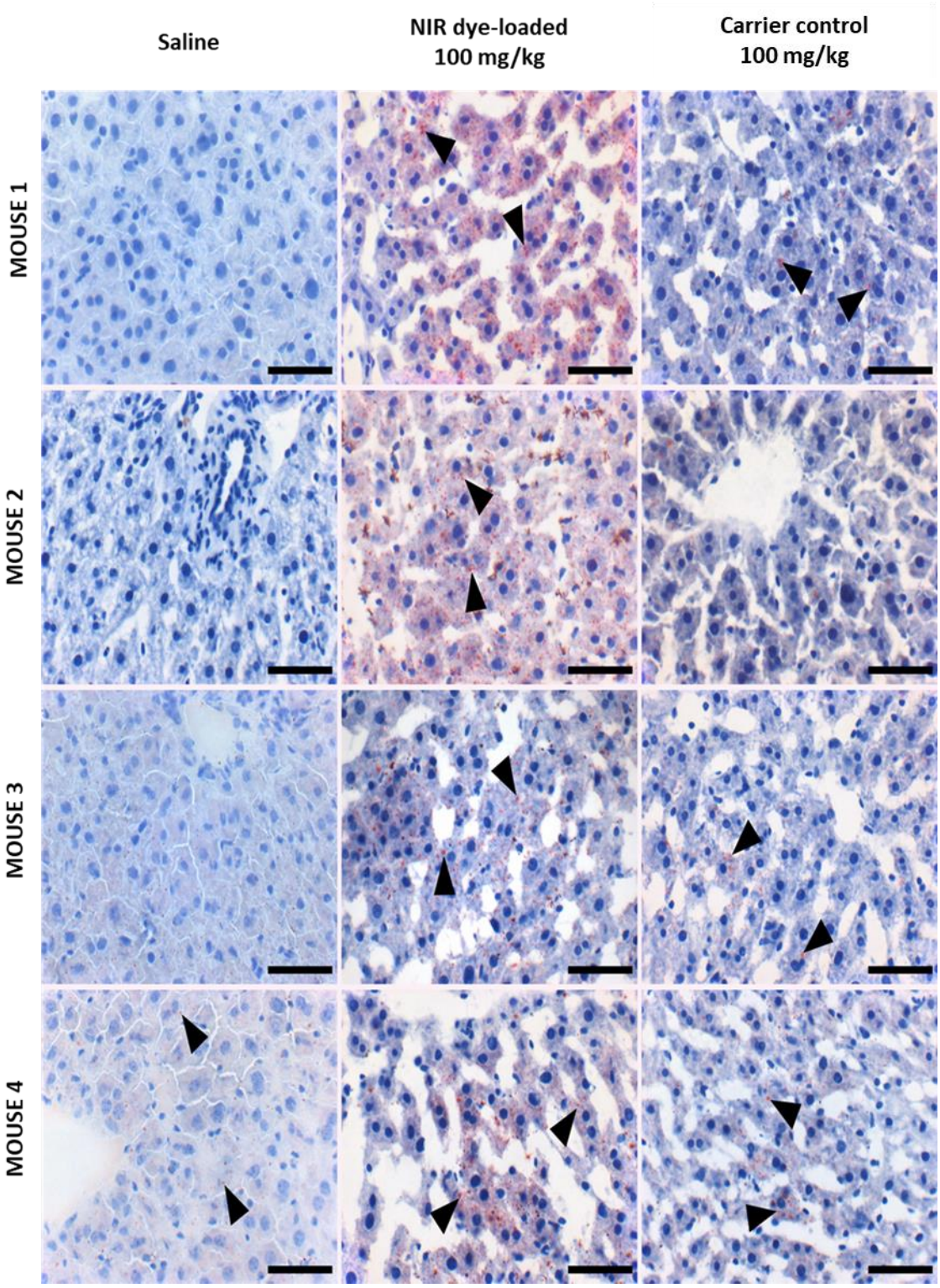

Supplementary figure 8.12: Lipid content in female livers
Representative photomicrographs of ORO stained liver tissue collected from female C57BL/6 mice. Females injected with NIR dye-loaded liposome at 100 mg/kg concentration (middle column) showed higher accumulation of lipid (black arrowhead) in comparison to females injected with soybean-oil filled liposome as vehicle control at 100 mg/kg concentration (right column) or those injected with saline (left column). Representative images were acquired with 40x lens; Scale bar represents 50 µm.

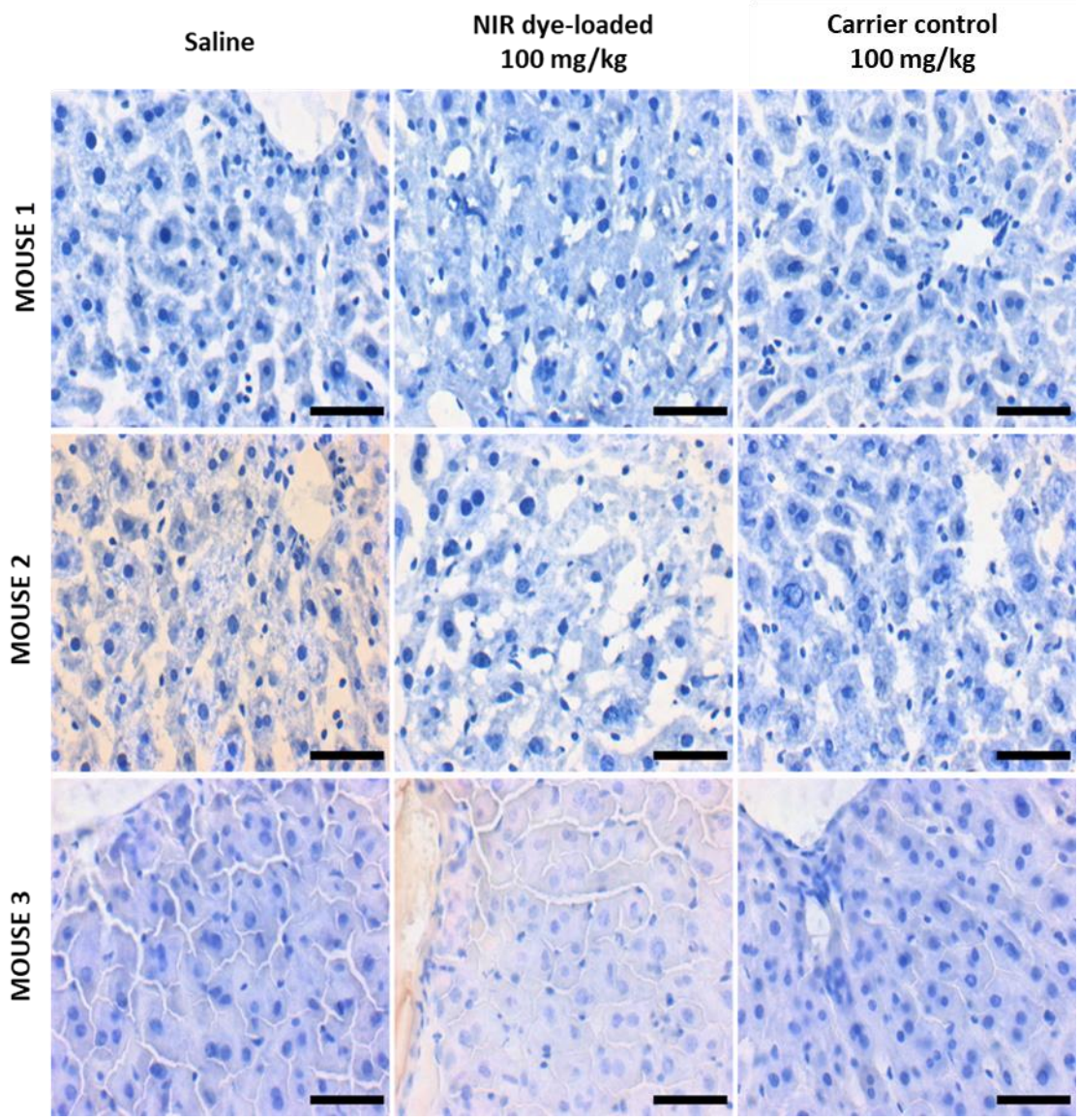

Supplementary figure 8.13: Lipid content in male livers
Representative photomicrographs of ORO stained liver tissue collected from male C57BL/6 mice. No accumulation of lipids was seen in males injected with saline (left column), NIR dye-loaded liposome at 100 mg/kg concentration (middle column) or soybean-oil filled liposome vehicle control at 100 mg/kg concentration (right column). Images were acquired with 40x lens; Scale bar represents 50 µm.

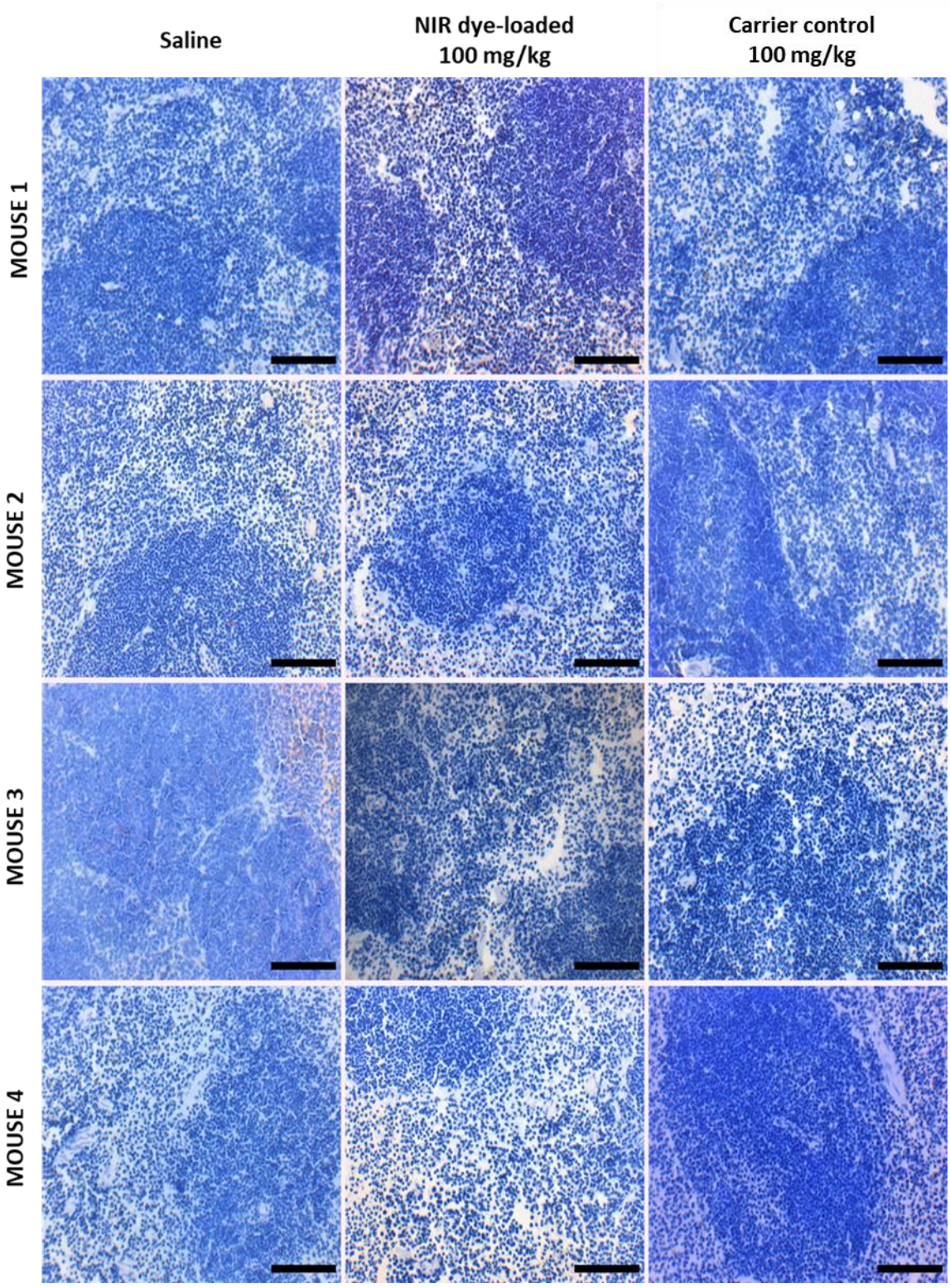

Supplementary figure 8.14: Lipid accumulation in female spleen
Representative photomicrographs of ORO stained spleen tissue collected from female C57BL/6 mice used in case study 1. No accumulation of lipids was seen in females injected with saline (left column), NIR dye-loaded liposome at 100 mg/kg concentration (middle column) or soybean-oil filled liposome vehicle control at 100 mg/kg concentration (right column). Images were acquired with 40x lens; Scale bar represents 50 µm.

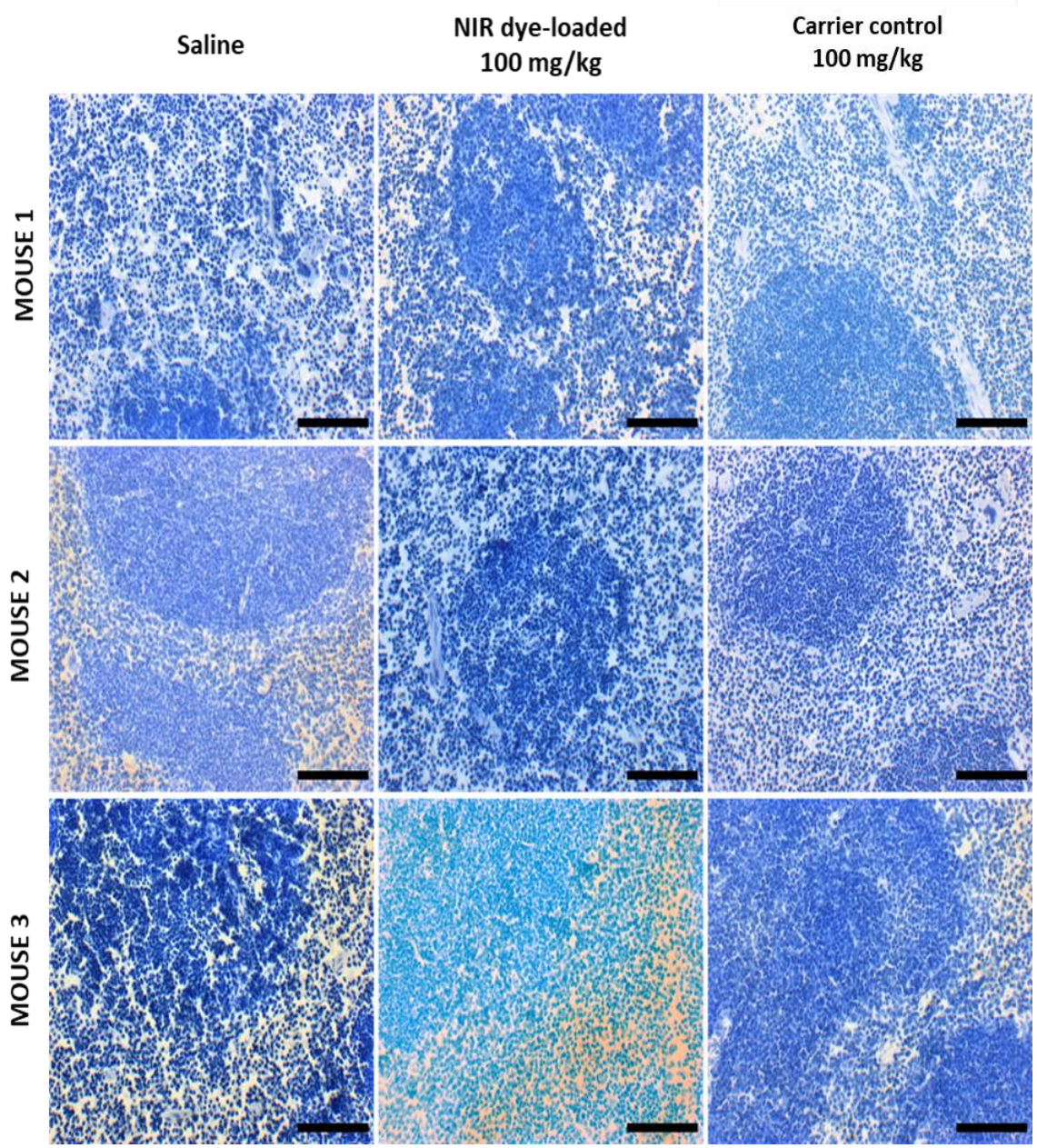

Supplementary figure 8.15: Lipid accumulation in male spleen
Representative photomicrographs of ORO stained spleen tissue collected from male C57BL/6 mice in case study 1. No accumulation of lipids was seen in males injected with saline (left column), NIR dye-loaded liposome at 100 mg/kg concentration (middle column) or soybean-oil filled liposome vehicle control at 100 mg/kg concentration (right column). Images were acquired with 40x lens; Scale bar represents 50 µm.

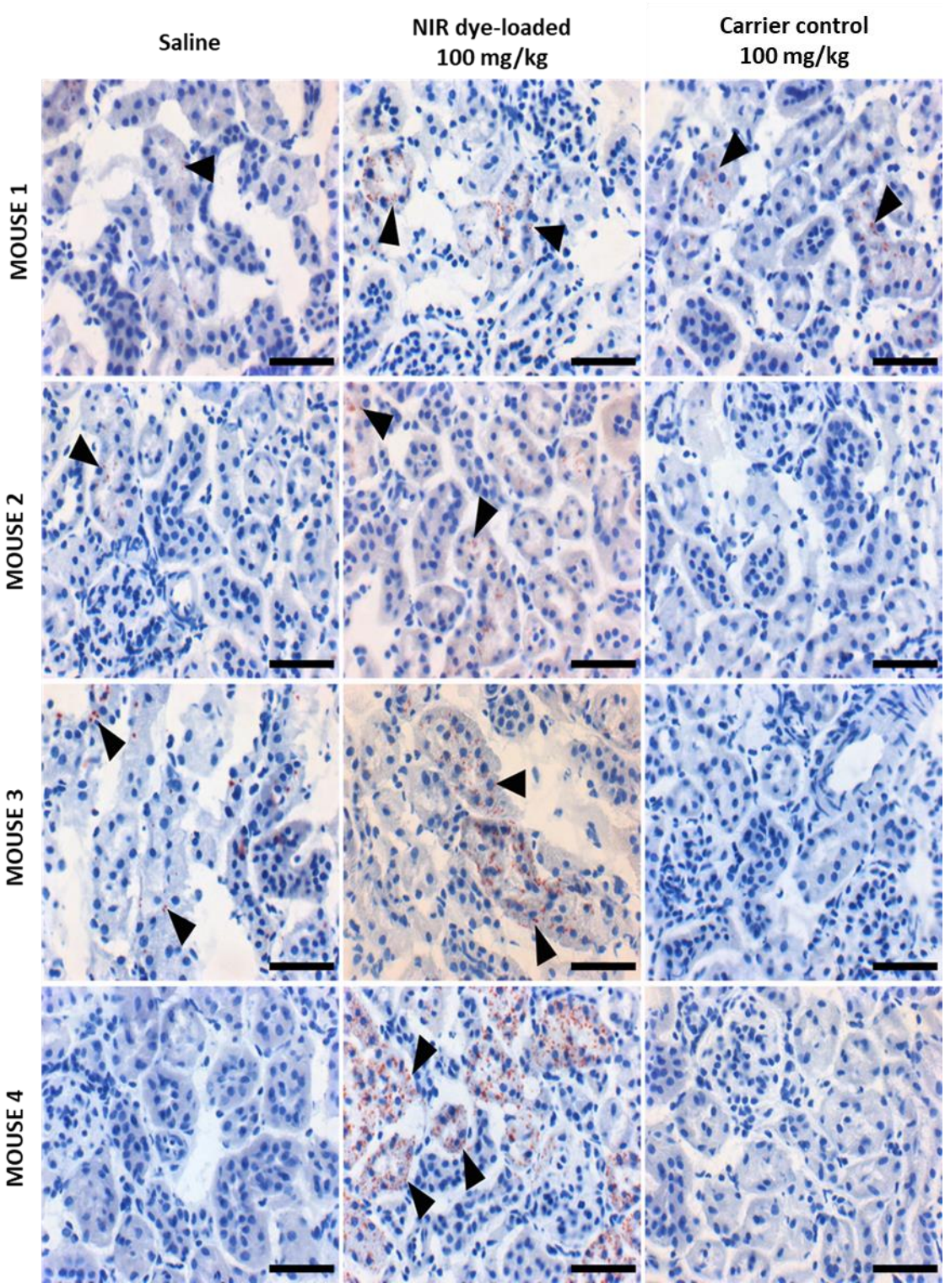

Supplementary figure 8.16: Lipid accumulation in female kidneys
Representative photomicrographs of ORO stained kidney tissue collected from female C57BL/6 mice used in case study 1. Lipids (black arrowheads) were detected in females from all treatment groups. Females injected with NIR dye-loaded liposome at 100 mg/kg concentration (middle column) showed higher accumulation of lipid in comparison to females injected with soybean-oil filled liposome carrier control at 100 mg/kg concentration (right column) or those injected with saline (left column). Representative images were acquired with 40x lens; Scale bar represents 50 µm.

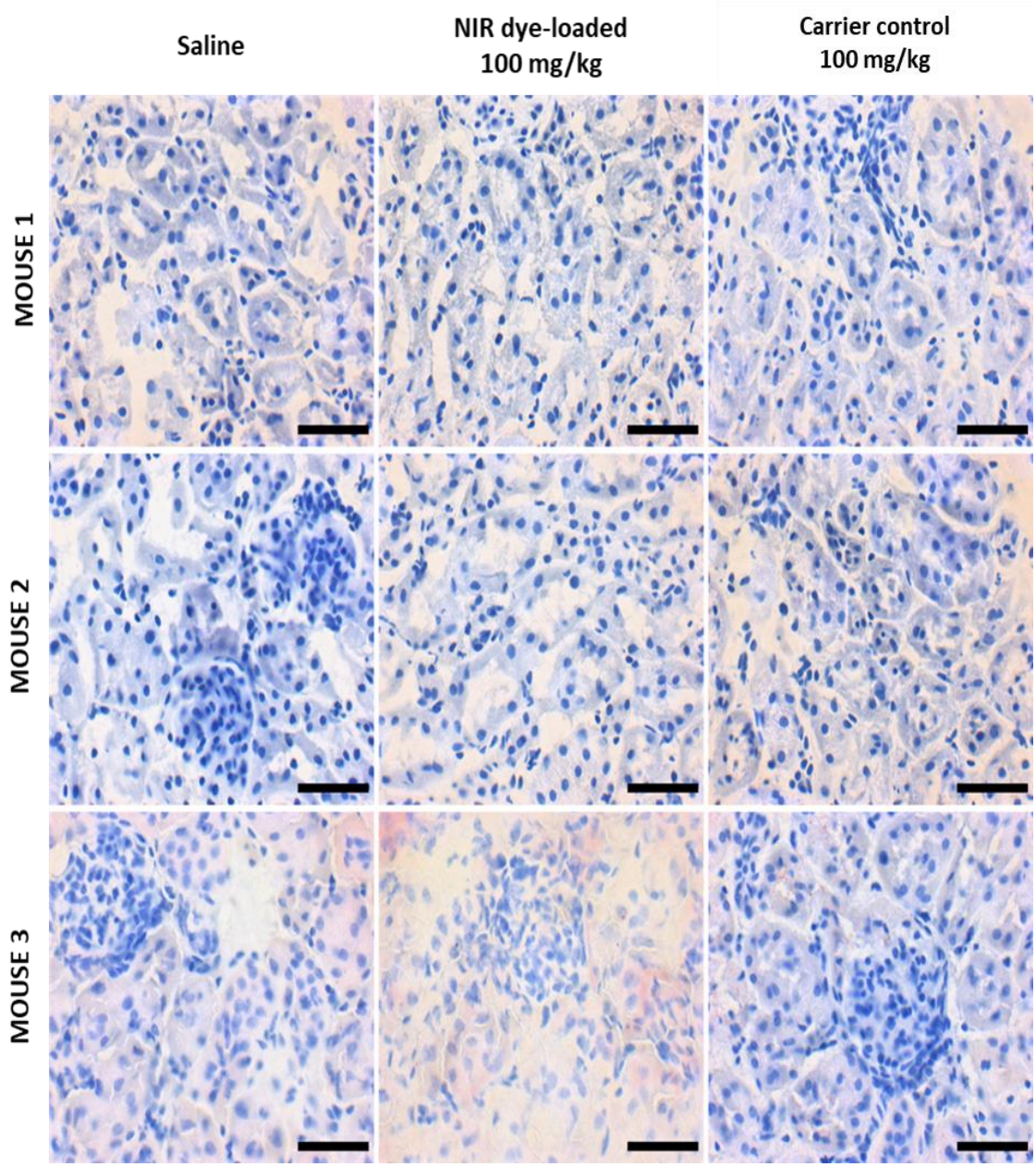

Supplementary figure 8.17: Lipid accumulation in male kidneys
Representative photomicrographs of ORO stained kidney tissue collected from male C57BL/6 mice. No significant accumulation of lipids was seen in males injected with saline (left column), NIR dye-loaded liposome at 100 mg/kg concentration (middle column) or soybean-oil filled liposome vehicle control at 100 mg/kg concentration (right column). Images were acquired with 40x lens; Scale bar represents 50 µm.

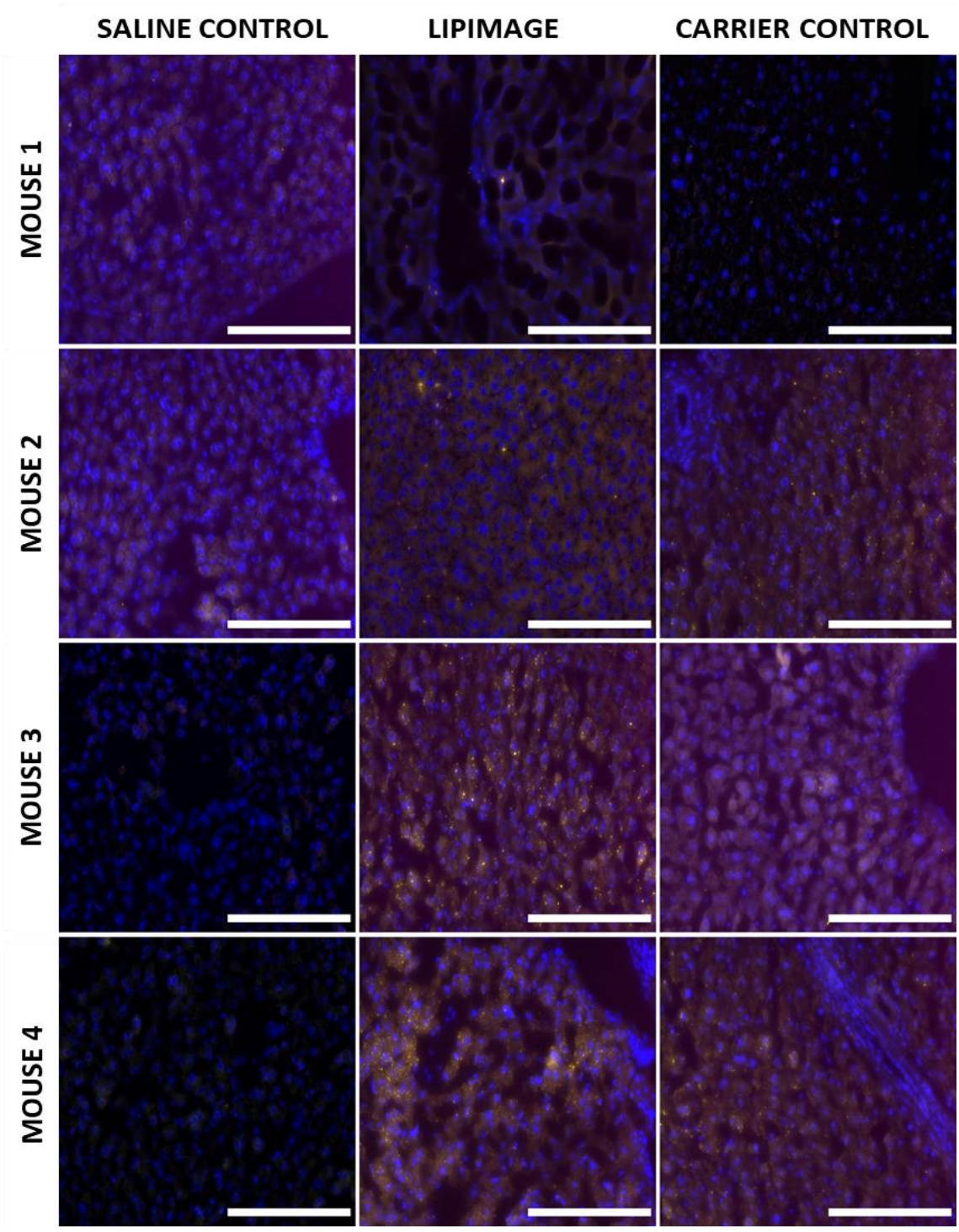

Supplementary figure 8.18: Detection of lipids and IR-780 dye in female livers using fluorescent microscopy

Representative photomicrographs showing lipid and IR-780 dye accumulation in livers of male C57BL/6 mice used in case study 1. Left hand side column shows sections from animals injected with saline; animals in the middle column were injected with dye-loaded liposome at 100 mg/kg of lipid concentration; animals in the right hand side column were injected with a carrier control liposome filled with soybean-oil (right column) at 100 mg/kg of lipid concentration. Objects of interest were assigned pseudo colour in the images as follows: nuclei are seen in blue, lipids in yellow, IR-780 dye in magenta. Representative images were acquired with 20x lens on LionHeart FX automated microscope. Scale bar represents 200μm.

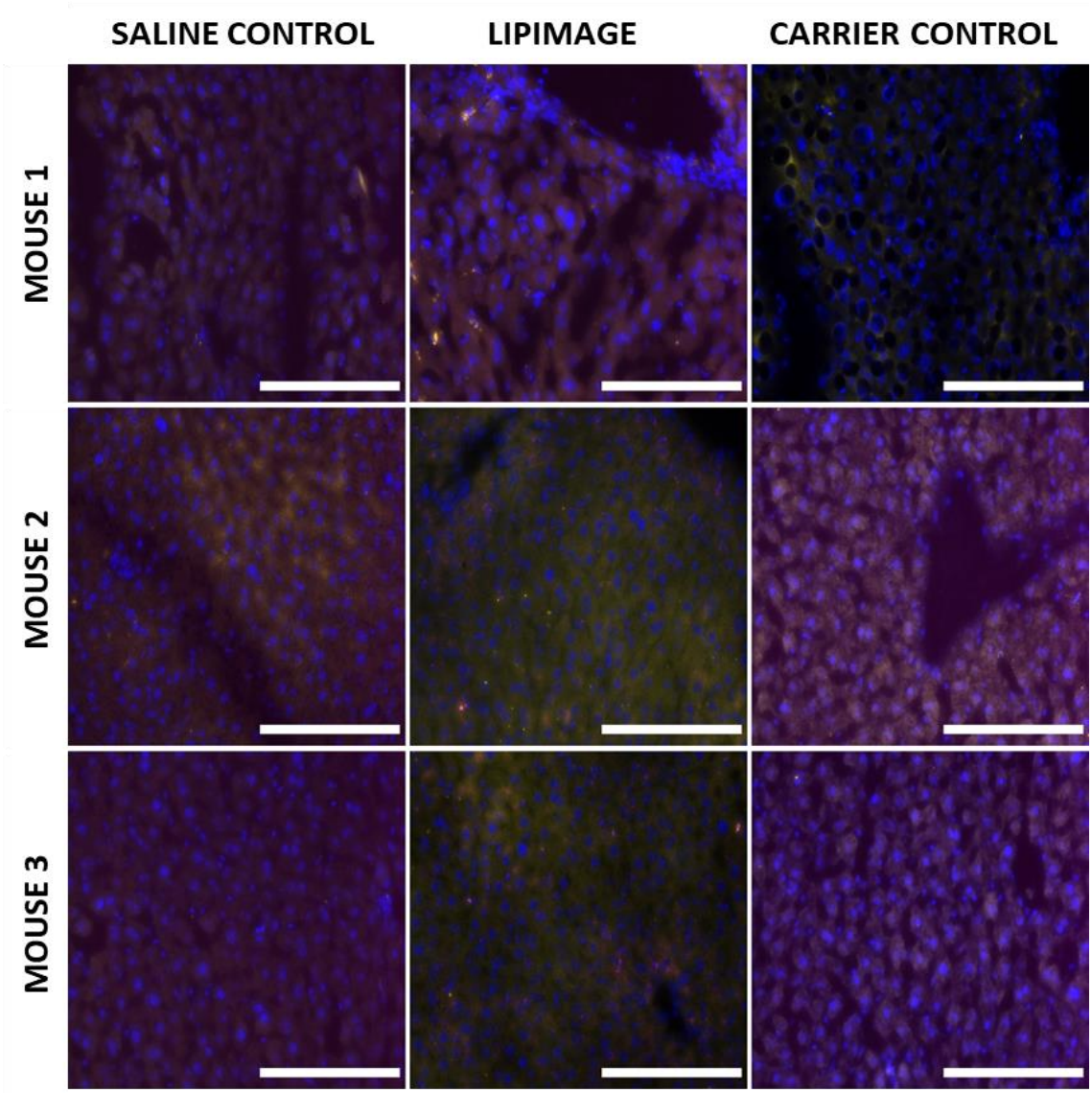

Supplementary figure 8.19: Detection of lipids and IR-780 dye in male livers using fluorescent microscopy

Representative photomicrographs showing lipid and IR-780 dye accumulation in livers of male C57BL/6 mice used in case study 1. Left hand side column shows sections from animals injected with saline; animals in the middle column were injected with dye-loaded liposome at 100 mg/kg of lipid concentration; animals in the right hand side column were injected with a carrier control liposome filled with soybean-oil (right column) at 100 mg/kg of lipid concentration. Objects of interest were assigned pseudo colour in the images as follows: nuclei are seen in blue, lipids in yellow, IR-780 dye in magenta. Representative images were acquired with 20x lens on LionHeart FX automated microscope. Scale bar represents 200µm.

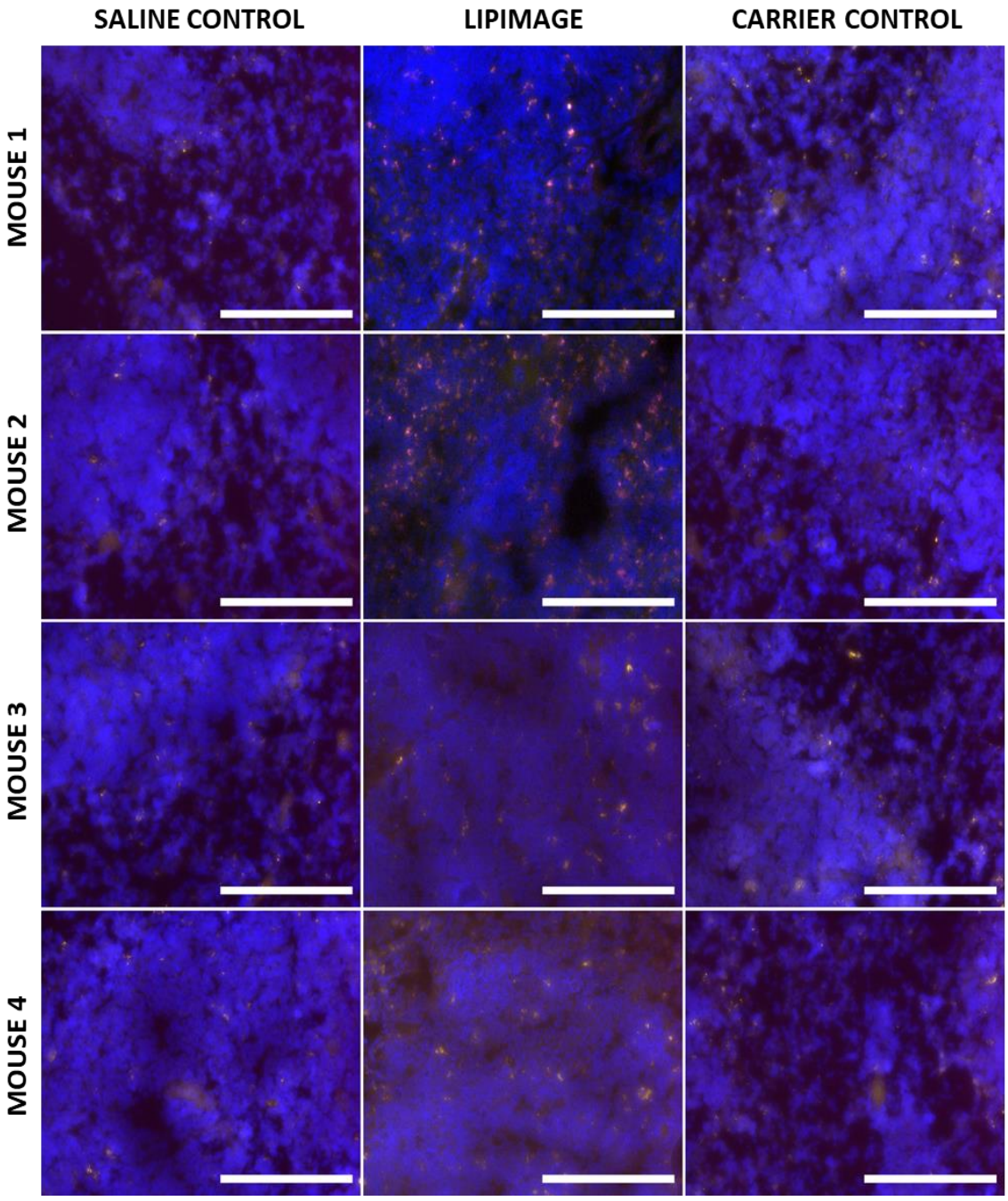

Supplementary figure 8.20: Detection of lipids and IR-780 dye in female spleens using fluorescent microscopy

Representative photomicrographs showing lipid and IR-780 dye accumulation in spleens of female C57BL/6 mice used in case study 1. Left hand side column shows sections from animals injected with saline; animals in the middle column were injected with dye-loaded liposome at 100 mg/kg of lipid concentration; animals in the right hand side column were injected with a carrier control liposome filled with soybean-oil (right column) at 100 mg/kg of lipid concentration. Objects of interest were assigned pseudo colour in the images as follows: nuclei are seen in blue, lipids in yellow, IR-780 dye in magenta. Representative images were acquired with 20x lens on LionHeart FX automated microscope. Scale bar represents 200μm.

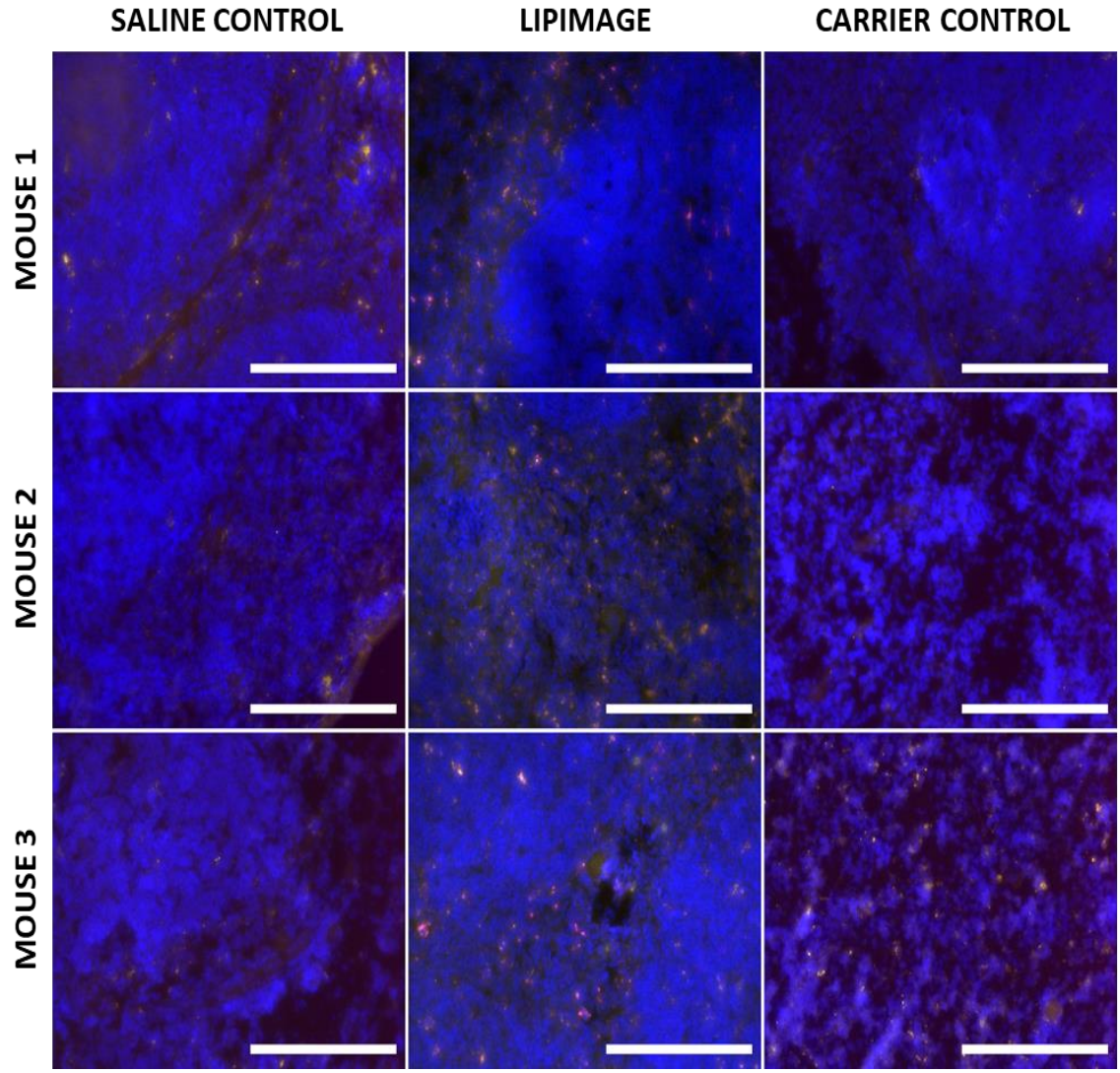

Supplementary figure 8.21: Detection of lipids and IR-780 dye in male spleens using fluorescent microscopy

Representative photomicrographs showing lipid and IR-780 dye accumulation in spleens of male C57BL/6 mice used in case study 1. Left hand side column shows sections from animals injected with saline; animals in the middle column were injected with dye-loaded liposome at 100 mg/kg of lipid concentration; animals in the right hand side column were injected with a carrier control liposome filled with soybean-oil (right column) at 100 mg/kg of lipid concentration. Objects of interest were assigned pseudo colour in the images as follows: nuclei are seen in blue, lipids in yellow, IR-780 dye in magenta. Representative images were acquired with 20x lens on LionHeart FX automated microscope. Scale bar represents 200μm.

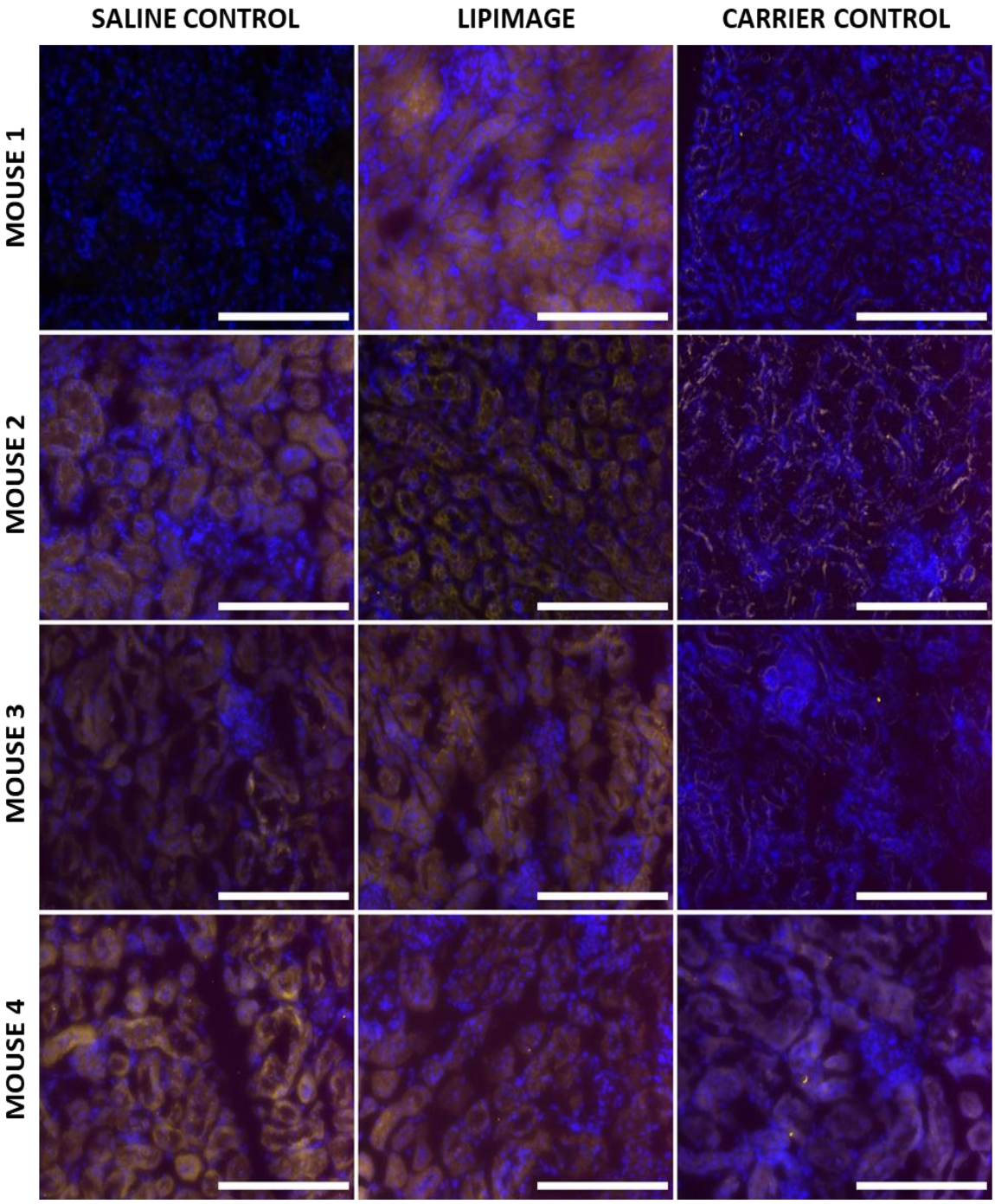

Supplementary figure 8.22: Detection of lipids and IR-780 dye in female kidneys using fluorescent microscopy

Representative photomicrographs showing lipid and IR-780 dye accumulation in kidneys of female C57BL/6 mice used in case study 1. Left hand side column shows sections from animals injected with saline; animals in the middle column were injected with dye-loaded liposome at 100 mg/kg of lipid concentration; animals in the right hand side column were injected with a carrier control liposome filled with soybean-oil (right column) at 100 mg/kg of lipid concentration. Objects of interest were assigned pseudo colour in the images as follows: nuclei are seen in blue, lipids in yellow, IR-780 dye in magenta. Representative images were acquired with 20x lens on LionHeart FX automated microscope. Scale bar represents 200μm.

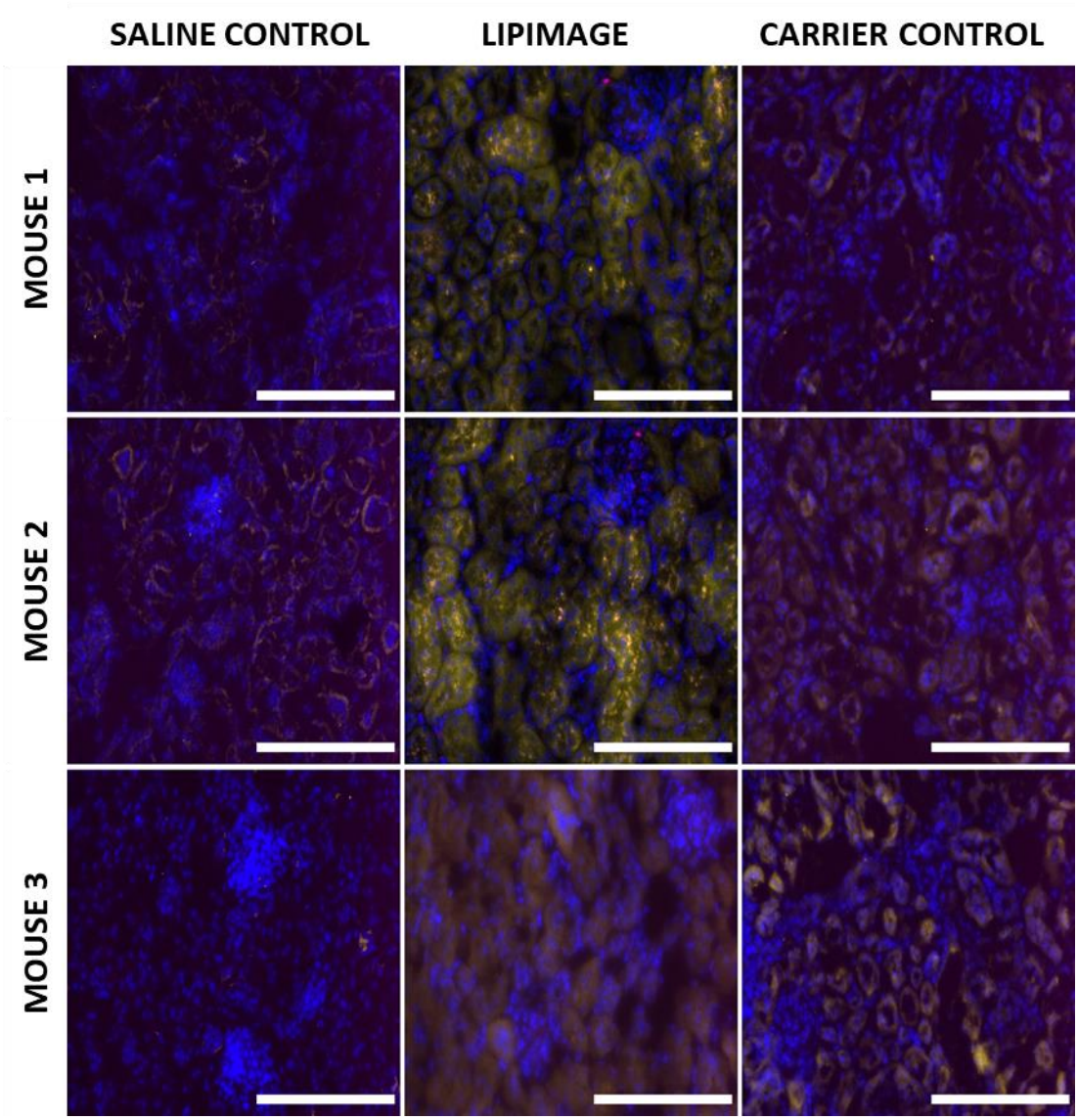

Supplementary figure 8.23: Detection of lipids and IR-780 dye in male kidneys using fluorescent microscopy

Representative photomicrographs showing lipid and IR-780 dye accumulation in kidneys of male C57BL/6 mice used in case study 1. Left hand side column shows sections from animals injected with saline; animals in the middle column were injected with dye-loaded liposome at 100 mg/kg of lipid concentration; animals in the right hand side column were injected with a carrier control liposome filled with soybean-oil (right column) at 100 mg/kg of lipid concentration. Objects of interest were assigned pseudo colour in the images as follows: nuclei are seen in blue, lipids in yellow, IR-780 dye in magenta. Representative images were acquired with 20x lens on LionHeartFX automated microscope. Scale bar represents 200μm.

8.3.2 *Supplementary data for Case study 2: proof of concept*

8.3.2.1 Toxicity

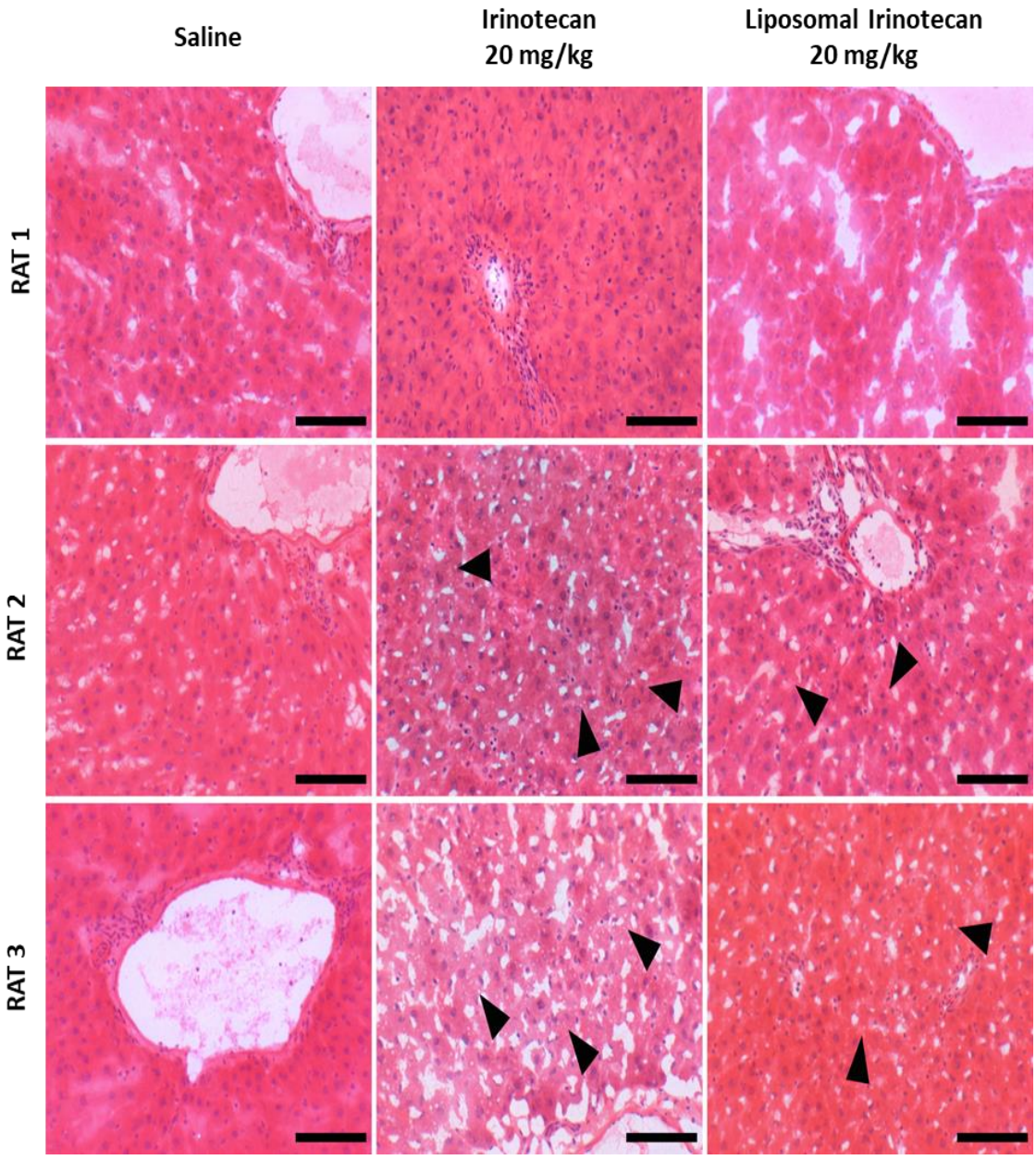

Supplementary figure 8.24: Structural changes in liver following treatment with irinotecan or Onivyde®

Representative photomicrographs of H&E stained liver sections of Wistar rats. Animals were injected with either saline (left column), Irinotecan at 20 mg/kg (middle column), or liposomal Irinotecan at 20 mg/kg (right column). Small vacuoles (black arrowheads) were found within the hepatocytes of some animals treated with Irinotecan and liposomal Irinotecan. Animals were culled 48h post injection and harvested organs were cryopreserved by freezing in OCT media. 10µm sections were cut with a cryostat, stained with H&E stain, and examined using a brightfield microscope. Representative images were acquired with 20x lens. Scale bar represents 100 µm.

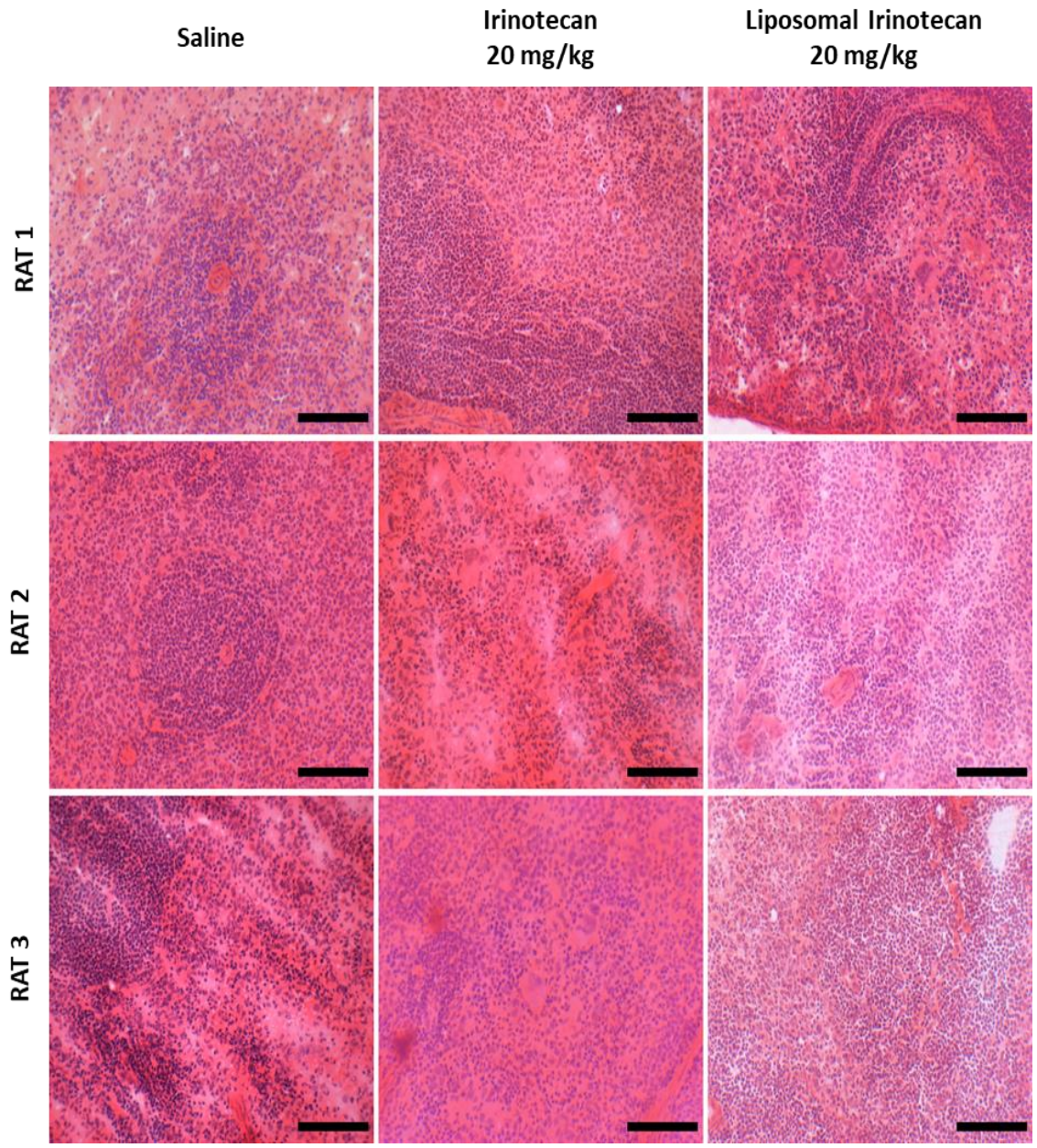

Supplementary figure 8.25: Structural changes in spleen following treatment with irinotecan or Onivyde®

Representative photomicrographs of H&E stained spleen sections of Wistar rats. Animals were injected with either saline (left column), Irinotecan at 20 mg/kg (middle column), or liposomal Irinotecan at 20 mg/kg (right column). No abnormal changes suggestive of toxicity were seen in any of the animals used in this study. Animals were culled 48h post injection and harvested organs were cryopreserved by freezing in OCT media. 10µm sections were cut with a cryostat, stained with H&E stain, and examined using a brightfield microscope. Representative images were acquired with 20x lens. Scale bar represents 100 µm.

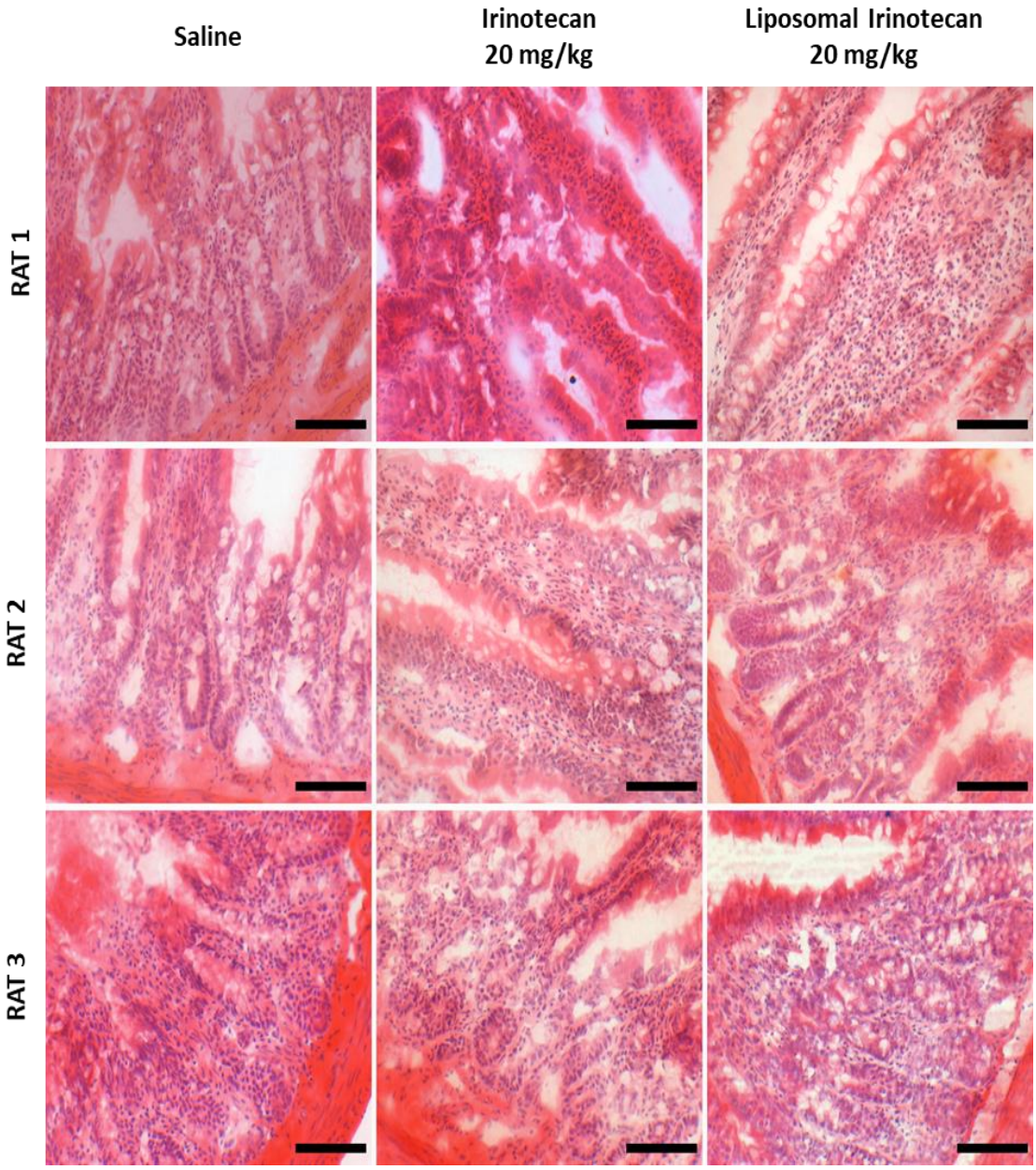

Supplementary figure 8.26: Structural changes in small intestines following treatment with irinotecan or Onivyde ®

Representative photomicrographs of H&E stained small intestine sections of Wistar rats. Animals were injected with either saline (left column), Irinotecan at 20 mg/kg (middle column), or liposomal Irinotecan at 20 mg/kg (right column). No abnormal changes suggestive of toxicity were seen in any of the animals used in this study. Animals were culled 48h post injection and harvested organs were cryopreserved by freezing in OCT media. 10µm sections were cut with a cryostat, stained with H&E stain, and examined using a brightfield microscope. Representative images were acquired with 20x lens. Scale bar represents 100 µm.

8.3.2.2 Accumulation

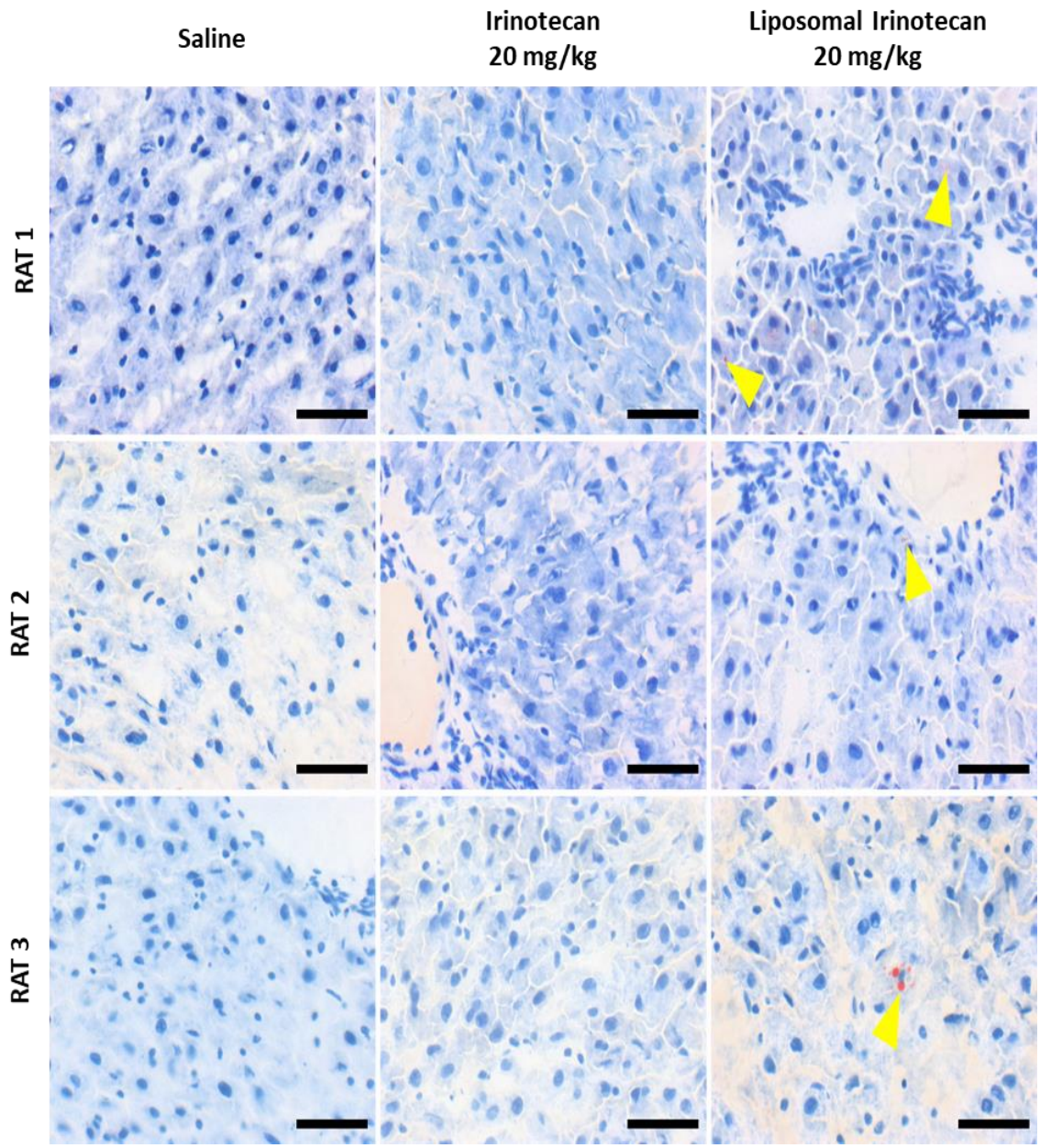

Supplementary figure 8.27: Lipid accumulation in liver following treatment with irinotecan or liposomal irinotecan

Representative photomicrographs of liver from Wistar rats injected with saline (left column) irinotecan at 20 mg/kg (middle column), or Onivyde® at 20 mg/kg of Irinotecan equivalent (right column). Lipid droplets visible as bright red deposits (yellow arrowhead) were seen in animals injected with liposomal Irinotecan. Animals were culled 48h post injection and harvested organs were cryopreserved by freezing in OCT media. 10µm sections were cut with a cryostat, stained with ORO stain, and examined using a brightfield microscope. Representative images were acquired with 40x lens. Scale bar represents 50 µm.

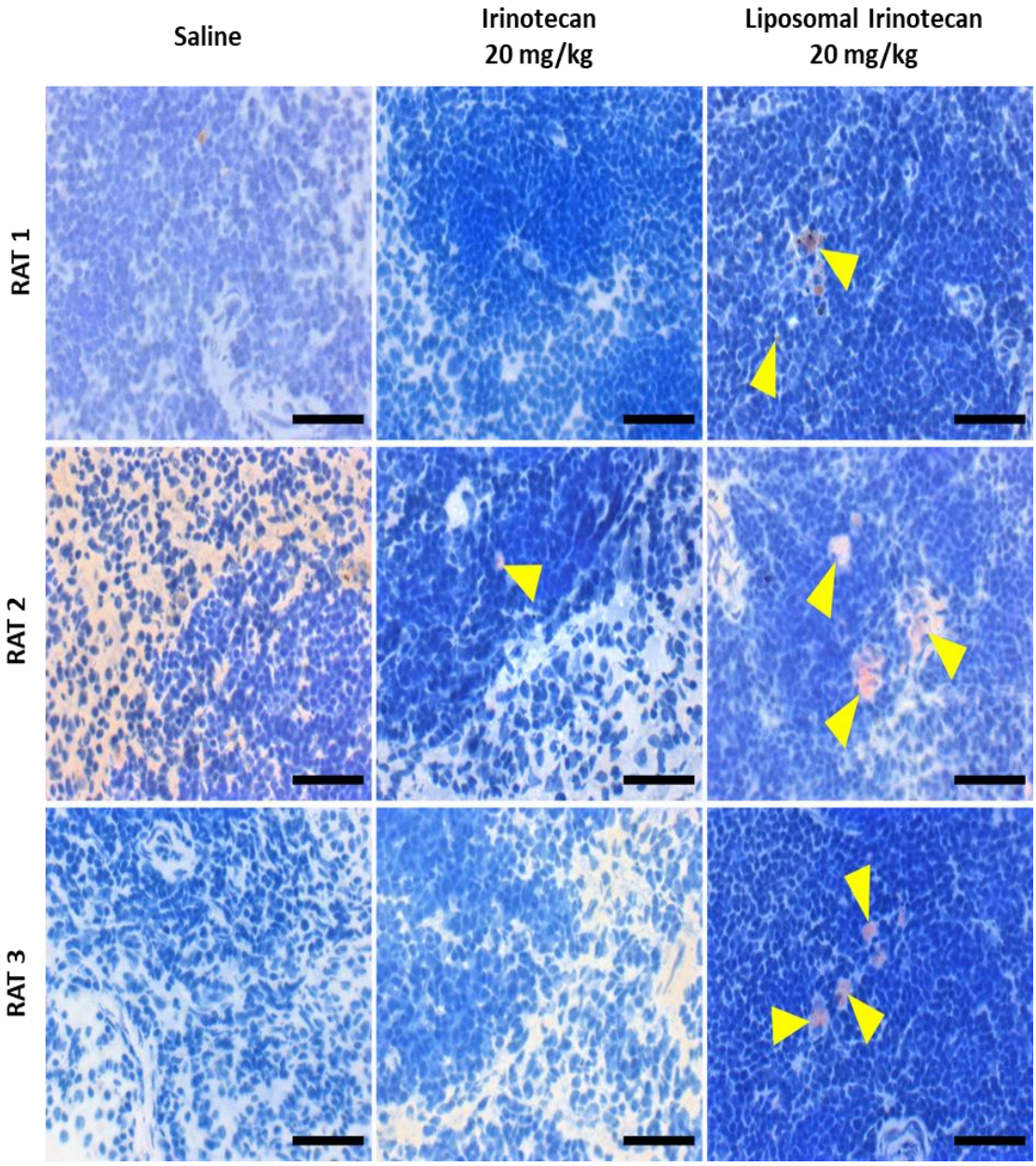

Supplementary figure 8.28: Lipid accumulation in spleen following treatment with irinotecan or liposomal irinotecan

Representative photomicrographs of spleen from Wistar rats injected with saline (left column) irinotecan at 20 mg/kg (middle column), or Onivyde® at 20 mg/kg of Irinotecan equivalent (right column). Lipid droplets visible as bright red deposits (yellow arrowhead) were seen predominantly in animals injected with liposomal Irinotecan, with one animal injected with Irinotecan also showing lipid accumulation. Animals were culled 48h post injection and harvested organs were cryopreserved by freezing in OCT media. 10µm sections were cut with a cryostat, stained with ORO stain, and examined using a brightfield microscope. Representative images were acquired with 40x lens. Scale bar represents 50 µm.

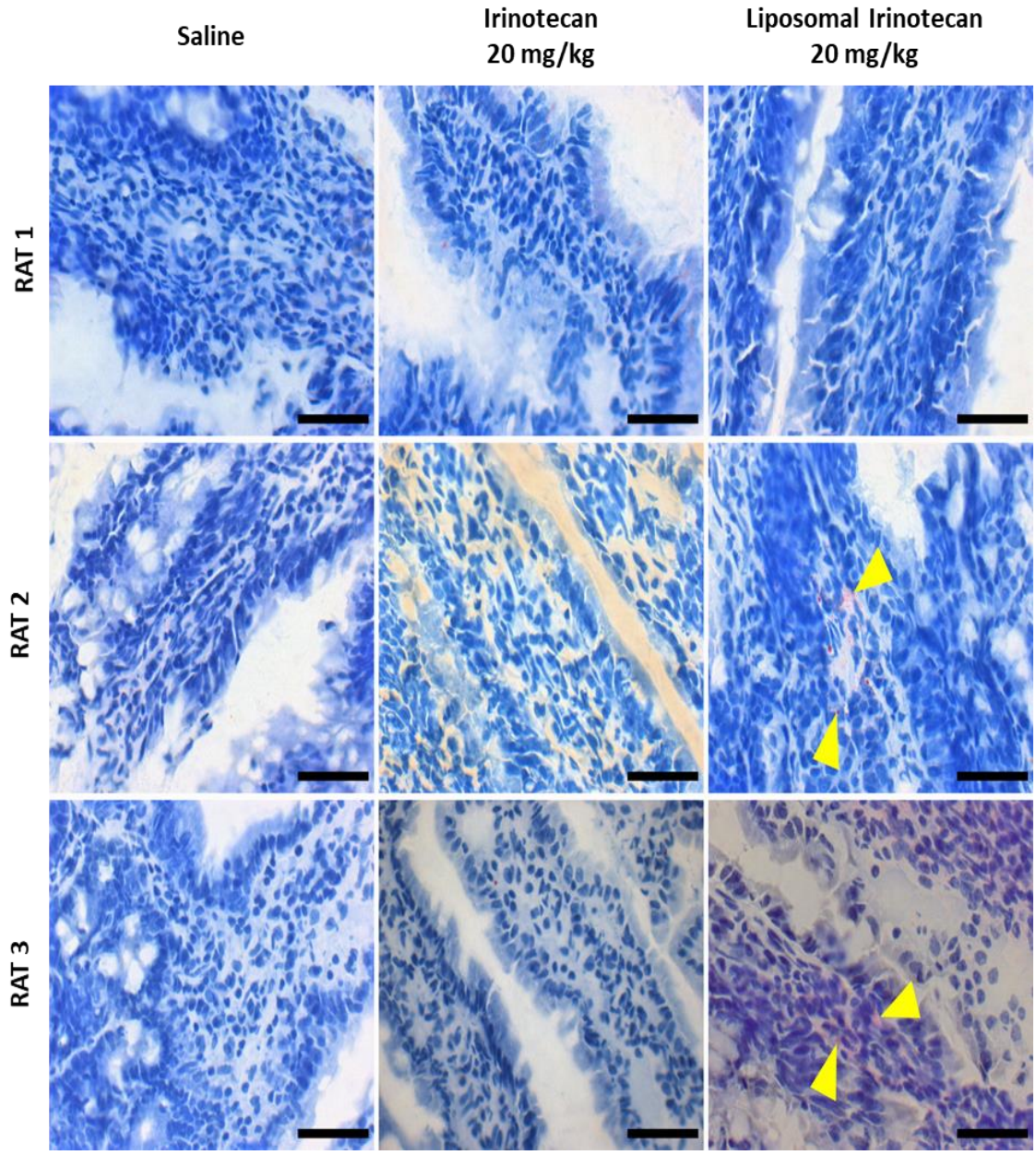

Supplementary figure 8.29: Lipid accumulation in small intestine following treatment with irinotecan or liposomal irinotecan

Representative photomicrographs of spleen from Wistar rats injected with saline (left column) irinotecan at 20 mg/kg (middle column), or Onivyde® at 20 mg/kg of Irinotecan equivalent (right column). Lipid droplets visible as bright red deposits (yellow arrowhead) were seen predominantly in animals injected with liposomal Irinotecan, with one animal injected with Irinotecan also showing lipid accumulation. Representative images were acquired with 40x lens. Scale bar represents 50 μm.

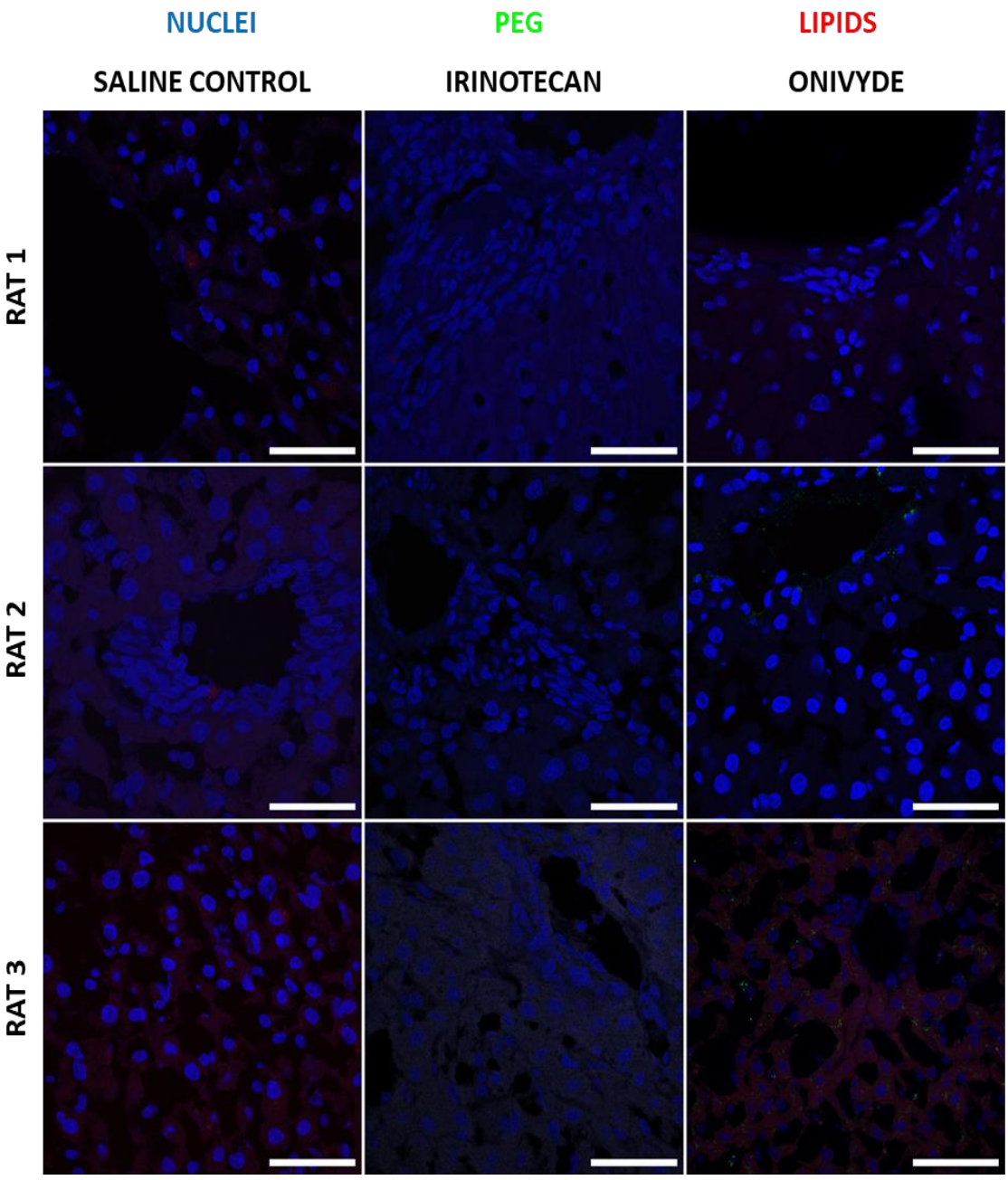

Supplementary figure 8.30: Immunofluorescent detection of lipids and PEG in liver
Representative photomicrographs showing lipid and PEG accumulation in livers of Wistar rats used in case study 2. Animal were injected with saline (left column), free irinotecan at 20 mg/kg (middle column), or Onivyde® at 20 mg/kg of irinotecan equivalent (right column). Objects of interest were assigned pseudo colour as follows: nuclei in blue, PEG in green, lipids in red. Co-localisation of lipid and PEG (white arrowheads) was seen in the animals injected with Onivyde®. Representative images were acquired with 63x lens. Scale bar represents 50 μm.

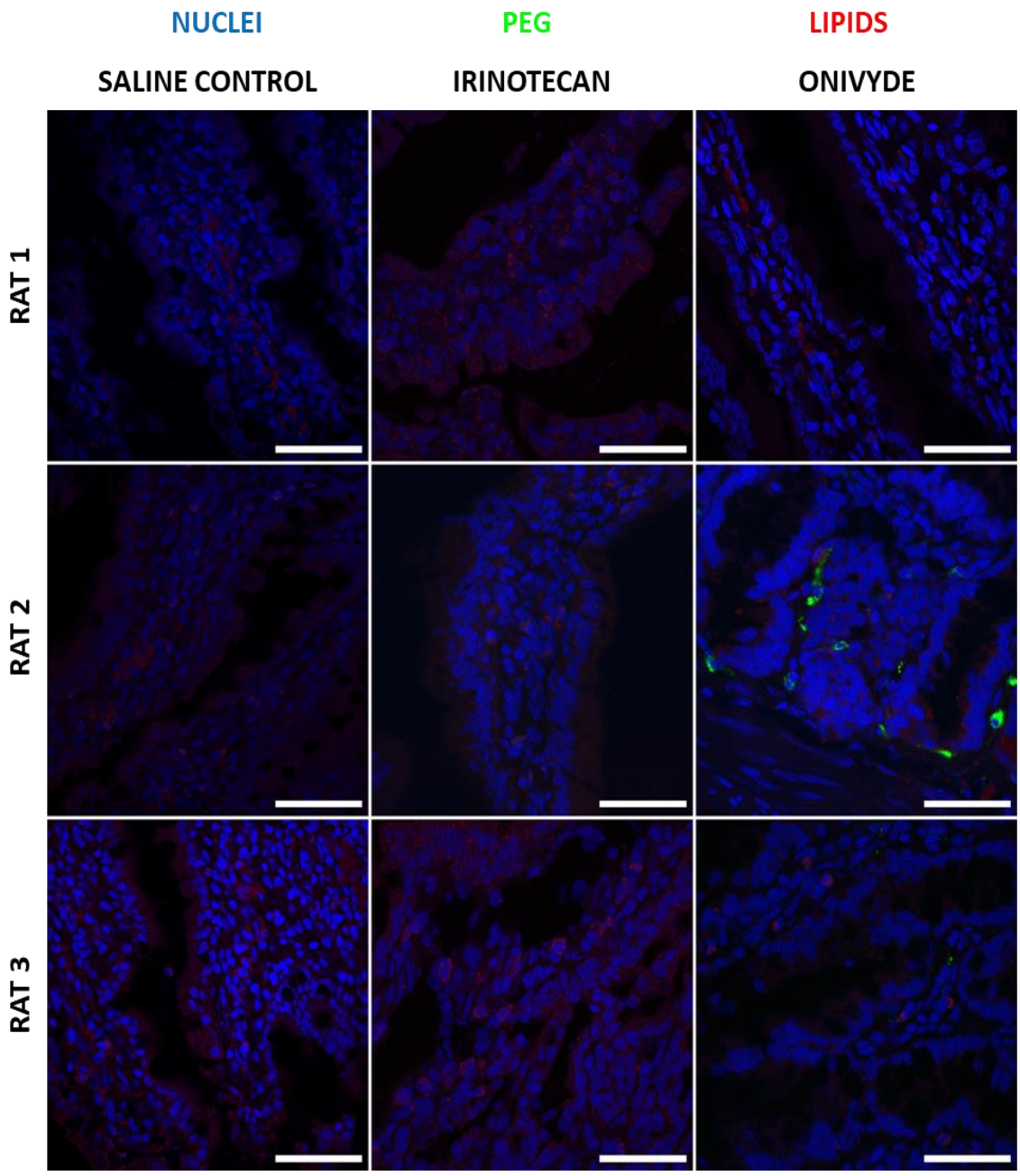

Supplementary figure 8.31: Immunofluorescent detection of lipids and PEG in small intestine
Representative photomicrographs showing lipid and PEG accumulation in small intestines of Wistar rats used in case study 2. Animal were injected with saline (left column), free irinotecan at 20 mg/kg (middle column), or Onivyde® at 20 mg/kg of irinotecan equivalent (right column). Objects of interest were assigned pseudo colour as follows: nuclei in blue, PEG in green, lipids in red. Co-localisation of lipid and PEG (white arrowheads) was seen in the lacteal of the animals injected with Onivyde®. Representative images were acquired with 63x lens. Scale bar represents 50 μm.

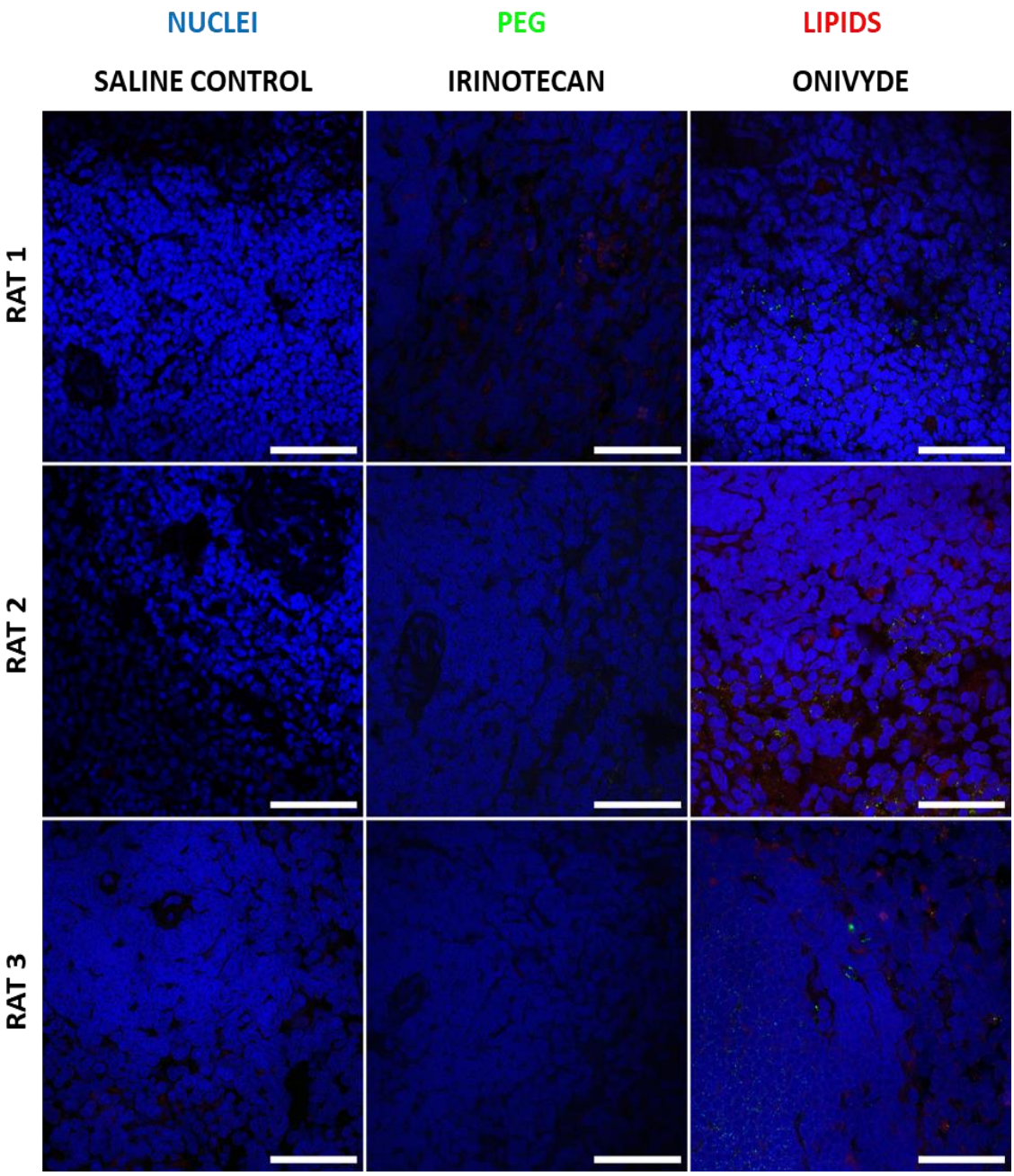

Supplementary figure 8.32: Immunofluorescent detection of lipids and PEG in spleen.
Representative photomicrographs showing lipid and PEG accumulation in spleens of Wistar rats used in case study 2.. Animal were injected with saline (left column), free irinotecan at 20 mg/kg concentration (middle column), or Onivyde® at 20 mg/kg of irinotecan equivalent (right column). Objects of interest were assigned pseudo colour as follows: nuclei in blue, PEG in green, lipids in red. Co-localisation of lipid and PEG (white arrowheads) was seen in the animals injected with Onivyde®. Representative images were acquired with 63x lens. Scale bar represents 50 μm.

8.3.2.3 Pharmacokinetics

CPT-11 is a prodrug which undergoes de-esterification by carboxylesterases to yield its active metabolite SN-38, which is up to 1000-fold more potent than irinotecan [225]. SN-38 is detoxified in the liver by the polymorphic enzyme UGT-1A1 to SN-38-glucuronide and both metabolites are eliminated by biliary excretion. The reverse deglycosylation reaction can also take place in the intestinal lumen by bacterial-derived β-glucuronidase activity.

Plasma profile of CPT-11, SN-38 and SN-38 glucuronide was evaluated with MS (Supplementary figure 8.33). As expected, higher concentrations of CPT-11 were retained up to 48h post injection in the Onivyde® treated animals (Onivyde group). None of the metabolites were detected in the plasma of irinotecan treated animals (irinotecan group) at 48h post injection. The same pattern was observed for other two metabolites of irinotecan.

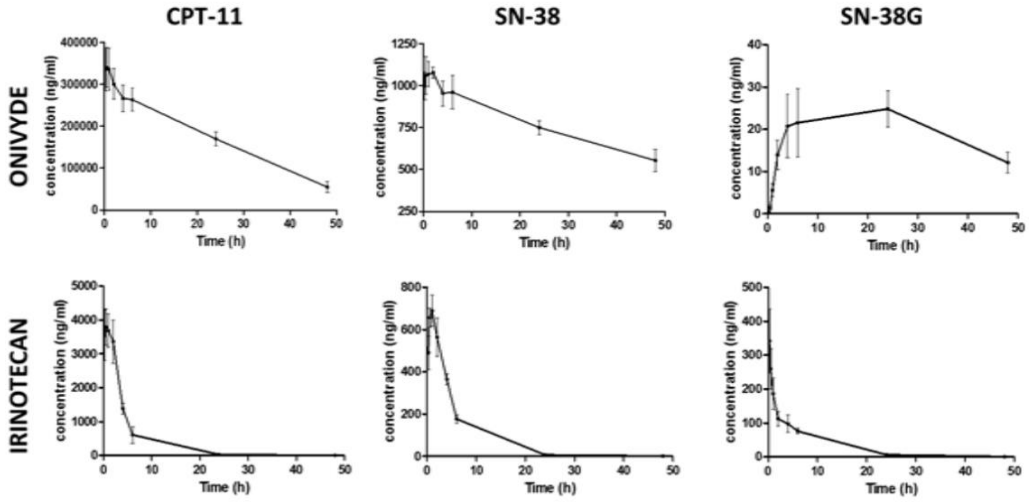

Supplementary figure 8.33: Pharmacokinetic profile of CPT-11, SN-38 and SN-38 glucuronide in plasma.
Animals were injected intravenously with a single dose of irinotecan or Onivyde® at 20 mg/kg irinotecan equivalent. MS was carried out by the collaborators on the project Dr. Sven Even Borgos and Dr. Astrid Hyldbakk at SINTEF in Norway.

8.3.2.4 Clearance

As it has been previously reported that irinotecan is mainly excreted via faeces [226], samples were collected, if available at 24 and 48 h post drug injection and analysed with MS for presence of CPT-11, SN-38 and SN-38G. In both treatment groups, faecal content of CPT-11 was higher compared to other metabolites. Animals treated with nanoliposomal formulation retained

relatively low concentration of CPT-11 in faeces up to 48h post-injection (Supplementary figure 8.34). This highlights prolonged retention time achieved by using liposome as a drug delivery method.

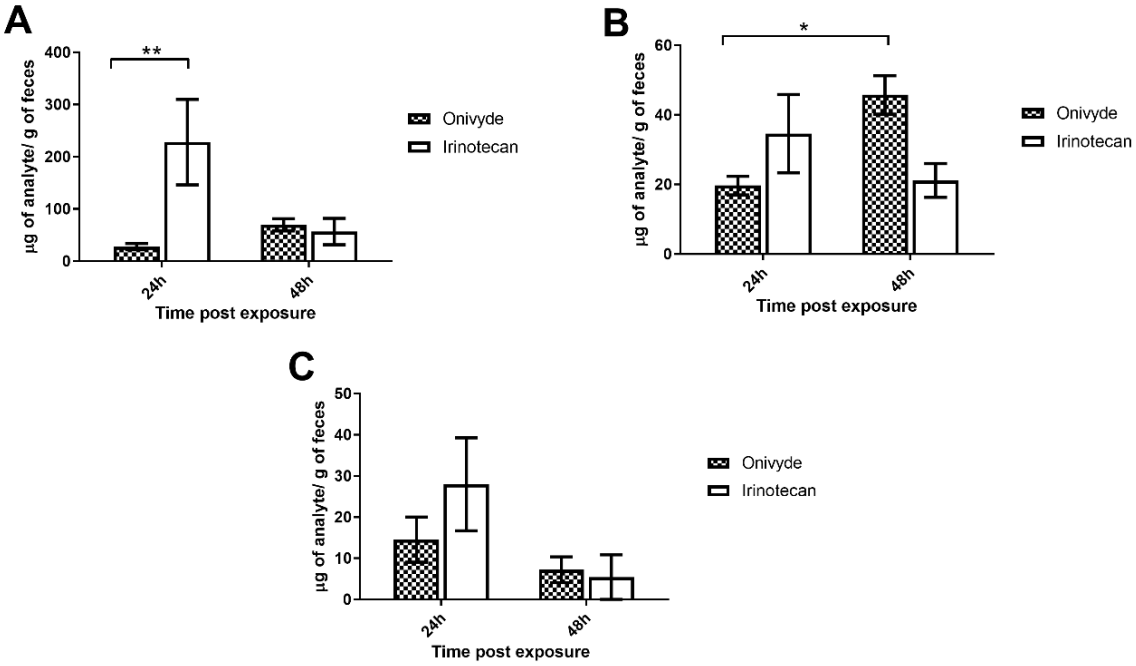

Supplementary figure 8.34: Faecal profile of CPT-11, SN-38 and SN-38G
Faecal profile of CPT-11 (A), SN-38 (B), and SN-38G (C). Faeces were collected at 24 and 48h after single dose intravenous administration of Onivyde® (checker pattern) or irinotecan (white fill) at 20 mg/kg irinotecan equivalent. Samples were dried in the oven and shipped to the collaborator (SINTEF, Norway) for the analysis. Data represent mean ± SEM. MS was carried out by the collaborators on the project Dr. Sven Even Borgos and Dr. Astrid Hyldbakk at SINTEF in Norway.

8.3.3 *Supplementary data for Case study 3: In vivo toxicity and biodistribution of MF66 MNPs*

8.3.3.1 Macro script for image processing

Representative images from Perl's Prussian blue stained slides were acquired using a 10x lens on an automated microscope LionHeart FX and were subjected to a number of processes coded in the macro language as detailed below.

8.3.3.1.1 Image pre-processing

```
run("Subtract Background...", "rolling=50 light");
run("Sharpen");
```

8.3.3.1.2 Macro script for particle analysis

```
setOption("ScaleConversions", true);
run("8-bit");
setAutoThreshold("Default dark");
//run("Threshold...");
setThreshold(191, 255);
//setThreshold(191, 255);
setOption("BlackBackground", true);
run("Convert to Mask");
run("Analyze Particles...", "display clear summarize");
```

8.3.3.1.3 Macro script for measuring tissue area

```
setOption("ScaleConversions", true);
run("8-bit");
setAutoThreshold("Default dark");
//run("Threshold...");
setThreshold(191, 255);
//setThreshold(191, 255);
setOption("BlackBackground", true);
run("Convert to Mask");
run("Measure");
```

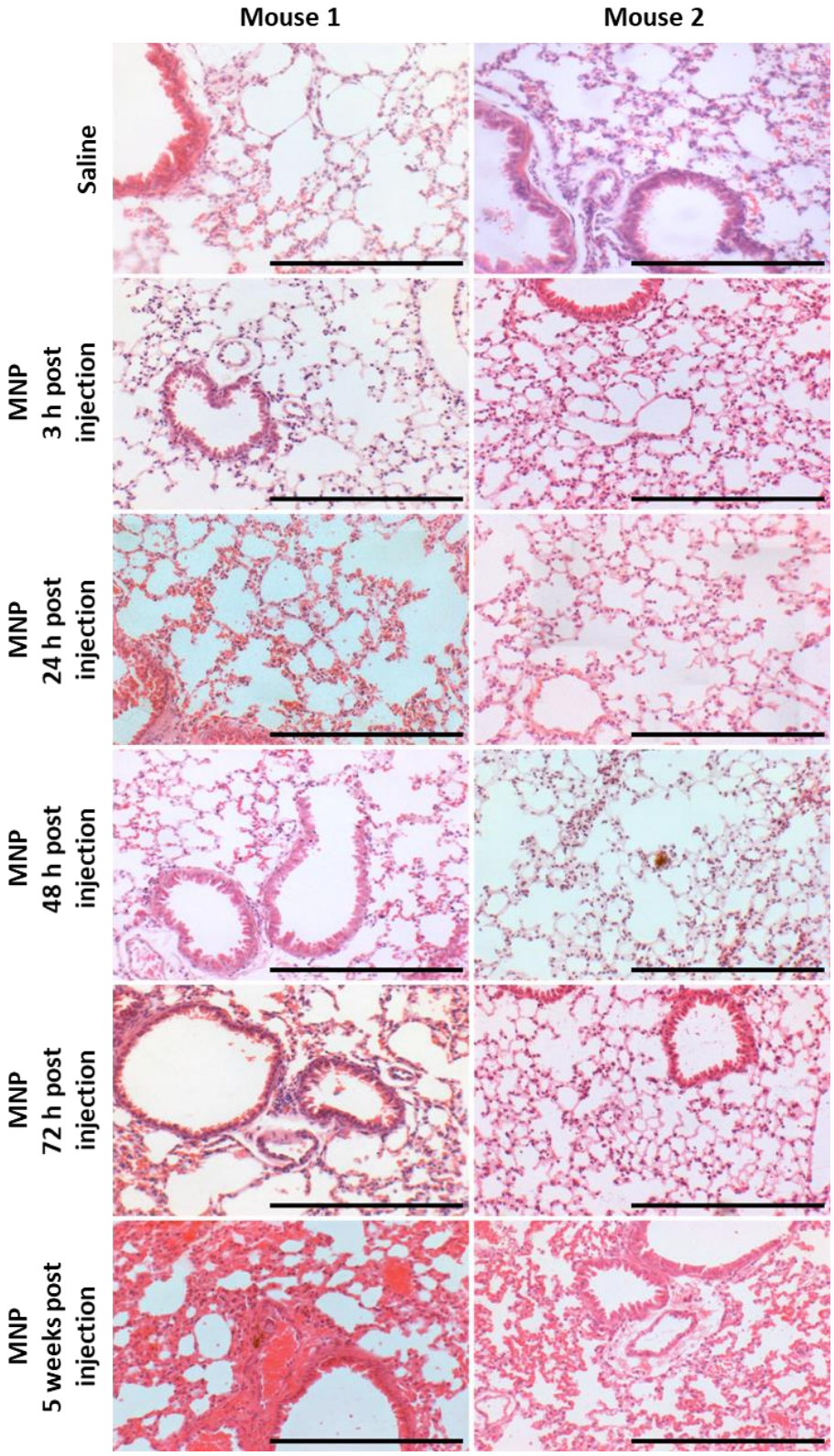

Supplementary figure 8.35: Structural changes induced by MNPs in lungs
Representative photomicrographs of H&E stained lung sections of BALB/c mice injected with saline (top row) or 10 mg/ml of MNPs and sacrificed at 3h, 24h, 48h, 72h and 5 weeks. No abnormal changes suggestive of toxicity were seen in any of the animals used in this study. MNPs aggregates can be seen as granular brown deposits. Images were acquired with 20x lens; scale bar represents 250 µm.

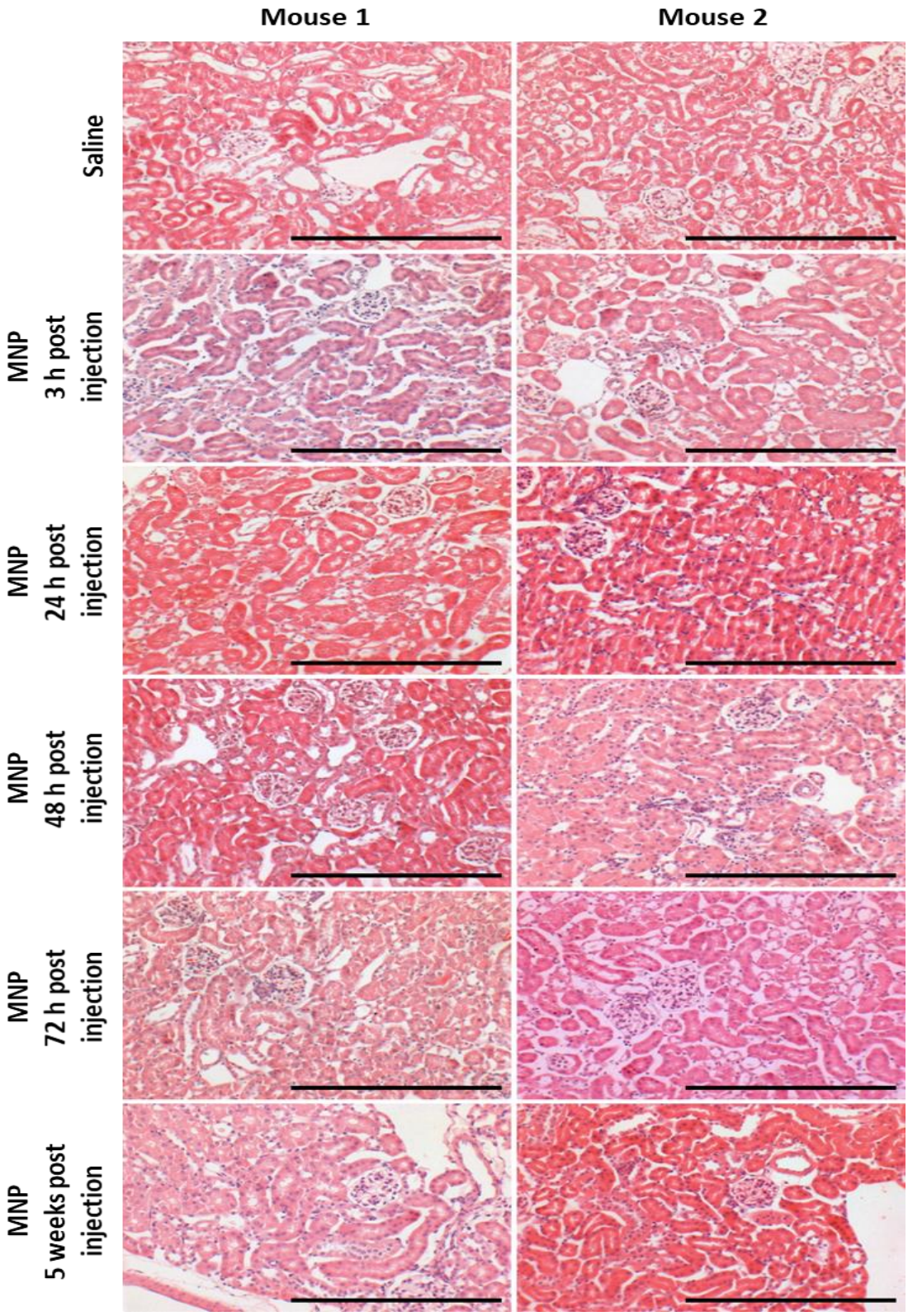

Supplementary figure 8.36: Structural changes induced by MNPs in kidneys
Representative photomicrographs of H&E stained kidney sections of BALB/c mice injected with saline (top row) or 10 mg/ml of MNPs and sacrificed at 3h, 24h, 48h, 72h and 5 weeks. No abnormalities suggestive of toxicity were seen in any of the animals. Images were acquired with 20x lens; scale bar represents 250 µm.

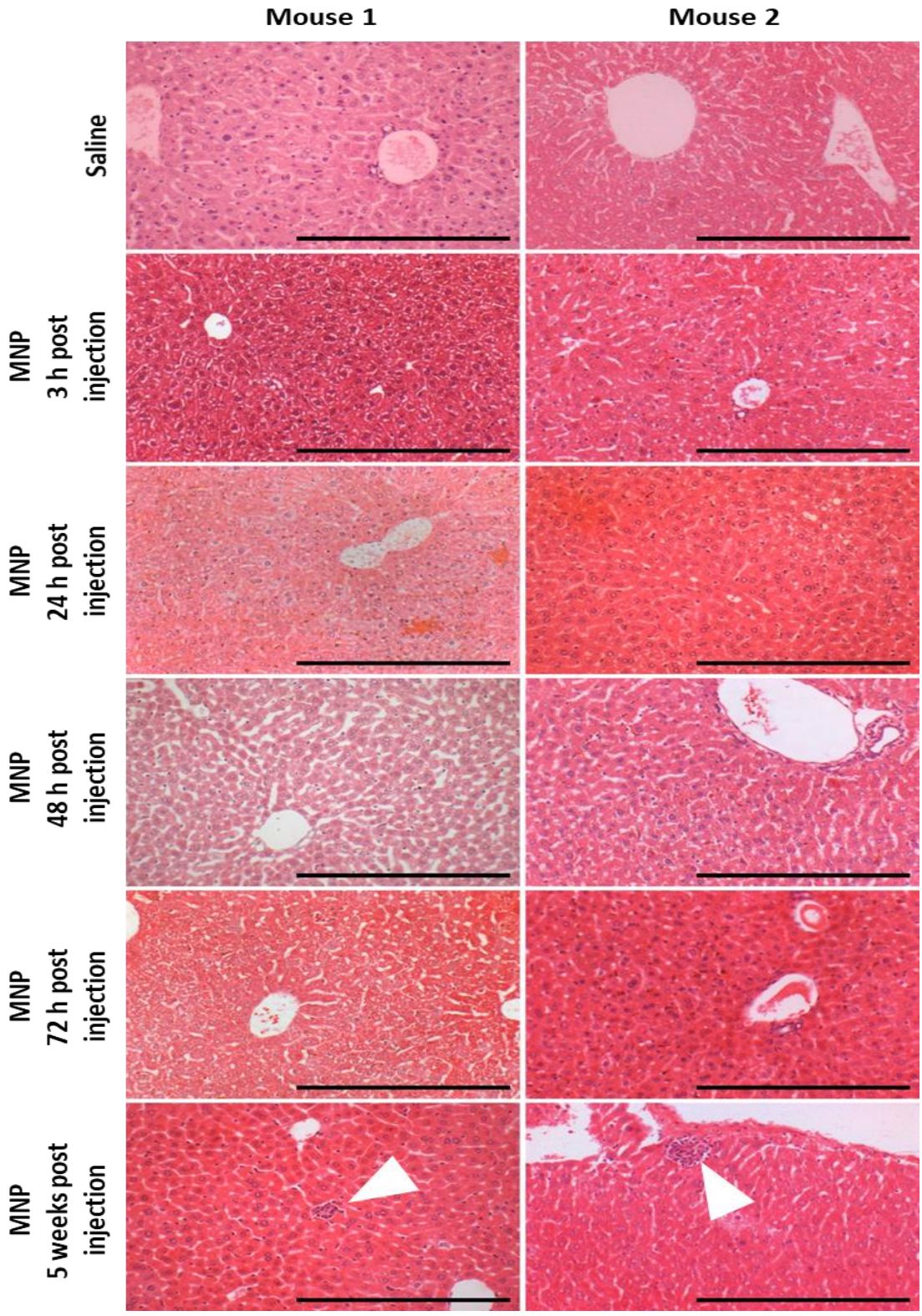

Supplementary figure 8.37: Structural changes induced by MNPs in liver
Representative photomicrographs of H&E stained liver sections of BALB/c mice injected with saline (top row) or 10 mg/ml of MNPs and sacrificed at 3h, 24h, 48h, 72h and 5 weeks. Small foci of inflammation (white arrowhead) were predominantly found in animals sacrificed 5 weeks post injection. Images were acquired with 20x lens; scale bar represents 250 µm.

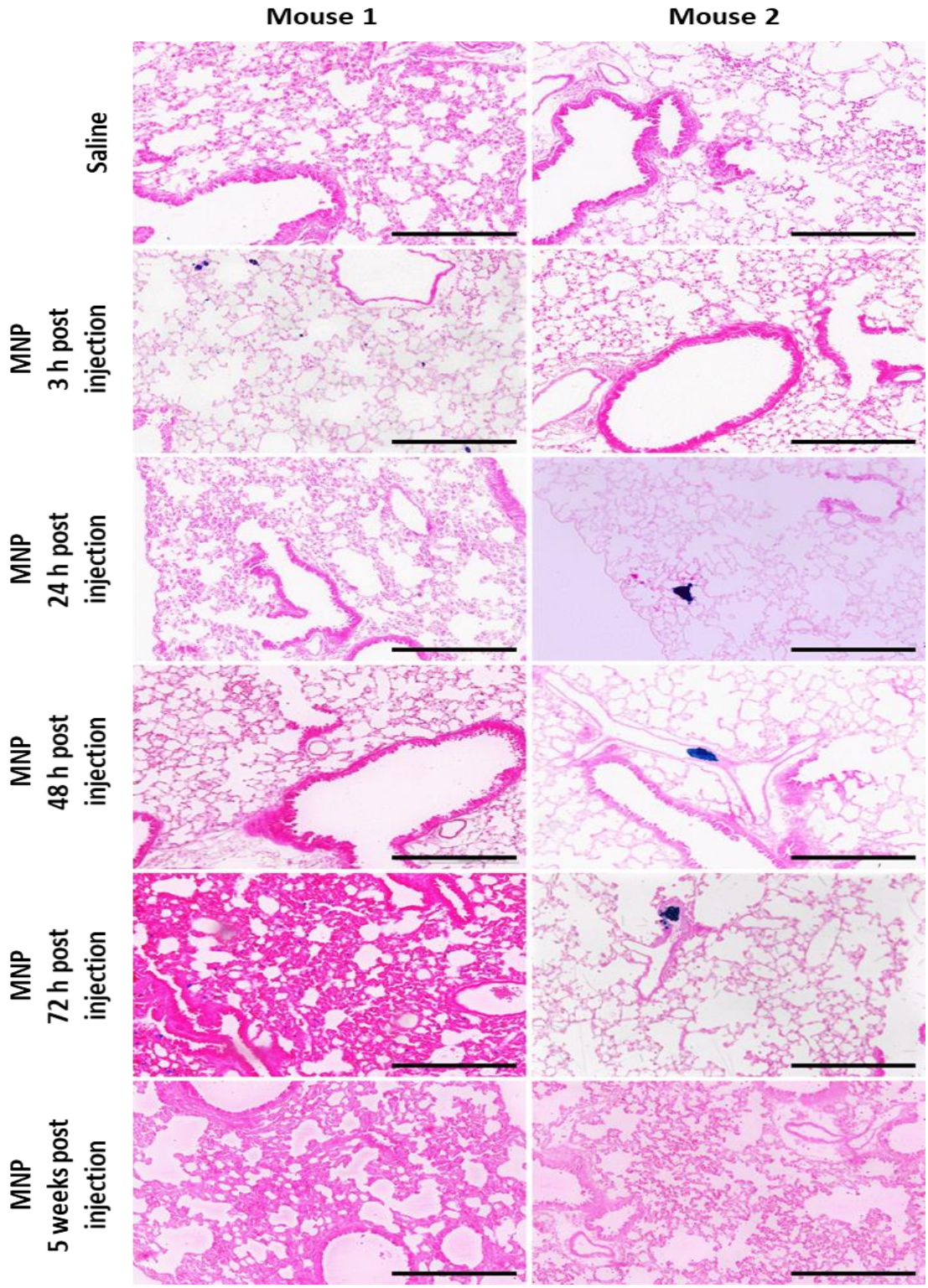

Supplementary figure 8.38: Accumulation of MNPs in lungs
Representative photomicrographs of PPB stained lung sections from BALB/c mice showing accumulation and distribution of MNPs (blue deposits). Animals were injected with either saline (top row) or 10 mg/ml of MNPs and sacrificed at 3h, 24h, 48h, 72h and 5 weeks. Representative images from all animals used in this study highlight animal to animal variation at each time post injection examined. Images were acquired with a 10x lens. Scale bar represents 200 µm.

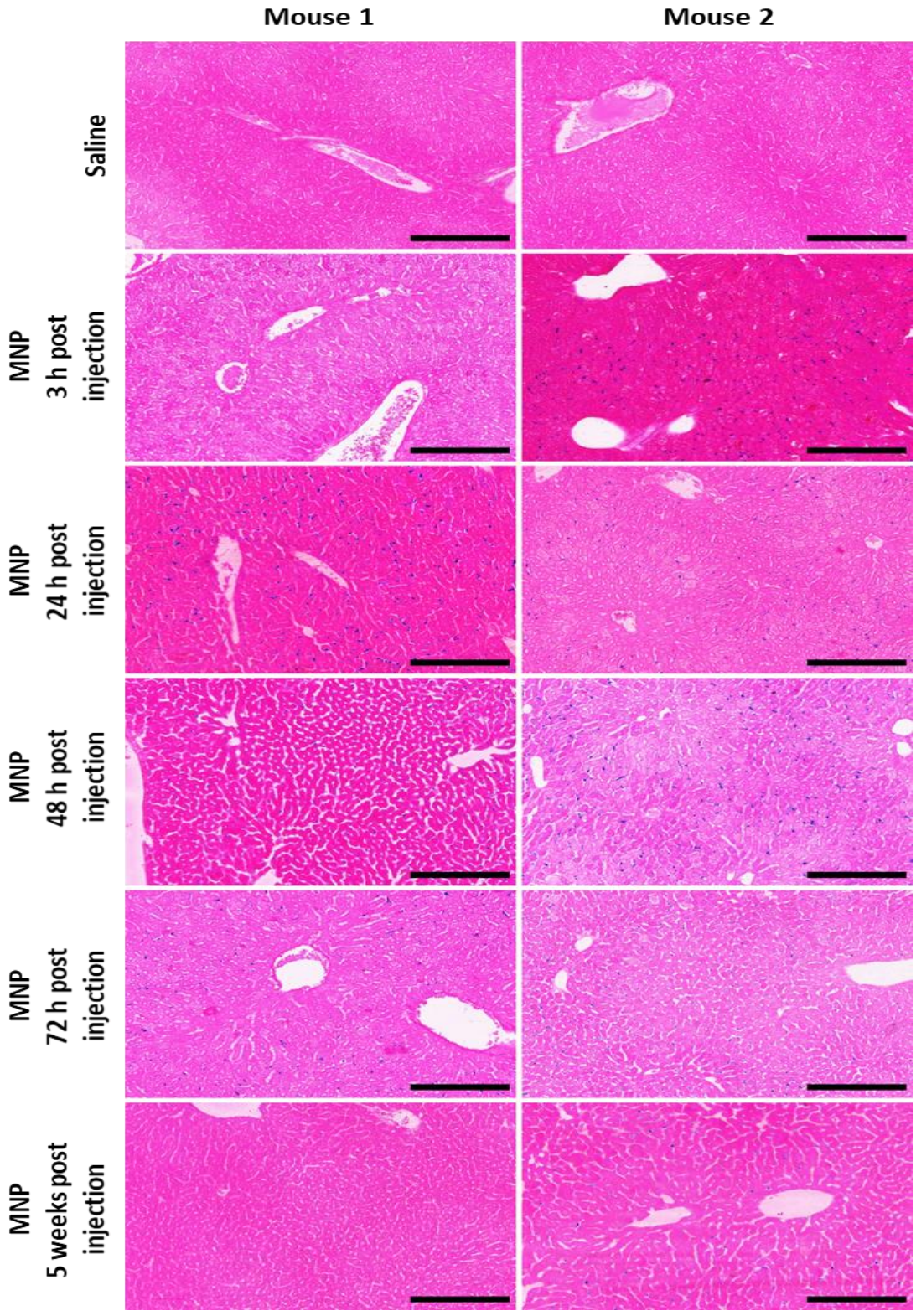

Supplementary figure 8.39: Accumulation of MNPs in liver
Representative photomicrographs of PPB stained liver sections from BALB/c mice showing accumulation and distribution of MNPs (blue deposits). Animals were injected with either saline (top row) or 10 mg/ml of MNPs and sacrificed at 3h, 24h, 48h, 72h and 5 weeks. Representative images from all animals used in this study highlight animal to animal variation at each time post injection examined. Images were acquired with a 10x lens. Scale bar represents 200 µm.

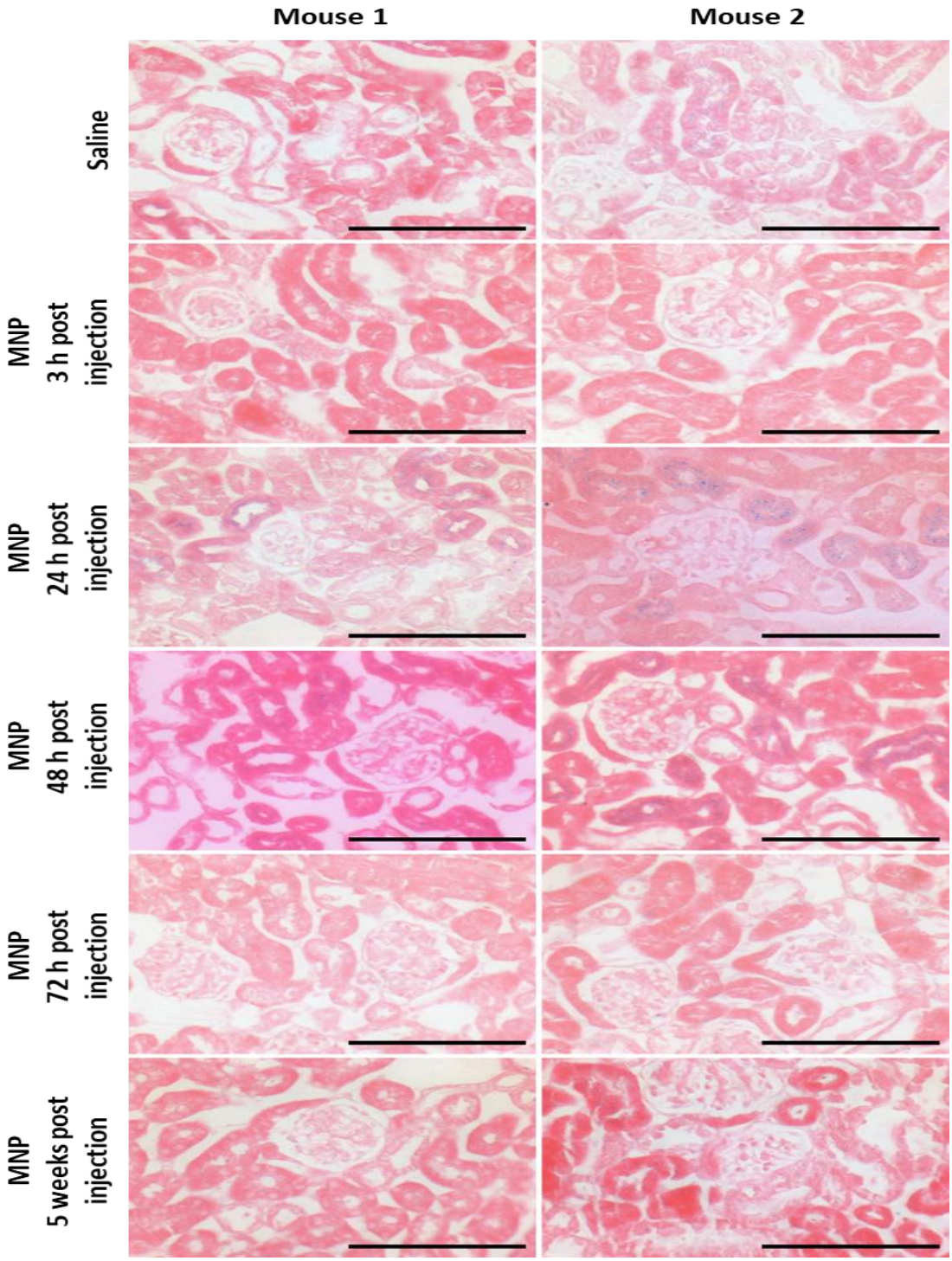

Supplementary figure 8.40: Accumulation of MNPs in kidneys
Representative photomicrographs of PPB stained kidney sections from BALB/c mice showing accumulation and distribution of MNPs (blue deposits). Animals were injected with either saline (top row) or 10 mg/ml of MNPs and sacrificed at 3h, 24h, 48h, 72h and 5 weeks. Magnitude of the animal to animal variation was much smaller in comparison to lung and liver. Images were acquired with a 40x lens. Scale bar represents 50 µm.

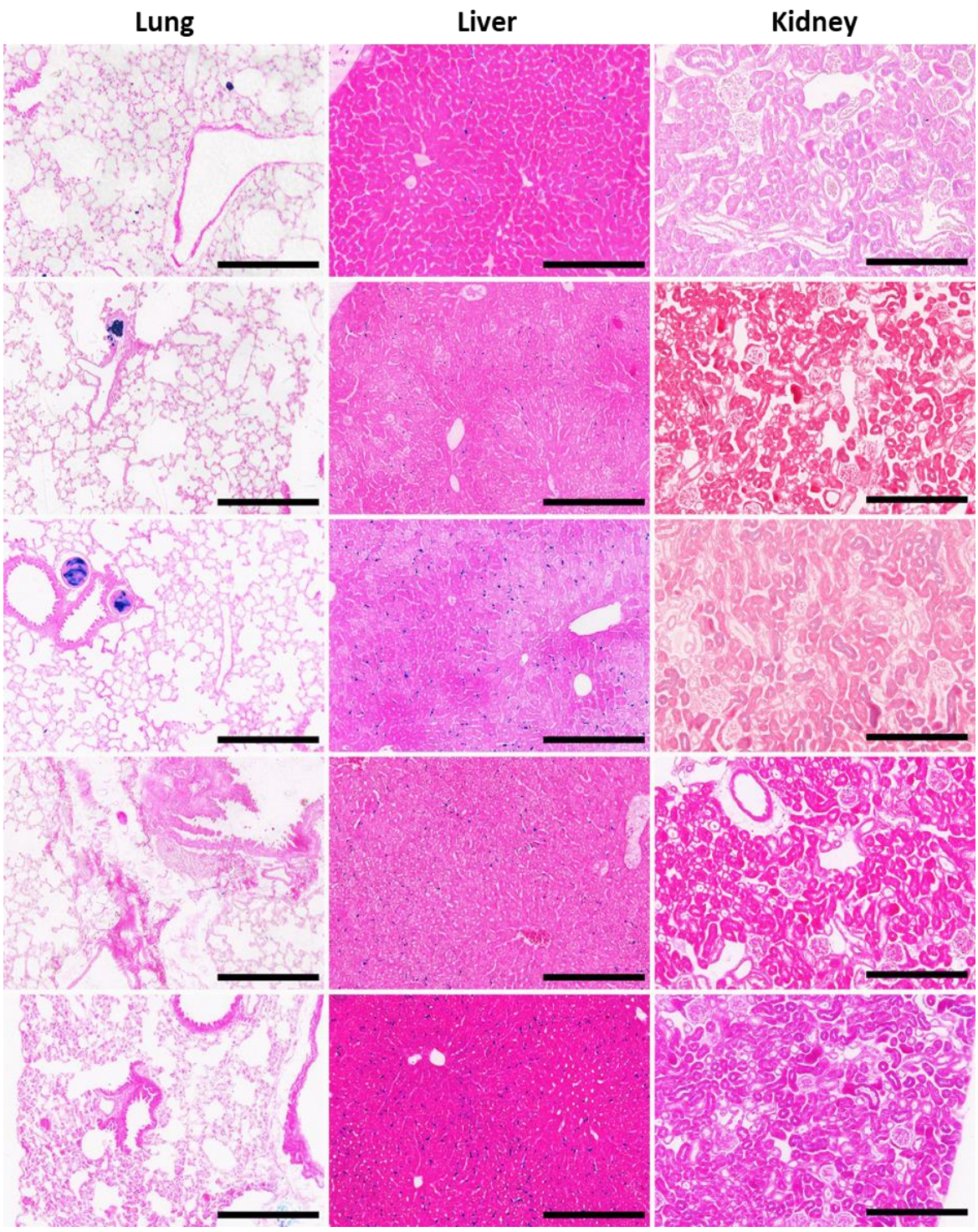

Supplementary figure 8.41: Representative images selected for training WEKA classifier
For training the classifier, 5 images from each organ of interest were selected to account for diversity in obtained data in terms of size of iron deposits, intensity of staining and variation in tissue structure. Images were acquired using an automated microscope LionHeartFX with a 10x lens. Scale bar represents 250 µm

.

8.3.4 *Supplementary data for case study 4: In vivo acute toxicity study of NOC0007 and RCL-01*

8.3.4.1 Toxicity

Supplementary table 8.8: Full description of iron accumulation and pathological changes in all organs from animals tested inNOC0007 experimental block in case study 4 .
Summary of findings reported by the certified pathologist from St. James' Central Pathology Laboratory on histological changes and accumulation of iron for slices obtained from the organs of experimental animal used in case study 4. Pathologist was blinded to type of injection given. Slides were assessed on a scale of 1-4 for both toxicity and iron accumulation. NAD: nothing abnormal detected

Animal ID	Organ	Diagnosis		Iron accumulation	
		Score	description	Score	description
1 MNPs 30 mg/kg	Liver	0	NAD	2	In Kupffer cells in sinusoids only
	Lung	0	NAD	1	Staining macrophages around blood vessels
	Spleen	0	NAD	4	Predominantly in the red pulp
	Kidney	1	tubular dilation	1	iron in the tubules
2 MNPs 30 mg/kg	Liver	2	congestion	2	In Kupffer cells in sinusoids only
	Lung	1	Thrombus/iron in blood vessels	0	N/A
	Spleen	1	presence of giant cells	4	Predominantly in the red pulp
	Kidney	1	calcification	1	iron in the tubules
3 MNPs 45 mg/kg	Liver	1	congestion	0	N/A
	Lung	0	NAD	0	N/A
	Spleen	1	presence of giant cells	4	Predominantly in the red pulp
	Kidney	2	tubular dilation, vacuolar change	1	iron in the tubules
4 MNPs 60 mg/kg	Liver	1	congestion	2	In Kupffer cells in sinusoids only
	Lung	2	Pigment in blood vessels	1	Staining macrophages around blood vessels, iron in blood vessels
	Spleen	1	presence of giant cells	4	Predominantly in the red pulp
	Kidney	1	tubular dilation	1	iron in the tubules

5 Saline	Liver	1	congestion	0	N/A
	Lung	0	NAD	0	N/A
	Spleen	1	presence of giant cells	4	Predominantly in the red pulp
	Kidney	1	calcification, tubular atrophy/autolysis	2	iron in the tubules
6 MNPs 45 mg/kg	Liver	0	NAD	2	In Kupffer cells in sinusoids only
	Lung	1	Pigment in blood vessels	1	Iron in blood vessels
	Spleen	1	presence of giant cells	4	Predominantly in the red pulp
	Kidney	1	calcification	1	iron stain in the tubules
7 MNPs 60 mg/kg	Liver	0	NAD	2	In Kupffer cells in sinusoids only
	Lung	1	Pigment deposition in blood vessels, no alveolar damage	1	Staining macrophages around blood vessels
	Spleen	1	presence of giant cells	4	Predominantly in the red pulp
	Kidney	0	NAD	1	iron in the tubules
8 Saline	Liver	1	congestion	0	N/A
	Lung	0	NAD	0	N/A
	Spleen	2	presence of giant cells	4	Predominantly in the red pulp
	Kidney	2	tubule dilation, vacuolar change	1	iron in the tubules
9 MNPs 30 mg/kg	Liver	1	congestion	2	In Kupffer cells in sinusoids only
	Lung	1	Pigment deposition in blood vessels, no alveolar damage	1	Thrombus/iron in blood vessels
	Spleen	1	presence of giant cells	4	Predominantly in the red pulp
	Kidney	1	tubule dilation	1	iron in the tubules
10 MNPs 60 mg/kg	Liver	0	NAD	2	In Kupffer cells in sinusoids only
	Lung	0	NAD	1	Staining macrophages around blood vessels
	Spleen	1	presence of giant cells	4	Predominantly in the red pulp

	Kidney	0	NAD	1	iron in the tubules
11 MNPs 45 mg/kg	Liver	0	NAD	2	In Kupffer cells in sinusoids only
	Lung	1	Pigment deposition in small blood vessels	1	Staining macrophages around blood vessels, iron in blood vessels
	Spleen	1	presence of giant cells	4	Predominantly in the red pulp
	Kidney	0	NAD	1	iron in the tubules
12 Saline	Liver	0	NAD	1	In Kupffer cells in sinusoids only
	Lung	0	NAD	0/1	Staining macrophages around blood vessels
	Spleen	1	presence of giant cells	4	Predominantly in the red pulp
	Kidney	1	calcification	2	iron in the tubules
13 Saline	Liver	1	congestion	1	In Kupffer cells in sinusoids only
	Lung	0	NAD	1	Staining macrophages around blood vessels
	Spleen	1	presence of giant cells	4	Predominantly in the red pulp
	Kidney	1	Mild dilation of tubules and vacuolation on the surface only. Calcification within the cortex	2	iron in the tubules
14 MNPs 30 mg/kg	Liver	0	NAD	0	N/A
	Lung	0	NAD	1	Staining macrophages around blood vessels
	Spleen	1	scattered giant cells	4	Predominantly in the red pulp
	Kidney	1	mild vacuolation and dilated tubules on the surface (may be artifactual)	2	iron in the tubules
15 MNPs 30 mg/kg	Liver	1	mild hepatic congestion	2	In Kupffer cells in sinusoids only
	Lung	1	Pigment in blood vessels and capillaries	1	Iron in blood vessels and capillaries

	Spleen	1	presence of giant cells	3	Predominantly in the red pulp
	Kidney	1	tubular dilation, vacuolar change	1	iron in the tubules
16 MNPs 30 mg/kg	Liver	0	NAD	2	In Kupffer cells in sinusoids only
	Lung	1	Pigment deposition in blood vessels	1	Staining macrophages around blood vessels, iron in the blood vessels
	Spleen	1	presence of giant cells	4	Predominantly in the red pulp
	Kidney	0	NAD	1	iron in the tubules
17 Saline	Liver	0	NAD	0	N/A
	Lung	0	NAD	0	N/A
	Spleen	1	presence of giant cells	4	Predominantly in the red pulp
	Kidney	0	NAD	1	iron in the tubules
18 MNPs 45 mg/kg	Liver	0	NAD	1	In Kupffer cells in sinusoids only
	Lung	0	NAD	1	Staining macrophages around blood vessels
	Spleen	2	reduced white pulp, expanded red pulp, presence of Giant cells	4	Predominantly in the red pulp
	Kidney	0	NAD	2	iron in the tubules
19 MNPs 45 mg/kg	Liver	1	mild hepatic congestion	2	In Kupffer cells in sinusoids only
	Lung	1	Pigment deposition in blood vessels	1	staining in macrophages around blood vessels (no staining of epithelial cells) staining within capillaries also
	Spleen	1	presence of giant cells	4	Predominantly in the red pulp
	Kidney	0	NAD	1	iron in the tubules
20 MNPs 45 mg/kg	Liver	1	mild hepatic congestion	2	In Kupffer cells in sinusoids only
	Lung	1	Pigment deposition in blood vessels	1	Staining macrophages around blood vessels, iron within small vessels and capillaries
	Spleen	0	NAD	4	Predominantly in the red pulp

	Kidney	0	NAD	2	iron in the tubules
21 Saline	Liver	0	NAD	0	N/A
	Lung	0	NAD	0	N/A
	Spleen	1	presence of giant cells	4	Predominantly in the red pulp
	Kidney	0	NAD	1	iron in the tubules
22 MNPs 60 mg/kg	Liver	0	NAD	2	In Kupffer cells in sinusoids only
	Lung	0	NAD	1	Staining macrophages around blood vessels
	Spleen	1	presence of giant cells	4	Predominantly in the red pulp
	Kidney	1	mild vacuolation of the renal tubules	3	iron in the tubules
23 MNPs 60 mg/kg	Liver	0	NAD	2	In Kupffer cells in sinusoids only
	Lung	1	Pigment deposition in blood vessels	1	Staining macrophages around blood vessels, iron within the blood vessels
	Spleen	1	presence of giant cells	4	Predominantly in the red pulp
	Kidney	0	NAD	1	iron in the tubules
24 MNPs 60 mg/kg	Liver	1	congestion	2	In Kupffer cells in sinusoids only
	Lung	2	Pigment in blood vessels	2	Staining macrophages around blood vessels, thrombus and iron deposition in large blood vessels
	Spleen	1	presence of giant cells	4	Predominantly in the red pulp
	Kidney	1	calcification	1	iron stain in the tubules

Supplementary table 8.9: Full description of iron accumulation and pathological changes in all organs from animals tested in RCL-01 experimental block in case study 4.

Summary of findings reported by the certified pathologist from St. James' Central Pathology Laboratory on histological changes and accumulation of iron for slices obtained from the organs of experimental animal used in case study 4. Pathologist was blinded to type of injection given. Slides were assessed on a scale of 1-4 for both toxicity and iron accumulation. NAD: nothing abnormal detected

Animal ID	**Organ**	**Diagnosis**		**Iron accumulation**	
		Score	**description**	**Score**	**description**
1 MNPs 30 mg/kg	Liver	0	NAD	2	Kupffer cells in sinusoids only
	Lung	0	NAD	0	N/A
	Spleen	1	presence of giant cells	4	Predominantly in the red pulp
	Kidney	1	calcification	1	iron in the tubules
2 MNPs 30 mg/kg	Liver	0	NAD	0	N/A
	Lung	0	NAD	0	N/A
	Spleen	1	presence of giant cells	4	Predominantly in the red pulp
	Kidney	1	calcification	1	iron in the tubules
3 MNPs 30 mg/kg	Liver	0	NAD	2	Kupffer cells in sinusoids only
	Lung	0	NAD	0	N/A
	Spleen	1	presence of giant cells	4	Predominantly in the red pulp
	Kidney	0	NAD	1	iron in the tubules
4 Saline	Liver	0	NAD	0	N/A
	Lung	0	NAD	0	N/A
	Spleen	0	NAD	4	Predominantly in the red pulp

	Kidney	1	calcification	1	iron in the tubules
5 MNPs 45 mg/kg	Liver	0	NAD	2	Kupffer cells in sinusoids only
	Lung	0	NAD	2	perivascular space
	Spleen	1	presence of giant cells	4	Predominantly in the red pulp
	Kidney	2	calcification, tubular dilation	1	iron in the tubules
6 Saline	Liver	0	NAD	0	N/A
	Lung	0	NAD	0	N/A
	Spleen	1	presence of giant cells	4	Predominantly in the red pulp
	Kidney	1	vacuolar degeneration	1	iron in the tubules
7 MNPs 45 mg/kg	Liver	0	NAD	0	N/A
	Lung	0	NAD	1	staining macrophages around blood vessels
	Spleen	1	presence of giant cells	4	Predominantly in the red pulp
	Kidney	1	mild vacuolation of the renal tubules	1	iron in the tubules
8 MNPs 45 mg/kg	Liver	0	NAD	2	Kupffer cells in sinusoids only
	Lung	0	NAD	1	staining macrophages around blood vessels
	Spleen	1	presence of giant cells	4	Predominantly in the red pulp
	Kidney	1	mild vacuolation of the renal tubules, calcification	1	iron in the tubules
9 Saline	Liver	1	Mild hepatic congestion	1	in the hepatocytes
	Lung	0	NAD	1	staining macrophages around blood vessels
	Spleen	1	presence of giant cells	3	Predominantly in the red pulp in macrophages

	Kidney	2	glomerular shrinkage and vacuolar degeneration	2	iron in the tubules
10 MNPs 60 mg/kg	Liver	2	congestion	1	in the hepatocytes
	Lung	0	NAD	1	staining macrophages around blood vessels
	Spleen	1	presence of giant cells	3	Predominantly in the red pulp in macrophages
	Kidney	1	mild vacuolation of the renal tubules, calcification	2	iron in the tubules
11 MNPs 60 mg/kg	Liver	0	NAD	0	N/A
	Lung	0	NAD	1	staining macrophages around blood vessels
	Spleen	1	presence of giant cells	4	Predominantly in the red pulp in macrophages
	Kidney	1	mild vacuolation of the renal tubules, calcification	1	iron in the tubules
12 MNPs 60 mg/kg	Liver	0	NAD	0	N/A
	Lung	0	NAD	1	staining macrophages around blood vessels
	Spleen	1	presence of giant cells	4	Predominantly in the red pulp in macrophages
	Kidney	1	vacuolar degeneration of tubules	1	iron in the tubules
14 MNPs 30 mg/kg	Liver	0	NAD	2	Kupffer cells in sinusoids only
	Lung	0	NAD	1	staining macrophages around blood vessels
	Spleen	1	presence of giant cells	4	Predominantly in the red pulp in macrophages
	Kidney	1	vacuolar degeneration of tubules	1	iron in the tubules
15 MNPs 30 mg/kg	Liver	0	NAD	2	Kuppfer cells in sinusoids only
	Lung	0	NAD	1	staining macrophages around blood vessels

	Spleen	2	presence of giant cells	4	Predominantly in the red pulp in macrophages
	Kidney	0	NAD	1	iron in the tubules
16 MNPs 30 mg/kg	Liver	0	NAD	2	Kupffer cells in sinusoids only
	Lung	0	NAD	0	N/A
	Spleen	1	presence of giant cells	4	Predominantly in the red pulp in macrophages
	Kidney	1	calcification	2	iron in the tubules
17 MNPs 45 mg/kg	Liver	0	NAD	1	Kupffer cells in sinusoids only
	Lung	0	NAD	0	N/A
	Spleen	2	presence of giant cells	4	Predominantly in the red pulp in macrophages
	Kidney	1	vacuolar change	3	in some tubules only
18 MNPs 45 mg/kg	Liver	0	NAD	2	Kupffer cells in sinusoids only
	Lung	0	NAD	1	staining macrophages around blood vessels
	Spleen	1	presence of giant cells	4	Predominantly in the red pulp in macrophages
	Kidney	2	calcifications in low cortex, vacuolar change of tubules	1	iron in the tubules
19 MNPs 45 mg/kg	Liver	0	NAD	3	in the hepatocytes
	Lung	0	NAD	0	N/A
	Spleen	1	presence of giant cells	4	Predominantly in the red pulp in macrophages
	Kidney	0	NAD	2	iron in the tubules
20 MNPs 60 mg/kg	Liver	0	NAD	2	Kupffer cells in sinusoids only
	Lung	0	NAD	1	staining macrophages around blood vessels

	Spleen	1	presence of giant cells	4	Predominantly in the red pulp in macrophages
	Kidney	0	NAD	1	iron in the tubules
21 MNPs 60 mg/kg	Liver	0	NAD	3	in the hepatocytes
	Lung	0	NAD	1	staining macrophages around blood vessels
	Spleen	1	presence of giant cells	4	Predominantly in the red pulp in macrophages
	Kidney	2	vacuolar degeneration of tubules, calcification	1	iron in the tubules
22 MNPs 60 mg/kg	Liver	1		2	in the hepatocytes surrounding portal tracts
	Lung	0	NAD	1	staining macrophages around blood vessels
	Spleen	1	presence of giant cells	4	Predominantly in the red pulp in macrophages
	Kidney	2	calcifications in low ccortex, vacuolar change of tubules	1	iron in the tubules
23 Saline	Liver	1	congestion	1	in the hepatocytes
	Lung	0	NAD	0	N/A
	Spleen	1	presence of giant cells	4	Predominantly in the red pulp
	Kidney	1	calcification	1	iron in the tubules
24 Saline	Liver	0	NAD	0	N/A
	Lung	0	NAD	0	N/A
	Spleen	1	presence of giant cells	4	Predominantly in the red pulp
	Kidney	0	NAD	1	iron in the tubules

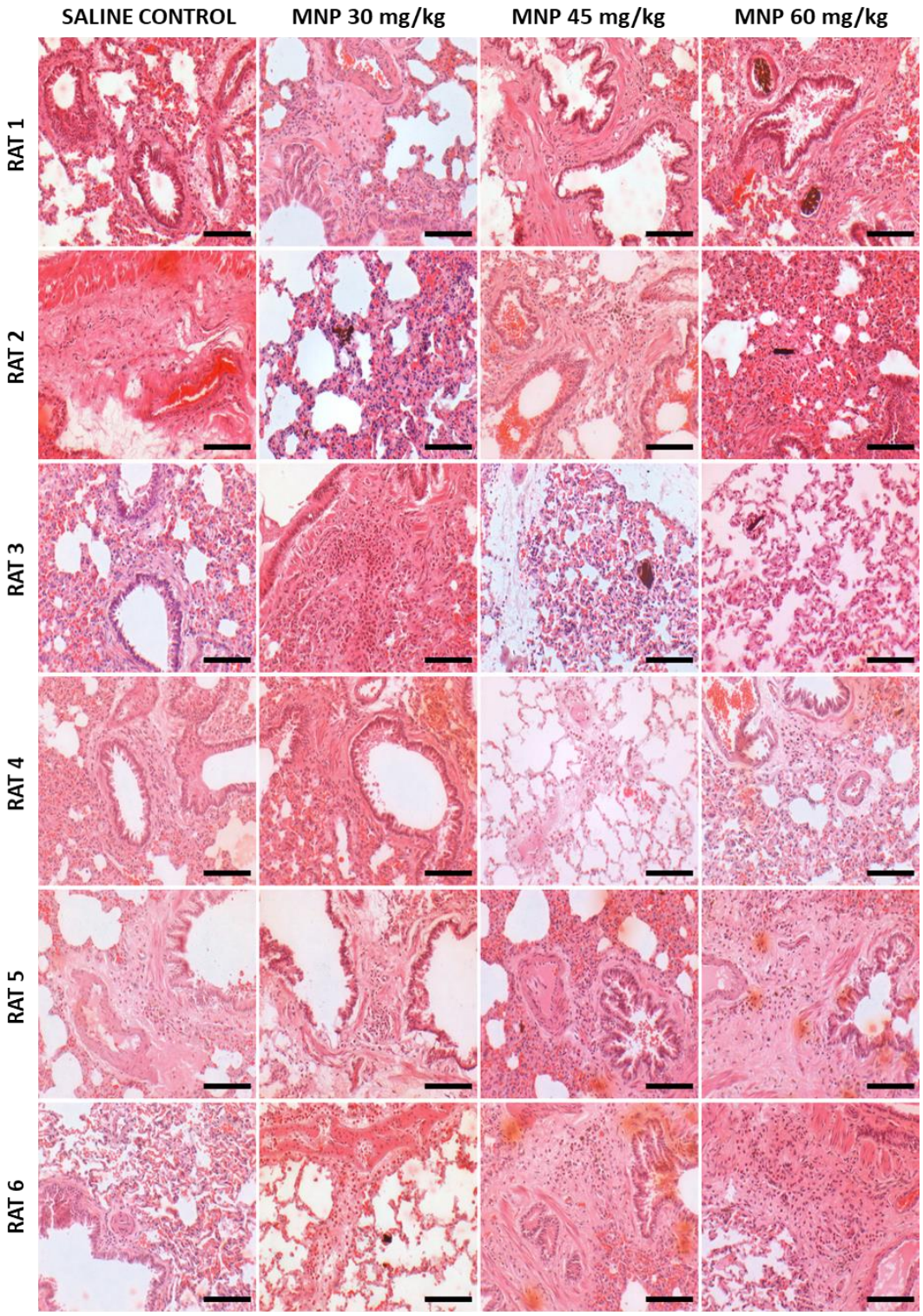

Supplementary figure 8.42: Immune response in lungs following injection of NOC 0007 MNPs
Representative photomicrographs of H&E stained lung sections from WIstar rats. Animals were injected with either saline, or MNP at 30 mg/kg, 45 mg/kg, and 60 mg/kg. Animals were sacrificed 7 days post injection. Tissue was formalin fixed and paraffin embedded. 5µm thick sections were cut with rotary microtome and collected at four levels through the block spaced at least 50 µm apart. An influx of immune cells was observed in the perivascular and peribronchial space of all animals injected with MNPs. Images were acquired with a 20x lens; scale bar represents 100 µm.

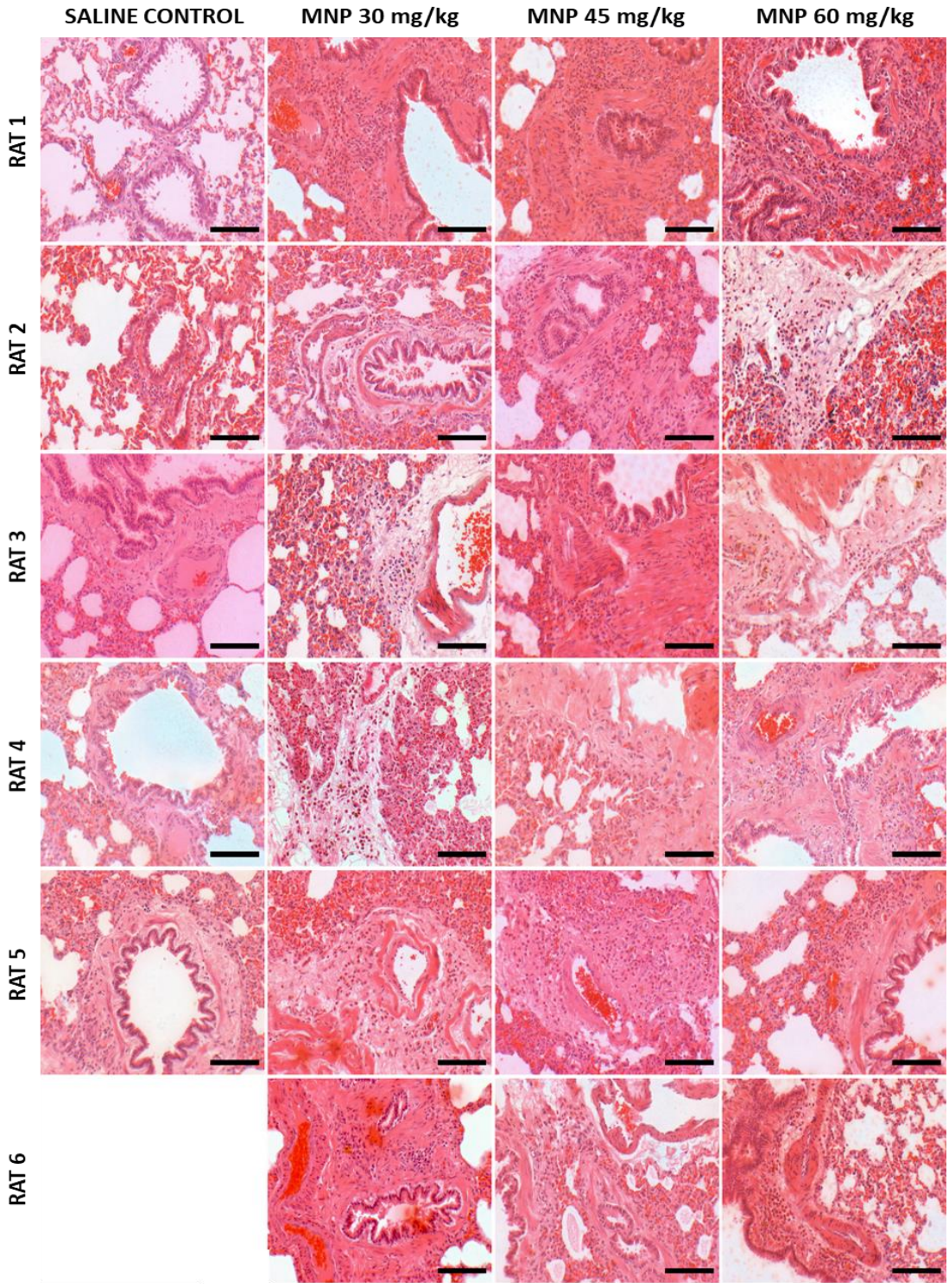

Supplementary figure 8.43: Immune response in lungs following injection of RCL-01 MNPs
Representative photomicrographs of H&E stained lung sections from Wistar rats. Animals were injected with either saline, or MNP at 30 mg/kg, 45 mg/kg, and 60 mg/kg. Animals were sacrificed 7 days post injection. Tissue was formalin fixed and paraffin embedded. 5µm thick sections were cut with rotary microtome and collected at four levels through the block spaced at least 50 µm apart. An influx of immune cells was observed in the perivascular and peribronchial space of all animals injected with MNPs. Tissue samples from one of the control animals were damaged during processing and were excluded from the study. Images were acquired with a 20x lens; scale bar represents 100 µm.

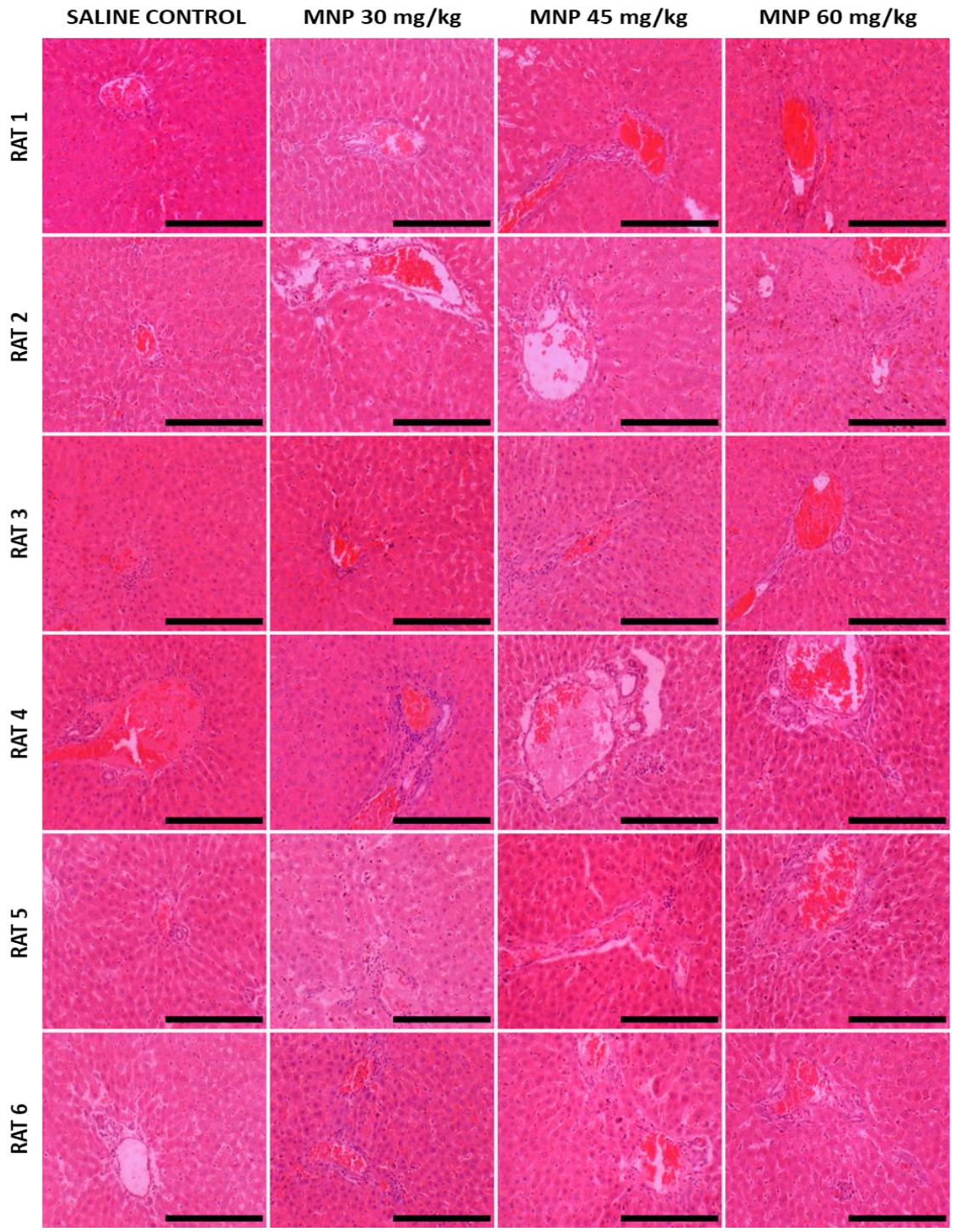

Supplementary figure 8.44: Pathological changes in liver following injection of NOC0007
Representative photomicrographs of H&E stained liver sections from Wistar rats. Animals were injected with either saline, or MNPs at 30 mg/kg, 45 mg/kg, and 60 mg/kg. Animals were sacrificed 7 days post injection. Tissue was formalin fixed and paraffin embedded. 5µm thick sections were cut with rotary microtome and collected at four levels through the block spaced at least 50 µm apart. Mild hepatic congestion was seen in all animals in this study, with no significant differences reported between the control animals and those injected with MNPs. Images were acquired with a 20x lens; scale bar represents 100 µm.

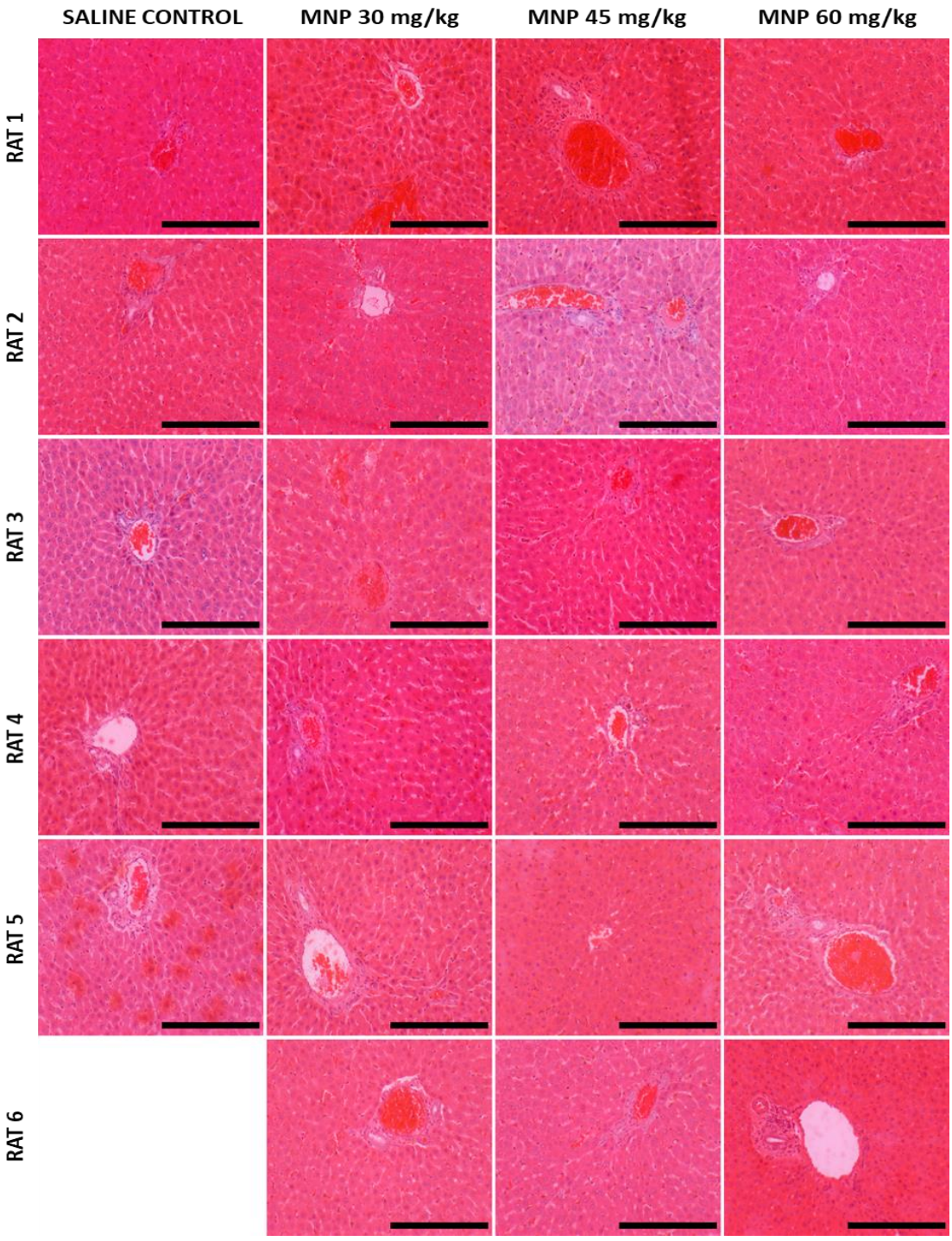

Supplementary figure 8.45: Pathological changes in liver following injection of RCL-01
Representative photomicrographs of H&E stained liver sections from Wistar rats. Animals were injected with either saline, or MNPs at 30 mg/kg, 45 mg/kg, and 60 mg/kg. Animals were sacrificed 7 days post injection. Tissue was formalin fixed and paraffin embedded. 5µm thick sections were cut with rotary microtome and collected at four levels through the block spaced at least 50 µm apart. Mild hepatic congestion was seen in all animals in this study, with no significant differences reported between the control animals and those injected with MNPs. Tissue samples from one of the control animals were damaged during processing and were excluded from the study. Images were acquired with a 20x lens; scale bar represents 100 µm.

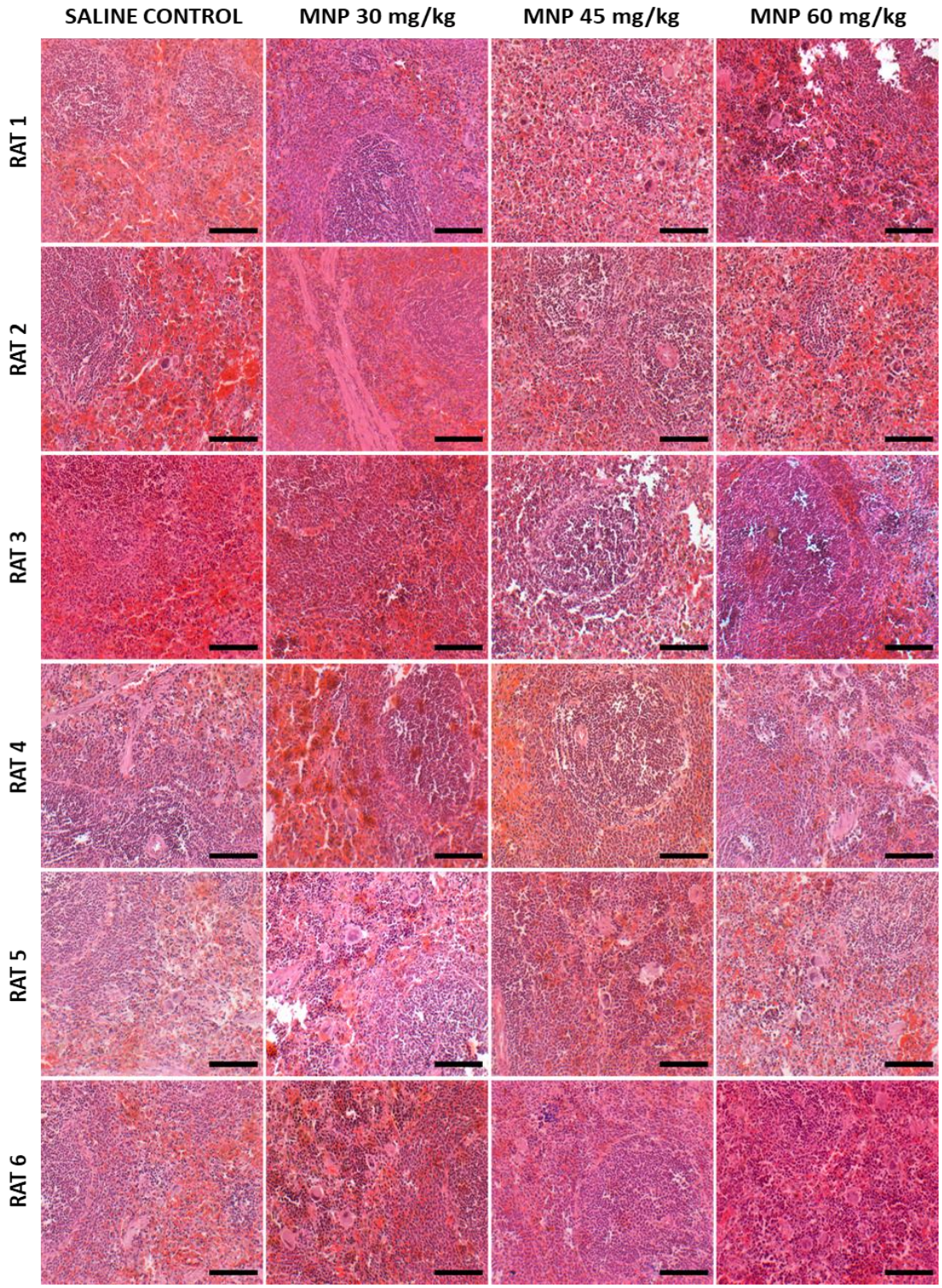

Supplementary figure 8.46: Histological changes in spleen following NOC 0007 injection
Representative photomicrographs of H&E stained spleen sections from Wistar rats. Animals were injected with either saline, or MNPs at 30 mg/kg, 45 mg/kg, and 60 mg/kg. Animals were sacrificed 7 days post injection. Tissue was formalin fixed and paraffin embedded. 5µm thick sections were cut with rotary microtome and collected at four levels through the block spaced at least 50 µm apart. Increased extramedullary haematopoiesis was seen in the animals injected with MNPs, with an increased number of megakaryocytes seen in the red pulp. Images were acquired with a 20x lens; scale bar represents 100 µm.

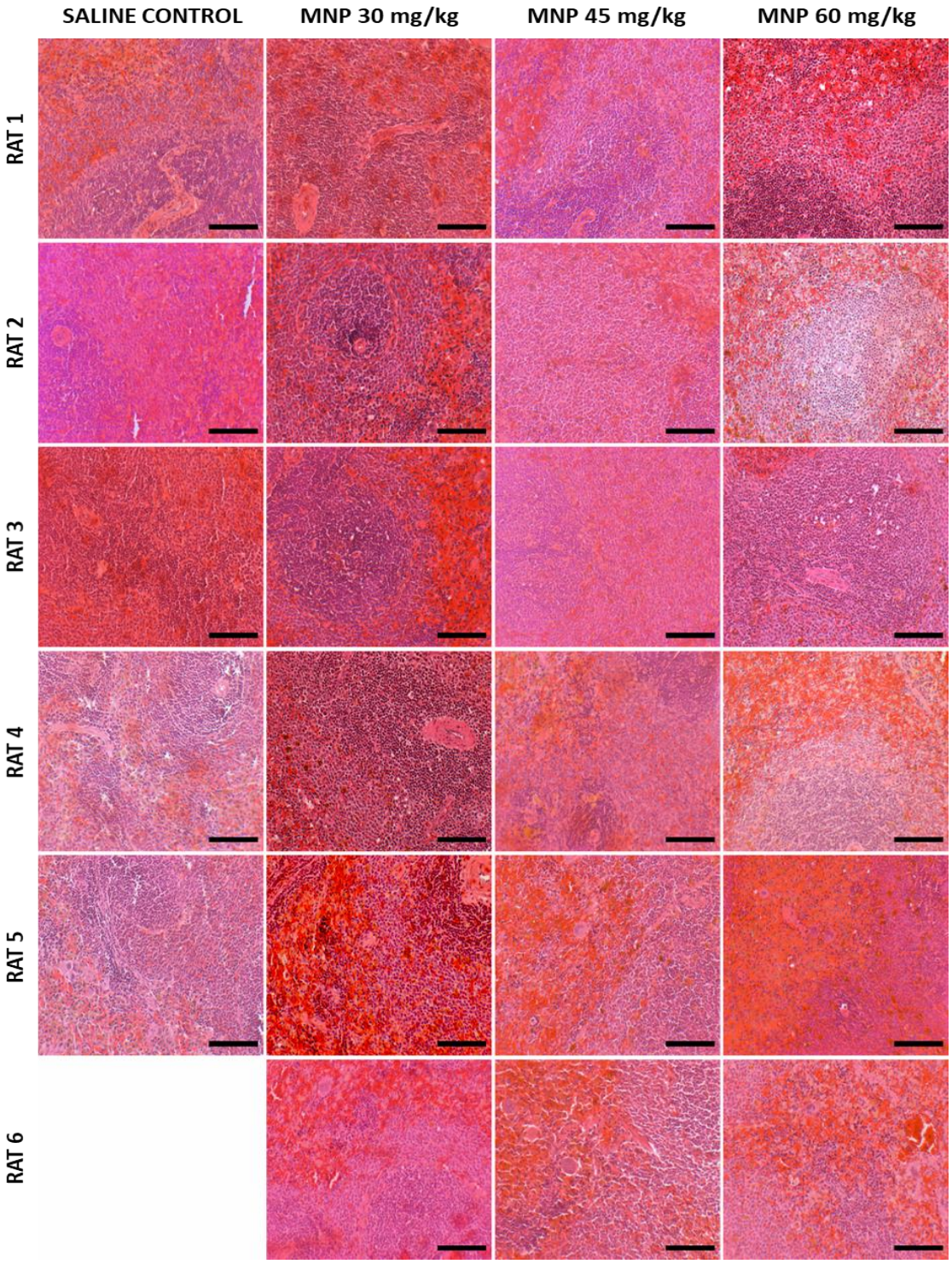

Supplementary figure 8.47: Histological changes in spleen following RCL-01 injection
Representative photomicrographs of H&E stained spleen sections from Wistar rats. Animals were injected with either saline or MNPs at 30 mg/kg, 45 mg/kg, and 60 mg/kg. Animals were sacrificed 7 days post injection. Tissue was formalin fixed and paraffin embedded. 5µm thick sections were cut with rotary microtome and collected at four levels through the block spaced at least 50 µm apart. No significant abnormalities were seen between the control animals and those injected with MNPs. Tissue samples from one of the control animals were damaged during processing and were excluded from the study. Images acquired with a 20x lens; scale bar represents 100 µm.

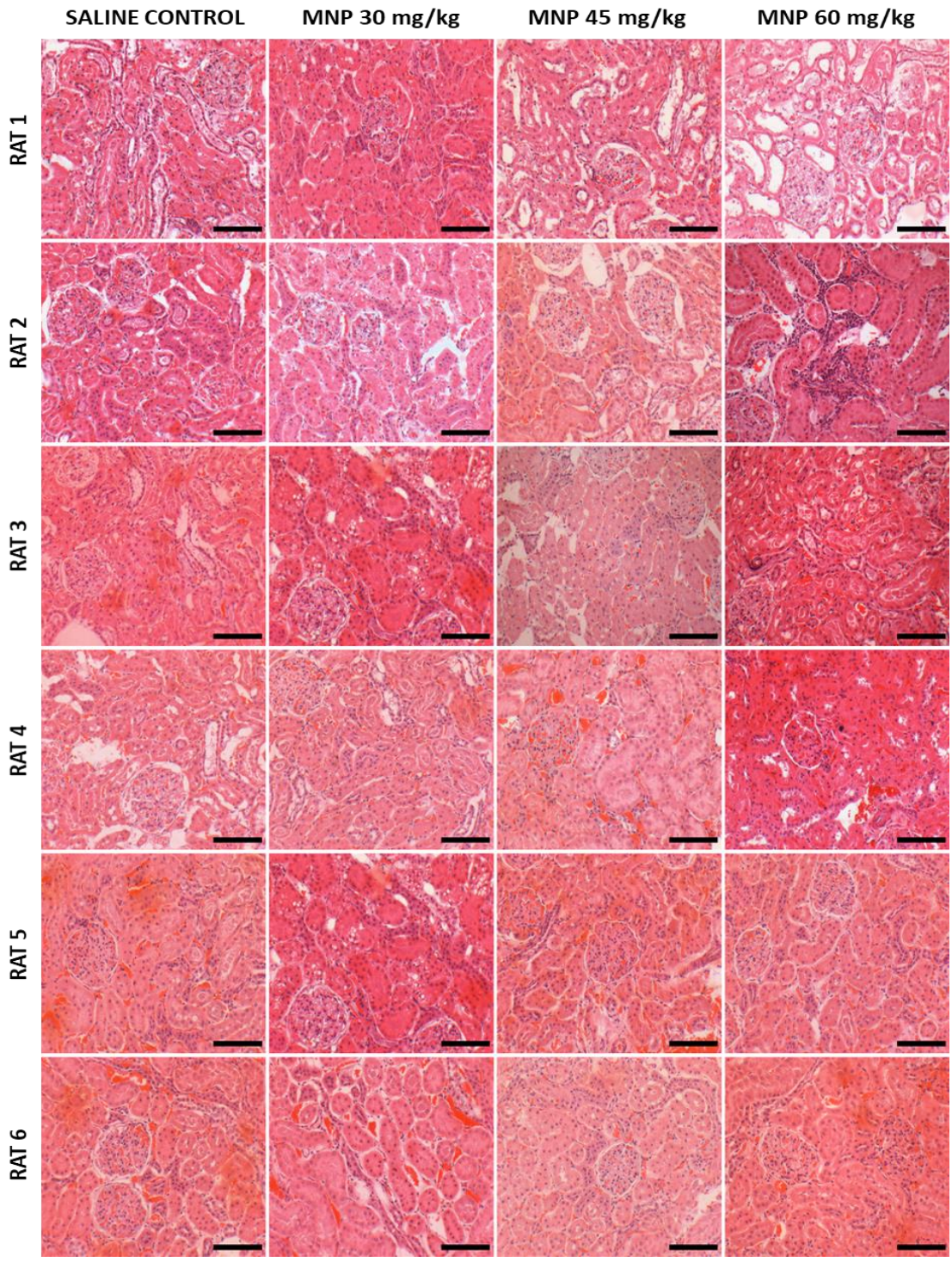

Supplementary figure 8.48: Histological changes in kidney following NOC 0007 injection
Representative photomicrographs of H&E stained kidney sections from Wistar rats. Animals were injected with either saline or MNPs at 30 mg/kg, 45 mg/kg, and 60 mg/kg concentrations. Animals were sacrificed 7 days post injection. Tissue was formalin fixed and paraffin embedded. 5µm thick sections were cut with rotary microtome and collected at four levels through the block spaced at least 50 µm apart. Abnormal histological changes were seen in both control and treated animals. Images acquired with a 20x lens; scale bar represents 100 µm.

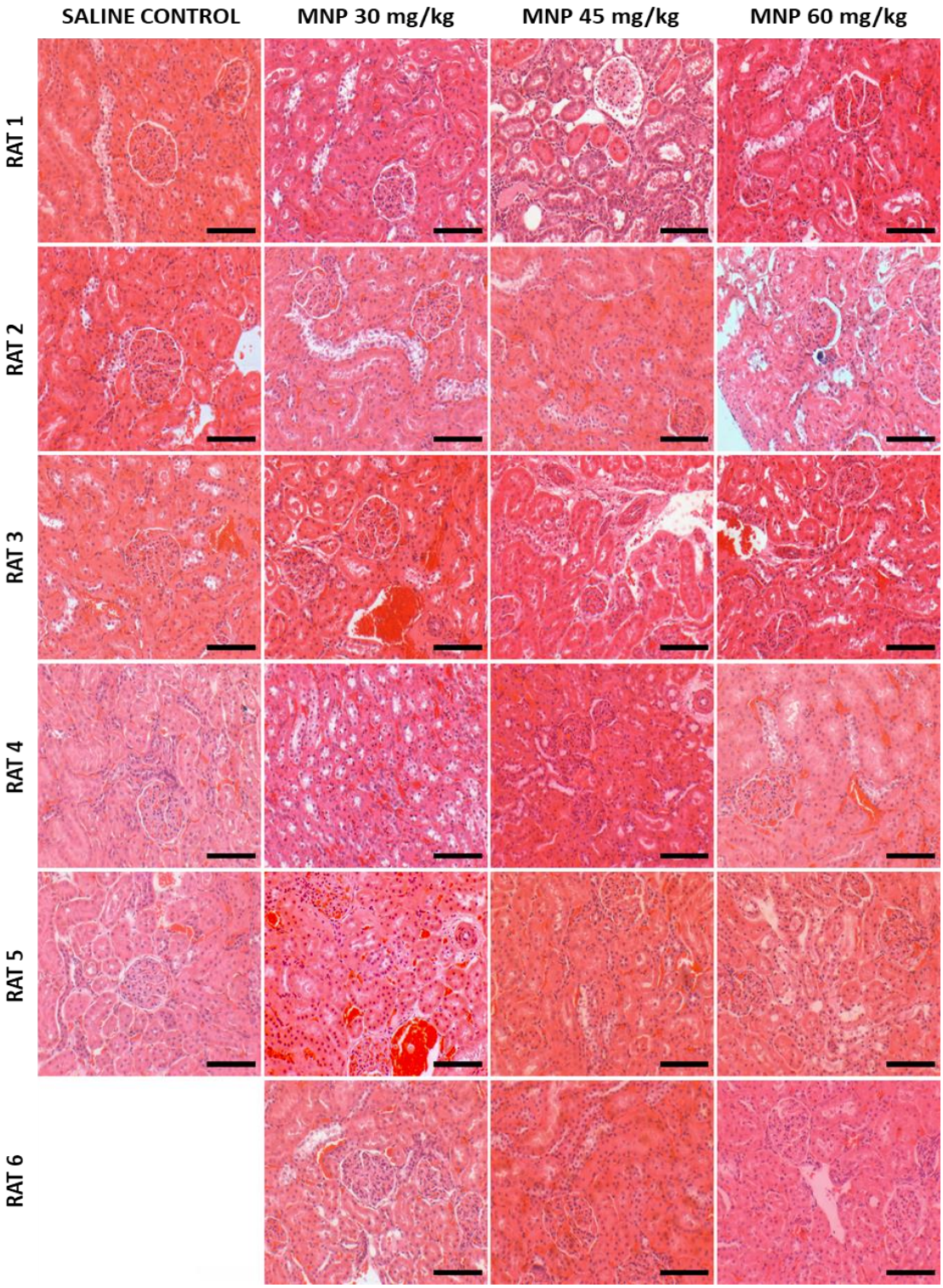

Supplementary figure 8.49: Histological changes in kidney following RCL-01 injection
Representative photomicrographs of H&E stained kidney sections of Wistar rats. Animals were injected with either saline or MNPs at 30 mg/kg, 45 mg/kg, and 60 mg/kg concentrations. Animals were sacrificed 7 days post injection. Tissue was formalin fixed and paraffin embedded. 5µm thick sections were cut with rotary microtome and collected at four levels through the block spaced at least 50 µm apart. Abnormal histological changes were seen in both control animals and those injected with MNPs. Images acquired with a 20x lens; scale bar represents 100 µm.

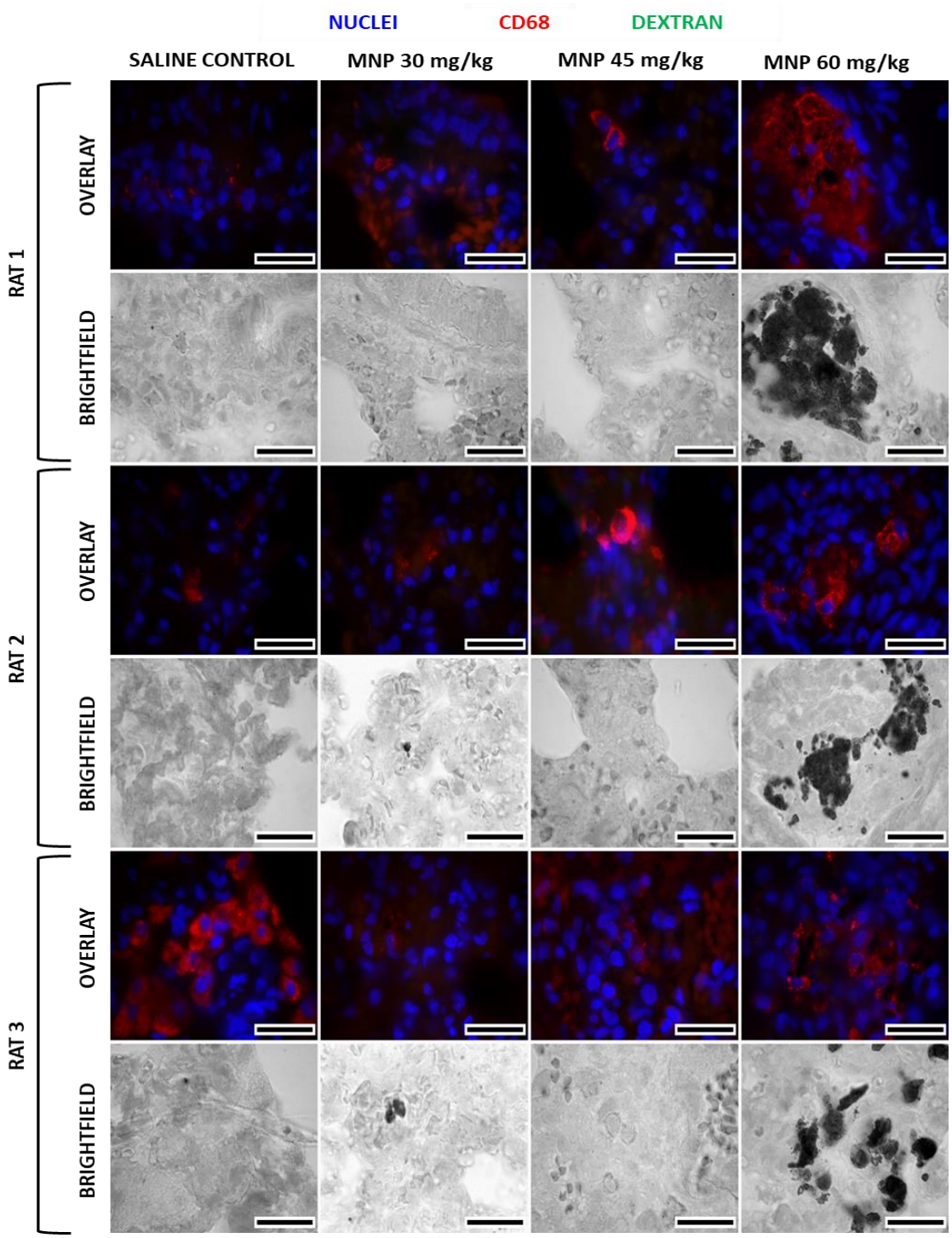

Supplementary figure 8.50: Uptake of NOC0007 MNPs by lung macrophages
High magnification photomicrographs showing uptake of NOC0007 by resident macrophages in lungs of Wistar rats. Animals were injected with either saline or MNPs at 30 mg/kg, 45 mg/kg, and 60 mg/kg concentrations. Animals were sacrificed 7 days post injection. Tissue was formalin fixed and paraffin embedded. 5µm thick sections were cut with rotary microtome and collected at four levels through the block spaced at least 50 µm apart. Nuclei can be seen in blue, dextran in green, and CD68+ cells in red. Corresponding brightfield image can be seen under each fluorescent overlay. Tissue sample from three out of six animals per treatment were used for this staining. Images were acquired with Nikon Eclipse E800 fluorescent microscope using 100x lens. Scale bar represents 25µm.

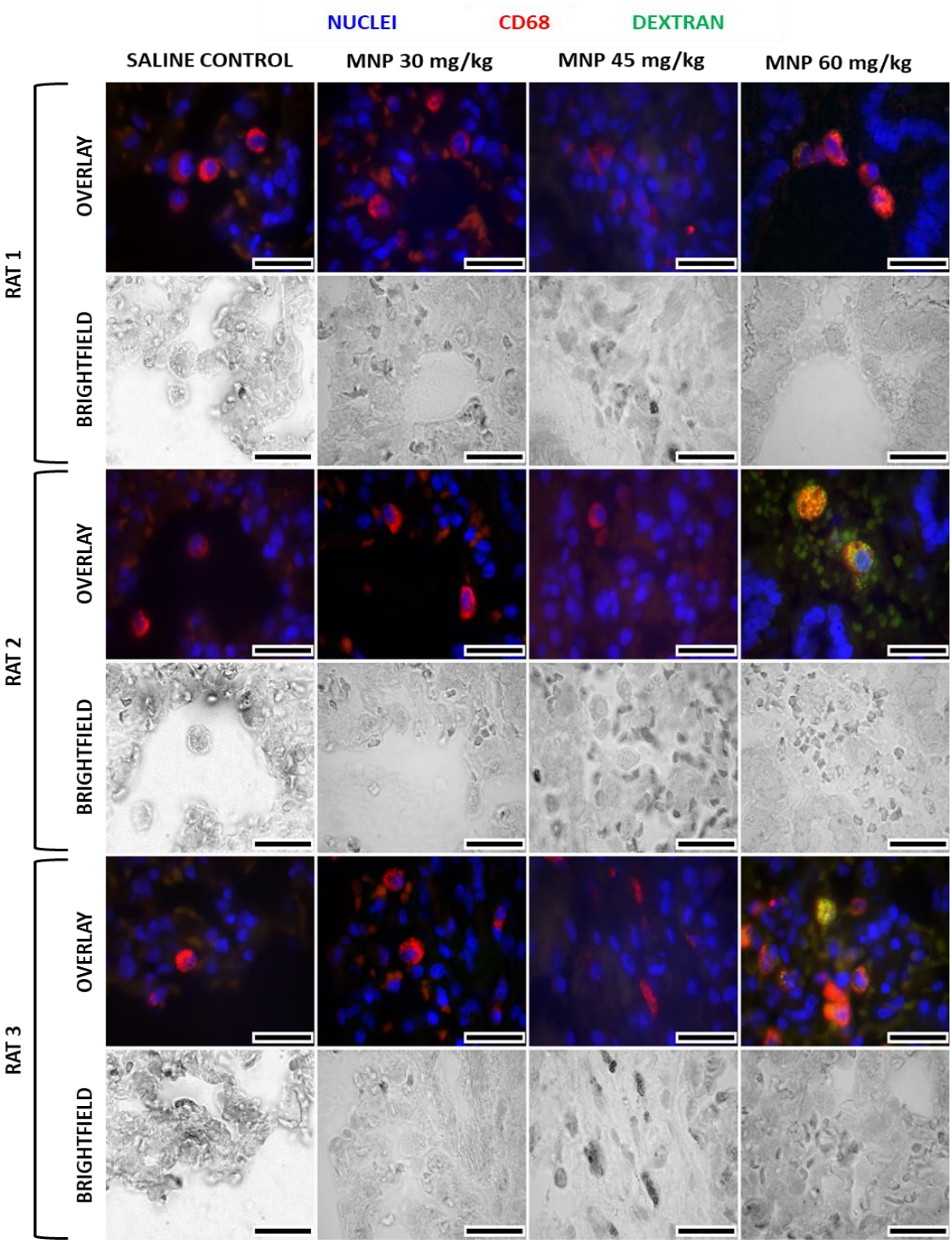

Supplementary figure 8.51: Uptake of RCL-01 MNPs by lung macrophages
High magnification photomicrographs showing uptake of RCL-01 MNPs by resident macrophages in lungs of Wistar rats. Animals were injected with either saline or MNPs at 30 mg/kg, 45 mg/kg, and 60 mg/kg concentrations. Animals were sacrificed 7 days post injection. Tissue was formalin fixed and paraffin embedded. 5µm thick sections were cut with rotary microtome and collected at four levels through the block spaced at least 50 µm apart. Nuclei can be seen in blue, dextran in green, and CD68+ cells in red. Corresponding brightfield image can be seen under each fluorescent overlay. Tissue sample from three out of six animals per treatment were used for this staining. Images were acquired with Nikon Eclipse E800 fluorescent microscope using 100x lens. Scale bar represents 25µm.

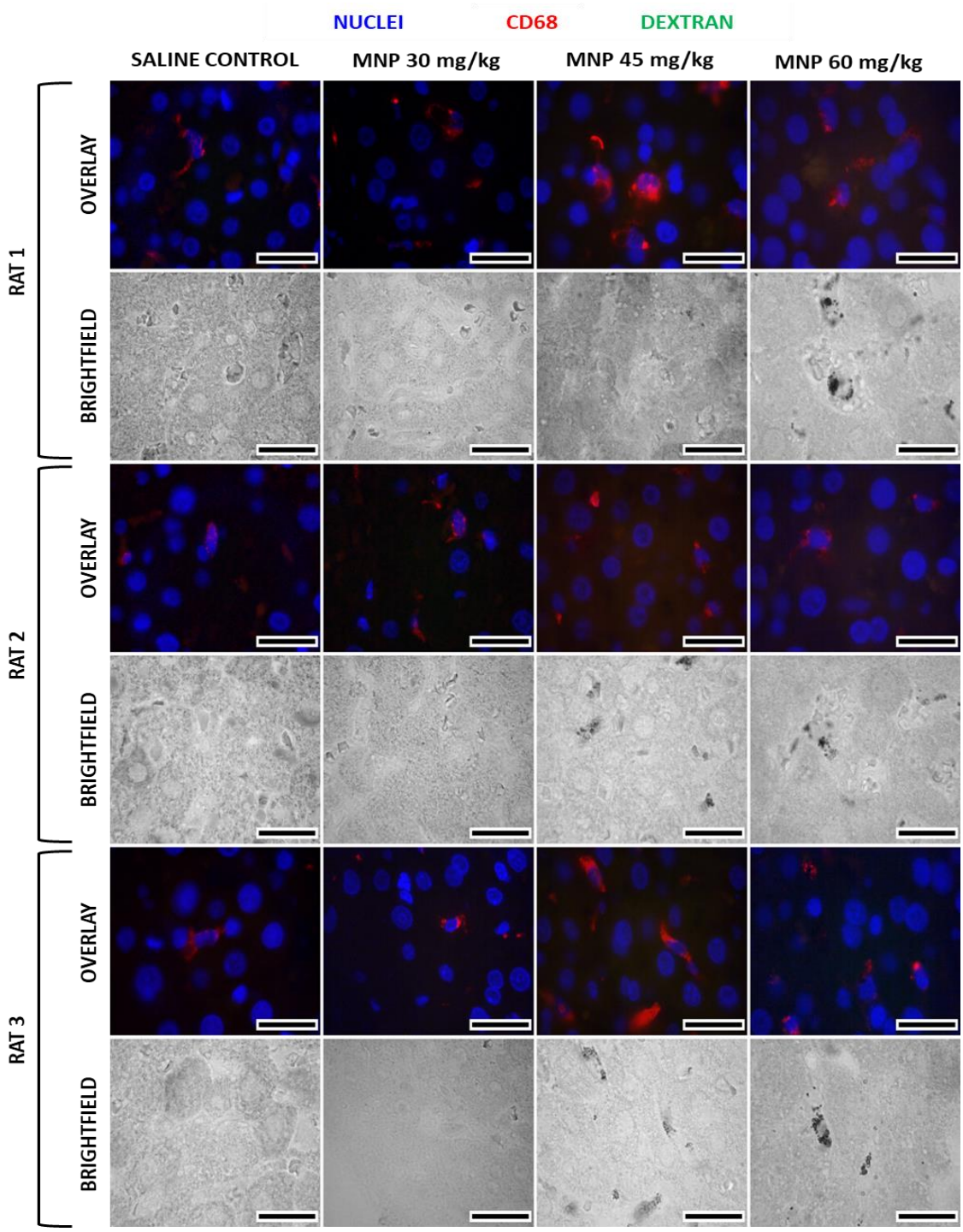

Supplementary figure 8.52: Uptake of NOC0007 MNPs by Kupffer cells in liver
High magnification photomicrographs showing uptake of NOC0007 by Kupffer cells in the liver of Wistar rats.Animals were injected with either saline or MNPs at 30 mg/kg, 45 mg/kg, and 60 mg/kg concentrations. Animals were sacrificed 7 days post injection. Tissue was formalin fixed and paraffin embedded. 5µm thick sections were cut with rotary microtome and collected at four levels through the block spaced at least 50 µm apart. Nuclei can be seen in blue, dextran in green, and CD68+ cells in red. Corresponding brightfield image can be seen under each fluorescent overlay. Tissue sample from three out of six animals per treatment were used for this staining. Images were acquired with Nikon Eclipse E800 fluorescent microscope using 100x lens. Scale bar represents 25µm.

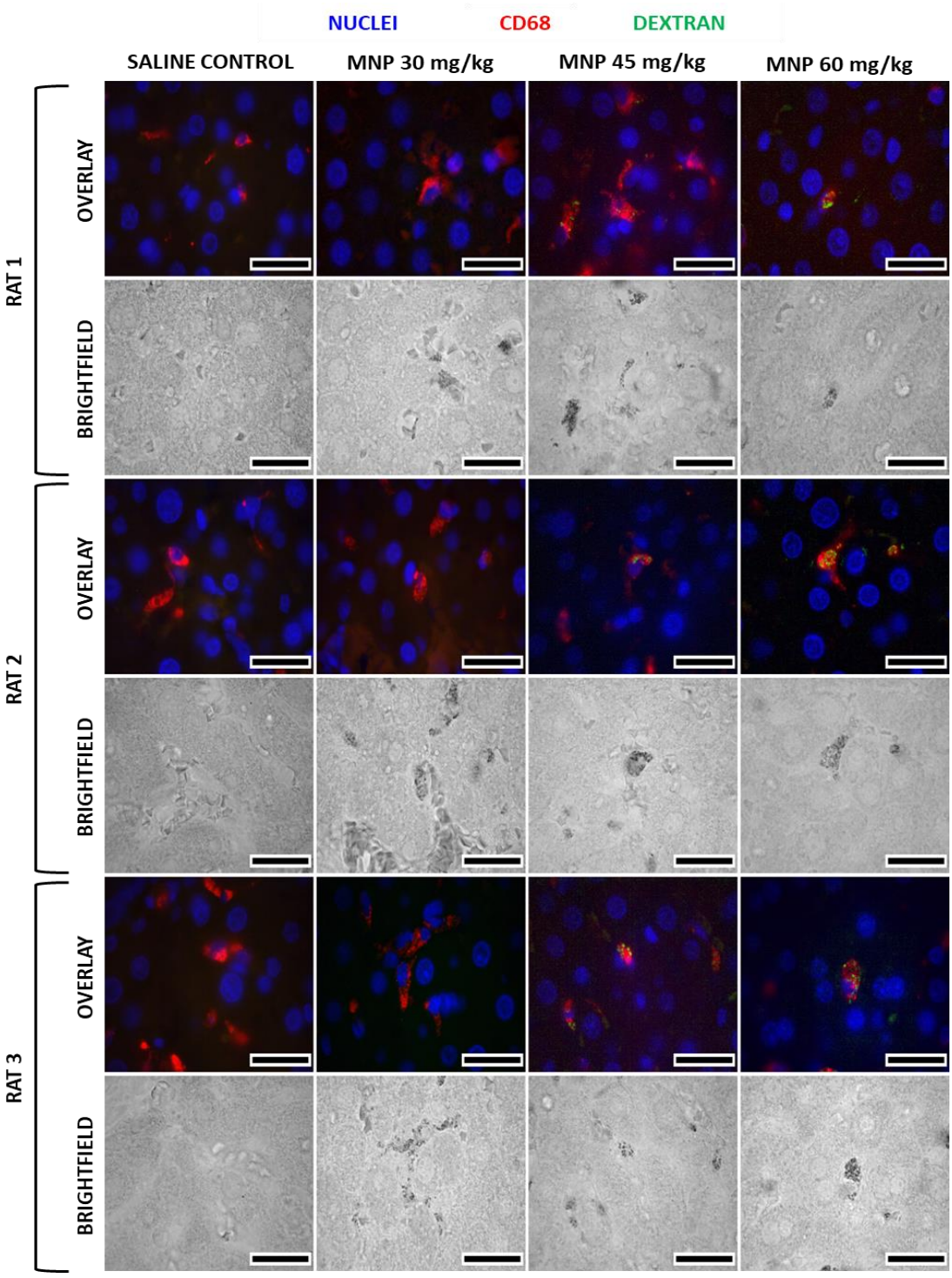

Supplementary figure 8.53: Uptake of RCL-01 MNPs by Kupffer cells in liver
High magnification photomicrographs showing uptake of RCL-01 by Kupffer cells in the liver of Wistar rats.Animals were injected with either saline or MNPs at 30 mg/kg, 45 mg/kg, and 60 mg/kg concentrations. Animals were sacrificed 7 days post injection. Tissue was formalin fixed and paraffin embedded. 5µm thick sections were cut with rotary microtome and collected at four levels through the block spaced at least 50 µm apart. Nuclei can be seen in blue, dextran in green, and CD68+ cells in red. Corresponding brightfield image can be seen under each fluorescent overlay. Tissue sample from three out of six animals per treatment were used for this staining. Images were acquired with Nikon Eclipse E800 fluorescent microscope using 100x lens. Scale bar represents 25µm.

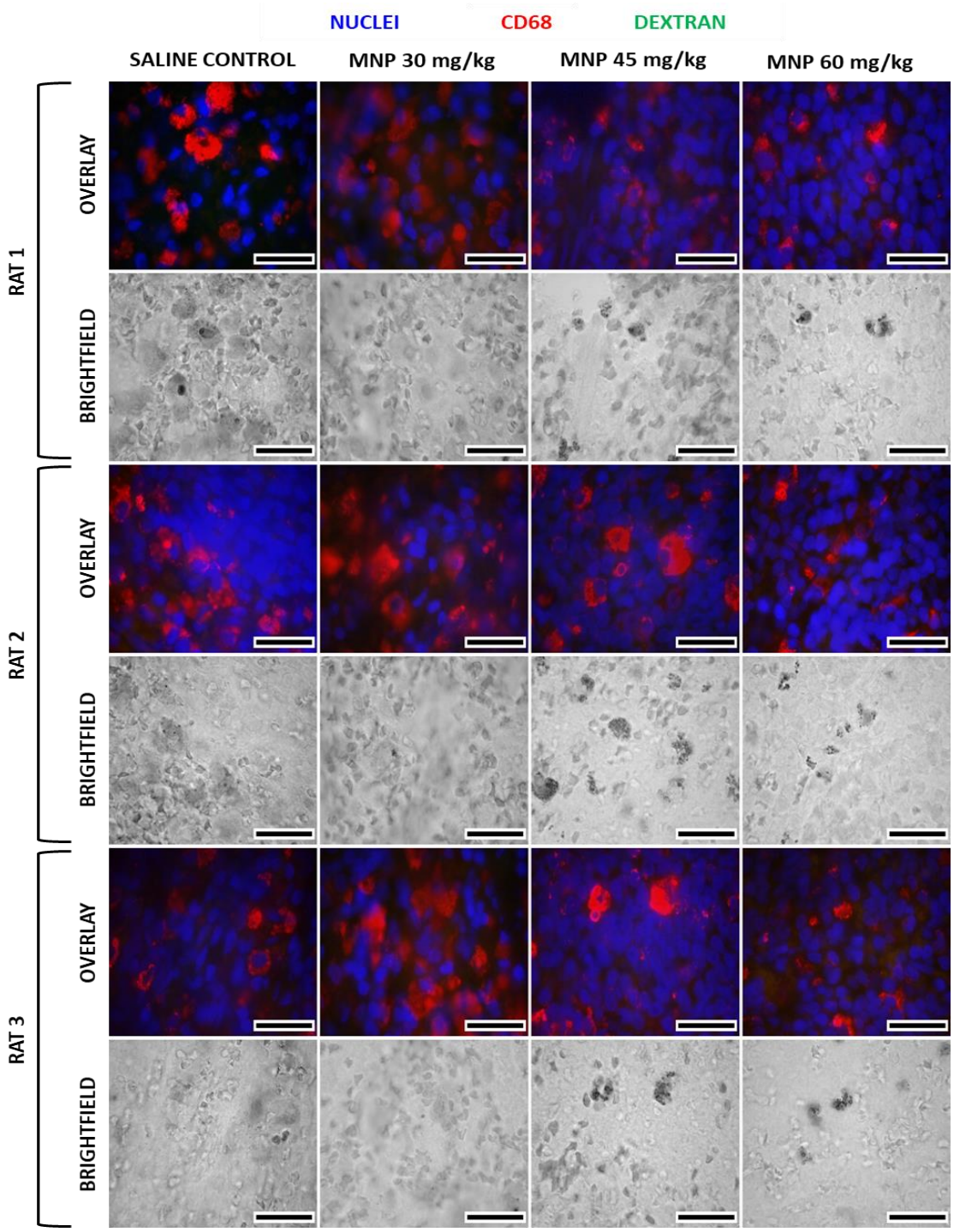

Supplementary figure 8.54: Uptake of NOC0007 MNPs by splenic macrophages
High magnification photomicrographs showing uptake of NOC0007 by splenic macrophages in Wistar rats. Animals were injected with either saline or MNPs at 30 mg/kg, 45 mg/kg, and 60 mg/kg concentrations. Animals were sacrificed 7 days post injection. Tissue was formalin fixed and paraffin embedded. 5µm thick sections were cut with rotary microtome and collected at four levels through the block spaced at least 50 µm apart. Nuclei can be seen in blue, dextran in green, and CD68+ cells in red. Corresponding brightfield image can be seen under each fluorescent overlay. Tissue sample from three out of six animals per treatment were used for this staining. Images were acquired with Nikon Eclipse E800 fluorescent microscope using 100x lens. Scale bar represents 25µm.

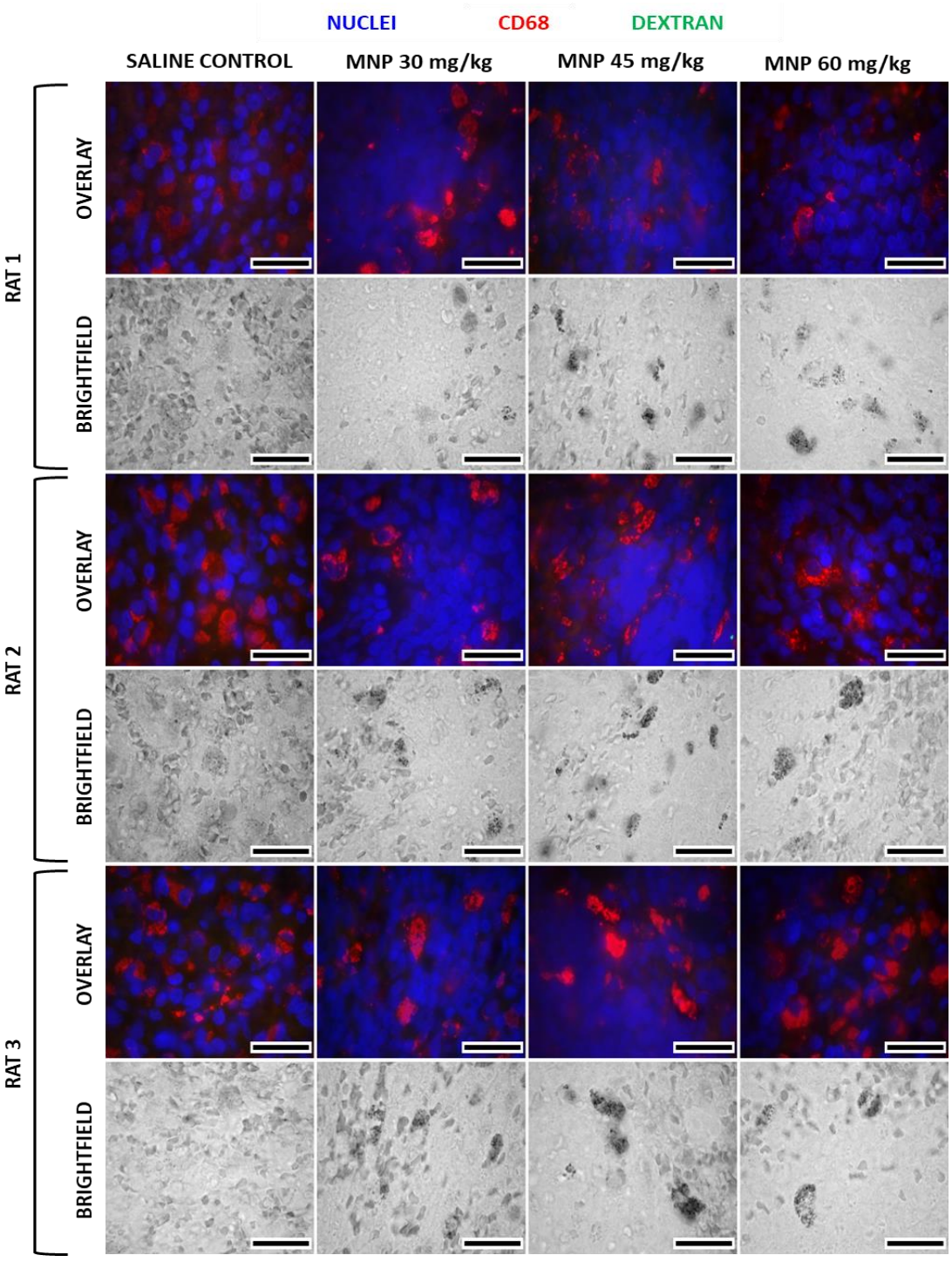

Supplementary figure 8.55: Uptake of RCL-01 MNPs by splenic macrophages
High magnification photomicrographs showing uptake of RCL-01 by splenic macrophages in Wistar rats. Animals were injected with either saline or MNPs at 30 mg/kg, 45 mg/kg, and 60 mg/kg concentrations. Animals were sacrificed 7 days post injection. Tissue was formalin fixed and paraffin embedded. 5µm thick sections were cut with rotary microtome and collected at four levels through the block spaced at least 50 µm apart. Nuclei can be seen in blue, dextran in green, and CD68+ cells in red. Corresponding brightfield image can be seen under each fluorescent overlay. Tissue sample from three out of six animals per treatment were used for this staining. Images were acquired with Nikon Eclipse E800 fluorescent microscope using 100x lens. Scale bar represents 25µm.

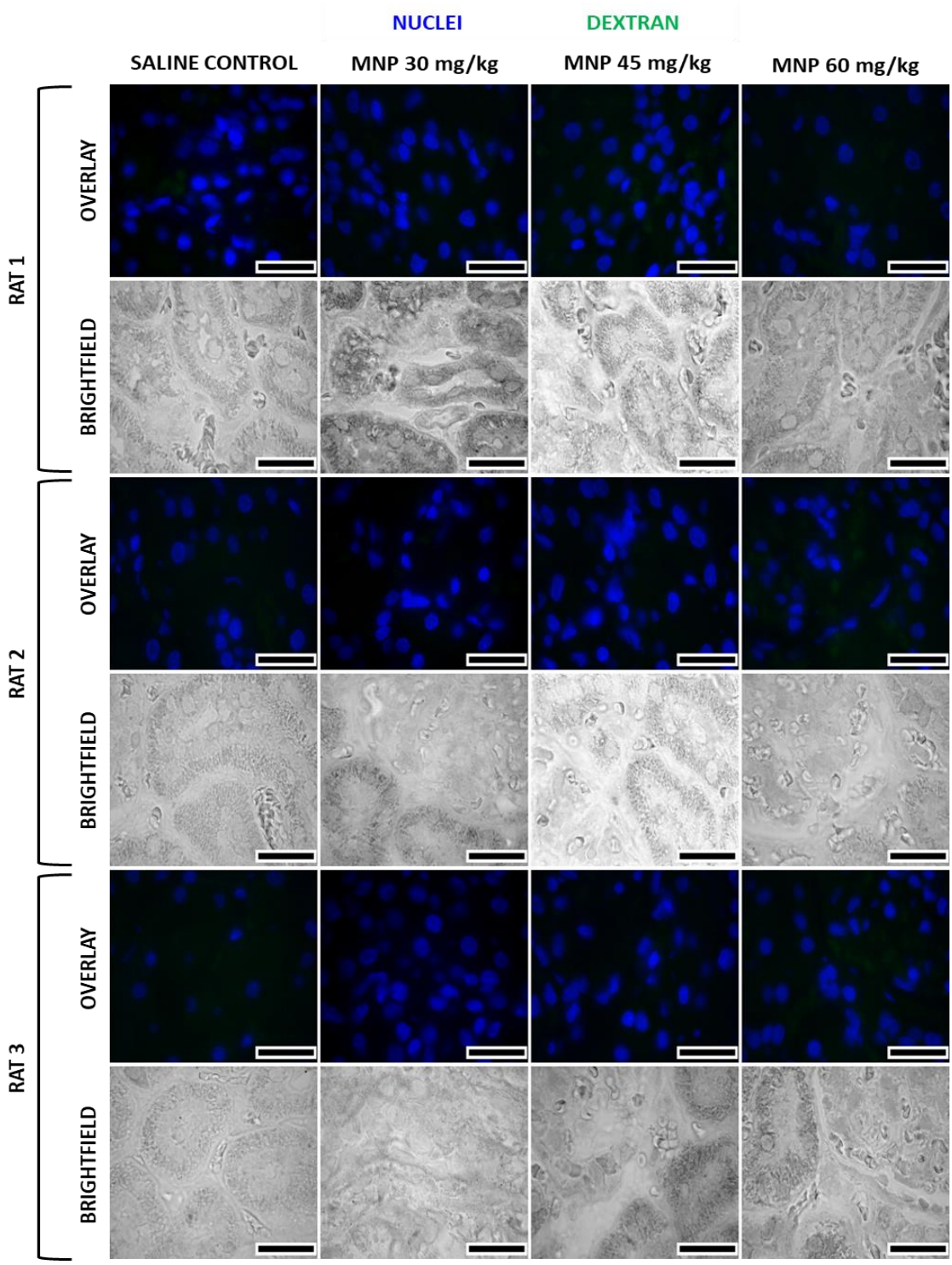

Supplementary figure 8.56: Immunofluorescent detection of dextran in kidneys of animals injected with NOC0007

Representative photomicrographs of kidney sections from Wistar rats injected with NOC0007 MNPs. Animals were injected with either saline or MNPs at 30 mg/kg, 45 mg/kg, and 60 mg/kg concentrations. Animals were sacrificed 7 days post injection. Tissue was formalin fixed and paraffin embedded. 5µm thick sections were cut with rotary microtome and collected at four levels through the block spaced at least 50 µm apart. Dextran was not detected in any of the animals examined. Scale bar represents 50µm.

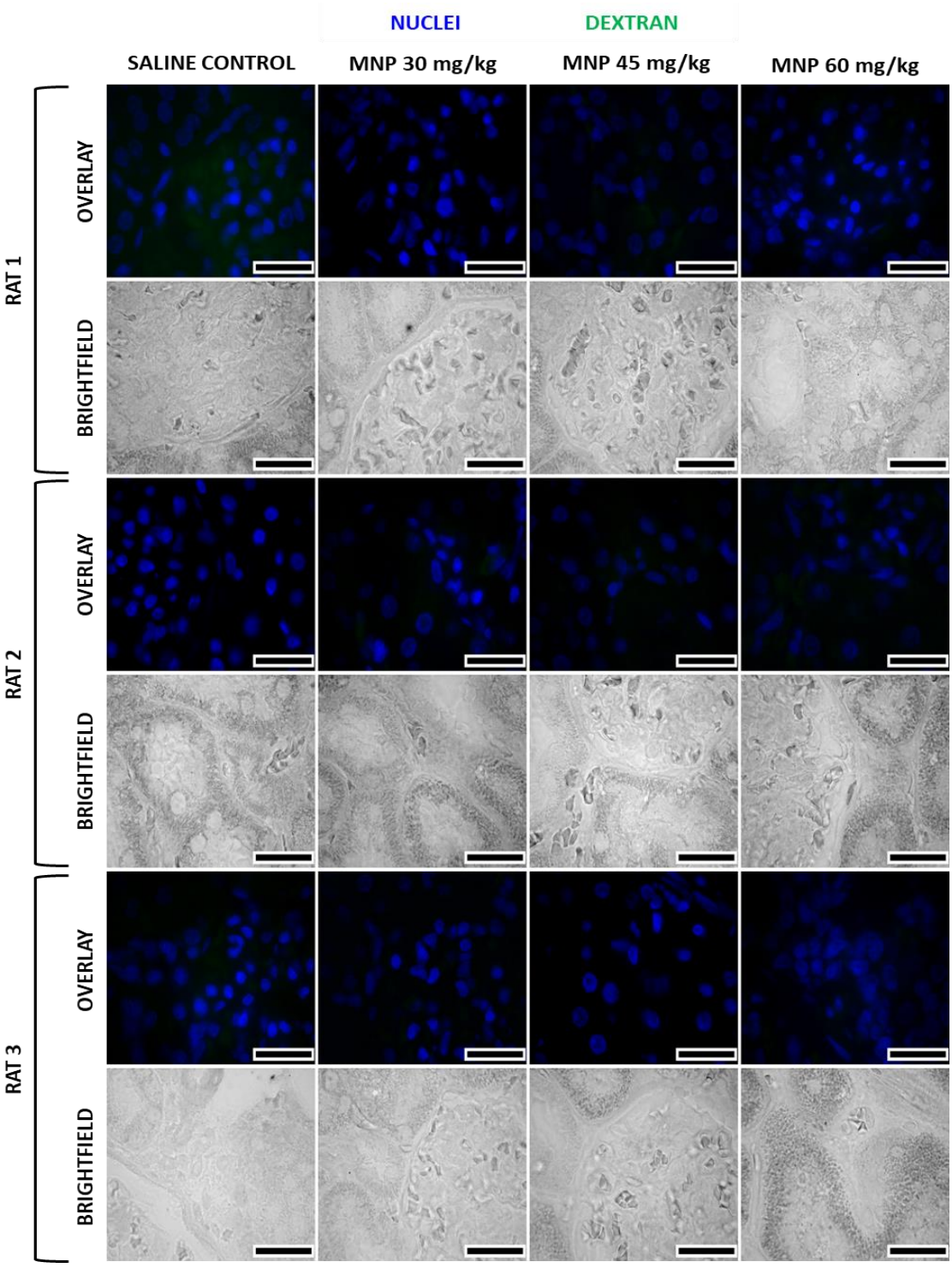

Supplementary figure 8.57: Immunofluorescent detection of dextran in kidneys of animals injected with RCL-01

Representative photomicrographs of kidney sections from animal treated with RCL-01 MNPs. Animals were injected with either saline or MNPs at 30 mg/kg, 45 mg/kg, and 60 mg/kg concentrations. Animals were sacrificed 7 days post injection. Tissue was formalin fixed and paraffin embedded. 5µm thick sections were cut with rotary microtome and collected at four levels through the block spaced at least 50 µm apart. Dextran was not detected in any of the animals examined. Scale bar represents 50µm.

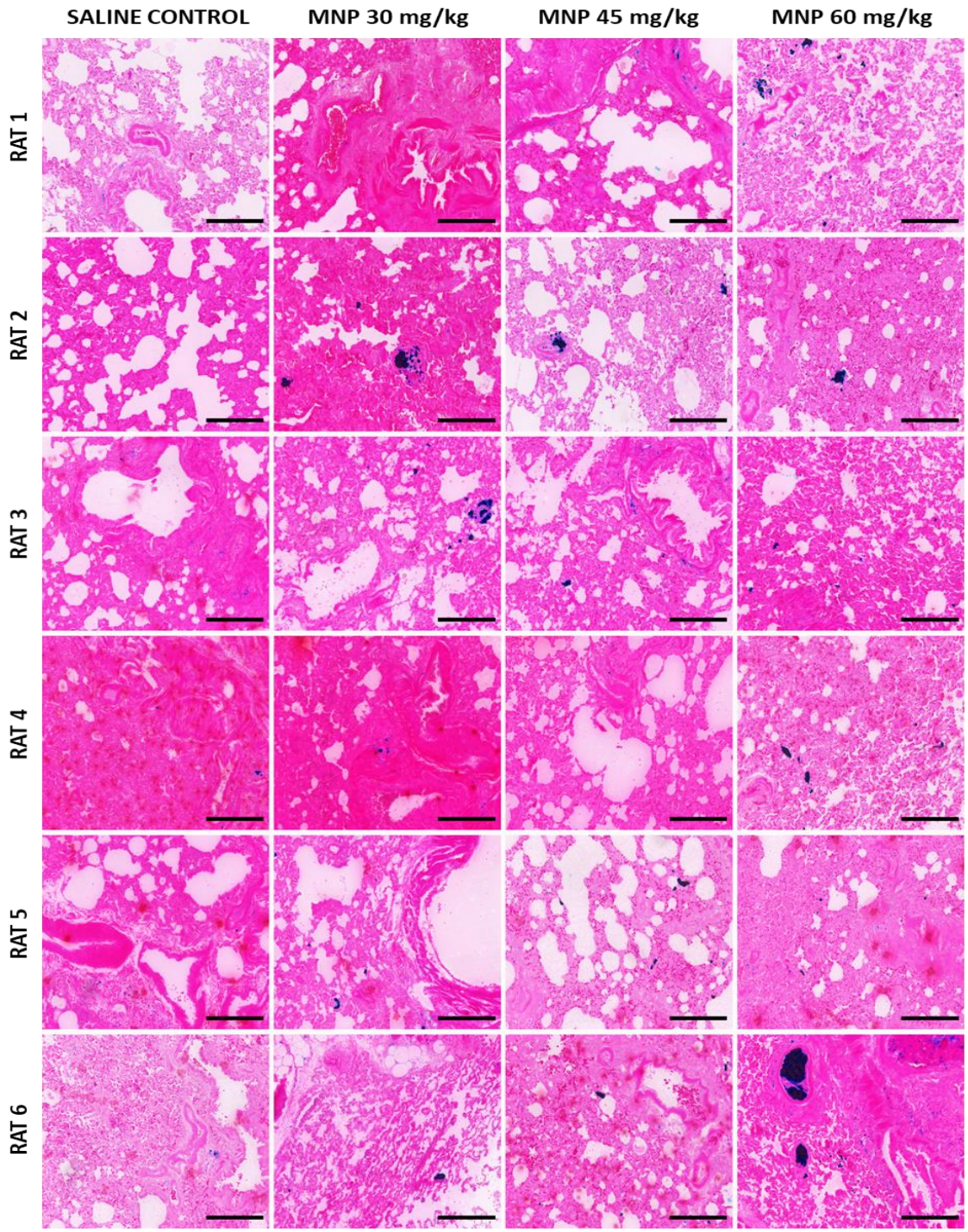

Supplementary figure 8.58: Distribution and accumulation of NOC 0007 MNPs in lungs
Representative photomicrographs of PPB stained lung sections of Wistar rats showing accumulation and distribution of iron (blue deposits) in every animal used in this study. Animals were injected with either saline or MNPs at 30 mg/kg, 45 mg/kg, and 60 mg/kg concentrations. Animals were sacrificed 7 days post injection. Tissue was formalin fixed and paraffin embedded. 5µm thick sections were cut with rotary microtome and collected at four levels through the block spaced at least 50 µm apart. Iron was found in perivascular and peribronchial space. Additionally, in animals injected with MNPs, iron was found in form of relatively large aggregates obstructing the vasculature such as the one seen in the image in the bottom right corner. Images were acquired with 10x lens; scale bar represents 200 µm.

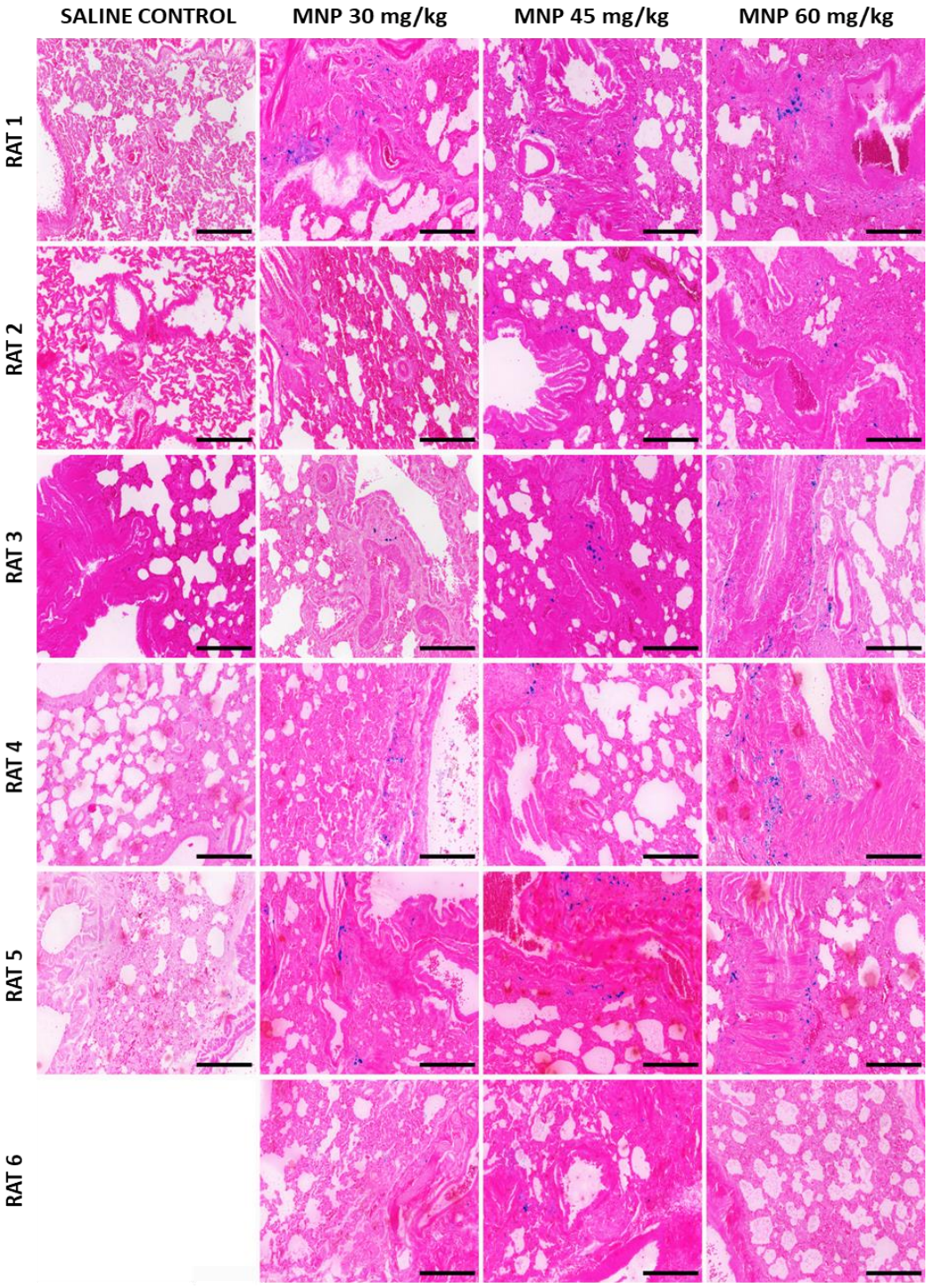

Supplementary figure 8.59: Distribution and accumulation of RCL-01 MNPs in lungs
Representative photomicrographs of PPB stained lung sections of Wistar rats showing accumulation and distribution of iron (blue deposits) in every animal used in this study. Animals were injected with either saline or MNPs at 30 mg/kg, 45 mg/kg, and 60 mg/kg concentrations. Animals were sacrificed 7 days post injection. Tissue was formalin fixed and paraffin embedded. 5µm thick sections were cut with rotary microtome and collected at four levels through the block spaced at least 50 µm apart. Iron was found in the perivascular and peribronchial space. Images were acquired with 10x lens; scale bar represents 200 µm.

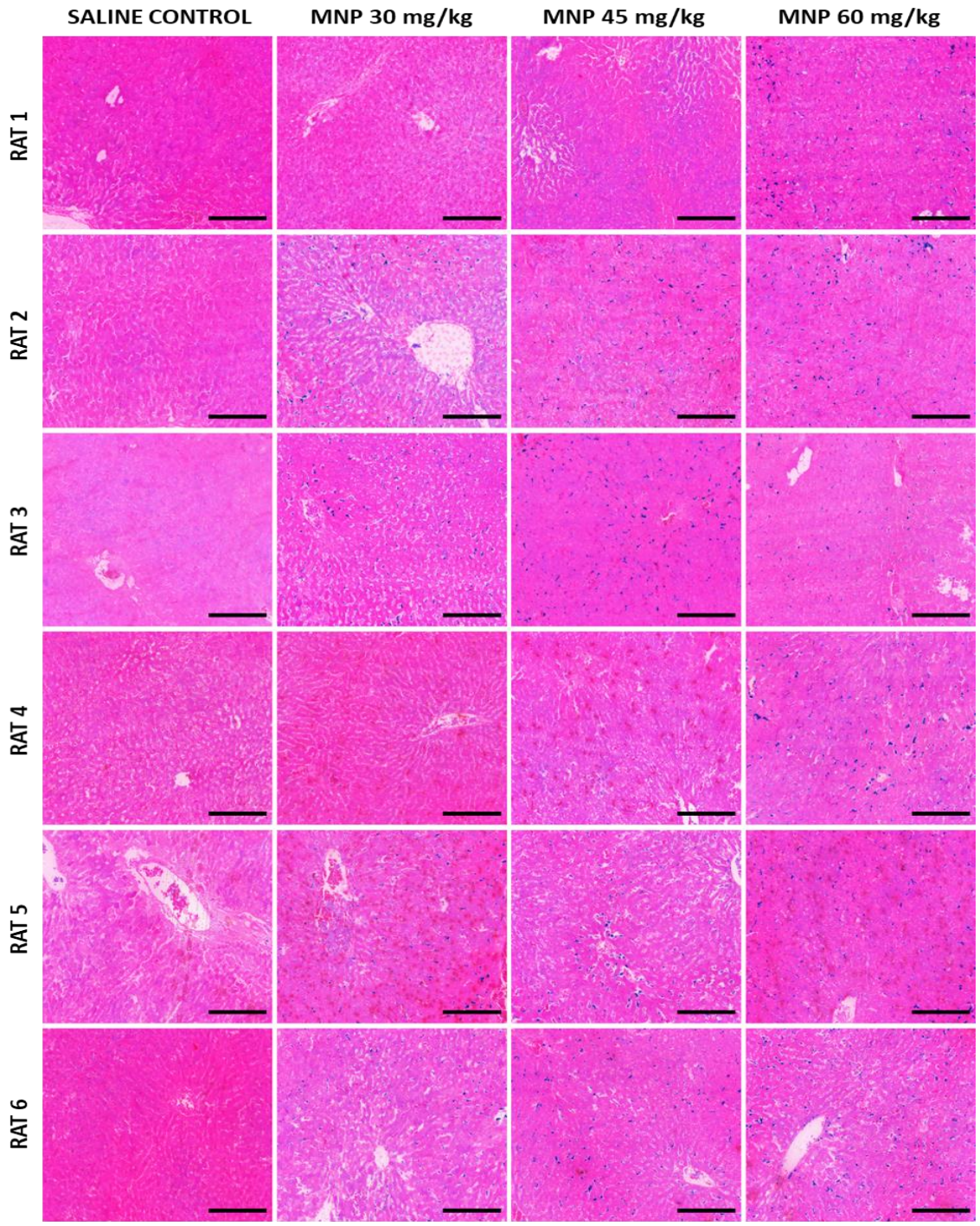

Supplementary figure 8.60: Distribution and accumulation of NOC 0007 MNPs in liver
Representative photomicrographs of PPB stained liver sections of Wistar rats showing accumulation and distribution of iron (blue deposits) in every animal used in this study. Animals were injected with either saline or MNPs at 30 mg/kg, 45 mg/kg, and 60 mg/kg concentrations. Animals were sacrificed 7 days post injection. Tissue was formalin fixed and paraffin embedded. 5µm thick sections were cut with rotary microtome and collected at four levels through the block spaced at least 50 µm apart. Images were acquired with 10x lens; scale bar represents 200 µm.

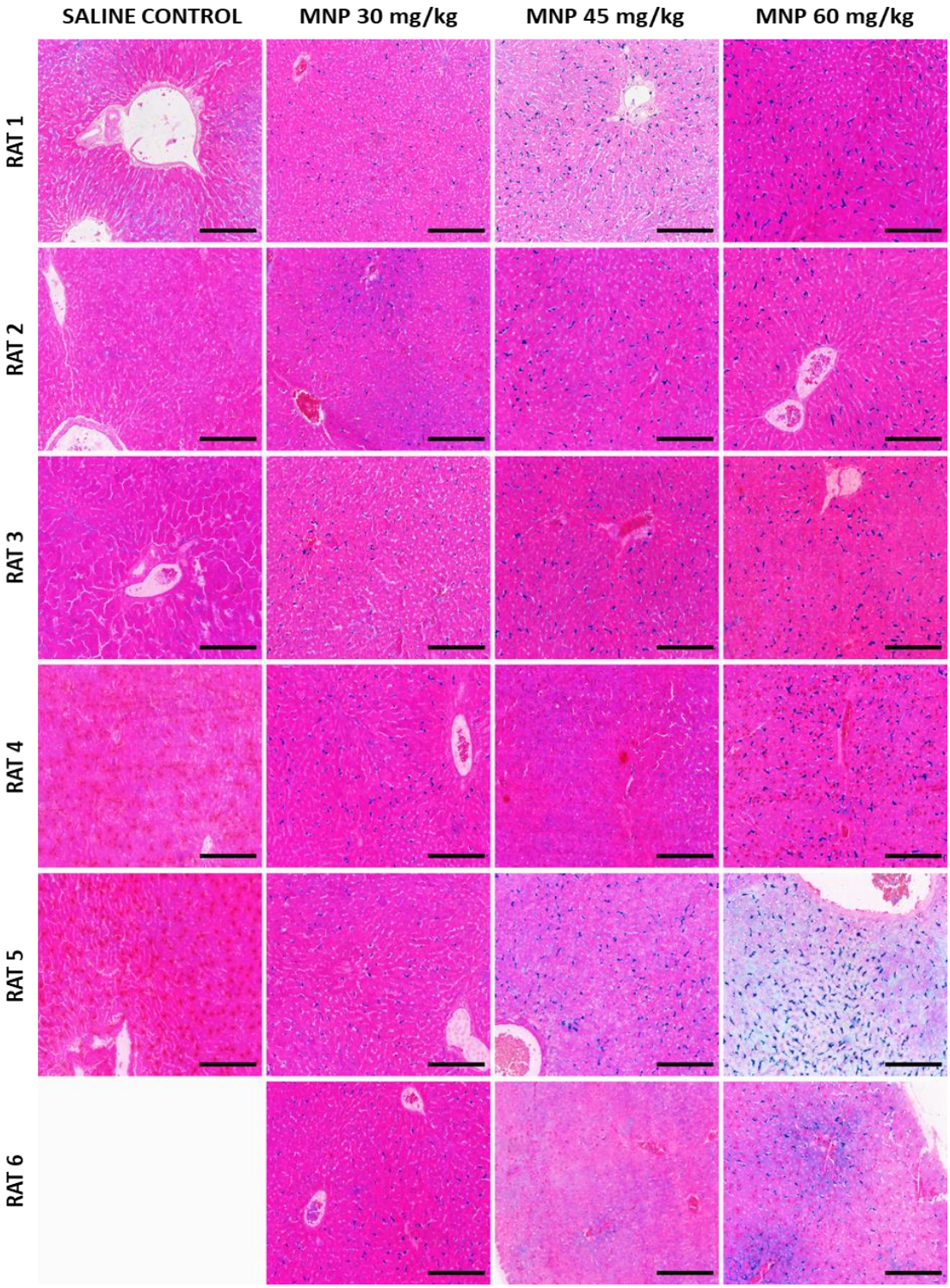

Supplementary figure 8.61: Distribution and accumulation of RCL-01 MNPs in liver
Representative photomicrographs of PPB stained liver sections of Wistar rats showing accumulation and distribution of iron (blue deposits) in every animal used in this study. Animals were injected with either saline or MNPs at 30 mg/kg, 45 mg/kg, and 60 mg/kg concentrations. Animals were sacrificed 7 days post injection. Tissue was formalin fixed and paraffin embedded. 5µm thick sections were cut with rotary microtome and collected at four levels through the block spaced at least 50 µm apart. Iron was predominantly found in the sinusoids within resident Kupffer cells. Images were acquired with 10x lens; scale bar represents 200 µm.

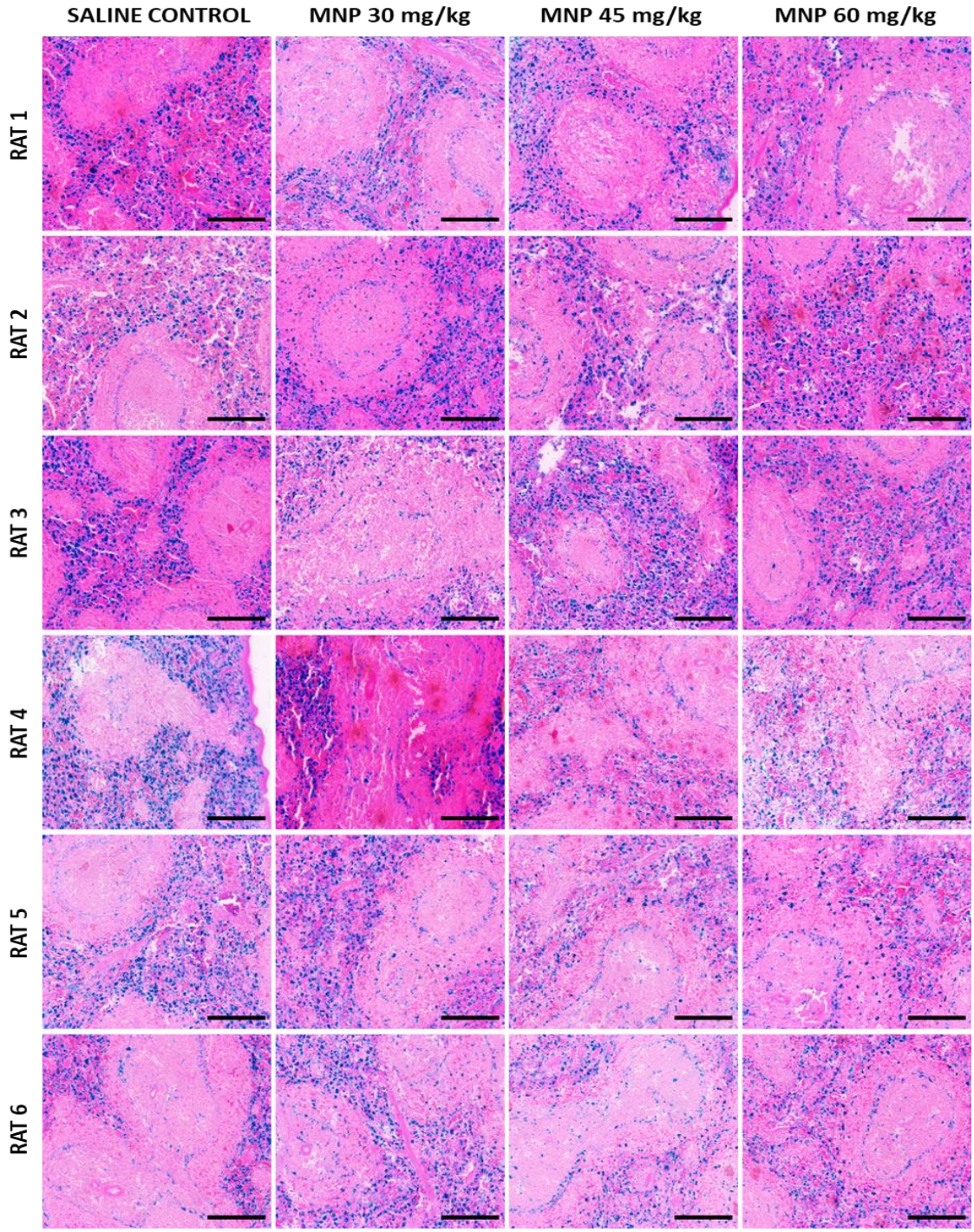

Supplementary figure 8.62: Distribution and accumulation of NOC 0007 MNPs in spleen
Representative photomicrographs of PPB stained spleen sections of Wistar rats showing accumulation and distribution of iron (blue deposits) in every animal used in this study. Animals were injected with either saline or MNPs at 30 mg/kg, 45 mg/kg, and 60 mg/kg concentrations. Animals were sacrificed 7 days post injection. Tissue was formalin fixed and paraffin embedded. 5µm thick sections were cut with rotary microtome and collected at four levels through the block spaced at least 50 µm apart. Iron was detected in all animals regardless of the treatment and was mainly located in the red pulp. Number of iron loaded cells were also seen in the marginal zone of animals injected with MNPs. Images were acquired with 10x lens; scale bar represents 200 µm

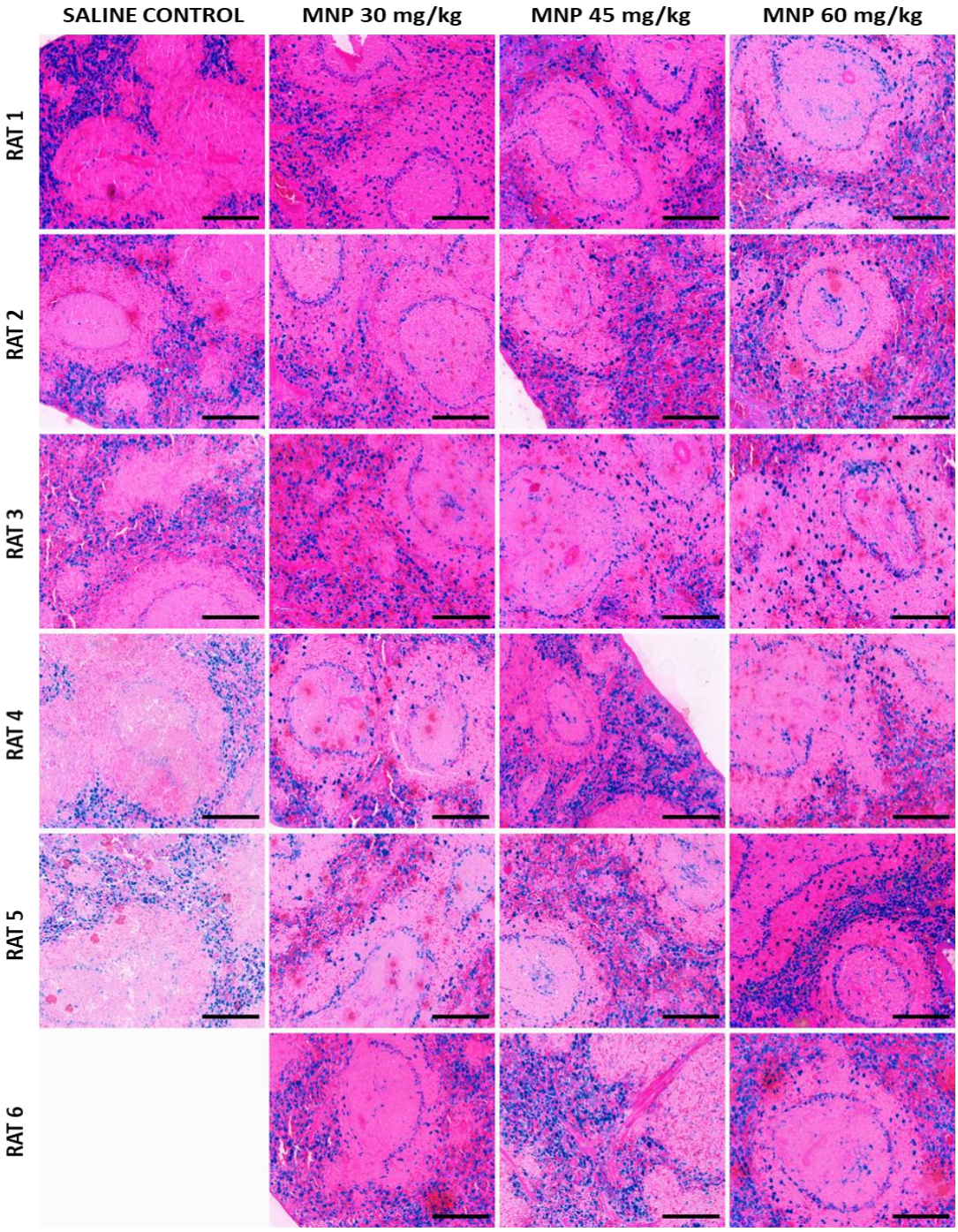

Supplementary figure 8.63: Distribution and accumulation of RCL-01 MNPs in spleen
Representative photomicrographs of PPB stained spleen sections of Wistar rats showing accumulation and distribution of iron (blue deposits) in every animal used in this study. Animals were injected with either saline or MNPs at 30 mg/kg, 45 mg/kg, and 60 mg/kg concentrations. Animals were sacrificed 7 days post injection. Tissue was formalin fixed and paraffin embedded. 5µm thick sections were cut with rotary microtome and collected at four levels through the block spaced at least 50 µm apart. Iron was detected in all animals regardless of the treatment and was mainly located in the red pulp. Number of iron loaded cells were also seen in the marginal zone of animals injected with MNPs. Images were acquired with 10x lens; scale bar represents 200 µm.

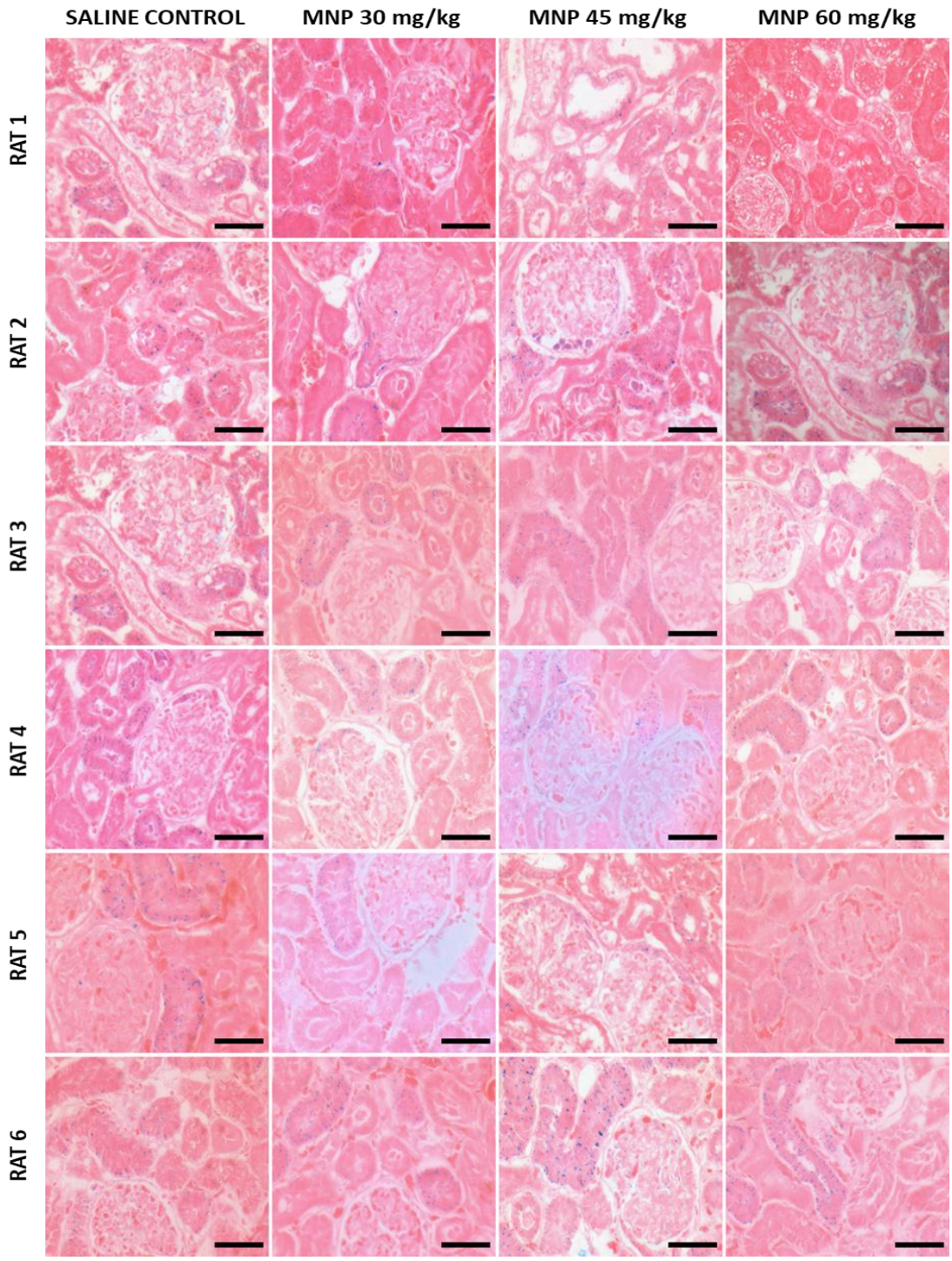

Supplementary figure 8.64: Distribution and accumulation of NOC 0007 MNPs in kidneys
Representative photomicrographs of PPB stained kidney sections of Wistar rats showing accumulation and distribution of iron (blue deposits) in every animal used in this study. Animals were injected with either saline or MNPs at 30 mg/kg, 45 mg/kg, and 60 mg/kg concentrations. Animals were sacrificed 7 days post injection. Tissue was formalin fixed and paraffin embedded. 5µm thick sections were cut with rotary microtome and collected at four levels through the block spaced at least 50 µm apart. Iron was detected in all animals regardless of the treatment and was mainly located in the renal tubules and glomeruli. Images were acquired with 40x lens; scale bar represents 50 µm.

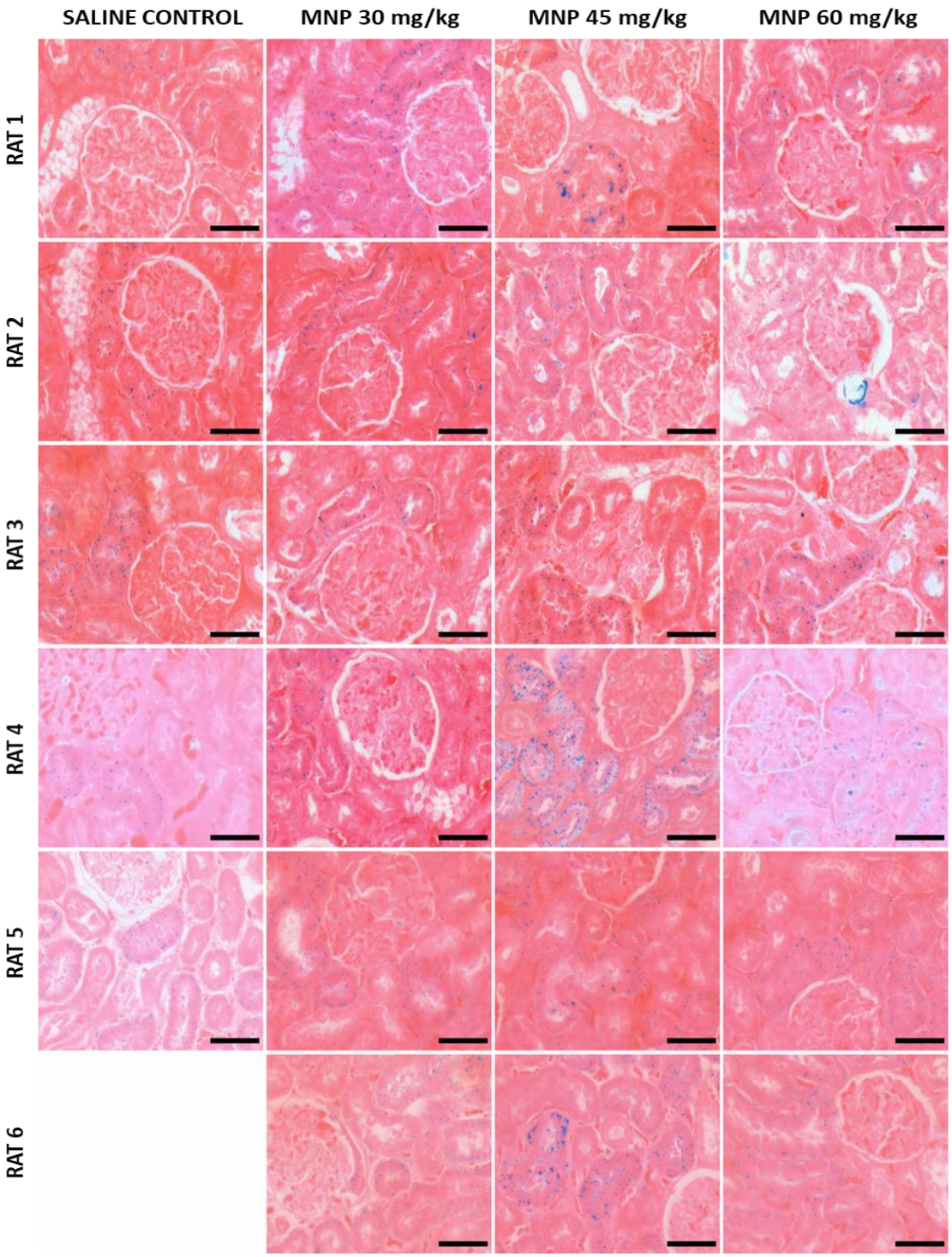

Supplementary figure 8.65: Distribution and accumulation of RCL-01 MNPs in kidneys
Representative photomicrographs of PPB stained kidney sections of Wistar rats showing accumulation and distribution of iron (blue deposits) in every animal used in this study. Animals were injected with either saline or MNPs at 30 mg/kg, 45 mg/kg, and 60 mg/kg concentrations. Animals were sacrificed 7 days post injection. Tissue was formalin fixed and paraffin embedded. 5µm thick sections were cut with rotary microtome and collected at four levels through the block spaced at least 50 µm apart. Iron was detected in all animals regardless of the treatment and was mainly located in the renal tubules and glomeruli. Images were acquired with 40x lens; scale bar represents 50 µm.

8.3.5 *Macro script for image pre-processing*

Representative images from Perl's Prussian blue stained slides were acquired using a 10x lens on an automated microscope LionHeart FX and were subjected to a pre-processing step Fiji software, which was coded in a macro language as detailed below.

```
run("Subtract Background...", "rolling=300 light");
run("Gamma...", "value=1.30");
```

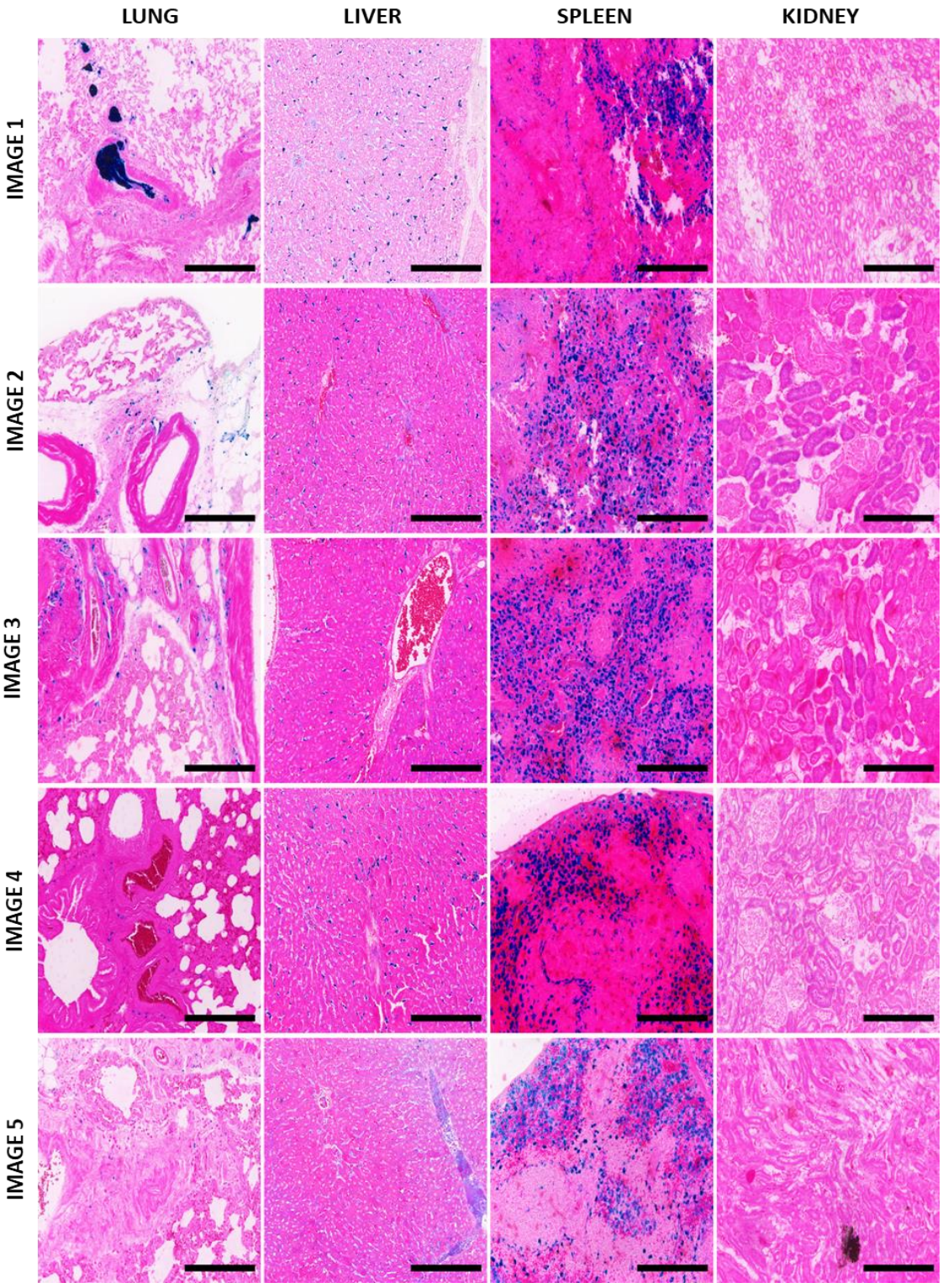

Supplementary figure 8.66: Representative images selected for validating WEKA classifiers
Five images from each organ of interest were selected to account for diversity in obtained data in terms of size of iron deposits, intensity of staining, variation in tissue structure, presence of staining aggregates (bottom right corner). Images were acquired using an automated microscope LionHeartFX with a 10x lens. Scale bar represents 250 µm.